

#### 4.1. Physical Layer: IoT Layer

The physical layer considers the physical infrastructure that a microgrid requires to enable the energy trading feature. The microgrid is composed of three main actors: the prosumer, the consumer, and the microgrid control center (MCC). A prosumer is a consumer who has the capability of generating energy through photovoltaic systems or wind turbines. The energy stored in a battery energy storage system can be used as a power supply to satisfy its own consumption or to sell energy to the rest of the microgrid. Consumers consume the energy provided by the MCC, but they can also employ a BESS to store energy bought from the grid. The MCC manages the energy present in the microgrid. It also provides the power infrastructure for energy flow. This energy is bought or sold by households of the microgrid. Energy can be from decentralized energy resources or from the utility service provider. This will define the operation mode of the microgrid, by island mode or grid-connected mode, respectively.

The physical layer generates plenty of energy-related data, which are required to be stored and/or transmitted to the cloud layer in order to enable several smart grid applications. This challenge is addressed by IoT devices, which enable the collection of the intended energy measurements while also communicating the data to cloud-based services on the internet. The devices in the context of microgrids are smart meters. Smart meters are digital hardware devices that allow the reading of energy consumption from households on a regular basis. Other IoT-related devices are HEMSs, which aggregate energy-related data such as state of charge of BESS, appliance loads consumption, or the main household consumption.

#### 4.2. Virtual Layer: Off-Chain Layer

The virtual layer of the IoT–blockchain architecture for P2P energy trading in a microgrid encompasses both energy data and energy trading transactions generated by the physical layer's IoT devices. This virtual layer is comprised of two sub-layers: the off-chain layer and the blockchain layer. The off-chain layer functions as a mediator between the real-world data captured by the IoT devices and the blockchain layer. The data are stored in cloud-based systems belonging to the HEMS provider and used for various purposes, such as load scheduling, load monitoring, alarm triggers, and forecasting. These features are available through cloud-based services offered by various HEMS providers. In addition, the MCC acts as a microgrid energy manager, collecting energy data from smart meters. This function enables the MCC to manage different processes and services on its own cloud servers. Both HEMSs and MCC cloud services may be self-hosted on-premise or through public cloud platforms such as Amazon Web Services (AWS), Google Cloud Platform (GCP), or Microsoft Azure. As these services manage energy storage data that are not stored on the blockchain, they are considered part of the off-chain layer.

#### 4.3. Virtual Layer: Blockchain Layer

The blockchain layer plays a critical role in enabling secure and transparent energy trading in the microgrid. It provides a decentralized and trusted platform for energy transactions. The use of distributed ledger technology (DLT) ensures that all energy trading transactions are recorded in a tamper-proof and transparent manner. Furthermore, it enables all participants to have access to the same information and reduces the risk of fraudulent or malicious activities. The use of consensus mechanisms, such as PoA, PoW, or PoS, enables the platform to validate and confirm energy trading transactions in a decentralized manner. This ensures that all parties involved in the energy trading platform can trust the outcome of the transaction and reduces the risk of fraud or errors.

### 5. Market Setup

This section provides a description of the market setup process for P2P energy trading in the microgrid. The following are the definitions of main elements, including the P2P market type, market design, price mechanism, types of market participants, market value

proposition, market scale, and market operation. In order to establish a functional and efficient market, these key elements are crucial for P2P energy trading.

- **Market Type:** It is set up as a peer-to-peer, meaning that the participants are able to exchange energy directly among each other without intermediaries. This allows for greater autonomy and more flexibility in energy trading.
- **Market Design:** It is selected as a future market design, which means that the participants trade for future delivery of energy. Such a design allows for greater predictability and flexibility in energy trading.
- **Price Formation Mechanism:** The market price is determined by the intersection of the energy offered by the prosumer and the energy demanded by the consumer. This mechanism ensures efficiency and fairness in the energy trading process.
- **Market Participants:** The participants in the market are defined as prosumers, pure consumers, and the microgrid control center (MCC). The MCC is responsible for the overall operation of the microgrid and acts as a combination of both the market operator and the grid operator. The decentralization of the system through the use of blockchain technology ensures more efficient management of the microgrid.
- **Market Value Proposition:** The commodity traded in the market is energy, and the main benefit of the model is to put prosumers at the forefront of energy production and supply to consumers. This allows for a more sustainable and decentralized energy system.
- **Market Scale:** The market is defined as small-scale, with participants confined to a single microgrid. This allows for more efficient and localized energy trading.
- **Market Operation:** The market operation involves two categories: data related, including state of charge (SoC) data from the battery energy storage system (BESS), energy consumption and generation data from IoT devices, and trade-related, including price and quantity. The settlement and gate closure procedures are defined in detail in a subsequent figure, promoting a transparent and fair energy trading system.

Settlement and gate closure policy is depicted in Figure 7. The energy trading window and the energy trading sequence diagram are defined as part of the market setup. The trading window is composed of four sequential phases which make up the trading process:

1. **Bidding and Offering Period:** This is a 10 min phase in which consumers and prosumers can submit bidding and offer requests, respectively.
2. **Matching Period:** This is a 2 min phase in which the bids and offers are processed to make a match between them.
3. **Energy Transfer Period:** This is a 60 min phase during which energy is transferred from prosumers to consumers.
4. **Settlement Period:** This is a 3 min phase in which the settlement of funds takes place. The settlement period verifies how much consumers should pay to prosumers based on the actual energy received.

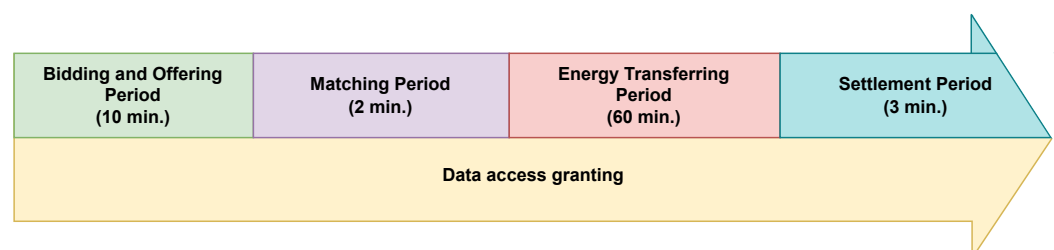
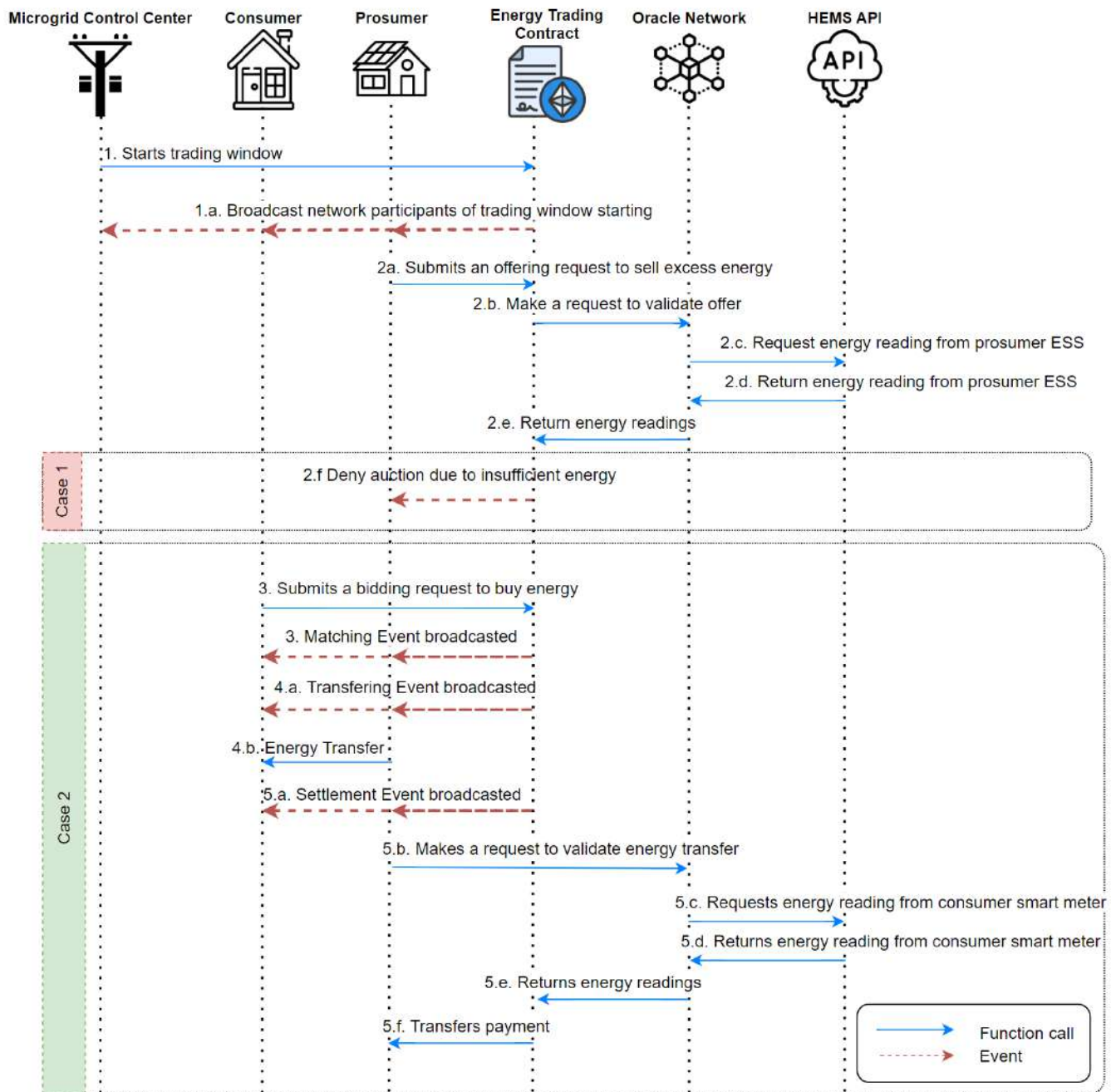


Figure 7. Trading window.

The four phases are modeled in the trading smart contract as valid states that a trading window can take. The transition between the states is executed autonomously by the microgrid control center using the smart contract when the expiration time elapses. Regarding the market operation, Figure 8 presents the interaction in which participants

manage to bid and offer energy. Before any trading operation is executed by the households, every householder has to grant permission to the trading smart contract to request energy data from its data sources, which is depicted as the data access granting phase from the trading window.



**Figure 8.** Test case sequence diagram for energy trading in a microgrid.

1. The MCC starts a new energy trading window, which begins with the bidding and offering phase. This is broadcasted as an event in the blockchain network.
2. The prosumer submits an offer to sell excess energy. The energy trading smart contract validates the offer request by obtaining energy readings from the HEMS through an oracle network. If the prosumer is unable to provide the offered energy, the smart contract emits an event to notify the prosumer that their offer will not be considered, and this is depicted in “Case 1”. This ensures fairness and transparency by preventing

- false offers. If the prosumer has enough energy, the smart contract records the energy offer as valid, and this is depicted in “Case 2”.
3. A consumer submits a bid to buy energy, which is recorded in the record of bids. After 10 min, the smart contract matches available energy offerings with the record of bids, providing a match between prosumers and consumers for energy transfer.
  4. In the energy-transferring phase, which lasts for 60 min, the prosumer becomes the energy provider of the consumer who charges its ESS with the energy provided. A maximum of 10 kWh is set for this phase due to technological restrictions of a common residential system to transfer more than 10 kW over an hour to the battery.
  5. In the settlement phase, the energy trading smart contract obtains energy readings from the consumer smart meter on the HEMS API through an oracle network. If the consumer received less energy than they requested, funds are returned to cover the energy mismatch. The payment is then transferred to the prosumer based on the revenue generated from the sale of energy, which is determined by market demand through the use of bid pricing. The mathematical representation of this process can be represented as  $R = E * B$ , where  $R$  represents the revenue,  $E$  represents the energy received by the consumer, and  $B$  represents the bid price.

## 6. Implementation

The testbed was carried out in the research laboratory B110 at Universidad Tecnica Federico Santa Maria in Valparaiso, Chile. In the laboratory, two Raspberry Pi 4 Model B units were used to represent the prosumer and consumer participants. An all-in-one (AIO) computer was used to set the blockchain-related elements and for the MCC operations. Additional services were implemented in Amazon Web Services (AWS). As seen in Figure 9, the implementation is divided into three main components:

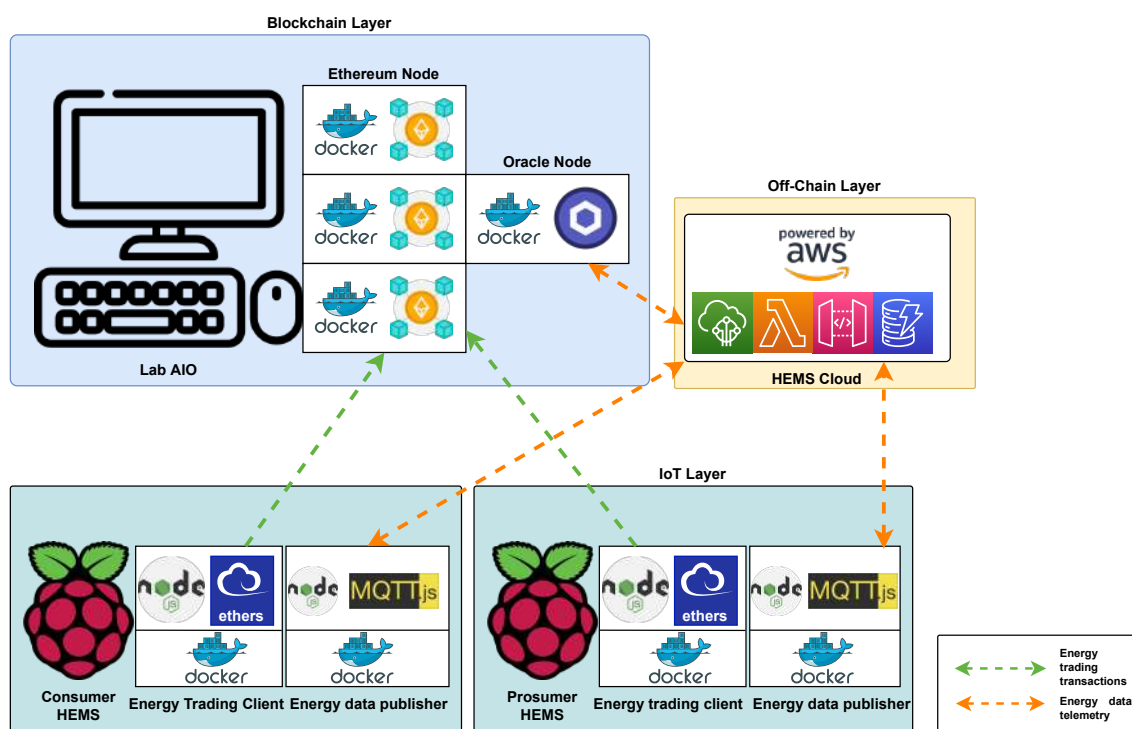


Figure 9. Testbed diagram.

### 6.1. Off-Chain Layer

The off-chain layer of the home energy management system (HEMS) was implemented on the AWS platform. AWS IoT Core was utilized to provide an MQTT broker for messaging between the energy data publisher microservice available in both the consumer and



prosumer HEMS. This broker allows energy consumption and generation data to be sent to the cloud, where it is stored and made available through an API. Energy data for each household can be requested using a unique identifier assigned to each smart meter.

The two HTTP get endpoints implemented are:

- `/battery-soc/id`: This endpoint returns an object with the readings from the last measurement of the state of charge (SoC) of a battery energy storage system (BESS). The readings are randomly generated each hour, and the id represents the identifier of the battery.
- `/smartmeter/id`: This endpoint returns the last hour energy consumption in kWh from a user's smart meter. The id represents the identifier of the smart meter.

The implementation of the off-chain layer allows the collection and storage of energy data from both the consumer and prosumer HEMS. The use of AWS and the energy data publisher microservice ensures the feasibility of the IoT-blockchain energy trading system in microgrids. The source code for this implementation is provided in a GitHub repository. (<https://github.com/pipegreyback/EViG-Server> accessed on 3 November 2022).

## 6.2. Blockchain Layer

The blockchain layer of the IoT-blockchain energy trading system was implemented in a laboratory using an all-in-one (AIO) computer, which featured an AMD Ryzen 7 5300U CPU, 16 GB RAM, and a 1 TB hard drive. The Hyperledger Besu, an open-source Ethereum client, was used to implement a private Ethereum network. To speed up the network setup, Hyperledger Besu Docker quickstart was used, which allowed for the deployment of four validator nodes and three client nodes. The validator nodes were configured to operate using IBFT 2.0 consensus [47], which was chosen due to its high throughput and finality compared to other consensus mechanisms. This is also the consensus mechanism set by default in Hyperledger Besu. This consensus mechanism uses a dynamic mechanism for validator selection and requires at least a 2/3 validator signature in order to confirm a block. In case no consensus is reached, further validation rounds are required until the consensus is reached. Additional tools, such as a block explorer, were also provided to simplify the development process. Finally, to develop smart contracts, Remix, a popular online Solidity compiler, and a debugger were used.

### 6.2.1. Smart Contracts

Four smart contracts were deployed to enable energy trading. Figure 10 shows a summary of each smart contract by category.

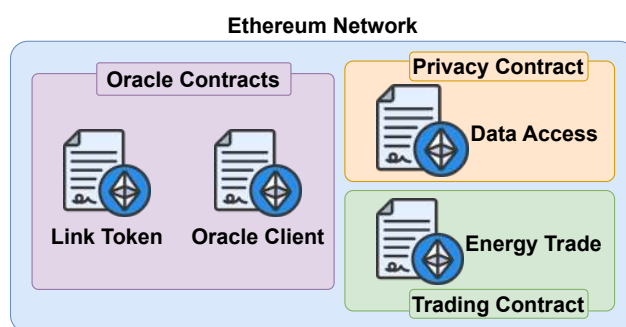


Figure 10. Deployed smart contracts by category.

- In the privacy contract category, the data access contract was implemented to manage an access control list containing entities authorized to request energy data from a user's HEMS. This permission is granted by the user. This smart contract helps ensure that the energy data are only accessible to authorized parties, which helps to protect the privacy and security of the energy data.

- In the trading contract category, the energy trade smart contract was developed, which contains the main business logic of the energy trading system. This smart contract implements a trading window consisting of four states: a bidding and offering state, a matching state, an energy-transferring state, and a settlement state. During the initial phase, the bidding and offering period is initialized when a new trading window is requested in the trading smart contract. Additionally, the trading window allows granting data access at any time, which is required to participate in a trading window. A class diagram is presented in Figure 11, where the solidity structures are presented as classes, that possess attributes and functions.
- In the oracle contracts category, two contracts were developed. The Link Token contract issues the ERC-20 Link Token, which is required to pay for data requests through the oracle network. The oracle client contract is used to request energy data using the HEMS APIs, and this request is handled by the oracle network, which processes the request and provides a callback with the results of the request. Both the Link Token contract and the oracle client contract can be found in the Chainlink official repository (<https://github.com/smartcontractkit/chainlink/tree/develop/contracts/src> accessed on 3 November 2022).

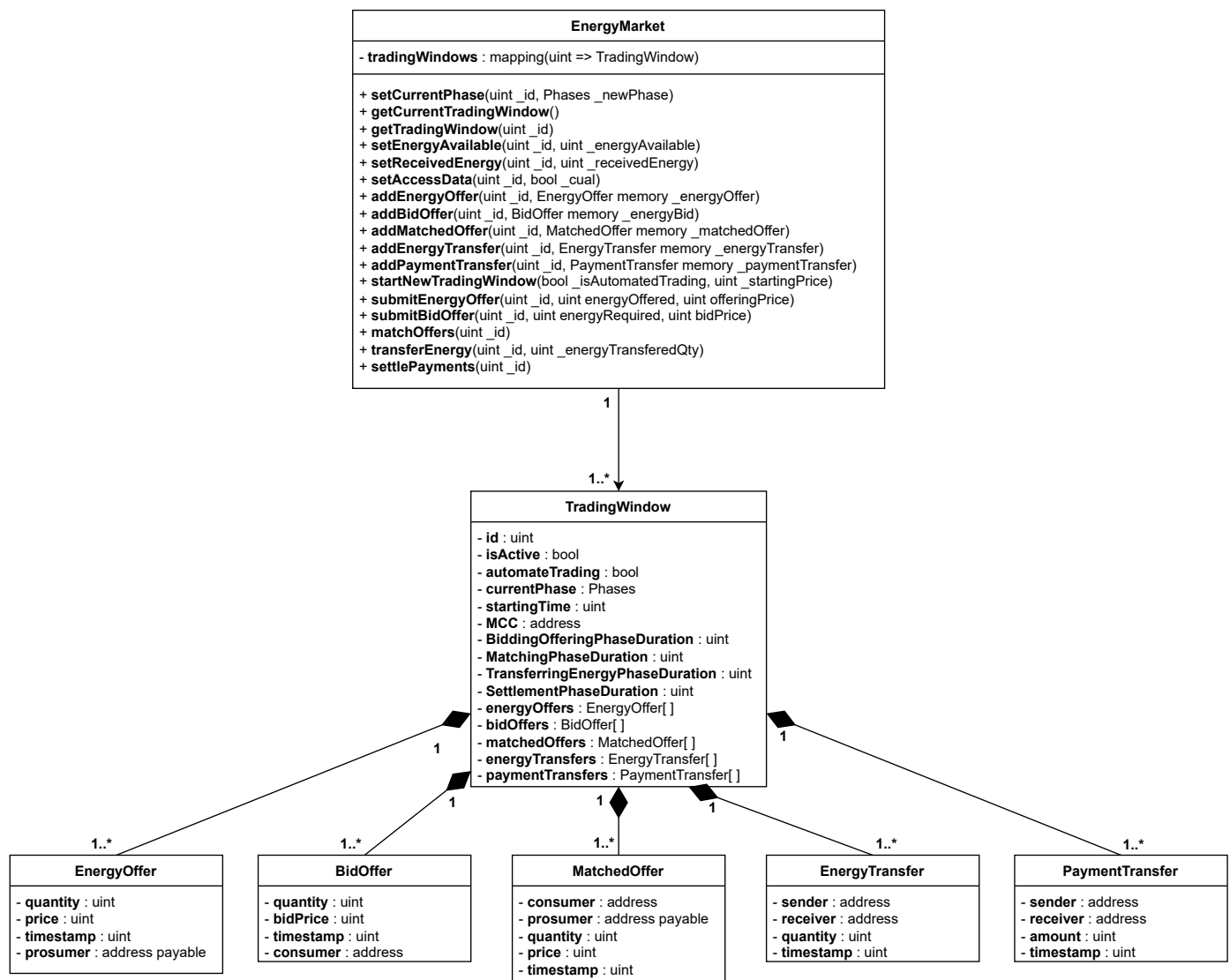
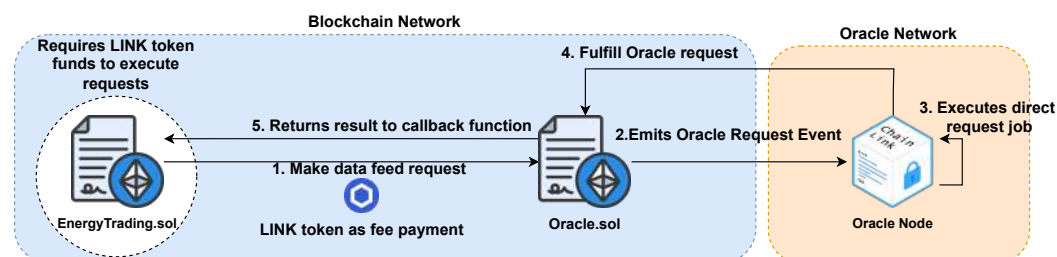


Figure 11. Class diagram of energy trading contract.

### 6.2.2. oracle Nodes

In order to enable smart contracts to utilize the available API, the deployment of a Chainlink oracle network using docker containers was necessary. Additionally, a PostgreSQL database was deployed using docker containers to support the Chainlink oracle network. Configuration between the Ethereum network and the Chainlink oracle node was established to facilitate interaction between smart contracts and the oracle within the Ethereum network. The primary parameters utilized for communication between the two networks include the RPC URL and the chainId. Figure 12 shows the interaction diagram for the data feed request between smart contracts and oracle nodes.



**Figure 12.** oracle smart contract deployment and invocation diagram.

In order to access the endpoints provided by the HEMS API, it is necessary to create and deploy a job within the oracle node. A job comprises a sequence of steps, called tasks, that fulfill the data feed requirement of a smart contract. In this specific case, a direct request job was created. This job involved requesting data from the HEMS API, parsing the response, encoding the data into a format compatible with Solidity, and ultimately submitting the transaction back to the requesting smart contract. Figure A1 shows the direct request job configured.

### 6.3. IoT Layer

For the IoT layer, the two Raspberry Pi units were used. Docker was employed to run containers of the services required to enable the energy data client and the energy trading client.

#### 6.3.1. Energy Data Client

The implementation of the IoT layer was done using the AWS platform and the energy data publisher microservice was developed using Node.js and MQTT.js. This microservice sends energy data to the HEMS cloud service using MQTT, allowing the collection and storage of energy data from each household. The microservice was packaged into a docker container for easy deployment and running on any operating system that supports docker containers.

#### 6.3.2. Energy Trading Client

Both the consumer and the prosumer were configured with an energy trading client, which allows for submitting bids and offers to the blockchain to participate in the energy trading within the microgrid. The energy trading client was developed using Node.js and the ethers.js library, which is an Ethereum client that allows the execution of operations within a blockchain network. The energy trading client was also packaged into a docker container for ease of deployment. The trading client subscribes to the four events that the smart contract emits to the blockchain network. The event subscription and execution of smart contract functions are managed by ethers.js. Table 2 describes the operations that any participant in the microgrid can execute within the energy trading smart contract. The client source code is provided in the repository, and it considers three possible configurations: consumer, prosumer, and MCC.

**Table 2.** Available operations for the energy trading smart contract.

Operation	Description
Constructor	Initialize the contract's state variables when the smart contract is deployed.
Phase Transition	Update the current phase of the trading process based on a predetermined timeline or other criteria.
Start Trading Window	Mark the beginning of the trading phase and set the initial trading parameters, such as the duration of the trading window and the maximum amount of energy that can be traded.
Submit Energy Offer	Allow sellers to submit offers to sell their energy at a certain price and quantity. These offers are stored in the contract's state variables until they are matched with a corresponding bid.
Submit Energy Bid	Allow buyers to submit bids to buy energy at a certain price and quantity. These bids are stored in the contract's state variables until they are matched with a corresponding offer.
Matching Phase	Match the submitted offers and bids based on their price and quantity, and assign the matched pairs to a transfer list for the transferring phase.
Transferring Phase	Transfer the energy between the matched parties based on the agreed-upon price and quantity. This phase ensures that the energy is delivered securely and efficiently.
Settlement Phase	Transfer the payment between the matched parties based on the agreed-upon price and quantity, and update the state variables to reflect the completed trade. This phase ensures that the payment is made accurately and securely.

#### 6.4. Use Case and Validation

The testbed consists of one prosumer, one consumer, and a microgrid control center. We assumed that a prosumer owns a PV system and BESS, which will offer excess energy, the consumer with BESS will bid to fulfill his energy consumption requirements, and the microgrid control center will provide the power infrastructure for all households in the microgrid. The smart contract for energy trading was deployed by the lab all-in-one (AIO) computer acting as the MCC. Both the prosumer and consumer grant data access permission to the energy trading smart contract for making energy requests to the HEMS API. Figure A2 shows the event log where the prosumer executes the grant data access function passing the energy trading smart contract address and the smart meter id as the parameters in the invocation.

The energy trading window starts with an energy price of 60,000 gwei per kWh, which was set by the microgrid control center (MCC). This price is equivalent to around CLP 102 per kWh, which is the rate provided by energy utility Chilquinta in Chile (<https://www.chilquinta.cl/informacion-de-interes/tarifas-vigentes> accessed on 3 November 2022) for the cost of energy per kWh, and the cost of transmission per kWh, for the BT1A tariff. The trading window has now entered the offering and bidding phase, allowing consumers and prosumers to submit their offers to sell or bids to buy energy at the specified price. The energy starting window event is broadcasted to all participants in the trading system, enabling them to react to the event on the clients by event subscription and execute their own state machines. This enhances the overall efficiency and transparency of the trading process, allowing participants to respond quickly and accurately to changes in the trading window and the energy price. The log message shown in Figure A3 confirms the current phase of the trading window and the energy price broadcasted in the event. This information is essential for understanding the initial pricing conditions and the current state of the energy trading system.

Later, a prosumer submits an offer to sell 10 kWh. This offer request triggers the oracle smart contract for making a request to the HEMS API for checking the prosumer available

energy. The event of an energy offering being denied due to insufficient energy is illustrated in Figure A4. An event with an error message indicating the reason for the denial, and in this case, “insufficient energy” is provided. In the event that a participant has not granted the energy trading smart contract the required permission to access the energy data, an error is returned by the contract validations, as seen in Figure A5.

In the case of valid energy offers and energy bids, when the matching phase finishes, a result event is broadcasted to the matched participants, as seen in Figure A6. This event indicates that the energy trading smart contract has reached the matching state, where a consumer and prosumer have agreed on a trade for 10 units of energy at a price of 54,000 gwei per unit. The smart contract has successfully matched the consumer’s energy demand with the prosumer’s energy supply at the agreed price, and the settlement phase can proceed.

Regarding the received energy by the consumer, Figure A7 shows the log from the oracle request. This log was emitted by the energy trading smart contract during the energy-transferring phase, indicating that the consumer received 8 kWh of energy from the prosumer, as measured by the smart meter. It is important to note that the energy data are managed by the Chainlink oracle, and the energy trading smart contract interacts with the oracle contracts to retrieve the data. The discrepancy between the initially agreed 10 kWh, and the 8 kWh received by the consumer may be due to a delay in the initial transfer from the prosumer, or external factors such as network congestion or power outages. However, the flexibility provided by the smart contract allows for mismatches between agreed energy and received energy to be addressed during the settlement phase.

The settlement phase, which follows the energy-transferring phase, is responsible for determining the proportional payment to be made to the prosumer based on the amount of energy received by the consumer. Figure A8 shows an example of the proportional payment calculation for the scenario where the consumer received 8 kWh of energy, which was less than the initially agreed 10 kWh. The implementation of the energy trading smart contract provides a degree of flexibility by allowing for adjustments to be made during the settlement phase in case of mismatches between agreed and received energy.

### 6.5. Cost Analysis Results

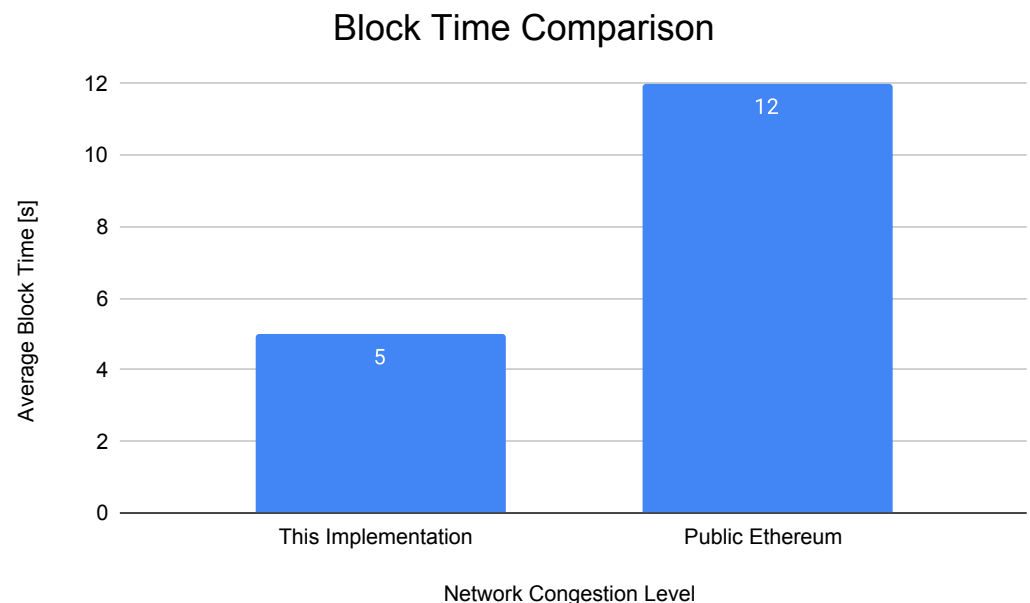
Table 3 shows a cost comparison of different energy trading smart contract operations performed in our energy trading platform and in various speed-based configurations on the public Ethereum network. As our implementation uses a private Ethereum network, there were no transaction fees incurred during contract deployment or execution. Therefore, the gas values listed in the table represent the resources used to perform the operations. In comparison, public Ethereum networks charge transaction fees for contract execution, and gas prices can vary based on the user’s preference for transaction speed. This is because the public Ethereum network tends to become congested, where validators prioritize transactions with a higher gas price to process and receive a reward. As a result, users may choose to pay a higher gas price to increase the chances of their transaction being processed sooner. The public Ethereum network offers suggested gas prices for different transaction speeds, namely slow, average, or fast. For the public Ethereum network, each transaction speed has a corresponding gas price, which on the date of this study were 20 gwei, 22 gwei, and 24 gwei. To simplify the comparison, the transaction costs in the table are presented in Chilean pesos (CLP) using the conversion rate from ETH to CLP on 10 April 2023.

Block time in the Ethereum network is dynamic and reflects the network congestion and performance. In the case of Hyperledger Besu, the block time is a critical parameter that determines the block frequency. This time has a direct impact on both throughput and latency. If the block time is very short (e.g., 1 s), blocks will be generated frequently, which results in low latency and high throughput. However, in the case of a block period being very long, the performance will be reduced because the transactions will need to wait a long time to be added to the next block [48].

**Table 3.** Cost comparison of different energy trading smart contract operations based on the network execution.

Contract Operation	Gas Utilization	Cost in CLP in Our System	Cost in CLP in Slow Public Ethereum	Cost in CLP in Average Public Ethereum	Cost in CLP in Fast Public Ethereum
Constructor Phase	2,619,703	\$0	\$81.010	\$89.112	\$97.213
Transition	161,524	\$0	\$4.995	\$5.494	\$5.994
Start Trading Window	286,403	\$0	\$8.857	\$9.742	\$10.628
Submit Energy Offer	129,613	\$0	\$4.008	\$4.409	\$4.810
Submit Energy Bid	130,354	\$0	\$4.031	\$4.434	\$4.837
Matching Phase	153,400	\$0	\$4.744	\$5.218	\$5.692
Transferring Phase	134,179	\$0	\$4.149	\$4.564	\$4.979
Settlement Phase	144,247	\$0	\$4.461	\$4.907	\$5.353

In our implementation of the energy trading smart contract, the created Ethereum network provided a 5 s validation block time. In comparison, the last average block time of the public Ethereum network is around 12 s (<https://etherscan.io/chart/blocktime> accessed on 10 January 2023), as shown in Figure 13. The difference in block times could be due to various factors, such as network congestion or the consensus mechanism used by the network. Understanding the impact of block time on the energy trading smart contract's performance, throughput, and gas usage is critical for future optimizations and improvements.

**Figure 13.** Block time comparison between EnergyAuction network and public Ethereum.

The maximum block size in gas units for a regular block in our implementation and in public Ethereum networks is 30 million gas units. Figure 14 shows a bar chart where the eight operations of the energy trading smart contract are presented in terms of the percentage of block usage. The constructor is the most gas-consuming operation and



utilizes 8.73% of the available gas in a block. The remaining operations present lower gas consumption, between 0.43% and 0.95% of gas usage for the available gas in a block. An analysis of the gas usage for the energy trading smart contract revealed that no more than 12 constructors or 200 trading operations could be performed within a single block. This indicates that the platform may face limitations in terms of scalability and network congestion with an increasing number of participants. However, given the 5 s block time of the private Ethereum network used in this work, and the number of participants for the use case validation scenario, this limitation was not explored in detail. Future research could investigate ways to optimize the gas usage of the smart contract or explore alternative solutions to address scalability and congestion issues.

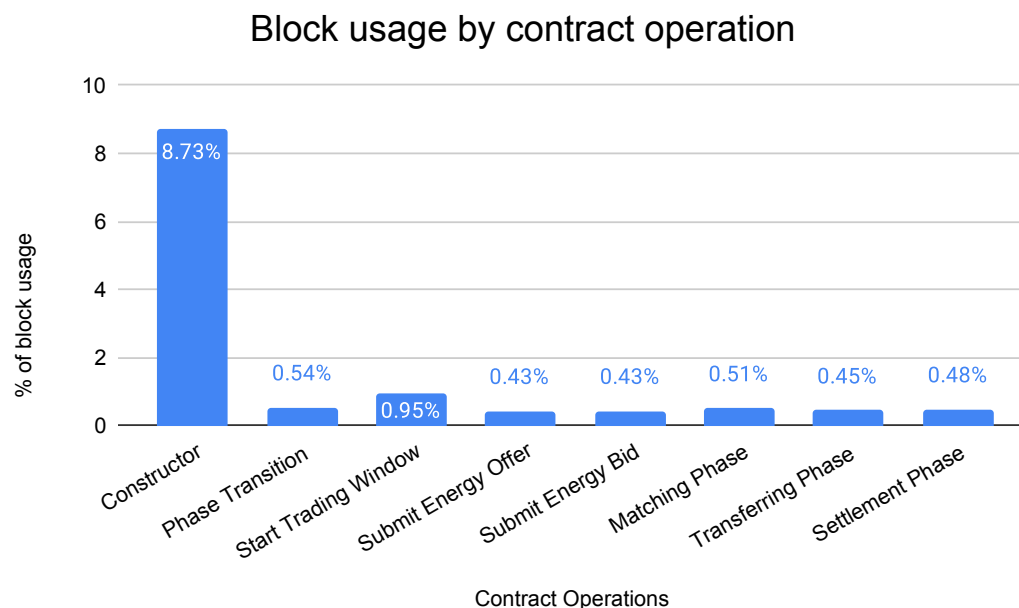


**Figure 14.** Percentage of block usage per smart contract operation.

## 7. Discussion and Limitations

The implemented energy trading platform successfully demonstrates the feasibility of a permissioned blockchain network for energy trading. The platform was designed to support energy trading between prosumers and consumers, with the support of an MCC. While the use of an access control list in conjunction with oracles allows the energy trading smart contract to access energy information, the relationship is established between the consumer or prosumer and the contract, instead of using IoT devices as a separate entity in the interaction. Recent developments in the field propose the use of Non-Fungible Tokens (NFTs) as a digital representation or “digital twin” of IoT devices. These tokens, standardized by Ethereum under the ERC-721 and ERC-1155 interfaces, enable the establishment of ownership relationships between the householder, consumer, or prosumer and their energy data-collecting devices. This feature includes the data access functionality, which can simplify the addition of further implementations, such as the one presented here.

In terms of cost analysis, the results indicate that a private implementation of the energy trading platform is more cost-effective than implementing the same business logic in the public Ethereum network. This is mainly due to the public network’s high transactional fee and longer validation block times, caused by network congestion and a different consensus mechanism. Therefore, it is recommended to implement such platforms in private Ethereum networks or shared private networks, such as consortiums involving multiple entities related to smart grid applications. If by any means there is a requirement to deploy such a platform in a public network, it is recommended to make a prospection into layer two (L2) solutions, which present lower transactional fees and faster validation block time.

The privacy of the energy trading system is achieved through the use of a permissioned blockchain network, which restricts access to only authorized nodes. However, it is important to note that while the access control list and the oracles provide privacy for off-chain data access, the transactions that occur within the energy trading smart contract are still recorded on the blockchain. This includes the funds transferred between parties during the settlement phase and the readings from the off-chain data that are accessed via the oracles. Therefore, further research is needed to ensure the privacy of on-chain transactions in the energy trading system. For example, a technology that could be used to enhance the privacy and security of energy trading platforms is the zero-knowledge proof (Zk-proofs). Zk-proofs enable the verification of data without revealing the data itself. This could be useful in scenarios where the privacy of the energy trading data is of utmost importance, such as trading between competitors or sensitive business transactions.

The analysis of the gas usage of the smart contract revealed that the constructor had an average gas usage of 9%, while the average gas usage for each function call was 0.5%. Although the implementation was successful in supporting the energy trading use case, the gas usage results suggest that there is room for improvement in the smart contract design. Future work could explore the use of more advanced smart contract technologies, such as verifiable computing (VC) or zero-knowledge proof (ZKP), to optimize gas usage and enable the implementation of more complex business logic.

In this work, the old transactions are still kept on the blockchain. However, the concept of offloading can be applied, but a different approach is needed regarding the blockchain network configuration, IoT data, transactions executed by devices, and energy trading participants. For example, in [49], the authors introduced using different types of nodes including full nodes, semi-full nodes, and light nodes, while in [50], the authors developed a hierarchical blockchain storage structure for industrial IoT architectures.

Regarding the law and regulations, in Chile, the current regulation allows prosumers with PV systems to only inject surplus energy to the power grid; however, consumers and prosumers are not allowed to conduct direct energy trading with one another. To enable such opportunities, new regulations should be developed that will bring benefits not only to utility companies but also all participants, including prosumers, consumers, and utilities.

## 8. Conclusions

This paper presents the development and deployment of a microgrid-based local peer-to-peer energy trading system in a laboratory environment. It thoroughly examined and discussed the conceptual architecture of a distributed peer-to-peer network. To establish a blockchain-based system in a test environment, a Chainlink oracle and a private Ethereum blockchain network were employed as foundational components. The research focused on exploring the capabilities of oracles as intermediaries between off-chain data sources, such as smart meter energy readings, and the business logic implemented within smart contracts, which typically lack the ability to directly request off-chain data. Overall, this work highlights the potential of IoT and blockchain technologies to enable sustainable and efficient energy management practices. Despite the promising results, the proposed platform has some limitations and challenges that require further research and development. The following are the main directions to extend the current work:

- To support a large number of participants, there is a need to optimize the platform performance and scalability. This includes optimizing the smart contract code, data storage, and processing algorithms.
- To support real-time energy trading, different business models and trading schemes should be developed where participants trade energy in real time based on the current market conditions.
- Cybersecurity and privacy are important factors to be considered. This includes the data exchange among different participants as well as the sensors, smart meters, and networking infrastructure.

**Author Contributions:** Conceptualization, M.A.A., J.M.M. and F.C.; methodology, M.A.A., J.M.M., F.C., P.F., A.M.E. and Y.-C.K.; software, F.C.; validation, M.A.A., J.M.M. and F.C.; formal analysis, M.A.A., J.M.M., F.C., P.F., A.M.E. and Y.-C.K.; investigation, M.A.A., J.M.M., F.C., P.F., A.M.E. and Y.-C.K.; writing—original draft preparation, F.C. and M.A.A.; writing—review and editing, M.A.A., J.M.M., F.C., P.F., A.M.E. and Y.-C.K.; funding acquisition, M.A.A. and Y.-C.K. All authors have read and agreed to the published version of the manuscript.

**Funding:** This work was supported in part by the Agencia Nacional de Investigación y Desarrollo (ANID) through the Proyecto Fondecyt de Iniciación en Investigación 2020 under Project ID11200178, DGIIP-UTFSM Chile, and in part by the National Research Foundation of Korea (NSF) Grant through the Korean Government under Grant (2021R1I1A305872911).

**Institutional Review Board Statement:** Not applicable.

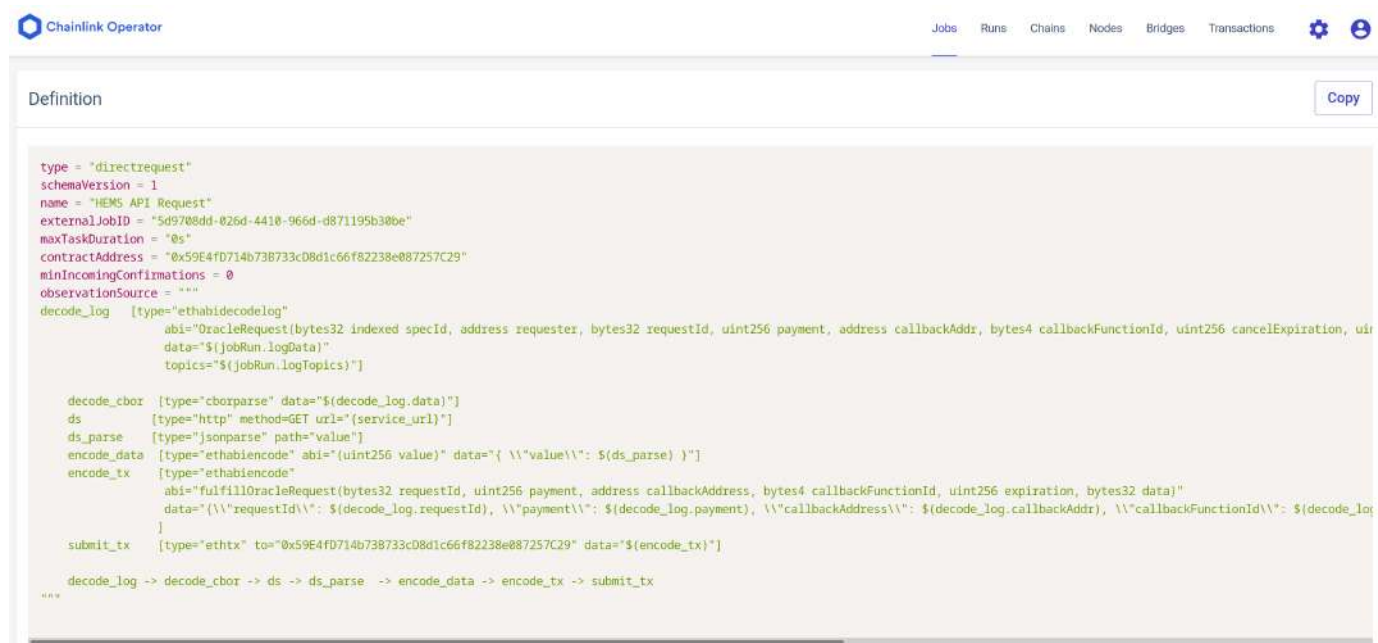
**Informed Consent Statement:** Not applicable.

**Data Availability Statement:** Not applicable.

**Acknowledgments:** The authors would like to acknowledge Proyecto Fondecyt de Iniciación en Investigación 2020 under Project ID11200178, DGIIP-UTFSM Chile, and National Research Foundation of Korea (NSF) Grant through the Korean Government under Grant (2021R1I1A305872911).

**Conflicts of Interest:** The authors declare no conflict of interest.

## Appendix A



```

type = "directrequest"
schemaVersion = 1
name = "HEMS API Request"
externalJobID = "5d9708dd-026d-4410-966d-d871195b30be"
maxTaskDuration = "0s"
contractAddress = "0x59E4fD714b738733cD8d1c66f82238e087257C29"
minIncomingConfirmations = 0
observationSource = ""

decode_log [type="ethabiencode"
  abi="OracleRequest(bytes32 indexed specId, address requester, bytes32 requestId, uint256 payment, address callbackAddr, bytes4 callbackFunctionId, uint256 cancelExpiration, uint256 dataVersion, bytes data)"
  data="{jobRun.logData}"
  topics="{jobRun.logTopics}"]

decode_cbor [type="cborparse" data="{decode_log.data}"]
ds [type="http" method=GET url="{service_url}"]
ds_parse [type="jsonparse" path="value"]
encode_data [type="ethabiencode" abi="(uint256 value)" data="{ \"value\": \"{ds_parse}\" }"]
encode_tx [type="ethabiencode"
  abi="fulfillOracleRequest(bytes32 requestId, uint256 payment, address callbackAddress, bytes4 callbackFunctionId, uint256 expiration, bytes32 data)"
  data="{ \"requestId\": \"{decode_log.requestId}\", \"payment\": \"{decode_log.payment}\", \"callbackAddress\": \"{decode_log.callbackAddr}\", \"callbackFunctionId\": \"{decode_log.callbackFunctionId}\" }"]
submit_tx [type="ethtx" to="0x59E4fD714b738733cD8d1c66f82238e087257C29" data="{encode_tx}"]

decode_log -> decode_cbor -> ds -> ds_parse -> encode_data -> encode_tx -> submit_tx

```

**Figure A1.** Job definition in the oracle node operator.

```
[
  {
    "from": "0x9209a142C1DFa4C746B19c4bf3e91BbC96737dC7",
    "topic": "0xb4c6779ceb4a20f448e76a0e11f39bd183cff9c9dbac53df6bfcc202e2eb32f1",
    "event": "AccessGranted",
    "args": {
      "0": "0x1e553735F5DA2B5A68bB37F90fbFb9551c229c8B",
      "1": "2474156",
      "_contract": "0x1e553735F5DA2B5A68bB37F90fbFb9551c229c8B",
      "_id": "2474156"
    }
  }
]
```

Figure A2. Log message from granting permission operation.

```
[
  {
    "from": "0x46cb39166e52d7Ea8077CAa6a764C5507e813FA6",
    "topic": "0x9569a998635142ff1e15cd543af337ca0d78b279ed2ffdecf5568e75625d121f",
    "event": "phaseTransition",
    "args": {
      "0": 0,
      "1": 0,
      "2": "This trading window is transitioning to the bidding and offering phase",
      "currentPhase": 0,
      "newPhase": 0,
      "message": "This trading window is transitioning to the bidding and offering phase"
    }
  },
  {
    "from": "0x46cb39166e52d7Ea8077CAa6a764C5507e813FA6",
    "topic": "0x8c2c6508c93167c2281369e462ef650683fa9108d9c74d5b84649b00520162ef",
    "event": "BiddingStarting",
    "args": {
      "0": "60000",
      "1": "Bidding/Offering",
      "price": "60000",
      "message": "Bidding/Offering"
    }
  }
]
```

Figure A3. Log message from a new energy trading window initialization.

```
[
  {
    "from": "0xf9565D6c300882b79800C8Ab16Fb9189Fe518Af7",
    "topic": "0xe13f19f70b29c7eaa932e468eb44464bcba87a95c33cf47888b63d1983b5893",
    "event": "OfferDenied",
    "args": {
      "0": "0x9625900fa6E5418B327E05997F546CAac473BB16",
      "1": "15",
      "2": "Insufficient energy",
      "prosumer": "0x9625900fa6E5418B327E05997F546CAac473BB16",
      "energyOffered": "15",
      "reason": "Insufficient energy"
    }
  }
]
```

Figure A4. Error log when prosumer is offering more energy than available.

```
[
  {
    "from": "0xEB231F11704c3d6e7E7969eE2dc0Ff80ef46697C",
    "topic": "0x903e4d60b59021f14ee487f61a98a583f3a2762ddcd38603816527688de4db",
    "event": "noPermission",
    "args": {
      "0": "0xEB231F11704c3d6e7E7969eE2dc0Ff80ef46697C",
      "1": "This contract does not have permission to access the smart meter data.",
      "contract": "0xEB231F11704c3d6e7E7969eE2dc0Ff80ef46697C",
      "message": "This contract does not have permission to access the smart meter data."
    }
  }
]
```

**Figure A5.** Error log when the energy trading smart contract does not have permission to request energy data from smart meters.

```
[
  {
    "from": "0x46cb39166e52d7Ea8077CAa6a764C5507e813FA6",
    "topic": "0x62830dd5377daa0dd3d791f401e84cbc08818150be0d78afd850cbf3db239afe",
    "event": "MatchingState",
    "args": {
      "0": "0xD8229d99515faB9159A9b33BA4d868eDeD92Dadc",
      "1": "0xb45CFB124677b22553e88b2B6189bD1055aC7bE7",
      "2": "10",
      "3": "54000",
      "consumer": "0xD8229d99515faB9159A9b33BA4d868eDeD92Dadc",
      "prosumer": "0xb45CFB124677b22553e88b2B6189bD1055aC7bE7",
      "quantity": "10",
      "price": "54000"
    }
  }
]
```

**Figure A6.** Log from the results of the matching phase.

```
[
  {
    "from": "0x46cb39166e52d7Ea8077CAa6a764C5507e813FA6",
    "topic": "0xb496c71060c8c1de109c75b6a2dacb7d8a9d1cbc9b6f573913b811cf37a0701e",
    "event": "EnergyRecieved",
    "args": {
      "0": "0xb496c71060c8c1de109c75b6a2dacb7d8a9d1cb",
      "1": "0x46cb39166e52d7Ea8077CAa6a764C5507e813FA6",
      "2": "8",
      "oracleAggregator": "0xb496c71060c8c1de109c75b6a2dacb7d8a9d1cb",
      "energyTradingContract": "0x46cb39166e52d7Ea8077CAa6a764C5507e813FA6",
      "energyReceived": "8"
    }
  }
]
```

**Figure A7.** Log from the oracle request for obtaining the received energy by the smart meter of the consumer.



```
[
  {
    "from": "0x46cb39166e52d7Ea8077CAa6a764C5507e813FA6",
    "topic": "0x7bdd298fee8520ef5fb09d30ad01cd090f764b284bf6ee61c6fa184132705f6b",
    "event": "SettlementState",
    "args": {
      "0": "0xb45CFB124677b22553e88b2B6189bD1055aC7bE7",
      "1": "0x46cb39166e52d7Ea8077CAa6a764C5507e813FA6",
      "2": "432000000000000",
      "prosumer": "0xb45CFB124677b22553e88b2B6189bD1055aC7bE7",
      "lockedFundsContract": "0x46cb39166e52d7Ea8077CAa6a764C5507e813FA6",
      "payment": "432000000000000"
    }
  }
]
```

**Figure A8.** Log from the settlement phase, where the prosumer is paid proportionally to what we provided.

## References

- Bouhafs, F.; Mackay, M.; Merabti, M. Links to the Future: Communication Requirements and Challenges in the Smart Grid. *IEEE Power Energy Mag.* **2012**, *10*, 24–32. [\[CrossRef\]](#)
- Bayram, I.S.; Shakir, M.Z.; Abdallah, M.; Qaraqe, K. A survey on energy trading in smart grid. In Proceedings of the 2014 IEEE Global Conference on Signal and Information Processing (GlobalSIP), Atlanta, GA, USA, 3–5 December 2014. [\[CrossRef\]](#)
- Hamari, J.; Sjölint, M.; Ukkonen, A. The sharing economy: Why people participate in collaborative consumption. *J. Assoc. Inf. Sci. Technol.* **2015**, *67*, 2047–2059. [\[CrossRef\]](#)
- Jamil, F.; Iqbal, N.; Ahmad, S.; Kim, D. Peer-to-Peer Energy Trading Mechanism Based on Blockchain and Machine Learning for Sustainable Electrical Power Supply in Smart Grid. *IEEE Access* **2021**, *9*, 39193–39217. [\[CrossRef\]](#)
- Kabalci, Y.; Kabalci, E.; Padmanaban, S.; Holm-Nielsen, J.B.; Blaabjerg, F. Internet of Things Applications as Energy Internet in Smart Grids and Smart Environments. *Electronics* **2019**, *8*, 972. [\[CrossRef\]](#)
- Tan, S.; Wu, Y.; Xie, P.; Guerrero, J.M.; Vasquez, J.C.; Abusorrah, A. New Challenges in the Design of Microgrid Systems: Communication Networks, Cyberattacks, and Resilience. *IEEE Electr. Mag.* **2020**, *8*, 98–106. [\[CrossRef\]](#)
- Wu, Y.; Wu, Y.; Guerrero, J.M.; Vasquez, J.C.; Palacios-Garcia, E.J.; Li, J. Convergence and Interoperability for the Energy Internet: From Ubiquitous Connection to Distributed Automation. *IEEE Ind. Electron. Mag.* **2020**, *14*, 91–105. [\[CrossRef\]](#)
- Leitao, J.; Gil, P.; Ribeiro, B.; Cardoso, A. A Survey on Home Energy Management. *IEEE Access* **2020**, *8*, 5699–5722. [\[CrossRef\]](#)
- Zafar, U.; Bayhan, S.; Sanfilippo, A. Home Energy Management System Concepts, Configurations, and Technologies for the Smart Grid. *IEEE Access* **2020**, *8*, 119271–119286. [\[CrossRef\]](#)
- Llaria, A.; Dos Santos, J.; Terrasson, G.; Boussaada, Z.; Merlo, C.; Curea, O. Intelligent Buildings in Smart Grids: A Survey on Security and Privacy Issues Related to Energy Management. *Energies* **2021**, *14*, 2733. [\[CrossRef\]](#)
- Chander, B.; Kumaravelan, G. Internet of Things: Foundation. In *Principles of Internet of Things (IoT) Ecosystem: Insight Paradigm*; Peng, S.L., Pal, S., Huang, L., Eds.; Springer International Publishing: Cham, Switzerland, 2020; pp. 3–33. [\[CrossRef\]](#)
- Zhang, C.; Wu, J.; Cheng, M.; Zhou, Y.; Long, C. A Bidding System for Peer-to-Peer Energy Trading in a Grid-connected Microgrid. *Energy Procedia* **2016**, *103*, 147–152. [\[CrossRef\]](#)
- Mengelkamp, E.; Gärttner, J.; Rock, K.; Kessler, S.; Orsini, L.; Weinhardt, C. Designing microgrid energy markets: A case study: The Brooklyn Microgrid. *Appl. Energy* **2018**, *210*, 870–880. [\[CrossRef\]](#)
- Zhou, Y.; Wu, J.; Long, C.; Ming, W. State-of-the-Art Analysis and Perspectives for Peer-to-Peer Energy Trading. *Engineering* **2020**, *6*, 739–753. [\[CrossRef\]](#)
- Soto, E.A.; Bosman, L.B.; Wollega, E.; Leon-Salas, W.D. Peer-to-peer energy trading: A review of the literature. *Appl. Energy* **2021**, *283*, 116268. [\[CrossRef\]](#)
- Wu, Y.; Wu, Y.; Guerrero, J.M.; Vasquez, J.C. Digitalization and decentralization driving transactive energy Internet: Key technologies and infrastructures. *Int. J. Electr. Power Energy Syst.* **2021**, *126*, 106593. [\[CrossRef\]](#)
- Condon, F.; Martínez, J.M.; Kim, Y.C.; Ahmed, M.A. EnergyAuction: oracle Blockchain-Based Energy Trading System for Microgrids. In Proceedings of the 2023 IEEE Conference on Power Electronics and Renewable Energy (CPERE), Luxor, Egypt, 15–17 February 2023; pp. 1–6.
- Mengelkamp, E.; Notheisen, B.; Beer, C.; Dauer, D.; Weinhardt, C. A blockchain-based smart grid: Towards sustainable local energy markets. *Comput. Sci. Res. Dev.* **2018**, *33*, 207–214. [\[CrossRef\]](#)
- Luo, Y.; Itaya, S.; Nakamura, S.; Davis, P. Autonomous cooperative energy trading between prosumers for microgrid systems. In Proceedings of the 39th Annual IEEE Conference on Local Computer Networks Workshops, Edmonton, AB, Canada, 8–11 September 2014. [\[CrossRef\]](#)



20. Zhang, C.; Wu, J.; Zhou, Y.; Cheng, M.; Long, C. Peer-to-Peer energy trading in a Microgrid. *Appl. Energy* **2018**, *220*, 1–12. [\[CrossRef\]](#)
21. Andoni, M.; Robu, V.; Flynn, D.; Abram, S.; Geach, D.; Jenkins, D.; McCallum, P.; Peacock, A. Blockchain technology in the energy sector: A systematic review of challenges and opportunities. *Renew. Sustain. Energy Rev.* **2019**, *100*, 143–174. [\[CrossRef\]](#)
22. Li, Z.; Kang, J.; Yu, R.; Ye, D.; Deng, Q.; Zhang, Y. Consortium Blockchain for Secure Energy Trading in Industrial Internet of Things. *IEEE Trans. Ind. Inform.* **2018**, *14*, 3690–3700. [\[CrossRef\]](#)
23. Aitzhan, N.Z.; Svetinovic, D. Security and Privacy in Decentralized Energy Trading Through Multi-Signatures, Blockchain and Anonymous Messaging Streams. *IEEE Trans. Dependable Secur. Comput.* **2018**, *15*, 840–852. [\[CrossRef\]](#)
24. Wang, S.; Sheng, H.; Zhang, Y.; Yang, D.; Shen, J.; Chen, R. Blockchain-Empowered Distributed Multi-Camera Multi-Target Tracking in Edge Computing. *IEEE Trans. Ind. Inform.* **2023**, 1–10. [\[CrossRef\]](#)
25. Cao, B.; Wang, X.; Zhang, W.; Song, H.; Lv, Z. A Many-Objective Optimization Model of Industrial Internet of Things Based on Private Blockchain. *IEEE Netw.* **2020**, *34*, 78–83. [\[CrossRef\]](#)
26. Mihaylov, M.; Jurado, S.; Avellana, N.; Van Moffaert, K.; de Abril, I.M.; Nowé, A. NRGcoin: Virtual currency for trading of renewable energy in smart grids. In Proceedings of the 11th International Conference on the European Energy Market (EEM14), Krakow, Poland, 28–30 May 2014; pp. 1–6. [\[CrossRef\]](#)
27. Wang, W.; Hoang, D.T.; Hu, P.; Xiong, Z.; Niyato, D.; Wang, P.; Wen, Y.; Kim, D.I. A Survey on Consensus Mechanisms and Mining Strategy Management in Blockchain Networks. *IEEE Access* **2019**, *7*, 22328–22370. [\[CrossRef\]](#)
28. Liu, C.; Zhang, X.; Chai, K.K.; Loo, J.; Chen, Y. A survey on blockchain-enabled smart grids: Advances, applications and challenges. *IET Smart Cities* **2021**, *3*, 56–78.
29. Szabo, N. Formalizing and securing relationships on public networks. *First Monday* **1997**, *2*. [\[CrossRef\]](#)
30. Caldarelli, G. Overview of Blockchain oracle Research. *Future Internet* **2022**, *14*, 175. [\[CrossRef\]](#)
31. Xu, X.; Pautasso, C.; Zhu, L.; Lu, Q.; Weber, I. A Pattern Collection for Blockchain-Based Applications. In Proceedings of the 23rd European Conference on Pattern Languages of Programs, New York, NY, USA, 19 February 2018.
32. Antal, C.; Cioara, T.; Antal, M.; Mihailescu, V.; Mitrea, D.; Anghel, I.; Salomie, I.; Raveduto, G.; Bertoncini, M.; Croce, V.; et al. Blockchain based decentralized local energy flexibility market. *Energy Rep.* **2021**, *7*, 5269–5288. [\[CrossRef\]](#)
33. Al Breiki, H.; Al Qassem, L.; Salah, K.; Habib Ur Rehman, M.; Sevtnovic, D. Decentralized Access Control for IoT Data Using Blockchain and Trusted oracles. In Proceedings of the 2019 IEEE International Conference on Industrial Internet (ICII), Orlando, FL, USA, 11–12 November 2019; pp. 248–257. [\[CrossRef\]](#)
34. Wu, Y.; Wu, Y.; Cimen, H.; Vasquez, J.C.; Guerrero, J.M. Towards collective energy Community: Potential roles of microgrid and blockchain to go beyond P2P energy trading. *Appl. Energy* **2022**, *314*, 119003. [\[CrossRef\]](#)
35. Pradhan, N.R.; Singh, A.P.; Verma, S.; Kavita; Wozniak, M.; Shafi, J.; Ijaz, M.F. A blockchain based lightweight peer-to-peer energy trading framework for secured high throughput micro-transactions. *Sci. Rep.* **2022**, *12*, 14523. [\[CrossRef\]](#)
36. Appasani, B.; Mishra, S.K.; Jha, A.V.; Mishra, S.K.; Enescu, F.M.; Sorlei, I.S.; Birleanu, F.G.; Takorabet, N.; Thounthong, P.; Bizon, N. Blockchain-Enabled Smart Grid Applications: Architecture, Challenges, and Solutions. *Sustainability* **2022**, *14*, 8801. [\[CrossRef\]](#)
37. Capper, T.; Gorbacheva, A.; Mustafa, M.A.; Bahloul, M.; Schwidtal, J.M.; Chitchyan, R.; Andoni, M.; Robu, V.; Montakhabi, M.; Scott, I.J.; et al. Peer-to-peer, community self-consumption, and transactive energy: A systematic literature review of local energy market models. *Renew. Sustain. Energy Rev.* **2022**, *162*, 112403. [\[CrossRef\]](#)
38. Frieden, D.; Tuerk, A.; Neumann, C.; d’Herbemont, S.; Roberts, J. Collective self-consumption and energy communities: Trends and challenges in the transposition of the EU framework. *Compil. Integr. Community Power Energy Isl.* **2020**. [\[CrossRef\]](#)
39. Chen, S.; Liu, C.C. From demand response to transactive energy: State of the art. *J. Mod. Power Syst. Clean Energy* **2017**, *5*, 10–19. [\[CrossRef\]](#)
40. Parag, Y.; Sovacool, B.K. Electricity market design for the prosumer era. *Nat. Energy* **2016**, *1*, 16032. [\[CrossRef\]](#)
41. Wang, Q.; Zhang, C.; Ding, Y.; Xydis, G.; Wang, J.; Østergaard, J. Review of real-time electricity markets for integrating Distributed Energy Resources and Demand Response. *Appl. Energy* **2015**, *138*, 695–706. [\[CrossRef\]](#)
42. Koirala, B.P.; Koliou, E.; Friege, J.; Hakvoort, R.A.; Herder, P.M. Energetic communities for community energy: A review of key issues and trends shaping integrated community energy systems. *Renew. Sustain. Energy Rev.* **2016**, *56*, 722–744. [\[CrossRef\]](#)
43. Saad, W.; Han, Z.; Poor, H.V.; Basar, T. Game-Theoretic Methods for the Smart Grid: An Overview of Microgrid Systems, Demand-Side Management, and Smart Grid Communications. *IEEE Signal Process. Mag.* **2012**, *29*, 86–105. [\[CrossRef\]](#)
44. Abdella, J.; Shuaib, K. Peer to Peer Distributed Energy Trading in Smart Grids: A Survey. *Energies* **2018**, *11*, 1560. [\[CrossRef\]](#)
45. Mohanta, B.K.; Panda, S.S.; Jena, D. An Overview of Smart Contract and Use Cases in Blockchain Technology. In Proceedings of the 2018 9th International Conference on Computing, Communication and Networking Technologies (ICCCNT), Bengaluru, India, 10–12 July 2018; pp. 1–4. [\[CrossRef\]](#)
46. Al-Breiki, H.; Rehman, M.H.U.; Salah, K.; Svetinovic, D. Trustworthy Blockchain oracles: Review, Comparison, and Open Research Challenges. *IEEE Access* **2020**, *8*, 85675–85685. [\[CrossRef\]](#)
47. Saltini, R.; Hyland-Wood, D. Ibft 2.0: A safe and live variation of the ibft blockchain consensus protocol for eventually synchronous networks. *arXiv* **2019**, arXiv:1909.10194.
48. Fan, C.; Lin, C.; Khazaei, H.; Musilek, P. Performance Analysis of Hyperledger Besu in Private Blockchain. In Proceedings of the 2022 IEEE International Conference on Decentralized Applications and Infrastructures (DAPPS), San Francisco, CA, USA, 15–18 August 2022; pp. 64–73. [\[CrossRef\]](#)

49. Zhao, P.; Cheng, H.; Fang, Y.; Wang, X. A Secure Storage Strategy for Blockchain Based on MCMC Algorithm. *IEEE Access* **2020**, *8*, 160815–160824. [[CrossRef](#)]
50. Wang, G.; Shi, Z.; Nixon, M.; Han, S. ChainSplitter: Towards Blockchain-Based Industrial IoT Architecture for Supporting Hierarchical Storage. In Proceedings of the 2019 IEEE International Conference on Blockchain (Blockchain), Atlanta, GA, USA, 14–17 July 2019; pp. 166–175. [[CrossRef](#)]

**Disclaimer/Publisher’s Note:** The statements, opinions and data contained in all publications are solely those of the individual author(s) and contributor(s) and not of MDPI and/or the editor(s). MDPI and/or the editor(s) disclaim responsibility for any injury to people or property resulting from any ideas, methods, instructions or products referred to in the content.

## Article

# An Evaluation of ANN Algorithm Performance for MPPT Energy Harvesting in Solar PV Systems

Md Tahmid Hussain <sup>1</sup>, Adil Sarwar <sup>1</sup>, Mohd Tariq <sup>1</sup>, Shabana Urooj <sup>2,\*</sup>, Amal BaQais <sup>3</sup> and Md. Alamgir Hossain <sup>4,\*</sup>

<sup>1</sup> Department of Electrical Engineering, ZHCET, Aligarh Muslim University, Aligarh 202002, India; gk3910@myamu.ac.in (M.T.H.); adil.sarwar@zhcet.ac.in (A.S.); tariq.ee@zhcet.ac.in (M.T.)

<sup>2</sup> Department of Electrical Engineering, College of Engineering, Princess Nourah bint Abdulrahman University, P.O. Box 84428, Riyadh 11671, Saudi Arabia

<sup>3</sup> Department of Chemistry, College of Science, Princess Nourah bint Abdulrahman University, P.O. Box 84428, Riyadh 11671, Saudi Arabia; aabaqais@pnu.edu.sa

<sup>4</sup> Queensland Micro and Nanotechnology Centre, Griffith University, Nathan, QLD 4111, Australia

\* Correspondence: smurooj@pnu.edu.sa (S.U.); mdalamgir.hossain@griffith.edu.au (M.A.H.)

**Abstract:** In this paper, the Levenberg–Marquardt (LM), Bayesian regularization (BR), resilient backpropagation (RP), gradient descent momentum (GDM), Broyden–Fletcher–Goldfarb–Shanno (BFGS), and scaled conjugate gradient (SCG) algorithms constructed using artificial neural networks (ANN) are applied to the problem of MPPT energy harvesting in solar photovoltaic (PV) systems for the purpose of creating a comparative evaluation of the performance of the six distinct algorithms. The goal of this analysis is to determine which of the six algorithms has the best overall performance. In the study, the performance of managing the training dataset is compared across the algorithms. The maximum power point tracking energy harvesting system is created using the environment of MATLAB or Simulink, and the produced model is examined using the artificial neural network toolkit. A total of 1000 datasets of solar irradiance, temperature, and voltage were used to train the suggested model. The data are split into three categories: training, validation, and testing. Eighty percent of the total data is used for training the model, and the remaining twenty percent is divided equally for testing and validation. According to the results, the regression values of LM, RP, BR, and BFGS are 1, whereas the regression values for SCG and GDM are less than 1. The gradient values for LM, RP, BFGS, SCG, BR, and GDM are  $7.983 \times 10^{-6}$ ,  $0.033415$ ,  $1.0211 \times 10^{-7}$ ,  $0.14161$ ,  $0.00010493$ , and  $11.485$ , respectively. Similarly, the performance values for these algorithms are  $2.0816 \times 10^{-10}$ ,  $2.8668 \times 10^{-6}$ ,  $9.98 \times 10^{-17}$ ,  $0.052985$ ,  $1.583 \times 10^{-7}$ , and  $0.15378$ . Overall, the results demonstrate that the LM and BFGS algorithms exhibit superior performance in terms of gradient and overall performance. The RP and BR algorithms also perform well across various metrics, while the SCG and GDM algorithms show comparatively less effectiveness in addressing the proposed problem. These findings provide valuable insights into the relative performance of the six evaluated algorithms for MPPT energy harvesting in solar PV systems.

**Citation:** Hussain, M.T.; Sarwar, A.; Tariq, M.; Urooj, S.; BaQais, A.; Hossain, M.A. An Evaluation of ANN Algorithm Performance for MPPT Energy Harvesting in Solar PV Systems. *Sustainability* **2023**, *15*, 11144. <https://doi.org/10.3390/su151411144>

Academic Editor: Mohamed A. Mohamed

Received: 30 April 2023

Revised: 1 June 2023

Accepted: 12 June 2023

Published: 17 July 2023

**Keywords:** artificial neural network (ANN); solar photovoltaic (PV); maximum power point tracking; Levenberg–Marquardt (LM); Bayesian regularization (BR); scaled conjugate gradient (SCG); resilient backpropagation (RP)



**Copyright:** © 2023 by the authors. Licensee MDPI, Basel, Switzerland. This article is an open access article distributed under the terms and conditions of the Creative Commons Attribution (CC BY) license (<https://creativecommons.org/licenses/by/4.0/>).

## 1. Introduction

Our energy usage includes solar PV electricity, which is also a crucial element of renewable energy networks. The cost of PV modules is falling as technology advances quickly, and PV panels are becoming more reliable. National economies are investing heavily in off-grid and grid-connected PV networks [1,2]. PV electricity is unstable and dependent on solar radiation as well as other meteorological conditions, such as humidity, wind speed direction, cloud cover temperature, and precipitation. This makes it different from typical

energy production methods [3]. Power networks have had significant issues because of the advent of large-scale grid-connected solar PV facilities, including a lack of device flexibility, energy balance, and efficiency [4]. For PV networks to have a consistent electricity supply, it is essential to anticipate the solar output energy. The accuracy of the predictive models boosts the device dependability, decreases the cost of extra equipment maintenance, and limits the impact of solar PV performance [5]. Irradiation and temperature are features of a PV module's I-V properties. Solar cell arrays are followed by MPPT controllers for the best utilization performance. A thorough list of 40 distinct MPPT approaches and their categorization was developed in [6]. Several MPPT algorithms and designs are covered in a number of publications in the literature to improve the performance of PV device [7]. The most efficient and widely used methods are perturb and observe (P&O) [8], incremental conductance (INC) [9], fuzzy logic controller (FLC) [10], a P&O technique based on particle swarm optimization (PSO) [11], and ANN [12]. For each of these options, there are differences in the pace of convergence, oscillation across the absolute maximum power point (MPP) complexity, stability, cost, and necessary electrical equipment [13].

After a quick irradiance change that causes a distortion in the algorithm of P&O and the working parameters of PV systems, the controller struggles at first to surpass the MPP [14]. The controller nonetheless mitigates the mistakes of the algorithm, which, with some lag time, follows the MPP once again. Furthermore, the MPP's terminal voltage fluctuates as a consequence amid a power outage. The smallest possible disruption phase size is used to counteract these oscillations. The minor phase again minimizes the transient startup and changes the system sensitivity to the weather. Inc. algorithm; it works well to use a controller such as proportional integral (PI) to deal with quick changes in irradiance and corresponding declines in the oscillation of the MPP during rips. Hence, the response and, according to the INC method, swing pace would still be balanced, but often breaks away from the MPP with sudden irradiance shifts. Authors in [15] claim that these algorithms cannot quickly and accurately detect the entire power because there are oscillations at the highest point. The biological neural networks of the human brain are the motivation for the ANN system development. It is used to train and assess the PV system I-V and P-V nonlinearity relationship. ANN retrieves inputs such as the input voltage, input current, temperature, irradiance, and metrological information and continuously learns to modify how the solar power system behaves for the highest impact [16]. The design of an FLC model is possible using ANN for a more accurate and simple converter actualization [17]. The dataset comes from simply using a simulation or hardware configuration and also introducing solar irradiances, temperatures, and/or the voltage or current of a solar power system to ANN to determine the necessary maximum power ( $P_{max}$ ) or maximum output voltage ( $V_{max}$ ). This information is converted into training data that is provided to the system to teach the desired ANN how to operate. Test datasets are used after training to evaluate the built-in ANN's performance, and for further correction, errors are sent to the ANN [18], which has the capability of predicting MPP by state estimation and SMC filtering (also known as sequential Monte Carlo). The framework of the incremental conductance maximum power point tracking approach (IC MPPT) might be expanded to include a model of state space estimations for successive maximum power points (MPP). The voltage or current and irradiance statistics are used to predict the global MPP (GMPP) in the ANN model to enhance the SMC estimation [19]. Among the advantages of ANN are exceptional precision in modelling and the ability to resolve nonlinearity issues without prior knowledge or models [20]. To speed up and improve tracking through solar power system modelling and forecasting, ANN may be used [21]. It has been demonstrated to have a quicker response time and less oscillation than MPP [22]. In actual operational circumstances, MPPT based on ANN can monitor MPP with little effort. Low ripple and transient time [23]. The square error method is used in the error calculation as a feedback correction [24]. A proper, precise, and systematic training set of data, however, is an important constraint to function well with the ANN without much training error [25]. Yet, the variations in instruction and operation when creating an ANN model and solar system

settings make the training technique challenging. The authors in [26] thus recommended using a particle swarm optimization (PSO) model in MATLAB and Simulink to determine the best starting weights for ANN models by selecting the best topology to improve the accuracy of the ANN model. Hence, with the conflict processing speed and the most accurate regression after resolution of the ANN model, the minimization of the mean squared error occurs. The results show that using the real-world approach of the improved feedforward ANN depends on data from the PSO method; the peak power is accurately predicted with average hourly efficiencies of over 99.67% on bright and 99.30% on overcast days, respectively. An ANN-based MPPT controller demonstrates reduced steady-state error and a quicker response to abrupt changes in solar temperature and irradiance in contrast to both P&O and IC [27]. Nevertheless, an improved algorithm of P&O with variable step size aims to improve the tracking speed and reduce the steady-state fluctuation or oscillation under abrupt changes in irradiance or partial shading conditions (PSC). Integrating FLC and ANN with more established MPPT methods such as IC and P&O is a good fit. The ANN method calculates the MPP even when there is no shade or temperature information available from the panel; nevertheless, the hill-climbing (HC) methodology further enhances the outcome. IC-ANN and P&O-ANN are two more hybrid MPPTs that are linked with the stacked autoencoder (SAE) controller via the use of building blocks and deep learning (DL) training. It is recommended to use a greedy layer-wise method to harvest the maximum amount of energy possible from the solar energy system. Backpropagation and supervised learning are then used to fine-tune the deep neural network using traditional MPPT-IC and P&O. This allows for the greatest amount of power to be extracted [28].

In the literature study, different artificial intelligence (AI) algorithms for energy harvesting with the PV system are highlighted; however, only a few studies have made use of LM algorithms, BR algorithms, SCG algorithms, etc. There is reason to be optimistic about the ability of AI systems to anticipate optimum power with low error under a variety of meteorological situations. Processing vast volumes of data is achieved much more speedily and effectively via the use of neural networks [29]. Even though there has been some study on contrasting various MPPT topologies for solar PV systems, there is still a significant research gap when it comes to evaluating the performance of different ANN algorithm-based MPPT methods for solar energy harvesting. In addition to evaluating the performance of ANN algorithms for MPPT energy harvesting in solar PV systems, the study proposed in [30] also aims to contribute to the literature by introducing a new model predictive control method for buck-boost inverter-based photovoltaic systems. By incorporating this study into the proposed study, we expand the scope and relevance of our research. The proposed model predictive control method offers a novel approach to optimize the operation of buck-boost inverters in photovoltaic systems, thereby enhancing the energy harvesting efficiency. This integration of the new control method into the evaluation of ANN algorithms provides a comprehensive analysis of advanced techniques for improving the performance of solar PV systems. Similarly, the study presented in [31] aims to contribute to the literature by considering the topic of optimal control of an energy-storage system in a microgrid for reducing wind-power fluctuations. By incorporating this work into the study, we can also broaden the scope of our research and address the challenges associated with integrating wind power into microgrid systems. The optimal control of an energy-storage system plays a crucial role in mitigating the intermittent nature of wind power generation and ensuring a stable and reliable energy supply. This integration of the optimal control strategy into the evaluation of ANN algorithms provides a comprehensive analysis of advanced techniques for improving the stability and efficiency of renewable energy systems. By considering both solar and wind power aspects, our study offers insights into the integration of multiple renewable energy sources and their control mechanisms, thereby contributing to the overall understanding of sustainable energy systems.

It is also crucial to investigate alternate methods for training neuro-fuzzy systems in addition to analyzing the effectiveness of different ANN algorithms for MPPT energy

harvesting in solar PV systems. A notable topic in this context is the training of neuro-fuzzy systems using meta-heuristic algorithms presented in [32]. These algorithms offer a promising approach to optimize the parameters of neuro-fuzzy models and enhance their MPPT capabilities. By incorporating meta-heuristic algorithms into the training process, such as genetic algorithms, particle swarm optimization, or simulated annealing, the neuro-fuzzy models can effectively learn the mapping between input data and optimal power outputs. This integration of meta-heuristic algorithms with neuro-fuzzy systems has the potential to improve the accuracy and efficiency of MPPT algorithms, ultimately leading to enhanced energy harvesting in solar PV systems. Therefore, investigating the training of neuro-fuzzy systems using meta-heuristic algorithms presents an intriguing avenue for further research and advancement in the field of MPPT energy harvesting. Furthermore, recent advancements in cooperative optimization techniques for assessing the performance of various ANN algorithms for MPPT energy harvesting in solar PV systems should also be considered. One such notable topic is the improved cooperative artificial neural network–particle swarm optimization (ANN-PSO) approach for solar photovoltaic systems with maximum power point tracking (MPPT) [33]. This approach combines the power of artificial neural networks and particle swarm optimization to enhance the efficiency and accuracy of MPPT algorithms in solar PV systems. By leveraging the cooperative nature of ANN-PSO, the system can benefit from the collective intelligence of multiple agents working together to find the optimal power output. This cooperative approach offers a promising solution for addressing the challenges of MPPT in solar PV systems, including non-linearity, partial shading, and varying environmental conditions. Therefore, incorporating the improved cooperative ANN-PSO approach in the evaluation of ANN algorithms for MPPT energy harvesting would provide valuable insights into its effectiveness and potential as an advanced optimization technique in solar PV systems.

In [34], a comparative analysis of three algorithm is proposed for energy harvesting of solar PV. The proposed work is compared in terms of the performance of handling the trained dataset, and the authors have described the algorithms in a clear and detailed way.

However, this work provides a detailed performance comparison of six different ANN-based algorithms (LM, BR, RP, GDM, BFGS, and SCG) for MPPT solar energy harvesting and also provides an explanation of each algorithm. Recent research on ANN-based MPPT has solely concentrated on fewer approaches. The created model gives a good grasp of how practical and applicable these algorithms are. It also contributes significantly to the existing literature in several ways. Firstly, it provides a comprehensive evaluation of six different ANN algorithms, specifically in the context of MPPT for solar PV systems. By comparing the performance of these algorithms, the study offers valuable insights into their effectiveness, convergence properties, and accuracy. This comparative analysis helps researchers and practitioners make informed decisions when selecting the most suitable algorithm for MPPT in solar PV systems. Additionally, the study incorporates real-time data on the solar irradiance, panel temperature, and generated voltage for training the ANN algorithms. This aspect enhances the practical relevance of the research findings and increases their applicability to real-world scenarios. The methodology and dataset used in this study can serve as a valuable resource for further research and algorithm development in the field. Furthermore, the study introduces and evaluates various performance metrics, such as regression, error at the middle bin, gradient, performance, momentum parameter, and epochs. These metrics provide a comprehensive framework for assessing the efficacy of ANN algorithms in MPPT energy harvesting. By establishing these metrics, the study contributes to the existing literature by providing a standardized approach to evaluate and compare the performance of different algorithms. Overall, this study advances the understanding of ANN algorithm performance for MPPT energy harvesting in solar PV systems and provides valuable insights and guidance for researchers, engineers, and practitioners working in this field. It sets a foundation for further research and development of advanced algorithms and methodologies for optimizing energy harvesting efficiency in solar PV systems. The performance of the six ANN algorithms is evaluated using a



thorough method, which includes training, validation, and testing using generated data of the solar irradiance, temperature, and produced voltage. This method is used to determine how well the algorithm functions. The performance of these algorithms is analyzed via the use of a simulated model that is deployed on MATLAB/Simulink. This offers clear knowledge of the application of ANN algorithms for MPPT in solar PV systems. The (ANN)-based MPPT algorithm is trained using data taken from the actual world, proving both the usefulness and efficacy of this technology.

The article's remaining sections are organized as follows: the status of ANN and MPPT technology is discussed in Section 2. Section 3 describes the modelling of ANN-based MPPT for solar PV system. The results and comments for six training algorithms are shown and discussed in Section 4. Lastly, the work is concluded in Section 5.

## 2. The State of the Art of ANNs and MPPTs

Artificial neural networks, often known as ANNs, are a specific form of machine learning algorithm that attempt to replicate the function and structure of the biological neural networks found in the human brain [35]. They are designed to connect various parameters to particular data points without the need for mathematical equations or complex mathematical bases [36]. In order to train ANNs, a technique known as supervised learning is applied. In this approach, datasets consisting of input–output parameter values are utilized in order to train the network. The datasets are often divided into two groups: a training dataset and a validation dataset. The training dataset is used to train the network, and the validation dataset is used to assess how well the trained network performed. An artificial neural network (ANN) is made up of many different neurons, all of which are linked together by a fractional number that is referred to as weight [37]. In order to accurately forecast the results of the process, the weights are changed while it is in the training phase. The weights become constant once the error falls below a permissible value. The most common form of ANN is the two-layer model, which is shown in Figure 1.

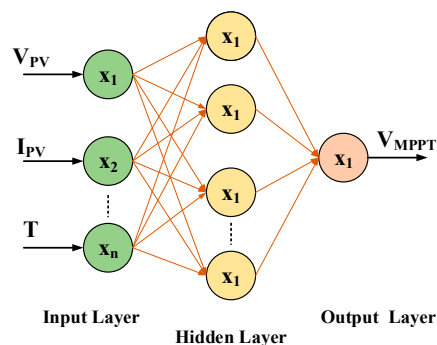


**Figure 1.** The fundamental design of a two-layer ANN.

The network's inputs are incorporated into the network at various times. The training dataset is used to create the neural network, and the validation dataset is used to assess how well it performed. Once the network has been trained and the error is within permissible limits [38], the validation dataset parameters of input are imported, and the associated values of output parameter are predicted [39]. This process helps to ensure that the ANN is accurate and reliable.

By contrasting the anticipated output parameter values from the validation dataset with the corresponding actual values, the trained ANN's performance is assessed. The trained ANN may be regarded as the best prediction model if the difference between the predicted and actual values is less than the allowable maximum. For the selected training method and number of training iterations, the ANN can forecast the matching input values and output parameters.

The trained ANN along with the training procedure is selected as the optimized model if the error magnitude is smaller than the allowed value. However, if the error is still high,

different training algorithms or more training iterations may be tried before an allowable error is obtained [40]. The results obtained from the validation dataset using the optimal ANN model validate the generalization of the trained ANN [41].

MPPT in Solar PV systems is one of the many power electronics applications where ANNs have found widespread usage. By changing the operating point to the MPP under various environmental circumstances, MPPT aims to maximize the power output from a PV system. The MPP of a PV system is a nonlinear and time-varying function that is difficult to model analytically. ANNs have been shown to be effective tools for modeling this nonlinear relationship, making them a popular choice for MPPT in PV systems.

For MPPT in PV systems, a variety of ANN algorithms, such as radial basis function (RBF) and multi-layer perceptron (MLP) networks, may be utilized. A sort of feedforward neural network called an MLP network is made up of layers of linked neurons. They are commonly used for supervised learning tasks, such as function approximation and regression. One of the most common ANN-based MPPT techniques is the Perturb and Observe (P&O) method with an MLP network. In this method, the PV system operating point is perturbed and the change in power is observed. The change in power and the operating point are used as inputs to the ANN, which is trained to predict the MPP. The ANN output is then used to adjust the operating point to the MPP. This process is repeated in real time to track the MPP as it changes due to varying environmental conditions. Another popular ANN-based MPPT technique is the incremental conductance (IC) method with an RBF network. In this method, the PV system operating point is adjusted incrementally, and the change in power is used as an input to the ANN. The ANN is trained to predict the direction of the MPP, and the operating point is adjusted in the direction predicted by the ANN. This process is also repeated in real time to track the MPP as it changes. There are also ANN-based MPPT techniques that combine multiple algorithms, such as the hybrid MPPT algorithm that uses both the P&O and IC methods. In this method, the P&O method is used to quickly find the initial MPP, and the IC method is used to track the MPP as it changes. One of the main advantages of ANN-based MPPT techniques is that they can effectively model the nonlinear relationship between the PV system output power and the operating conditions. They can also adapt to changing environmental conditions in real time, which is essential for efficient MPPT in PV systems. Additionally, ANNs are relatively easy to implement and can be used with a variety of PV systems, from small-scale systems to large-scale power plants. The fact that ANN-based MPPT approaches need a lot of data to train the network properly is one of their key drawbacks. This can be a significant obstacle for some applications, particularly those that are remote or have limited data collection capabilities. Additionally, the training procedure may also be time-consuming and computationally demanding, which can be problematic for real-time applications.

A variety of maximum power point tracking (MPPT) algorithms for photovoltaic (PV) systems were examined and classified in a study that was referenced in [42]. The classifications were based on the number of control variables and the types of control strategies. In order to examine the dynamic response of the PV voltage ripple, the authors made use of MATLAB/Simulink and the dSPACE framework. They provided a hands-on assessment for commonly used MPPT algorithms [43] and compared them with a PI controller. The research modified environmental variables, including changing irradiance and increasing temperatures, to emphasize the benefits and drawbacks of the P&O and INC algorithms in simulated findings. To improve the P&O algorithm in the context of unforeseen irradiance variations, they put up a novel method [44], which includes two algorithms: an original disturbance algorithm and an adaptive control algorithm. Experimental findings were also compared with the proposed algorithm and traditional algorithms. In another study [45], the authors proposed an updated P&O algorithm to address the root cause of the drift phenomenon and compared the results of experiments and simulations using conventional P&O methods using adaptive measures.

The INC MPPT algorithm has been evaluated in [45]. The authors tested the INC algorithm using an isolated PV pumping approach, which impacted service speeds and altered the reference voltage. Here, the influence of prior disturbances on the phase size and disturbance size has been made clear, which often reveals the algorithm's uncertainty as a result of sudden changes in irradiance. The accomplishment also has something to do with the recommended algorithm.

To monitor the PV properties of MPP, a comparison study is performed between the P&O method and the INC algorithm. In contrast, the transient solution for the INC job ratio disturbance and reference voltage disturbance is more quickly implemented. It was shown that the INC MPPT technique is less susceptible to device dynamics and noise. Greater stability at rapidly changing irradiance has been shown by this phenomenon in the suggested device. The authors of [26] have written up experimental studies with high INC algorithm perturbation rates. At greater disruption speeds, INC is shown to provide a quicker transitional reaction. The method also offers a speedier MPP recovery when the MPP is affected by noise or brightness fluctuations. There have been several MPPT algorithms using PI controllers used so far. However, the most uncomfortable and unusual idea for implementing PV systems was using ANN as the MPPT controllers.

The ANN MPPT was characterized as having a number of off-line preparation characteristics, including nonlinear mapping, a faster response time, and less computing effort in [46]. A novel neural network (NN) MPPT controller for PV systems was proposed by the authors in [47]. Using MATLAB and Simulink, data were extracted from the P&O system to be used in the training and testing of the NN model. The simulation results showed that using the suggested NN controllers for swiftly moving insulation will increase monitoring accuracy, response time, and control. In order to accomplish the electronic power grids' optimal design using AI, the research is important because it integrates configuration parameters with reliability measurements [48]. This article explains how switching the frequency and voltage series may be used to determine a device's stability, efficiency, and cost. Additionally, it provides a thorough examination of the data extraction and training for artificial neural networks. The findings of another ANN MPPT [49] are superior to those of the climbing algorithms.

To locate the global peak using the MATLAB NN-Tool, the authors created a feedback network using the LM backpropagation method. The simulation findings demonstrate that the suggested model is effective and has a smaller root mean square error (RMSE) than the climbing method. The fundamental nature and purpose of diverse MPPTs are achieved using modified methodologies. It is recommended that a technique employ a NN controller instead of a PI controller when utilizing conventional MPPT algorithms. PI-dependent algorithms may thus provide better dynamic stability with abrupt changes in the environment.

### 3. Modelling of ANN-Based MPPT for Solar PV System

#### 3.1. Solar Photovoltaic (PV) System

A solar photovoltaic (PV) cell, also known as a solar cell, is a device that uses a process known as the photovoltaic effect to transform light energy into electrical energy. The photovoltaic effect occurs when photons from sunlight knock electrons into a higher state of energy, allowing them to flow as an electrical current. Solar PV cells are made of semiconductor materials, typically silicon, and are designed to capture the energy from sunlight and convert it into usable electrical power.

Solar PV cells are connected together to form a solar panel, which can then be connected in series to form a solar array. The efficiency of solar PV cells, or the percentage of sunlight energy that is transformed into electrical energy, varies, but most commercial solar cells have an efficiency of around 15–20%. The performance of a solar cell is also influenced by temperature, shading, and other environmental factors.

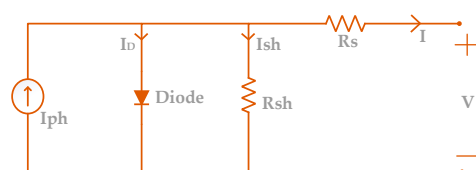
The equivalent circuit of a solar cell is a mathematical model that represents the behavior of a solar cell as an electrical circuit. This model is used to analyze and understand the performance of a solar cell, including its voltage, current, and power output.

A current source, a series resistance (denoted by  $R_s$ ), a shunt resistance (denoted by  $R_{sh}$ ), and a diode are the standard components that make up the equivalent circuit of a solar cell. The current source is symbolic of the photocurrent that is produced by the solar cell, and the  $R_s$  is symbolic of the resistance that is posed by the material and connections that are included inside the cell. The  $R_{sh}$  represents the resistance to current flow through pathways other than the intended path, such as cracks or defects in the cell. The diode represents the non-linear behavior of the solar cell, including its short-circuit current and open-circuit voltage.

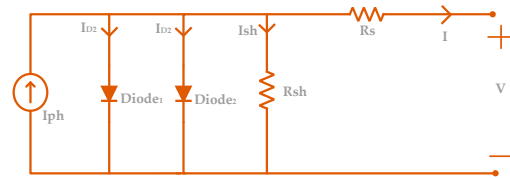
By analyzing the equivalent circuit, one can better understand the factors that influence the performance of a solar cell and make design improvements to increase its efficiency. For example, reducing the values of  $R_s$  and  $R_{sh}$  can increase the overall performance of the solar cell. Additionally, the equivalent circuit can be used to determine the MPP of a solar cell, which is the point at which the solar cell produces the maximum amount of power.

There are several different types of equivalent circuits used to model the behavior of solar cells, each with its own advantages and limitations. The most common types of equivalent circuits are:

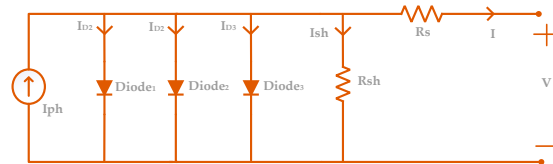
1. One-diode model (Scheme 1): The one-diode model is the simplest type of equivalent circuit and is often used as a first approximation of the behavior of a solar cell. It consists of only a current source and a diode and is relatively easy to analyze and understand. The main advantage of the one-diode model is its simplicity, which makes it suitable for many applications where a quick estimate of the performance of a solar cell is needed.
2. Two-diode model (Scheme 2): The two-diode model is a more sophisticated equivalent circuit that includes two diodes and a series resistance. This model is used to represent the behavior of a solar cell more accurately and is particularly useful for analyzing the performance of cells under varying light and temperature conditions. The main advantage of the two-diode model is its improved accuracy compared to the one-diode model, which makes it suitable for applications where a more detailed understanding of the behavior of a solar cell is needed.
3. Circular model: The circular model is an advanced equivalent circuit that includes a series resistance, a shunt resistance, and a diode. This model represents the behavior of a solar cell more accurately than the one-diode or two-diode models and is particularly useful for analyzing the behavior of cells under complex environmental conditions. The main advantage of the circular model is its improved accuracy and the ability to model the effects of shading and other environmental factors on the performance of a solar cell.
4. Three-diode model (Scheme 3): It is a more sophisticated equivalent circuit that consists of three diodes and a series resistance. This model is used to represent the behavior of a solar cell more accurately, particularly under conditions of high light intensity and high temperature. The three-diode model takes into account the non-linear behavior of a solar cell under these conditions and provides a more accurate representation of the behavior of a solar cell than the circular model or the one- or two-diode models.



**Scheme 1.** Equivalent circuit of one diode model.



Scheme 2. Equivalent circuit of two diode model.



Scheme 3. Equivalent circuit of three diode model.

A simulation model for a photovoltaic (PV) cell is created to optimize its power conversion efficiency. This is achieved by taking into account the impact of light intensity and temperature on the cell's production capacity. The analogous electrical circuit of the PV cell, as displayed in Figure 2, is used as the basis for this simulation model. This permits the measurement of the maximum power point of the solar panels and provides a more accurate forecast of the performance of the cell under various environmental circumstances. Additionally, this makes it possible to determine the maximum power point.

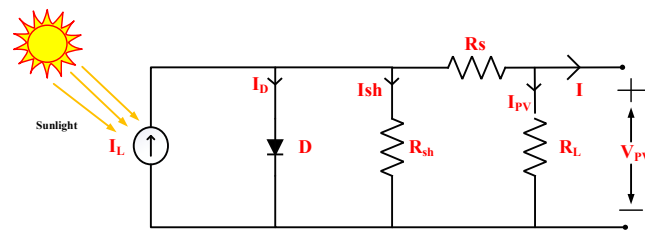


Figure 2. Analogous circuit of a solar PV cell.

In Figure 3a, the current and voltage for a photovoltaic cell are shown in response to various levels of irradiance, including ( $200 \text{ W/m}^2$ ,  $400 \text{ W/m}^2$ ,  $600 \text{ W/m}^2$ ,  $800 \text{ W/m}^2$ , and  $1000 \text{ W/m}^2$ ) at  $25^\circ\text{C}$ . The voltage and current of the cell fluctuate as a consequence of variations in the sun irradiation.

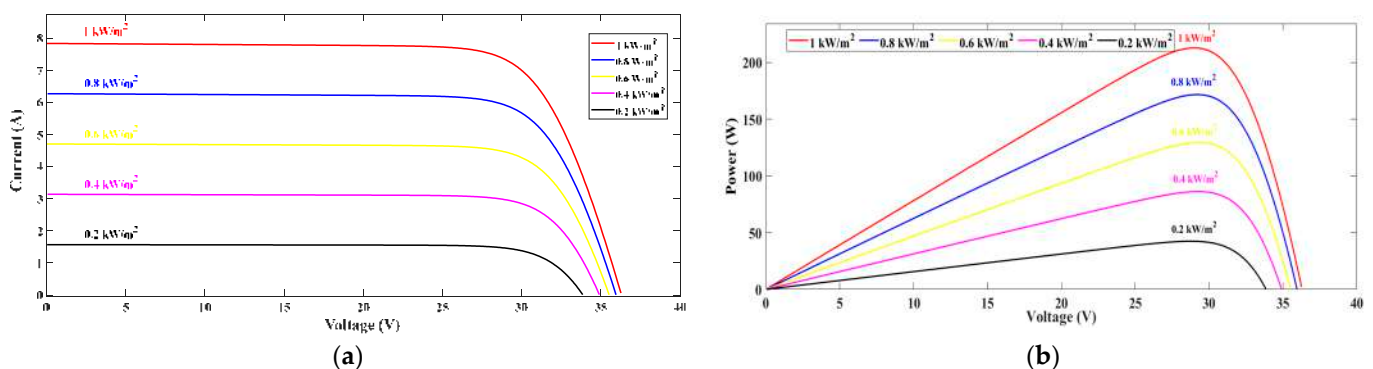


Figure 3. Characteristic curve of module 1Soltech ISTH-215-P: (a) I-V curve; (b) P-V curve.

Figure 3b demonstrates the impact of light intensity on the production capacity of the photovoltaic cell. It shows that even with the same temperature, the optimal energy point for the cell occurs at a constant level of light intensity.

The solar cell current can be expressed using the variables such as short circuit current ( $I_{sc}$ ), saturation current ( $I_0$ ), diode ideality constant ( $a$ ), number of series-connected cells

( $N_s$ ), temperature of the cell (T), Boltzmann constant (K), charge of an electron ( $q$ ), series resistance ( $R_s$ ), and shunt resistance ( $R_{sh}$ ) of the array. These variables are used in Equations (1) and (2) to represent the solar cell current [50].

$$I = I_{sc} - I_0 \left( e^{\frac{V + IR_s}{\frac{N_s k T}{q} a}} - 1 \right) - \frac{V + IR_s}{R_{sh}} \quad (1)$$

$$I = I_{sc} - I_o \left( e^{\frac{V + IR_s}{V_{Ta}}} - 1 \right) - \frac{V + IR_s}{R_{sh}} \quad (2)$$

where the value of  $K$  and  $q$  are  $1.38 \times 10^{-23}$  J/K and  $1.6 \times 10^{-19}$  C, respectively. Equation (1) can be rewritten as Equation (2), if the array thermal voltage is replaced by  $V_T = \frac{N_s K T}{q}$ .

### 3.2. ANN-Based MPPT for Solar PV System

The MATLAB/Simulink—based simulated model of the solar PV system, illustrated in Figure 4, has been developed. It utilizes the 1Soltech ISTH-215-P solar panel, with the electrical specifications provided in Table 1. The simulated model consists of two primary subsystems: the ANN\_MPPT and Switching block. The proposed system incorporates an ANN algorithm, which is represented by an ANN block as depicted in Figure 5.

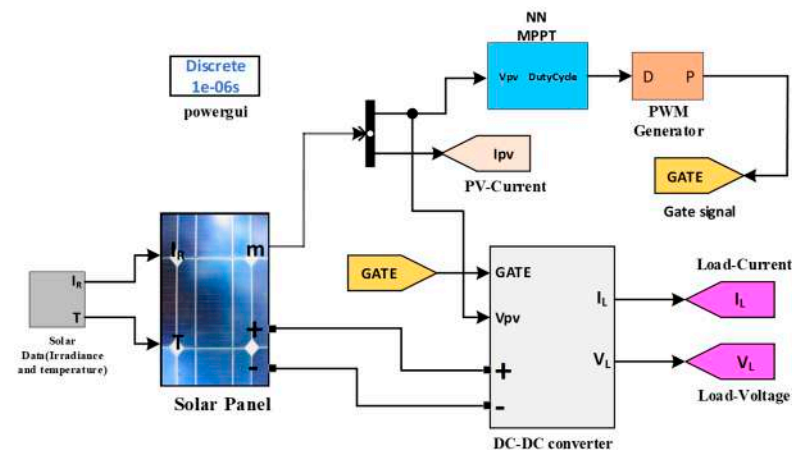


**Figure 4.** ANN-Based MPPT Solar PV Model.

**Table 1.** Specification of 1Soltech ISTH-215-P Solar Module.

Specification	Value
Power at STC (W)	215
Power at PTC (W)	189.4
V <sub>mp</sub> : Voltage at Max Power (V)	29.0
I <sub>mp</sub> : Current at Max power (A)	7.35
V <sub>oc</sub> : Open Circuit Voltage (V)	36.3
I <sub>sc</sub> : Short Circuit Current (A)	7.84
Nominal Operating Cell Temperature (°C)	47.4
Open Circuit Voltage Temp Coefficient (%/°C)	−0.361
Short Circuit Current Temp Coefficient (%/°C)	0.102
Max power Temp Coefficient (%/°C)	−0.495
Power Density at STC (W/m <sup>2</sup> )	136.943
Power Density at PTC (W/m <sup>2</sup> )	120.637



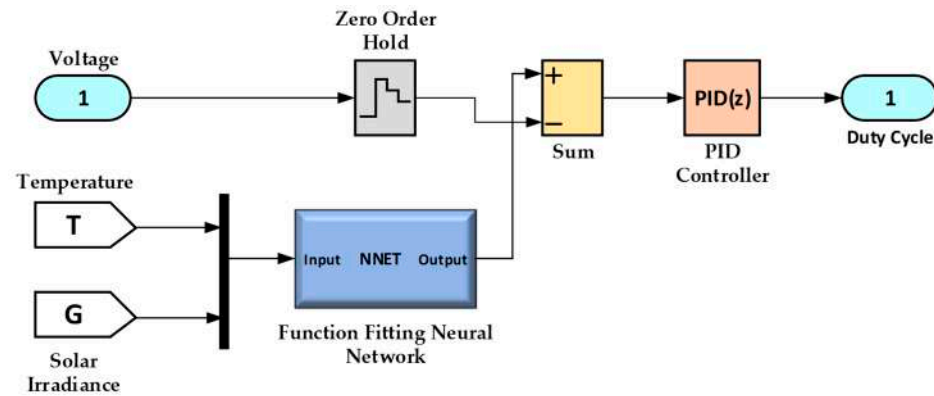


Figure 5. Proposed Block Diagram of ANN Algorithm.

Within the ANN\_MPPT subsystem, a comparator compares the output voltage,  $V_1$ , of the ANN with the voltage generated by the PV array. This generated voltage serves as the reference for the comparator. A Proportional Integral Derivative (PID) controller generates a duty cycle signal based on the difference between  $V$  and  $V_1$ . The Switching block incorporates a boost converter where the insulated-gate bipolar transistor (IGBT) is activated by the gate signal produced by the pulse width modulated (PWM) generator. The duty cycle of PWM is controlled by the voltage difference observed by the comparator. The ANN algorithm ensures a consistent duty cycle for PWM through the ideal correlation between the target and trained values, leading to smooth IGBT switching operations. Additionally, the solar data subsystem sequentially provides input data (irradiance and array temperature) to the PV array, ensuring that the simulation time corresponds to the time taken for transferring the input data.

Solar radiation intensity and panel temperature both have an impact on how much power can be generated by solar panels. Hence, the input data for the artificial neural network (ANN) model is computed depends on the solar irradiance and temperature using Formulas (3) and (4).

Irradiance Calculation,  $G$  ( $\text{W}/\text{m}^2$ ):

$$G = [(G_{max} - G_{min}) \times rand] + G_{min} \quad (3)$$

Temperature Calculation,  $T$  ( $^{\circ}\text{C}$ ):

$$T = [(T_{max} - T_{min}) \times rand] + T_{min} \quad (4)$$

Maximum Voltage ( $V_{MP}$ ), at given  $G$  and  $T$

$$V_{MP} = V_{OC} + (beta \times (T - T_s)) \quad (5)$$

where  $V_{OC}$  is open circuit voltage of panel and  $T_s$  is standard temperature.

Maximum Current ( $I_{MP}$ ) at given  $G$  and  $T$

$$I_{MP} = I_M \times \left(\frac{G}{G_s}\right) \times (1 + (alpha \times (T - T_s))) \quad (6)$$

Maximum Power ( $P_{MP}$ ) at given  $G$  and  $T$

$$P_{MP} = I_{MP} \times V_{MP} \quad (7)$$

The MPPT technology that is used for the solar panel system is built with the help of data on solar irradiation, the maximum voltage produced and temperature. The solar PV array receives specific data about the amount of solar irradiation as well as the temperature from the solar data system. Equations (5)–(7) are used in order to compute the solar panel

maximum produced power ( $P_{MP}$ ), maximum generated voltage ( $V_{MP}$ ), and maximum generated current ( $I_{MP}$ ) for a variety of irradiance and temperature conditions. The data that are considered to be the output of the neural network are the voltage that is produced by the solar panel.

The rated current and temperature coefficient and rated voltage of the solar panel (1Soltech ISTH-215-P) were used as the basis for the input and output datasets that were used in the design process for the MPPT technology. Both the standard irradiance ( $G_s$ ) of the sun and the standard temperature ( $T_s$ ) are assumed to be  $1000 \text{ W/m}^2$  and 25 degrees Celsius, respectively. The irradiance levels that are regarded as the highest, or  $G_{max}$ , and the lowest, or  $G_{min}$ , are, respectively,  $1000 \text{ W/m}^2$  and  $0 \text{ W/m}^2$ . The highest temperature, denoted by the notation  $T_{max}$ , is determined to be 35 degrees Celsius, while the lowest temperature, denoted by  $T_{min}$ , is determined to be 15 degrees Celsius.

In Figure 6, the flowchart of proposed ANN algorithm is shown in order to implement the MPPT technology. In MATLAB/Simulink, the neural network toolbox function is used to construct the ANN algorithm. In order to collect data, develop and train a network, and assess the network performance, the fitting application of the ANN toolbox is utilized.

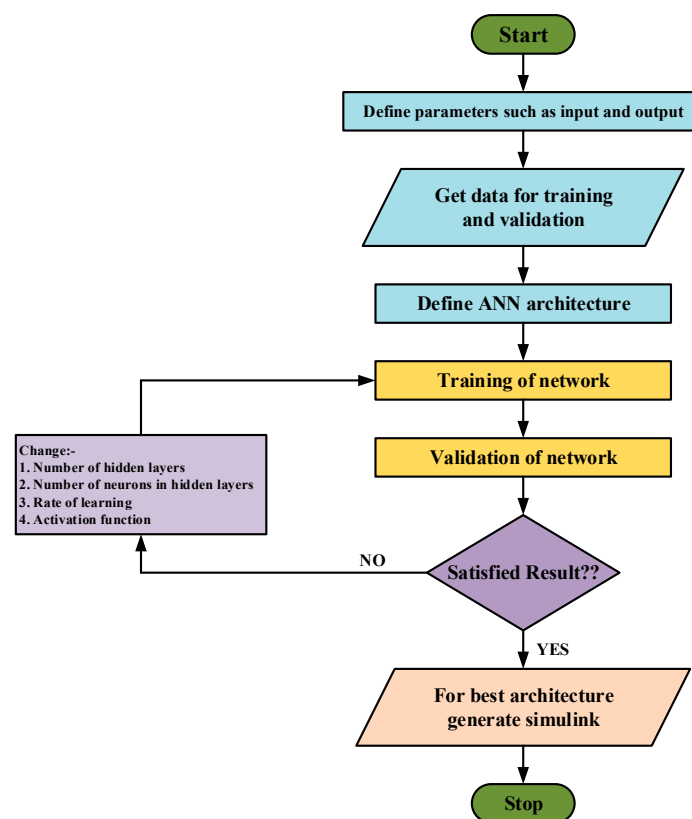


**Figure 6.** Flowchart of ANN Algorithm.

The created ANN is made up of sigmoid hidden neurons and linear output neurons, and it is built as a two-layer feedforward network. This kind of network is well-suited for solving multi-dimensional mapping issues. In order to train the neural network, one thousand datasets, including information on the temperature, irradiance and produced voltage of the chosen 1Soltech ISTH-215-P solar panel, are used. The data are then arbitrarily split into thirds: 10 percent for validation, 80 percent for training, and 10 percent for testing.

During the process of building the feedforward network, the number of neurons for the hidden layer is estimated to be 20. For training ANN datasets, a number of different training algorithms, including RP, GDM, LM, BR, SCG, and BFGS, may be used. The mean squared error, or MSE, is defined as the average squared difference between outputs and

objectives and is used by the LM algorithm, which is sometimes referred to as the damped least-squares approach.

In the LM strategy, “steepest descent” and “Gauss–Newton” are combined as two optimization techniques. When the estimated values are near to the final solution, the LM technique shifts to the Gauss–Newton method, which is initially more resistant to beginning values. This allows for a faster convergence rate. The transition from the steepest descent to the Gauss–Newton method is controlled by the “damping factor” parameter, ensuring the efficient use of the LM approach.

The parameters in question are adjusted at each iteration according to the Equation (8) [51]. The equation involves modifying the parameters based on the Jacobian matrix ( $J$ ), the damping factor ( $\lambda$ ), the identity matrix ( $I$ ), the discrepancy between the network’s intended and actual performance ( $\epsilon$ ), the number of iterations ( $k$ ), and the Hessian matrix ( $J'J + \lambda_k I$ ).

$$\theta_{k+1} = \theta_k - \left( \frac{J' \epsilon}{J'J + \lambda_k I} \right)_{\theta=\theta_k} \quad (8)$$

The damping factor must be positive for the algorithm to converge. The LM algorithm is fast and has a built-in solution in MATLAB, making it efficient to use in that environment. The MSE is used to quantify the performance of the network, with a lower number signifying greater performance. The number 1 represents a perfect correlation, the value 0 represents a random association, and the regression coefficient  $R$  determines the degree to which the outputs and targets are correlated with one another.

Since they need fewer cross-validation steps, Bayesian regularized artificial neural networks (BRANNs) are a more reliable substitute for conventional backpropagation nets. BRANNs use mathematical methods to make ridge regression, such as nonlinear regression, a well-posed statistical problem. With this technique, only one iteration is needed to generate the model that is the “most generalizable”, but it must reach a local minimum instead of a global minimum. In contrast to the hundreds or thousands of repetitions required for unregularized ANNs, testing has shown that repeating the approach five times is sufficient to prevent any aberrant behavior. The mathematical model and all aspects of BRANN are described in detail in [52,53].

When it comes to training, the SCG strategy is one that is often used for a number of different kinds of issues. It employs knowledge of the second order rather than the line-search approach, which enables the amount of memory that is utilized to be decreased. Previous research [54,55], provides a full grasp of the approach by offering a detailed description of the final algorithm for the SCG. Similarly, when it comes to handle noisy and ill-conditioned data, resilient backpropagation (RP) is a robust optimization algorithm. RP uses only the sign of the gradient to update the weights and biases, which makes it computationally efficient and suitable for large-scale problems [56]. RP does not require any learning rate parameter to be tuned, which simplifies the training process and makes it less sensitive to hyperparameter tuning.

Broyden–Fletcher–Goldfarb–Shanno (BFGS) is a quasi-Newton optimization algorithm that approximates the inverse Hessian matrix of the loss function, which makes it converge faster than first-order optimization algorithms such as gradient descent [57]. Similar to the RP algorithm, BFGS does not require any learning rate parameter to be tuned, which simplifies the training process and makes it less sensitive to hyperparameter tuning. BFGS is relatively robust to noisy and ill-conditioned data and can handle non-convex optimization problems. Furthermore, for gradient descent momentum, the momentum parameter in GDM allows the algorithm to overcome local minima and converge faster to the global minimum of the loss function [58]. GDM reduces the oscillations and noise in the update direction and therefore provides a smoother convergence path. GDM is easy to implement and computationally efficient compared to other optimization algorithms.

#### 4. Results and Discussion

The suggested model for solar energy collection involves simulating 1000 s of data transfer from a photovoltaic (PV) array to assess optimal analysis. This simulation uses a discrete approach instead of a continuous one. The accuracy of the artificial neural network (ANN) depends on the amount of training data and the selected training algorithm. Generally, larger training datasets result in less error from the ANN. The input data for the solar panel, consisting of solar irradiance and panel temperature, are supplied using a lookup table and a clock for synchronization.

The suitability of six algorithms for solar energy harvesting is also compared in this article. To assess the efficacy and performance of each method, regression, gradient, mean square error, Mu, and validation check are all employed. Regression measures the output's ability to predict the inputs, and error is determined by deducting the goal from the output. The neural network uses three main types of samples: training, validation, and testing. Data are trained through training, and the network is then modified in response to error. By terminating training if faults are found, validation checks the network's generalizability. Contrarily, testing does not alter the training data and offers a neutral evaluation of the network's performance after training.

When referring to the training dataset, an "epoch" is a single cycle. A neural network has to be trained across a number of epochs. The iteration, or quantity of partitioned training data batches or steps required to complete one epoch, is connected to the epoch. Heuristically, the network has the opportunity to view the prior data and revise the parameters of the model. The model is impartial towards the most recent few data points during training. To adjust the ANN's parameters and keep the output divergence to a minimum, a gradient is a numerical computation. Each matrix or vector representation of the network parameters is employed as a reference point in this multivariable derivative of the loss function. The ANN sometimes encounters the local minimum issue and fails to converge; thus, the Mu is added to the weight update phrase to prevent this issue. As a result, its value, which ranges from 0 to 1, directly influences the error of convergence during dataset training. The validation check is represented in training data as error minimization.

One or more selected error metrics are used to evaluate and validate a neural network (ANN) prediction model. An approximation of a function is achieved by the ANN algorithm via the use of a continuous error matrix, such as mean square error (MSE), mean absolute error (MAE), or root mean square error (RMSE).

After tallying up the mistakes across all of the inputs and outputs of the validation set, the results are then normalized based on the size of the set. Each data instance receives an application of a loss function that has been squared and then averaged across the entire dataset in order to maximize the predictive model's operation as a whole. By using error minimization, commonly known as "backpropagation," the ANN modifies its anticipated output in relation to its actual output.

##### 4.1. Levenberg–Marquardt (LM)

Levenberg–Marquardt (LM) is an optimization algorithm widely used for training ANNs. It is particularly effective in solving non-linear regression problems and finding the optimal set of weights to minimize the difference between the network's predicted outputs and the target outputs. LM is known for its fast convergence and robustness, making it a popular choice in the field of machine learning. The LM algorithm combines the benefits of both the Gauss–Newton and steepest descent methods. It iteratively updates the weights of the network by considering both local and global search directions. The primary objective of LM is to minimize a given error function, often represented by the mean squared error (MSE), which quantifies the discrepancy between the predicted and target outputs. The core idea behind LM is to adaptively adjust the step size of weight updates based on the local curvature of the error surface. It achieves this by introducing a damping parameter that controls the trade-off between the local and global search directions. In regions where the error surface is steep and narrow, the damping parameter reduces the step size to

avoid overshooting the optimal solution. Conversely, in regions where the error surface is flat, the damping parameter increases the step size to speed up convergence. The LM algorithm starts with an initial set of weights and computes the Jacobian matrix, which represents the sensitivity of the network's outputs to changes in the weights. The Jacobian is used to approximate the Hessian matrix, which describes the curvature of the error surface. The Hessian matrix is modified by adding a damping term to ensure its positive definiteness, which guarantees the convergence of the algorithm. During each iteration, the LM algorithm updates the weights by solving a system of linear equations derived from the modified Hessian matrix and the gradient of the error function. This update step is performed iteratively until the error function reaches a minimum or a convergence criterion is met. The convergence criterion is often based on the change in the error function between iterations. One of the key advantages of LM is its ability to handle non-linear regression problems effectively. Unlike other gradient-based methods, the LM does not require explicit computation of the Hessian matrix, which can be computationally expensive for large networks. Instead, it approximates the Hessian using the Jacobian matrix and adapts the damping parameter to ensure stable convergence.

Another advantage of LM is its robustness to local minima. The combination of local and global search directions allows LM to escape from shallow local minima and find better solutions. This property makes LM particularly useful in situations where the error surface is complex and contains multiple local minima. Implementing LM for ANN training requires careful initialization of the weights and tuning of the damping parameter. In practice, the initial weights can be randomly assigned or set based on prior knowledge of the problem domain. The damping parameter is typically adjusted dynamically during the training process based on the convergence behavior of the algorithm. In conclusion, the Levenberg–Marquardt (LM) algorithm is a powerful optimization method for training artificial neural networks (ANNs). Its combination of local and global search directions, adaptive step size adjustment, and robustness to local minima make it an effective tool for solving non-linear regression problems. LM's fast convergence and stability contribute to its widespread use in the field of machine learning. With its ability to handle complex error surfaces and find optimal solutions, LM plays a significant role in the successful training of ANNs and the advancement of the field.

The plot in Figure 7 demonstrates the accuracy of the ANN's prediction of output in relation to input, indicated by the regression ( $R = 1$ ) measurement. Error is defined as the variance between the solar panel's produced voltage output and its intended generated voltage, which is determined by deducting the output from the target. The regression plot illustrates that the LM algorithm has effectively trained the data with minimal error, as the output follows the desired value quite closely.

This approach for ANN is further validated by Figure 8, which shows zero error in the data matching training phase, validation phase, and test phases. The bins indicate how many vertical bars there are in the error histogram in Figure 8, where the total ANN error varies from  $-0.0004$  (the leftmost bin) to  $0.0000512$  (the rightmost bin). It is shown how many samples from the chosen dataset fit into each of the 20 smaller bins that make up the error range. For 100 samples from the validation dataset, the bin with the error value  $-0.0000015$  is in the center of the error histogram. The use of ANN for MPPT shows convergence at 20 bins with 0% error in the error histogram.

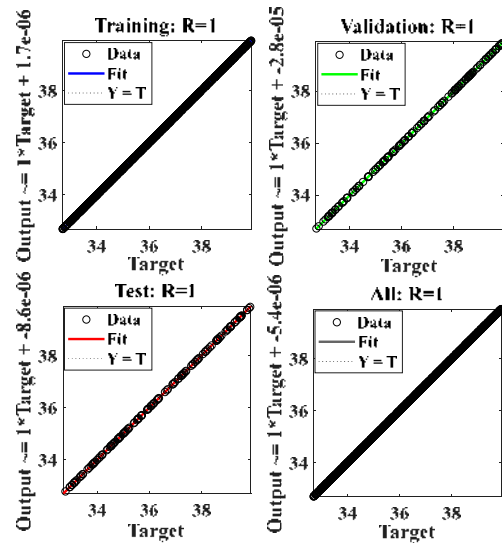


Figure 7. Regression plot of LM algorithm.

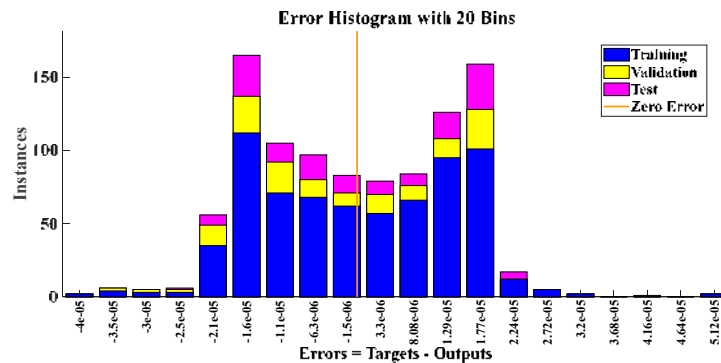


Figure 8. Error histogram plot of LM algorithm.

Figures 9 and 10 illustrate the training stage and performance phase of the ANN for the purpose of processing the selected dataset, respectively. The validation check, as well as the gradient and momentum parameter ( $\mu$ ), for the training dataset are shown in Figure 9 at 1000 epochs. The simulation indicates that the gradient is  $7.983 \times 10^{-6}$  at the 1000 epoch, which represents the insignificant variances from the training data with a small loss function. The simulation's findings indicate that a choice to produce zero outputs and the mean for each input vector make up the cumulative error. The LM algorithm suitability for MPPT is justified by the extremely low value of gradient,  $\mu$  and validation tests of the training dataset.

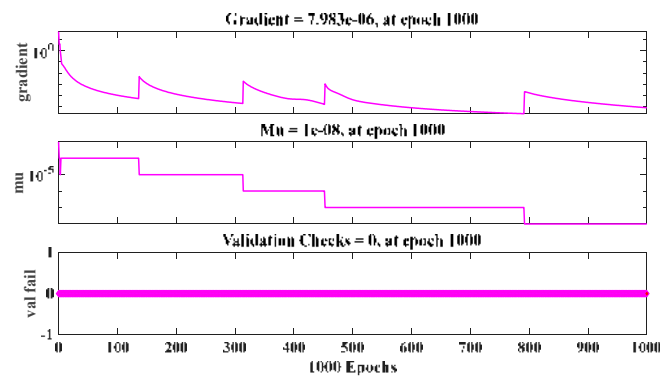
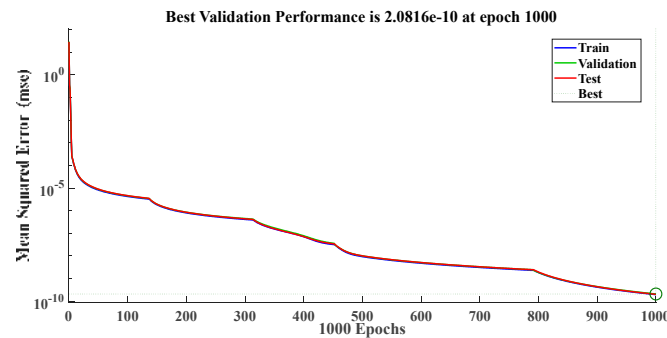


Figure 9. Training test plot of LM algorithm.





**Figure 10.** Performance plot of LM algorithm.

Figure 10 depicts the MSE for the trained dataset samples at different epochs, with the best training result being achieved at 1000 epochs. As a consequence of this, the trained dataset displays the highest level of validation performance after 1000 epochs have passed. In accordance with the findings of the simulation, the validation performance of  $2.0816 \times 10^{-10}$ , which is reached at the 1000 epoch, is the best possible value. The estimation of MPPT provided by the LM method had a nearly zero validation performance, which means that its error was minimal.

#### 4.2. Bayesian Regularization (BR)

BR is a mathematical method like ridge regression that is used to solve nonlinear regression problems in a well-posed way. In this method, the nonlinear regression is turned into a statistical problem, and a conjugate gradient descent or a similar minimizer is used to find a solution. The advantage of using BR over traditional backpropagation methods is that it is more stable and eliminates the importance of thorough cross-validation. The method only requires a single iteration to create the model that is “most generalizable”, although repeating the process several times may be necessary to ensure a local minimum is reached instead of a global minimum. BRANN is a type of neural network that uses BR for training and is successful in solving a broad range of problems. It uses second-order knowledge instead of line-search methods, which uses less memory. The BR is a powerful technique used for training ANNs that addresses the challenges of overfitting and model complexity. By incorporating Bayesian principles into the training process, BR provides a probabilistic framework that allows for more robust and stable learning. The primary objective of BR is to find the optimal balance between fitting the training data well and avoiding overfitting. Overfitting occurs when the model becomes too complex and starts to memorize the training data instead of generalizing well to unseen data. BR tackles this issue by introducing a regularization term into the training objective, which encourages simpler and more robust models. The core idea behind BR is to impose a prior distribution over the weights of the network and update this distribution during the training process. The prior distribution reflects our prior beliefs about the values of the weights before observing the data. By incorporating prior knowledge, BR provides a regularization mechanism that constrains the model’s complexity and prevents it from overfitting.

During training, BR aims to find the posterior distribution of the weights given the observed data. This is achieved by maximizing the posterior probability using the training data and the prior distribution. The posterior distribution represents the updated beliefs about the weights after observing the data. The optimization process involves finding the weight values that maximize the posterior probability, which can be approached using various methods such as Markov chain Monte Carlo (MCMC) or variational inference. In conclusion, Bayesian regularization (BR) is a powerful technique for training artificial neural networks (ANNs) that addresses the challenges of overfitting and model complexity. By incorporating Bayesian principles, BR provides a probabilistic framework that allows for more robust and stable learning. Its ability to automatically determine the regularization strength and provide uncertainty estimates for predictions makes it a valuable tool in

the field of machine learning. With its adaptability and robustness, BR contributes to the advancement of ANN training and its successful application in various domains.

From the regression plot in Figure 11, the trained dataset does not need to go through a validation step. In the regression diagram, the best correlation between output and desired generated voltage is shown by the value  $R = 1$ , which indicates that the data for the solar PV system were appropriately trained.

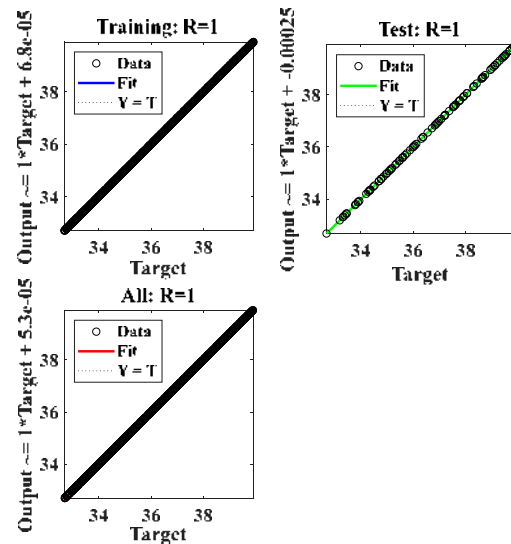


Figure 11. Regression plot of BR algorithm.

Figure 12 depicts the trained dataset, which contains zero errors in both the training and testing phases and total errors that range from  $-0.00111$  (the bin on the left) to  $0.00116$  (the bin on the right) (the rightmost bin). The gradient and Mu in the training state phase are, at the 1000th epoch,  $0.00010493$  and  $5000$ , respectively. The error histogram plot of the BR algorithm is shown in Figure 13; there are 20 smaller bins, and the central bin has a near-zero error of  $0.000037$  for 100 samples, which is larger than that of the LM approach.

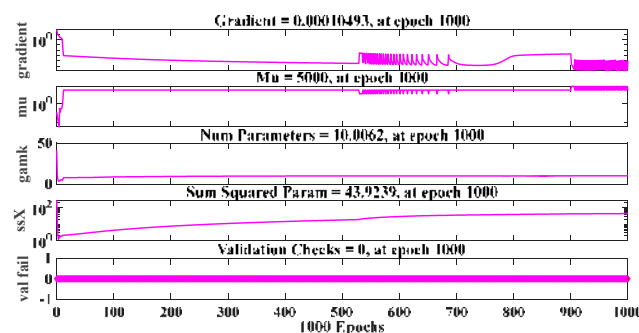


Figure 12. Training test plot of BR.

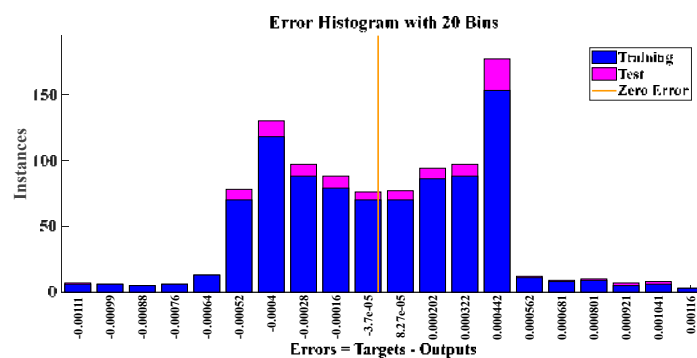
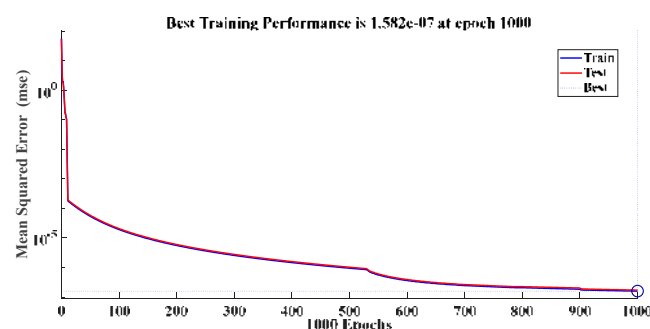


Figure 13. Error histogram plot of BR.

The actual number of parameters at the 1000th epoch is 10.0062; however, the total squared parameters at that time amount to 43.9239. This is shown by the LM method's slower backpropagation capacity for the training dataset and by the high value of Mu as well as an efficient number of parameters and absence of any validation tests.

Compared to the BR approach, which starts with an objective function for the prediction and adds the residual sum of squares and sum of squared weights for reducing the prediction error, the LM algorithm gives quicker convergence in predicting training data with near to zero error. As a consequence, the LM approach generally performs training dataset processing faster than the BR technique. Figure 14, which shows convergence of trained data with the optimum training outcome after 1000 iterations, shows the mean squared error at various epochs. The robustness of the BR method is shown by the best training performance of  $1.582 \times 10^{-7}$  at the 1000 epoch with no validation phase.



**Figure 14.** Performance plot of BR.

#### 4.3. Scaled Conjugate Gradient (SCG)

The scaled conjugate gradient (SCG) algorithm is a powerful optimization technique commonly used for training artificial neural networks (ANNs). It offers an efficient and effective approach to updating the network's weights, facilitating convergence and improving the network's performance. ANNs are computational models inspired by the structure and functioning of the human brain. They are composed of interconnected nodes, known as neurons, which work together to process and transmit information. ANNs have gained significant attention in various fields due to their ability to learn from data and make accurate predictions. Training an ANN involves adjusting the weights of its connections to minimize the difference between the predicted outputs and the target outputs. The optimization algorithm used for weight adjustment plays a crucial role in determining the network's performance. The SCG algorithm is a popular choice for this task due to its desirable properties.

The SCG algorithm is based on the conjugate gradient (CG) method, a well-known optimization technique. The CG method aims to find the minimum of a function by iteratively updating the weight values. However, the SCG algorithm introduces a scaling factor that ensures the gradients have the same magnitude, which accelerates convergence. This scaling property allows the algorithm to adaptively adjust the learning rate for each weight update, leading to efficient weight adjustments and improved convergence speed. One of the key advantages of the SCG algorithm is that it eliminates the need for an explicit line search procedure, which is often required in traditional gradient-based optimization algorithms [59]. The line search procedure is responsible for determining an appropriate learning rate at each iteration. By incorporating second-order information and using a scaling approach, the SCG algorithm estimates the learning rate without the need for repetitive line search calculations. This feature significantly reduces the computational burden and makes the algorithm more efficient. The SCG algorithm exhibits excellent performance in handling non-linear optimization problems, making it particularly suitable for training ANNs with complex architectures. It has been successfully applied in various domains, including pattern recognition, data mining, and control systems. Researchers and practitioners often rely on the SCG algorithm to optimize the performance of their

neural network models and achieve accurate predictions in real-world applications. One notable advantage of the SCG algorithm is its robustness to noise and ill-conditioned problems. Ill-conditioned problems refer to situations where slight changes in input data or initial weights can have a significant impact on the optimization process. The SCG algorithm's adaptive learning rate and scaling properties help mitigate the effects of such issues, making it more stable and reliable. Another significant benefit of the SCG algorithm is its good generalization capability. Generalization refers to the ability of a trained network to perform well on unseen data. The SCG algorithm's efficient weight adjustments and convergence properties contribute to improved generalization, allowing the network to make accurate predictions on new and unseen instances. To summarize, the SCG algorithm offers several advantages for training ANNs. Its efficient weight adjustment scheme, adaptive learning rate estimation, and scaling properties contribute to faster convergence and improved generalization capabilities. The algorithm's robustness to noise and ill-conditioned problems makes it a reliable choice for various applications. Researchers and practitioners rely on the SCG algorithm to optimize the performance of their neural network models and achieve accurate predictions in diverse fields.

In comparison to the LM and BR algorithms, the  $R$  is somewhat less than 1, as seen by the regression plot in Figure 15. A regression value less than 1 for the SCG algorithm implies that there might be some level of inconsistency or error in the predictions made by the algorithm. The deviation from a perfect correlation suggests that there is room for improvement in the algorithm's ability to accurately predict the output based on the given input. In comparison, when the regression value is 1, it indicates a perfect correlation between the input and output data, suggesting that the algorithm is able to accurately capture the relationship between the variables.

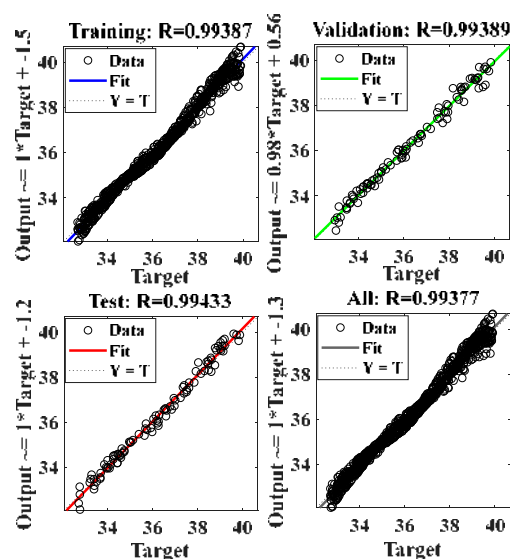


Figure 15. Regression plot of SCG algorithm.

As can be seen in Figure 16, the total error for the trained dataset varies from  $-0.7406$  (the leftmost bin) to  $0.8365$  (the rightmost bin) when there is no mistake at any point throughout the training phase, validation phase, or test phase. The error histogram shows that the center bin has a value that is  $-0.006443$  (100 samples) higher than the value produced by the LM and BR algorithms. After 75 iterations, Figure 17 displays a gradient with a value of  $0.14161$ , while the validation tests have a value of 6. When data training is terminated after 75 epochs, the SCG's performance in terms of achieving the target objective suffers as a direct result.

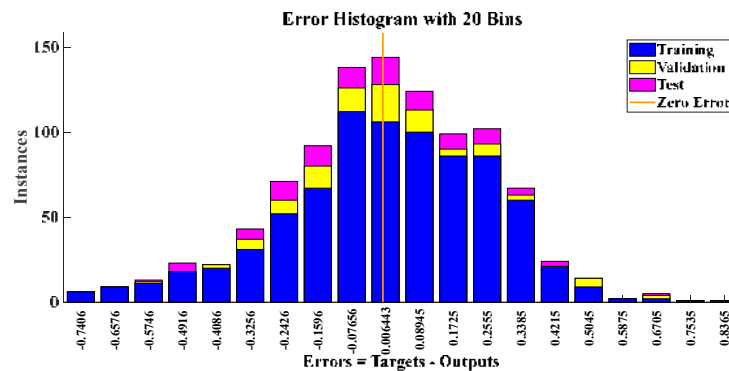


Figure 16. Error histogram of SCG algorithm.

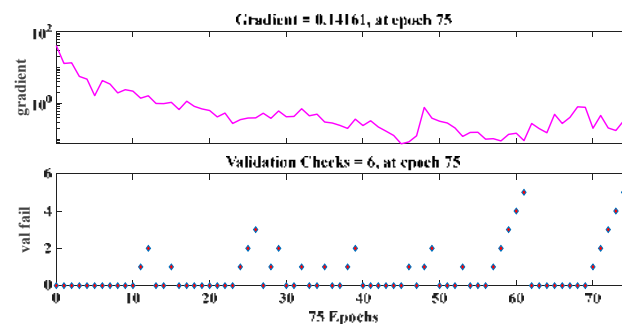


Figure 17. Training test plot of SCG.

The performance gradient for validation is higher than the maximum time for failure and lower than the lowest gradient. Figure 18, which represents the convergence of training data with the highest validation performance of 0.052985 at 75 epochs, displays the mean squared error at various epochs. The learned dataset for the solar PV system do not suit the SCG algorithm, despite having greater validation performance and a lower total training performance than the LM and BR algorithms. Similar to this, the BR method is less suitable than the LM algorithm due to the high processing time for prediction and the large momentum parameter.

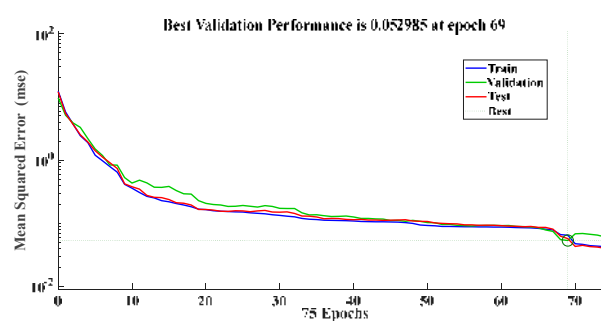


Figure 18. Performance plot of SCG.

#### 4.4. Resilient Backpropagation (RP)

Resilient backpropagation (RP) is a gradient-based optimization algorithm commonly used in training artificial neural networks (ANNs). It is a variation of the traditional backpropagation algorithm that uses a different update rule for adjusting the weights of the neural network during training.

The key feature of the RP algorithm is its use of a dynamic learning rate for each weight in the network. The learning rate determines the step size used to update the weights during the backpropagation process and can have a significant impact on the convergence and stability of the training process. In traditional backpropagation, a fixed learning rate is

used for all weights, which can lead to slow convergence or even divergence if the learning rate is set too high or too low.

The RP algorithm overcomes this problem by using two different update rules based on the sign of the gradient of the error function with respect to the weight. If the gradient changes sign from one iteration to the next, indicating that the optimization process is moving in the wrong direction, the learning rate for that weight is reduced by a factor (e.g., 0.5). If the gradient has the same sign as the previous iteration, indicating that the optimization process is moving in the right direction, the learning rate is increased by a factor (e.g., 1.2). If the gradient is zero, indicating that the weight has reached a stationary point, the learning rate is unchanged.

This approach is known as a “resilient” update rule, as it allows the algorithm to recover quickly from bad updates and adapt to changing conditions during the optimization process. By adjusting the learning rate dynamically for each weight, the RP algorithm can achieve faster convergence and better stability compared to traditional backpropagation. Another advantage of the RP algorithm is its ability to handle noisy or ill-conditioned data, which can cause traditional optimization algorithms to become stuck in local minima. By adjusting the learning rate dynamically, the RP algorithm is able to navigate complex, high-dimensional search spaces more effectively and avoid becoming trapped in local minima. Hence, the RP algorithm is a robust and efficient optimization algorithm that is well-suited for training ANNs. Its ability to adapt to changing conditions and handle noisy data make it a popular choice for many machine learning applications.

From the regression plot in Figure 19, the trained dataset does not need to go through a validation step. In the regression diagram, the best correlation between output and desired generated voltage is shown by the value  $R = 1$ , which indicates that the data for the solar PV system were appropriately trained.

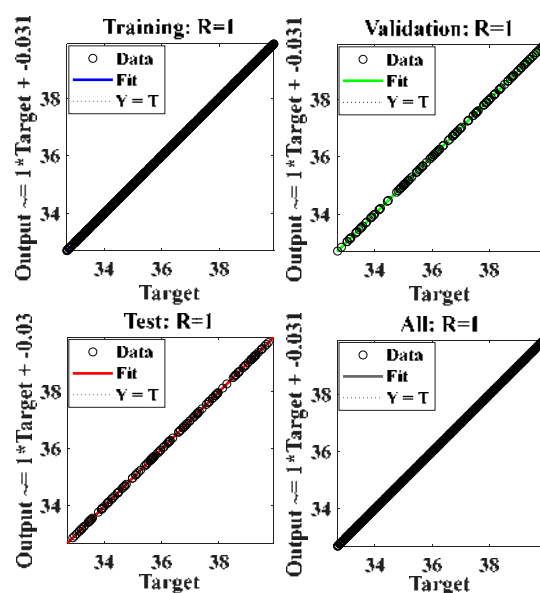


Figure 19. Regression plot of RP algorithm.

After 21 iterations, Figure 20 displays a gradient with a value of 0.033415, while the validation tests have a value of 6 at 21 epochs. A gradient value of 0.033415 indicates the rate of change or steepness of the objective function with respect to the algorithm’s parameters. A low gradient value indicates that the algorithm is making progress towards the optimal solution, and the estimate is close to the true minimum. This value suggests that the RP algorithm is making significant progress towards optimizing the objective function and reaching the desired solution. The validation tests having a value of 6 at 21 epochs implies that the algorithm’s predictions during the validation phase have a relatively larger deviation from the true values compared to desired accuracy. This indicates that the



algorithm may not be performing optimally in terms of accurately predicting the target values during the validation phase.

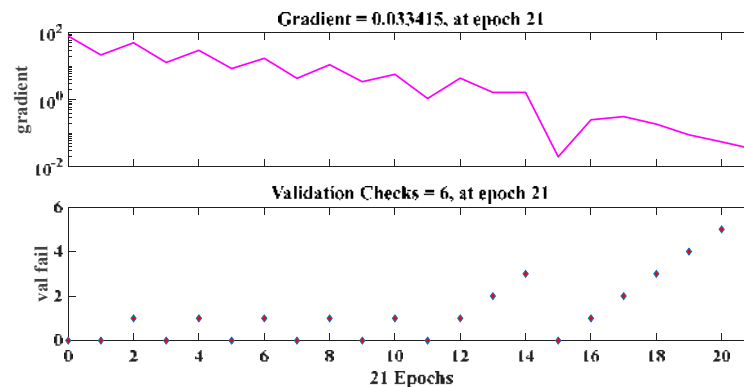


Figure 20. Training plot of RP algorithm.

Figure 21 displays the mean squared error at a number of different epochs. This figure illustrates the convergence of trained data with the optimal training result after 15 iterations. The greatest training performance of  $2.8668 \times 10^{-6}$  was achieved at the 15 epoch even though there was no validation phase, which demonstrates the resilience of the RP algorithm.

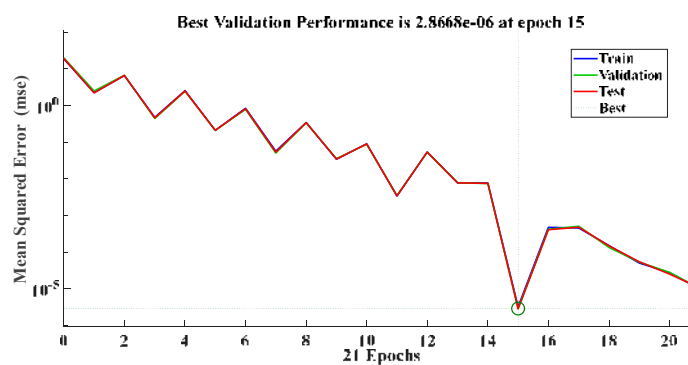


Figure 21. Performance test plot of Rp algorithm.

#### 4.5. Gradient Descent Momentum (GDM)

Gradient descent momentum (GDM) is a popular optimization algorithm for training artificial neural networks (ANNs). It is a variation of the traditional gradient descent algorithm that incorporates a momentum term to help speed up the convergence of the optimization process. The momentum term allows the algorithm to “remember” the direction it has been moving in the past and use that information to help accelerate the optimization process.

The basic idea behind gradient descent with momentum is to add a “velocity” term to the weight updates that takes into account the direction and magnitude of previous weight updates. Specifically, the velocity for weight ‘ $w$ ’ at iteration ‘ $t$ ’ is given by:

$$V_t(w) = \alpha \times V_{t-1}(w) - \eta \times \nabla \in (w_t) \quad (9)$$

where  $\alpha$  is the momentum coefficient (typically set to a value between 0 and 1),  $\eta$  is the learning rate,  $\in (w_t)$  is the error function at iteration  $t$ , and  $\nabla \in (w_t)$  is the gradient of the error function with respect to weight  $w$  at iteration  $t$ .

The weight update at iteration  $t$  is then given by:

$$w_{t+1} = w_t + V_t(w) \quad (10)$$

The momentum term allows the algorithm to “smooth out” the weight updates over time, reducing the impact of small, noisy changes in the gradient and helping to avoid getting stuck in local minima. The momentum term can also help the algorithm to accelerate when the gradient is pointing consistently in the same direction, allowing it to move more quickly towards the global minimum. One of the key advantages of GDM is its ability to handle noisy or ill-conditioned data, which can cause traditional optimization algorithms to become stuck in local minima. By incorporating information about the direction and magnitude of previous weight updates, the momentum term allows the algorithm to navigate complex, high-dimensional search spaces more effectively and avoid becoming trapped in local minima. Another advantage of gradient descent with momentum is its ability to handle non-convex objective functions. Non-convex objective functions can be difficult to optimize using traditional gradient descent, as the optimization process can become stuck in local minima. By incorporating information about the direction and magnitude of previous weight updates, the momentum term allows the algorithm to explore more of the search space and avoid becoming trapped in local minima. Hence, gradient descent with momentum is a powerful and efficient optimization algorithm that is well-suited for training ANNs. Its ability to handle noisy or ill-conditioned data and to navigate complex, high-dimensional search spaces make it a popular choice for many machine learning applications.

In comparison to the LM, RP, BFGS, and BR algorithms, the R is somewhat less than 1, as seen by the regression plot in Figure 22 for GDM algorithm.

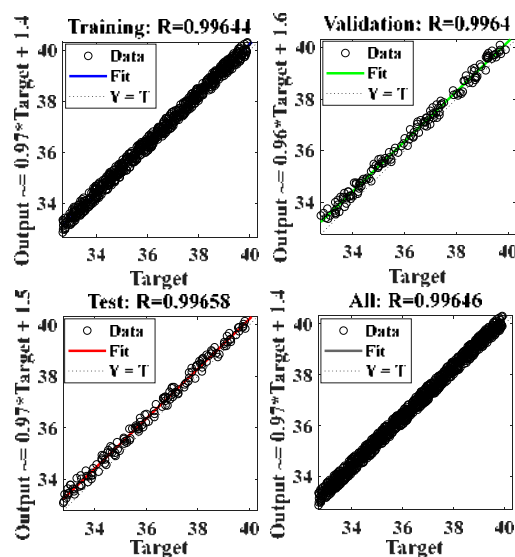


Figure 22. Regression plot of GDM algorithm.

A regression value of 0.996 indicates a strong positive correlation between the predicted values and the actual values in the training dataset, while a regression value of 1 indicates a perfect positive correlation between the predicted values and the actual values.

Figure 23 displays a gradient with a value of 11.485, while the validation tests have a value of 6 at 8 epochs. The higher value of gradient for GDM algorithm indicates that the current estimate is far from the true minimum, and the algorithm needs to take large steps to get closer to it. This could result in overshooting the minimum or becoming stuck in a local minimum instead of the global minimum, which can lead to poor performance.

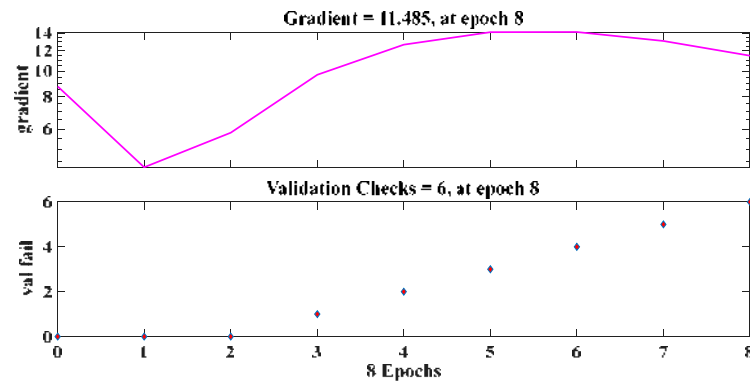


Figure 23. Training plot of GDM algorithm.

Figure 24 displays the performance plot of GDM algorithm. The plot shows that the algorithm achieves its best validation performance of 0.15378 at 2 epochs. A validation performance of 0.15378 indicates that the algorithm's predictions have a relatively moderate level of deviation from the true values of the validation dataset. Although not as low as achieving near-zero validation performance, this value still demonstrates a reasonable level of accuracy in estimating the desired output within a very short training time.

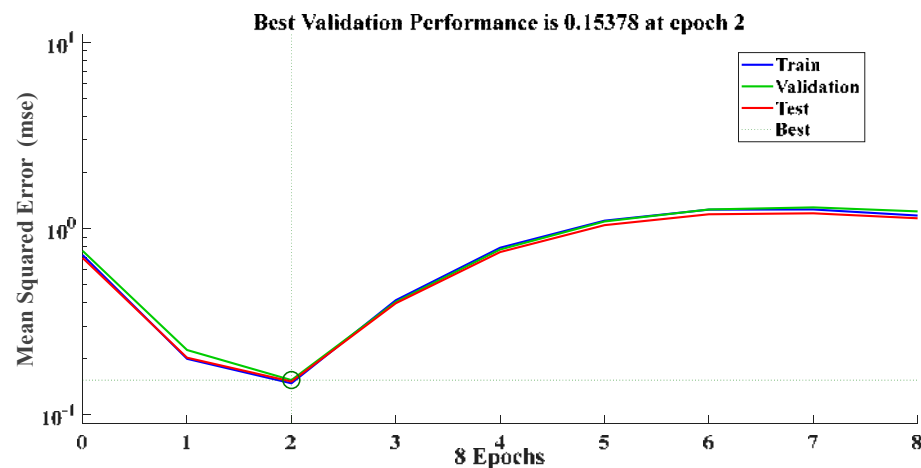


Figure 24. Performance plot of GDM algorithm.

#### 4.6. Broyden–Fletcher–Goldfarb–Shanno (BFGS) Quasi Newton

The Broyden–Fletcher–Goldfarb–Shanno (BFGS) algorithm is a popular quasi-Newton method for unconstrained optimization, commonly used in training artificial neural networks (ANNs). The basic idea behind the BFGS algorithm is to approximate the inverse Hessian matrix of the objective function, which is a measure of how the gradient of the function changes as the weights of the network are updated. By using this approximation, the algorithm is able to estimate the direction and magnitude of weight updates that are likely to lead to a decrease in the objective function.

The BFGS algorithm works by iteratively updating an approximation of the inverse Hessian matrix, denoted by  $H_k$ , at each iteration  $k$ . The weight update at iteration  $k$  is then given by:

$$W_{k+1} = W_k - \alpha_k \times H_k \times \nabla \in (W_k) \quad (11)$$

where  $\alpha_k$  is a step size parameter,  $\nabla \in (W_k)$  is the gradient of the objective function with respect to the weights at iteration  $k$ , and  $H_k$  is the approximate inverse Hessian matrix.

The BFGS algorithm uses a rank-2 update formula to update the approximate inverse Hessian matrix at each iteration. Specifically, the update formula is given by:

$$H_{k+1} = (1 - P_k \times S_k \times Y_{kT}) \times H_k (1 - P_k \times Y_k \times S_{kT}) + P_k \times S_k \times S_{kT} \quad (12)$$

where  $S_k = W_{k+1} - W_k$ ,  $Y_k = \nabla \in (W_{k+1}) - \nabla \in (W_k)$ , and  $P_k = \frac{1}{(Y_k^T \times S_k)}$ . This update formula is designed to approximate the true inverse Hessian matrix, while also maintaining the positive definiteness of the approximation.

One of the key advantages of the BFGS algorithm is its ability to handle non-convex objective functions, which are commonly encountered in ANNs. Non-convex objective functions can be difficult to optimize using traditional gradient descent methods, as the optimization process can become stuck in local minima. The BFGS algorithm is able to overcome this problem by using an approximation of the inverse Hessian matrix, which allows it to navigate complex, high-dimensional search spaces more effectively.

Another advantage of the BFGS algorithm is its ability to handle ill-conditioned or noisy data. Traditional optimization algorithms can be sensitive to noisy or ill-conditioned data, which can cause them to become stuck in local minima. The BFGS algorithm is able to overcome this problem by using an approximation of the inverse Hessian matrix, which allows it to smooth out noisy or ill-conditioned data and navigate the search space more effectively. Hence, the BFGS algorithm is a powerful and efficient optimization algorithm that is well-suited for training ANNs. Its ability to handle non-convex objective functions and ill-conditioned or noisy data makes it a popular choice for many machine learning applications. However, like all optimization algorithms, it may require careful tuning of the step size parameter and other hyperparameters to achieve optimal performance on a given problem.

Figure 25 is a figure that indicates how accurate the ANN's prediction of output in relation to input is. This accuracy is demonstrated by the regression measurement of  $R = 1$ , which is shown in the plot. The regression plot demonstrates that the BFGS method has successfully trained the data with a small amount of error by displaying the output in a manner that closely reflects the intended value. In other words, the BFGS algorithm accurately captures the relationship between the input variables (such as solar irradiance and temperature) and the corresponding output variable (such as voltage and power output in energy harvesting applications). This high regression value signifies that the BFGS algorithm is effectively modeling and predicting the behavior of the energy harvesting system, making it a reliable and precise algorithm for optimizing energy extraction from solar photovoltaic systems.

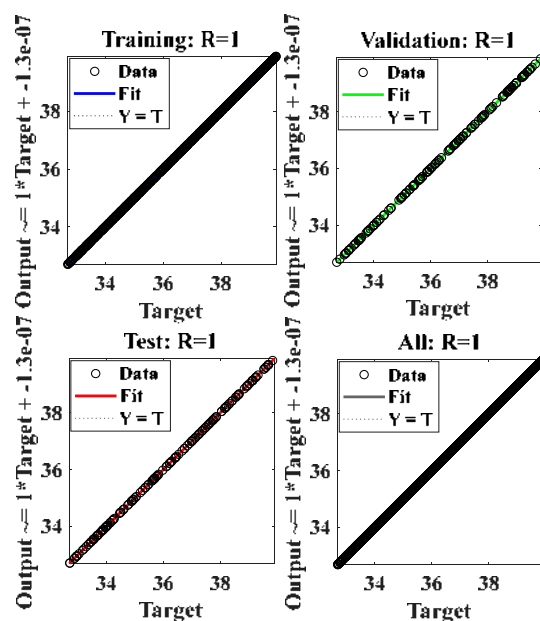


Figure 25. Regression plot of BFGS algorithm.

In Figure 26, a training plot of the BFGS algorithm is shown. The validation check as well as the gradient and reset values for the training dataset are shown at 10 epochs.

The algorithm attained a gradient with a value of  $1.0211 \times 10^{-7}$ , while the validation tests and resets had no value at 10 epochs. A gradient value of  $1.0211 \times 10^{-7}$  indicates that the algorithm's estimate of the optimal solution is very close to the true minimum. In general, a lower gradient value suggests that the algorithm is converging well and making small, steady steps towards the optimal solution. This indicates that the algorithm is effectively adjusting its parameters to minimize the difference between predicted and actual values, resulting in improved accuracy. The fact that the validation tests and resets have no value at 10 epochs suggests that the algorithm has successfully learned and generalized the underlying patterns in the training data. This means that the algorithm's predictions align well with the validation dataset, and there is no need for further adjustments or resets at this point. Overall, these findings indicate that the algorithm has achieved a high level of accuracy and convergence, making it a reliable choice for MPPT (maximum-power point tracking) energy harvesting in solar PV systems.

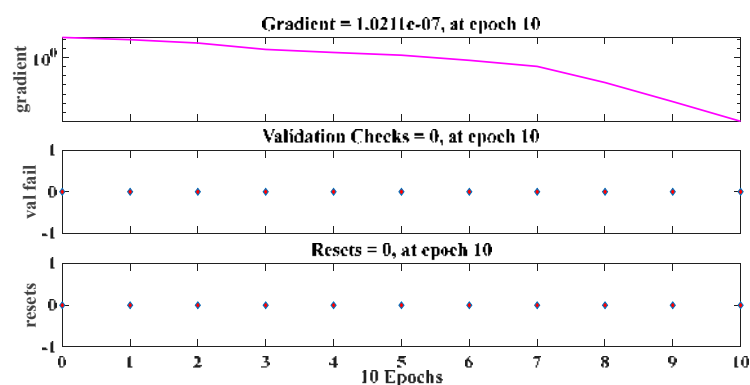


Figure 26. Training plot of BFGS algorithm.

In Figure 27, The convergence of training data with the highest performance value of the BFGS algorithm is displayed. The algorithm attained the best validation performance of  $9.98 \times 10^{-17}$  at 10 epochs. A validation performance of  $9.98 \times 10^{-17}$  indicates that the algorithm's predictions are extremely close to the true values of the validation dataset. This near-zero validation performance suggests that the algorithm has successfully learned the underlying patterns and relationships in the training data, and it can generalize its predictions accurately to unseen data. It also suggests that the algorithm is capable of accurately capturing the complex relationships between input variables and the desired output, enabling it to make precise predictions for MPPT (maximum-power point tracking) energy harvesting in solar PV systems.

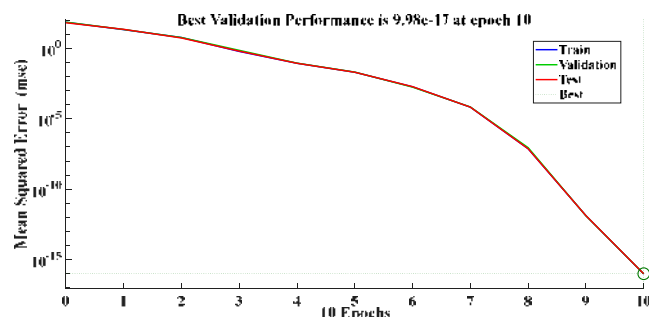
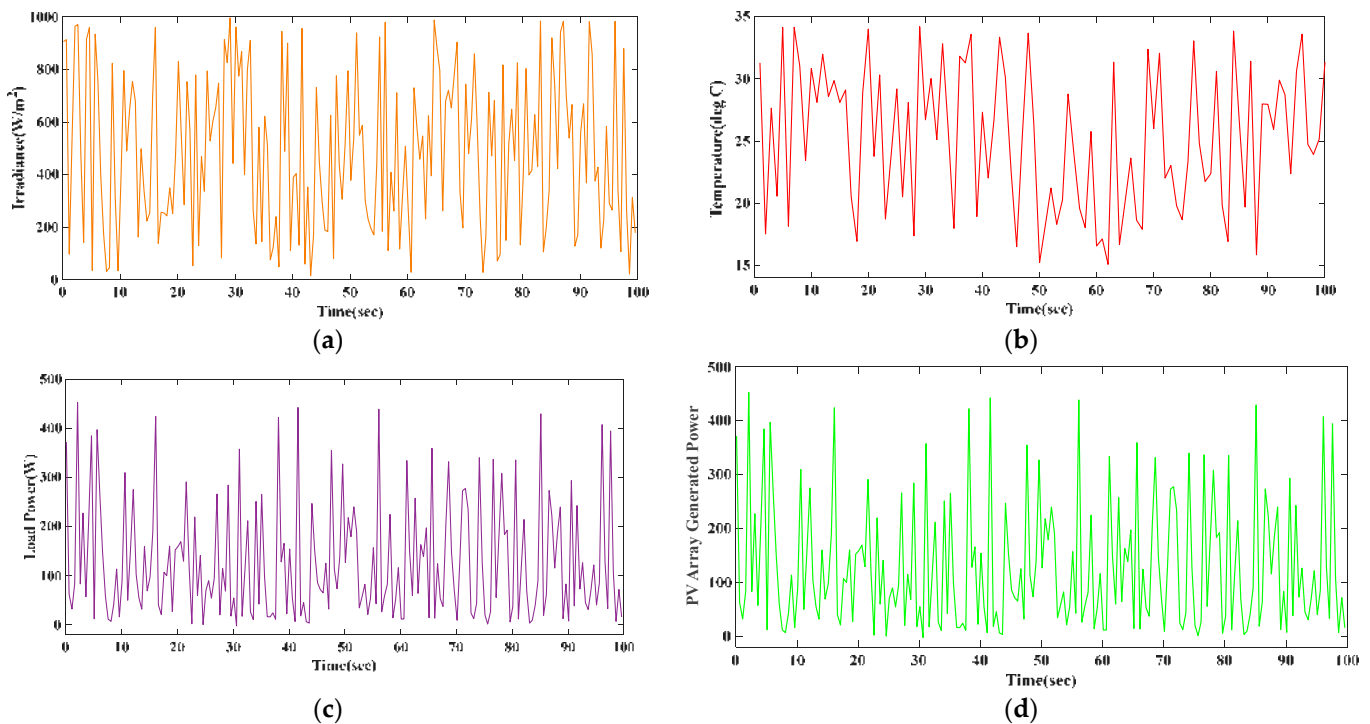


Figure 27. Performance plot of BFGS algorithm.

In relation to solar radiation and array temperature, respectively, Figure 28a–d show the output power and load power of the PV array. According to the MPPT topology of ANN, both powers are claimed to follow the solar irradiation and the temperature of the PV array. Based on the amount of simulation time that has passed, the PV array's

produced power, load power, irradiance, and temperature are shown here. The MPPT is satisfied when the array temperature is 15 degrees Celsius and the sun irradiance is 200 watts per square meter. This results in the lowest power output of 100 watts. With an array temperature of 35 degrees Celsius and a solar irradiation of 1000 watts per square meter, the power output reaches its maximum of 450 watts. The ripples in the output power are not smoothed out by this model since it does not have filter component. As a direct consequence of this, the power waveforms that are created and loaded have discernible ripples.



**Figure 28.** (a) Irradiance ( $\text{W}/\text{m}^2$ ) versus time (s) plot of the solar panel, (b) temperature ( $^{\circ}\text{C}$ ) versus time (s) plot of the solar panel, (c) load power (W) versus time (s) plot of the solar panel, (d) and power generated (W) versus time (s) of the panel.

Table 2 presents a dataset consisting of matching values for solar irradiance ( $G$ ) in watts per square meter ( $\text{W}/\text{m}^2$ ), temperature ( $T$ ) in degrees Celsius ( $^{\circ}\text{C}$ ), and maximum voltage ( $V_{\text{max}}$ ) in volts (V). The table contains 120 rows, each representing a specific observation or data point. These 120 data points are sample data among 1000 data points. Using Equations (3)–(5) of solar irradiance, temperature, and maximum voltage, the data in Table 2 were generated. These equations are used to calculate the solar irradiance ( $G$ ), temperature ( $T$ ), and maximum voltage ( $V_{\text{MP}}$ ) based on specific parameters and random values. Furthermore, the data were used to train the neural network.

**Table 2.** ANN databases of matching values of solar irradiance,  $G$  ( $\text{W}/\text{m}^2$ ), temperature,  $T$  ( $^{\circ}\text{C}$ ), and maximum voltage,  $V_{\text{max}}$  (V).

S. No.	Solar Irradiance ( $\text{W}/\text{m}^2$ )	Temperature ( $^{\circ}\text{C}$ )	Maximum Voltage ( $V_{\text{max}}$ )
1	905.7919371	31.29447373	34.02775793
2	913.3758561	17.53973633	38.99308058
3	97.540405	27.64718492	35.34439271
4	546.8815192	20.56996438	37.89919856



Table 2. Cont.

S. No.	Solar Irradiance (W/m <sup>2</sup> )	Temperature (°C)	Maximum Voltage (V <sub>max</sub> )
5	964.8885352	34.15013671	32.99689215
6	970.5927818	18.15226163	38.77196507
7	485.3756487	34.14333896	32.99934607
8	141.8863386	31.00560938	34.13203507
9	915.7355252	23.43522565	36.86486789
10	959.4924264	30.84414659	34.19032152
11	35.71167857	28.11481398	35.1755833
12	933.9932478	31.98258612	33.77935624
13	757.7401306	28.5747031	35.00956793
14	392.2270195	29.86264936	34.54463221
15	171.1866878	28.1095578	35.17748073
16	31.83284638	29.12092176	34.81238845
17	46.17139063	20.5384597	37.91057143
18	823.4578283	16.94263562	39.20862797
19	317.0994801	28.89657246	34.89337631
20	34.4460805	34.00444098	33.04948685
21	381.5584571	23.77488719	36.74225347
22	795.1999011	30.31033576	34.38302189
23	489.7643958	18.73745209	38.56071717
24	646.3130101	23.91172401	36.69285675
25	754.686682	29.18729662	34.78842779
26	679.7026769	20.52050154	37.91705415
27	162.6117352	28.10196008	35.18022343
28	498.364052	17.37995363	39.05076054
29	340.3857267	34.19487917	32.98074057
30	223.8119395	26.70535502	35.68438389
31	255.0951155	30.02534119	34.48590209
32	699.0767227	25.11914103	36.25699128
33	959.2914252	32.81806505	33.4777567
34	138.6244428	25.9443106	35.95911332
35	257.5082541	17.98588011	38.83202714
36	254.282179	31.81434512	33.84008956
37	243.5249687	31.28569652	34.03092641
38	349.983766	33.58527246	33.20080249
39	251.083858	18.93190501	38.49052161
40	473.2888489	27.32089352	35.46218065
41	830.8286279	22.03319014	37.37098869
42	549.7236083	26.70528182	35.68441031
43	285.8390188	33.34387328	33.28794519
44	753.7290943	30.14400458	34.44306579

Table 2. Cont.

S. No.	Solar Irradiance (W/m <sup>2</sup> )	Temperature (°C)	Maximum Voltage (V <sub>max</sub> )
45	567.8216407	22.60891694	37.16315707
46	53.95011867	16.51708579	39.3622472
47	779.1672301	25.61595106	36.07764783
48	129.9062085	33.68021368	33.16652966
49	469.3906411	26.37647322	35.80310693
50	337.1226444	15.23804139	39.82396944
51	794.2845407	18.24364616	38.73897617
52	528.5331355	21.22430084	37.66298964
53	601.9819414	18.31297459	38.7139493
54	654.0790985	20.25942569	38.01129992
55	748.1515928	28.78429006	34.93390913
56	83.821378	24.01083197	36.65707977
57	913.3373615	19.57953937	38.25673208
58	825.8169775	18.04756038	38.80976118
59	996.1347166	25.76684871	36.02317529
60	442.6782698	16.56351058	39.34548832
61	961.8980809	17.1330554	39.13988833
62	774.9104647	15.09268448	39.87644183
63	868.6947054	31.34606441	34.00913421
64	399.7826491	16.68871691	39.30029008
65	800.0684802	20.19740806	38.03368767
66	910.6475944	23.62827655	36.79517845
67	263.8029165	18.63694057	38.59700083
68	136.0685587	17.91077961	38.85913767
69	579.7045874	32.38584415	33.63378412
70	144.9547982	25.99720404	35.94001931
71	622.0551315	32.06062235	33.75118594
72	513.2495399	22.01904762	37.376094
73	75.96669169	23.03616068	37.00892636
74	123.3189348	19.79832307	38.17775335
75	239.9525257	18.67815577	38.58212255
76	49.65443033	23.34534138	36.89731521
77	944.7871897	33.0543222	33.39247023
78	489.2526384	24.81728185	36.36595943
79	900.0538464	21.7543882	37.4716334
80	111.2027553	22.38493562	37.24401209
81	389.738837	30.60504137	34.27663612
82	403.9121456	19.83382572	38.16493725
83	131.9732926	16.9290905	39.21351762
84	956.1345402	33.84101182	33.10848314

Table 2. Cont.

S. No.	Solar Irradiance (W/m <sup>2</sup> )	Temperature (°C)	Maximum Voltage (V <sub>max</sub> )
85	59.77954295	26.5041719	35.75700899
86	353.1585712	19.69559827	38.21483598
87	15.40343765	31.4238808	33.98104327
88	168.9900295	15.86047603	39.59927676
89	731.7223857	27.9823095	35.22341609
90	450.9237064	27.95491926	35.2333037
91	296.3208056	25.94017785	35.9606052
92	188.955015	29.89385614	34.53336687
93	183.5111557	28.73550867	34.95151873
94	625.6185607	22.36969193	37.24951491
95	81.12576887	30.6045487	34.27681396
96	775.7126786	33.58771942	33.19991917
97	435.8585886	24.73583265	36.39536177
98	306.349472	23.93567499	36.68421069
99	510.7715642	25.17017311	36.23856921
100	794.8314169	31.35255417	34.00679147
101	378.6093827	27.8863626	35.25805196
102	532.8255888	31.23160917	34.05045141
103	939.001562	22.01454207	37.37772046
104	550.1563429	32.51885623	33.58576809
105	587.0447045	27.44950172	35.41575437
106	301.2463303	19.15484585	38.41004219
107	230.4881602	24.41846697	36.50992761
108	194.7642896	31.88617585	33.81415938
109	170.7080471	19.51843562	38.27878993
110	435.6986841	19.55328596	38.2662093
111	923.3796421	21.22204573	37.66380371
112	184.8163201	23.60414783	36.80388868
113	979.7483784	33.09761937	33.37684038
114	111.1192234	23.77739946	36.74134657
115	408.7198461	20.16129392	38.04672451
116	262.2117478	26.89792148	35.61486932
117	711.2157804	27.05686179	35.55749346
118	117.4176509	19.43493468	38.30893293
119	318.7783019	20.93351746	37.76795953
120	507.8582847	23.48333519	36.84750083

Table 3 compares the efficacy of six different ANN algorithms—the LM algorithm, BR algorithm, SCG algorithm, RP algorithm, GDM algorithm, and BFGS algorithm—in this regard.

**Table 3.** Comparison of the ANN algorithms' performance.

Parameters	Algorithm					
	LM	RP	SCG	BR	GDM	BFGS
Regression	1	1	0.993	1	0.996	1
Error at middle bin	−0.0000015	-	−0.006443	−0.000037	-	-
Gradient	$7.983 \times 10^{-6}$	0.033415	0.14161	0.00010493	11.485	$1.0211 \times 10^{-7}$
Performance	$2.0816 \times 10^{-10}$	$2.8668 \times 10^{-6}$	0.052985	$1.583 \times 10^{-7}$	0.15378	$9.98 \times 10^{-17}$
Momentum parameter	$1.00 \times 10^{-8}$	-	-	5000	-	-
Epochs	1000	15	69	1000	2	10

The table shows various performance parameters for each algorithm, including regression, error at the middle bin, gradient, performance, momentum parameter, and epochs. The regression value for the LM, BR, RP, and BFGS algorithms is 1, indicating a perfect correlation between the input and output data, while the SCG and GDM algorithms have a slightly lower regression value of 0.993 and 0.996, respectively. The error at the middle bin is negative for the LM algorithm (−0.0000015), indicating that the algorithm is performing better than the other algorithms. The gradient value for the BFGS algorithm ( $1.0211 \times 10^{-7}$ ) is much lower than that for the BR, RP, SCG, LM, and GDM algorithms, which are 0.00010493, 0.033415, 0.14161,  $7.983 \times 10^{-6}$ , and 11.485, respectively, which indicates that the BFGS algorithm has better convergence properties. The lower gradient value of BFGS indicates that the algorithm is making progress towards the optimal solution, and the estimate is close to the true minimum. This suggests that the algorithm is converging well and making small, steady steps towards the optimal solution. Similarly, the higher gradient value of the GDM algorithm indicates that the current estimate is far from the true minimum, and the algorithm needs to take large steps to get closer to it. This could result in overshooting the minimum or becoming stuck at a local minimum instead of the global minimum, which can lead to poor performance.

The performance value for the BFGS algorithm ( $9.98 \times 10^{-17}$ ) is significantly better than that for the BR algorithm ( $1.583 \times 10^{-7}$ ), SCG algorithm (0.052985), RP algorithm ( $2.8668 \times 10^{-6}$ ), GDM algorithm (0.15378), and LM algorithm ( $2.0816 \times 10^{-10}$ ), indicating that the BFGS algorithm provides the most accurate predictions. The LM algorithm secures second place in terms of performance and accuracy of predictions. The momentum parameter is only specified for the LM and BR algorithms, with the LM algorithm having a value of 0.00000001 and the BR algorithm having a value of 5000. The momentum parameter was not applicable for RP, SCG, GDM, and BFGS algorithms, as they do not use momentum. Finally, looking at the number of epochs required for convergence, the RP and BR algorithms required the fewest epochs at 15 and 2, respectively. The LM, GDM, and BFGS algorithms required moderate numbers of epochs, while the SCG algorithm required a relatively large number of epochs at 69. Overall, the results illustrate that the LM algorithm outperforms the other two algorithms in terms of accuracy, convergence, and performance, making it the best choice for MPPT energy harvesting in a solar PV system.

Overall, the results suggest that the LM and BFGS algorithms are the best performers in terms of gradient and performance, while the RP and BR algorithms also perform well across the various metrics. The SCG and GDM algorithms appear to be less effective for this particular problem.

## 5. Conclusions

In conclusion, this paper presented a novel approach for evaluating the efficacy of six ANN algorithms (LM, BR, RP, GDM, BFGS, and SCG) in the context of MPPT for solar PV systems. The authors utilized a two-layer feedforward neural network from the ANN toolbox and trained it with generated data on solar irradiance, panel temperature, and generated voltage. Based on the outcomes, the regression values of the LM, RP, BR, and BFGS algorithms are all equal to 1, whereas the regression values for the SCG and GDM

algorithms are less than 1. The gradient values for the LM, RP, BFGS, SCG, BR, and GDM algorithms are  $7.983 \times 10^{-6}$ , 0.033415,  $1.0211 \times 10^{-7}$ , 0.14161, 0.00010493, and 11.485, respectively. Likewise, the performance values for these algorithms are  $2.0816 \times 10^{-10}$ ,  $2.8668 \times 10^{-6}$ ,  $9.98 \times 10^{-17}$ , 0.052985,  $1.583 \times 10^{-7}$ , and 0.15378. Overall, the findings demonstrated that the LM and BFGS algorithms performed exceptionally well in terms of performance and gradient, with LM showing almost no error in the middle epoch. At 1000 epochs, the validation efficiency was highest, indicating close-to-zero values for the momentum parameter, validation, and gradient checks. The LM and BFGS algorithms exhibit superior performance in terms of regression, gradient, and overall performance. Additionally, the RP and BR algorithms also demonstrate good performance across various metrics, while the SCG and GDM algorithms show relatively less effectiveness in addressing the proposed problem. These findings provide valuable insights into the relative performance of the six evaluated algorithms for MPPT energy harvesting in solar PV systems.

The proposed ANN-based MPPT energy harvesting concept holds potential for solving problems on a large scale and can be incorporated into multilayer neural networks, making it highly versatile. Furthermore, the study revealed a perfect correlation between input and output data, exemplified by the consistency between generated power and load power after MPPT. This ANN-based MPPT energy harvesting model can find applications in standalone and grid-connected solar PV systems, as well as military equipment, telecommunications, and space satellites. The suggested ANN-based MPPT energy harvesting model exhibits applicability across various domains and can be integrated into numerous technologies. Additionally, the model can be utilized for solar radiation and temperature prediction, energy estimation, energy management in smart homes and cities, and forecasting solar radiation and temperature. Looking ahead, the future scope of solar PV MPPT based on ANN appears promising, offering several areas for research and development. One potential direction is exploring the use of reinforcement learning algorithms to further optimize MPPT control in solar PV systems. Additionally, integrating AI-based control systems with power electronics devices, such as DC–DC converters and inverters, could enhance overall system efficiency. Advancements in sensors and data acquisition systems hold the potential to develop more sophisticated and accurate ANN models for MPPT control. Furthermore, investigating hybrid control algorithms that combine multiple AI-based techniques could lead to improved performance in solar PV MPPT. The proposed work offers valuable insights but has limitations. Firstly, it focuses only on six specific ANN algorithms, potentially limiting the understanding of the overall algorithmic landscape. Secondly, the evaluation is based on specific performance parameters, which may not capture all aspects of algorithm performance. Additionally, the study focuses solely on solar PV systems, excluding other renewable energy sources. This limits the applicability of the findings to a broader range of energy harvesting systems. Overall, this research contributes valuable insights into the evaluation of ANN algorithm performance for MPPT in solar PV systems and sets the stage for future advancements in the field.

**Author Contributions:** Conceptualization, A.S. and M.T.; formal analysis, M.T.H., A.S., M.T., S.U. and M.A.H.; funding acquisition, S.U. and A.B.; investigation, M.T.H., A.S., M.T. and S.U.; methodology, M.T.H., A.S., M.T. and M.A.H.; project administration, M.T., S.U. and A.B.; resources, M.T.; supervision, A.S. and M.T.; validation, M.T.H., A.S., M.T., A.B. and M.A.H.; writing—original draft, M.T.H., A.S. and M.T.; writing—review and editing, S.U., A.B. and M.A.H. All authors have read and agreed to the published version of the manuscript.

**Funding:** Princess Nourah bint Abdulrahman University (43-PRFA-P-38), Princess Nourah bint Abdulrahman University, Riyadh, Saudi Arabia.

**Institutional Review Board Statement:** Not applicable.

**Informed Consent Statement:** Not applicable.

**Data Availability Statement:** Not applicable.

**Acknowledgments:** This research project was funded by the Deanship of Scientific Research, Princess Nourah bint Abdulrahman University, through the Program of Research Project Funding After Publication, grant No (43-PRFA-P-38).

**Conflicts of Interest:** The authors declare no conflict of interest.

## References

1. Kouro, S.; Leon, J.I.; Vinnikov, D.; Franquelo, L.G. Grid-Connected Photovoltaic Systems: An Overview of Recent Research and Emerging PV Converter Technology. *IEEE Ind. Electron. Mag.* **2015**, *9*, 47–61. [CrossRef]
2. Tarroja, B.; Shaffer, B.; Samuelson, S. The importance of grid integration for achievable greenhouse gas emissions reductions from alternative vehicle technologies. *Energy* **2015**, *87*, 504–519. [CrossRef]
3. Rokouzzaman; Mishu, M.K.; Amin, N.; Nadarajah, M.; Roy, R.B.; Rahman, K.S.; Buhari, A.M.; Binzaid, S.; Shakeri, M.; Pasupuleti, J. Self-Sustained Autonomous Wireless Sensor Network with Integrated Solar Photovoltaic System for Internet of Smart Home-Building (IoSHB) Applications. *Micromachines* **2021**, *12*, 653. [CrossRef]
4. Koohi-Kamali, S.; Rahim, N.; Mokhlis, H.; Tyagi, V. Photovoltaic electricity generator dynamic modeling methods for smart grid applications: A review. *Renew. Sustain. Energy Rev.* **2016**, *57*, 131–172. [CrossRef]
5. De Giorgi, M.G.; Congedo, P.M.; Malvoni, M. Photovoltaic power forecasting using statistical methods: Impact of weather data. *IET Sci. Meas. Technol.* **2014**, *8*, 90–97. [CrossRef]
6. Karami, N.; Moubayed, N.; Outbib, R. General review and classification of different MPPT Techniques. *Renew. Sustain. Energy Rev.* **2017**, *68*, 1–18. [CrossRef]
7. Mishu, M.K.; Rokouzzaman, M.; Pasupuleti, J.; Shakeri, M.; Rahman, K.S.; Hamid, F.A.; Tiong, S.K.; Amin, N. Prospective Efficient Ambient Energy Harvesting Sources for IoT-Equipped Sensor Applications. *Electronics* **2020**, *9*, 1345. [CrossRef]
8. Rokouzzaman; Shakeri, M.; Hamid, F.A.; Mishu, M.K.; Pasupuleti, J.; Rahman, K.S.; Tiong, S.K.; Amin, N. IoT-Enabled High Efficiency Smart Solar Charge Controller with Maximum Power Point Tracking—Design, Hardware Implementation and Performance Testing. *Electronics* **2020**, *9*, 1267. [CrossRef]
9. Sivakumar, P.; Kader, A.A.; Kaliavaradhan, Y.; Arutchelvi, M. Analysis and enhancement of PV efficiency with incremental conductance MPPT technique under non-linear loading conditions. *Renew. Energy* **2015**, *81*, 543–550. [CrossRef]
10. Roy, R.B.; Basher, E.; Yasmin, R.; Rokouzzaman, M. Fuzzy logic based MPPT approach in a grid connected photovoltaic system. In Proceedings of the 8th International Conference on Software, Knowledge, Information Management and Applications (SKIMA 2014), Dhaka, Bangladesh, 18–20 December 2014; pp. 1–6. [CrossRef]
11. Bhatti, A.R.; Salam, Z.; Sultana, B.; Rasheed, N.; Awan, A.B.; Sultana, U.; Younas, M. Optimized sizing of photovoltaic grid-connected electric vehicle charging system using particle swarm optimization. *Int. J. Energy Res.* **2018**, *43*, 500–522. [CrossRef]
12. Dixit, T.V.; Yadav, A.; Gupta, S. Experimental assessment of maximum power extraction from solar panel with different converter topologies. *Int. Trans. Electr. Energy Syst.* **2018**, *29*, e2712. [CrossRef]
13. Rokouzzaman, H.-E.-H. Design and implementation of maximum power point tracking solar charge controller. In Proceedings of the 2016 3rd International Conference on Electrical Engineering and Information Communication Technology (ICEEICT), Dhaka, Bangladesh, 22–24 September 2016; pp. 1–5. [CrossRef]
14. Mishu, M.K.; Rokouzzaman; Pasupuleti, J.; Shakeri, M.; Rahman, K.S.; Binzaid, S.; Tiong, S.K.; Amin, N. An Adaptive TE-PV Hybrid Energy Harvesting System for Self-Powered IoT Sensor Applications. *Sensors* **2021**, *21*, 2604. [CrossRef] [PubMed]
15. Esram, T.; Chapman, P.L. Comparison of Photovoltaic Array Maximum Power Point Tracking Techniques. *IEEE Trans. Energy Convers.* **2007**, *22*, 439–449. [CrossRef]
16. Basha, C.H.; Rani, C. Different Conventional and Soft Computing MPPT Techniques for Solar PV Systems with High Step-Up Boost Converters: A Comprehensive Analysis. *Energies* **2020**, *13*, 371. [CrossRef]
17. Lopez-Guede, J.M.; Ramos-Hernandez, J.; Altun, N.; Ozdemir, S.; Kurt, E.; Azkune, G. Neural Modeling of Fuzzy Controllers for Maximum Power Point Tracking in Photovoltaic Energy Systems. *J. Electron. Mater.* **2018**, *47*, 4519–4532. [CrossRef]
18. Khanam, J.J.F.; Simon, Y. Modeling of a photovoltaic array in MATLAB simulink and maximum power point tracking using neural network. *J. Electr. Electron. Syst.* **2018**, *7*, 40–46.
19. Chen, L.; Wang, X. Enhanced MPPT method based on ANN-assisted sequential Monte-Carlo and quickest change detection. *IET Smart Grid* **2019**, *2*, 635–644. [CrossRef]
20. Chtouki, I.; Wira, P.; Zazi, M. ICIT—Comparison of several neural network perturb and observe MPPT methods for photovoltaic applications. In Proceedings of the 2018 IEEE International Conference on Industrial Technology (ICIT), Lyon, France, 20–22 February 2018; pp. 909–914. [CrossRef]
21. Bouakkaz, M.S.; Boukadoum, A.; Boudebouz, O.; Bouraiou, A.; Attoui, I. ANN based MPPT Algorithm Design using Real Operating Climatic Condition. In Proceedings of the 2020 2nd International Conference on Mathematics and Information Technology (ICMIT), Adrar, Algeria, 18–19 February 2020. [CrossRef]
22. Algarín, C.R.; Hernández, D.S.; Leal, D.R. A Low-Cost Maximum Power Point Tracking System Based on Neural Network Inverse Model Controller. *Electronics* **2018**, *7*, 4. [CrossRef]



23. Divyasharon, R.; Banu, R.N.; Devaraj, D. Artificial Neural Network based MPPT with CUK Converter Topology for PV Systems Under Varying Climatic Conditions. In Proceedings of the 2019 IEEE International Conference on Intelligent Techniques in Control, Optimization and Signal Processing (INCOS), Tamilnadu, India, 11–13 April 2019; pp. 1–6. [CrossRef]
24. Fatima, K.; Alam, M.A.; Minai, A.F. Optimization of Solar Energy Using ANN Techniques. In Proceedings of the 2019 2nd International Conference on Power Energy, Environment and Intelligent Control (PEEIC), Greater Noida, India, 18–19 October 2019. [CrossRef]
25. Al-Majidi, S.D.; Abbod, M.F.; Al-Raweshidy, H.S. Design of an intelligent MPPT based on ANN using a real photovoltaic system data. In Proceedings of the 2019 54th International Universities Power Engineering Conference (UPEC), Bucharest, Romania, 3–6 September 2019. [CrossRef]
26. Elgendy, M.A.; Atkinson, D.J.; Zahawi, B. Experimental investigation of the incremental conductance maximum power point tracking algorithm at high perturbation rates. *IET Renew. Power Gener.* **2016**, *10*, 133–139. [CrossRef]
27. Jyothy, L.P.; Sindhu, M.R. An Artificial Neural Network based MPPT Algorithm For Solar PV System. In Proceedings of the 2018 4th International Conference on Electrical Energy Systems (ICEES), Chennai, India, 7–9 February 2018. [CrossRef]
28. Vimalarani, C.; Kamaraj, N. Improved method of maximum power point tracking of photovoltaic (PV) array using hybrid intelligent controller. *Optik* **2018**, *168*, 403–415. [CrossRef]
29. Roy, R.B.; Cros, J.; Nandi, A.; Ahmed, T. Maximum Power Tracking by Neural Network. In Proceedings of the 2020 8th International Conference on Reliability, Infocom Technologies and Optimization (Trends and Future Directions) (ICRITO), Noida, India, 4–5 June 2020. [CrossRef]
30. Danyali, S.; Aghaei, O.; Shirkhani, M.; Aazami, R.; Tavoosi, J.; Mohammadzadeh, A.; Mosavi, A. A New Model Predictive Control Method for Buck-Boost Inverter-Based Photovoltaic Systems. *Sustainability* **2022**, *14*, 11731. [CrossRef]
31. Aazami, R.; Heydari, O.; Tavoosi, J.; Shirkhani, M.; Mohammadzadeh, A.; Mosavi, A. Optimal Control of an Energy-Storage System in a Microgrid for Reducing Wind-Power Fluctuations. *Sustainability* **2022**, *14*, 6183. [CrossRef]
32. Kaya, C.B.; Kaya, E.; Gökkuş, G. Training Neuro-Fuzzy by Using Meta-Heuristic Algorithms for MPPT. *Comput. Syst. Sci. Eng.* **2023**, *45*, 69–84. [CrossRef]
33. Ibnelouad, A.; El Kari, A.; Ayad, H.; Mjahed, M. Improved cooperative artificial neural network-particle swarm optimization approach for solar photovoltaic systems using maximum power point tracking. *Int. Trans. Electr. Energy Syst.* **2020**, *30*, 12439. [CrossRef]
34. Roy, R.B.; Rokonzaman, M.; Amin, N.; Mishu, M.K.; Alahakoon, S.; Rahman, S.; Pasupuleti, J. A Comparative Performance Analysis of ANN Algorithms for MPPT Energy Harvesting in Solar PV System. *IEEE Access* **2021**, *9*, 102137–102152. [CrossRef]
35. Li, Z.; Rahman, S.M.; Vega, R.; Dong, B. A Hierarchical Approach Using Machine Learning Methods in Solar Photovoltaic Energy Production Forecasting. *Energies* **2016**, *9*, 55. [CrossRef]
36. Xia, L.; Ma, Z.; Kokogiannakis, G.; Wang, Z.; Wang, S. A model-based design optimization strategy for ground source heat pump systems with integrated photovoltaic thermal collectors. *Appl. Energy* **2018**, *214*, 178–190. [CrossRef]
37. Ding, M.; Wang, L.; Bi, R. An ANN-based Approach for Forecasting the Power Output of Photovoltaic System. *Procedia Environ. Sci.* **2011**, *11*, 1308–1315. [CrossRef]
38. Porrazzo, R.; Cipollina, A.; Galluzzo, M.; Micale, G. A neural network-based optimizing control system for a seawater-desalination solar-powered membrane distillation unit. *Comput. Chem. Eng.* **2013**, *54*, 79–96. [CrossRef]
39. Chine, W.; Mellit, A.; Lughi, V.; Malek, A.; Sulligoi, G.; Pavan, A.M. A novel fault diagnosis technique for photovoltaic systems based on artificial neural networks. *Renew. Energy* **2016**, *90*, 501–512. [CrossRef]
40. Vaz, A.; Elsinga, B.; van Sark, W.; Brito, M. An artificial neural network to assess the impact of neighbouring photovoltaic systems in power forecasting in Utrecht, the Netherlands. *Renew. Energy* **2016**, *85*, 631–641. [CrossRef]
41. Elsheikh, A.H.; Sharshir, S.W.; Abd Elaziz, M.; Kabeel, A.E.; Guilan, W.; Haiou, Z. Modeling of solar energy systems using artificial neural network: A comprehensive review. *Sol. Energy* **2019**, *180*, 622–639. [CrossRef]
42. Subudhi, B.; Pradhan, R. A Comparative Study on Maximum Power Point Tracking Techniques for Photovoltaic Power Systems. *IEEE Trans. Sustain. Energy* **2013**, *4*, 89–98. [CrossRef]
43. De Brito, M.A.G.; Galotto, L.; Sampaio, L.P.; Melo, G.D.A.E.; Canesin, C.A. Evaluation of the Main MPPT Techniques for Photovoltaic Applications. *IEEE Trans. Ind. Electron.* **2013**, *60*, 1156–1167. [CrossRef]
44. Kollimalla, S.K.; Mishra, M.K. A Novel Adaptive P&O MPPT Algorithm Considering Sudden Changes in the Irradiance. *IEEE Trans. Energy Convers.* **2014**, *29*, 602–610. [CrossRef]
45. Elgendy, M.A.; Zahawi, B.; Atkinson, D.J. Assessment of the Incremental Conductance Maximum Power Point Tracking Algorithm. *IEEE Trans. Sustain. Energy* **2013**, *4*, 108–117. [CrossRef]
46. Elobaid, L.M.; Abdelsalam, A.K.; Zakzouk, E.E. Artificial neural network-based photovoltaic maximum power point tracking techniques: A survey. *IET Renew. Power Gener.* **2015**, *9*, 1043–1063. [CrossRef]
47. Mohammed, K.K.; Buyamin, S.; Shams, I.; Mekhilef, S. Maximum power point tracking based on adaptive neuro-fuzzy inference systems for a photovoltaic system with fast varying load conditions. *Int. Trans. Electr. Energy Syst.* **2021**, *31*, e12904. [CrossRef]
48. Dragicevic, T.; Wheeler, P.; Blaabjerg, F. Artificial Intelligence Aided Automated Design for Reliability of Power Electronic Systems. *IEEE Trans. Power Electron.* **2019**, *34*, 7161–7171. [CrossRef]

49. Ramana, V.V.; Jena, D. Maximum power point tracking of PV array under non-uniform irradiance using artificial neural network. In Proceedings of the 2015 IEEE International Conference on Signal Processing, Informatics, Communication and Energy Systems (SPICES), Kozhikode, India, 19–21 February 2015; pp. 1–5. [CrossRef]
50. Ali, F.; Sarwar, A.; Bakhsh, F.I.; Ahmad, S.; Shah, A.A.; Ahmed, H. Parameter extraction of photovoltaic models using atomic orbital search algorithm on a decent basis for novel accurate RMSE calculation. *Energy Convers. Manag.* **2023**, *277*, 116613. [CrossRef]
51. Dkhichi, F.; Oukarfi, B.; Fakkar, A.; Belbounaguia, N. Parameter identification of solar cell model using Levenberg–Marquardt algorithm combined with simulated annealing. *Sol. Energy* **2014**, *110*, 781–788. [CrossRef]
52. Gimazov, R.; Shidlovskiy, S. Simulation Modeling of Intelligent Control Algorithms for Constructing Autonomous Power Supply Systems with Improved Energy Efficiency. In *MATEC Web of Conferences*; EDP Sciences: Les Ulis, France, 2018; Volume 155, p. 01032. [CrossRef]
53. Macaulay, J.; Zhou, Z. A Fuzzy Logical-Based Variable Step Size P&O MPPT Algorithm for Photovoltaic System. *Energies* **2018**, *11*, 1340. [CrossRef]
54. Cho, T.-H.; Hwang, H.-R.; Lee, J.-H.; Lee, I.-S. Comparison of Intelligent Methods of SOC Estimation for Battery of Photovoltaic System. *Int. J. Adv. Comput. Sci. Appl.* **2018**, *9*, 90907. [CrossRef]
55. Ul-Haq, A.; Sindi, H.F.; Gul, S.; Jalal, M. Modeling and Fault Categorization in Thin-Film and Crystalline PV Arrays Through Multilayer Neural Network Algorithm. *IEEE Access* **2020**, *8*, 102235–102255. [CrossRef]
56. Abd Ellah, A.R.; Essai, M.H.; Yahya, A. Comparison of different backpropagation training algorithms using robust M-estimators performance functions. In Proceedings of the 2015 Tenth International Conference on Computer Engineering & Systems (ICCES), Cairo, Egypt, 23–24 December 2015; pp. 384–388. [CrossRef]
57. Dong, C.L.; Nocedal, J. On the limited memory BFGS method for large scale optimization. *Math. Program* **1989**, *45*, 503–528. Available online: <https://link.springer.com/content/pdf/10.1007%2F01589116.pdf> (accessed on 11 June 2023).
58. Luo, X.; Qin, W.; Dong, A.; Sedraoui, K.; Zhou, M. Efficient and High-quality Recommendations via Momentum-incorporated Parallel Stochastic Gradient Descent-Based Learning. *IEEE/CAA J. Autom. Sin.* **2020**, *8*, 402–411. [CrossRef]
59. Møller, M.F. A scaled conjugate gradient algorithm for fast supervised learning. *Neural Netw.* **1993**, *6*, 525–533. [CrossRef]

**Disclaimer/Publisher’s Note:** The statements, opinions and data contained in all publications are solely those of the individual author(s) and contributor(s) and not of MDPI and/or the editor(s). MDPI and/or the editor(s) disclaim responsibility for any injury to people or property resulting from any ideas, methods, instructions or products referred to in the content.

Article

# Tourism Service Scheduling in Smart City Based on Hybrid Genetic Algorithm Simulated Annealing Algorithm

Pannee Suanpang <sup>1,\*</sup>, Pitchaya Jamjuntr <sup>2</sup>, Kittisak Jermsittiparsert <sup>3,4,5,6,7</sup> and Phuripoj Kaewyong <sup>1</sup>

<sup>1</sup> Faculty of Science & Technology, Suan Dusit University, Bangkok 10300, Thailand

<sup>2</sup> Faculty of Engineering, King Mongkut's University of Technology Thonburi, Bangkok 10140, Thailand

<sup>3</sup> Faculty of Education, University of City Island, Famagusta 9945, Cyprus

<sup>4</sup> Faculty of Social and Political Sciences, Universitas Muhammadiyah Sinjai, Kabupaten Sinjai 92615, Sulawesi Selatan, Indonesia

<sup>5</sup> Faculty of Social and Political Sciences, Universitas Muhammadiyah Makassar, Kota Makassar 90221, Sulawesi Selatan, Indonesia

<sup>6</sup> Publication Research Institute and Community Service, Universitas Muhammadiyah Sidenreng Rappang, Sidenreng Rappang Regency 91651, South Sulawesi, Indonesia

<sup>7</sup> Sekolah Tinggi Ilmu Administrasi Abdul Haris, Kota Makassar 90000, Sulawesi Selatan, Indonesia

\* Correspondence: pannee\_sua@dusit.ac.th

**Abstract:** The disruptions in this era have caused a leap forward in information technology being applied in organizations to create a competitive advantage. In particular, we see this in tourism services, as they provide the best solution and prompt responses to create value in experiences and enhance the sustainability of tourism. Since scheduling is required in tourism service applications, it is regarded as a crucial topic in production management and combinatorial optimization. Since workshop scheduling difficulties are regarded as extremely difficult and complex, efforts to discover optimal or near-ideal solutions are vital. The aim of this study was to develop a hybrid genetic algorithm by combining a genetic algorithm and a simulated annealing algorithm with a gradient search method to the optimize complex processes involved in solving tourism service problems, as well as to compare the traditional genetic algorithms employed in smart city case studies in Thailand. A hybrid genetic algorithm was developed, and the results could assist in solving scheduling issues related to the sustainability of the tourism industry with the goal of lowering production requirements. An operation-based representation was employed to create workable schedules that can more effectively handle the given challenge. Additionally, a new knowledge-based operator was created within the context of function evaluation, which focuses on the features of the problem to utilize machine downtime to enhance the quality of the solution. To produce the offspring, a machine-based crossover with order-based precedence preservation was suggested. Additionally, a neighborhood search strategy based on simulated annealing was utilized to enhance the algorithm's capacity for local exploitation, and to broaden its usability. Numerous examples were gathered from the Thailand Tourism Department to demonstrate the effectiveness and efficiency of the proposed approach. The proposed hybrid genetic algorithm's computational results show good performance. We found that the hybrid genetic algorithm can effectively generate a satisfactory tourism service, and its performance is better than that of the genetic algorithm.

**Keywords:** service scheduling; hybrid genetic algorithms; simulated annealing algorithms; tourism services; sustainability tourism

**Citation:** Suanpang, P.; Jamjuntr, P.; Jermsittiparsert, K.; Kaewyong, P. Tourism Service Scheduling in Smart City Based on Hybrid Genetic Algorithm Simulated Annealing Algorithm. *Sustainability* **2022**, *14*, 16293. <https://doi.org/10.3390/su142316293>

Academic Editor: Mohamed A. Mohamed

Received: 27 October 2022

Accepted: 2 December 2022

Published: 6 December 2022



**Copyright:** © 2022 by the authors. Licensee MDPI, Basel, Switzerland. This article is an open access article distributed under the terms and conditions of the Creative Commons Attribution (CC BY) license (<https://creativecommons.org/licenses/by/4.0/>).

## 1. Introduction

In this era of disruption, people around the world are utilizing information technology to create competitive advantages, especially in the tourism industry. This approach should provide the best solutions and prompt responses that will improve experiences and enhance sustainability tourism. Since scheduling is involved in tourism service applications, it is

regarded as a crucial topic in production management and combinatorial optimization. One of the most significant subjects with a wide range of applications in tourism services is scheduling. When assigning resources to a collection of tasks, scheduling must take time, capability, and capacity limits into consideration [1]. To increase profit, the fundamental goal is to increase production efficiency and resource use. Many scheduling issues in the industrial sector are regarded as being extremely complicated, making it challenging to resolve them using precise techniques and standard algorithms. Since 1950, scheduling issues have drawn the attention of several scholars, and significant research efforts have been made in a variety of engineering and scientific domains, including operations research, computer science, industrial engineering, mathematics, and management science.

Scheduling problems are well-known, significant, and difficult issues in the domains of combinatorial optimization and production management. The complexity of scheduling difficulties can be estimated in relation to all potential schedules, and as the size of the problem increases, this complexity increases dramatically.

Scheduling issues are among the hardest problems, and Garey et al. [2] and Ullman [3] demonstrated that this means that polynomial time methods cannot be used to solve them. In cases of scheduling issues have primarily been addressed using traditional approaches and exact methods, such as Lagrangian relaxation, branch and bound, heuristic rules, and shifting bottleneck (e.g., Carlier and Pinson [4], Adams et al. [5], Vanecheeswaran and Townsend [6], Brucker et al. [7], and Lageweg et al. [8]). Various techniques have drawn inspiration from nature, biology, and physical processing over the last ten years. These methods have been effectively used to solve a variety of optimization issues, including scheduling issues. Genetic algorithms [9–11], ant colony optimization [12], imperialist competitive algorithms [13,14], tabu search [15], simulated annealing (SA) [16,17], particle swarm optimization [18], and immune systems [19] are a few of these metaheuristic approaches. For further information, see the thorough studies of scheduling problem solutions performed by Jain and Meeran [20] and Aliş and Bulkan [21].

A potent search method that mimics biological evolution and natural selection is the genetic algorithm (GA). Holland [22] was the first to come up with the idea for GA, and David Goldberg expanded on it. In contrast to other algorithms, this metaheuristic approach is frequently used to locate optimal or nearly optimal solutions to a variety of optimization problems. Davis [23] was the one who first used GA in the scheduling problem, and several GA-based methods for solving scheduling problems have since been introduced. A GA for solving scheduling problems with an encoding technique based on preference rules was proposed by Croce et al. in [11]. A GA with a novel representation technique based on operation completion time was proposed by Yamada and Nakano [24], and its crossover can provide active schedules. For the scheduling problems, Lee et al. [25] presented a GA with an operation-based representation and an order-based crossover that preserves precedence. For scheduling problems, Sun et al. [26] created a modified GA with clonal selection and a life span strategy. Out of 23 key instances, the generated algorithm was able to discover the 21 best solutions. The literature makes it clear that GA is a potent search approach with strong global search capabilities; yet, this metaheuristic algorithm suffers from early convergence and poor local search capabilities.

The major goal of the hybridization strategy is to improve the efficiency and potency of GA by addressing its limitations in terms of local search capability and premature convergence. In their hybrid optimization technique, Wang and Zheng [27] combined local search and GA. The hybrid framework of this method lowers the parameter dependence of both algorithms and reduces the likelihood of GA becoming stuck on local optima. In order to solve the scheduling problems using an adaptive mutation operator and avoid premature convergence, Zhou et al. [28] created a hybrid heuristic GA. In this approach, heuristics were utilized to identify the remaining operations in the constrained solution space, while GA was applied to the machines' first operations.

In order to further boost the quality of the hybrid heuristic GA-derived solutions, a neighborhood search strategy was used. A deadlock-free local search GA with an operation-

based representation and UOX crossover was presented by Ombuki and Ventresca [29], and this was able to produce workable solutions. In this technique, a local search operator was used for local exploitation, while the GA was used to perform global search. They also created a second hybrid genetic algorithm that uses tabu search; according to computational results, the hybrid GA with tabu search performed better than the local search GA. Gonçalves et al. [30] combined GA, a schedule builder, and a local search operator to create a hybrid GA for addressing scheduling problems. In this approach, a priority rule was utilized to produce schedules, and GA was employed to establish priorities. The quality of the solutions was then further enhanced using a local search operator. A hybrid approach using the novel representation technique known as random keys encoding was created by Lin and Yugeng [31]. In this approach, a neighborhood search was added to perform local exploitation and improve the quality of the solution acquired by GA, after the GA was used to obtain an optimal schedule. A hybrid GA was suggested by Zhou et al. [32] to reduce weighted tardiness in the scheduling problem. The first operations of this algorithm were determined using GA, and the remaining operations were assigned using a heuristic. This method was utilized to produce optimal solutions. The hybrid framework outperformed GA and heuristic used alone, according to the results. Agents were employed to implement the parallel GA that Asadzadeh and Zamanifar [33] proposed, as well as to establish the initial populations. A hybrid SA immune system algorithm was presented by Zhang and Wu [17] for reducing the overall weighted tardiness of workshop scheduling. A hybrid micro-GA created by Yusof et al. [34,35] was used in scheduling problems. This method combined an autonomous immigration GA with subpopulations with an asynchronous colony GA, which had colonies with low populations. This algorithm is suitable for use in the complex optimization problem, and can also be applied in tourism service scheduling.

The problem addressed in this research is to find effective algorithms for a tourism recommendation system in Thailand. For the purpose of solving non-preemptive scheduling problems, an efficient hybrid GA is described in this study. An operation-based representation is utilized to more efficiently address the given problem. Additionally, the context of function evaluation involves the invention and use of a new knowledge-based operator. In order to determine the operations of machines during their downtime, this knowledge-based operator mimics the features of the scheduling problem. In order to create offspring and mutants during the reproduction phase of the GA, two different mutation operators and a machine-based, precedence-preserving and order-based crossover are devised. Additionally, SA is used to some extent to increase the population variety in GA, as well as to improve the solution quality of the schedules obtained from GA. After highlighting its key components, the suggested approach is designed to reduce time of schedules. Finally, the computational outcomes of the given issues are given to demonstrate the effectiveness of the suggested algorithm.

To bridge the gap in knowledge regarding the research problem, the aim of this study was to develop a hybrid genetic algorithm by combining a genetic algorithm and a simulated annealing algorithm using a gradient search method to optimize the complex processes used to deal with the tourism service problem, and to compare this to the traditional genetic algorithms used in Chiang Mai smart city case studies in Thailand. The remainder of this paper is structured as follows: The scheduling problems are described in Section 2, while Section 3 contains the suggested hybrid GA. In Section 4, the computational results of exemplar instances are shown, followed by the discussion. Section 5 provides the reasons for choosing the GA and SAA algorithms as effective approaches, then we give our recommendations for tourism systems, ideas, conclusions and proposals for further research.

## 2. Materials and Methods

### 2.1. Tourism Package Tours and Service Scheduling

Package tours, according to Enoch [36], are a useful and more economical way to see tourist locations, but they lack flexibility because of their predetermined itinerary. The

advantages of package vacations frequently exceed their drawbacks for travel agents and customers. Travelers can save money, for instance, when travel agents offer them a discount due to bulk purchasing. Additionally, through the tour operator, the travel firms handle every aspect of travel, transfers, and lodging. By making just one call to confirm their package trip, passengers can save a lot of time compared to having to communicate with several service providers separately. Due to the benefits they provide, package tours are frequently chosen by customers as their means of departure.

Tour operators cater to particular customer groups and provide a variety of excursions, including fully escorted, adventure, special interest, city or regional, and group trips. GPTs are frequently used by citizens of Asian nations and regions, including Taiwan, Japan, South Korea, Hong Kong, and China, as one of their preferred outbound modes of transportation [37]. These trips are now crucial for the growth of individual nations' economies, as well as the global tourist industry [38].

With a wealth of literature on GPT services, previous studies on GPT management have focused on issues with passenger happiness, consumer behavior, and customer service [39]. The practice of combining airline seats and beds in hotels (or other forms of accommodation), in a manner that will make the purchase price acceptable to potential vacationers [39], is termed a package holiday. Seddighi and Theocharous [40] established a framework for analyzing the nature, shape, and character of vacation decision-making, as well as a micro-econometric approach to individual travel. The topic of vertical integration in the European tourism sector was investigated by [41]. Jin et al. [41] looked into how customer decision behavior in similar package tours was affected by the selection framework for upgrading and downgrading. From the viewpoint of the asymmetry in tourism information, Ref. [42] addressed the causes of low tourism quality.

Alao and Batabyal [43] indicated that the characteristics associated with the problem of how to sell package tours to tourists include asymmetric information, uncertain demands, and differentiated customers. Taking these three factors into account, they applied the first contract-theoretic analysis in order to provide the sharing of valuable information between package tour-selling firms and tourists. Aguiar-Quinatna et al. [44] analyzed customers' motivations and perceptions, and proposed strategies to improve the competitiveness of traditional travel agencies in Spain.

Seddighi and Theocharous [45] developed a framework for analyzing the nature, shape, and personality of vacation decision-making, as well as a micro-econometric approach to individual travel. The subject of vertical integration in the European tourism sector was examined by Theuvsen [46]. Jin et al. [47] looked into how client decision-making in similar package trips is impacted by the choice framework for upgrading and downgrading. From the standpoint of information asymmetry in the tourism business, Chen et al. [48] investigated the causes of low tourist quality.

Batabyal and Yoo [49] used probabilistic analysis to determine the long-run loss in demand for guided tours during the low season by modeling the pattern of client arrival as a stochastic process. In their investigation of the UK package tour market in 2007, Davies and Downward examined the dynamics of profitability and market share, as well as the function of pricing and non-pricing decisions, in order to identify the causal mechanisms behind both pricing and competition. In order to examine how Norwegians' income levels affect their demand for inclusive tour charters during a specific time period, Jrgensen and Solvoll [50] created an econometric model. Some tour providers are also focused on offering package holidays or single-destination included tours (Tepelus) [51]. However, to the best of our knowledge, no research has looked at tour selection and bus planning. A number of specific studies have also been conducted on themes relating to package tour management. Portfolio management, facility location selection, supplier selection, and investment portfolio management are examples of issues that are somewhat linked to our research (e.g., Arabani and Farahani [52]).

There is no requirement to take into account whether a preset minimum demand or load is met when assessing a reward or service in relation to these issues. Revenue

is counted once a product has been purchased—for instance, in the product portfolio management problem. When an investment is sold off in the portfolio investment problem, a profit or loss is realized. If a facility can deliver a service to a geographic area within a given distance, the facility location-selection problem's requirement is satisfied. The issue with staff assignments includes any service provided to a customer by an allocated employee. These observations help us understand how the proposed selection differs from other selection-related problems.

The proposed selection problem relates to the minimal number of passengers, whereas other challenges do not. This is the first distinction between the tour portfolio and other portfolio selection problems. The second difference is that while lost sales in most industries are caused by excessive demand, they can also result from insufficient demand in the tourism sector. In other words, new reservations are only turned down once the number of customers who have made reservations has reached capacity.

However, if there are fewer than the required number of consumers for a tour, all reserved clients are refused the service product. This issue is crucial for the tourism sector, because bad proposed selection and bus planning can result in financial losses and a negative business image. There is a research gap in the analysis of proposed selection and bus planning as a result.

Our research offers a mathematical model to look at the particular issues so as to close this gap in the literature. Through the use of a mathematical model, travel companies can profit from quicker and more accurate decision-making by analyzing the costs and benefits via data from the actual world. Travel agencies can utilize the selection method to arrange their package tours and their sightseeing buses, which can provide insights into how to do so. Because they are computationally challenging, the majority of portfolio selection problems that fall under the category of combinatorial optimization problems and traditional mathematical techniques frequently fall short of producing ideal or promising solutions. Due to their high computational efficiency, meta-heuristics-like genetic algorithms have been effectively used to solve real-world combinatorial optimization issues (e.g., Luan et al. [53]; Niknamfar and Niaki [54]). This article also suggests a hybrid heuristic based on using a genetic algorithm to solve the suggested mathematical model in order to accelerate computation.

## 2.2. Tourism Service Scheduling in Smart City

A smart city is a city with physical characteristics, and complex social and digital innovation and information technology. The concept of a smart city refers to a city that is as physically and socially connected as it is digitally [55]. Since the beginning of smart city development, the smart tourism city has emerged as a new concept for utilizing information technology to support the tourists and also the tourism industry in a city [55,56].

In Thailand, Chiang Mai is one of the smart cities that was developed in 2017 to build smart agriculture, smart economy, smart safety, smart health and smart tourism. The policy of smart tourism, which implements ICT infrastructure and technology to serve tourists, aims to support good living and the provision of useful information to people in the area, and also support the tourism industry [57].

In order to improve the competitiveness of the tourism industry, many scholars have addressed the problem of tourist trip design and tour route planning. An attempt to schedule tour guides for the tourism and leisure industry was carried out by Chen and Wang [58]. Their findings demonstrate that the Genetic Algorithm is useful for tourism scheduling service centers. Furthermore, Thumrongvut, Sethanan, Pitakaso, Jamrus, and Golinska-Dawson [59] created a mobile application using a mixed-integer linear programming approach for small-size problems, to help the suppliers of tourism services arrange trip and route planning for visitors, in order to improve the timeliness of visitor services.



### 2.3. Hybrid Genetic Algorithm

There is still much to learn about the extent of the flow shop scheduling challenge established in earlier investigations. Initializing the population will enable us to begin the process in GA. Numerous methods have been employed due to the significance of this process, including opposition-based (Li and Yin, [60]), quasi-oppositional, space transformation searches, and linear regression (Hassanat et al.) [61].

Due to a flow's increased complexity, metaheuristics must be used instead of the traditional heuristic approach (Lee and Loong) [62]. Instead of a memetic or hybrid scheme, a single algorithm dominates the majority of the previous studies (Tosun et al.) [63]. The first metaheuristic used to solve shop flow was simulated annealing (Osman and Potts). GA (Rahman et al.) and the well-known local search optimization technique TS were the next two (Ben Cheikh-Graiet et al.) [64]. Integrating the GA and TS is an alternative technique of solving shop flow, since the hybridization concept provides a more reliable method by combining two or more algorithms. The reason for choosing the GA and SAA algorithms is that they are effective in verifying our recommendations for the tourism system.

Some hybridized algorithms, particularly metaheuristic algorithms, have been used to tackle optimization issues, such as GA, which has already been merged with TS via a scatter search mechanism (Glover et al., 1995). There is the general algorithm (GA) that has been hybridized with the insertion of the search cut and repair algorithm (GA-ISCR) (Tseng and Lin, 2010), the co-evolutionary quantum genetic algorithm (CQGA) (Deng et al. [65]), and the general algorithm combined with simulated annealing (HGSA) (Wei et al.) [66].

In addition to GA, a number of different metaheuristics have been proposed to decrease the life span of shop flows, including those by Ding et al. (2015), who developed a local search approach using variable neighborhood search, called the tabu-mechanism with improved iterated greedy algorithm (TMIIG); there is also the iterated greedy with jumping probability (IG-JP), developed by Tasgetiren et al. [67], and Davendra and Bialic-Davendra (2013) developed DSOMA. Additionally, the aquila optimizer, which is based on how an aquila behaves when hunting its prey, has been applied in general optimization problems in recent years (Abualigah et al.) [68]. CFD analysis and the optimization of the design of a centrifugal pump use an effective, artificially intelligent algorithm that optimizes the compliant gripper mechanism's design by employing an effective bialgorithm comprising fuzzy logic and ANFIS, which is an efficient hybrid approach to the finite element method. The artificial neural network-based multi-objective genetic algorithm has also been used for the computational optimization of a linear compliant mechanism of a nanoindentation tester.

Wang et al. (2022) [69] proposed a cutting-edge strategy to raise the efficiency, power, and head of centrifugal pumps. First, an ideal numerical model that took pump efficiency and head into consideration was explored in order to set restrictions. Before conducting testing, the pump was built, and an artificial intelligence algorithmic technique was applied to the pump. By choosing the parameters for the centrifugal pump's casing section area, the impeller interference, the volute tongue length, and the volute tongue angle were investigated in a number of models. On the optimization indices, the weights of the safety and displacement factors were estimated. The weights matrix for the ideal process ranged from less than 38% to more than 62%. This method ensures that the optimization approach is strong and multi-objective. The outcomes demonstrate an improvement in centrifugal pump performance.

### 2.4. Simulated Annealing Algorithm

The original single-objective simulated annealing algorithm was slightly modified by Serafini (1994) by changing the method of calculating the probability of accepting new candidate solutions to narrow the search. This was one of the first works to use a simulated annealing algorithm to solve multi-objective problems. In addition to the well-known traveling salesman issue, a smaller problem with two objectives was also solved using the

approach. The technique performs well for minor issues, but with large problems, only limited parts of the Pareto front can be reached, as claimed by Czyzak and Jaskiewicz [70].

In order to find a good approximation of the entire Pareto front in somewhat large multi-objective knapsack problems with two, three, and four objectives, they invented Pareto-simulated annealing (PSA). In an effort to ensure the dispersion of the nondominated solutions discovered throughout the procedure, PSA employs objective weights that are changed after each iteration. In order to solve the two-objective knapsack problem, Ulungu et al. [71] proposed the UMOSA (Ulungu Multi-Objective Simulated Annealing) approach and investigated the impact of various neighborhood architectures (for candidate solution generation) and aggregation functions. All of these older MOSA techniques combine the goals using a variety of aggregation functions and objective weights, and the aggregated values are then minimized, much like in the case of a single simulated annealing process. Although it is necessary to create objective weights in advance, doing so can be difficult because, as Das and Dennis [72] found when using a number of instances, inadequate weight values render some areas of the Pareto front unreachable.

Following these initial attempts, several academics began utilizing the dominance idea to direct the algorithm. SMOSA (Suppaitnarm multi-objective simulated annealing), a technique developed by Suppaitnarm et al. in 2000, uses nondominated solutions that are archived in a solution list. The nondominated solutions discovered during the procedure had to be saved in an archive because SMOSA only produces one solution in each iteration (as opposed to MOEAs algorithms, which deal with populations of solutions). It employs a cutting-edge “return to base” tactic. In order to repeat the search and attempt to reach a new area of the front, the return to base approach occasionally chooses a random solution from the archive. Sankararao and Yoo [73] claim that even with this revised formulation, few nondominated solutions are found, and the convergence velocity is slow due to the search method employed. The acceptance determination process for this algorithm is primarily based on direct comparisons between the candidate and existing solution, which means that several excellent solutions may be overlooked while searching.

In his 2003 study, Suman [33] compared the performance of the UMOSA, SMOSA, and PSA algorithms, as well as two new ones: the PDMOSA (Pareto dominance multi-objective simulated annealing), which uses the Pareto dominance concept to direct the search, and the WMOSA (weighted multi-objective simulated annealing), which uses a weight vector to handle the constraints that are not verified. Certain comparisons aim to demonstrate how effective these algorithms are at addressing multi-objective optimization problems.

All of the approaches reached nondominated solutions, according to the comparisons, although the PDMOSA results are subpar compared to those of the other methods, and in some cases, PSA performs best. To assure a large collection of nondominated solutions, the authors contend that all five techniques need little processing effort and should be applied simultaneously. This means that if each of these methods is utilized independently, a larger number of front-end solutions cannot be guaranteed.

Suman and Kumar [74] reviewed SA-based algorithms and suggested new lines of inquiry to enhance MOSA algorithm performance. Suman et al. [75] proposed the orthogonal simulated annealing (OSA) technique in order to avoid utilizing conventional approaches that could inadvertently choose a new candidate solution at random, rendering the algorithm ineffective in exploring the solution space in complicated optimization problems. To increase the algorithm’s convergence, they suggested employing methods to first search the space of potential candidate solutions in the vicinity of the current solution, and then pick the best candidate solution. However, when compared to other algorithms, OSA’s performance was problem-dependent; while there are some situations in which OSA succeeds, there are other instances in which it fails. It is essential to develop an algorithm that performs well in a wide range of circumstances.

Bandyopadhyay et al. [76], who pioneered the archive multi-objective simulated annealing (AMOSA) approach, made a significant advancement in this subject. To calculate trade-offs between solutions, this algorithm makes use of an archive that holds the nondom-

inated solutions discovered during the optimization process. Additionally, they devised a process that uses the notion of the quantity of domination and the domination status amongst solutions to direct the algorithm search.

AMOSAs results were superior to those provided by NSGA-II (Deb et al.) [77] and PAES (Knowles and Corne) [78], in that a greater number of nondominated solutions were obtained, according to the results of various tests. The archive taken into account by AMOSA has two separate size restrictions, with an upper limit on the number of nondominated solutions that can be stored. The number of answers is then reduced to a smaller limit using a clustering strategy, which involves controlling and separating a huge amount of data into groups or subsets with comparable characteristics. This lowers the algorithm's computing requirements.

No constraints should be taken into account, however, to arrive at a more varied collection of nondominated solutions. Furthermore, as Sankararao and Yoo [79] did not seek a process to obtain a uniform Pareto front, it was discovered that the large number of solutions obtained by AMOSA were concentrated in specific regions of the front. Sankararao and Yoo [80] developed the multi-objective simulated annealing technique (rMOSA). This is a process to select the "most uncrowded solution" in the archive to generate a new candidate solution and obtain a well-distributed number of solutions in the algorithm's final results. This process seeks to select a random solution from the archive to generate a new candidate solution, with the aim of increasing the convergence speed of the algorithm.

The optimization process begins with the simultaneous employment of these search techniques, and they are applied periodically during the iterations. On the basis of comparisons with the existing solution, rMOSA employs a straightforward process for accepting candidate solutions. This can be ineffective, since it is important to consider the nondominated solutions that have already been found when accepting new candidate solutions (Cao and Tang) [81]. Additionally, the result derived when utilizing both processes concurrently from the start ignores the algorithm's evolution.

In an effort to improve the intensification and diversity aspects of the UMOSA algorithm, Rincón-García et al. [82] created a variation of the algorithm. They proposed various aggregation strategies for meeting the aims. The fundamental drawback of this form of weight-based algorithm is still, however, the establishment of weights allocated to targets in advance.

To address issues in air traffic control systems, Mateos and Jiménez-Martín [83] suggested a better AMOSA. To calculate the likelihood of adopting inferior solutions in comparison to the original AMOSA scheme, a new "element" was proposed. By only accepting solutions that increase the variety of the front, this element is utilized to speed up the algorithm's convergence rate. The authors showed that the algorithm performs well, but they contend that in order to demonstrate its superiority, it should be compared to other algorithms that have been applied to the same problem. It is important to carefully consider throwing out some answers that would increase the convergence velocity.

Sengupta and Saha [84] introduced a novel unconstrained many-objective optimization technique that was evaluated on academic optimization issues—the reference point-based simulated annealing (RSA) method. In contrast to the earlier "point-to-point" MOSA algorithms, the authors suggested an "archive-to-archive" procedure, which greatly improves the outcomes. The authors demonstrated that RSA performs effectively in many types of problems, based on comparisons with the outcomes of other methods.

Similar to the AMOSA algorithm, RSA uses clustering to shrink the archive, and as previously mentioned, this should be carefully considered to maintain the variety in the final set of answers. The AMOSA method is also used by Saadatpour et al. [85] to tackle a multi objective waste load allocation problem in rivers. In this instance, the archive is designed to hold just a small number of nondominated solutions. As a result, the finished front's quality may suffer.

Our work introduces a novel MOSA-GR technique, which was motivated by the encouraging outcomes from a wide range of applications of MOSA algorithms. The new

method was developed by using the finest ideas from the MOSA algorithms already mentioned above, and avoiding their shortcomings, notably with regard to the convergence and spreading of solutions along the front. The procedure for creating new candidate solutions and the reannealing of the algorithm are the two key areas where we suggest new enhancements to a previous version that Marques et al. [86] already provided. By utilizing a special tool that excels in a wide range of situations, this novel method seeks to identify a nearly optimal and sizable collection of nondominated, well-dispersed solutions.

Furthermore, there are two studies related to our research that apply an optimization technique in other areas of industry; for example, Zhang et al. (2018) [87] evaluated trade-offs between the main factors in green manufacturing (energy, noise and cost) through cutting parameter optimization, which introduces the new optimization technique to the manufacturing industry. Moreover, Zhang et al. (2020) [88] studied a multi-objective cellular genetic algorithm for the energy-oriented balancing and sequencing problem in a mixed-model assembly line in the energy industry. Finally, many algorithms have been designed to solve multi-objective optimization issues in the literature. However, the creation of new algorithms continues to be crucial. New algorithms are required to solve these problems in an acceptable amount of time, because the complexity of the problems is continuously increasing.

### 3. Methodology

#### 3.1. Simulated Annealing Algorithm

##### Problem Definition

The JSSP can be expressed as follows: JOB SHOP SCHEDULING PROBLEM. Each of the “ $n$ ” jobs consists of a number of procedures that must be carried out on “ $m$ ” different machines. A single machine is employed for a set amount of time for each operation. Each operation can only be processed by one machine at a time, and processing must continue uninterrupted until completion once processing on a given machine begins. A specific job’s processes must be completed in a specific sequence. The fundamental goal of the challenge is to plan the activities or operations of the tasks on the machines so that the overall time to complete all of the jobs, or the makespan ( $C_{max}$ ), is as short as possible. The phrase “makespan” describes the total amount of time needed to finish all operations for all tasks on all machines. It is a measurement of the amount of time elapsed between the beginning of the first operation and its conclusion. Sometimes, there may be several solutions with the shortest makespan, but the objective is to identify any one of them; finding all feasible optimum solutions is not always necessary.

The scheduling problem is a broad kind of the following classical scheduling problems:

given tourists  $n$ ,  $N = \{j1, j2, \dots, jn\}$ ;

given tourists consists of  $s$  operations  $S = \{Oj1, Oj2, \dots, Oj,s\}$ .

Each tourist gives rise to tasks that need to be completed on services in a specific technological order:  $S = \{Oj1, Oj2, \dots, Oj,s\}$ . The notation indicates the third operation of a project that must be completed on one of the services and has a known processing time. In this setting, each computer can only handle one operation at a time, and a single tourist’s operation cannot be handled by two services concurrently. Operation  $Oj,s$  must be processed on one of the designated machines until it is finished, without being interrupted. Additionally, a job can only visit one machine once; subsequent visits to the same machine are not permitted. Additionally, it is believed that the machines are always available and that operation travel times are minimal. In contrast to flow shop scheduling, scheduling problems assign each job a certain planned route. The order of all activities on all machines is planned to reduce  $C_{max}$ , or the maximum time for a project to be completed ( $\max C1, C2, \dots, Cj$ ).

A scheduling problem uses a mathematical model with the goal of reducing the makespan. In this model,  $B$  is taken to be a large integer, where  $tj,s$  represents the start of

operation  $O_{j,s}$ ,  $S_{mi,l}$  represents the start of machine  $I$  in the priority of  $l$ , and  $h_{i,j,s}$  is given a value of 1 if operation  $O_{j,s}$  is carried out on machine  $I$ , and a value of 0 if otherwise:

$$\min Z = \max \{C1, C2, \dots, Cj\} \quad j = 1, 2, \dots, n \quad (1)$$

$$S.t. \quad t_{j,s} + P_{j,s} \leq t_{j,s+1} \quad j = 1, 2, \dots, n; s = 1, 2, \dots, sj - 1 \quad (2)$$

$$S_{mi,l} + P_{j,s} X_{i,j,s,l} \leq S_{mi,l+1} \quad i = 1, 2, \dots, m; j = 1, 2, \dots, n; l = 1, 2, \dots, li - 1; s = 1, 2, \dots, sj \quad (3)$$

$$S_{mi,l} \leq t_{j,s} + (1 - X_{i,j,s,l}) B \quad i = 1, 2, \dots, m; j = 1, 2, \dots, n; l = 1, 2, \dots, li; s = 1, 2, \dots, sj \quad (4)$$

$$X_{i,j,s,l} \leq h_{i,j,s} \quad i = 1, 2, \dots, m; j = 1, 2, \dots, n; l = 1, 2, \dots, li; s = 1, 2, \dots, sj \quad (5)$$

$$\sum_j \sum_s X_{i,j,s,l} = 1 \quad i = 1, 2, \dots, m; l = 1, 2, \dots, li \quad (6)$$

$$\sum_i \sum_l X_{i,j,s,l} = 1 \quad j = 1, 2, \dots, n; s = 1, 2, \dots, sj \quad (7)$$

$$t_{j,s} \geq 0 \quad j = 1, 2, \dots, n; s = 1, 2, \dots, sj \quad (8)$$

$$X_{i,j,s,l} \in \{0, 1\} \quad i = 1, 2, \dots, m; j = 1, 2, \dots, n; l = 1, 2, \dots, li; s = 1, 2, \dots, sj. \quad (9)$$

Constraint (2) in this model deals with the sequences of operations that must occur in a particular order. The third constraint forbids machine overlap and mandates that no machine process more than one operation at once. Constraint (4) forbids operations from running simultaneously; therefore, an operation is assigned to a specific idle machine under the condition that its preceding operation is completed. Additionally, a machine is selected in a constraint for each of the operations (5). Operations are assigned to the machines and are performed in the order specified by constraint (6). The number of operations that can be carried out on a single machine is constrained by constraint (7), based on the priority of the machine.

### 3.2. The Proposed Hybrid Genetic Algorithm-Simulated Annealing Algorithm

Even though the proposed hybrid genetic algorithm–simulated annealing algorithm is a traditional algorithm, it still works effectively for our recommendation system. The hybrid algorithm that is being suggested combines the GA and SA algorithms. The benefits of both algorithms are combined in the suggested framework to get the best answers to the scheduling problems. A flowchart for the suggested hybrid genetic algorithm (HGA) is shown in Figure 1. The random initialization of the population is where it all begins. A new knowledge-based operator is used in this stage to enhance the individual's solution quality, as the formed population is assessed using the fitness function. This knowledge-based operator also integrates with the function assessment stage and operates during machine downtime.

A selection operator is used during the reproduction phase to choose the mating pool's parents, followed by a crossover to create the progeny, when the operator is used. To create the mutants, a mutation operator is also applied to a group of people chosen at random. The evaluation of the produced offspring and mutants is followed by consideration of the termination circumstances, which directs the algorithm in the appropriate direction. Section 3.7 details the termination requirements.

However, the simulated annealing algorithm will converge to a fixed point in simulated annealing; the acceptance probability for a new state in step  $k$  is traditionally defined as

$$(\text{accept new}) = \begin{cases} \exp\left(-\frac{\Delta}{T_k}\right) & , \text{if } \Delta \geq 0 \\ 1 & , x < 0 \end{cases}$$

where  $\Delta = f(\text{new}) - f(\text{old})$  is the change in objective function  $f$ , which is to be minimized, and  $T_k$  is a strictly decreasing positive sequence with  $\lim_{k \rightarrow \infty} T_k = 0$ .

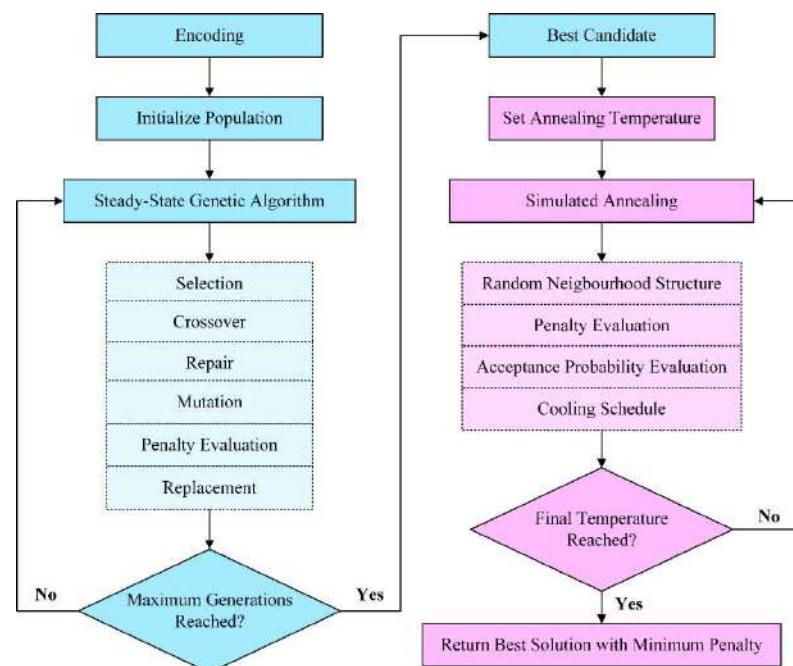


**Figure 1.** The proposed hybrid genetic algorithm–simulated annealing algorithm.

When the algorithm runs through the termination condition, which is when GA's generations come to an end, SA will begin with the top GA performer. In SA, a neighborhood search structure is used with three separate operators as the proposal mechanism: swapping, insertion, and reversion. Additionally, as each SA cooling criterion is met, a pool of people with the beta percent of accepted solutions is maintained.

In Section 3.6, the SA algorithm is covered in detail. Three conditions are set in this phase of the algorithm to either stop it or proceed with fresh parameters. The parameters of SA are reset and fresh GA parameters are applied if the most recent condition, or condition 4, which is the termination of SA's outer loop, is reached. Additionally, from the migration pool of SA, zeta percent of unique persons are relocated to GA.

### 3.3. Encoding and Decoding

Finding the right encoding and decoding techniques to describe the problem is the first and most crucial stage in any algorithm. The permutation of operations for various occupations is represented in this paper using an operation-based representation [34,37]. If the technology limitations are met, the timetable could be built using this representational approach. According to this method, a chromosome is made up of  $nm$  genes, each of which encodes the order of operations to be carried out on the machines.

Each operation is indicated by a positive integer number ranging from 1 to  $n$  (see in Figure 2). Each of the integer values has an equal number of occurrences and operations. In other words, the  $k$ th instance of an integer value in a chromosome corresponds to the  $k$ th technological procedure of the task. Each tourist on this chromosome consists of three processes, and as a result, every job appears three times along the length of the chromosome. For instance, this chromosome's sixth and ninth genes, respectively, reflect the second and third operations of jobs one and two. Each chromosome also has other data that are related to it, such as the machine number, processing time, start time, and finish time.

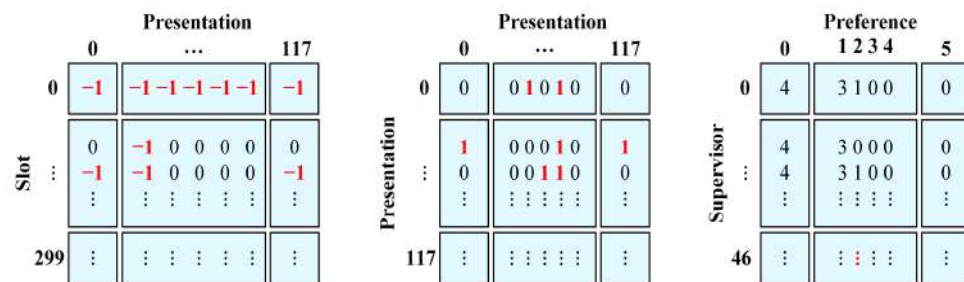


**Figure 2.** From the left, presentation-by-presentation matrix, supervisor-by-preference matrix, and slot-by-presentation matrix.

### 3.4. The Knowledge-Based Operator and the Fitness Function

The likelihood that a solution can be passed on to the following generation in an optimization problem is often determined by the fitness function. In other words, by using this operator, the solution quality is assessed, and the better-fitting chromosomes will have a higher chance of survival; nevertheless, the less well-fitting chromosomes must be eliminated from the population. There are numerous possible performance evaluators for defining the fitness function in scheduling problems. In this study, the fitness function used to assess each chromosome is either makespan or Cmax. A new knowledge-based operator is created in this algorithm and in the context of the fitness function based on the characteristics of the challenge. Based on the machine idle times present in job shop settings, this operator was created. Additionally, in order to shorten the algorithm's computation time and cover all the chromosomes that need to be evaluated, this knowledge-based operator is used during the function evaluation phase. The next stages are used to develop this operator more effectively.

The first step is to locate each machine's idle positions. The idle start time, idle finish time, and idle time must then be determined for each of these inactive points.

Step 2. Taking into account the length of idle time as well as the processing time of the candidate operation, a candidate operation is selected from the right side of the machine sequence list based on the position of the idle point on the machine sequence list.

Step 3: If the amount of idle time is greater than or equal to the candidate operation's processing time, it will be conditionally accepted. If not, it will be turned down.

Step 4. If the candidate operation is not accepted for transfer, the operator returns to step 2 and selects the next operation.

Step 5: To decide whether to accept or reject the shift for the conditionally accepted candidate operation, all processing limitations must be taken into account. For instance, the candidate operation's previous operation must be finished.

Step 6: The candidate operation will be moved to its new location if all of the constraints are met. If not, the candidate operation will remain in its current place.

Step 7. Steps 2 through 6 should be repeated for each machine until the very last action on the machine sequence list.

### 3.5. Encoding Selection Operator

An effective selection method can improve GA's performance by enabling it to find the best solutions more quickly. The most popular operator, the Roulette Wheel selection technique, is used in this study to choose the parents [34]. Additionally, the elitism strategy is used in this selection process to keep the fittest chromosomes for the following generation and stop the problem from getting worse over time.

We determined the likelihood of each chromosome in Roulette Wheel selection using Boltzmann Probability  $P(x) = \exp(f(x))/f(x)$ .  $P(x)$  in this equation stands for the likelihood of each chromosome, indicating selection pressure, while  $f(x)$  stands for each individual's fitness, and  $f(x)$  is the fitness of the generation's lowest performer. It should be noted that in order to make the selection pressure independent of the problem scale,  $f(x)$  was



added to the original Boltzmann Probability equation. Additionally, each chosen person's normalized probability is stated as  $P(x)_{\text{norm}} = P(x) / \max.\text{pop} \times 1 P(x)$ .

### 3.6. Crossover

In GA, crossover is the most crucial operator compared to other operators, and is actually the algorithm's foundation. By merging the data from the first and second parents, the crossover operator creates offspring with traits from both parents that may be better or worse than their parents. Additionally, the major objective of this operator is to create viable offspring using parental knowledge that is better.

In this study, a realistic offspring generation method called a machine-based precedence-preserving order-based crossover (POX) is proposed [25]. The POX operator is implemented using the specific steps listed below. Figure 3 show the process of chromosome which in the red frame show the presentation of process by the following step.

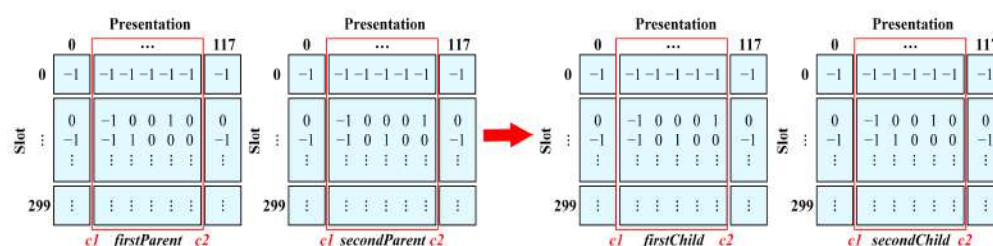


**Figure 3.** Process of a chromosome.

Step 1: Using Roulette Wheel selection, two people are first chosen to serve as parents (P1, P2).

Step 2: Next, two groups of tourists are chosen and given the names sj1 and sj2. One of the tourists is chosen at random from the remaining n jobs, and one is chosen from the bottleneck machines.

Step 3 copies the components of the first tourists (sj1) from the first parent (P1) to the precise locations; in other words, the elements of the second tourists (sj2) are replicated exactly from the second parent (P2) to the alleles in the second child (O2), and the same is true for the second tourists (sj2).

Step 4: In the first tourists (sj1) and the second tourists (sj2), all of the alleles are deleted in the second parent (P2) and, in the case of the second tourists (sj2), all of the alleles are deleted in the first parent (P1).

Step 5: From the furthest left to the furthest right, the second and first children (O2, O1) receive the remaining alleles from the first and second parents (P1, P2), respectively.

### 3.7. Mutation

Mutation is the second method of examining the solution space during the reproduction phase. The mutation operator can make the algorithm faster at finding better solutions and prevent it from getting stuck in the local optima. Additionally, it might alter the chromosome to broaden the diversity of the population.

Two different kinds of mutation operators, namely, swapping and insertion, are used in this approach. The insertion operator could perform a thorough search in addition to increasing the population's variety through mutation. It should be emphasized that one of these mutation operators, which are listed below, should be chosen at random in order to produce an offspring. Figure 4 show the process of chromosome mutation which the red frame shows the result of the process of the following operator.

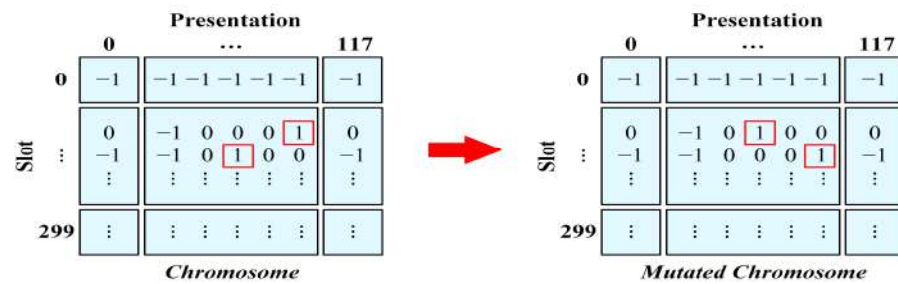


Figure 4. Process of chromosome mutation.

(1) Swapping operator: Before using the swapping operator, two random values ( $R = 2, 5$ , for example) are created that represent the locations of two alleles on the chromosome. Except for the randomly chosen alleles that must be switched or exchanged in the offspring, all of the parental information is then copied to the exact places in the child. Consider the parent who was chosen at random from the population.

(2) Insertion operator: To use the insertion operator, two random values are first created to represent the locations of two alleles on the chromosome. The offspring's genetic makeup is then identically duplicated from the parent, with the exception of the randomly chosen alleles. The other randomly chosen allele with a greater job-value is positioned to the left of the smaller randomly chosen allele.

Figure 5 show the simulated annealing process to evaluate the accuracy of this algorithm via convergence, the plot of cost vs. iterations makes it simple to see how the SAA is convergent. Other elements with a similar viewpoint include round-off errors and local extrema. In Figure 6, the cost function is the minimum, beginning at generation 1125.

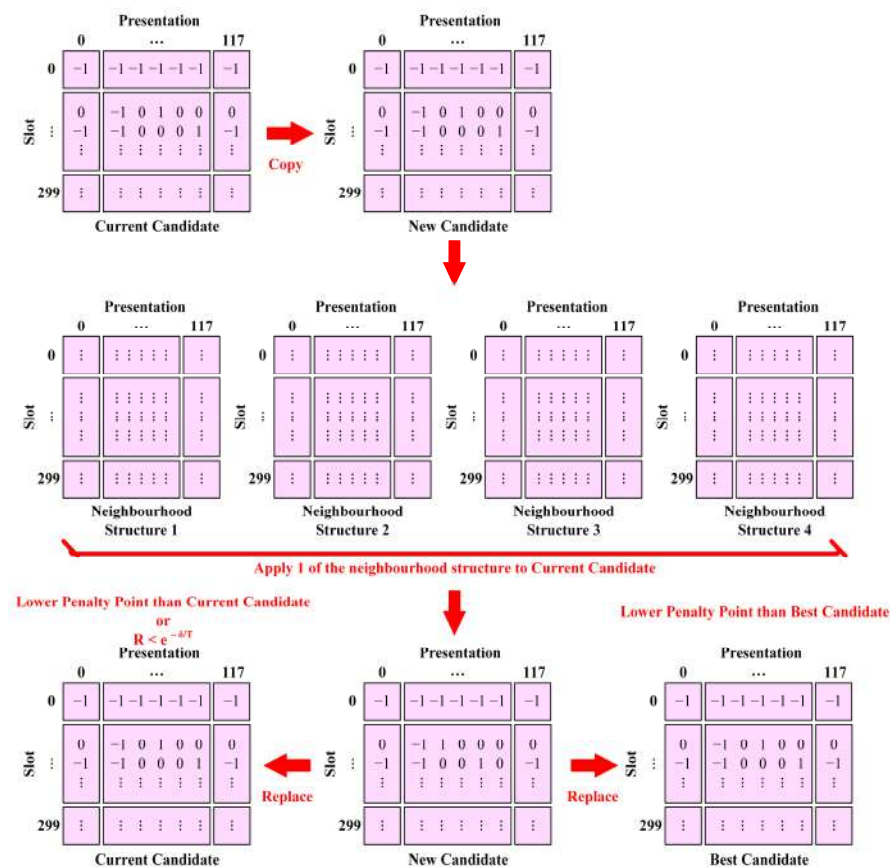


Figure 5. Simulated annealing process.

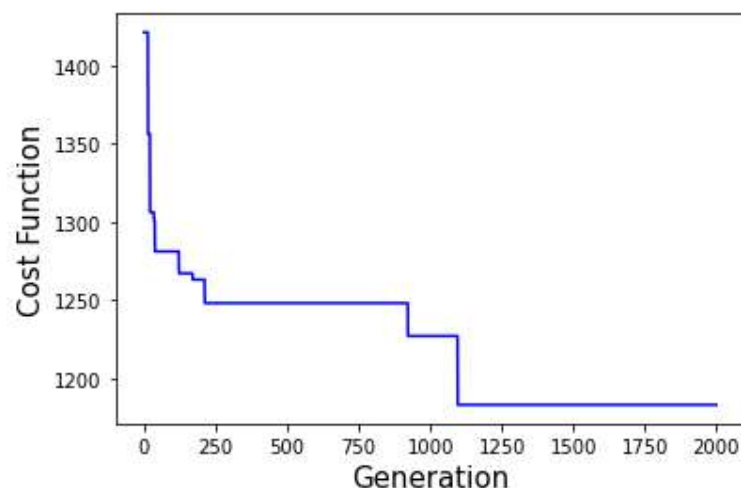


Figure 6. Cost function.

## 4. Results

### 4.1. Simulated Annealing

The SA technique, which is categorized as a stochastic local search approach, was motivated by the physical annealing process of solid materials [35]. In SA, the search operator is periodically allowed to take bad turns, which allows the algorithm to divert from local solutions and move toward global ones. In SA, this trait could be acquired by probabilistically opting for the less desirable options.

In the suggested HGA, SA begins with the top GA solution. Then, using the current solution (S), a proposal mechanism made up of the three operators (swapping, insertion, and reversal) is used to create a new neighborhood solution (S). The freshly created solution (S) is subjected to the new knowledge-based operator, after which it is assessed using the objective function. The newly evaluated neighborhood solution will be accepted ( $f(S)$   $f(S)$ ) if it is on par with or superior to the current solution. If not, the algorithm will carry on searching for a solution (S or S) determined by a probabilistic acceptance function. Acceptance of a solution is also determined by the value of the individual's goal function and the algorithm's current temperature (T) ( $e^{[(f(S)-f(S))/T]}$ ). An acceptable answer is maintained among a fresh group of people in each inner loop of SA. The starting value of the temperature should be changed in accordance with the annealing schedule as the algorithm's inner loops are ended. Additionally, in each outer loop of SA, the remaining individuals from the new pool of individuals are discarded, while a beta percent of the unique individuals are maintained. Additionally, 25% of unique individuals are retained once the outer loop is closed for migration-related purposes, while the remaining remainders are deleted. It should be emphasized that a low migration rate is required in order to somewhat increase the variety of the GA population. Three operators (swapping, insertion, and reversion) are utilized in SA's proposal method, and one of them is arbitrarily chosen and used to produce the neighborhood solution.

### 4.2. Ending Conditions

Four distinct conditions are offered in the proposed HGA in order to fully or partially terminate the algorithm. The achievement of the best-known solution serves as the first termination condition, and the maximum number of generations in the HGA main loop serves as the third termination condition. The entire algorithm will be terminated at once if it meets either the first or third criteria. The maximum number of generations in GA and the maximum number of outer loops in SA are the second and fourth partial conditions, respectively.

#### 4.3. Computational Experiments and Discussion

The following table provides a comparison between the planned HGA and the traditional GA. The same parameters are used to implement GA and HGA in a Python 3 environment. The fitness and execution time associated with the quantity of convergence iterations serves as the comparison criterion. For the HGA, all parameters are set for the best result after a specific number of iterations (in Table 1).

**Table 1.** Parameters.

Parameters	Values
Total number of iterations	2000
Number of individuals per generation	50
Chromosomes' size	8
Mutation probability	0.2
Mutant gene per individual	1
Crossover probability	1
Number of individuals chosen during the selection	1
Number of iterations for the LS	6
Number of neighbors per individual	4

The optimization results are compiled in the table. One thousand repetitions later, the ideal value had been reached. By providing a solid resolution, this also demonstrates that all genetic processes function effectively in general. In actuality, the program consistently moves closer to the ideal outcome. HGA, on the other hand, offers a reduction in the number of iterations required to converge from 15 s to 11 s. As a result, HGA can perform better than regular GA on an optimization problem, which demonstrates the hybridization mechanism's ability to improve convergence (in Table 2).

**Table 2.** Genetic algorithm and hybrid genetic algorithm performance.

	Convergence (Iterations/Time CPU)
Genetic Algorithm	15/60 s
Hybrid Genetic Algorithm	11/46 s

The proposed HGA was implemented using Python, and the technique was tested on a machine running Windows 10, an Intel Core i5 running at 2.5 GHz, with 8 GB of RAM. The results of the computational experiments were derived using the 10 well-researched tourism services with the aforementioned tweaked parameters and 10 replications for each benchmarked instance (Figure 7). The dimension of the problem is tourism services, the best-known solution, and the outcomes of our proposed HGA, which are presented in columns and include the best replication-level solution, relative deviation (RD), average solution, and worst algorithmic solution over ten runs. These are the most crucial indexes to compare in order to evaluate the algorithm's efficiency and consistency.

The notion of the "smart city" has improved the effectiveness and procedure of city management while integrating connection in many different domains. It requires strategic and innovative thinking to implement the smart city program, because it is not simple to do so. The first steps in this strategic program include problem identification, problem grouping, an abstraction process, solution selection, selection of efficient techniques, and implementation planning. The community and organizations can benefit from the innovative and valuable works produced by creativity. It is possible to research a variety of organizational traits, including human resource management and leadership planning. One tactic for raising public service companies' effectiveness is innovation. The limitations in the implementation of smart cities have not stopped efforts to advance numerous applications and other technologies. Chiang Mai has a plan to become a smart city, aiming to improve services to the community by utilizing local knowledge and maximizing the application

of technology. One of the applications is called the Chiang Mai Smart City For Smart Mobility, which stores all the route data in Chiang Mai such that our proposed method can be applied effectively. A smart city is a form of the application of digital technology or information and communication to enhance the efficiency and quality of travel services, and help reduce costs and population consumption. Increasing the capacity of people to achieve a better quality of life, the smart city is a project that many cities around the world have sought to develop, in order to keep up with the new era by using technology. Technology is integrated with the life of the people, whether in terms of transportation power consumption or infrastructure, to make the city more comfortable. Chiang Mai is ready to drive smart city developments via a strategy to improve performance in a systematic way, and thus facilitate the development of a pattern that will drive Chiang Mai to truly become a city of life and wealth.

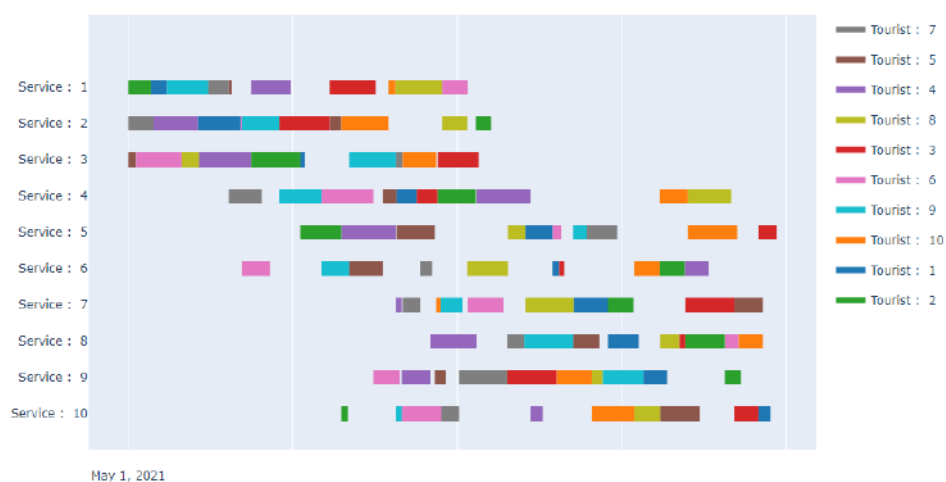


**Figure 7.** Tourism service scheduling.

## 5. Conclusions and Discussion

The algorithm's result was encoded in an operation-based form. The problem features were used to develop a new knowledge-based operator, which was able to improve the schedule solutions' quality. In order to boost population variety and sharpen the search, a machine-based precedence-preserving order-based crossover and two types of mutation operators, namely, swapping and insertion, were used to produce the offspring and mutants. Additionally, the SA method was used to further enhance the GA solution's quality due to its neighborhood search functionality.

The research library's well-studied benchmarked cases were used to test the proposed HGA, and the results were compared to those of other methods.

The usefulness and efficiency of the suggested technique are demonstrated by the computational results, which generally reveal that the proposed algorithm has a lower average relative deviation than the compared algorithms.

This paper adopts a hybrid genetic algorithm–simulated annealing algorithm to create schedules for tourism services, which meets the interests of active tourists by collecting data from Thailand's tourism industry on the preferences of tourists. Our proposed algorithm is able to create schedules for tourism services and develop recommendations. The system employs minimum costs to create schedules for tourism services by the using genetic algorithm approach. Our proposed hybrid recommendation algorithm focuses on the tourists in Thailand. In future research, this can be extended to compare with other algorithms and improve the recommendation system. The result of this study is a recommended system, related to the study of Duan et al. (2020) [89], for the optimal scheduling and management of a smart city within a safe framework. Moreover, the results show that the hybrid genetic algorithm can effectively generate a satisfaction tourism

service that saves energy which related the study of Alsokhiry et al. (2022) [90]—and thus develops a framework using pricing-based energy management.

A limitation of this study is that the method is time-consuming, which can cause the amount of services to vary if this method is applied in a large area, and will result in a very long time for the result to be output. Moreover, the accuracy of this work will be developed in future research.

We advise future researchers to consider the greenness issue in scheduling, because it is a new field that is expanding in manufacturing sectors. Additionally, recently created algorithms, such as the imperialist competitive algorithm, can be tested using the proposed framework and knowledge-based operator.

Additionally, one might think about creating new operators to further broaden the algorithm's population diversity, and even creating an operator to quantify population diversity.

**Author Contributions:** Conceptualization, P.S. and P.J.; methodology, P.S. and P.J.; software, P.S. and P.J.; validation, P.S. and P.J.; formal analysis P.S. and P.J.; investigation, P.S. and P.J.; resources, P.S. and P.J.; data curation, P.S. and P.J.; writing—original draft preparation, P.S. and P.J.; writing—review and editing, P.S., P.J., and P.K.; visualization, P.S. and P.J.; supervision, K.J.; project administration, P.S.; funding acquisition, P.S. All authors have read and agreed to the published version of the manuscript.

**Funding:** This research was funded by Suan Dusit University under the Ministry of Higher Education, Science, Research and Innovation, Thailand, grant number 65-FF-003 “Innovation of Smart Tourism to Promote Tourism in Suphan Buri Province”.

**Institutional Review Board Statement:** The study was conducted in accordance with the ethical and approved by the Ethics Committee of Suan Dusit University (SDU-RDI-SHS 2022-030, 1 June 2022) for studies involving humans.

**Informed Consent Statement:** Not applicable.

**Data Availability Statement:** Not applicable.

**Acknowledgments:** The research team would like to thank Suan Dusit University for the support with funding. Also, we would like to thank AVIC Research Center, Chulalongkorn University for consulting this paper. Finally, we would like to thank the Chiang Mai Municipality for all their cooperation and for providing the necessary information for the research.

**Conflicts of Interest:** The authors declare no conflict of interest.

## References

1. AuPinedo, M.L. Introduction. In *Scheduling: Theory, Algorithms, and Systems*; Springer: New York, NY, USA, 2012; pp. 1–10.
2. Garey, M.R.; Johnson, D.S.; Sethi, R. The complexity of flowshop and jobshop scheduling. *Math. Oper. Res.* **1976**, *1*, 117–129. [CrossRef]
3. Ullman, J.D. NP-complete scheduling problems. *J. Comput. Syst. Sci.* **1975**, *10*, 384–393. [CrossRef]
4. Carlier, J.; Pinson, E. An algorithm for solving the job-shop problem. *Manag. Sci.* **1989**, *35*, 164–176. [CrossRef]
5. Adams, J.; Balas, E.; Zawack, D. The shifting bottleneck procedure for job shop scheduling. *Manag. Sci.* **1988**, *34*, 391–401. [CrossRef]
6. Vancheeswaran, R.; Townsend, M.A. Two-stage heuristic procedure for scheduling job shops. *J. Manuf. Syst.* **1993**, *12*, 315–325. [CrossRef]
7. Brucker, P.; Jurisch, B.; Sievers, B. A branch and bound algorithm for the job-shop scheduling problem. *Discret. Appl. Math.* **1994**, *49*, 107–127. [CrossRef]
8. Lageweg, B.J.; Lenstra, J.K.; Rinnooy Kan, A.H. Job-shop scheduling by implicit enumeration. *Manag. Sci.* **1977**, *24*, 441–450. [CrossRef]
9. Fisher, H.; Thompson, G.L. *Probabilistic Learning Combinations of Local Job-Shop Scheduling Rules*; Prentice-Hall: Englewood Cliffs, NJ, USA, 1963.
10. Qing-Dao-Er-Ji, R.; Wang, Y.; Wang, X. Inventory based two-objective job shop scheduling model and its hybrid genetic algorithm. *Appl. Soft Comput.* **2013**, *13*, 1400–1406. [CrossRef]
11. Croce, F.D.; Tadei, R.; Volta, G. A genetic algorithm for the job shop problem. *Comput. Oper. Res.* **1995**, *22*, 15–24. [CrossRef]
12. Zhang, J.; Hu, X.; Tan, X.; Zhong, J.H.; Huang, Q. Implementation of an ant colony optimization technique for job shop scheduling problem. *Trans. Inst. Meas. Control* **2006**, *28*, 93–108. [CrossRef]
13. Zhang, J.; Zhang, P.; Yang, J.; Huang, Y. Solving the Job Shop Scheduling Problem using the imperialist competitive algorithm. *Adv. Mater. Res.* **2012**, *845*, 737–740. [CrossRef]

14. Piroozfard, H.; Wong, K.Y. An imperialist competitive algorithm for the job shop scheduling problems. In Proceedings of the IEEE International Conference on Industrial Engineering and Engineering Management (IEEM '14), Selangor, Malaysia, 9–12 December 2014; pp. 69–73.
15. Armentano, V.A.; Schich, C.R. Tabu search for minimizing total tardiness in a job shop. *Int. J. Prod. Econ.* **2000**, *63*, 131–140. [CrossRef]
16. Rakkiannan, T.; Palanisamy, B. Hybridization of genetic algorithm with parallel implementation of simulated annealing for job shop scheduling. *Am. J. Appl. Sci.* **2012**, *9*, 1694–1705.
17. Zhang, R.; Wu, C. A hybrid immune simulated annealing algorithm for the job shop scheduling problem. *Appl. Soft Comput. J.* **2010**, *10*, 79–89. [CrossRef]
18. Lei, D. A Pareto archive particle swarm optimization for multi-objective job shop scheduling. *Comput. Ind. Eng.* **2008**, *54*, 960–971. [CrossRef]
19. Coello, C.A.C.; Rivera, D.C.; Cortés, N. Use of an artificial immune system for job shop scheduling. In *Artificial Immune Systems*; Timmis, J., Bentley, P., Hart, E., Eds.; Springer: Berlin/Heidelberg, Germany, 2003; pp. 1–10.
20. Jain, A.S.; Meeran, S. Deterministic job-shop scheduling: Past, present and future. *Eur. J. Oper. Res.* **1999**, *113*, 390–434.
21. Çaliş, B.; Bulkan, S. A research survey: Review of AI solution strategies of job shop scheduling problem. *J. Intell. Manuf.* **2015**, *26*, 961–973. [CrossRef]
22. Holland, J.H. Genetic algorithms. *Sci. Am.* **1992**, *267*, 66–72. [CrossRef]
23. Davis, L. Job shop scheduling with genetic algorithms. In Proceedings of the 1st International Conference on Genetic Algorithms, Hillsdale, NJ, USA, 1 July 1985; pp. 136–140.
24. Yamada, T.; Nakano, R. A genetic algorithm applicable to large-scale job-shop problems. In Proceedings of the Parallel Problem Solving from Nature (PPSN-II '92), Brussels, Belgium, 28–30 September 1992; Elsevier Science: Amsterdam, The Netherlands, 1992; pp. 281–290.
25. Lee, K.M.; Yamakawa, T.; Lee, K.M. Genetic algorithm for general machine scheduling problems. In Proceedings of the 1998 Second International Conference. Knowledge-Based Intelligent Electronic Systems. Proceedings KES'98 (Cat. No.98EX111), Adelaide, SA, Australia, 21–23 April 1998; Volume 2, pp. 60–66. [CrossRef]
26. Sun, L.; Cheng, X.; Liang, Y. Solving job shop scheduling problem using genetic algorithm with penalty function. *Int. J. Intell. Inf. Process.* **2010**, *1*, 65–77.
27. Wang, L.; Zheng, D.Z. An effective hybrid optimization strategy for job-shop scheduling problems. *Comput. Oper. Res.* **2001**, *28*, 585–596. [CrossRef]
28. Zhou, H.; Feng, Y.; Han, L. The hybrid heuristic genetic algorithm for job shop scheduling. *Comput. Ind. Eng.* **2001**, *40*, 191–200. [CrossRef]
29. Ombuki, B.M.; Ventresca, M. Local search genetic algorithms for the job shop scheduling problem. *Appl. Intell.* **2004**, *21*, 99–109. [CrossRef]
30. Gonçalves, J.F.; Mendes, J.J.D.M.; Resende, M.G.C. A hybrid genetic algorithm for the job shop scheduling problem. *Eur. J. Oper. Res.* **2005**, *167*, 77–95. [CrossRef]
31. Lin, L.; Yugeng, X. A hybrid genetic algorithm for job shop scheduling problem to minimize makespan. In Proceedings of the 2006 6th World Congress on Intelligent Control and Automation, Dalian, China, 21–23 June 2006; pp. 3709–3713. [CrossRef]
32. Zhou, H.; Cheung, W.; Leung, L.C. Minimizing weighted tardiness of job-shop scheduling using a hybrid genetic algorithm. *Eur. J. Oper. Res.* **2009**, *194*, 637–649. [CrossRef]
33. Asadzadeh, L.; Zamanifar, K. An agent-based parallel approach for the job shop scheduling problem with genetic algorithms. *Math. Comput. Model.* **2010**, *52*, 1957–1965. [CrossRef]
34. Yusof, R.; Khalid, M.; Hui, G.T.; Md Yusof, S.; Othman, M.F. Solving job shop scheduling problem using a hybrid parallel micro genetic algorithm. *Appl. Soft Comput. J.* **2011**, *11*, 5782–5792. [CrossRef]
35. Kirkpatrick, S.; Gelatt, C.D., Jr.; Vecchi, M.P. Optimization by simulated annealing. *Science* **1983**, *220*, 671–680. [CrossRef]
36. Enoch, Y. Contents of tour packages: A cross-cultural comparison. *Ann. Tour. Res.* **1996**, *23*, 599–616. [CrossRef]
37. March, R. The Japanese travel life cycle. *J. Travel Tour. Mark.* **2000**, *9*, 185–200. [CrossRef]
38. Seddighi, H.R.; Theoharous, A.L. A model of tourism destination choice: A theoretical and empirical analysis. *Tour. Manag.* **2002**, *23*, 475–487. [CrossRef]
39. Wang, K.C.; Hsieh, A.T.; Chou, S.H.; Lin, Y.S. GPTCCC: An instrument for measuring group package tour service. *Tour. Manag.* **2007**, *28*, 361–376. [CrossRef]
40. Seddighi, H. Does cultural background of tourists influence the destination choice? an empirical study with special reference to political instability. *Tour. Manag.* **2001**, *22*, 181–191. [CrossRef]
41. Theuvsen, L. Vertical integration in the European package tour business. *Ann. Tour. Res.* **2004**, *31*, 475–478. [CrossRef]
42. Chen, Y.; Mak, B.; Li, Z. Quality deterioration in package tours: The interplay of asymmetric information. *Tour. Manag.* **2013**, *38*, 43–54. [CrossRef]
43. Alao, O.; Batabyal, A.A. Selling package tours to tourists: A contract theory perspective. *Ann. Tour. Res.* **2013**, *42*, 439–442. [CrossRef]
44. Aguiar-Quinatna, T.; Moreno-Gil, S.; Patricia-Peral, P. How could traditional travel agencies improve their competitiveness and survive? A qualitative study in Spain. *Tour. Manag.* **2016**, *20*, 98–108.



45. Reay, P.; Seddighi, H. An empirical evaluation of management and operational capabilities for innovation via co-creation. *European. J. Innov. Manag.* **2012**, *15*, 259–275. [CrossRef]
46. Nuray, A.; Theuvsen, L. Organic agriculture in Turkey: Status, achievements, and shortcomings. *Organ. Agric.* **2021**, *11*, 501–507. [CrossRef]
47. Jin, L.; He, Y.; Song, H. Service customization: To upgrade or to downgrade? An investigation of how option framing affects tourists' choice of package-tour service. *Tour. Manag.* **2012**, *33*, 266–275. [CrossRef]
48. Chen, H.; Weiler, B.; Young, M. Examining service shortfalls: A case study of Chinese group package tours to Australia. *J. Vacat. Market.* **2018**, *24*, 371–386. [CrossRef]
49. Batabyal, A.A.; Yoo, S.J. A probabilistic analysis of guided tours for tourists during the slack season. *Tour. Manag.* **2010**, *31*, 482–485. [CrossRef]
50. Jørgensen, F.; Solvoll, G. Demand models for inclusive tour charter: The Norwegian case. *Tour. Manag.* **1996**, *17*, 17–24. [CrossRef]
51. Tepelus, C. Aiming for sustainability in the tour operating business. *J. Clean. Prod.* **2005**, *13*, 99–107. [CrossRef]
52. Arabani, A.B.; Farahani, R.Z. Facility location dynamics: An overview of classifications and applications. *Comput. Ind. Eng.* **2012**, *62*, 408–420. [CrossRef]
53. Luan, J.; Yao, Z.; Zhao, F.; Song, X. A novel method to solve supplier selection problem: Hybrid algorithm of genetic algorithm and ant colony optimization. *Math. Comput. Simul.* **2019**, *76*, 294–309. [CrossRef]
54. Niknamfar, A.H.; Niaki, S.T.A. A binary-continuous invasive weed optimization algorithm for a vendor selection problem. *Knowl. Based Syst.* **2018**, *140*, 158–172. [CrossRef]
55. Tyan, I.; Yagüe, M.I.; Guevara-Plaza, A. Blockchain Technology for Smart Tourism Destinations. *Sustainability* **2021**, *12*, 9715. [CrossRef]
56. Koo, C.; Park, J.; Lee, J.N. Smart tourism: Traveler, business, and organizational perspectives. *Inf. Manag.* **2017**, *54*, 683–686. [CrossRef]
57. Taweesaengsakulthai, S.; Laochankham, S.; Kamnuansilpa, P.; Wongthanavas, S. Thailand Smart Cities: What is the Path to Success? *Asian Politics Policy* **2019**, *11*, 144–156. [CrossRef]
58. Chen, R.C.; Wang, H.L. Application of Genetic Algorithm to Scheduling of Tour Guides for Tourism and Leisure Industry. *INFOS Cairo-Egypt* **2008**, *43*, 4083–4101. [CrossRef]
59. Thumrongvut, P.; Sethanan, K.; Pitakaso, R.; Jamrus, T.; Golinska-Dawson, P. Application of Industry 3.5 approach for planning of more sustainable supply chain operations for tourism service providers. *Int. J. Logist. Res. Appl.* **2022**, 1–24. [CrossRef]
60. Li, X.; Yin, M. An opposition-based differential evolution algorithm for permutation flow shop scheduling based on diversity measure. *Adv. Eng. Softw.* **2013**, *55*, 10–31. [CrossRef]
61. Hassanat, A.B.; Prasath, V.B.S.; Abbadi, M.A.; Abu-Qdari, S.A.; Faris, H. An improved genetic algorithm with a new initialization mechanism based on Regression techniques. *Information* **2018**, *9*, 167. [CrossRef]
62. Lee, T.S.; Loong, Y.T. A review of scheduling problem and resolution methods in flexible flow shop. *Int. J. Ind. Eng. Comput.* **2019**, *10*, 67–88. [CrossRef]
63. Tosun, Ö.; Marichelvam, M.K.; Tosun, N. A literature review on hybrid flow shop scheduling. *Int. J. Adv. Oper. Manag.* **2020**, *12*, 156–194. [CrossRef]
64. Ben Cheikh-Graiet, S.; Dotoli, M.; Hammadi, S. A tabu search based metaheuristic for dynamic carpooling optimization. *Comput. Ind. Eng.* **2020**, *140*, 106217. [CrossRef]
65. Deng, G.; Wei, M.; Su, Q.; Zhao, M. An effective co-evolutionary quantum genetic algorithm for the no-wait flow shop scheduling problem. *Adv. Mech. Eng.* **2015**, *7*, 1687814015622900. [CrossRef]
66. Wei, H.; Li, S.; Jiang, H.; Hu, J.; Hu, J.J. Hybrid genetic simulated annealing algorithm for improved flow shop scheduling with makespan criterion. *Appl. Sci.* **2018**, *8*, 2621. [CrossRef]
67. Tasgetiren, M.F.; Kizilay, D.; Pan, Q.K.; Suganthan, P.N. Iterated greedy algorithms for the blocking flowshop scheduling problem with makespan criterion. *Comput. Oper. Res.* **2017**, *77*, 111–126. [CrossRef]
68. Wang, C.-N.; Yang, F.-C.; Nguyen, V.T.T.; Vo, N.T.M. CFD Analysis and Optimum Design for a Centrifugal Pump Using an Effectively Artificial Intelligent Algorithm. *Micromachines* **2022**, *13*, 1208. [CrossRef]
69. Abualigah, L.; Yousri, D.; Abd Elaziz, M.; Ewees, A.A.; Al-qaness, M.A.A.; Gandomi, A.H. Aquila Optimizer: A novel meta-heuristic optimization algorithm. *Comput. Ind. Eng.* **2021**, *157*, 107250. [CrossRef]
70. Czyżżak, P.; Jaskiewicz, A. Pareto simulated annealing—A metaheuristic technique for multiple-objective combinatorial optimization. *J. Multi-Criteria Decis. Anal.* **1998**, *7*, 34–47. [CrossRef]
71. Ulungu, E.L.; Teghem, J.; Fortemps, P.H.; Tuytens, D. MOSA method: A tool for solving multiobjective combinatorial optimization problems. *J. Multi-Criteria Decis. Anal.* **1999**, *8*, 221–236. [CrossRef]
72. Das, I.; Dennis, J.E. A closer look at drawbacks of minimizing weighted sums of objectives for Pareto set generation in multicriteria optimization problems. *Struct. Optim.* **1997**, *14*, 63–69. [CrossRef]
73. Sankararao, B.; Yoo, C.K. Development of a robust multiobjective simulated annealing algorithm for solving multiobjective optimization problems. *Ind. Eng. Chem. Res.* **2011**, *50*, 6728–6742. [CrossRef]
74. Suman, B. Simulated annealing-based multiobjective algorithms and their application for system reliability. *Eng. Optim.* **2003**, *35*, 391–416. [CrossRef]

75. Suman, B.; Kumar, P. A survey of simulated annealing as a tool for single and multiobjective optimization. *J. Oper. Res. Soc.* **2006**, *57*, 1143–1160. [CrossRef]
76. Suman, B.; Hoda, N.; Jha, S. Orthogonal simulated annealing for multiobjective optimization. *Comput. Chem. Eng.* **2010**, *34*, 1618–1631. [CrossRef]
77. Bandyopadhyay, S.; Saha, S.; Maulik, U.; Deb, K. A simulated annealing-based multiobjective optimization algorithm: AMOSA. *IEEE Trans. Evol. Comput.* **2008**, *12*, 269–283. [CrossRef]
78. Deb, K.; Pratap, A.; Agarwal, S.; Meyarivan, T. A fast and elitist multiobjective genetic algorithm: NSGA-II. *IEEE Trans. Evol. Comput.* **2002**, *6*, 182–197. [CrossRef]
79. Knowles, J.; Corne, D. The Pareto archived evolution strategy: A new baseline algorithm for Pareto multiobjective optimization. In Proceedings of the 1999 Congress on Evolutionary Computation-CEC99 (Cat. No. 99TH8406), Washington, DC, USA, 6–9 July 1999; Volume 1, pp. 98–105. [CrossRef]
80. Liu, H.; Kim, M.; Kang, O. Sensor Validation for Monitoring Indoor Air Quality in a Subway Station. *Indoor Built Environ.* **2012**, *21*, 205–221. [CrossRef]
81. Cao, P.; Tang, J. A reinforcement learning hyper-heuristic in multi-objective single point search with application to structural fault identification. *arXiv* **2018**, arXiv:1812.07958.
82. Rincón-García, E.A.; Gutiérrez-Andrade, M.A.; De-Los-Cobos-Silva, S.G.; Lara-Velázquez, P.; Ponsich, A.S.; Mora-Gutiérrez, R.A. A multiobjective algorithm for redistricting. *J. Appl. Res. Technol.* **2013**, *11*, 324–330. [CrossRef]
83. Mateos, A.; Jiménez-Martín, A. Multiobjective simulated annealing for collision avoidance in ATM accounting for three admissible maneuvers. *Math. Probl. Eng.* **2016**, *2016*, 8738014. [CrossRef]
84. Sengupta, R.; Saha, S. Reference point based archived many objective simulated annealing. *Inf. Sci.* **2018**, *467*, 725–749. [CrossRef]
85. Saadatpour, M.; Afshar, A.; Khoshkam, H. Multi-objective multi-pollutant waste load allocation model for rivers using coupled archived simulated annealing algorithm with QUAL2Kw. *J. Hydroinformatics* **2019**, *21*, 397–410. [CrossRef]
86. Marques, J.; Cunha, M.; Savić, D. Many-objective optimization model for the flexible design of water distribution networks. *J. Environ. Manag.* **2018**, *226*, 308–319. [CrossRef] [PubMed]
87. Zhang, L.; Zhang, B.; Bao, H.; Huang, H. Optimization of Cutting Parameters for Minimizing Environmental Impact: Considering Energy Efficiency, Noise Emission and Economic Dimension. *Int. J. Precis. Eng. Manuf.* **2018**, *19*, 613–624. [CrossRef]
88. Zhang, B.; Xu, L.; Zhang, J. A multi-objective cellular genetic algorithm for energy-oriented balancing and sequencing problem of mixed-model assembly line. *J. Clean. Prod.* **2020**, *244*, 118845. [CrossRef]
89. Duan, Q.; Nguyen, V.Q.; Heba, A.; Abdulaziz, A. Optimal scheduling and management of a smart city within the safe framework. *IEEE Access* **2020**, *8*, 161847–161861. [CrossRef]
90. Alsokhry, F.; Siano, P.; Annuk, A.; Mohamed, M.A. A Novel Time-of-Use Pricing Based Energy Management System for Smart Home Appliances: Cost-Effective Method. *Sustainability* **2022**, *14*, 14556. [CrossRef]

## Article

# GIS Fault Prediction Approach Based on IPSO-LSSVM Algorithm

Hengyang Zhao <sup>1,\*</sup>, Guobao Zhang <sup>2</sup> and Xi Yang <sup>3</sup>

<sup>1</sup> State Grid Anhui Electric Power Company Limited, Hefei 230022, China

<sup>2</sup> Electric Power Research Institute, State Grid Anhui Electric Power Co., Ltd., Hefei 230601, China

<sup>3</sup> School of Electrical Engineering and Automation, Hefei University of Technology, Hefei 230009, China

\* Correspondence: jianyanghubei@gmail.com

**Abstract:** With the improvement of industrialization, the importance of equipment failure prediction is increasing day by day. Accurate failure prediction of gas-insulated switchgear (GIS) in advance can reduce the economic loss caused by the failure of the power system to operate normally. Therefore, a GIS fault prediction approach based on Improved Particle Swarm Optimization Algorithm (IPSO)-least squares support vector machine (LSSVM) is proposed in this paper. Firstly, the future gas conditions of the GIS to determine the characteristic data of SF<sub>6</sub> decomposition gas are analyzed; Secondly, a GIS fault prediction model based on LSSVM is established, and the IPSO algorithm is used to normalize the parameters LSSVM. The parameters of  $c$  and radial basis kernel function  $\sigma^2$  are optimized, which can meet the needs of later search accuracy while ensuring the global search capability in the early stage. Finally, the effectiveness of the proposed method is verified by the fault data of gas-insulated switch. Simulation results shows that, compared with the prediction methods based on IGA-LSSVM and PSO-LSSVM, the prediction accuracy rate of the proposed method reached 92.1%, which has the smallest prediction absolute error, higher accuracy and stronger prediction ability.

**Keywords:** gas-insulated switchgear; failure prediction; parameter optimization; improved particle swarm optimization algorithm

**Citation:** Zhao, H.; Zhang, G.; Yang, X. GIS Fault Prediction Approach Based on IPSO-LSSVM Algorithm. *Sustainability* **2023**, *15*, 235. <https://doi.org/10.3390/su15010235>

Academic Editor: Mohamed A. Mohamed

Received: 27 November 2022  
Revised: 12 December 2022  
Accepted: 15 December 2022  
Published: 23 December 2022



**Copyright:** © 2022 by the authors. Licensee MDPI, Basel, Switzerland. This article is an open access article distributed under the terms and conditions of the Creative Commons Attribution (CC BY) license (<https://creativecommons.org/licenses/by/4.0/>).

## 1. Introduction

Gas-insulated switchgear (GIS) has the advantages of a small footprint, high operational reliability, and a long maintenance cycle [1–3]. So, it has been widely used in power systems, especially in high-voltage power grids [4,5]. Although GIS equipment has the advantage of high operational reliability, insulation and mechanical defects and failures still occur from time to time during its operation [6–8]. In order to meet the high efficiency and reliability of equipment operation, fault prediction can process the information measured by each sensor through certain theories and algorithms to infer the trend of fault development, so as to check the equipment to reduce the loss caused by the fault [9]. Therefore, to propose a GIS fault prediction method for accurate fault prediction in advance is of great significance to ensure the stable operation of the power system [10].

Because the fault prediction is carried out before the fault occurs, it often has the characteristics of small fault amplitude, inconspicuous fault characteristics, and easy to be covered by noise. Therefore, the signal processing and analysis before the fault occurs are the focus of fault prediction technology research [11–13]. The authors in [14] used the combination of deep neural network (DNN) and principal component analysis (PCA) to realize the early diagnosis and life prediction of small and slowly changing faults. In [15], in order to realize the active early warning of familial defect faults of power grid equipment, a familial defect fault database is established, and a probability prediction model between a single influencing factor and the defect decision data is established by the

Copula function. In order to solve the problem of large error and low accuracy in predicting equipment failure rate with a single model, a method for equipment failure rate prediction based on Autoregressive Moving Average Model-Back Propagation (ARMA-BP) combined model was proposed in [16]. The prediction results show that compared with the single prediction model, the equipment failure rate prediction result of the ARMA-BP combined model is more accurate. Reference [17] predicts the next batch of statistic values in GIS by establishing an autoregressive model, and compares the calculated value with the control limit, thereby realizing the prediction of S fault, but this method assumes that the trend of the fault is linear, and prediction results of the quantity are independent, so it is difficult to predict the nonlinear and multi-coupling data.

SF<sub>6</sub> gas-insulated metal-enclosed combined electrical appliances have become the main component of modern power systems because of their small footprint and high reliability [18]. Reference [19] proposed a fault detection method for gas-insulated switchgear based on a support vector machine and nuclear principal component analysis, and verified the reliability and accuracy of the algorithm through the actual sample test. Reference [20] established a GIS internal insulation electric field degradation calculation model, and used the central limit theorem to estimate the failure probability of the most harmful metal tip. In the literature [21], the online monitoring of the content of SO<sub>2</sub>, SOF<sub>2</sub>, H<sub>2</sub>S, CO and other components in the SF<sub>6</sub> gas decomposition products can quickly find the location of the gas chamber where the fault point is located, but no research has been conducted on the types of faults that cause gas composition changes. Reference [22] proposes a GIS state assessment method combining the subjective weighting method and the objective weighting method to judge the operating status of GIS equipment. This method can systematically and comprehensively evaluate the health status of GIS, but it cannot provide a reference for more detailed troubleshooting, which is difficult to apply in practical engineering. The applicability of the model to the data characteristics is not highly consistent, and the prediction accuracy cannot meet the requirements.

In summary, how to accurately diagnose GIS faults according to operating parameters has become a key technology that needs to be overcome. For this reason, a GIS fault prediction approach based on IPSO-LSSVM is proposed in this paper. The contributions are as follows:

- (1) A GIS fault prediction model based on IPSO-LSSVM is established.
- (2) The PSO algorithm is improved through weight nonlinear adjustment and iterative speed optimization, so as to improve the optimization ability and convergence speed of the algorithm.
- (3) The normalization parameter  $c$  of LSSVM and the parameter of radial basis kernel function  $\sigma^2$  are optimized by the improved PSO algorithm, so as to improve the accuracy of the prediction model.

The organization of this paper is as follows: Section 2 analyzes the GIS fault characteristics; Section 3 introduces the GIS fault prediction model based on the improved PSO-LSSVM; Section 4 introduces the improvement strategy of the PSO algorithm; the Section 4 is the simulation verification; Section 5 is the conclusion.

## 2. GIS Fault Feature Analysis

The main faults of SF<sub>6</sub> electrical equipment are discharge and overheating. The discharge mainly includes three types: arc discharge, spark discharge and corona discharge [23]. Both discharge and overheating will generate energy to promote the decomposition of SF<sub>6</sub> gas. The main components decomposed under the action of discharge are SF<sub>6</sub> and metal oxides of electrodes or containers. In the presence of water vapor and oxygen, SF<sub>6</sub> reacts with them and finally generates SO<sub>2</sub>, HF, SO<sub>2</sub>F<sub>2</sub> and SOF<sub>2</sub> and other compounds.

In the discharge state, the energy generated by different discharge types is different, which promotes the decomposition of SF<sub>6</sub> gas into different stable substances under different energy conditions. Studies have found that the ratio of SO<sub>2</sub>F<sub>2</sub>/SO<sub>2</sub> has certain regularity [24]. During corona discharge, its ratio is often in the range of 4.0~6.0 or even

higher, and spark discharges are mostly concentrated in 2.0~3.5. During arc discharge, the ratio is the smallest, mostly 0.1~0.3, which decreases with the increase in intensity of discharge.  $\text{SO}_2$  and  $\text{SO}_2\text{F}_2$  are substances that are produced in large quantities during discharge faults. Considering that they have good stability at the same time, monitoring will be more convenient and accurate. Based on the observation data of 220 kV voltage level GIS in a substation, some data of  $\text{SF}_6$  decomposition gas characteristics are shown in Table 1.

**Table 1.** Characteristic data of  $\text{SF}_6$  decomposition gas.

Fault State	Sample Eigenvalues		
	$\text{SO}_2/(\mu\text{L}\cdot\text{L}^{-1})$	$\text{SO}_2\text{F}_2/(\mu\text{L}\cdot\text{L}^{-1})$	$\text{SO}_2\text{F}_2/\text{SO}_2$
Arc discharge	19.47	4.14	0.213
Arc discharge	16.41	3.70	0.225
Arc discharge	12.73	3.29	0.258
Spark discharge	18.74	55.95	0.986
Spark discharge	21.11	44.87	2.126
Spark discharge	17.55	45.35	2.584
Corona discharge	26.77	151.91	5.675
Corona discharge	20.99	84.50	4.026
Corona discharge	23.12	121.07	5.237

When predicting the future failure condition of GIS, it is necessary to analyze the future gas condition of GIS. In this paper, based on the historical data of decomposed gas content in GIS gas chamber, the GIS fault prediction method based on IPSO-LSSVM is used to predict the decomposition gas of GIS gas chamber in the future.

### 3. GIS Fault Prediction Approach Based on Improved PSO-LSSVM

#### 3.1. Least Squares Support Vector Machine

The least squares support vector machine is a new type of support vector machine developed on the basis of the standard support vector machine. It replaces the inequality constraints of the traditional support vector machine (SVM) with equality constraints, and uses the sum of squares of errors as the empirical loss of the training set [25]. By transforming the quadratic programming problem into a system of linear equations, the solution speed and convergence accuracy are improved.

For the training sample set  $\text{Tr} = \{(x_1, y_1), (x_2, y_2), \dots, (x_n, y_n)\}$   $x_i \in R^d$ ,  $y_i \in \{1, 2, \dots, k\}$ ,  $i = 1, 2, \dots, n$ . The sample is mapped from the input space  $R^d$  to the feature space, the nonlinear mapping is  $\varphi(\cdot)$ , namely:

$$\psi(x) = (\varphi(x_1), \varphi(x_2), \dots, \varphi(x_n)) \quad (1)$$

construct an optimal decision function in the mapped feature space as follows:

$$y = w^T \cdot \varphi(x) + b \quad (2)$$

The decision function parameters  $w$  and  $b$  are determined based on the principle of structural risk minimization, and the solution process can be equivalent to solving the following optimization problems:

$$\begin{cases} \min R = c \cdot \sum_{i=1}^n \xi_i^2 + \frac{1}{2} \cdot \|w\|^2 \\ \text{s.t. } y_i = w^T \cdot \varphi(x_i) + b \quad i = 1, 2, \dots, n \end{cases} \quad (3)$$

The solution using the Lagrange method can be written as:

$$L(w, b, \xi_i, \alpha) = c \cdot \sum_{i=1}^n \xi_i^2 + \frac{1}{2} \|w\|^2 - \sum_{i=1}^n \left\{ \alpha_i \cdot [w^T \cdot \varphi(x_i) + b - y_i] \right\} \quad (4)$$

where  $\alpha = [\alpha_1, \alpha_1, \dots, \alpha_n]$  is the Lagrange multiplier.

According to the optimization conditions  $\frac{\partial L}{\partial w} = 0$ ,  $\frac{\partial L}{\partial b} = 0$ ,  $\frac{\partial L}{\partial \xi_i} = 0$ ,  $\frac{\partial L}{\partial \alpha_i} = 0$ , we can get:

$$w = \sum_{i=1}^n \alpha_i \cdot \varphi(x_i) \quad (5)$$

$$\sum_{i=1}^n \alpha_i = 0 \quad (6)$$

$$2c\xi_i = \alpha_i \quad (7)$$

$$y_i = w^T \cdot \varphi(x_i) + b + \xi_i \quad (8)$$

Substituting Equations (5) and (7) into Equation (8), we can get:

$$y_i = \sum_{j=1}^n (\alpha_i \cdot \langle \varphi(x_j), \varphi(x_i) \rangle) + b + \frac{1}{2c} \alpha_i \quad (9)$$

Assuming that the kernel function  $K(x_j, x_i) = \langle \varphi(x_j), \varphi(x_i) \rangle$  is defined, then

$$y_i = \sum_{j=1}^n (\alpha_i \cdot K(x_i, x_j)) + b + \frac{1}{2c} \alpha_i \quad (10)$$

Combining Equations (6) and (10) into a system of linear equations is as follows:

$$\begin{bmatrix} 0 & 1 & 1 & \dots & 1 \\ 1 & K(x_1, x_2) + \frac{1}{2c} & K(x_1, x_2) & \dots & K(x_1, x_n) \\ 1 & K(x_2, x_1) & K(x_2, x_2) + \frac{1}{2c} & \dots & K(x_2, x_n) \\ \vdots & \vdots & \vdots & \ddots & \vdots \\ 1 & K(x_n, x_1) & K(x_n, x_2) & \dots & K(x_n, x_n) + \frac{1}{2c} \end{bmatrix} \cdot \begin{bmatrix} b \\ \alpha_1 \\ \alpha_2 \\ \vdots \\ \alpha_n \end{bmatrix} = \begin{bmatrix} 0 \\ y_1 \\ y_2 \\ \vdots \\ y_n \end{bmatrix} \quad (11)$$

Based on the previously set training sample set  $(x_i, y_i), i = 1, 2, \dots, n, x \in R^d, y \in R$ , the model parameters can be obtained by solving the linear equation system (11). Then the decision function  $[b \ \alpha_1 \ \alpha_2 \ \dots \ \alpha_n]$  can be determined:

$$f(x) = \sum_{i=1}^n \alpha_i \cdot K(x, x_i) + b \quad (12)$$

In the coefficient  $\alpha$  of the support vector machine, if the element  $\alpha_i$  is not equal to zero, the so-called support vector  $\alpha_i$  is the corresponding sample  $(x_i, y_i)$ .

On the basis of LSSVM binary classification, a one-to-many classification algorithm is used to establish a multi-class classifier. For the  $k$  ( $k > 2$ ) class classification problem, take all the training samples of  $y = i$  and  $y \neq i$ , and construct  $k$  training subsets  $Tr_i$ . When constructing the  $m$ -th classifier among the  $k$  classifiers ( $m \in y_i$ ), the  $m$ -class training samples are used as the first class, the class number is  $y_i^m = \pm 1$ , and the other  $m-1$  classes are used as one class, the class number is  $y_i^m = -1$ .

When classifying the test sample, the test sample is first input to the classifier 1. If the output of the discriminant function is 1, the judgment category is the first type of fault; otherwise, it is automatically input to the next classifier 2, and so on, until the classifier  $k$ . If the output of the judgment function is 1, the judgment category is the  $k$ -th fault; if the output is  $-1$ , the test sample is not in the  $k$  categories and belongs to other categories.

### 3.2. Kernel Function and Parameter Selection

LSSVM transforms the optimization problem into solving a system of linear equations, which makes its model have better generalization ability, and the parameters in LSSVM have a great influence on the performance of the algorithm. In this paper, the Gaussian radial basis kernel function is selected as the kernel function. The normalization parameter  $c$  and the parameters of the radial basis kernel function  $\sigma^2$  play a key role in the learning ability, generalization ability and training calculation amount of the algorithm [26]. The size of  $\sigma^2$  is closely related to the sparsity of the coefficient matrix in formula (11). Another thing that needs to be determined is the regularization parameter  $c$  (also called penalty factor) of the model. Based on the principle of minimizing structural risk, its size determines the proportion of empirical risk in structural risk. The smaller  $c$  is the weaker the proportion of empirical risk will be, so the model will be simpler, but the accuracy will be reduced. If  $c$  is larger, the proportion of empirical risk will be larger, which can improve the accuracy of the model, but the cost is the model will be more complicated. Therefore, in practical applications, an optimal choice should be made between the accuracy and complexity of the model. Take a section of  $c$  and  $\sigma^2$ , and form a two-dimensional plane with the two sections, and perform continuous search based on the accuracy rate. It can be determined that the only one  $(c, \sigma^2)$  has the highest accuracy rate. It should be noted that this  $(c, \sigma^2)$  may be not the optimal solution of above, but it is also an acceptable satisfactory solution. Therefore, finding the most parameters and applying them to the state estimation model of LSSVM will improve the accuracy of state estimation.

This paper has utilized the improved particle swarm optimization algorithm to find the optimal parameters of LSSVM.

### 4. Improved LSSVM Parameter Optimization for PSO

In the prediction method proposed in this paper, the parameters  $c$  and  $\sigma^2$  of the LSSVM are determined by the improved particle swarm optimization algorithm, and the behavior of a group of particles with randomly selected initial values is modeled by the particle swarm optimization algorithm. The position and velocity of each particle over  $k$  iterations in the search space are described by  $X_k^i$  and  $V_k^i$ , respectively, and each particle records its best local position  $P_{\text{best}}^i$ . Then, at  $(k + 1)$  iterations, the velocity of particle  $i$  is obtained by the following equation:

$$V_{k+1}^i = \omega \cdot V_k^i + C_1 \cdot R_1 \left( P_{\text{best}}^i - X_k^i \right) + C_2 \cdot R_2 \left( P_{\text{global}}^i - X_k^i \right) \quad (13)$$

where  $R_1$  and  $R_2$  are random functions that generate random numbers between 0 and 1;  $C_1$  and  $C_2$  are training coefficients;  $\omega$  is inertia weight factors, which linearly decrease from 0.9 to 0.4, and it can be obtained by the following formula:

$$\omega = \omega_{\text{max}} - ((\omega_{\text{max}} - \omega_{\text{min}}) / k_{\text{max}}) \times k \quad (14)$$

where  $k_{\text{max}}$  is the maximum number of iteration. At the end of each iteration, the new position of each particle is obtained by the sum of its old position and new velocity:

$$X_{k+1}^i = X_k^i + V_{k+1}^i \quad (15)$$



In addition to improving the accuracy of the GIS fault prediction, the training time and convergence speed are also particularly important. Therefore, we use the particle swarm algorithm to optimize the parameters of the LSSVM model in this section, the particle swarm algorithm is mainly improved in terms of optimization effect and calculation time.

#### 4.1. PSO Weight Nonlinear Adjustment

The inertia weight factor  $\omega$  has a great influence on the position update of the PSO algorithm. When the inertia weight factor  $\omega$  is relatively large, the particle can quickly converge to the optimal position, but the volatility is large; when the inertia weight factor is relatively small, the particle convergence speed is slow, and it is easy to fall into the local optimum when faced with uncertain bionic optimization. Equation (14) is only processed by linearly decreasing the weight, and there is still room for improvement in the actual optimization process. Therefore, in this paper, the formula (14) is improved, and the weight is decreased by a nonlinear method. The improved inertia weight factor  $\omega$  is:

$$\omega = \omega_{\min} \left( \frac{\omega_{\max}}{\omega_{\min}} \right)^{\frac{1}{1+\sqrt{k}/k_{\max}}} \quad (16)$$

The nonlinear decreasing change of the inertia weight factor can be realized through the above formula, which not only ensures the global search ability in the early stage, but also meets the needs of the later search accuracy.

#### 4.2. PSO Iteration Speed Optimization

After each iteration, the new position of each particle will also change, so the search state will also be different. To adapt to this situation, this chapter optimizes and improves the iteration speed of Equation (15), namely:

$$X_{k+1}^i = X_k^i + \xi V_{k+1}^i \quad (17)$$

where  $\xi$  is the speed coefficient.

The parameter optimization process is shown in the Figure 1.

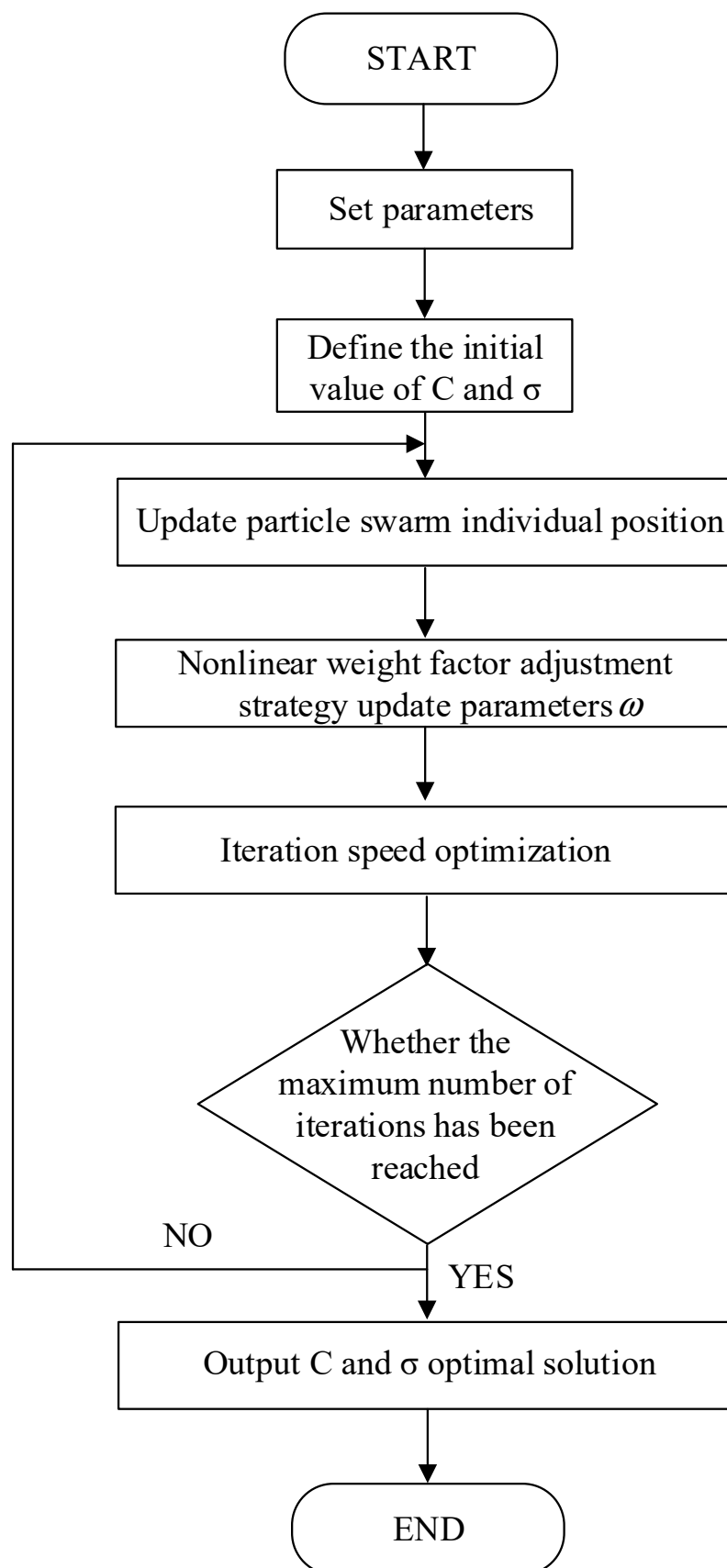


Figure 1. LSSVM parameter optimization process.

## 5. Simulation Results

Taking the data collected by the SF<sub>6</sub> online monitoring device of GIS in a distribution network as an example. A total of 400 sets of data from 1 March to 5 December 2021 are selected as the training set, and a total of 50 sets of samples of fault type data are selected as the test set. Code  $c$  and  $\sigma^2$  according to the real number coding mode, and the optimization interval is (0, 200), (0, 15), respectively. The basic parameters of the PSO algorithm are shown in Table 2. The IPSO iteration curve is shown in Figure 2.

**Table 2.** Related parameters of PSO.

Parameter	Numerical Value
$\omega_{\max}$	0.8
$\omega_{\min}$	0.5
$k_{\max}$	25
$C_1, C_2$	1.5
number of particles	100

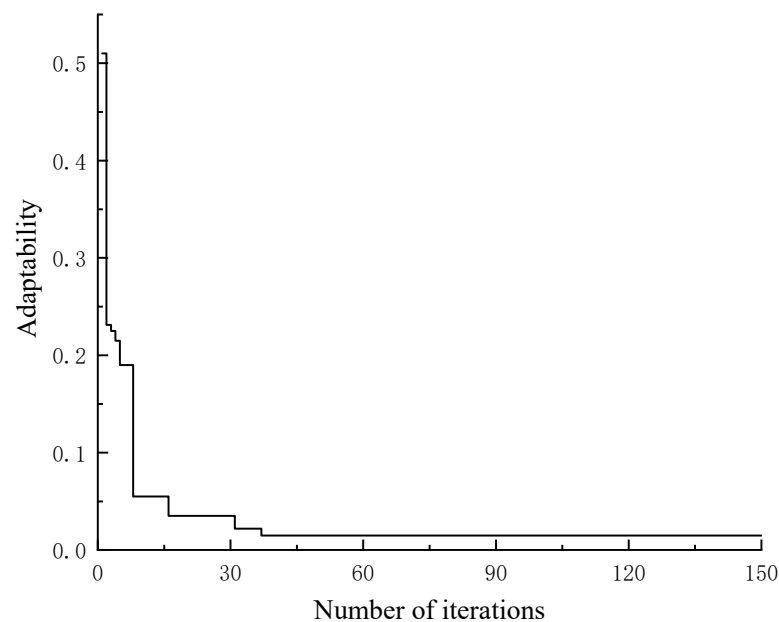


**Figure 2.** IPSO iteration curve.

It can be seen from Figure 2 that IPSO reaches the minimum fitness value after 37 iterations, and after that the value no longer changed. In addition, the corresponding optimal solutions  $c$  and  $\sigma^2$  are 64.35 and 2.47, respectively. In order to compare the optimization effect of IPSO, PSO and IGA are used to optimize  $c$  and  $\sigma^2$ , respectively, and the maximum number of iterations is set to 300. The calculation results of the three optimization algorithms are shown in Table 3.

**Table 3.** Comparison of optimization algorithms.

Optimization Algorithm	IGA	PSO	IPSO
Number of iterations at convergence	154	126	52
Minimum fitness value	0.0918	0.0642	0.0223
Convergence time/ms	7.49	8.66	4.24

It can be seen from Table 3 that IPSO is better than PSO and IGA in terms of the number of iterations, optimal value and convergence time. It can be seen that the improvement

strategy of the improved PSO algorithm proposed in this paper is successful. IPSO can effectively reduce the number of iterations and accelerate the convergence of the algorithm.

The ratio of  $\text{SO}_2\text{F}_2/\text{SO}_2$  was calculated to find the PD fault types, in which the number of samples of arc discharge fault types was 14, the classification error was 2 times, and the model prediction accuracy was 85.7%. There are 10 spark discharge fault type samples, one classification error, and the prediction accuracy rate is 90.3%. There are 18 normal samples, one prediction error, and the prediction accuracy rate is 94.4%. The overall accuracy of the model reached 92.1%. Prediction results and accuracy comparisons of different algorithms are shown in Tables 4 and 5.

**Table 4.** Analysis data of GIA gas prediction results.

Method of Prediction	$\text{SO}_2$	HF	$\text{SO}_2\text{F}_2$	$\text{SOF}_2$
Actual value	11.84	0.67	0.15	0.8
IGA-LSSVM predictive value	11.21	0.69	0.175	0.72
Absolute error	−0.63	0.02	0.025	0.08
PSO-LSSVM predictive value	11.19	0.64	0.159	0.75
Absolute error	0.65	−0.03	0.009	−0.05
IPSO-LSSVM predictive value	11.79	0.68	0.143	0.82
Absolute error	−0.05	0.01	0.007	0.02

**Table 5.** Comparison of prediction results of different algorithms.

Fault Type	Number of Samples	Accuracy		
		IGA-LSSVM	PSO-LSSVM	IPSO-LSSVM
1	15	86.4	77.6	85.7
2	10	81.7	89.5	90.1
3	8	77.4	87.4	99.8
4	20	83.2	85.2	95.6

It can be seen from Tables 4 and 5, compared with the prediction methods based on IGA-LSSVM and PSO-LSSVM, the method proposed in this paper has the smallest prediction absolute error, higher accuracy and stronger prediction ability.

## 6. Conclusions

A GIS fault prediction approach based on IPSO-LSSVM is proposed in this paper. The PSO algorithm is improved by nonlinear weight adjustment and iterative speed optimization, so as to optimize the normalization parameters of LSSVM. Simulation results show that: on the one hand, the improved PSO algorithm is superior to PSO and IGA in terms of the number of iterations, optimal value and convergence time, which can effectively reduce the number of iterations and speed up the algorithm convergence; on the other hand, compared with the traditional algorithm, prediction results of the proposed method are more accurate, so that the failure trend can be detected before the failure occurs, which can provide reference for the relevant staff.

In the aspect of power transformer fault diagnosis, with the development of electronic technology and sensor technology, the means of monitoring power transformers are increasing day by day. How to make full use of multi-dimensional information to comprehensively diagnose power transformers is a problem that needs further research in the field of power transformer fault diagnosis.

**Author Contributions:** All authors contributed equal. All authors have read and agreed to the published version of the manuscript.

**Funding:** This research received no external funding.

**Institutional Review Board Statement:** Not applicable.

**Informed Consent Statement:** Not applicable.

**Data Availability Statement:** Not applicable.

**Conflicts of Interest:** The authors declare no conflict of interest.

## References

1. Liu, L.; Wang, B.; Ma, F.; Zheng, Q.; Yao, L.; Zhang, C.; Mohamed, M.A. A concurrent fault diagnosis method of transformer based on graph convolutional network and knowledge graph. *Front. Energy Res.* **2022**, *10*, 127. [CrossRef]
2. Zhuang, Y.; Hu, X.; Tang, B.; Wang, S.; Cui, A.; Hou, K.; He, Y.; Zhu, L.; Li, W.; Chu, J. Effects of SF6 decomposition components and concentrations on the discharge faults and insulation defects in GIS equipment. *Sci. Rep.* **2020**, *10*, 15039–15048. [CrossRef] [PubMed]
3. Orrù, P.F.; Zoccheddu, A.; Sassu, L.; Mattia, C.; Cozza, R.; Arena, S. Machine learning approach using MLP and SVM algorithms for the fault prediction of a centrifugal pump in the oil and gas industry. *Sustainability* **2020**, *12*, 4776. [CrossRef]
4. Wang, Q.; Xiao, Y.; Dampage, U.; Alkuhayli, A.; Alhelou, H.H.; Annuk, A. An effective fault section location method based three-line defense scheme considering distribution systems resilience. *Energy Rep.* **2022**, *8*, 10937–10949. [CrossRef]
5. Wang, Q.; Jin, T.; Mohamed, M.A. An innovative minimum hitting set algorithm for model-based fault diagnosis in power distribution network. *IEEE Access* **2019**, *7*, 30683–30692. [CrossRef]
6. Faraz, B.; Alesheikh, A.A.; Sharif, M.; Farnaghi, M. FLCSS: A fuzzy-based longest common subsequence method for uncertainty management in trajectory similarity measures. *Trans. GIS* **2022**, *26*, 2244–2262.
7. Wen, T.; Zhang, Q.; Ma, J.; Wu, Z.; Shimomura, N.; Chen, W. A new method to evaluate the effectiveness of impulse voltage for detecting insulation defects in GIS equipment. *IEEE Trans. Dielectr. Electr. Insul.* **2019**, *26*, 1301–1307. [CrossRef]
8. Thacker, H.; Shah, Y.; Borah, A.J.; Jadeja, Y.; Thakkar, M.; Bhimani, S.; Chauhan, G. Assessment of groundwater potential zones across Katrol hill fault, Kachchh, Western India: A remote sensing and GIS approach. *Open J. Geol.* **2022**, *12*, 25–33. [CrossRef]
9. Wang, Q.; Jin, T.; Mohamed, M.A.; Deb, D. A novel linear optimization method for section location of single-phase ground faults in neutral noneffectively grounded systems. *IEEE Trans. Instrum. Meas.* **2021**, *70*, 1–10. [CrossRef]
10. Chen, Z.; He, G.; Li, J.; Liao, Y.; Gryllias, K.; Li, W. Domain adversarial transfer network for cross-domain fault diagnosis of rotary machinery. *IEEE Trans. Instrum. Meas.* **2020**, *23*, 61–73. [CrossRef]
11. Wu, Y.; Zhao, R.; Jin, W.; He, T.; Ma, S.; Shi, M. Intelligent fault diagnosis of rolling bearings using a semi-supervised convolutional neural network. *Appl. Intell.* **2020**, *5*, 21–29. [CrossRef]
12. Wu, Z.; Zhang, Q.; Ma, J.; Li, X.; Wen, T. Effectiveness of on-site dielectric test of GIS equipment. *IEEE Trans. Dielectr. Electr. Insul.* **2018**, *25*, 1454–1460. [CrossRef]
13. Zhang, L.; He, C.; Guo, R.; Yuan, W.; Li, J. Research on effectiveness of lightning impulses with different parameters for detecting protrusion defects in GIS. *IEEE Trans. Dielectr. Electr. Insul.* **2020**, *27*, 1354–1362. [CrossRef]
14. Wen, T.; Zhang, Q.; Ma, J.; Liu, X.; Wu, Z.; Zhang, L.; Zhao, J.; Shimomura, N.; Chen, W. Research on the detecting effectiveness of on-site lightning impulse test for GIS equipment with insulation defects. *IEEE Trans. Dielectr. Electr. Insul.* **2018**, *25*, 551–558. [CrossRef]
15. Deng, X.; Zhang, G. Family defect early warning of multi-factor GIS equipment based on ARMA and copula theory. *High Volt. Electr. Appl.* **2022**, *58*, 9–16.
16. Xu, D.; Zhou, C.; Guan, C.; Wang, X. Equipment failure rate prediction method based on ARMA-BP combined model. *Firepower Command. Control.* **2021**, *46*, 83–87.
17. Ji, H.; Ma, G.; Li, C.; Pang, Z.; Zheng, S. Influence of voltage waveforms on partial discharge characteristics of protrusion defect in GIS. *IEEE Trans. Dielectr. Electr. Insul.* **2016**, *23*, 1058–1067. [CrossRef]
18. Han, X.; Li, J.; Zhang, L.; Liu, Z. Partial discharge characteristics of metallic protrusion in GIS under different lightning impulse voltage waveforms based on UHF method. *IEEE Trans. Dielectr. Electr. Insul.* **2017**, *24*, 3722–3729. [CrossRef]
19. He, S.; Zhang, T.; Zhou, L.; Peng, X.; He, L. GIS fault diagnosis strategy based on feature classification algorithm. *Autom. Instrum.* **2019**, *232*, 197–200.
20. Wu, X.; Li, Y.; Pang, W. Research on the electric field degradation characteristics and fault probability prediction of GIS bus latent faults. *Power Grid Technol.* **2014**, *12*, 1–12.
21. Wu, Z.; Lyu, B.; Zhang, Q.; Liu, L.; Zhao, J. Phase-space joint resolved PD characteristics of defects on insulator surface in GIS. *IEEE Trans. Dielectr. Electr. Insul.* **2020**, *27*, 156–163. [CrossRef]
22. Yuan, Y.; Ma, S.; Wu, J.; Jia, B.; Li, W.; Luo, X. Frequency feature learning from vibration information of GIS for mechanical fault detection. *Sensors* **2019**, *19*, 1949. [CrossRef] [PubMed]
23. Yang, Y.; Ma, S.; Wu, J.; Jia, B.; Li, W.; Luo, X. Fault diagnosis in gas insulated switchgear based on genetic algorithm and density-based spatial clustering of applications with noise. *IEEE Sens. J.* **2019**, *21*, 965–973. [CrossRef]
24. Ma, S.; Chen, M.; Wu, J.; Wang, Y.; Jia, B.; Jiang, Y. Intelligent fault diagnosis of HVCB with feature space optimization-based random forest. *Sensors* **2018**, *18*, 1221. [CrossRef] [PubMed]

25. He, L.; Yang, J.; Zhang, Z.; Li, Z.; Ding, D.; Yuan, M.; Li, R.; Chen, M. Research on mechanical defect detection and diagnosis method for GIS equipment based on vibration signal. *Energies* **2021**, *14*, 5507. [CrossRef]
26. Zhang, C.; Dong, M.; Ren, M.; Huang, W.; Zhou, J.; Gao, X.; Albarracín, R. Partial discharge monitoring on metal-enclosed switchgear with distributed non-contact sensors. *Sensors* **2018**, *18*, 551. [CrossRef]

**Disclaimer/Publisher’s Note:** The statements, opinions and data contained in all publications are solely those of the individual author(s) and contributor(s) and not of MDPI and/or the editor(s). MDPI and/or the editor(s) disclaim responsibility for any injury to people or property resulting from any ideas, methods, instructions or products referred to in the content.

## Article

# An Efficient MPPT Technique-Based Single-Stage Incremental Conductance for Integrated PV Systems Considering Flyback Central-Type PV Inverter

Ahmed Ismail M. Ali <sup>1,\*</sup>, Zuhair Muhammed Alaas <sup>2</sup>, Mahmoud A. Sayed <sup>1</sup>, Abdulaziz Almalaq <sup>3</sup>, Anouar Farah <sup>3</sup> and Mohamed A. Mohamed <sup>4,\*</sup>

<sup>1</sup> Electrical Engineering Department, South Valley University, Qena 83523, Egypt

<sup>2</sup> Electrical Engineering Department, Jazan University, Jazan 45142, Saudi Arabia

<sup>3</sup> Department of Electrical Engineering, Engineering College, University of Ha'il, Ha'il 55476, Saudi Arabia

<sup>4</sup> Electrical Engineering Department, Faculty of Engineering, Minia University, Minia 61519, Egypt

\* Correspondence: a.ismail@eng.svu.edu.eg (A.I.M.A.); dr.mohamed.abdelaziz@mu.edu.eg (M.A.M.)

**Abstract:** Central-type photovoltaic (PV) inverters are used in most large-scale standalone and grid-tied PV applications due to the inverter's high efficiency and low-cost per kW generated. The perturbation and observation (P&O) and incremental conductance (IncCond) have become the most common techniques for maximum power point tracking (MPPT) strategies of PV/wind generation systems. Typically, the MPPT technique is applied in a two-stage operation; the first stage tracks the MPP and boosts the PV voltage to a certain level that complies with grid voltage, whereas the second stage represents the inversion stage that ties the PV system to the grid. Therefore, these common configurations increase the system size and cost as well as reduce its overall footprint. As a result, this paper applies two IncCond MPPT techniques on a proposed single-stage three-phase differential-flyback inverter (DFI). In addition, the three-phase DFI is analyzed for grid current negative-sequence harmonic compensation (NSHC). The proposed system efficiently provides a MPPT of the PV system and voltage boosting property of the DC-AC inverter in a single-stage operation. Moreover, the MPPT technique has been applied through the DFI using the conventional and modified IncCond tracking strategies. Furthermore, the system is validated for the grid-tied operation with the negative-sequence harmonic compensation strategy using computer-based simulation and is tested under uniform, step-change, as well as fast-changing irradiance profiles. The average efficiencies of the proposed system, considering the conventional and modified IncCond MPPT techniques, are 94.16% and 96.4% with tracking responses of 0.062 and 0.035 s and maximum overshoot of 46.15% and 15.38%, respectively.

**Keywords:** MPPT; incremental conductance (IncCond); differential inverter; differential flyback inverter (DFI); high-frequency transformer (HFT); continuous modulation scheme (CMS); harmonic compensation

**Citation:** Ali, A.I.M.; Alaas, Z.M.; Sayed, M.A.; Almalaq, A.; Farah, A.; Mohamed, M.A. An Efficient MPPT Technique-Based Single-Stage Incremental Conductance for Integrated PV Systems Considering Flyback Central-Type PV Inverter. *Sustainability* **2022**, *14*, 12105. <https://doi.org/10.3390/su141912105>

Academic Editor: Alberto-Jesus Perea-Moreno

Received: 10 August 2022

Accepted: 21 September 2022

Published: 25 September 2022



**Copyright:** © 2022 by the authors. Licensee MDPI, Basel, Switzerland. This article is an open access article distributed under the terms and conditions of the Creative Commons Attribution (CC BY) license (<https://creativecommons.org/licenses/by/4.0/>).

## 1. Introduction

Photovoltaic (PV) energy supplies the utility grid with electricity for public utilization purposes. PV energy generation offers many advantages compared with conventional fossil fuels, such as inexhaustible energy sources, environmentally-friendly nature of energy resources, and reduced cost per kWh [1,2]. Moreover, the modular operation characteristic of the PV generation system allows for the construction of solar energy systems at different power levels and load ratings. However, PV generation systems suffer from the drawback of low conversion efficiency and high installation cost [3]. In addition, the level of generated power from the PV system depends on many aspects, such as solar irradiance level and ambient temperature. However, the recent advancement in the interfaced power electronic technologies provides different solutions for solar energy



utilization with enhanced operational efficiency [4]. Considering different irradiance levels, there is only a unique point where the PV system generates the maximum power, as depicted in Figure 1. Therefore, it is very important for solar energy applications to track the point of peak power for better solar energy utilization.

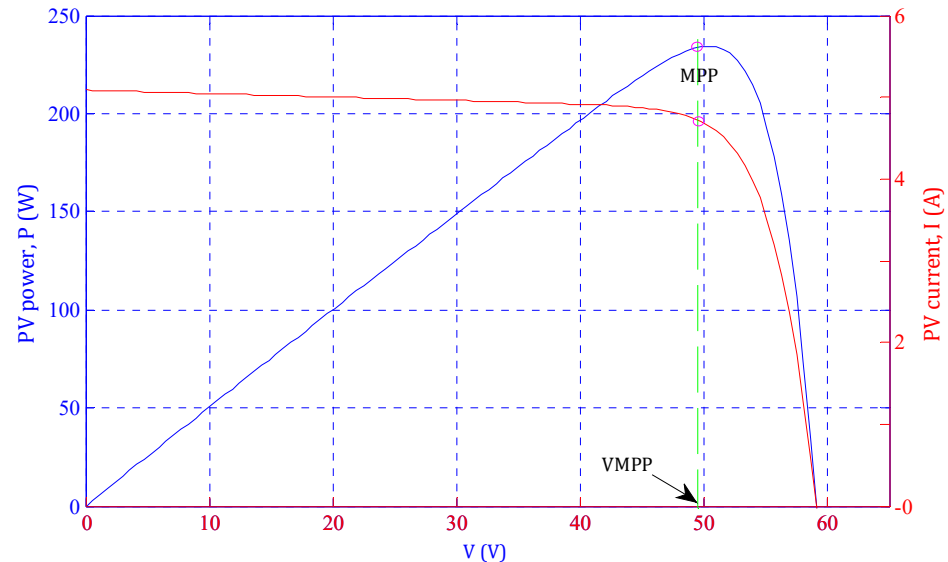


**Figure 1.** Characteristic curves of PV module.

To track the optimal power point, numerous maximum power point tracking (MPPT) techniques have been presented through interfaced power electronic circuits [5–7]. These MPPT algorithms vary in many aspects, such as tracking efficiency, system dynamic response (system settling time and overshoot), cost, and the required implementation equipment. An analysis of more than 30 different MPPT topologies is illustrated in [7,8]. Among the different MPPT topologies, perturbation and observation (P&O) [9–15] and incremental conductance (IncCond) [16–19] MPPT techniques are the most common topologies due to their simplicity, low implementation cost, and direct operation as a result of their independency on PV array parameters. In addition, different MPPT techniques have been proposed based on the parameters of the array, such as the fractional short-circuit current that predicts the location of optimal power from the short-circuit current [14,20], fractional open-circuit voltage that estimates the MPP from the array open-circuit voltage [21], fuzzy logic control-based tracker [22,23], neural network control-based algorithm [24], model-predictive control-based algorithm [25], and the sliding mode control-based MPPT techniques [26,27]. These tracking topologies are iterative MPPT topologies, which track the MPP with high precision under uniform irradiance conditions. However, these topologies suffer from slow response under load change and fast-changing weather conditions. In addition, the MPP spends a large execution time for MPPT control decision, which slows the system tracking response. In [28], an enhanced P&O technique has been presented to improve the PV system tracking operation under fast-changing irradiance conditions. In this control technique, the I-V curve of PV array has been used to differentiate between the irradiance change and operating point perturbation. However, this topology exhibits a slow system dynamic response with high contained steady-state oscillations. Moreover, an improved IncCond MPPT algorithm has been proposed in [16], which applies an allowable error level to improve the dynamic response of the conventional MPPT strategy under fast-changing irradiance conditions. However, it executes complex calculations that slow the system response. In [29], a modified IncCond strategy has been presented that efficiently tracks the optimal power point under fast-changing irradiance conditions. The presented topology improves the steady-state oscillations. However, the algorithm implements this function through complex computations that slows the system dynamic response. In [10], a modified P&O MPPT technique has been recommended to improve

the tracking efficiency. However, the proposed controller slows the system response to the long computational execution time. In [30], the basic IncCond MPPT technique has been implemented through Cuk converter, which directly perturbs the duty-cycle of the Cuk converter to track the MPP until the optimal power point location is reached. However, it uses the conventional fixed step-size voltage perturbation that slows the system dynamic response and decreases the system tracking efficiency. Therefore, many research efforts are exerted to improve the tracking efficiency as well as system efficiency by applying a few variable step-size perturbation control algorithms [31,32]. However, the fixed and variable step-size MPPT techniques are applied to improve the tracking efficiency and dynamic behavior of the proposed controller through the DC-DC converter or two-stage DC-AC conversion stage, which increases the system size and cost, and controls complexity. Recently, different MPPT control parameters and topics are raised for the optimal operation of MPPT techniques for modern distribution networks with multi-types of intermittent renewable energy resources [33–35].

### 1.1. Motivation

Stimulated by the aforementioned literature survey, this work aims to apply a modified IncCond MPPT algorithm via a single-stage isolated DC-AC grid-connected differential flyback inverter (DFI). Both MPPT techniques are direct MPPT controllers, which can operate directly with the PV without any pre-stored data requirements [1,2]. In addition, the conventional and modified IncCond MPPT algorithms are compared by a grid-connected PV system through the three-phase isolated DFI. The two MPPT algorithms are applied to the grid-tied PV system under uniform, step-changing, and fast-changing irradiance profiles. The modified MPPT algorithm improves the system dynamic performance by decreasing the system overshoot by 30% and the settling time by 0.03 s compared with the conventional fixed-step MPPT algorithm. Ultimately, the average tracking efficiency of the isolated three-phase grid-integrated PV system is increased from 94.17% to 96.42%.

### 1.2. Contribution

The significant contributions of this paper are summarized as follows:

1. The study provides a simple single-stage three-phase isolated grid-tied PV system through a differential flyback inverter.
2. The proposed system is applicable under conventional as well as modified MPPT algorithms and at different irradiance conditions.
3. The single-stage operation of the PV system exhibits improved average efficiencies of 94.17% and 96.42% for the conventional and modified algorithms, respectively, with grid isolation for protection purposes.
4. The modified MPPT algorithm enhances the system overshoot from 46.45% to 15.38% and the system settling time from 0.062 to 0.035 s.
5. The paper exhibits a simple, low-cost, and efficient single-stage three-phase isolated grid-tied PV system through DFI with a 1:2 voltage boosting property.

### 1.3. Organization

This paper is organized into the following sections. Section 2 illustrates the PV array model with a detailed analysis of PV array specifications. Section 3 analyzes the single-stage three-phase DFI circuit structure and operation, whereas the single-stage conventional and modified IncCond MPPT techniques are explained in Section 4. The system specifications and results considering the conventional and modified single-stage IncCond MPPT algorithms are deeply analyzed in Section 5. Finally, the conclusions are provided in Section 6.

## 2. Solar Cell Modeling

In general, different mathematical modeling topologies are presented for the solar cell, which form the basic constructional element in the PV array [3]. A single-diode model has

been used for simplicity purposes as depicted in Figure 2. The solar cell voltage-current mathematical relationship formula is as follows [1]:

$$I = I_{Ph} - I_{Sat} \cdot \left[ \exp \left\{ q \cdot \frac{V_{PV} + I_{PV} \cdot R_s}{A \cdot K \cdot T} \right\} - 1 \right] - \frac{V_{PV} + I_{PV} \cdot R_s}{R_{Sh}} \quad (1)$$

where

$I_{Ph}$ : light-produced current/photocurrent (A).

$I_{Sat}$ : reverse saturation-current (A).

$q$ : electron charge (C).

$V_{PV}$ : solar-cell output-voltage (V).

$I_{PV}$ : solar-cell output-current (A).

$R_s$  and  $R_{Sh}$ : series and shunt resistors ( $\Omega$ ), respectively.

$A$ : P-N junction ideality-factor.

$K$ : Boltzmann's constant ( $1.38 \times 10^{-23}$  J/K)

$T$ : solar-cell temperature (K)

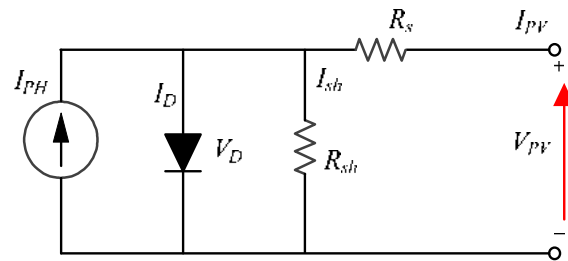


Figure 2. Solar cell model.

In addition, the produced photo-current depends on the level of irradiance ( $G$ ) and the cell ambient temperature ( $T$ ) as follows [2]:

$$I_{Ph} = \{I_{sc}^* + K_i(T - T^*)\} \cdot \frac{G}{G^*} \quad (2)$$

where  $I_{sc}^*$  is the short-circuit current of PV array at standard temperature and irradiation conditions (STICs) ( $T^* = 298$  K,  $G^* = 1000$  W/m<sup>2</sup>) and  $K_i$  is the PV array temperature co-efficient. In addition, the reverse saturation current is related to the cell temperature as follows [2]:

$$I_{Sat} = \frac{I_{sc}^* + K_i(T - T^*)}{\exp \left[ \frac{V_{oc}^* + K_v(T - T^*)}{V_t} \right] - 1} \quad (3)$$

where  $V_{oc}^*$ ,  $K_v$ , and  $V_t$  are the cell open-circuit voltage at STICs, open-circuit voltage co-efficient, and the thermal voltage ( $V_t = K \cdot T / q$ ), respectively.

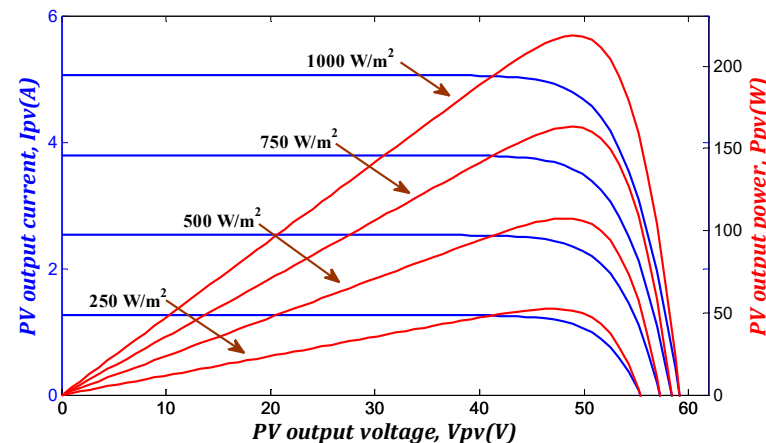
For a PV array combining series-connected cells of  $N_s$  per string and parallel-connected strings of  $N_p$ , the PV array generated output-current can be formulated as follows [36]:

$$I = N_p \cdot I_{Ph} - N_p \cdot I_{Sat} \cdot \left[ \exp \left\{ q \cdot \frac{\frac{V_{PV}}{N_s} + I_{PV} \cdot \frac{R_s}{N_p}}{A \cdot K \cdot T} \right\} - 1 \right] - \frac{\frac{N_p}{N_s} \cdot V_{PV} + I_{PV} \cdot R_s}{R_{Sh}} \quad (4)$$

Moreover, Canadian solar module CSP-220M PV is utilized in the proposed single-stage grid-tied system, where its characteristics under a uniform irradiance profile (1000 W/m<sup>2</sup>) are depicted in Table 1. In addition, the system characteristics are directly related to the applied irradiance level as depicted in Figure 3.

**Table 1.** Canadian solar module characteristics CSP-220M PV.

Maximum power, PMPP	220 (W)
MPP Voltage, VMPP	48.3159 (V)
MPP Current, IMPP	4.54758 (A)
Open-circuit voltage, VOC	59.2618 (V)
Short-circuit current, ISC	5.09261 (A)
Temperature, STC	25 °C

**Figure 3.** Output characteristics of the solar cell under different irradiance levels [1].

### 3. Three-Phase Single-Stage DFI

Figure 4 shows the three-phase DFI circuit structure, which consists of three parallel-connected input and differential-connected output flyback converter modules. Therefore, each module utilizes two switches ( $S_{Mx}$ ,  $S_{Rx}$ ), high frequency transformer ( $T_{rx}$ ), and output capacitor ( $C_{ox}$ ), where  $x = a, b$ , or  $c$ . Each flyback module temporarily transfers the input power to the secondary side with voltage bucking/boosting property as depicted in the operational modes in Figure 5. In addition, a variable duty-cycle is applied to control each flyback module under a wide range of duty-cycle changes to form DC output-voltage over module-output capacitors, which have a sinusoidal envelope and  $120^\circ$  phase-shift between the different modules (see Figure 4). Consequently, the differential connection between the flyback modules cancels the DC-voltage component and forms sinusoidal voltage waveforms at the grid terminals. Moreover, the success of the single-stage DFI depends on the flyback HFT design. As the DFI transfers the power temporarily to the grid, the HFT performs two main operational functions: (a) Storage element for the input power over the HFT magnetizing inductance,  $L_M$ , (b) Galvanic isolation for grid integration applications. In addition, the HFT offers further voltage bucking/boosting properties.

Different modulation schemes are used to control variable duty-cycle inverter topologies as reported in [37,38]. The grid-tied DFI synthesizes a sinusoidal grid current deceived with low-order harmonics due to the voltage boosting property with a mismatch between the converter modules and the input-to-output nonlinear relationship [39]. Therefore, the continuous modulation scheme (CMS) combined with the static linearization method (SLM) is used for low-frequency odd harmonics elimination in the grid-injected currents [40]. However, a feedback separate compensation loop is required for NS low-frequency even harmonics compensation. In addition, the CMS-based control scheme improves the input current ripple for PV applications as well as grid current THD to follow the IEEE and IEC standard harmonic limitations [41,42].

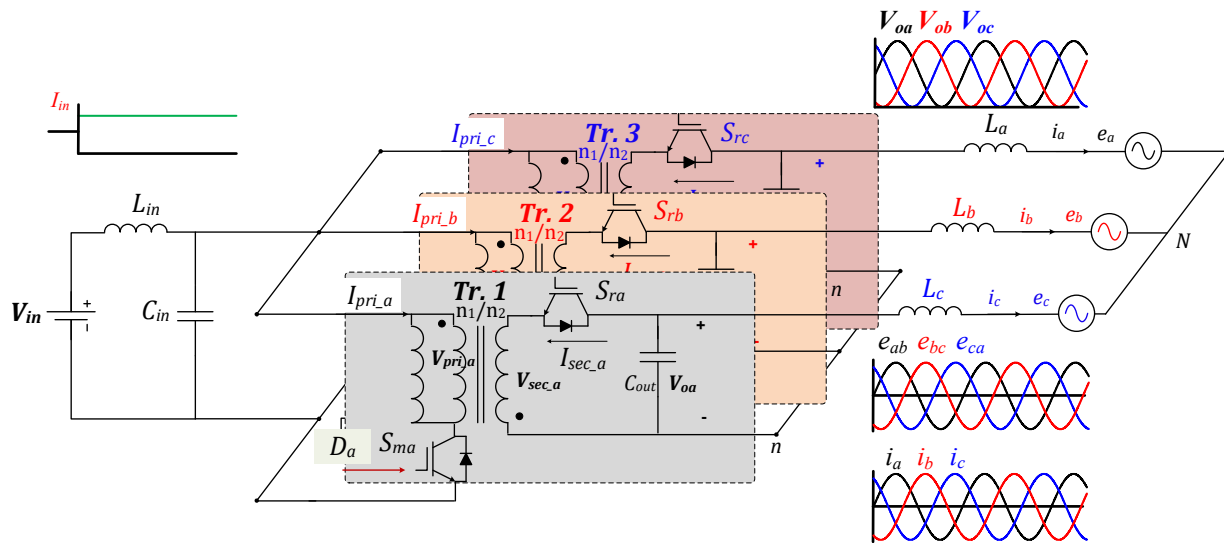


Figure 4. Differential-based three-phase flyback inverter.

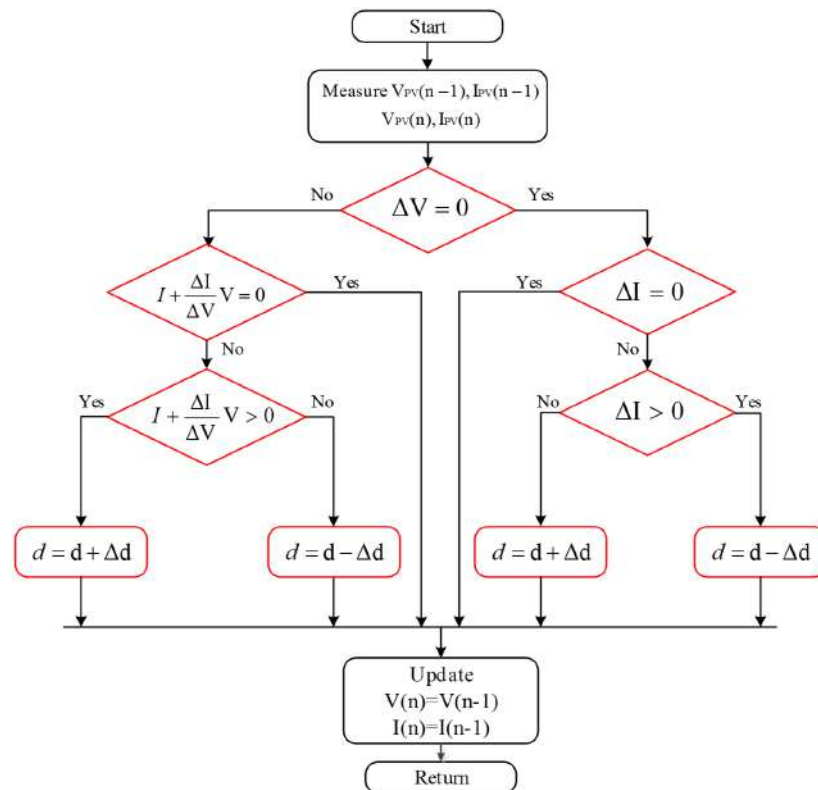


Figure 5. Conventional IncCond MPPT algorithm flowchart.

#### 4. Incremental Conductance MPPT

The incremental conductance is a common MPPT technique that tracks the optimal PV array power directly without pre-defined information about the PV system [1]. It tracks the MPP by comparing the addition of the instantaneous conductance ( $I/V$ ) and the incremental conductance ( $\Delta i/\Delta v$ ) with zero to decide the location of the MPP ( $I/V + \Delta i/\Delta v$ ). The slope of the solar array P-V curve is positive on the left side of MPP, zero at the MPP, and negative on the right side of MPP. Consequently, the MPPT algorithm adjusts the PV array voltage to control the operating point location. Therefore, when the P-V curve slope is negative, the controller moves the operating point to the left side toward the MPP locations by decreasing the PV array voltage. Similarly, when the slope is positive, it increases the

PV array voltage to move the operating point to the right side toward the MPP. Finally, as a null slope is reached, the voltage adjustment stops and the MPP is reached as depicted in the control algorithm in Figure 5. This simple and conventional MPPT algorithm tracks the MPP effectively at a uniform irradiance condition. However, it causes oscillations around the steady-state location and can easily divert the MPPT under fast-changing irradiance conditions. This conventional algorithm has the former handicap since it cannot differentiate between the fast-changing irradiance effects and the MPP location change.

Considering the former drawbacks, a modified IncCond MPPT technique is applied to track the optimal operating point location for efficient MPPT as shown in the algorithm flowchart in Figure 6 [3]. The modified algorithm tracks the MPP efficiently by checking the current variation sign with voltage variations. If the voltage perturbation results in current variations of the same sign, a sudden irradiance change is applied to the solar array (see Figure 6). Otherwise, the conventional IncCond technique is adequate to track the optimal MPP efficiently. In addition, the modified IncCond MPPT technique uses different step sizes in the PV array perturbation according to the location of the MPP on the P-V curve. Therefore, the closer the operating point to the MPP, the smaller the step size of voltage perturbation as depicted in the modified technique flowchart in Figure 6.

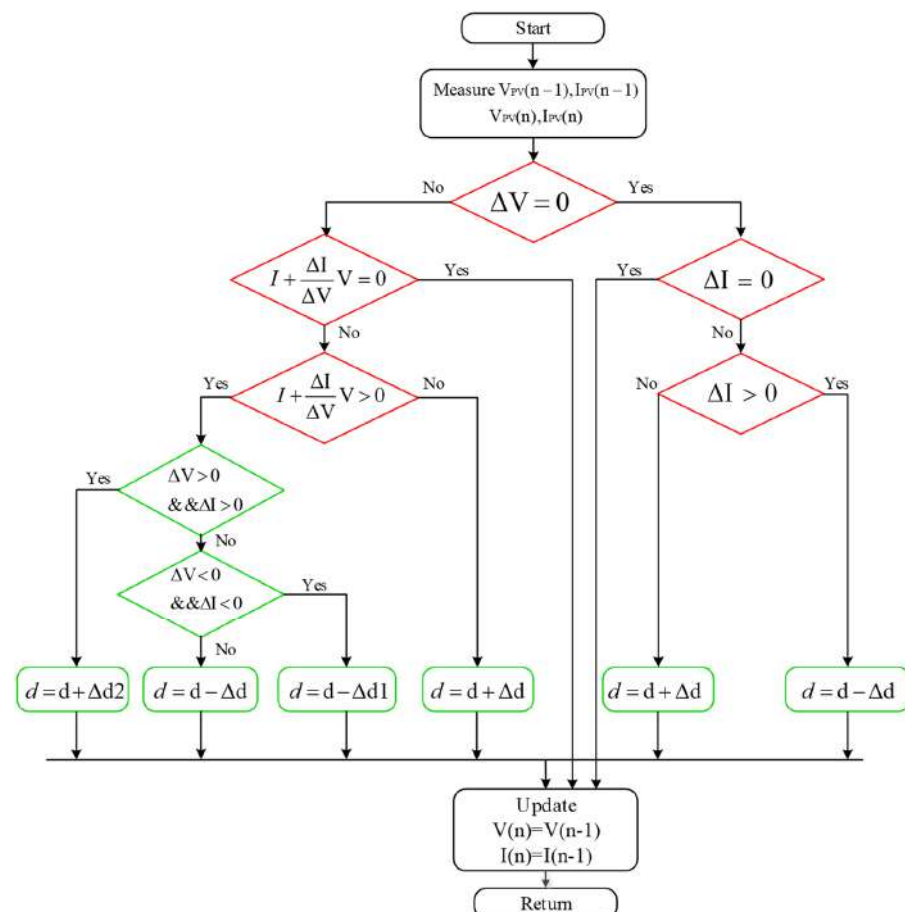


**Figure 6.** Modified IncCond MPPT algorithm flowchart.

## 5. System Results and Discussion

### 5.1. System Specifications

Based on the aforementioned analysis and modeling of different parts of the proposed system, the PSIM software is used to simulate the single-stage grid-tied PV system combined with the MPPT algorithm. In addition, the paper did not consider the experimental system verifications due to the unavailability of the system prototype at this moment, which will be considered in the future with low power capacity. This section illustrates the

validation of the three-phase DFI using CMS control techniques through 200 V, 5 kW, and 50 kHz switching frequencies as the down-scale system for central-type PV inverters. The DFI closed-loop control scheme with the main and secondary control-loops is described in Figure 7. The parameters of the grid-tied system are listed in Table 2, which consists of the input PV array-based Canadian solar module with the parameters in Table 1, the DFI power-stage, and the grid-tied current filter (grid-inductance). Moreover, a stringent designed snubber-circuit is used to mitigate the high voltage spikes over the power switches.

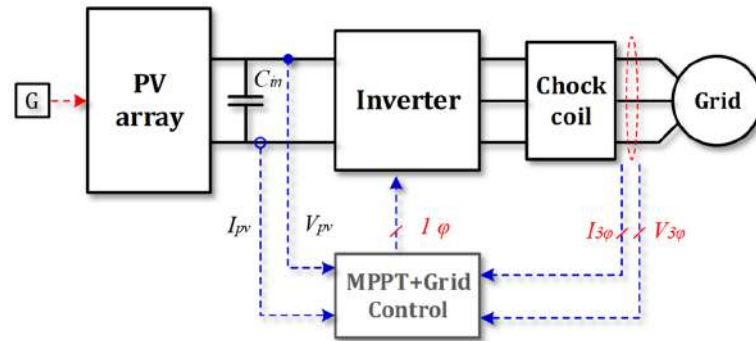


Figure 7. Proposed DFI control scheme.

Table 2. Overall DFI system parameters.

Inverter rating, P	5 kW
Input DC-voltage, $V_{in}$	100 V
Input-filter, $L_{in}, C_{in}$	150 $\mu$ H, 10 $\mu$ F
Input filter-resistance, $r_{in}$	4 $\Omega$
Grid-voltage (L.L.), $E, \omega$	200 V, $2 \times \pi \times 60$ rad/s
HFT magnetizing-inductance, $L_m$	100 $\mu$ H
HFT primary-resistance, $r_m$	2 m $\Omega$
Output-capacitor, $C_o$	10 $\mu$ F
HFT leakage-inductance, $L_{Leakage}$	2.25 $\mu$ H
HFT turns-ratio, $n$	1:1
Grid-inductance, $L_g$	4 mH
Grid inductor-resistance, $r_g$	5 m $\Omega$
Switching-frequency, $F_{SW}$	50 kHz
MPPT update frequency	0.025 ms [43]
PI controller-gains, $K_p, K_I$	0.097 A/V, 280 rad.s <sup>-1</sup>
PV array specifications	Canadian solar module
$\Delta d, \Delta d1, \Delta d2$	0.0002, 0.0005, 0.00006 s

In addition, this section aims to exhibit the performance of the conventional and proposed IncCond MPPT techniques through a compact three-phase DFI under a uniform irradiance profile and constant temperature fixed at 25 °C. Moreover, the fast-changing irradiance profile is applied to the proposed grid-tied system to investigate the MPPT response under stringent irradiance conditions. Furthermore, the DFI connects the PV system to the utility grid with a voltage boosting factor of (2), as shown in the input and grid voltage specifications listed in Table 2. The system circuit diagram has been illustrated in Figure 4 and the duty-cycle increments are listed in Table 2.

## 5.2. System Results

First, the proposed single-stage grid-tied PV system is tested under the conventional and modified IncCond MPPT techniques using a step-change uniform irradiance profile, as depicted in Figure 8. The solar irradiance profile is depicted in Figure 8a. The solar irradiance is uniform at 1000 W/m<sup>2</sup> for 1 s of the operating period, which is step-changed to 500 W/m<sup>2</sup> for another 1 s. Figure 8b shows the PV output-voltage using the conventional and modified IncCond MPPT techniques compared with the reference PV voltage, which



is plotted in red color as depicted in the legend of each waveform. In addition, the MPP reference voltage variations are small compared to the variations in the actual waveforms. The results of the two tracking techniques are matched. However, the modified IncCond algorithm improves the system settling time and overshoot from (0.062 s and 46.15%) for the conventional algorithm to (0.035 s and 15.38%), respectively, as shown in the two zoomed regions. In addition, the d-axis current of the conventional and modified MPPT techniques are compared with the reference value as depicted in Figure 8c,d, respectively. Therefore, it proves the single-stage IncCond-based MPPT operation of the proposed grid-tied PV system under the two tracking algorithms using a step-changing irradiance profile. In addition, the settling time and overshoot of the d-axis current is improved using the modified IncCond from (0.062 s and 46.15%) for the conventional technique to (0.035 s and 15.38%), respectively.

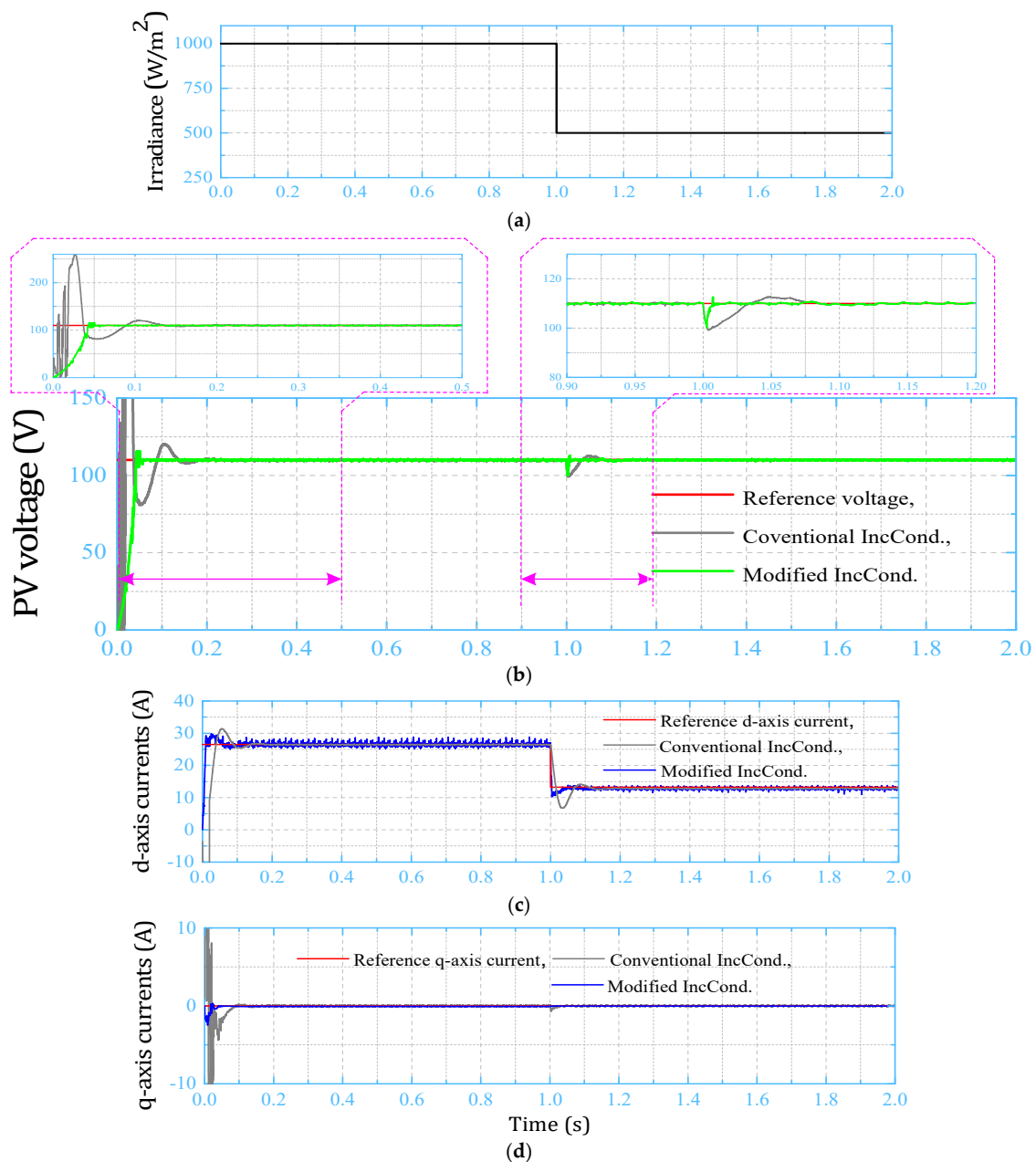


**Figure 8.** Grid-tied system results under the step-change uniform irradiance profile. (a) Step-change irradiance profile; (b) PV output-voltage under the two IncCond MPPT techniques; (c) grid-injected d-axis current; (d) grid-injected q-axis current.



Furthermore, the fast-changing irradiance profile is applied to the single-stage grid-connected PV system to reveal the tracking response of the conventional and modified IncCond MPPT techniques under these hard and fast-changing irradiance conditions. The fast-changing irradiance profile is depicted in Figure 9a,b. As can be seen, the PV output-voltage under the conventional and modified MPPT techniques is compared with the reference value. The system output-voltage using the modified IncCond MPPT technique shows an improved response compared with the conventional one. The d-axis current of the conventional and modified MPPT algorithms is compared with the reference value in Figure 9a,c comparison of the q-axis current is illustrated in Figure 9d.

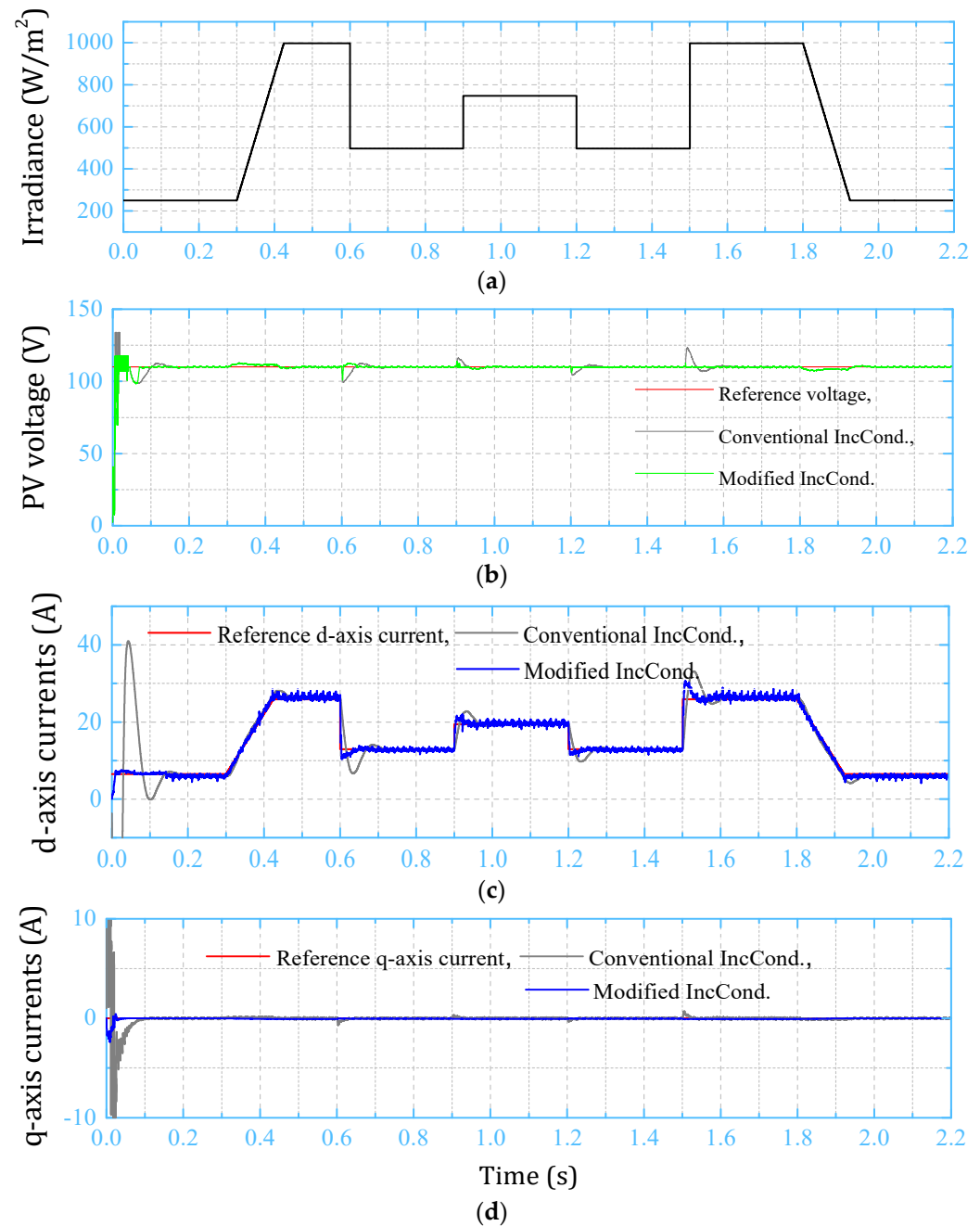


**Figure 9.** Grid-tied system results under the fast-changing irradiance profile. (a) Step-change irradiance profile; (b) PV output-voltage under the two IncCond MPPT techniques; (c) grid-injected d-axis current; (d) grid-injected q-axis current.

It is clear that the PV-side and grid-side results guaranteed the single-stage DC-AC PV system under the conventional and modified IncCond MPPT techniques. Moreover, the modified algorithm exhibits a better performance and dynamic response than the conventional algorithm's poor response. It improves the classical tracking behavior by decreasing the system settling time and dynamic overshoot. In addition, Figure 10 shows the FFT harmonic spectrum of the grid-injected current. The grid current THD is (3.95%), which follows the IEC-61000 and IEEE-519 harmonic standard limits.

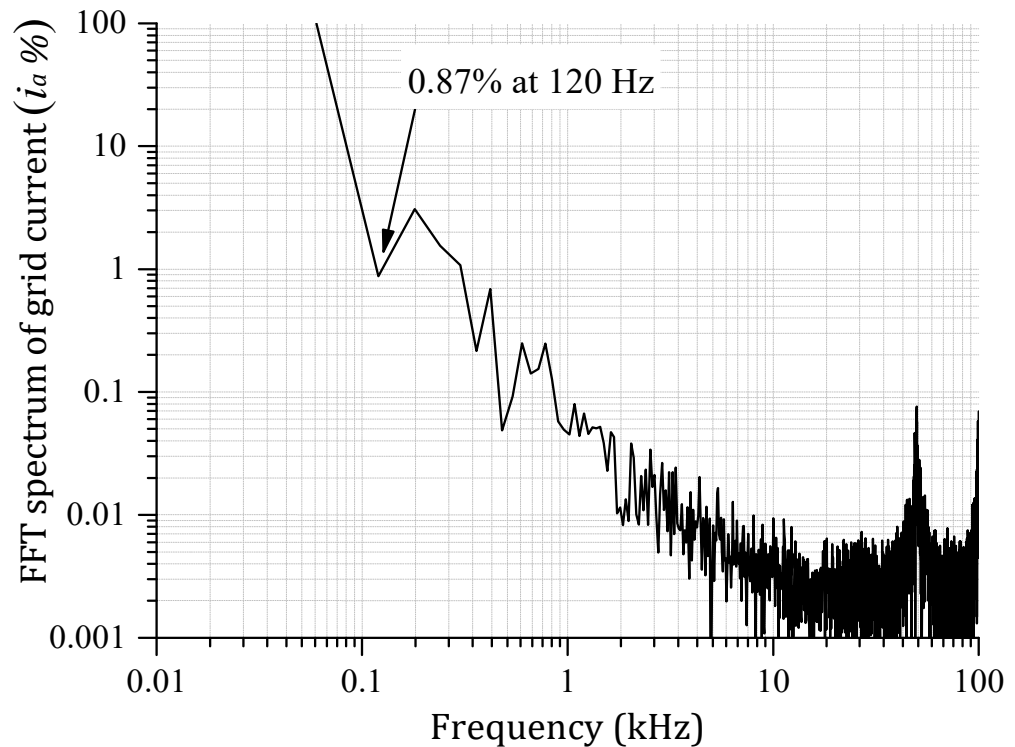


**Figure 10.** Grid current FFT harmonic spectrum (3.95%).

In addition, Figure 11 shows the instantaneous grid-injected powers and instantaneous tracking efficiency of the proposed single-stage PV system based on the following formula [1]:

$$\eta_T = \frac{P_G}{P_{th}} \cdot 100[\%] \quad (5)$$

where  $\eta_T$  is the instantaneous tracking efficiency,  $P_G$  is the grid-injected power, and  $P_{th}$  refers to the theoretical grid-injected power. In addition, the average tracking efficiency can be calculated from the following formula [2]:

$$\eta_{avg} = \langle \eta_T \rangle = \frac{\int_0^t P_G}{\int_0^t P_{th}} \cdot 100[\%] \quad (6)$$

The grid-injected power of the conventional and modified MPPT techniques is compared with the theoretical grid-injected power in Figure 11a. Moreover, Figure 11b shows the instantaneous tracking efficiency of the two IncCond-based MPPT algorithms based on Equation (5). Therefore, the modified algorithm improved the system average efficiency from 94.46% to 96.41%, which improved the system efficiency by 2.25%. Finally, the aforementioned results guaranteed the single-stage IncCond MPPT algorithm operation for the grid-tied PV system through the three-phase DFI.

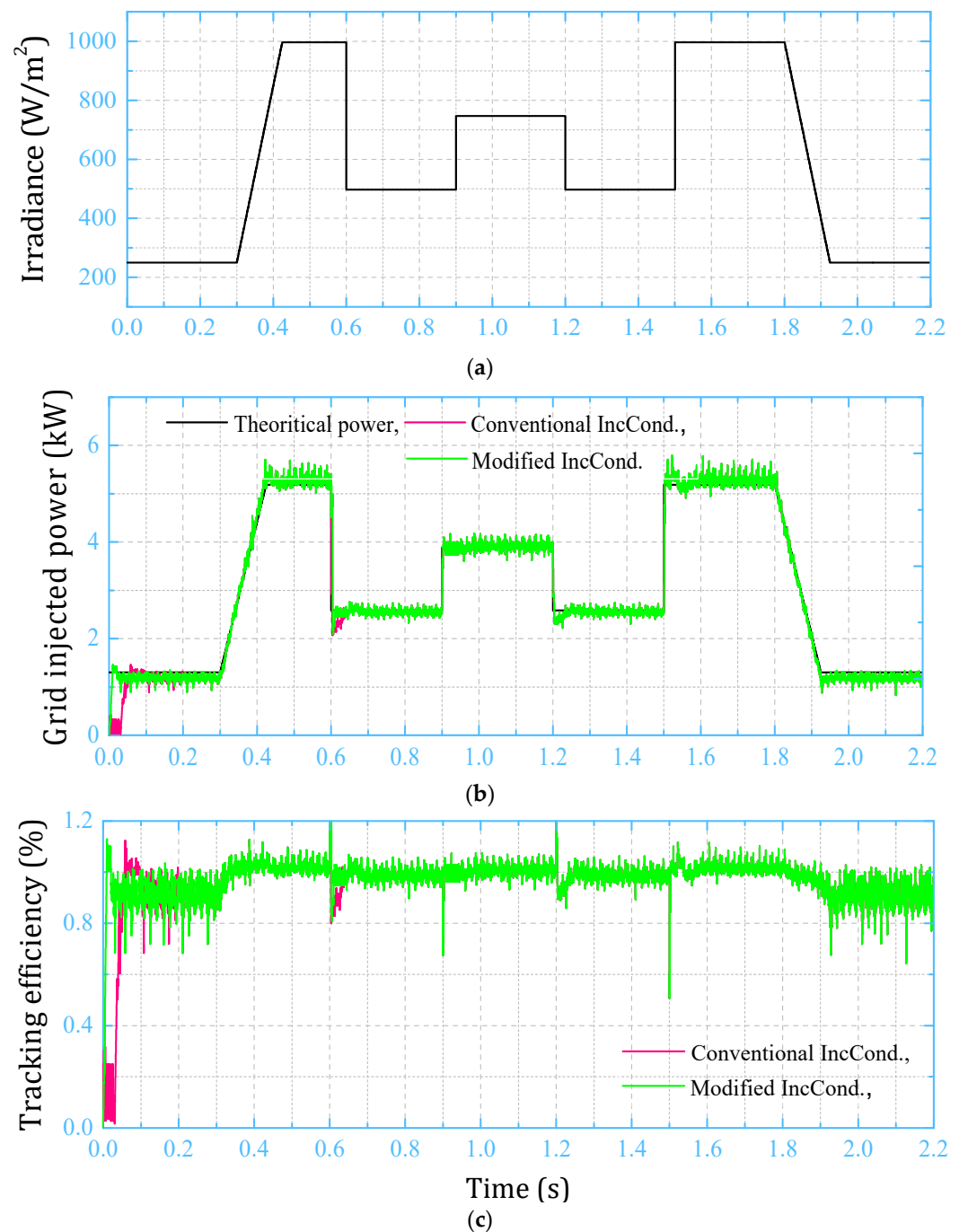


**Figure 11.** Grid current FFT harmonic spectrum. (a) Fast-changing irradiance profile; (b) grid-injected power comparison with theoretical power; (c) PV system tracking efficiency comparison.

## 6. Conclusions

This paper proposes a single-stage incremental conductance-based MPPT technique for the grid-tied PV system through the three-phase DC-AC isolated DFI. The proposed system decreases the required number of operational stages, components, and footprints. In addition, the system operation has been investigated by considering the conventional and modified IncCond MPPT algorithms. Moreover, the two tracking techniques are applied to the PV system under the step-change uniform irradiance as well as fast-changing irradiance profile. The system results guaranteed the single-stage operation of the proposed grid-tied PV system under the two MPPT techniques. Furthermore, the proposed modified IncCond algorithm exhibits an improved dynamic response compared with the conventional

technique. It improves the system overshoot and settling time by (0.027 s and 30.77%), respectively. Ultimately, the tracking efficiency of the proposed single-stage grid-tied PV system has been improved from (94.16%) for the conventional IncCond algorithm to (96.41%) for the modified algorithm, as listed in Table 3. As a result, this paper achieved the single-stage MPPT operation using two techniques with the efficiency enhancement and minimized inverter footprint, which is applicable for industrial central-type PV tracking systems. Finally, the experimental verification of the proposed system will be investigated in future work considering a low-scale system capacity and standalone operation.

**Table 3.** Conventional vs. modified IncCond MPPT technique comparison at 1000 W/m<sup>2</sup> and 25 °C.

MPPT Algorithm	Settling Time (s)	Max. Overshoot (%)	$\eta_T$ (%)
Conventional IncCond	0.062	46.15	94.1648
Modified IncCond	0.035	15.38	96.4168

**Author Contributions:** Conceptualization, A.I.M.A., Z.M.A., M.A.S. and M.A.M.; methodology, A.I.M.A.; software, A.I.M.A.; validation, A.I.M.A., Z.M.A., M.A.S., A.A., A.F. and M.A.M.; formal analysis, A.I.M.A., Z.M.A., M.A.S., A.A., A.F. and M.A.M.; investigation, A.I.M.A., Z.M.A., M.A.S., A.A., A.F. and M.A.M.; resources, A.I.M.A., Z.M.A., M.A.S., A.A., A.F. and M.A.M.; data curation, A.I.M.A., Z.M.A., M.A.S., A.A., A.F. and M.A.M.; writing—original draft preparation, A.I.M.A.; writing—review and editing, A.I.M.A., Z.M.A., M.A.S., A.A., A.F. and M.A.M.; visualization, A.I.M.A., Z.M.A., M.A.S., A.A., A.F. and M.A.M.; supervision, A.I.M.A., Z.M.A., M.A.S., A.A., A.F. and M.A.M. All authors have read and agreed to the published version of the manuscript.

**Funding:** This research has been funded by Scientific Research Deanship at the University of Ha'il—Saudi Arabia through project number RG-21079.

**Institutional Review Board Statement:** Not applicable.

**Informed Consent Statement:** Not applicable.

**Data Availability Statement:** Not applicable.

**Conflicts of Interest:** The authors declare no conflict of interest.

## References

1. Ali, A.I.; Sayed, M.A.; Mohamed, E.E. Modified efficient perturb and observe maximum power point tracking technique for grid-tied PV system. *Int. J. Electr. Power Energy Syst.* **2018**, *99*, 192–202. [CrossRef]
2. Ali, A.I.M.; Mohamed, H.R.A. Improved P&O MPPT algorithm with efficient open-circuit voltage estimation for two-stage grid-integrated PV system under realistic solar radiation. *Int. J. Electr. Power Energy Syst.* **2022**, *137*, 107805.
3. Eltamaly, A.M.; Mohamed, M.A.; Abo-Khalil, A.G. Design and Comprehensive Analysis of Maximum Power Point Tracking Techniques in Photovoltaic Systems. In *Advanced Technologies for Solar Photovoltaics Energy Systems*; Springer: Cham, Switzerland, 2021; pp. 253–284.
4. Chen, W.; Liu, B.; Nazir, M.S.; Abdalla, A.N.; Mohamed, M.A.; Ding, Z.; Bhutta, M.S.; Gul, M. An Energy Storage Assessment: Using Frequency Modulation Approach to Capture Optimal Coordination. *Sustainability* **2022**, *14*, 8510. [CrossRef]
5. Rao, C.; Hajjiah, A.; El-Meligy, M.A.; Sharaf, M.; Soliman, A.T.; Mohamed, M.A. A novel high-gain soft-switching DC-DC converter with improved P&O MPPT for photovoltaic applications. *IEEE Access* **2021**, *9*, 58790–58806.
6. Subudhi, B.; Pradhan, R. A comparative study on maximum power point tracking techniques for photovoltaic power systems. *IEEE Trans. Sustain. Energy* **2012**, *4*, 89–98. [CrossRef]
7. Ali, M.N.; Mahmoud, K.; Lehtonen, M.; Darwish, M.M. An efficient fuzzy-logic based variable-step incremental conductance MPPT method for grid-connected PV systems. *IEEE Access* **2021**, *9*, 26420–26430. [CrossRef]
8. Hanzaei, S.H.; Gorji, S.A.; Ektesabi, M. A scheme-based review of MPPT techniques with respect to input variables including solar irradiance and PV arrays' temperature. *IEEE Access* **2020**, *8*, 182229–182239. [CrossRef]
9. Bianconi, E.; Calvente, J.; Giral, R.; Mamarelis, E.; Petrone, G.; Ramos-Paja, C.A.; Spagnuolo, G.; Vitelli, M. Perturb and observe MPPT algorithm with a current controller based on the sliding mode. *Int. J. Electr. Power Energy Syst.* **2013**, *44*, 346–356. [CrossRef]
10. Ahmed, J.; Salam, Z. An improved perturb and observe (P&O) maximum power point tracking (MPPT) algorithm for higher efficiency. *Appl. Energy* **2015**, *150*, 97–108.
11. Tafticht, T.; Agbossou, K.; Doumbia, M.; Cheriti, A. An improved maximum power point tracking method for photovoltaic systems. *Renew. Energy* **2008**, *33*, 1508–1516. [CrossRef]

12. Ishaque, K.; Salam, Z.; Lauss, G. The performance of perturb and observe and incremental conductance maximum power point tracking method under dynamic weather conditions. *Appl. Energy* **2014**, *119*, 228–236. [CrossRef]
13. Femia, N.; Petrone, G.; Spagnuolo, G.; Vitelli, M. Optimization of perturb and observe maximum power point tracking method. *IEEE Trans. Power Electron.* **2005**, *20*, 963–973. [CrossRef]
14. Kollimalla, S.K.; Mishra, M.K. A new adaptive P&O MPPT algorithm based on FSCC method for photovoltaic system. In Proceedings of the 2013 International Conference on Circuits, Power and Computing Technologies (ICCPCT), Nagercoil, India, 21–22 March 2013; pp. 406–411.
15. Kamran, M.; Mudassar, M.; Fazal, M.R.; Asghar, M.U.; Bilal, M.; Asghar, R. Implementation of improved Perturb & Observe MPPT technique with confined search space for standalone photovoltaic system. *J. King Saud Univ. Eng. Sci.* **2020**, *32*, 432–441.
16. Elgendy, M.A.; Zahawi, B.; Atkinson, D.J. Assessment of the incremental conductance maximum power point tracking algorithm. *IEEE Trans. Sustain. Energy* **2012**, *4*, 108–117. [CrossRef]
17. Sayed, M.A.; Mohamed, E.; Ali, A. Maximum power point tracking technique for grid tie PV system. In Proceedings of the 7th International Middle-East Power System Conference, (MEPCON'15), Mansoura, Egypt, 15–17 December 2015; Mansoura University: Mansoura, Egypt, 2015.
18. Lin, C.-H.; Huang, C.-H.; Du, Y.-C.; Chen, J.-L. Maximum photovoltaic power tracking for the PV array using the fractional-order incremental conductance method. *Appl. Energy* **2011**, *88*, 4840–4847. [CrossRef]
19. Radjai, T.; Rahmani, L.; Mekhilef, S.; Gaubert, J.P. Implementation of a modified incremental conductance MPPT algorithm with direct control based on a fuzzy duty cycle change estimator using dSPACE. *Sol. Energy* **2014**, *110*, 325–337. [CrossRef]
20. Hiyama, T.; Kouzuma, S.; Imakubo, T. Identification of optimal operating point of PV modules using neural network for real time maximum power tracking control. *IEEE Trans. Energy Convers.* **1995**, *10*, 360–367. [CrossRef]
21. Ahmad, J. A fractional open circuit voltage based maximum power point tracker for photovoltaic arrays. In Proceedings of the 2010 2nd International Conference on Software Technology and Engineering, San Juan, PR, USA, 3–5 October 2010; pp. V1-247–V1-250.
22. Alajmi, B.N.; Ahmed, K.H.; Finney, S.J.; Williams, B.W. Fuzzy-logic-control approach of a modified hill-climbing method for maximum power point in microgrid standalone photovoltaic system. *IEEE Trans. Power Electron.* **2010**, *26*, 1022–1030. [CrossRef]
23. Salam, Z.; Ahmed, J.; Merugu, B.S. The application of soft computing methods for MPPT of PV system: A technological and status review. *Appl. Energy* **2013**, *107*, 135–148. [CrossRef]
24. Rai, A.K.; Kaushika, N.; Singh, B.; Agarwal, N. Simulation model of ANN based maximum power point tracking controller for solar PV system. *Sol. Energy Mater. Sol. Cells* **2011**, *95*, 773–778. [CrossRef]
25. Ali, A.I.; Mohamed, E.E.; Youssef, A.-R. MPPT algorithm for grid-connected photovoltaic generation systems via model predictive controller. In Proceedings of the 2017 Nineteenth International Middle East Power Systems Conference (MEPCON), Cairo, Egypt, 19–21 December 2017; pp. 895–900.
26. Farhat, M.; Barambones, O.; Sbita, L. Real-time efficiency boosting for PV systems using MPPT based on sliding mode. *Energy Procedia* **2015**, *75*, 361–366. [CrossRef]
27. Farhat, M.; Barambones, O.; Sbita, L. A new maximum power point method based on a sliding mode approach for solar energy harvesting. *Appl. Energy* **2017**, *185*, 1185–1198. [CrossRef]
28. Ghassami, A.A.; Sadehghzadeh, S.M.; Soleimani, A. A high performance maximum power point tracker for PV systems. *Int. J. Electr. Power Energy Syst.* **2013**, *53*, 237–243. [CrossRef]
29. Tey, K.S.; Mekhilef, S. Modified incremental conductance MPPT algorithm to mitigate inaccurate responses under fast-changing solar irradiation level. *Sol. Energy* **2014**, *101*, 333–342. [CrossRef]
30. Safari, A.; Mekhilef, S. Implementation of incremental conductance method with direct control. In Proceedings of the TENCON 2011—2011 IEEE Region 10 Conference, Bali, Indonesia, 21–24 November 2011; pp. 944–948.
31. Liu, F.; Duan, S.; Liu, F.; Liu, B.; Kang, Y. A variable step size INC MPPT method for PV systems. *IEEE Trans. Ind. Electron.* **2008**, *55*, 2622–2628.
32. Yau, H.-T.; Liang, Q.-C.; Hsieh, C.-T. Maximum power point tracking and optimal Li-ion battery charging control for photovoltaic charging system. *Comput. Math. Appl.* **2012**, *64*, 822–832. [CrossRef]
33. Zhou, S.; Han, Y.; Yang, P.; Mahmoud, K.; Lehtonen, M.; Darwish, M.M.; Zalhaf, A.S. An optimal network constraint-based joint expansion planning model for modern distribution networks with multi-types intermittent RERs. *Renew. Energy* **2022**, *194*, 137–151. [CrossRef]
34. Al-Gabalawy, M.; Mahmoud, K.; Darwish, M.M.; Dawson, J.A.; Lehtonen, M.; Hosny, N.S. Reliable and robust observer for simultaneously estimating state-of-charge and state-of-health of lifepo4 batteries. *Appl. Sci.* **2021**, *11*, 3609. [CrossRef]
35. Ghoneim, S.S.; Mahmoud, K.; Darwish, M.M. Effective Transmission Congestion Management via Optimal DG Capacity Using Hybrid Swarm Optimization for Contemporary Power System Operations. *IEEE Access* **2022**, *10*, 71091–71106.
36. Ali, A.I.; Sayed, M.A.; Mohamed, E.E. Maximum Power Point Tracking technique applied on partial shaded grid connected PV system. In Proceedings of the 2016 Eighteenth International Middle East Power Systems Conference (MEPCON), Cairo, Egypt, 27–29 December 2016; pp. 656–663.
37. Diab, M.; Elserougi, A.; Abdel-Khalik, A.; Massoud, A.; Ahmed, S. Modified modulation scheme for photovoltaic fed grid-connected three-phase boost inverter. In Proceedings of the IECON 2013-39th Annual Conference of the IEEE Industrial Electronics Society, Vienna, Austria, 10–13 November 2013; pp. 1735–1740.

38. Ali, A.I.M.; Takeshita, T.; Sayed, M.A. In depth mathematical-analysis and experimentation of high-power SiC-FET based single-stage three-phase differential-based flyback inverter with practical design issues for grid-tied applications. *Int. J. Electr. Power Energy Syst.* **2022**, *140*, 108041. [CrossRef]
39. Mehrnami, S.; Mazumder, S.K.; Soni, H. Modulation scheme for three-phase differential-mode Ćuk inverter. *IEEE Trans. Power Electron.* **2015**, *31*, 2654–2668. [CrossRef]
40. Darwish, A.; Massoud, A.M.; Holliday, D.; Ahmed, S.; Williams, B. Single-stage three-phase differential-mode buck-boost inverters with continuous input current for PV applications. *IEEE Trans. Power Electron.* **2016**, *31*, 8218–8236. [CrossRef]
41. Ali, A.I.M.; Tuan, C.A.; Takeshita, T.; Sayed, M.A.; Alaas, Z.M. Modular Single-Stage Three-Phase Flyback Differential Inverter for Medium/High-Power Grid Integrated Applications. *Sensors* **2022**, *22*, 2064. [CrossRef] [PubMed]
42. Hammami, M.; Grandi, G. A single-phase multilevel PV generation system with an improved ripple correlation control MPPT algorithm. *Energies* **2017**, *10*, 2037. [CrossRef]
43. Zurbriggen, I.G.; Ordonez, M. PV energy harvesting under extremely fast changing irradiance: State-plane direct MPPT. *IEEE Trans. Ind. Electron.* **2018**, *66*, 1852–1861. [CrossRef]

## Article

# Investigation on New Metaheuristic Algorithms for Solving Dynamic Combined Economic Environmental Dispatch Problems

Benyekhlef Larouci <sup>1,\*</sup>, Ahmed Nour El Islam Ayad <sup>1</sup>, Hisham Alharbi <sup>2</sup>, Turki E. A. Alharbi <sup>2</sup>, Houari Boudjella <sup>1</sup>, Abdelkader Si Tayeb <sup>3</sup>, Sherif S. M. Ghoneim <sup>2,\*</sup> and Saad A. Mohamed Abdelwahab <sup>4,5</sup>

- <sup>1</sup> Department of Electrical Engineering, Kasdi Merbah University, Ghardaia Road, P.O. Box 511, Ouargla 30000, Algeria; ayad.ahmed@univ-ouargla.dz (A.N.E.I.A.); boudjella.houari@univ-ouargla.dz (H.B.)
  - <sup>2</sup> Department of Electrical Engineering, College of Engineering, Taif University, P.O. Box 11099, Taif 21944, Saudi Arabia; h.alharbi@tu.edu.sa (H.A.); turki.alharbi@tu.edu.sa (T.E.A.A.)
  - <sup>3</sup> Applied Research Unit for Renewable Energies “URAER Ghardaia”, Renewable Energy Development Center (CDER), Ghardaia 47133, Algeria; si\_tayeb12@yahoo.fr
  - <sup>4</sup> Electrical Department, Faculty of Technology and Education, Suez University, Suez 43533, Egypt; saad.abdelwahab@suezuniv.edu.eg
  - <sup>5</sup> Department of Computers and Systems Engineering, High Institute of Electronic Engineering, Ministry of Higher Education, Bilbis-Sharqiya 44621, Egypt
- \* Correspondence: larouci.benyekhlef@univ-ouargla.dz (B.L.); s.ghoneim@tu.edu.sa (S.S.M.G.)

**Abstract:** In this paper, the dynamic combined economic environmental dispatch problems (DCEED) with variable real transmission losses are tackled using four metaheuristics techniques. Due to the consideration of the valve-point loading effects (VPE), DCEED have become a non-smooth and more complex optimization problem. The seagull optimization algorithm (SOA), crow search algorithm (CSA), tunicate swarm algorithm (TSA), and firefly algorithm (FFA), as both nature and biologic phenomena-based algorithms, are investigated to solve DCEED problems. Our proposed algorithms, SOA, TSA, and FFA, were evaluated and applied on the IEEE five-unit test system, and the effectiveness of the proposed CSA approach was applied on two-unit, five-unit, and ten-unit systems by considering VPE. We defined CSA for different objective functions, such as cost of production, emission, and CEED, by considering VPE. The obtained results reveal the efficiency and robustness of the CSA compared to SOA, TSA, FFA, and to other optimization algorithms reported recently in the literature. In addition, Matlab simulation results show the advantages of the proposed approaches for solving DCEED problems.

**Keywords:** dynamic economic environmental dispatch; cow search algorithm; seagull optimization algorithm; tunicate swarm algorithm; firefly algorithm; optimal scheduling; optimization methods

**Citation:** Larouci, B.; Ayad, A.N.E.I.; Alharbi, H.; Alharbi, T.E.A.; Boudjella, H.; Tayeb, A.S.; Ghoneim, S.S.M.; Abdelwahab, S.A.M. Investigation on New Metaheuristic Algorithms for Solving Dynamic Combined Economic Environmental Dispatch Problems. *Sustainability* **2022**, *14*, 5554. <https://doi.org/10.3390/su14095554>

Academic Editors: Mohamed A. Mohamed and Elena Cristina Rada

Received: 13 March 2022

Accepted: 28 April 2022

Published: 5 May 2022



**Copyright:** © 2022 by the authors. Licensee MDPI, Basel, Switzerland. This article is an open access article distributed under the terms and conditions of the Creative Commons Attribution (CC BY) license (<https://creativecommons.org/licenses/by/4.0/>).

## 1. Introduction

A competitive electricity generation market necessitates high concentration to solve the economic load dispatch (ELD) problem of power generation. The essential objective of the ELD is to distribute the production of the available production units in such a way that the load demand is covered with a minimum total cost of fuel, taking into account the physical and operational limitations of the electrical system [1].

Due to these physical and operational limitations, the ELD problem is a non-linear optimization problem [1]. As a result, the conventional mathematical methods fall somewhat short in solving such a problem. On the other hand, with the growing concern about polluting emissions and the total cost of fuel, finding a solution to emissions has become a critical issue for the power generation systems around the world. However, the functions of pollutant emission and operating cost are incompatible; reducing emissions increases operating costs and vice versa [2]. Therefore, a grid operator allocates generation units to

the tradeoff between the total operation cost reduction and/or reducing emissions under the newest generations, such as prohibited operating zones [3] and ramp rate limits [4], which have a high order of nonlinearities, discontinuities, dimensions, and valve loading points that determine the characteristics of the ELD problem [5]. Therefore, considering more non-convex and multiple local minima increases the complexity of obtaining the optimal fuel cost function. In contrast, metaheuristic optimization techniques have become common to find the best solution to the DEED problem. Such algorithms include a colony optimizer [6], multi-verse optimizer [7], particle swarm optimization [8], gray wolf optimizer [9], biogeography-based optimization [10], enhanced exploratory whale optimization algorithm (EEOOA) [7], and hybrid bat–crow search algorithm (HBACSA); they are used exceptionally, in a unique, improved, or hybrid form with others approaches.

Thermal power plants release toxic gases into the atmosphere, endangering human health. Environmental pollution caused by these chemicals has the potential to harm not only humans but also animals and birds. It also has a negative impact on visibility, material quality, and contributes to global warming. DEED provides a solution to these problems by scheduling a renewable energy source and backup power generation based on the predicted load demand to decrease the operational generator's cost and emissions [2].

## 2. Literature Review

According to the importance of DEED, researchers have adapted and proposed these new algorithms to address the DEED problem. In [11], the authors proposed a method based on improved sailfish algorithm to solve the hybrid dynamic economic emission dispatch (HDEED). In addition, the paper in [12] presented a novel multi-objective optimization based on enhanced moth-flame optimization approach to locate the optimal solution of the hybrid DEED, including renewable energy generation. Ref. [13] proposed an improved tunicate swarm method to explore the search space for DEED. The proposed ITSA in [13] was applied to the 5, 10, and 15-unit systems, respectively. Ref. [14] proposed a novel approach, namely a multi-objective differential evolution algorithm, to deal with the constraints in DEED problems by considering the difference in the power generation range of the units. Authors in [15] suggested a multi-objective virus colony search algorithm (MOVCS) for solving the DEED problem in the power system integrated electric vehicle and wind units over a 24 h period. Ref. [16] formulated DEED as a third-order polynomial fitting curve method to balance between emissions gas and fuel cost by utilizing renewable energy and PEVs. In [17], the authors proposed an enhanced exploratory whale optimization algorithm (EEOOA) to solve the dynamic economic dispatch (DED), which coordinates the behavior of whales, random exploration, and local random search. The feasibility of EEOOA is validated on 5, 10, and 15 units considering VPE and power loss constraints.

In the last two years, various research works have focused on solving the DEED problems by using novel metaheuristic techniques. The research in [18] developed a new model of the multi-objective DCEED using a hybridized flower pollination algorithm (FPA) with sequential quadratic programming (SQP). The FPA–SQP is tested on 5 and 10-unit systems for a 24 h period. Ref. [19] suggested a novel multi-objective hybrid optimization-algorithm-based equilibrium optimizer (EO) and differential evolution (DE) to solve the DEED. The proposed algorithm is validated and verified on the test system containing ten thermal power generators and one wind farm. The study showed that the hybrid EO–DE method with a constraint management system is able to counter balance the tasks of exploitation and exploration. The results obtained in [20] show that the new chaotic artificial bee colony (IABC) rides the local trap and improves the convergence of the solution in terms of solving the CEED with different constraints. A 10-unit system without and with a wind farm and a 40-unit system were investigated to prove the effectiveness and accuracy of the suggested IABC for tackling the CEED problem. In [21], the improved slime mold algorithm (ISMA) is developed and applied to optimize the single-and bi-objective economic emission dispatch (EED) problems considering VPE. Five test systems



(6-unit, 10-unit, 11-unit, 40-unit, and 110-unit) are used to validate the proposed ISMA. Additionally, ref. [22] presented an optimal allocation of the power system for the combined economic emission dispatch problem using a moth swarm algorithm (MSA). The method was tested on two different systems. The first system is a combination of six thermal generators and thirteen solar plants, and the second test system comprises three thermal units combined with thirteen photovoltaic plants.

This paper proposes, presents, and applies more effective methods, such as, TSA, SOA, CSA, and FFA, for solving the DCEED problem, including VPE. The most important contributions of this article can be summarized as follows:

- Improvement of some optimization methods, such as TSA, SOA, CSA, and FFA.
- Application of the proposed algorithms to solve single-and bi-objective DEED problems.
- The four techniques are validated and tested by applying them on the IEEE standard five-unit test system to demonstrate their robustness and accuracy.

The rest of the article is organized as follows. The DEED problem with the mathematical model is presented in Section 3. Section 4 demonstrates the four metaheuristic approaches: TSA, SOA, CSA, and FA. The investigation of the simulation results and discussion are shown in Section 5. Finally, we conclude this paper in Section 6.

### 3. DCEED Problem Formulation Including VPE

Due to the dynamic behavior of the electrical network and the prodigious variations in load demand on the consumer side, the DCEED problem can be described as a multi-objective mathematical optimization problem, which is non-linear and dynamic. DCEED is a constraint optimization problem that minimizes simultaneously the fuel cost and emission effects in order to meet a power system's load demand over some appropriate periods while meeting certain equality and inequality constraints [23].

#### 3.1. Objective Function

DCEELD's objective is to minimize total fuel costs while also reducing the level of emissions emitted by generating units. Thus, the objective function is mathematically defined as the weighted summation of the production cost of generating units and emissions caused by fossil fuel thermal plants, which is shown below [16]:

$$\min F = \sum_{t=1}^T \sum_{i=1}^{Ng} C_{i,t}(P_{i,t}) + ppf_i \sum_{t=1}^T \sum_{i=1}^{Ng} E_{i,t}(P_{i,t}) \quad (1)$$

where  $F$  indicates the single objective to be minimized;  $C_{i,t}(P_{i,t})$  denotes the fuel cost of  $Ng$  generators in the  $t^{th}$  ( $t = 1, 2, \dots, T$ ) time interval in USD/h;  $E_{i,t}(P_{i,t})$  stands for the emissions generated by the generation stations over  $T$  dispatch intervals in kg/h;  $P_{i,t}$  denotes the dynamic dispatch power in MW.  $ppf_i$  is the price penalty factor determined by the ratio of  $C_i(P^{max})$  and  $E_i(P^{min})$  in USD/kg.

##### 3.1.1. Dynamic Economic Load Dispatch Model (DED)

The objective of the DED problem is to minimize the overall economic cost of fossil fuel during a 24-h period. In some large generators, their cost functions are also non-linear, due to the effect of the valve opening [24]. Consequently, the valve dynamics increase several local minimum points in the cost function, hence complicating the problem. The DED problem involved with VPE is expressed as minimization of the production cost of power dispatch in the following way [25]:

$$C_{i,t}(P_{i,t}) = a_i + b_i P_{i,t} + c_i P_{i,t}^2 + \left| e_i \times \sin \left( f_i \times \left( P_i^{min} - P_i \right) \right) \right| \quad (2)$$

where  $a_i$ ,  $b_i$ , and  $c_i$  are the coefficients of the fuel cost corresponding to the generator  $i$ ;  $e_i$ , and  $f_i$  stand for the fuel cost coefficients of the  $i^{th}$  generator due to VPE; and  $P_i^{min}$  denotes the minimum real power of the  $i^{th}$  ( $i = 1, 2, \dots, Ng$ ) generating unit.

### 3.1.2. Dynamic Environmental Dispatch Model (DEnD)

Global warming and increased movements to protect the environment have forced producers to reduce gas emissions caused by the combustion of fossil fuels in various power plants mainly due to sulfur dioxide ( $SO_2$ ) and nitrate oxide ( $NO_x$ ) [26,27].

Each thermal power plant will produce its power according to a dynamic non-smooth emission function given by the following quadratic form [28]:

$$E_{i,t}(P_{i,t}) = \alpha_i + \beta_i P_{i,t} + \gamma_i P_{i,t}^2 + \eta_i \times \exp(\delta_i P_{i,t}) \quad (3)$$

where  $\alpha_i$ ,  $\beta_i$ ,  $\gamma_i$ ,  $\eta_i$ , and  $\delta_i$  are the emission curve coefficients.

### 3.2. Constraints Functions

The minimization of the DCEED problem is subject to the following constraints and limits:

#### 3.2.1. Power Balance Constraint

The sum of total power generated by all generators at each time interval  $t$  should be matched with the load demand PD and the total transmission losses  $P_L$  in the corresponding time period, which is given as follows [29]:

$$\sum_{i=1}^{Ng} P_{i,t} = P_{D,t} + P_{L,t} \quad (4)$$

The power losses incurred in the transmission lines can be computed by using Kron's loss coefficients formula given below [30]:

$$P_{L,t} = \sum_{i=1}^{Ng} \sum_{j=1}^{Ng} P_{i,t} B_{i,j} P_{j,t} \quad (5)$$

where  $B_{i,j}$  denotes the transmission loss coefficients. Wood et al. in [31] provide detailed procedures for calculating the  $B$  coefficients.

#### 3.2.2. Power Output Limits

The dispatch active power outputs of each generator must be between the capacities of each specific generating unit at each time interval  $t$  [32]:

$$P_i^{min} \leq P_{i,t} \leq P_i^{max} \quad (6)$$

where  $P_i^{min}$  and  $P_i^{max}$  indicate, respectively, the minimum and the maximum power limits of  $P_{i,t}$ .

## 4. Metaheuristic Approaches Applied to DEED

### 4.1. Seagull Optimization Algorithm (SOA)

The seagull optimization algorithm (SOA) [33] is a recently proposed metaheuristic technique inspired by the natural behaviors of seagulls. The seagull optimization algorithm is a metaheuristic algorithm that mimics gull behavior. Seagulls live in colonies. Seagulls are omnivorous, eating reptiles, earthworms, insects, fish, and other animals.

Seagulls are highly intelligent birds. This aids the seagull in its hunt for prey. The migratory and hunting habits of seagulls are well known. Seagulls migrate in search of a new plentiful food source. After arriving at a new home, seagulls attack their prey (Figure 1 [33]).

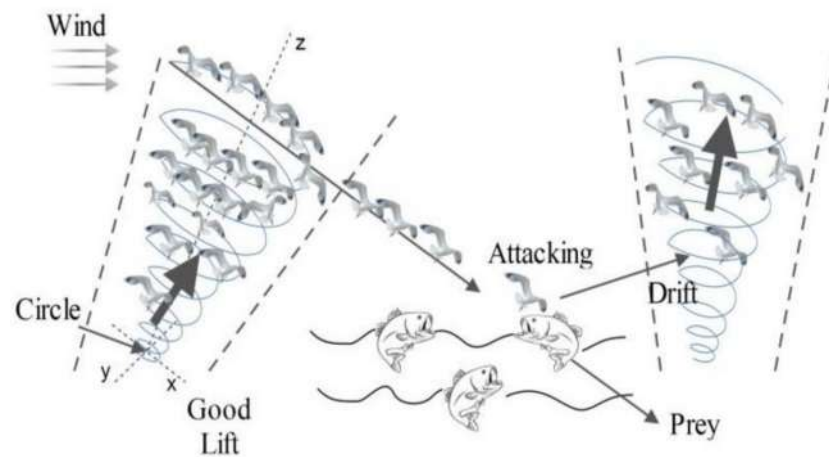


**Figure 1.** Migration and attacking behaviors of seagulls.

The most important thing about seagulls is their migrating and attacking behavior [34]. Thus, the SOA focuses on these two natural behaviors. This behavior is clarified as follows:

#### 4.1.1. Migration (Exploration)

During migration, the members of a seagull swarm should avoid colliding with each other (see Figure 2a). To achieve this purpose, an additional variable  $A$  is employed [35]:

$$\vec{C}_s = A \times \vec{P}_s(j) \quad (7)$$

where  $\vec{C}_s$  indicates the position of each agent,  $\vec{P}_s(j)$  denotes the current position of seagulls in the  $j$ th iteration ( $j = 1, 2, \dots, \text{Max}_{\text{iteration}}$ ), and  $A$  depicts the movement behavior of seagulls.

$$A = a - \left( j \times (a / \text{Max}_{\text{iteration}}) \right) \quad (8)$$

where  $a$  is a constant and responsible for controlling the frequency of employing variable  $A$ , which linearly decreases from  $a$  to 0.

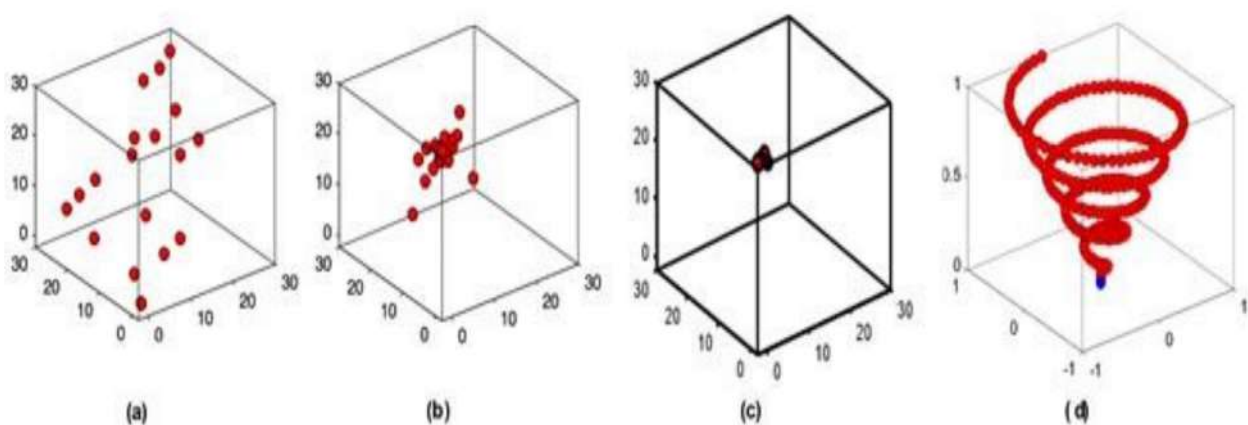


**Figure 2.** The basic comportment of seagull (a) Avoiding collisions between search agents, (b) Displacement of search agents toward the best seagull, (c) Convergence in the direction of the best seagull, and (d) Seagulls' natural aggressive behavior.

To find the richest food resources, seagulls move toward the best search agent as shown in Figure 2b.

$$\vec{M}_s = B \times \left( \vec{P}_{bs}(j) - \vec{P}_s(j) \right) \quad (9)$$

where  $\vec{M}_s$  indicates seagull position  $\vec{P}_s(j)$  toward the best search agent  $\vec{P}_{bs}(j)$ . The coefficient  $B$  is a random value responsible for making a tradeoff between exploitation and exploration and is expressed as follows:

$$B = 2 \times A^2 \times rd \quad (10)$$

where  $rd$  is a random number that lies in the interval (0,1).

As seagulls move toward the fittest search agent, they might remain close to each other (see Figure 2c). Thus, seagulls can update their position according to the following rule [33]:

$$\vec{D}_s = |\vec{C}_s + \vec{M}_s| \quad (11)$$

where  $\vec{D}_s$  stands for the distance between seagulls and the best search agent.

#### 4.1.2. Attacking (Exploitation)

Seagulls attack their prey in a spiral shape after arriving at a new place, as presented in Figure 2d. Their attacking behavior in the  $x$ ,  $y$ , and  $z$  planes is explained as follows [33]:

$$\begin{cases} x' = r \times \cos(k) \\ y' = r \times \sin(k) \\ z' = r \times k \end{cases} \quad (12)$$

$$r = u \times \exp(kv) \quad (13)$$

where  $r$  denotes the radius of each turn of the spiral;  $k$  is a random number with  $[0 \leq k \leq 2\pi]$ ;  $u$  and  $v$  are constants to define the spiral shape [33,36].

The updated position of the search agent  $\vec{P}_s(j)$  is determined by using Equations (11)–(13) [36].

$$\vec{P}_s(j) = (\vec{D}_s \times x' \times y' \times z') + \vec{P}_{bs}(j) \quad (14)$$

#### 4.2. Crow Search Algorithm (CSA)

Crow search algorithm (CSA) is a nature-inspired algorithm suggested by A. Askarzadeh in 2016 [37]. This evolutionary computation technique based-population algorithm imitates crow birds' conduct and social interaction [38].

One of the best indications of their cleverness is hiding food and remembering its location. Moreover, the mechanism of exploration and exploitation of CSA can be learned from Figure 3 [39]. As shown in Figure 3a, small values of  $fl$  ( $<1$ ) result in a solution to an optimum local; otherwise, if  $fl$  of more than 1 is selected, the optimal solution leads in the global search, as shown in Figure 3b. Overall, the pseudo code of CSA can be explained as shown in Algorithm 1.

The CSA process is discussed in this subsection [39]:

**Step 1:** Initializing crow swarm in the  $d$ -dimension randomly.

**Step 2:** A fitness function is used to evaluate each crow, and its value is put as an initial memory value. Each crow stores its hiding place in its memory variable  $P_i$ .

**Step 3:** The crow updates its position by selecting another random crow, (i.e,  $M_j$ ) and generating a random value. If this value is greater than the awareness probability " $AP$ ", then crow  $P_i$  will follow  $P_j$  to know  $M_j$ .

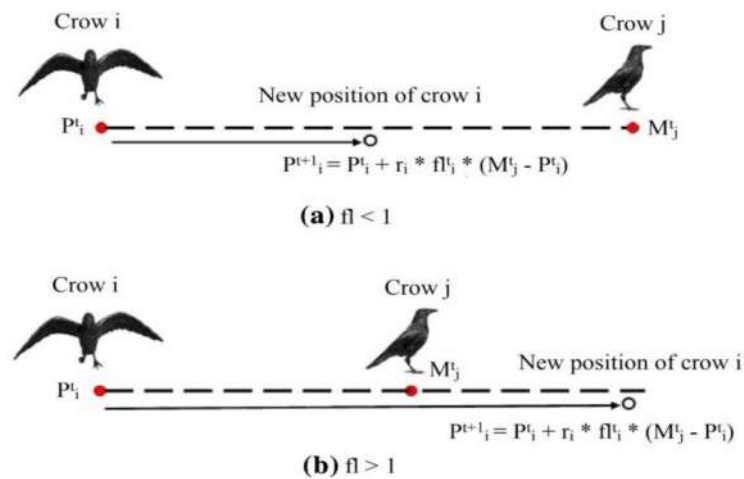


**Figure 3.** Searching mechanism by the crow in both states.

**Step 4:** The crow updates its position by selecting another random crow (i.e.,  $P_j$ ) and following it to know  $M_j$ . Then new  $P_j$  is calculated as follows:

$$P_i^{t+1} = \begin{cases} P_i^t + r_i \times fl_i^t \times (M_j^t - P_i^t) & r_j \geq AP_i^t \\ a \text{ random position} & \text{otherwise} \end{cases} \quad (15)$$

where  $t$  refers to iteration number;  $r_i$  and  $r_j$  refer to random numbers;  $fl_i^t$  is the crow  $i$  flight length to denote crow  $j$  memory.

**Step 5:** Updating memory

The crows' memory is updated as follows:

$$M_i^{t+1} = \begin{cases} P_i^{t+1} & f(P_i^{t+1}) < f(M_i^t) \\ M_i^t & \text{otherwise} \end{cases} \quad (16)$$

**Step 6:** Check termination criterion. Steps 3–5 are repeated until  $t_{max}$  is reached.

---

**Algorithm 1.** Crow Search Algorithm

---

```

1: Input: N number of crows in the population, and Maximum number of iteration ( $t_{max}$ ).
2: Output: Optimal crow position
3: Initialize position of crows, and crows' memory
4: while  $t < t_{max}$  do
5:   for  $i = 1:N$  (all N crows of the flock)
6:     Choose a random crow (i.e.  $M_j$ ), and determine a value of an awareness probability  $AP$ 
7:     if  $r_j \geq AP_i^t$ 
8:        $P_i^{t+1} = P_i^t + r_i \times fl_i^t \times (M_j^t - P_i^t)$ 
9:     else
10:       $P_i^{t+1} = a$  random position of search space
11:    end if
12:  end for
13: Check solution boundaries.
14: Calculate the fitness of each crow
15:   Update Crows' memory
16: end while

```

---

#### 4.3. Tunicate Swarm Algorithm (TSA)

The standard tunicate swarm algorithm is a very simple bio-inspired metaheuristic optimization technique, which was first proposed by S. Kaur et al. in 2020 [40]. Its inspiration and performance were proven over the seventy-four benchmark problems

compared to several other optimization approaches. Its efficacy and unpretentious structure draw the attention to employ and improve this algorithm for the considered problem. The swarm behavior of TSA is given in Figure 4 [40]. TSA main limitates the swarming behaviors of the marine tunicates and their jet propulsions during its navigation and foraging procedure [41].

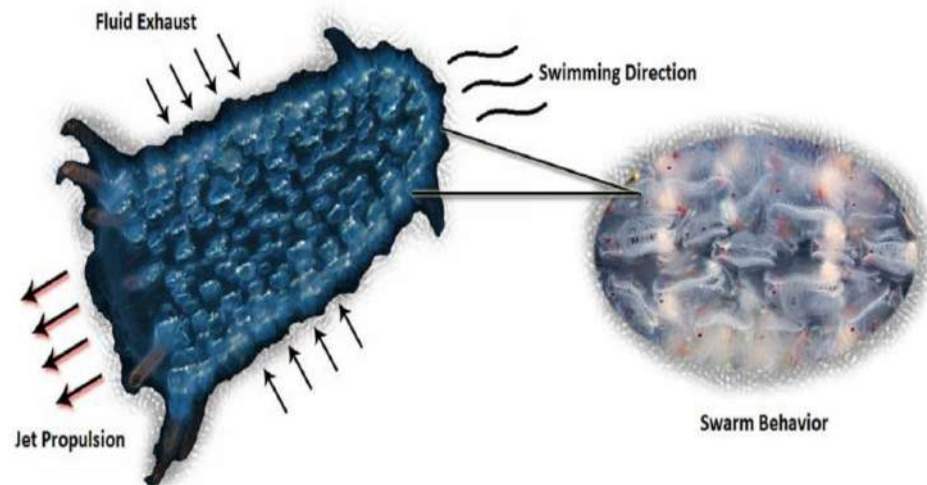


**Figure 4.** Inspiration of TSA.

In TSA, a population of tunicates ( $PT$ ) is swarming to search for the best source of food ( $SF$ ), representing the fitness function. In this swarming, the tunicates update their positions related to the first best tunicates stored and upgraded in each iteration. The TSA begins where the tunicate population is initialized randomly, considering the permissible bounds of the control variables. The dimension of the control variables composes each tunicate ( $T$ ), which can be initially created as [40]

$$T_n(m) = T_{min}^n + r \times (T_{max}^n - T_{min}^n) \quad \forall m \in PT_{size} \text{ \& } n \in Dim \quad (17)$$

where  $T(m)$  stands for the position of each tunicate ( $m$ );  $n$  refers to each control variable in dimension  $Dim$ ;  $r$  is a random number within the range (0:1); and  $PT_{size}$  indicates the number of tunicates in the population.

The update process of the tunicates position is executed by the following formula [41]:

$$T_n(m) = \frac{T_n^*(m) - T_n^*(m-1)}{2 + c_1} \quad (18)$$

where  $T^*$  denotes the updated position of the  $m^{th}$  tunicate based on Equation (18);  $T(m-1)$  refers to the neighbor tunicate;  $c_1$  is a random number, uniformly distributed between 0 and 1.

$$T_n^*(m) = \begin{cases} SF + A \times |SF - rand \times T_n(n)| & \text{if } rand \geq 0.5 \\ SF - A \times |SF - rand \times T_n(n)| & \text{if } rand < 0.5 \end{cases} \quad (19)$$

where  $SF$  is the source of food, which is represented by the best tunicate position in the whole population;  $A$  is a randomized vector to avoid any conflicts between tunicates and each other, which is expressed as: [40]

$$A = \frac{c_2 + c_3 - 2c_1}{VT_{min} + c_1(VT_{max} - VT_{min})} \quad (20)$$

where  $c_2$  and  $c_3$  are random numbers within the range (0:1);  $VT_{min}$  and  $VT_{max}$  represent the initial and subordinate speeds to produce social interaction.

The TSA method's key steps can be described as [42]:

- Step 1:** Create the initial tunicate population.  
**Step 2:** Determine the control units of TSA and stopping criteria.  
**Step 3:** Compute the fitness values of the initial population.  
**Step 4:** Select the position of the tunicate with the best fitness value.  
**Step 5:** Create the new position for each tunicate by using Equation (18).  
**Step 6:** Update the position of the tunicates that are out of the search space.  
**Step 7:** Compute the fitness values for the new positions of tunicates.  
**Step 8:** Until stopping criteria is satisfied, repeat steps 5–8.  
**Step 9:** After stopping criteria is satisfied, save the best tunicate position.

#### 4.4. Overview of the Firefly Algorithm (FEA)

The firefly algorithm developed by X-S. Yang in 2007 [43] is one of the swarm-based optimization algorithms, which works based on the sparkling performance of all the fireflies. Fireflies use their flashing property to communicate. There are three rules in the firefly algorithm, which are based on the idealized behavior of the flashing characteristics of fireflies [44].

##### 4.4.1. Attractiveness

All fireflies are unisex, and they will move toward more attractive and brighter ones regardless of their sex. In the firefly algorithm, the form of attractiveness function of a firefly is the following monotonically decreasing function [44]:

$$\beta(r) = \beta_0 \times \exp(-\gamma r^m), \quad m \geq 1 \quad (21)$$

where  $r$  is the distance between any two fireflies  $\beta_0$  is the initial attractiveness at  $r = 0$ , and  $\gamma$  is an absorption coefficient which controls the decrease in light intensity.

##### 4.4.2. Distance

The degree of attractiveness of a firefly is proportional to its brightness, which decreases as the distance from the other firefly increases because the air absorbs light. If there is no brighter or more attractive firefly than a particular one, it will move randomly [45].

The distance between any two fireflies  $i$  and  $j$ , at positions  $x_i$  and  $x_j$ , respectively, can be defined as a Cartesian or Euclidean distance as follows [46]:

$$r_{ij} = \|x_i - x_j\| = \sqrt{\sum_{k=1}^d (x_{i,k} - x_{j,k})^2} \quad (22)$$

where  $x_{i,k}$  is the  $k^{th}$  component of the spatial coordinate  $x_i$  of the  $i^{th}$  firefly.

In the dimensions 2- $d$ , we have:

$$r_{ij} = \sqrt{(x_i - x_j)^2 + (y_i - y_j)^2} \quad (23)$$

##### 4.4.3. Movement

The movement of a firefly  $i$ , which is attracted by a more attractive (brighter) firefly  $j$ , is calculated by [46]

$$x_i = x_i + \beta_0 \times \exp(-\gamma r_{ij}^2)(x_j - x_i) + \alpha \left( \text{rand} - \frac{1}{2} \right) \quad (24)$$

where the second term is due to the attraction, while the third term is randomization with  $\alpha$  being the randomization parameter, and rand is a random number within the range (0:1).

## 5. Simulation Results and Discussion

In order to solve the dynamic combined economic environmental dispatch problem, we developed and executed the CSA, SOA, TSA, and FFA algorithms in MATLAB 2017, and they were run on a personal computer with an Intel Core(TM) i5 with a processor of 2.60 GHz and a Ram of 8.0 GB under MS Windows 8.1. In the first part, the four proposed techniques were tested on the five-unit test system by considering VPE for three case studies, and in the second part, the CSA method was applied on the IEEE ten-unit system, including VPE, for three cases. The constraints involved in all cases were power balance limit with consideration of transmission losses and generator operating limits constraints.

The obtained results were compared with the optimization approaches recently published in the literature. Table 1 stands for the parameter values of CSA, SOA, TSA, and FFA algorithms, for all cases studies.

**Table 1.** Parameters of CSA, SOA, TSA, and FFA algorithms for DEED problem.

Algorithm	Parameters
SOA	$N = 50, t_{\max} = 1000, u = 1, v = 0.011$
CSA	$N = 50, \text{itermax} = 1000, fl = 2, AP = 0.1$
TSA	$m = 50, \text{iter}_{\max} = 1000, VT_{\min} = 1, VT_{\max} = 4$
FFA	$N = 100, \text{itermax} = 1000, \beta_0 = 1, \gamma = 1, \alpha = 0.1,$

### 5.1. IEEE Five-Unit Test System

The five-unit test system was derived from [47,48]. Tables 2 and 3 include the generation data. In this subsection, the dynamic load dispatch (DLD) cases through the application of the four metaheuristics techniques include:

- Case 1: Dynamic economic dispatch DED;
- Case 2: Dynamic environmental dispatch DENd;
- Case 3: Dynamic economic emission dispatch DEED.

**Table 2.** Cost and emission coefficients of generators for IEEE five-unit power system.

Unit	$a_i$ \$/h	$b_i$ \$/MWh	$c_i$ \$/MW <sup>2</sup> h	$e_i$ USD/h	$f_i$ rad/MW	$\alpha_i$ lb/h *	$\beta_i$ lb/MWh	$\gamma_i$ lb/MW <sup>2</sup> h	$\eta_i$ lb/h	$\delta_i$ 1/MW	$P_i^{\min}$ MW	$P_i^{\max}$ MW	$ppf_i$ \$/lb
$P_1$	25	2.0	0.0080	100	0.042	80	−0.805	0.0180	0.6550	0.02846	10	75	1.8201
$P_2$	60	1.8	0.0030	140	0.040	50	−0.555	0.0150	0.5773	0.02446	20	125	1.5436
$P_3$	100	2.1	0.0012	160	0.038	60	−1.355	0.0105	0.4968	0.02270	30	175	3.4911
$P_4$	120	2.0	0.0010	180	0.037	45	−0.600	0.0080	0.4860	0.01948	40	250	1.7278
$P_5$	40	1.8	0.0015	200	0.035	30	−0.555	0.0120	0.5035	0.02075	50	300	0.7578

\* Pound per hour (lb/h) = 0.453 59237 kilogram per hour (kg/h).

**Table 3.** Load demands.

Time (h)	Load (MW)	Time (h)	Load (MW)	Time (h)	Load (MW)
1	410	9	690	17	558
2	435	10	704	18	608
3	475	11	720	19	654
4	530	12	740	20	704
5	558	13	704	21	680
6	608	14	690	22	605
7	626	15	654	23	527
8	654	16	580	24	463



The B matrix of the test system we use is given by Equation (25) [48]:

$$B = 10^{-4} \times \begin{bmatrix} 0.49 & 0.14 & 0.15 & 0.15 & 0.20 \\ 0.14 & 0.45 & 0.16 & 0.20 & 0.18 \\ 0.15 & 0.16 & 0.39 & 0.10 & 0.12 \\ 0.15 & 0.20 & 0.10 & 0.40 & 0.14 \\ 0.20 & 0.18 & 0.12 & 0.14 & 0.35 \end{bmatrix} \quad (25)$$

#### 5.1.1. Case 1

The dynamic economic dispatch (DED) considering VPE with variables power losses is studied in this subsection (for total load = 14,577 MW).

The optimal schedule for a five-thermal-generator test system considering VPE and transmission losses, using the crow search algorithm (CSA), is presented in Table 4. The best results are highlighted in bold font.

**Table 4.** Simulation results of best solutions of CSA for Case 1.

Time h	$P_1$ MW	$P_2$ MW	$P_3$ MW	$P_4$ MW	$P_5$ MW	$P_D$ MW	$P_L$ MW	Fuel Cost USD/h	Emission Ib/h
1	84.804	98.539	50.652	40.000	139.759	410	3.756	<b>1363.640</b>	546.604
2	48.075	98.539	112.673	40.000	139.759	435	4.048	<b>1380.410</b>	510.742
3	88.876	98.539	112.673	40.000	139.759	475	4.849	<b>1423.790</b>	584.122
4	59.954	98.539	112.673	124.908	139.759	530	5.835	<b>1584.710</b>	590.865
5	84.139	98.539	112.673	40.000	229.519	558	6.872	<b>1604.790</b>	969.866
6	55.079	98.539	112.673	209.816	139.759	608	7.868	<b>1777.140</b>	784.062
7	73.529	98.539	112.673	209.816	139.759	626	8.317	<b>1783.770</b>	814.087
8	97.449	98.539	112.673	124.908	229.519	654	9.090	<b>1882.450</b>	1071.515
9	49.619	98.539	112.673	209.816	229.519	690	10.168	<b>1977.660</b>	1175.437
10	64.011	98.539	112.673	209.816	229.519	704	10.559	<b>1996.590</b>	1194.648
11	80.483	98.539	112.673	209.815	229.519	720	11.032	<b>1989.970</b>	1226.653
12	101.112	98.539	112.673	209.816	229.519	740	11.662	<b>2106.450</b>	1282.648
13	64.0110	98.539	112.673	209.816	229.519	704	10.559	<b>1996.590</b>	1194.648
14	49.619	98.539	112.673	209.816	229.519	690	10.168	<b>1977.660</b>	1175.437
15	97.449	98.539	112.673	124.908	229.519	654	9.090	<b>1882.450</b>	1071.515
16	84.800	40.058	112.673	209.816	139.759	580	7.108	<b>1746.070</b>	745.131
17	84.139	98.539	112.673	40.000	229.519	558	6.872	<b>1604.790</b>	969.866
18	55.079	98.539	112.673	209.816	139.759	608	7.868	<b>1777.140</b>	784.062
19	97.449	98.539	112.673	124.908	229.519	654	9.090	<b>1882.450</b>	1071.515
20	64.011	98.539	112.673	209.816	229.519	704	10.559	<b>1996.590</b>	1194.648
21	39.353	98.539	112.673	209.816	229.519	680	9.902	<b>1944.590</b>	1166.578
22	52.007	98.539	112.673	209.816	139.759	605	7.796	<b>1771.650</b>	780.351
23	56.889	98.539	112.673	124.908	139.759	527	5.771	<b>1581.460</b>	586.584
24	81.432	98.539	112.673	124.908	50.000	463	4.553	<b>1392.530</b>	468.968

The comparison results of the optimization techniques (CSA, SOA, TSA, and FFA) and the statistical analysis of the optimal results of Case 1 are given in Table 5. The best values, the robustness and effectiveness of the proposed CSA in finding optimal solutions to the DED problem with a reasonable number of iterations are compared and the constraints verified.

The results shown in Table 4 present the total cost found by the CSA algorithm, which is equal to 42,425.455 USD/h, is lower compared to that found by the SOA, TSA, and FFA algorithms, which is estimated at 48,609.77 USD/h, 46,672.4787 USD/h and 45,474.198 USD/h respectively.

As seen in Table 5, we infer that the CSA obtained the best fuel cost compared to PSO [47], SOGSA [48], NEHS [49], HS-NPSA [49], and DE-SQP [50].

The CSA algorithm, which offers the best production cost, on the other hand, offers a relatively higher amount of transmission losses compared to FFA, i.e., 193.393 MW for the CSA algorithm, 204.66 MW for SOA, 198.278 MW for TSA, and 191.298 MW for FFA.

**Table 5.** Comparison of CSA with previous algorithms for DED.

Methods	Total Loss MW	Total Fuel Cost USD/h	Total Emission lb/h
CSA	193.393	42,425.455	21,960.553
SOA	204.660	48,609.770	32,652.860
TSA	198.278	46,672.479	27,641.230
FFA	191.298	45,474.198	24,862.338
PSOGSA [48]	NA	42,853.339	22,087.887
NEHS [49]	NA	43,066.073	NA
MHS [49]	NA	45,497.740	NA
HS-NPSA [49]	NA	43,927.305	NA
DE-SQP [50]	NA	45,590.000	23,567.000
PSO [47]	NA	47,852.000	22,405.000

NA means not available in the corresponding literature.

It is also worth mentioning that in Table 5, the total emissions found by the CSA algorithm, which amount to 21,960.553 lb/h are more reduced compared to those found by the SOA, TSA, and FFA algorithms, which are estimated at 32,652.86 lb/h, 27,641.23 lb/h, and 24,862.338 lb/h respectively.

Figure 5, shows the graphical depiction of the convergence of the DED problem with time (iterations) obtained by applying our proposed methods corresponding to the peak hour ( $P_D = 740$  MW).

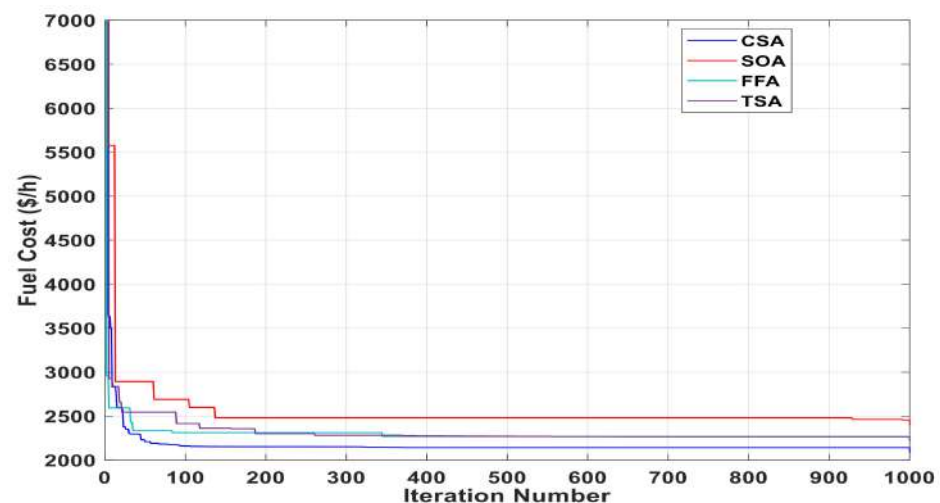


**Figure 5.** ° Convergence of the ED problem with time (iterations) for  $P_D = 740$  MW.

In comparison to SOA, TSA, and FFA, we can see that CSA has an incredibly fast convergence ability. In addition, CSA was trapped into the local optimum at around 230 iterations.

### 5.1.2. Case 2

The dynamic environmental dispatch (DEnD) considering the valve-point loading effect and transmission losses as given in Equation (3) are discussed in this case.

Table 6 shows the results of the optimum power dispatch for the five-unit system over 24 h obtained by CSA.

**Table 6.** Simulation results of best solutions of CSA for Case 2.

Time h	$P_1$ MW	$P_2$ MW	$P_3$ MW	$P_4$ MW	$P_5$ MW	$P_D$ MW	$P_L$ MW	Fuel Cost USD/h	Emission lb/h
1	54.679	58.236	116.571	110.598	73.364	410	3.448	352.453	<b>1723.627</b>
2	58.067	62.383	121.851	117.982	78.601	435	3.885	385.960	<b>1784.169</b>
3	63.526	69.080	130.221	129.751	87.063	475	4.641	446.642	<b>1912.114</b>
4	71.120	78.439	141.552	145.801	98.890	530	5.797	544.648	<b>2135.506</b>
5	75.032	83.262	147.232	153.895	105.008	558	6.431	601.208	<b>2203.616</b>
6	82.107	92.034	157.218	168.176	116.119	608	7.654	713.801	<b>2241.188</b>
7	84.684	95.241	160.760	173.252	120.183	626	8.121	758.078	<b>2229.487</b>
8	88.729	100.286	166.212	181.072	126.577	654	8.876	831.019	<b>2240.807</b>
9	93.996	106.880	173.119	190.970	134.934	690	9.898	932.292	<b>2270.804</b>
10	96.065	109.478	175.772	194.768	138.227	704	10.311	974.021	<b>2274.187</b>
11	98.446	112.472	178.783	199.072	142.020	720	10.794	1023.365	<b>2305.246</b>
12	101.444	116.253	182.514	204.393	146.809	740	11.414	1087.577	<b>2365.552</b>
13	96.065	109.478	175.772	194.768	138.227	704	10.311	974.021	<b>2274.190</b>
14	93.996	106.879	173.119	190.970	134.934	690	9.898	932.292	<b>2270.804</b>
15	88.729	100.286	166.212	181.072	126.577	654	8.876	831.019	<b>2240.804</b>
16	78.130	87.098	151.652	160.208	109.866	580	6.955	648.892	<b>2233.356</b>
17	75.032	83.262	147.233	153.895	105.008	558	6.431	601.208	<b>2203.615</b>
18	82.107	92.034	157.218	168.176	116.119	608	7.654	713.801	<b>2241.189</b>
19	88.729	100.286	166.212	181.072	126.577	654	8.876	831.019	<b>2240.807</b>
20	96.066	109.478	175.772	194.768	138.227	704	10.311	974.021	<b>2274.187</b>
21	92.525	105.036	171.212	188.239	132.596	680	9.609	903.298	<b>2265.782</b>
22	81.678	91.502	156.625	167.326	115.445	605	7.577	706.617	<b>2241.906</b>
23	70.703	77.915	140.940	144.931	98.239	527	5.727	538.858	<b>2126.253</b>
24	61.883	67.063	127.721	126.227	84.514	463	4.407	427.514	<b>1850.281</b>

The optimal results of the pollutant power generation, fuel cost, and active power loss obtained by the CSA are depicted in Table 6.

The total losses, total fuel cost, and total emissions computed by our proposed approaches are illustrated in Table 7. We compared them with those determined by other algorithms recently applied in the literature.

**Table 7.** Comparison of CSA with previous algorithms for DEnD.

Methods	Total Loss MW	Total Fuel Cost USD/h	Total Emission lb/h
CSA	187.901	51,149.500	17,733.600
SOA	189.766	51,385.300	18,743.100
TSA	188.825	51,878.700	18,602.800
FFA	187.070	51,263.500	19,840.200
NEHS [49]	NA	NA	17,853.003
MHS [49]	NA	NA	17,937.408
HS-NPSA [49]	NA	NA	17,872.348
PSOGSA [48]	NA	51,953.905	17,852.979
DE-SQP [50]	NA	52,611.000	18,955.000
PSO [47]	NA	53,086.000	19,094.000

By analyzing the results given in Table 7, we infer that the total emissions found by the CSA algorithm, which amount to 17,733.6 lb/h, are lower, compared to those found by the SOA TSA, and FFA algorithms, which are estimated at 18,743.1 lb/h, 18,602.8 lb/h, and 19,840.2 lb/h, respectively.

From the results shown in Table 7, we notice that the total cost determined by the CSA algorithm, which amounts to 51,149.5 USD/h, is lower compared to that found by the SOA, TSA, and FFA algorithms, which is estimated at 51,385.3 USD/h, 51,878.7 USD/h, and 51,263.5 USD/h, respectively.

In addition, when compared to CSA, SOA, and TSA, FFA has a relatively low amount of active power losses. The CS algorithm, which offers the minimum pollutant power generation, in return offers relatively higher transmission losses than FFA, and lower than SOA and TSA, i.e., 187.901 MW, 204.66MW, 188.825 MW, and, 187.07 MW for CSA, SOA, TSA, and FFA, respectively.

Figure 6 represents the convergence curves of our proposed approaches for the DEnD problem. It describes the stable convergence of the objective function of the problem given in Equation (3). The convergence characteristics shown in Figure 6 prove that CSA has better qualities than SOA, TSA, and FFA. We conclude that CSA is favorable for large-scale power systems.

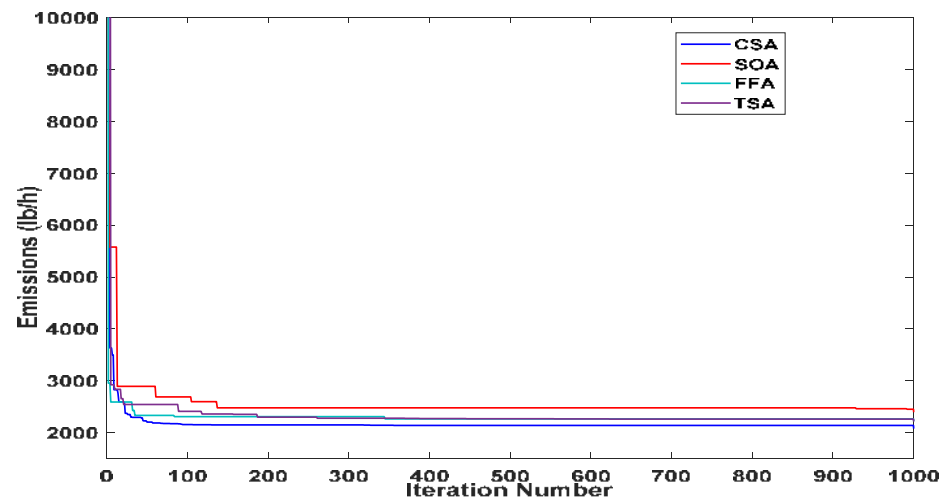


**Figure 6.** Convergence characteristics of the EnD with iterations for  $P_D = 740$  MW.

### 5.1.3. Case 3

In this case, we deal with the dynamic combined economic environmental dispatching (DCEED) with the variable losses by applying the price penalty factor under the impact of the valve-point. Electrical losses are variable depending on the power generated.

Table 8 summarizes the best solutions achieved for DCEED for a given load. We can deduce from the same table that CSA and our three competitive algorithms adjust the value of the output power ( $P_1 - P_5$ ) such that load demand and the constraint limits are satisfied, and the best fuel cost and pollutants emission results are achieved.

**Table 8.** The best solutions obtained by CSA for the DCEED of the IEEE five-unit test system.

Time h	$P_1$ MW	$P_2$ MW	$P_3$ MW	$P_4$ MW	$P_5$ MW	$P_D$ MW	$P_L$ MW	Fuel Cost USD/h	Emission lb/h	CEED USD/h
1	23.221	95.066	118.179	125.507	51.646	410.00	3.619	1343.493	400.897	1814.930
2	42.464	84.193	112.348	124.800	75.142	435.00	3.946	1607.846	399.951	2078.248
3	46.363	94.690	111.484	87.447	139.713	475.00	4.697	1670.469	519.509	2254.467
4	26.838	99.530	114.280	126.507	168.745	530.00	5.899	1745.194	669.218	2475.641
5	33.564	92.891	123.185	175.142	139.753	558.00	6.536	1902.752	665.000	2649.852
6	73.336	98.983	157.530	146.016	139.760	608.00	7.625	2031.153	728.731	2893.762
7	57.750	99.767	123.604	210.658	142.515	626.00	8.294	1914.203	816.010	2838.928
8	51.884	88.674	103.432	204.515	214.625	654.00	9.131	2131.606	1040.647	3248.435
9	53.142	97.776	114.207	209.557	225.462	690.00	10.144	2019.883	1153.740	3260.318
10	54.142	109.352	112.662	209.810	228.632	704.00	10.598	2075.861	1204.781	3370.372
11	73.636	100.102	117.640	210.105	229.527	720.00	11.010	2052.002	1223.114	3381.405

Table 8. Cont.

Time h	$P_1$ MW	$P_2$ MW	$P_3$ MW	$P_4$ MW	$P_5$ MW	$P_D$ MW	$P_L$ MW	Fuel Cost USD/h	Emission Ib/h	CEED USD/h
12	72.069	116.167	123.841	210.056	229.502	740.00	11.635	2224.386	1274.535	3613.856
13	66.908	98.680	173.744	145.451	229.517	704.00	10.300	2236.929	1154.978	3523.693
14	61.029	98.536	102.648	209.815	228.176	690.00	10.204	2036.995	1171.356	3293.254
15	66.581	117.798	115.698	213.160	149.886	654.00	9.123	2078.304	903.466	3098.415
16	22.005	101.970	112.492	124.576	226.155	580.00	7.200	1701.781	948.532	2700.991
17	24.788	95.120	109.230	195.916	139.614	558.00	6.667	1740.035	706.614	2521.975
18	66.807	83.120	156.707	124.906	184.080	608.00	7.620	2199.492	803.606	3116.141
19	61.025	110.762	116.453	209.863	164.984	654.00	9.087	2122.958	915.351	3145.552
20	61.190	96.517	118.054	209.294	229.473	704.00	10.528	2049.371	1189.705	3333.294
21	61.279	77.640	112.693	208.694	229.519	680.00	9.825	2055.372	1140.486	3280.867
22	66.280	38.471	112.702	209.818	185.459	605.00	7.729	2051.944	873.120	3013.830
23	47.683	93.663	126.697	124.929	139.771	527.00	5.741	1693.775	582.538	2357.800
24	41.562	70.450	112.609	124.880	117.903	463.00	4.404	1696.097	452.880	2212.678

Table 9 shows the values of the active power losses, the best cost, the best emission, and the total cost objectives against 0.5 weight for the test system. The results displayed in the mentioned table are obtained from NEHS, MHS, HS-NPSA, PSO-GSA, DE-SQO, PSO, and our proposed approaches.

Table 9. The DCEED comparison results of different algorithms of the five-unit test system.

Methods	Total Loss MW	Total Fuel Cost USD/h	Total Emission Ib/h	Total Cost (0.5 Weight) USD/h	Change % w.r.t CSA
CSA	192.386	46,381.900	20,938.800	33,660.350	//
SOA	196.961	48,500.800	21,130.100	34,815.450	3.43
TSA	194.204	45,816.300	22,424.800	33,942.950	0.84
FFA	192.451	47,030.700	22,069.600	34,550.150	2.64
NEHS [49]	NA	45,398.016	18,392.337	31,895.177	−5.24
MHS [49]	NA	47,390.956	18,423.776	32,907.366	−2.24
MOHDESAT [51]	NA	48,214.000	18,011.000	33,112.500	−1.63
WOA [52]	NA	46,475.090	18,827.980	32,651.530	−2.99
PSOGSA [48]	NA	45,702.6001	18,267.179	31,984.985	−5.24
DE-SQP [50]	NA	46,625.000	20,527.000	33,576.000	−0.002
PSO [47]	NA	50,893.000	20,163.000	35,528.000	5.55
MONNDE [53]	NA	49,135.000	18,233.000	33,684.240	0.06
EP [54]	NA	48,628.000	21,154.000	34,891.000	3.66
SA [51]	NA	48,621.000	21,188.000	33,904.500	0.73
PS [55]	NA	47,911.000	18,927.000	33,419.000	−0.72
MODE [51]	NA	47,330.000	18,116.000	32,723.000	−2.78

Column five of Table 9 depicts the value of the single-objective function of the problem, as specified in Equation (1). The effectiveness of the suggested CSA is demonstrated by the percentage change of some algorithms listed in the same table.

As seen in Table 9, the results reveal that CSA has a good performance for solving DCEED at less than SOA (3.43%), than TSA (0.84%), than FFA (2.64%), than PSO (5.55%), and then EP (3.66%).

According to Table 9, we infer that minimizing the cost of generation and minimizing emissions are contradictory goals. Emissions are highest when the cost of production is minimized.

Figure 7 shows the convergence curves of the total cost with iterations, obtained by applying CSA, SOA, TSA, and FFA methods corresponding to the power demand equal to

740 MW. We infer that CSA and FFA reach the optimum solution more quickly than SOA and TSA, which is shown in Figure 7.

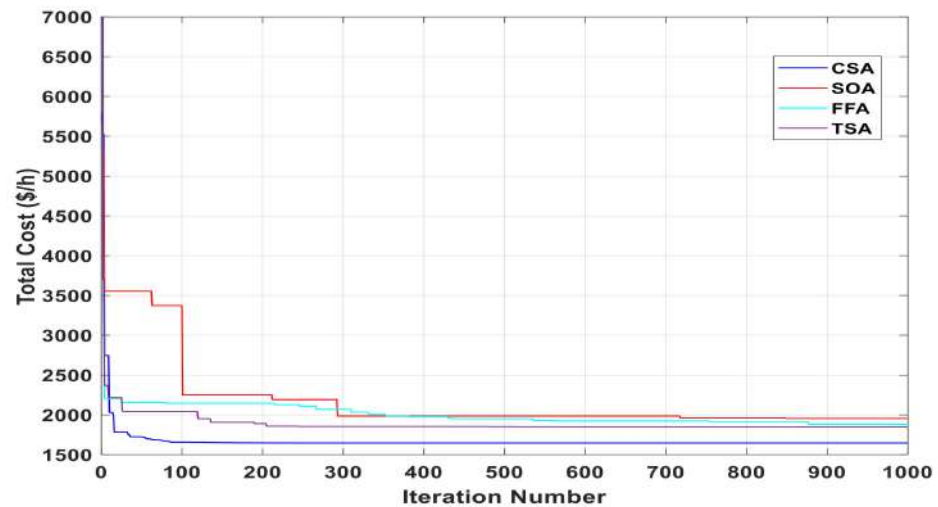


Figure 7. Convergence curves of the CEED with time (iterations) for  $P_D = 740$  MW.

Figure 8 presents a graphical comparison of the total fuel cost, the total emissions, and the total cost of our proposed methods and other algorithms for a five-unit test system. This clearly demonstrates that CSA has the lowest total cost when compared to other algorithms.

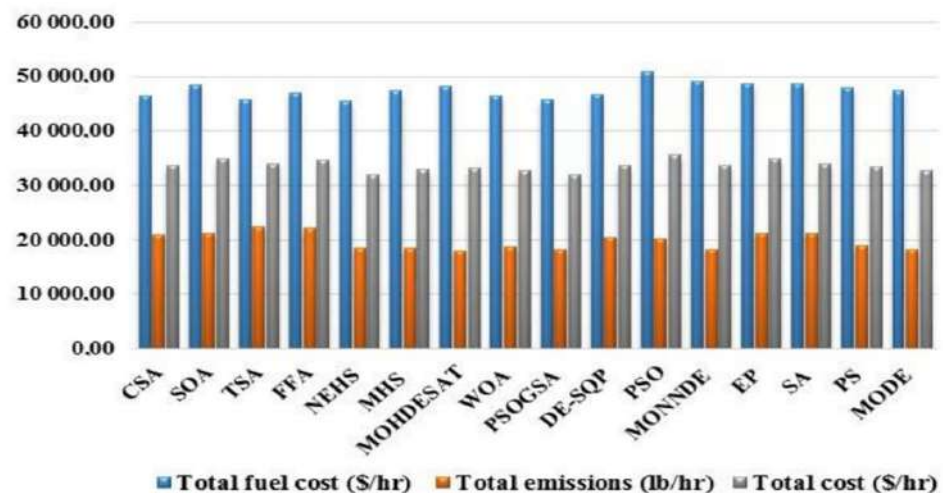


Figure 8. Total fuel cost, total emissions, and total cost obtained by CSA, SOA, TSA, and FFA vs. other algorithms applied on the IEEE five-unit test system.

Percentage enhancement of the suggested CSA over other algorithms is shown in Figure 9. From this figure, the positive bars show the largest values of the total cost compared to those obtained by CSA, and negative bars represent smaller values of the total cost compared to those obtained by CSA.

The statistical summary of 50 runs for each study case performed (i.e., Case 1 to Case 3) using CSA, SOA, TSA, and FFA approaches is depicted in Table 10.

The columns display the min, average, worst, and standard deviation values for the objective function in each case. According to Table 10, it is clear the CSA method delivers the best fitness, best mean, and best standard deviation values in all the cases.

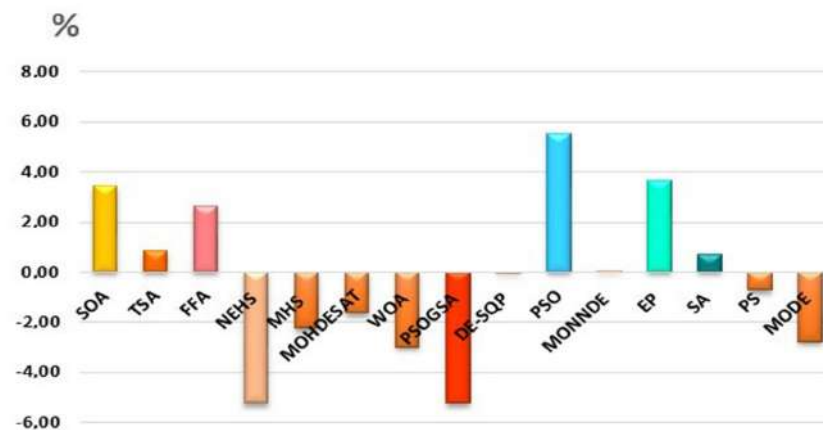


Figure 9. Percentage enhancement of CSA vs. other algorithms for the IEEE five-unit test system.

Table 10. Statistical summary of case studies using CSA, SOA, TSA, and FFA algorithms for load demand of 740 MW for a IEEE five-unit system.

Case 1		Economic Load Dispatch ELD (USD/h)			
Algorithm	Min	Average	Worst	Std Dev	
CSA	2142.3181	2164.8135	2593.5470	55.4145	
SOA	2456.3468	2537.9394	5577.4323	290.6773	
TSA	2269.2981	2293.2777	3635.3608	113.8379	
FFA	2265.5019	2310.7733	2926.1582	100.0485	
Case 2		Environmental Dispatch EnD (lb/h)			
CSA	1090.3380	1111.2373	1421.8938	58.9938	
SOA	1160.6740	1757.2506	3536.7399	499.4472	
TSA	1295.4652	1506.9932	1728.0597	83.5214	
FFA	1241.5852	1323.0107	5121.1719	331.6223	
Case 3		Combined Economic Emission Dispatch CEED (USD/h)			
CSA	1646.9098	1652.9305	1784.2619	22.1540	
SOA	1955.3266	2153.2196	3553.8243	418.7256	
TSA	1879.5231	1992.3606	2203.5179	99.1567	
FFA	1848.8820	1878.6942	2216.4237	67.0644	

Figure 10 obtained values (min, mean, and worst values) for 50 runs of the CSA approach for the case of reducing the cost of production (Case 1).

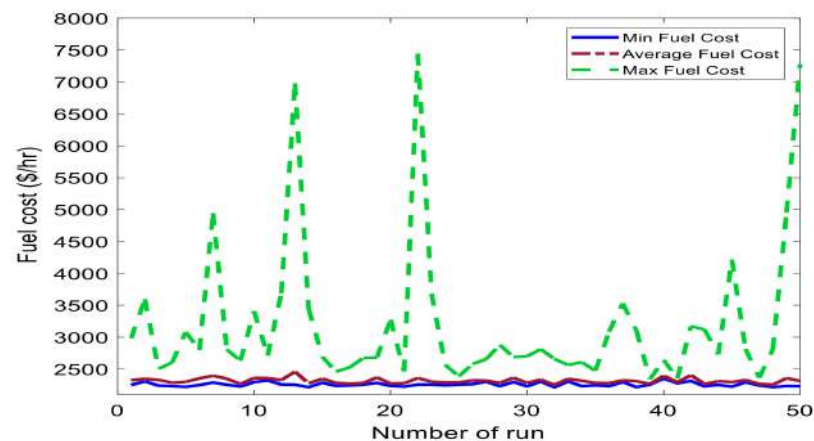


Figure 10. Min, Mean and Max Fuel cost obtained in 50 runs using CSA method.

### 5.2. IEEE 10-Unit Test System

In this case study, the then-unit generating system is utilized to evaluate the performance of the proposed CSA by considering the valve-point loading effect. In this experiment, a 24-h scheduling period with 1-h intervals is used. The original data of the 10-unit system are shown in Table 11, which are available in the literature [53]. Tables 12 and 13 are the 10-unit generator loads demand and the B matrix, respectively, which are derived from [53]. In this research, the weighting function approach (w.f.a) is used to convert multi-objective functions into a single problem [56]. Hence, by the usage of the w. f. a, Equation (1) can be reformulated as:

$$\min F = w_1 \sum_{t=1}^T \sum_{i=1}^{Ng} C_{i,t}(P_{i,t}) + w_2 \sum_{t=1}^T \sum_{i=1}^{Ng} E_{i,t}(P_{i,t}) \quad (26)$$

where  $\sum_{i=1}^n w_i = 1$  ( $n$ : number of problems).

**Table 11.** IEEE 10-unit generator coefficients.

Unit	$a_i$ \$/h	$b_i$ \$/MWh	$c_i$ \$/MW <sup>2</sup> h	$e_i$ \$/h	$f_i$ rad/MW	$\alpha_i$ lb/h*	$\beta_i$ lb/MWh	$\gamma_i$ lb/MW <sup>2</sup> h	$\eta_i$ lb/h	$\delta_i$ 1/MW	$p_i^{\min}$ MW	$p_i^{\max}$ MW
$P_1$	786.7988	38.5397	0.1524	450	0.0410	103.3908	−2.4444	0.0312	0.5035	0.0207	150	470
$P_2$	451.3251	46.1591	0.1058	600	0.0360	103.3908	−2.4444	0.0312	0.5035	0.0207	135	470
$P_3$	1049.9977	40.3965	0.0280	320	0.0280	300.3910	−4.0695	0.0509	0.4968	0.0202	73	340
$P_4$	1243.5311	38.3055	0.0354	260	0.0520	300.3910	−4.0695	0.0509	0.4968	0.0202	60	300
$P_5$	1658.5696	36.3278	0.0211	280	0.0630	320.0006	−3.8132	0.0344	0.4972	0.0200	73	243
$P_6$	1356.6592	38.2704	0.0179	310	0.0480	320.0006	−3.8132	0.0344	0.4972	0.0200	57	160
$P_7$	1450.7045	36.5104	0.0121	300	0.0860	330.0056	−3.9023	0.0465	0.5163	0.0214	20	130
$P_8$	1450.7045	36.5104	0.0121	340	0.0820	330.0056	−3.9023	0.0465	0.5163	0.0214	47	120
$P_9$	1455.6056	39.5804	0.1090	270	0.0980	350.0056	−3.9524	0.0465	0.5475	0.0234	20	80
$P_{10}$	1469.4026	40.5407	0.1295	380	0.0940	360.0012	−3.9864	0.0470	0.5475	0.0234	10	55

**Table 12.** IEEE 10-unit B matrix ( $\times 10^{-4}$ ).

0.49	0.14	0.15	0.15	0.16	0.17	0.17	0.18	0.19	0.20
0.14	0.45	0.16	0.16	0.17	0.15	0.15	0.16	0.18	0.18
0.15	0.16	0.39	0.10	0.12	0.14	0.14	0.16	0.16	0.16
0.15	0.16	0.10	0.40	0.14	0.10	0.11	0.12	0.14	0.15
0.16	0.17	0.12	0.14	0.35	0.11	0.13	0.13	0.15	0.16
0.17	0.15	0.12	0.10	0.11	0.36	0.12	0.12	0.14	0.15
0.17	0.15	0.14	0.11	0.13	0.12	0.38	0.16	0.16	0.18
0.18	0.16	0.14	0.12	0.13	0.12	0.16	0.40	0.15	0.16
0.19	0.18	0.16	0.14	0.15	0.14	0.16	0.15	0.42	0.19
0.20	0.18	0.16	0.15	0.16	0.15	0.18	0.16	0.19	0.44

**Table 13.** Load demands.

Time (h)	Load (MW)	Time (h)	Load (MW)	Time (h)	Load (MW)
1	1036	9	1924	17	1480
2	1110	10	2022	18	1628
3	1258	11	2106	19	1776
4	1406	12	2150	20	1972
5	1480	13	2072	21	1924
6	1628	14	1924	22	1628
7	1702	15	1776	23	1332
8	1776	16	1554	24	1184



Dynamic load dispatch (DLD) cases in this subsection include:

- Case 4: Dynamic economic dispatch DED ( $w_1 = 1$ ,  $w_2 = 0$ );
- Case 5: Dynamic environmental dispatch DEnD ( $w_1 = 0$ ,  $w_2 = 1$ );
- Case 6: Dynamic economic emission dispatch DEED ( $w_1 = 0.5$ ,  $w_2 = 0.5$ );

#### 5.2.1. Case 4

The dynamic economic dispatch (DED) considering VPE with variables power losses is studied in this subsection (for total load = 39.848 MW).

Hourly generation (MW) schedule obtained from DED using CSA for a 10-unit system by considering VPE and transmission losses are presented in Table 14. The best results are highlighted in bold font.

**Table 14.** Best solutions obtained from CSA for test Case 4.

Time h	$P_1$ MW	$P_2$ MW	$P_3$ MW	$P_4$ MW	$P_5$ MW	$P_6$ MW	$P_7$ MW	$P_8$ MW	$P_9$ MW	$P_{10}$ MW	$P_L$ MW	Fuel Cost USD/h	Emission lb/h
1	150.510	135.104	80.705	62.302	169.338	122.675	125.946	119.882	54.877	34.491	19.832	<b>61,600.519</b>	3803.894
2	150.006	135.034	146.567	120.465	175.863	122.983	128.759	118.303	20.993	13.373	22.336	<b>64,906.264</b>	4689.769
3	150.279	135.165	181.085	182.838	221.095	138.049	129.652	89.063	49.058	10.227	28.514	<b>72,304.859</b>	6228.359
4	150.009	135.007	224.237	191.995	242.419	159.944	129.963	119.998	44.613	43.418	35.606	<b>80,271.190</b>	7718.284
5	150.034	135.001	290.188	242.097	222.606	124.793	129.457	117.073	61.531	47.082	39.862	<b>84,408.221</b>	9763.984
6	150.032	144.110	339.873	298.516	242.647	159.853	98.936	118.058	79.997	44.509	48.532	<b>94,297.297</b>	13,307.920
7	222.445	135.032	330.607	299.754	239.465	159.924	129.960	116.990	70.059	51.333	53.563	<b>100,946.056</b>	13,761.749
8	224.611	213.686	339.936	291.807	242.827	139.143	129.115	119.997	79.959	54.035	59.116	<b>107,884.313</b>	14,564.055
9	272.168	323.499	339.776	299.530	242.880	159.038	129.950	120.000	65.817	42.489	71.142	<b>124,932.384</b>	17,534.742
10	299.063	395.517	339.995	293.040	242.928	159.991	122.587	114.212	79.889	55.000	80.219	<b>137,626.028</b>	20,656.966
11	341.347	449.088	339.950	296.452	243.000	159.982	129.965	110.813	79.997	44.020	88.609	<b>150,876.695</b>	26,836.868
12	386.873	450.590	339.134	299.972	242.996	156.337	129.852	119.998	79.960	37.402	93.114	<b>157,522.576</b>	29,006.003
13	312.707	441.906	332.353	299.267	242.973	144.923	128.829	119.947	79.461	54.994	85.359	<b>145,630.761</b>	24,855.409
14	272.168	323.499	339.776	299.530	242.880	159.038	129.950	120.000	65.817	42.489	71.142	<b>124,932.384</b>	17,534.742
15	224.611	213.686	339.936	291.807	242.827	139.143	129.115	119.997	79.959	54.035	59.116	<b>107,884.313</b>	14,564.055
16	152.831	135.356	293.140	299.998	237.653	158.625	129.971	93.751	52.366	44.230	43.915	<b>89,095.065</b>	11,635.439
17	150.034	135.001	290.188	242.097	222.606	124.793	129.457	117.073	61.531	47.082	39.862	<b>84,408.221</b>	9763.984
18	150.032	144.110	339.873	298.516	242.647	159.853	98.936	118.058	79.997	44.509	48.532	<b>94,297.297</b>	13,307.920
19	224.611	213.686	339.936	291.807	242.827	139.143	129.115	119.997	79.959	54.035	59.116	<b>107,884.313</b>	14,564.055
20	247.097	405.611	338.935	300.000	241.615	159.957	130.000	116.665	64.768	43.158	75.807	<b>131,752.041</b>	20,566.632
21	272.168	323.499	339.776	299.530	242.880	159.038	129.950	120.000	65.817	42.489	71.142	<b>124,932.384</b>	17,534.742
22	150.032	144.110	339.873	298.516	242.647	159.853	98.936	118.058	79.997	44.509	48.532	<b>94,297.297</b>	13,307.920
23	150.015	135.032	215.063	180.844	222.867	143.145	129.793	119.964	56.899	10.332	31.955	<b>76,082.212</b>	7006.619
24	150.001	135.024	184.626	131.224	222.612	123.171	129.588	86.119	24.598	22.486	25.447	<b>68,742.483</b>	5589.037

Total fuel cost and total emission results obtained from the CSA algorithm are compared with other methods in Table 15. As can be seen from Table 15, the proposed CSA algorithm produces fewer fuel cost value by  $2.487512 \times 10^6$  USD than other algorithms. CSA was able to achieve an enhanced in total fuel cost in rang  $10^6$  of 0.01659 USD, 0.013315 USD and 0.029288 USD, respectively as compared to MHS [49], SA [57], and NSGAI [58]. IBFA [59], GCABC [60], and TLBO [61] gives a best solutions (less than this obtained by our proposed approach of 5812 USD, 13,039 USD, and 15,396 USD, respectively).

To elaborate the transition of CSA for different phases of the search convergence characteristics for the 10-unit test system under a fixed hour ( $P_D = 2150$  MW) for 1000 iterations is shown in Figure 11. From the figure, we can be seen that CSA has an incredibly fast convergence ability it has been quickly trapped the optimal values.

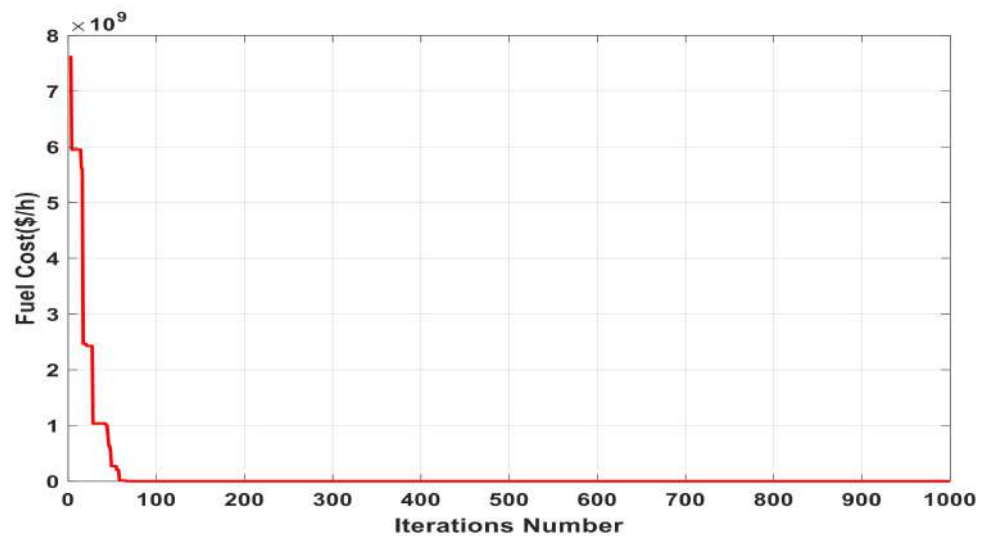


**Figure 11.** Convergence curve for 10-unit test system for a fixed hour ( $P_D = 2150$  MW).

**Table 15.** Comparison of the 10-unit test system with previous algorithms for best minimum cost solution (Case 4).

Methods	Total Fuel Cost ( $\times 10^6$ ) USD	Total Emission ( $\times 10^5$ ) lb
CSA	2.487512	3.38103
MHS [49]	2.504106	NA
SA [57]	2.537200	NA
NSGAII [58]	2.516800	3.17400
IBFA [59]	2.481700	3.27500
GCABC [60]	2.474473	NA
TLBO [61]	2.472116	3.30411

### 5.2.2. Case 5

The dynamic environmental dispatch (DEnD) considering the valve-point loading effect and transmission losses as given in Equation (3) is discussed in this case.

Table 16 shows the results of the optimum power dispatch for the 10-unit system over 24 h obtained by CSA. The optimal results of the pollutant power generation and fuel cost obtained by the CSA are depicted in Table 16. The total fuel cost and total emissions computed by the CSA method are illustrated in Table 17. We compared the obtained solutions with those determined by other algorithms recently published in the literature.

By analyzing the results given in Table 17, we infer that the total emissions found by the CSA algorithm, which amount to  $2.9354 \times 10^5$  lb, are lower, compared to that found by IHS [49], MHS in [49], NSGA-II [58], TLBO [61], CRO [62], and HCRO [62], which are estimated at 296,044 lb, 302,093 lb, 304,120 lb, 294,153 lb, 317,400 lb, and 327,500 lb, respectively.

Method GCABC in [60] obtains the less total emission values of 293,416 lb compared with those values obtained by the methods cited in Table 17.

According to Table 17, we notice that the total cost determined by the CSA algorithm which is equal to  $2.62594 \times 10^6$  USD is lower compared to that found by the NSGA-II [58] algorithm, which is estimated at  $2.6563 \times 10^6$  USD.

**Table 16.** Best solutions obtained from CSA for test Case 5.

Time h	P <sub>1</sub> MW	P <sub>2</sub> MW	P <sub>3</sub> MW	P <sub>4</sub> MW	P <sub>5</sub> MW	P <sub>6</sub> MW	P <sub>7</sub> MW	P <sub>8</sub> MW	P <sub>9</sub> MW	P <sub>10</sub> MW	P <sub>L</sub> MW	Fuel Cost USD/h	Emission lb/h
1	150.002	135.718	90.566	91.469	118.016	136.066	109.538	94.773	74.663	54.913	19.725	63,282.134	3479.107
2	157.856	153.661	110.735	93.173	142.569	139.932	110.889	89.120	79.790	54.989	22.712	68,271.277	3945.886
3	160.271	167.053	120.413	132.252	178.038	155.820	122.997	119.962	75.131	54.997	28.936	75,457.550	5060.796
4	204.728	221.786	134.213	140.423	197.409	159.938	129.528	119.976	79.999	55.000	37.000	86,669.943	6532.429
5	188.357	229.602	151.075	171.912	239.342	158.088	129.982	119.990	77.798	54.576	40.723	89,962.573	7507.212
6	277.420	270.540	161.914	183.738	242.939	159.996	130.000	117.692	79.999	54.583	50.822	105,456.159	9689.460
7	303.679	253.234	215.080	207.820	234.626	159.789	129.996	118.557	80.000	54.731	55.512	110,376.988	11,046.974
8	284.213	276.631	242.805	257.079	232.163	159.480	129.906	119.925	79.154	54.847	60.204	114,622.220	12,591.579
9	329.264	351.175	263.618	277.043	237.413	153.536	129.956	119.969	79.838	54.610	72.424	131,422.312	16,492.225
10	391.022	365.874	298.133	265.150	242.871	159.900	129.864	119.824	75.641	54.994	81.275	143,558.138	20,215.772
11	403.610	398.763	323.390	299.975	233.988	159.970	129.997	112.664	79.995	52.485	88.838	152,258.869	24,291.715
12	415.007	433.955	340.000	295.831	242.986	159.987	129.954	98.248	79.986	47.515	93.474	159,891.196	28,568.055
13	403.752	376.588	323.914	265.781	242.984	159.996	129.998	119.990	79.991	54.733	85.728	148,855.883	22,349.281
14	329.264	351.175	263.618	277.043	237.413	153.536	129.956	119.969	79.838	54.610	72.424	131,422.312	16,492.225
15	284.213	276.631	242.805	257.079	232.163	159.480	129.906	119.925	79.154	54.847	60.204	114,622.220	12,591.579
16	223.433	240.864	174.031	189.920	227.097	159.983	129.867	119.965	79.171	54.950	45.282	95,730.049	8464.578
17	188.357	229.602	151.075	171.912	239.342	158.088	129.982	119.990	77.798	54.576	40.723	89,962.573	7507.212
18	277.420	270.540	161.914	183.738	242.939	159.996	130.000	117.692	79.999	54.583	50.822	105,456.159	9689.460
19	284.213	276.631	242.805	257.079	232.163	159.480	129.906	119.925	79.154	54.847	60.204	114,622.220	12,591.579
20	349.961	338.292	287.234	299.742	242.953	157.864	129.890	119.878	68.079	54.236	76.132	134,994.987	18,062.886
21	329.264	351.175	263.618	277.043	237.413	153.536	129.956	119.969	79.838	54.610	72.424	131,422.312	16,492.225
22	277.420	270.540	161.914	183.738	242.939	159.996	130.000	117.692	79.999	54.583	50.822	105,456.159	9689.460
23	167.768	180.865	146.464	142.876	189.040	159.016	129.864	113.622	79.999	54.997	32.511	80,208.210	5752.844
24	166.459	153.534	105.409	106.892	152.447	159.990	110.254	119.831	79.968	54.989	25.774	71,963.076	4438.329

**Table 17.** Comparison of the 10-unit test system with previous algorithms for best minimum cost solution (Case 5).

Methods	Total Fuel Cost ( $\times 10^6$ ) USD	Total Emission ( $\times 10^5$ ) lb
CSA	2.625940	2.93540
GCABC [60]	NA	2.93416
TLBO [61]	2.594148	2.94153
IHS [49]	NA	2.96044
MHS [49]	NA	3.02093
NSGA-II [58]	2.656300	3.04120
CRO [62]	NA	3.17400
HCRO [62]	NA	3.27500

Figure 12 represents the convergence curves of our proposed approach for the DEnD problem. It describes the stable convergence of the objective function of the problem given in (3) (Case 5). The convergence characteristics shown in Figure 12 prove that CSA has good qualities. We conclude that CSA is favorable for large-scale power systems.

### 5.2.3. Case 6

In this case, we deal with the dynamic combined economic environmental dispatching (DCEED) by considering the power losses and the valve point-effect loading. Table 18 summarizes the best compromise solutions achieved for DCEED for a given load.

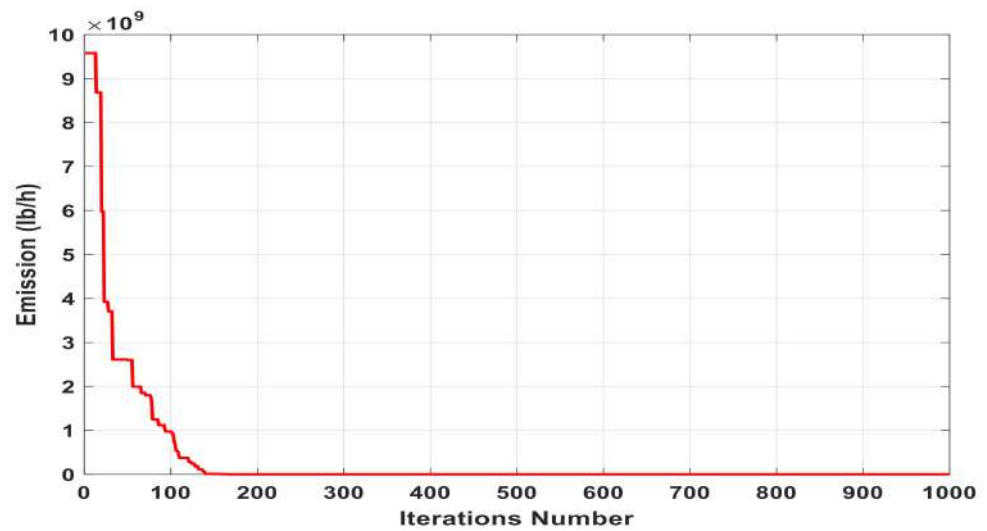


Figure 12. Convergence characteristics of the EnD with iterations for a fixed hour ( $P_D = 2150$  MW).

Table 18. The best solutions obtained by CSA for the DCEED of the IEEE 10-unit test system.

Time h	$P_1$ MW	$P_2$ MW	$P_3$ MW	$P_4$ MW	$P_5$ MW	$P_6$ MW	$P_7$ MW	$P_8$ MW	$P_9$ MW	$P_{10}$ MW	$P_L$ MW	FC USD/h	E lb/h	TC USD/h
1	150.406	135.246	85.444	94.209	181.135	122.376	129.280	94.366	20.605	42.622	19.691	61,700.233	3934.478	32,955.958
2	150.059	135.192	148.162	120.431	172.562	122.461	93.065	119.995	22.348	48.148	22.423	65,198.802	4454.610	34,966.155
3	150.093	135.208	101.472	182.259	221.659	149.384	129.872	119.939	55.572	41.141	28.607	72,288.444	5650.903	39,113.119
4	150.060	135.019	190.752	204.190	224.454	159.847	124.653	119.999	79.982	52.633	35.589	80,461.980	7112.270	43,928.263
5	150.231	135.171	241.644	242.567	241.338	159.980	129.383	119.991	52.892	46.297	39.493	84,292.688	9023.037	46,796.853
6	152.020	164.386	320.567	277.526	222.190	159.921	129.914	119.986	80.000	49.903	48.411	94,530.118	12,104.35	53,457.173
7	161.851	223.048	310.663	299.756	235.796	141.568	129.795	119.940	78.244	55.000	53.662	100,886.75	13,127.88	57,150.064
8	150.069	269.756	339.843	299.405	242.988	158.986	124.745	119.937	75.404	53.775	58.903	107,645.16	14,941.13	61,436.135
9	289.083	313.982	339.999	280.201	234.134	156.640	129.595	120.000	78.241	53.458	71.328	125,468.68	16,952.94	71,353.584
10	364.296	316.930	339.330	299.170	242.913	159.675	129.700	119.025	76.855	54.122	80.023	137,757.86	19,776.86	78,914.408
11	391.758	400.840	336.936	293.570	242.999	159.970	129.998	119.999	63.537	54.997	88.603	151,135.50	24,136.97	87,778.694
12	442.035	396.653	337.897	299.108	242.982	157.061	127.818	119.996	79.999	39.772	93.323	158,774.96	28,337.51	93,695.444
13	359.815	391.269	339.912	299.467	242.964	151.758	126.070	118.443	79.987	47.449	85.138	145,326.69	22,318.79	83,964.399
14	289.083	313.982	339.999	280.201	234.134	156.640	129.595	120.000	78.241	53.458	71.328	125,468.68	16,952.94	71,353.584
15	150.069	269.756	339.843	299.405	242.988	158.986	124.745	119.937	75.404	53.775	58.903	107,645.16	14,941.13	61,436.135
16	150.156	135.036	276.528	283.184	240.900	159.073	129.657	120.000	51.168	52.036	43.739	88,890.958	10,861.13	50,016.892
17	150.231	135.171	241.644	242.567	241.338	159.980	129.383	119.991	52.892	46.297	39.493	84,292.688	9023.037	46,796.853
18	152.020	164.386	320.567	277.526	222.190	159.921	129.914	119.986	80.000	49.903	48.411	94,530.118	12,104.35	53,457.173
19	150.069	269.756	339.843	299.405	242.988	158.986	124.745	119.937	75.404	53.775	58.903	107,645.16	14,941.13	61,436.135
20	326.074	347.521	309.290	299.994	242.997	160.000	129.970	119.999	67.957	44.017	75.820	133,249.35	18,331.48	75,929.053
21	289.083	313.982	339.999	280.201	234.134	156.640	129.595	120.000	78.241	53.458	71.328	125,468.68	16,952.94	71,353.584
22	152.020	164.386	320.567	277.526	222.190	159.921	129.914	119.986	80.000	49.903	48.411	94,530.118	12,104.35	53,457.173
23	150.173	137.534	180.818	163.649	238.569	149.328	129.739	117.812	51.515	44.869	32.009	76,243.211	6439.102	41,480.912
24	150.015	135.021	126.085	104.167	220.872	159.474	129.251	119.979	21.132	43.459	25.457	68,625.467	5068.830	36,985.679

Note: FC: Fuel cost, E: Emission and TC: Total cost (FC+E).

According to Table 18, we can deduce that CSA adjust the value of the output power ( $P_1 - P_{10}$ ) such that load demand and the constraint limits are satisfied, and the best fuel cost and pollutants emission results are achieved. However, the statistical comparative results of CSA method along with various other methods for both cost and emission objective functions are provided in Table 19. The minimum cost obtained by the proposed CSA approach is 2,492,050 USD among 50 trials in the economic dispatch problem and considered as the ever best solution. It is also clear from the simulation results that the proposed approach provides better statistical results as compared with many other available methods given in Table 19.

**Table 19.** The DCEED comparison results of different algorithms of the 10-unit test system.

Methods	Total Loss MW	Total Fuel Cost ( $\times 10^6$ ) USD	Total Emission ( $\times 10^5$ ) Ib	Total Cost ( $\times 10^6$ ) USD
CSA	<b>1298.9956</b>	<b>2.492050</b>	<b>3.19592</b>	<b>2.843985</b>
MONNDE [53]	1307.8000	2.557900	2.95220	2.769100
NSGA-II [58]	NA	2.521000	3.12460	2.823600
IBFA [59]	1299.8760	2.517117	2.99037	2.753743
TLBO [61]	1301.1900	2.472116	2.94153	2.776644
HCRO [62]	1299.8723	2.517076	2.99065	2.753863
CRO [62]	1298.4666	2.517821	3.01941	2.768615
NSPSO [63]	NA	2.474472	2.93416	2.704316
PSO-CSC [64]	1303.1000	2.524700	3.05240	2.788550

Figure 13 shows the convergence curves of the CEED with time (iterations) obtained by applying the CSA method corresponding to a fixed hour with a power demand of 2150 MW. It is observed from the convergence curve that a better reduction in combined cost and emission can be obtained with less number of iterations using the proposed CSA.

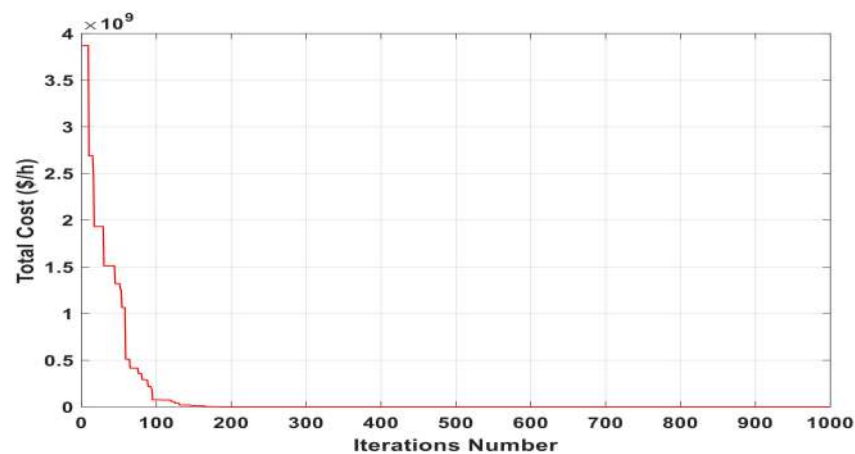
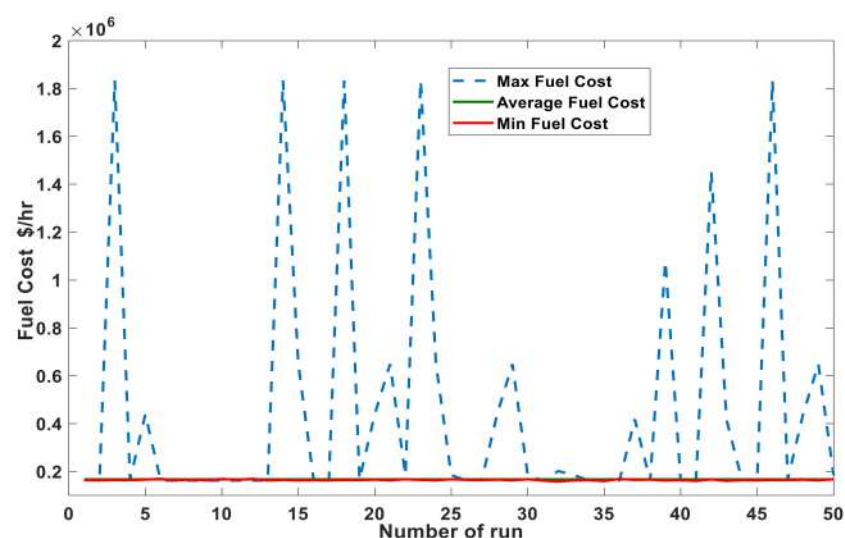
**Figure 13.** Convergence curves of the CEED with time (iterations) for a fixed hour ( $P_D = 2150$  MW).

Figure 14 displays the obtained values (best, average, and max values) among 50 runs of the CSA technique for the case of minimizing the fuel cost of production (Case 4).

**Figure 14.** Min, Mean, and Max Fuel cost obtained in 50 runs using CSA method for 10-unit system.

## 6. Conclusions and Future Work

In this paper, new optimization approaches were proposed, presented and applied to solve the problem of the dynamic economic emissions dispatch of generator units considering the valve-point loading effects. The main inspiration of these optimization techniques are the fact that metaheuristic algorithms are easy to implement and can be used for a variety of other problems.

The proposed strategies are validated by simulating MATLAB and testing on the two standard IEEE power systems, 5-unit and 10-unit systems. The numerical results of this system are presented to show the capabilities of the proposal algorithms to establish an optimal solution of the dynamics problem of combined economic emissions dispatch in several passages. From Tables 4, 6, 8, 14, 16 and 18, it is obviously clear that the optimal generation schedule of a 5-units and 10-unit system obtained by CSA satisfy power balance constraint with considering power losses and generator operating limits constraint. The proposed CSA gives better performance compared to methods cited in the literature.

In all cases, our proposed algorithms can reach the optimum solution more quickly which. In future works, we intend to combine CSA with TSA, and introduce it to other kinds of optimization issues, such as large-scale economic load dispatch problems, integrated renewable energy sources, multi-objective ED problems with many complex constraints.

**Author Contributions:** Conceptualization, B.L., A.N.E.I.A., H.B. and A.S.T.; Data curation, B.L.; Formal analysis, B.L., A.N.E.I.A. and H.B.; Funding acquisition, H.A., T.E.A.A., S.S.M.G. and S.A.M.A.; Investigation, H.A., T.E.A.A., A.S.T. and S.S.M.G.; Methodology, B.L., A.N.E.I.A. and H.B.; Project administration, B.L. and S.S.M.G.; Resources, A.N.E.I.A., H.A., T.E.A.A., S.S.M.G. and S.A.M.A.; Software, B.L., A.N.E.I.A., H.B. and A.S.T.; Supervision, B.L. and S.S.M.G.; Validation, B.L., A.N.E.I.A. and A.S.T.; Visualization, H.A., T.E.A.A., S.S.M.G. and S.A.M.A.; Writing—original draft, B.L., A.N.E.I.A., H.B. and A.S.T.; Writing—review and editing, H.A., T.E.A.A., S.S.M.G. and S.A.M.A. All authors have read and agreed to the published version of the manuscript.

**Funding:** This work was supported by Taif University Researchers Supporting Project number (TURSP-2020/34), Taif University, Taif, Saudi Arabia.

**Institutional Review Board Statement:** Not applicable.

**Informed Consent Statement:** Not applicable.

**Data Availability Statement:** Not applicable.

**Acknowledgments:** The authors appreciate Taif University Researchers Supporting Project number (TURSP-2020/34), Taif University, Taif, Saudi Arabia, and the General Directorate of Scientific Research and Technological Development (DGRSDT) of Algeria.

**Conflicts of Interest:** The authors declare no conflict of interest.

## Abbreviations

CEED	Combined economic environmental dispatch
DED	Dynamic economic dispatch
DEnD	Dynamic environmental dispatch
DEED	Dynamic economic emission dispatch
DCEELDP	Dynamic combined economic emission load dispatch problem
EED	Economic emission dispatch
FC	Fuel cost
$a_i, b_i, c_i$	Coefficients of the fuel cost corresponding of generator $i$
$e_i$ , and $f_i$	Fuel cost coefficients of $i^{th}$ generator due to VPE
$\alpha_i, \beta_i, \gamma_i, \eta_i$ , and $\delta_i$	Emission curve coefficients
$P_{L,t}$	Power losses
$w_i$	Weighting factor

## References

1. Larouci, B.; Benasla, L.; Belmadani, A.; Rahli, M. Cuckoo Search Algorithm for Solving Economic Power Dispatch Problem with Consideration of Facts Devices. *UPB Sci. Bull. Ser. C* **2017**, *79*, 43–54.
2. Ryu, H.-S.; Kim, M.-K. Combined Economic Emission Dispatch with Environment-Based Demand Response Using WU-ABC Algorithm. *Energies* **2020**, *13*, 6450. [CrossRef]
3. Razali, N.S.; Mansor, M.H.; Musirin, I.; Othman, M.M.; Akoury, M. Embedded Immune-Evolutionary Programming for Economic Dispatch of Generators with Prohibited Operating Zones. *Int. J. Eng. Technol.* **2018**, *7*, 183–186. [CrossRef]
4. Vahidi, M.; Vahdani, S.; Rahimian, A.; Jamshidi, M.-N.; Kanee, A.-T. Evolutionary-base finite element model updating and damage detection using modal testing results. *Struct. Eng. Mech.* **2019**, *70*, 339–350.
5. Al-Betar, M.A.; Awadallah, M.A.; Abu Doush, I.; Alsukhni, E.; Alkhraisat, H. A Non-convex Economic Dispatch Problem with Valve Loading Effect Using a New Modified  $\beta$ -Hill Climbing Local Search Algorithm. *Arab. J. Sci. Eng.* **2018**, *43*, 7439–7456. [CrossRef]
6. Gao, Y.; Li, X.; Dong, M.; Li, H.-P. An enhanced artificial bee colony optimizer and its application to multi-level threshold image segmentation. *J. Cent. South Univ.* **2018**, *25*, 107–120. [CrossRef]
7. Mirjalili, S.; Mirjalili, S.-M.; Hatamlou, A. Multi-verse optimizer: A nature-inspired algorithm for global optimization. *Neural Comput. Appl.* **2016**, *27*, 495–513. [CrossRef]
8. Wang, F.; Zhang, H.; Zhou, A. A particle swarm optimization algorithm for mixed-variable optimization problems. *Swarm Evol. Comput.* **2021**, *60*, 100808. [CrossRef]
9. Nadimi-Shahraki, M.H.; Taghian, S.; Mirjalili, S. An improved grey wolf optimizer for solving engineering problems. *Expert Syst. Appl.* **2021**, *166*, 113917. [CrossRef]
10. Albashish, D.; Hammouri, A.I.; Braik, M.; Atwan, J.; Sahran, S. Binary biogeography-based optimization based SVM-RFE for feature selection. *Appl. Soft Comput.* **2021**, *101*, 107026. [CrossRef]
11. Li, L.-L.; Shen, Q.; Tseng, M.-L.; Luo, S. Power system hybrid dynamic economic emission dispatch with wind energy based on improved sailfish algorithm. *J. Clean. Prod.* **2021**, *316*, 128318. [CrossRef]
12. Liu, Z.-F.; Li, L.-L.; Liu, Y.-W.; Liu, J.-Q.; Li, H.-Y.; Shen, Q. Dynamic economic emission dispatch considering renewable energy generation: A novel multi-objective optimization approach. *Energy* **2021**, *235*, 121407. [CrossRef]
13. Li, L.-L.; Liu, Z.-F.; Tseng, M.-L.; Zheng, S.-J.; Lim, M.K. Improved tunicate swarm algorithm: Solving the dynamic economic emission dispatch problems. *Appl. Soft Comput.* **2021**, *108*, 107504. [CrossRef]
14. Qiao, B.; Liu, J.; Hao, X. A multi-objective differential evolution algorithm and a constraint handling mechanism based on variables proportion for dynamic economic emission dispatch problems. *Appl. Soft Comput.* **2021**, *108*, 107419. [CrossRef]
15. Zou, Y.; Zhao, J.; Ding, D.; Miao, F.; Sobhani, B.F. Solving dynamic economic and emission dispatch in power system integrated electric vehicle and wind turbine using multi-objective virus colony search algorithm. *Sustain. Cities Soc.* **2021**, *67*, 102722. [CrossRef]
16. Yao, L.; Li, J.; Liang, H. Dynamic Economic/Emission Dispatch Considering Renewable Energy and PEVs. In Proceedings of the 2021 40th Chinese Control Conference (CCC), Shanghai, China, 26–28 July 2021. [CrossRef]
17. Yang, W.; Peng, Z.; Yang, Z.; Guo, Y.; Chen, X. An enhanced exploratory whale optimization algorithm for dynamic economic dispatch. *Energy Rep.* **2021**, *7*, 7015–7029. [CrossRef]
18. Gul, R.N.; Ahmad, A.; Fayyaz, S.; Sattar, M.K.; Haq, S.S.U. Hybrid Flower Pollination Algorithm with Sequential Quadratic Programming Technique for Solving Dynamic Combined Economic Emission Dispatch Problem. *Mehran Univ. Res. J. Eng. Technol.* **2021**, *40*, 371–382. [CrossRef]
19. Xia, A.; Wu, X.; Bai, Y. A new multi-objective hybrid optimization algorithm for wind-thermal dynamic economic emission power dispatch. *Int. Trans. Electr. Energy Syst.* **2021**, *31*, e12966. [CrossRef]
20. Alshammari, M.; Ramli, M.; Mehedi, I. A New Chaotic Artificial Bee Colony for the Risk-Constrained Economic Emission Dispatch Problem Incorporating Wind Power. *Energies* **2021**, *14*, 4014. [CrossRef]
21. Hassan, M.H.; Kamel, S.; Abualigah, L.; Eid, A. Development and application of slime mould algorithm for optimal economic emission dispatch. *Expert Syst. Appl.* **2021**, *182*, 115205. [CrossRef]
22. Ajayi, O.; Heymann, R. Day-ahead combined economic and emission dispatch with spinning reserve consideration using moth swarm algorithm for a data centre load. *Heliyon* **2021**, *7*, e08054. [CrossRef] [PubMed]
23. Fayyaz, S.; Sattar, M.K.; Waseem, M.; Ashraf, M.U.; Ahmad, A.; Hussain, H.A.; Alsubhi, K. Solution of Combined Economic Emission Dispatch Problem Using Improved and Chaotic Population-Based Polar Bear Optimization Algorithm. *IEEE Access* **2021**, *9*, 56152–56167. [CrossRef]
24. Larouci, B.; Si Tayeb, A.; Boudjella, H.; Ayad, A.N.E.I. Cuckoo search algorithm to solve the problem of economic emission dispatch with the incorporation of facts devices under the valve-point loading effect. *Facta Univ. Ser. Electron. Energ.* **2021**, *34*, 569–588. [CrossRef]
25. Si Tayeb, A.; Larouci, B.; Rezzak, D.; Houam, Y.; Bouzeoudja, H.; Bouchakour, A. Application of a new hybridization to solve economic dispatch problem on an algerian power system without or with connection to a renewable energy. *Diagnostyka* **2021**, *22*, 101–112. [CrossRef]

26. Kuk, J.N.; Gonçalves, R.A.; Pavelski, L.M.; Venske, S.M.G.S.; de Almeida, C.P.; Pozo, A.T.R. An empirical analysis of constraint handling on evolutionary multi-objective algorithms for the Environmental/Economic Load Dispatch problem. *Expert Syst. Appl.* **2021**, *165*, 113774. [CrossRef]
27. Prasad, R.S.; Sud, R. The pivotal role of UNFCCC in the international climate policy landscape: A developing country perspective. *Glob. Aff.* **2021**, *7*, 67–78. [CrossRef]
28. Van Hong, T.P.; Ngoc, D.V.; Tuan, K.D. Environmental Economic Dispatch Using Stochastic Fractal Search Algorithm. In Proceedings of the 2021 International Symposium on Electrical and Electronics Engineering (ISEE), Ho Chi Minh, Vietnam, 15–16 April 2021; pp. 214–219.
29. Chakrabarti, S.; Panja, A.K.; Mukherjee, A.; Bar, A.K. Application of Multi-Objective Particle Swarm Optimization Technique for Analytical Solution of Economic and Environmental Dispatch. In *Intelligent Electrical Systems: A Step towards Smarter Earth*; CRC Press: Boca Raton, FL, USA, 2021; pp. 313–319.
30. Boudjella, H.; Laouer, M.; Bouzeboudja, H.; Ayad, A.N.E.I.; Benhamida, F.; Saad, A. Solution of Economic Load Dispatch Problems Using Novel Improved Harmony Search Algorithm. *Int. J. Electr. Eng. Inform.* **2021**, *13*, 218–241. [CrossRef]
31. Wood, A.J.; Wollenberg, B.F.; Sheblé, G.B. *Power Generation, Operation, and Control*; John Wiley & Sons: Hoboken, NJ, USA, 2013.
32. Rezaee Jordehi, A. Dynamic environmental-economic load dispatch in grid-connected microgrids with demand response programs considering the uncertainties of demand, renewable generation and market price. *Int. J. Numer. Model. Electron. Netw. Devices Fields* **2021**, *34*, e2798. [CrossRef]
33. Dhiman, G.; Kumar, V. Seagull optimization algorithm: Theory and its applications for large-scale industrial engineering problems. *Knowl. Based Syst.* **2019**, *165*, 169–196. [CrossRef]
34. Kumar, V.; Kumar, D.; Kaur, M.; Singh, D.; Idris, S.A.; Alshazly, H. A Novel Binary Seagull Optimizer and its Application to Feature Selection Problem. *IEEE Access* **2021**, *9*, 103481–103496. [CrossRef]
35. Sharifi, M.R.; Akbarifard, S.; Qaderi, K.; Madadi, M.R. Comparative analysis of some evolutionary-based models in optimization of dam reservoirs operation. *Sci. Rep.* **2021**, *11*, 15611. [CrossRef] [PubMed]
36. Jia, H.; Xing, Z.; Song, W. A New Hybrid Seagull Optimization Algorithm for Feature Selection. *IEEE Access* **2019**, *7*, 49614–49631. [CrossRef]
37. Askarzadeh, A. A novel metaheuristic method for solving constrained engineering optimization problems: Crow search algorithm. *Comput. Struct.* **2016**, *169*, 1–12. [CrossRef]
38. Han, X.; Xu, Q.; Yue, L.; Dong, Y.; Xie, G.; Xu, X. An Improved Crow Search Algorithm Based on Spiral Search Mechanism for Solving Numerical and Engineering Optimization Problems. *IEEE Access* **2020**, *8*, 92363–92382. [CrossRef]
39. Meraihi, Y.; Gabis, A.B.; Ramdane-Cherif, A.; Acheli, D. A comprehensive survey of Crow Search Algorithm and its applications. *Artif. Intell. Rev.* **2021**, *54*, 2669–2716. [CrossRef]
40. Kaur, S.; Awasthi, L.K.; Sangal, A.; Dhiman, G. Tunicate Swarm Algorithm: A new bio-inspired based metaheuristic paradigm for global optimization. *Eng. Appl. Artif. Intell.* **2020**, *90*, 103541. [CrossRef]
41. Fetouh, T.; Elsayed, A.M. Optimal Control and Operation of Fully Automated Distribution Networks Using Improved Tunicate Swarm Intelligent Algorithm. *IEEE Access* **2020**, *8*, 129689–129708. [CrossRef]
42. Sharma, A.; Sharma, A.; Dasgotra, A.; Jatelly, V.; Ram, M.; Rajput, S.; Azzopardi, B.; Averbukh, M. Opposition-Based Tunicate Swarm Algorithm for Parameter Optimization of Solar Cells. *IEEE Access* **2021**, *9*, 125590–125602. [CrossRef]
43. Yang, X.S. Firefly algorithms for multimodal optimization. In Proceedings of the 5th International Symposium on Stochastic Algorithms, Sapporo, Japan, 26–28 October 2009; pp. 169–178.
44. Strumberger, I.; Bacanin, N.; Tuba, M. Enhanced firefly algorithm for constrained numerical optimization. In Proceedings of the 2017 IEEE Congress on Evolutionary Computation (CEC), Donostia, Spain, 5–8 June 2017; pp. 2120–2127. [CrossRef]
45. Chahnasir, E.S.; Zandi, Y.; Shariati, M.; Dehghani, E.; Toghrli, A.; Mohamad, E.T.; Shariati, A.; Safa, M.; Wakil, K.; Khorami, M. Application of support vector machine with firefly algorithm for investigation of the factors affecting the shear strength of angle shear connectors. *Smart Struct. Syst.* **2018**, *22*, 413–424.
46. Wang, C.-F.; Song, W.-X. A novel firefly algorithm based on gender difference and its convergence. *Appl. Soft Comput.* **2019**, *80*, 107–124. [CrossRef]
47. Basu, M. Particle Swarm Optimization Based Goal-Attainment Method for Dynamic Economic Emission Dispatch. *Electr. Power Components Syst.* **2006**, *34*, 1015–1025. [CrossRef]
48. Hardiansyah, H. Hybrid PSO-GSA technique for solving dynamic economic emission dispatch problem. *Eng. Rev.* **2020**, *40*, 96–104. [CrossRef]
49. Li, Z.; Zou, D.; Kong, Z. A harmony search variant and a useful constraint handling method for the dynamic economic emission dispatch problems considering transmission loss. *Eng. Appl. Artif. Intell.* **2019**, *84*, 18–40. [CrossRef]
50. Shehata, A.M.; Elaiw, A.M. Hybrid DE-SOP for solving dynamic economic emission dispatch with prohibited operating. *Int. J. Sci. Eng. Res.* **2015**, *6*, 1136–1141.
51. Zhang, H.; Yue, D.; Xie, X.; Hu, S.; Weng, S. Multi-elite guide hybrid differential evolution with simulated annealing technique for dynamic economic emission dispatch. *Appl. Soft Comput.* **2015**, *34*, 312–323. [CrossRef]
52. Mehdi, M.F.; Ahmad, A.; Haq, S.S.U.; Saqib, M.; Ullah, M.F. Dynamic economic emission dispatch using whale optimization algorithm for multi-objective function. *Electr. Eng. Electromech.* **2021**, *2*, 64–69. [CrossRef]



53. Mason, K.; Duggan, J.; Howley, E. A multi-objective neural network trained with differential evolution for dynamic economic emission dispatch. *Int. J. Electr. Power Energy Syst.* **2018**, *100*, 201–221. [CrossRef]
54. Basu, M. Dynamic Economic Emission Dispatch Using Evolutionary Programming and Fuzzy Satisfying Method. *Int. J. Emerg. Electr. Power Syst.* **2007**, *8*. [CrossRef]
55. Alsumait, J.S.; Qasem, M.; Sykulski, J.; Al-Othman, A.K. An improved Pattern Search based algorithm to solve the Dynamic Economic Dispatch problem with valve-point effect. *Energy Convers. Manag.* **2010**, *51*, 2062–2067. [CrossRef]
56. Kothari, D.P.; Dhillon, J.S. *Power System Optimization*, 2nd ed.; PHI Learning Private Ltd.: New Delhi, India, 2011.
57. Pattanaik, J.K.; Basu, M.; Dash, D.P. Dynamic economic dispatch: A comparative study for differential evolution, particle swarm optimization, evolutionary programming, genetic algorithm, and simulated annealing. *J. Electr. Syst. Inf. Technol.* **2019**, *6*, 1–8. [CrossRef]
58. Basu, M. Dynamic economic emission dispatch using nondominated sorting genetic algorithm-II. *Int. J. Electr. Power Energy Syst.* **2008**, *30*, 140–149. [CrossRef]
59. Pandit, N.; Tripathi, A.; Tapaswi, S.; Pandit, M. An improved bacterial foraging algorithm for combined static/dynamic environmental economic dispatch. *Appl. Soft Comput.* **2012**, *12*, 3500–3513. [CrossRef]
60. Marouani, I.; Boudjemline, A.; Guesmi, T.; Abdallah, H.H. A Modified Artificial Bee Colony for the Non-Smooth Dynamic Economic/Environmental Dispatch. *Eng. Technol. Appl. Sci. Res.* **2018**, *8*, 3321–3328. [CrossRef]
61. Alshammari, B.M. Teaching-Learning-Based Optimization Algorithm for the Combined Dynamic Economic Environmental Dispatch Problem. *Eng. Technol. Appl. Sci. Res.* **2020**, *10*, 6432–6437. [CrossRef]
62. Roy, P.K.; Bhui, S. A multi-objective hybrid evolutionary algorithm for dynamic economic emission load dispatch. *Int. Trans. Electr. Energy Syst.* **2016**, *26*, 49–78. [CrossRef]
63. Alshammari, M.E.; Ramli, M.A.; Mehedi, I.M. An Elitist Multi-Objective Particle Swarm Optimization Algorithm for Sustainable Dynamic Economic Emission Dispatch Integrating Wind Farms. *Sustainability* **2020**, *12*, 7253. [CrossRef]
64. Qian, S.; Wu, H.; Xu, G. An improved particle swarm optimization with clone selection principle for dynamic economic emission dispatch. *Soft Comput.* **2020**, *24*, 15249–15271. [CrossRef]

## Article

# Investigating the Impact of Wind Power Integration on Damping Characteristics of Low Frequency Oscillations in Power Systems

Jian Chen <sup>1,\*</sup>, Tao Jin <sup>2</sup>, Mohamed A. Mohamed <sup>3,\*</sup>, Andres Annuk <sup>4</sup> and Udaya Dampage <sup>5</sup>

<sup>1</sup> Robotics School of Fuzhou Polytechnic, Fuzhou 350108, China

<sup>2</sup> Department of Electrical Engineering, Fuzhou University, Fuzhou 350116, China; jintly@fzu.edu.cn

<sup>3</sup> Electrical Engineering Department, Faculty of Engineering, Minia University, Minia 61519, Egypt

<sup>4</sup> Institute of Forestry and Engineering, Estonian University of Life Sciences, 51006 Tartu, Estonia; andres.annuk@emu.ee

<sup>5</sup> Faculty of Engineering, Kotelawla Defence University, Kandawala Estate, Ratmalana 10390, Sri Lanka; dampage@kdu.ac.lk

\* Correspondence: chenjian@fvti.edu.cn (J.C.); dr.mohamed.abdelaziz@mu.edu.eg (M.A.M.)

**Abstract:** This paper investigates the impact of doubly-fed induction generator (DFIG) wind farms on system stability in multi-generator power systems with low-frequency oscillations (LFOs). To this end, this paper establishes the interconnection model of the equivalent generators and derives the system state equation. On this basis, an updated system state equation of the new power system with integrated wind power is further derived. Then, according to the updated system state equation, the impact factors that cause changes in the system damping characteristics are presented. The IEEE two-area four-machine power system is used as a simulation model in which the LFOs occur. The simulation results demonstrate that the connection of wind power to the power feeding area (PFA) increases the damping ratio of the dominant mode of inter-area oscillation from  $-0.0263$  to  $-0.0107$ , which obviously improves the system stability. Furthermore, the wind power integration into PFA, as the connection distance of the wind power increases, gradually decreases the damping ratio of the dominant mode of the inter-area oscillation to  $-0.0236$ , approaching that of no wind power in the system. Meanwhile, with the increase in the wind power output capacity, the damping ratio of the dominant mode of the intra-area and inter-area oscillation increases, and the maximum damping ratios reach  $0.1337$  and  $0.0233$ , respectively.

**Keywords:** wind power integration; low-frequency oscillations (LFOs); doubly-fed induction generators (DFIGs); power system stability; damping characteristics

**Citation:** Chen, J.; Jin, T.; Mohamed, M.A.; Annuk, A.; Dampage, U. Investigating the Impact of Wind Power Integration on Damping Characteristics of Low Frequency Oscillations in Power Systems. *Sustainability* **2022**, *14*, 3841. <https://doi.org/10.3390/su14073841>

Academic Editor: Marc A. Rosen

Received: 14 February 2022

Accepted: 20 March 2022

Published: 24 March 2022



**Copyright:** © 2022 by the authors. Licensee MDPI, Basel, Switzerland. This article is an open access article distributed under the terms and conditions of the Creative Commons Attribution (CC BY) license (<https://creativecommons.org/licenses/by/4.0/>).

## 1. Introduction

The expansion of the integration of clean and efficient renewable energy sources such as wind and solar energy has exacerbated the gradual expansion of the modern power grid interconnection and caused an unprecedented complexity of the energy system [1–3]. Hence, the security and stability of the power system should be taken seriously [4]. A typical hazard in a power system is the interaction among generators or regional power grids, which results in the damping characteristic changes of the power systems and thus may produce low-frequency oscillations (LFOs) [5]. The synchronous generator angles start oscillating with each other in low frequencies of  $0.1$ – $2.5$  Hz following grid disturbances. These oscillations are usually poorly damped and can lead to system collapse [6]. A famous example of a grid failure is the blackout that occurred at Western Systems Council Coordinated (WSCC) in August 1996 [7]. A series of system failures occurred in eastern North America, which eventually led to system instability and resulted in the blackout disaster on August 14, 2003 [8]. There was a major grid disturbance in the northern region at 02:33 on 30 July 2012. The northern regional grid load was about  $36,000$  MW at the time of the disturbance. Subsequently, there was another grid disturbance at 13:00 on 31 July

2012, resulting in the collapse of the northern, eastern, and north-eastern regional grids. A total load of about 48,000 MW was affected in this blackout [9]. The power oscillations at different stages and degrees were observed during these big blackouts. LFO seriously affects the power transmission capacity and threatens the stable operation of the power grid and even causes power failure accidents due to grid instability [10].

Due to the increase in power demand and to reduce global warming, the power grid is moving more and more to renewable energy integration, in which wind power is the most important renewable source of energy all over the world. The impact of integrated wind power on the power system stability is also a long-term problem which in turn arouses the interest of many researchers around the world [11]. The authors in [12] proposed the stability problems of the power systems early, including large-scale wind power in which the impact of intra-area and inter-area oscillations is studied under the condition of wind power integrated into the power systems. It is found that the damping effect of the constant speed wind turbine (WT) on the power systems is more effective than that of the variable speed WT because of the effects of the induction generator. In [13], the authors have analyzed the power system oscillation modes of the two-area four-machine system with small disturbance and studied the changes of the oscillation modes under the situation of a wind farm replacing a synchronous generator in the system. Aiming at the integration of the wind power into Norwegian power grids, E. Hagstrøm et al. [14] studied the impact of the integrated wind power on the interval oscillation damping of northern European power grids and tested the impact of different types of generators on the inter-area oscillation damping of Norway and Sweden. In [15], the generic dynamic model of WT with a doubly-fed induction generator (DFIG) is presented, and the small-signal stability mathematical model is derived. G. Tsourakis et al. [16] studied the response modes of DFIG in wind power plants and their impact on the electromechanical oscillation of interconnected power systems. L. Yang et al. [17] carried out a mathematical model for DFIG. Through eigenvalue sensitivity analysis, the most sensitive parameters of the Hopf bifurcation of DFIG power generation system can be determined. Thus, the Hopf bifurcation boundaries of the key parameters are analyzed to facilitate the parameterization of DFIG WT system and ensure system stability. H. Li et al. [18] proposed a fuzzy control strategy to suppress the LFOs of the power system after the doubly-fed induction generators (DFIGs) are integrated into the power grid. M. Singh et al. [19] studied the potential damping interval oscillation mode of the wind farm. The result shows that the intra-area oscillation mode is a phenomenon of oscillation in a single or a group of generators with another set of generators on a weak transmission link. R. Effatnejad et al. [20] studied the LFO suppression strategy of power systems in the case of the integrated wind power. The angular velocity difference signal of the two generators is used as the input signal of the damping controller. The conventional damping controller is replaced by the fuzzy controller, and the controller parameters are optimized by the intelligent optimization algorithm. In [21], a method was proposed for the separate examination of the two impact factors, the change of load flow and dynamic interaction brought about by the DFIG on the electromechanical oscillation modes of the power systems. J. G. Slootweg and W. L. Kling [22] established a 7-order WT mathematical model for doubly-fed wind turbines and revealed the impact of shafting and the wind speed on the system's forced LFOs in the condition of the wind power integrated into the power systems through the small-signal linear analysis method. In order to solve the dynamic stability problem of the large wind farms, X. Zhang et al. [23] proposed a power grid operation method based on variable inertia control. A variable inertia control strategy for WT was proposed to improve the damping and frequency stability of power oscillation between the areas. In [24], a line modal potential energy (LMPE) method was proposed for the inter-area oscillation analysis and damping control of DFIGs. The study attempts to design the damping control loop using the LMPE approach from the network viewpoint. L. Simon et al. [25] described an optimization enabled wide-area damping control (WADC) for DFIG to mitigate both the intra-area and the inter-area oscillations. The main purpose in [26] was to improve the synchrony generator's transient and dynamic performance

using local DFIGs. The impact of wind power integrated into the existing power system is multi-dimensional. There are still many uncertain results that cannot be ignored in the coordinated development of wind power and the large power grid to maintain system stability in the future power grid. Based on the above investigation and explanations, the main contributions of this research are summarized as follows:

- The two-area interconnection system and its mathematical model are established and analyzed, and the system state equation is deduced before and after the wind power integration.
- Three impact factors of the integrated wind power on the LFOs of the power system are proposed and the eigenvalues of the intra-area and inter-area oscillation of the power system are identified by the total least squares-estimation of signal parameters via rotational invariance techniques (TLS-ESPRIT) algorithm.
- By comparing the changes of the damping characteristics of the system before and after wind power integration, the impact on the LFOs of the system is obtained, which provides a reference for the design of the wind power plants, as well as the stability of the power system with small disturbance.

The remaining sections of this paper are organized as follows: Section 2 establishes the model of the two-area interconnection power system and derives the system state equation. The damping characteristics of the system integrated with the wind power consisting of the DFIGs are analyzed. The impact factors of wind power connection on the LFOs are mainly related to the area option of the integrated wind power, including a power feeding area (PFA) or a power receiving area (PRA), the connection distance, and the output capacity of the integrated wind power. Section 3 shows the example simulation and result analysis based on the simulation of the IEEE two-area four-machine power system. Firstly, the eigenvalues of the intra-area and inter-area oscillation modes of the system are calculated. Secondly, considering the variation of each impact factor, the changes in the damping characteristics of the simulation model are reflected by the eigenvalues of the modes of the intra-area and inter-area oscillation. Finally, through the quantitative analysis of the modal eigenvalues and the changes of the damping ratios, the effect of the different impact factors of the integrated wind power on the LFOs of the power system is obtained and discussed. Section 4 addresses the conclusion of the paper.

## 2. Analysis of Damping Characteristics

The LFOs of large-scale power systems usually include intra-area and inter-area oscillation. The intra-area oscillation is mainly the relative sway between different generators in the area. The inter-area oscillation is the relative swing between multiple generator groups in one area and multiple generator groups in other areas. According to the equivalent principle of the center of inertia (COI) [27], multiple generator groups in the area are taken to be COI equivalent, which can simplify the damping analysis of the system. Hence, the interconnection between two groups of generators can be studied by using a simplified system consisting of two equivalent generators.

### 2.1. Analysis of Damping Characteristics of the Two-Area Interconnection Power Systems

The equivalent model of the two-area interconnection system is shown in Figure 1. The inter-area oscillation is equivalent to the oscillation between the synchronous generators  $G_{eq1}$  and  $G_{eq2}$ . Taking the active power transmitted from area A1 to area A2 as an example, it can be said that area A1 is PFA, while area A2 is PRA. Then, the equivalent rotor angular velocity increment of  $G_{eq1}$  and  $G_{eq2}$  will show the same frequency reverse characteristic, as well as the equivalent power angle increment.

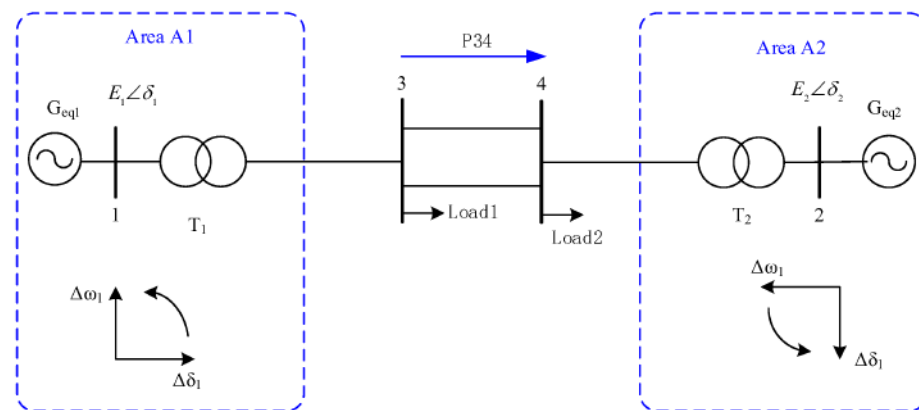


**Figure 1.** Equivalent model of the two-area interconnection system.

The classical second-order equations are adopted as the rotor motion mathematical model of  $G_{eq1}$  and  $G_{eq2}$ . The mechanical power of the prime movers is constant, and the excitation system dynamics are ignored while the load is treated as constant impedance. The rotor motion equation of the COI equivalent synchronous generator is represented as follows:

$$\begin{cases} \Delta\dot{\delta}_j = \Delta\omega_j \\ \Delta\dot{\omega}_j = \frac{1}{T_{j1}}(-\Delta P_{je} - D_j\Delta\omega_j) \end{cases} \quad (1)$$

Using the Heffron–Phillips model, rewriting (1) in the matrix form, it is represented as follows:

$$\begin{bmatrix} \Delta\dot{\delta}_1 \\ \Delta\dot{\delta}_2 \\ \Delta\dot{\omega}_1 \\ \Delta\dot{\omega}_2 \end{bmatrix} = \begin{bmatrix} 0 & 0 & 1 & 0 \\ 0 & 0 & 0 & 1 \\ -\frac{K_{11}}{T_{j1}} & -\frac{K_{12}}{T_{j1}} & -\frac{D_1}{T_{j1}} & 0 \\ -\frac{K_{21}}{T_{j2}} & -\frac{K_{22}}{T_{j2}} & 0 & -\frac{D_2}{T_{j2}} \end{bmatrix} \begin{bmatrix} \Delta\delta_1 \\ \Delta\delta_2 \\ \Delta\omega_1 \\ \Delta\omega_2 \end{bmatrix} = A_{eq} \begin{bmatrix} \Delta\delta_1 \\ \Delta\delta_2 \\ \Delta\omega_1 \\ \Delta\omega_2 \end{bmatrix} \quad (2)$$

According to the system's circuit analysis, based on the superposition theorem of the model shown in Figure 1, the output electromagnetic power  $P_{1e}$  and  $P_{2e}$  are calculated as represented in (3).

$$\begin{cases} P_{1e} = \frac{E_1^2}{|Z_{11}|} \sin \alpha_{11} + \frac{E_1 E_2}{|Z_{12}|} \sin(\delta_{12} - \alpha_{12}) \\ P_{2e} = \frac{E_2^2}{|Z_{22}|} \sin \alpha_{22} + \frac{E_1 E_2}{|Z_{21}|} \sin(\delta_{21} - \alpha_{12}) \end{cases} \quad (3)$$

where

$$Z_{12} = Z_{21}, Z_{11} = |Z_{11}| \angle \varphi_{11}, Z_{22} = |Z_{22}| \angle \varphi_{22}, Z_{12} = |Z_{12}| \angle \varphi_{12}, \alpha_{11} = 90^\circ - \varphi_{11}, \alpha_{22} = 90^\circ - \varphi_{22}, \alpha_{12} = 90^\circ - \varphi_{12}.$$

At a certain operating point, the rotor angle difference of  $G_{eq1}$  and  $G_{eq2}$  has the relation  $\delta_{120} = -\delta_{210}$ . According to (3), the synchronous torque coefficients  $K_{jk}$  can be calculated as follows:

$$\begin{cases} K_{11} = -K_{12} = \frac{E_1 E_2}{|Z_{12}|} \cos(\delta_{120} - \alpha_{12}) \\ K_{22} = -K_{21} = \frac{E_1 E_2}{|Z_{21}|} \cos(\delta_{210} - \alpha_{12}) \end{cases} \quad (4)$$

The state matrix  $A_{eq}$  can be extracted from (2), and its characteristic equation is represented by:

$$\det(A_{eq} - \lambda I) = 0 \quad (5)$$

Through matrix transformation and the Schur theorem, Equation (5) can be transformed into a fourth-degree equation with one variable with respect to  $\lambda$ , as represented in (6).

$$\lambda^4 + \left(\frac{D_1}{T_{j1}} + \frac{D_2}{T_{j2}}\right)\lambda^3 + \left(\frac{K_{11}}{T_{j1}} + \frac{K_{22}}{T_{j2}} + \frac{D_1 D_2}{T_{j1} T_{j2}}\right)\lambda^2 + \frac{1}{T_{j1} T_{j2}}(D_1 K_{22} + D_2 K_{11})\lambda = 0 \quad (6)$$

Idealizing the damping moment coefficient and the same inertia time constant of the equivalent generator results in  $D_1 = D_2$ ,  $T_{j1} = T_{j2}$ , or  $\frac{D_1}{T_{j1}} = \frac{D_2}{T_{j2}}$ . Therefore, (6) can be simplified as follows:

$$\lambda(\lambda + \gamma)\left(\lambda^2 + \gamma\lambda + \frac{K_{11}}{T_{j1}} + \frac{K_{22}}{T_{j2}}\right) = 0 \quad (7)$$

The eigenvalues are obtained by solving the equation as follows:

$$\begin{cases} \lambda_1 = 0 \\ \lambda_2 = -\gamma = -\frac{D_1}{T_{j1}} \\ \lambda_{3,4} = \sigma \pm j\omega = -\frac{D_1}{2T_{j1}} \pm j\sqrt{\left(-\frac{D_1}{T_{j1}}\right)^2 + 4\left(\frac{K_{11}}{T_{j1}} + \frac{K_{22}}{T_{j2}}\right)} \end{cases} \quad (8)$$

In general,  $K_{11}$ ,  $K_{22}$ ,  $D_1$ ,  $D_2$  are greater than zero in normal operation. According to the Routh system stability criterion, Equation (8) shows that the real parts of the three non-zero eigenvalues are all negative, and the conjugate eigenvalues  $\lambda_3$  and  $\lambda_4$  represent the electromechanical oscillation modes of the interconnected system. If the system is abnormal, such as  $D_1 \leq 0$  or  $D_2 \leq 0$ , that is  $-D_1/T_{j1} \geq 0$  or  $-D_2/T_{j2} \geq 0$ , the real part of eigenvalue will be located on the imaginary axis or the right half-space of the complex plane. The corresponding consequences are that the system damping is zero or negative, which results in continuous or growth oscillation of the power systems. If it is not intervened in, the power systems under the conditions of instability will be out-of-step, splitting finally.

## 2.2. Analysis of Damping Characteristics of the Two-Area Interconnection Power Systems Integrated with Wind Power

The wind farm marked by ellipse dotted lines in Figure 2 is incorporated into the two-area interconnection system. The wind farm can be represented by a single machine of a large-capacity DFIG [25]. The schematic diagram of a DFIG integrating the power grid is shown in Figure 3.

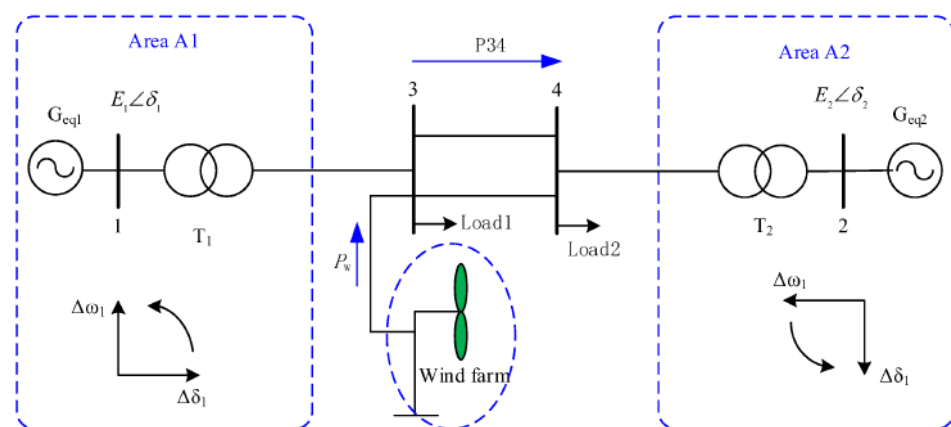
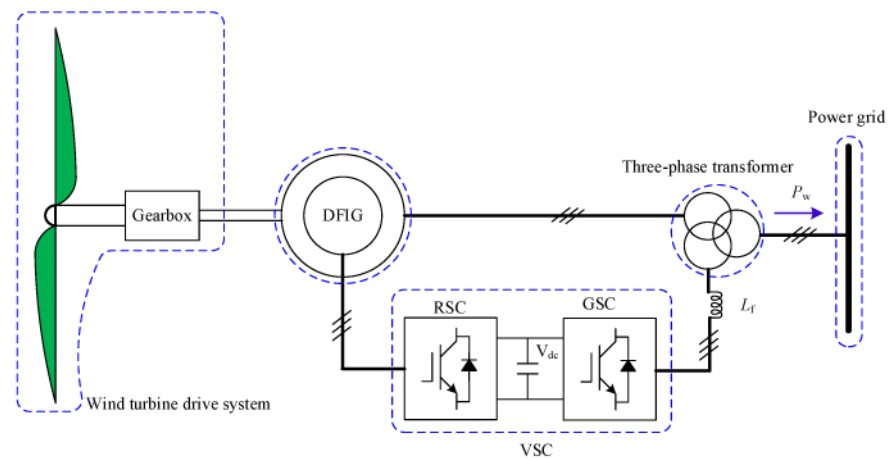


Figure 2. Two-area interconnection system integrated with wind farm.



**Figure 3.** Schematic diagram of DFIG integrated into power grid.

Neglecting the system line loss, the electromagnetic power increments  $\Delta P_{1e}$  and  $\Delta P_{2e}$  of  $G_{eq1}$  and  $G_{eq2}$  mentioned in (1) are rewritten as (9).

$$\begin{cases} \Delta P_{1e} = \frac{E_1 U_w}{X_{13}} \cos(\delta_{10} + \delta_{w0}) (\Delta \delta_1 + \Delta \delta_w) \\ \Delta P_{2e} = \frac{E_2 U_w}{X_{23}} \cos(\delta_{20} + \delta_{w0}) (\Delta \delta_2 + \Delta \delta_w) \end{cases} \quad (9)$$

Labeling  $k_1 = \frac{E_1 U_w}{X_{13}} \cos(\delta_{10} + \delta_{w0})$ ,  $k_2 = \frac{E_2 U_w}{X_{23}} \cos(\delta_{20} + \delta_{w0})$ , Equation (9) can be simplified as follows:

$$\begin{cases} \Delta P_{1e} = k_1 (\Delta \delta_1 + \Delta \delta_w) \\ \Delta P_{2e} = k_2 (\Delta \delta_2 + \Delta \delta_w) \end{cases} \quad (10)$$

As the system structure is stable and the load remains unchanged, the active power of the PFA and PRA is increased or decreased by the same amount. Hence, the active power increment of the interconnected two-area systems in Figure 2 remains in the balance after the integration of the wind farm to the grid, and the mathematical relationship is represented as follows:

$$\Delta P_{1e} + \Delta P_w = \Delta P_{2e} \quad (11)$$

$\Delta P_w$  is not a state variable. When LFOs occur in the system, the changing trend of the power increment at any node is consistent with that of the frequency increment at the same point of the system. The power and frequency for any point have the same oscillation mode. Therefore, it can be considered that their increments have a proportional relationship, which can be simplified as follows:

$$\Delta P_w = g_1 \cdot \Delta f_B \quad (12)$$

Similarly, there is a linear relationship between the frequency increment of the system and the rotor angular velocity of the system generator. In the case that the regional structure is not completely symmetrical, the proportional relation can be represented as follows:

$$\Delta f_B = g_2 \cdot \Delta \omega_1 = g_3 \cdot \Delta \omega_2 \quad (13)$$

The linear relationships between (12) and (13) with regard to the state variables  $\Delta \omega_1$  and  $\Delta \omega_2$  are represented in (14).

$$\begin{cases} \Delta P_w = k_3 \Delta \omega_1 = k_4 \Delta \omega_2 \\ k_3 = g_1 g_2 \\ k_4 = g_1 g_3 \end{cases} \quad (14)$$

Uniting (10)–(14), the state variables can represent  $\Delta P_{1e}$  and  $\Delta P_{2e}$ . Combining with rotor motion (1) derived from the above second-order classical model, the wind farm is incorporated into the PFA corresponding to area A1, and the state equation is represented in (15). When the wind power is incorporated into the PRA corresponding to area A2, the state equation is represented in (16).

$$\begin{bmatrix} \Delta \dot{\delta}_1 \\ \Delta \dot{\delta}_2 \\ \Delta \dot{\omega}_1 \\ \Delta \dot{\omega}_2 \end{bmatrix} = \begin{bmatrix} 0 & 0 & 1 & 0 \\ 0 & 0 & 0 & 1 \\ -\frac{k_1 k_2}{T_{j1}(k_1+k_2)} & \frac{k_1 k_2}{T_{j1}(k_1+k_2)} & -\frac{D_1}{T_{j1}} + \frac{k_1 k_3}{T_{j1}(k_1+k_2)} & 0 \\ -\frac{k_1 k_2}{T_{j2}(k_1+k_2)} & \frac{k_1 k_2}{T_{j2}(k_1+k_2)} & \frac{k_1 k_3}{T_{j2}(k_1+k_2)} & -\frac{D_2}{T_{j2}} \end{bmatrix} \begin{bmatrix} \Delta \delta_1 \\ \Delta \delta_2 \\ \Delta \omega_1 \\ \Delta \omega_2 \end{bmatrix} \quad (15)$$

$$\begin{bmatrix} \Delta \dot{\delta}_1 \\ \Delta \dot{\delta}_2 \\ \Delta \dot{\omega}_1 \\ \Delta \dot{\omega}_2 \end{bmatrix} = \begin{bmatrix} 0 & 0 & 1 & 0 \\ 0 & 0 & 0 & 1 \\ -\frac{k_1 k_2}{T_{j1}(k_1+k_2)} & \frac{k_1 k_2}{T_{j1}(k_1+k_2)} & -\frac{D_1}{T_{j1}} & \frac{k_1 k_4}{T_{j2}(k_1+k_2)} \\ -\frac{k_1 k_2}{T_{j2}(k_1+k_2)} & \frac{k_1 k_2}{T_{j2}(k_1+k_2)} & 0 & -\frac{D_2}{T_{j2}} + \frac{k_1 k_4}{T_{j2}(k_1+k_2)} \end{bmatrix} \begin{bmatrix} \Delta \delta_1 \\ \Delta \delta_2 \\ \Delta \omega_1 \\ \Delta \omega_2 \end{bmatrix} \quad (16)$$

The impact of integrated wind power on the power system damping is mainly investigated through the quantitative changes of the system damping characteristics. Before and after the integration, the change of damping characteristics can be discussed according to (2), (15), and (16).

Keeping the system structure unchanged, the damping sum of all the modes of the system is constant and equals the sum of all the characteristic roots of the system [28]. Furthermore, the sum of diagonal elements  $A_{eq}$  in (2) is always equal. When wind power is incorporated into the PFA, it can be seen from (15) that the damping sum of the system is  $-\frac{D_1}{T_{j1}} - \frac{D_2}{T_{j2}} + \frac{k_1 k_3}{T_{j1}(k_1+k_2)}$ . The damping increment is  $\frac{k_1 k_3}{T_{j1}(k_1+k_2)}$ , which is the relation of  $k_1$ ,  $k_2$ ,  $k_3$ .  $k_1 = \frac{E_1 U_w}{X_{13}} \cos(\delta_{10} + \delta_{w0})$ ,  $k_2 = \frac{E_2 U_w}{X_{23}} \cos(\delta_{20} + \delta_{w0})$ , and  $k_3 = g_1 g_2$  are a relation of  $E_1$ ,  $E_2$ ,  $U_w$ ,  $X_{13}$ , and  $X_{23}$ , which are fixed. However,  $\delta_{20}$ ,  $\delta_{w0}$ ,  $g_1$ , and  $g_2$  may result in changes of  $k_1$ ,  $k_2$ , and  $k_3$ , which cause the change of  $\frac{k_1 k_3}{T_{j1}(k_1+k_2)}$ . When the wind power is incorporated into the PRA, it can be observed from (16) that the damping sum of the system is  $-\frac{D_1}{T_{j1}} - \frac{D_2}{T_{j2}} + \frac{k_2 k_4}{T_{j2}(k_1+k_2)}$ . The damping increment is  $\frac{k_2 k_4}{T_{j2}(k_1+k_2)}$ , in which there is  $k_4 = g_2 g_3$ . Similarly,  $\delta_{20}$ ,  $\delta_{w0}$ ,  $g_2$ , and  $g_3$  result in the changes of  $k_1$ ,  $k_2$ , and  $k_4$ , which cause the change of  $\frac{k_2 k_4}{T_{j2}(k_1+k_2)}$ .

Based on the mathematical derivation and analysis above, the system damping increment may be positive or negative in the impact of the integrated wind power on the power systems. The effect depends on the various parameters of the integrated wind power, such as how far it is connected to the grid, how large-scale the capacity is, and in which area the integrated location is, PFA or PRA. The wind power impact is related to the actual changes of system damping, according to the practical structure of the power systems containing the wind farm.

### 3. Simulation Example and Result Analysis

#### 3.1. The Impact of the Different Areas of Wind Power on the System LFOs

In this paper, the wind farm is connected to the double loop line of the IEEE two-area four-machine power systems [27]. Before the connection of the wind farm, area A1 is mainly composed of generators G1 and G2, and area A2 is mainly composed of generators G3 and G4. Area A1 is set to transmit 413 MW of active power to area A2 through the tie line. Hence, area A1 is the PFA, and area A2 is the PRA. According to the literature [25], the wind farm consisting of DFIGs can be simulated by an equivalent DFIG denoted with  $G_w$ , which is connected to node 7 in the PFA and node 9 in the PRA, as shown in Figures 4 and 5, respectively. The green ellipse dotted line frame in Figures 4 and 5 is the integrated



wind farm. The wind farm is equivalent, practically, to the WT of 25 DFIGs, which has the capacity of 2 MW for each one. Hence, the capacity of  $G_w$  equals 50 MW.

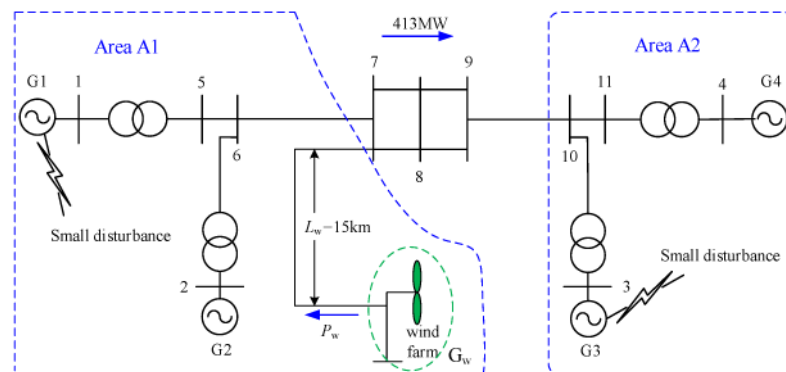


**Figure 4.** The wind power integrated into the PFA.

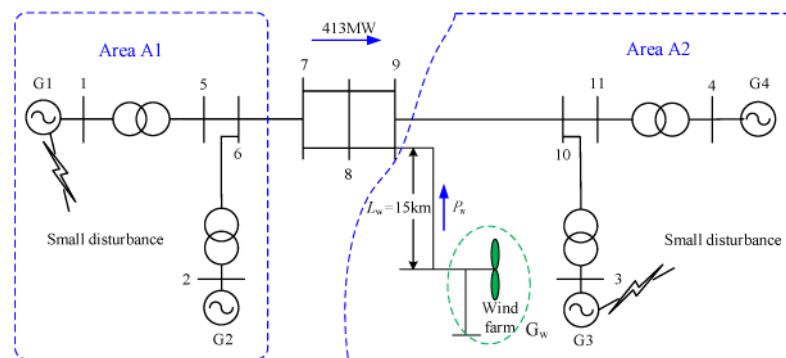


**Figure 5.** The wind power integrated into the PRA.

Before the DFIG reaches a stable operating state, it needs a period of 10–15 s from the start to the stable state. Therefore, the small disturbance is set at  $t = 20$  s after the DFIG starts. The square wave pulse signals, with 5% of the stable transmission voltage, which is set as the small disturbance with a duration of 0.1 s, are added to G1 and G3 at the same time. Under the perturbation excitation, the intra-area oscillation of the rotor angular velocity of the synchronous generator and the inter-area oscillation of the active power of the tie line between node 7 and node 9 are observed.

In the paper, three operating conditions are studied under the condition of the no-power system stabilizer (PSS) in the system. First, the IEEE two-area four-machine power systems suffer small disturbances without integrated wind power. Second, the power system suffers small disturbance with the wind power integrated into the PFA, as shown in Figure 4. Third, the power system suffers small disturbance with the wind power integrated into the PRA, as shown in Figure 5. According to the data of the oscillation modes in Tables 1–3, the mode distributions of the intra-area oscillation in G1–G4 are drawn out in Figure 6a–d and that of the intra-area oscillation in the tie line are illustrated in Figure 6e in three operating conditions. The variables  $\sigma$  and  $\omega$  denote the real part and imaginary part of the eigenvalue, respectively. The eigenvalues of the oscillation modes are identified by the TLS-ESPRIT algorithm [29] in the paper. The variable  $\xi$  is the damping ratio of the corresponding mode, which is equal to  $\frac{-\sigma}{\sqrt{\sigma^2 + \omega^2}}$ . The intra-area oscillation modes are characterized with the oscillation mode parameters of the rotor angular velocity of the four generators (G1–G4). The inter-area oscillation modes are characterized with the oscillation mode parameters of the active power in the tie line [30]. The conjugate eigenvalues are symmetrically distributed about the real axis in the complex plane; so, the imaginary part is not depicted in Figure 6.

**Table 1.** Oscillation modes of the system without wind power.

Object	Mode	$\sigma$	$\omega$ (rad/s)	$\xi$
G1	Mode #1	−0.5809	±7.0282	0.0824
	Mode #2	0.0871	±4.0228	−0.0217
	Mode #3	−1.0705	±1.1010	0.6971
G2	Mode #1	−0.6319	±7.0404	0.0894
	Mode #2	0.0620	±4.0274	−0.0154
	Mode #3	−0.1028	±0.8767	0.1165
G3	Mode #1	−0.5637	±7.2388	0.0776
	Mode #2	0.0927	±4.0292	−0.0230
	Mode #3	−0.8445	±1.0654	0.6212
G4	Mode #1	−0.6301	±7.2762	0.0863
	Mode #2	0.1092	±4.0185	−0.0272
	Mode #3	−0.0681	±0.8490	0.0800
$P_L$	Mode #1	−0.2247	±6.9636	0.0323
	Mode #2	0.1072	±4.0257	−0.0266
	Mode #3	−0.0695	±0.7260	0.0953

**Table 2.** Oscillation modes of the system with wind power integrated into PFA.

Object	Mode	$\sigma$	$\omega$ (rad/s)	$\xi$
G1	Mode#1	−0.5868	±7.0125	0.0834
	Mode #2	0.0463	±4.0702	−0.0114
	Mode #3	−1.3740	±1.7076	0.6269
G2	Mode #1	−0.5559	±6.9174	0.0801
	Mode #2	0.0438	±4.0686	−0.0108
	Mode #3	−0.0484	±0.6640	0.0727
G3	Mode #1	−0.5835	±7.2156	0.0806
	Mode #2	0.0429	±4.0650	−0.0106
	Mode #3	−0.1245	±0.7685	0.1599
G4	Mode #1	−0.6608	±7.2553	0.0907
	Mode #2	0.0451	±4.0676	−0.0111
	Mode #3	−0.0244	±0.7069	0.0345
$P_L$	Mode #1	0.0436	±4.0634	−0.0107
	Mode #2	0.0303	±1.1072	−0.0274

**Table 3.** Oscillation modes of the system with wind power integrated into PRA.

Object	Mode	$\sigma$	$\omega$ (rad/s)	$\xi$
G1	Mode #1	−0.5953	±7.0269	0.0844
	Mode #2	0.1081	±4.0544	−0.0267
	Mode #3	−0.9478	±1.0427	0.6726
G2	Mode #1	−0.5597	±6.9155	0.0807
	Mode #2	0.1108	±4.0523	−0.0273
	Mode #3	−0.0468	±0.5066	0.0920
G3	Mode #1	−0.5480	±7.2324	0.0756
	Mode #2	0.1084	±4.0557	−0.0267
	Mode #3	0.1571	±0.6128	−0.2483
G4	Mode #1	−0.5347	±7.1724	0.0743
	Mode #2	0.1089	±4.0558	−0.0268
	Mode #3	−0.0682	±0.4766	0.1417
$P_L$	Mode #1	0.1092	±4.0525	−0.0269
	Mode #2	0.2013	±0.7349	−0.2642

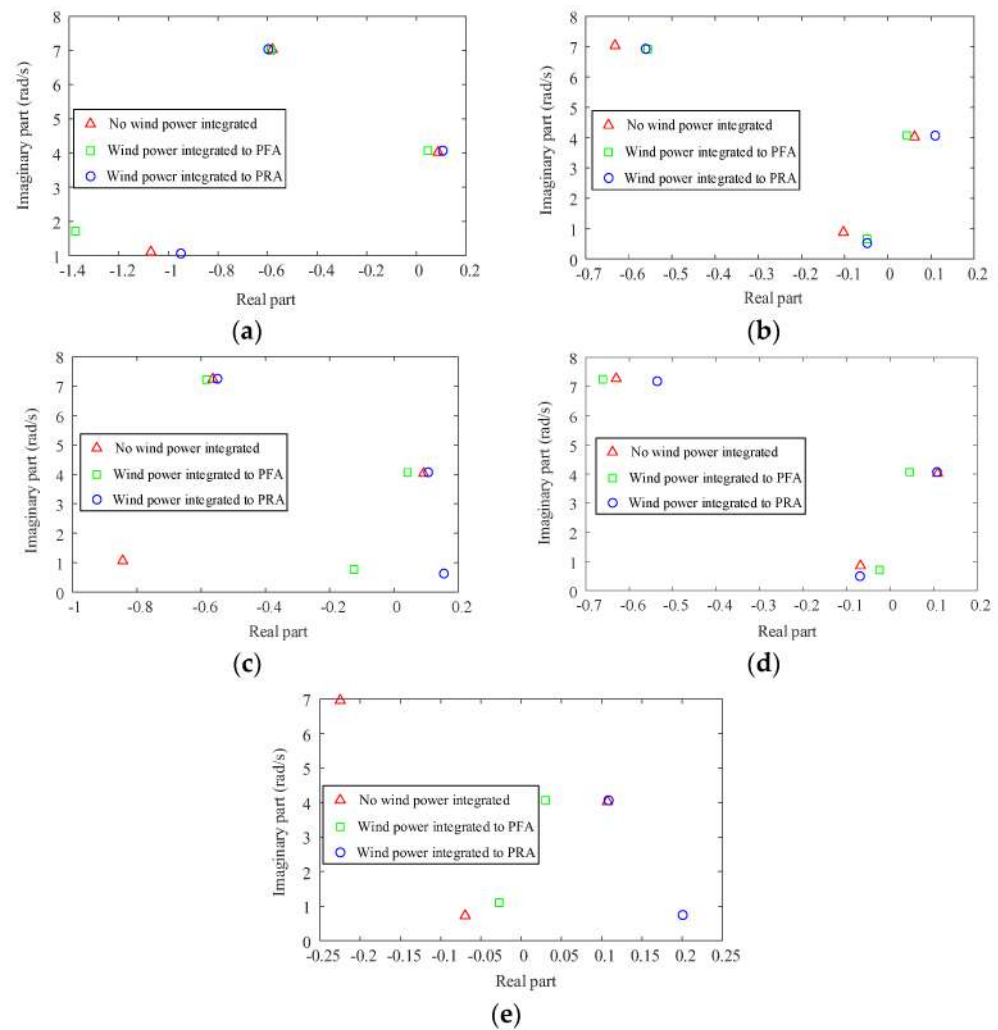


**Figure 6.** The modes distributions of intra-area oscillation and inter-area oscillation. (a) G1; (b) G2; (c) G3; (d) G4; and (e) tie line.

The following are the discussions on Figure 6:

(1) The green squares corresponding to the eigenvalues of each mode under the three conditions are mainly located on the left of the red angle. The eigenvalues on the corresponding complex plane generally shift to the left under the condition of wind power integrated into the PFA, compared with no wind power in the system. The damping characteristics are improved and the LFOs are suppressed.

(2) The blue circles corresponding to the eigenvalues of each mode in the three operating conditions are mainly located on the right of the red angle. The eigenvalues on the corresponding complex plane generally shift to the right when the wind power is integrated into the PRA, compared with the condition of no wind power in the system. When the wind power is integrated into the PRA, the damping characteristics become worse and the LFOs are aggravated slightly.

(3) The wind power integration has an impact on the dominant mode of the rotor angular velocity oscillation of the four generators G1~G4. The variation range of the eigenvalues is small, and the impact is not significant. However, the intra-area oscillation of the active power of the tie line is obviously suppressed, which can be observed from the existence of the red angle but no blue circle or green square nearby in Figure 6e. In addition, the corresponding eigenvalue of the blue circle in the lower right corner of Figure 6e indicates that wind power integrated into the PRA increases the oscillation modes and weakens the damping characteristics of the system.

Figure 7 represents the fact that the damping ratio of Mode#1 of the dominant mode of the intra-area oscillation fluctuates in the range of 0.07 to 0.09, which shows that the wind power has a slight impact. However, with the wind power integration into the PFA, the damping ratio of the dominant mode of the inter-area oscillation changes from  $-0.0266$  to  $-0.0107$ , which in turn improves the damping characteristics of the system. In contrast, the damping ratio of the wind power integration into PRA is  $-0.0269$ , which is a slight decrease. The minimum damping ratio of the intra-area oscillation is reduced to  $-0.2483$ , corresponding to Mode#3 on G3, and that of the inter-area oscillation in Mode#2 is reduced to  $-0.2642$ .

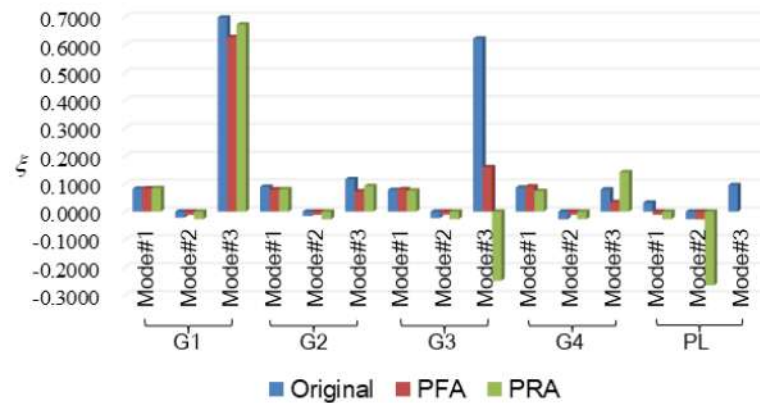


**Figure 7.** Changes of damping ratio before and after wind power integration.

### 3.2. The Impact of Connection Distance of the Wind Power on the System LFOs

The schematic diagram of a single line of the IEEE two-area four-machine power systems, including the integrated wind power whose connection distance can be adjusted, is shown in Figure 8. Area A1 consists of the generators G1 and G2 and the wind farm. The capacity of the wind farm is set at 50 MW, which is equivalently provided by 25 DFIGs of 2 MW in the simulation. The thick red line marked with  $l_w$  represents the connection distance of the wind power and is used as an adjustable object. The area A2 mainly consists of G3 and G4. As area A1 is set to transmit 413 MW of active power to area A2 through the tie line, A1 and A2 represent the PFA and the PRA, respectively. The small disturbance, including the disturbance amplitude and the disturbance period, is set the same as Section 3.1.  $l_w$  is set as 10 km, 50 km, 100 km, 200 km, and 300 km, respectively. With the different connection distances of the integrated wind power, the oscillation modes of the rotor angular velocity of G1–G4 and the active power of the tie line are tested and recorded in Tables 4–8.

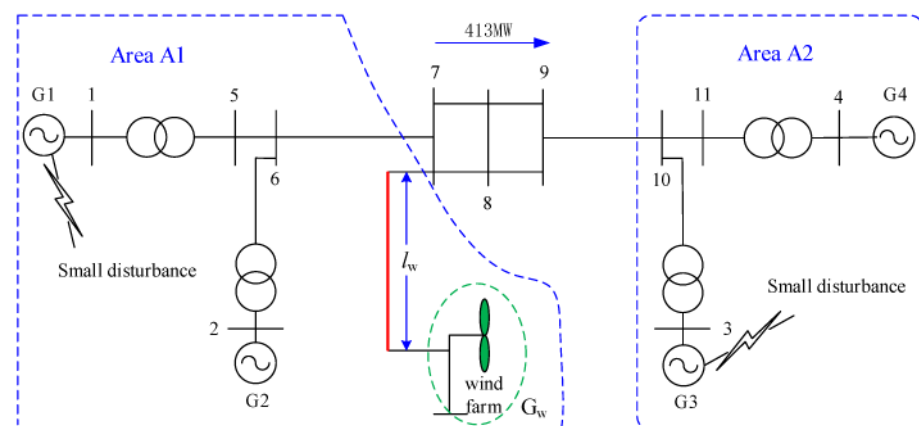


**Figure 8.** Schematic diagram of adjustable connection distance of integrated wind power.

**Table 4.**  $l_w = 10$  km.

Object	Mode	$\sigma$	$\omega$ (rad/s)	$\xi$
G1	Mode #1	−0.5869	±7.0114	0.0834
	Mode #2	0.0514	±4.1136	−0.0125
	Mode #3	−1.5415	±2.0295	0.6049
G2	Mode #1	−0.5544	±6.9159	0.0799
	Mode #2	0.0471	±4.1054	−0.0115
	Mode #3	−0.0512	±0.6694	0.0763
G3	Mode #1	−0.5832	±7.2138	0.0806
	Mode #2	0.0429	±4.1124	−0.0104
	Mode #3	−0.1772	±0.7630	0.2262
G4	Mode #1	−0.6592	±7.2562	0.0905
	Mode #2	−4.9058	±3.2432	0.8342
	Mode #3	0.0481	±4.1112	−0.0117
$P_L$	Mode #4	−0.0398	±0.7003	0.0567
	Mode #1	0.0468	±4.1099	−0.0114
	Mode #2	−0.2904	±6.2922	0.0461
	Mode #3	0.0964	±0.6716	−0.1421

**Table 5.**  $l_w = 50$  km.

Object	Mode	$\sigma$	$\omega$ (rad/s)	$\xi$
G1	Mode #1	−0.5897	±7.0044	0.0839
	Mode #2	0.0721	±3.9967	−0.0180
	Mode #3	−0.2326	±0.7583	0.2933
G2	Mode #1	−0.5646	±6.9093	0.0814
	Mode #2	0.0699	±3.9986	−0.0175
	Mode #3	−0.0710	±0.6669	0.1059
G3	Mode #1	−0.5054	±7.2594	0.0695
	Mode #2	0.0683	±3.9903	−0.0171
	Mode #3	−0.0708	±0.9064	0.0779
G4	Mode #1	−0.5606	±7.1206	0.0785
	Mode #2	0.0732	±3.9895	−0.0183
	Mode #3	−0.0461	±0.6661	0.0690
$P_L$	Mode #1	0.0696	±3.9922	−0.0174
	Mode #2	0.2988	±0.6986	−0.3933

**Table 6.**  $l_w = 100$  km.

Object	Mode	$\sigma$	$\omega$ (rad/s)	$\xi$
G1	Mode #1	−0.5768	±7.0187	0.0819
	Mode #2	0.0801	±3.9932	−0.0201
	Mode #3	−0.8717	±0.8444	0.7183
G2	Mode #1	−0.5540	±6.8997	0.0800
	Mode #2	0.0788	±3.9940	−0.0197
	Mode #3	−0.1318	±0.6801	0.1903
G3	Mode #1	−0.5027	±7.2622	0.0691
	Mode #2	0.0766	±3.9886	−0.0192
	Mode #3	0.0419	±0.8395	−0.0498
G4	Mode #1	−0.5194	±7.1183	0.0728
	Mode #2	0.0800	±3.9868	−0.0201
	Mode #3	−0.1182	±0.7211	0.1618
$P_L$	Mode #1	0.0775	±3.9902	−0.0194
	Mode #2	0.3224	±0.6805	−0.4281

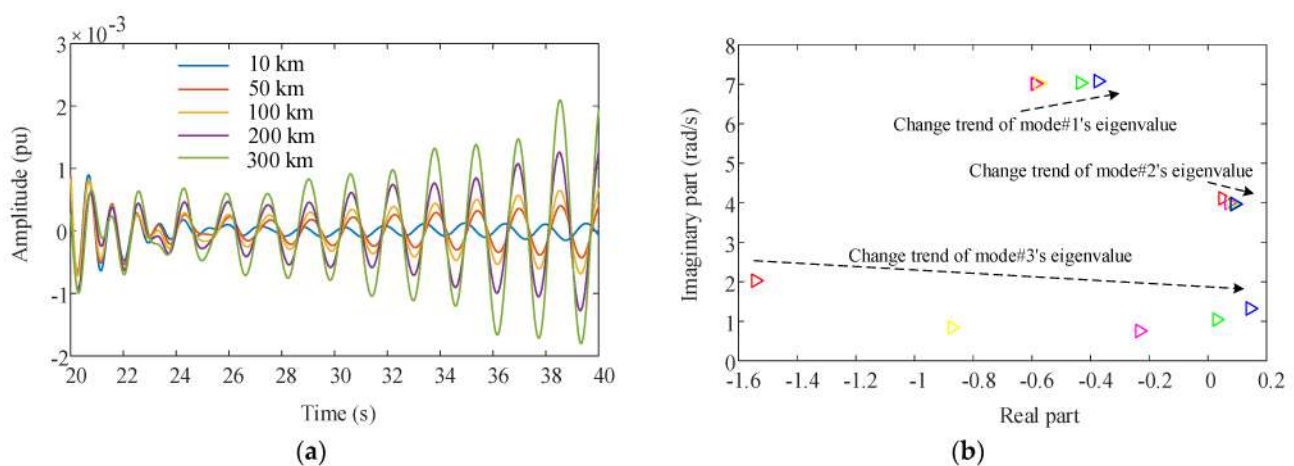
**Table 7.**  $l_w = 200$  km.

Object	Mode	$\sigma$	$\omega$ (rad/s)	$\xi$
G1	Mode #1	0.0891	$\pm 3.9848$	−0.0224
	Mode #2	−0.4344	$\pm 7.0341$	0.0616
	Mode #3	0.0302	$\pm 1.0444$	−0.0289
G2	Mode #1	−0.5224	$\pm 6.8893$	0.0756
	Mode #2	0.0840	$\pm 3.9819$	−0.0211
	Mode #3	−0.1453	$\pm 0.9354$	0.1535
G3	Mode #1	0.0837	$\pm 3.9824$	−0.0210
	Mode #2	−0.5783	$\pm 7.2186$	0.0799
	Mode #3	0.1729	$\pm 1.0368$	−0.1645
G4	Mode #1	0.0868	$\pm 3.9804$	−0.0218
	Mode #2	−0.3566	$\pm 7.0398$	0.0506
	Mode #3	0.0629	$\pm 1.0646$	−0.0590
$P_L$	Mode #1	0.0857	$\pm 3.9860$	−0.0215
	Mode #2	0.3259	$\pm 0.6785$	−0.4330

**Table 8.**  $l_w = 300$  km.

Object	Mode	$\sigma$	$\omega$ (rad/s)	$\xi$
G1	Mode #1	−0.3745	$\pm 7.0774$	0.0528
	Mode #2	0.0915	$\pm 3.9652$	−0.0231
	Mode #3	0.1439	$\pm 1.3245$	−0.1080
G2	Mode #1	0.2916	$\pm 7.5212$	−0.0387
	Mode #2	−0.4981	$\pm 6.8604$	0.0724
	Mode #3	0.0912	$\pm 3.9643$	−0.0230
G3	Mode #4	0.3169	$\pm 1.3077$	−0.2355
	Mode #1	−0.6302	$\pm 7.0251$	0.0893
	Mode #2	0.0913	$\pm 3.9695$	−0.0230
G4	Mode #3	0.3995	$\pm 1.3254$	−0.2886
	Mode #1	−0.2189	$\pm 6.9959$	0.0313
	Mode #2	0.0937	$\pm 3.9657$	−0.0236
$P_L$	Mode #3	0.3436	$\pm 1.3607$	−0.2448
	Mode #1	0.1813	$\pm 7.2515$	−0.0250
	Mode #2	0.0935	$\pm 3.9681$	−0.0236
	Mode #3	0.2956	$\pm 0.7389$	−0.3714

The following are discussions on Figures 9–13:

**Figure 9.** Rotor angular velocity oscillation of G1: (a) Oscillation output; (b) eigenvalues distribution.

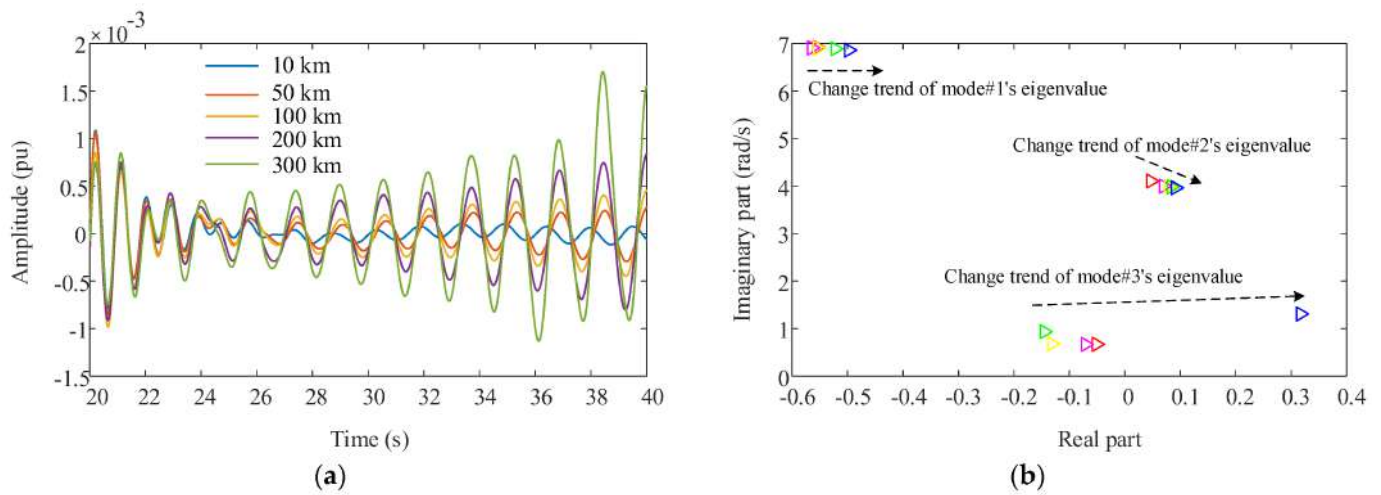


Figure 10. Rotor angular velocity oscillation of G2: (a) Oscillation output; (b) eigenvalues distribution.

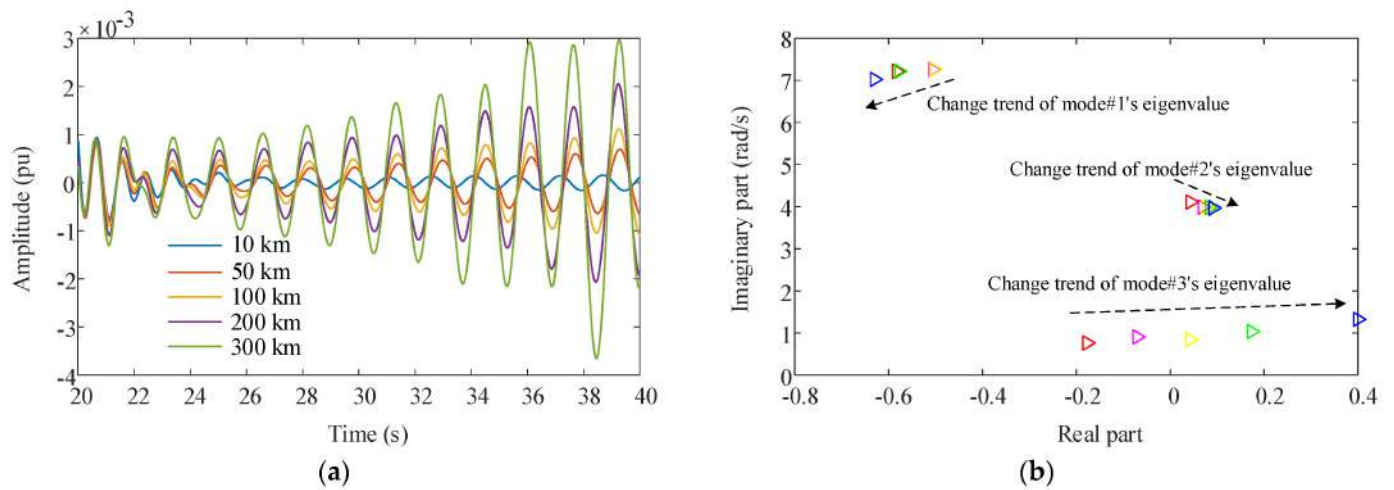


Figure 11. Rotor angular velocity oscillation of G3: (a) Oscillation output; (b) eigenvalues distribution.

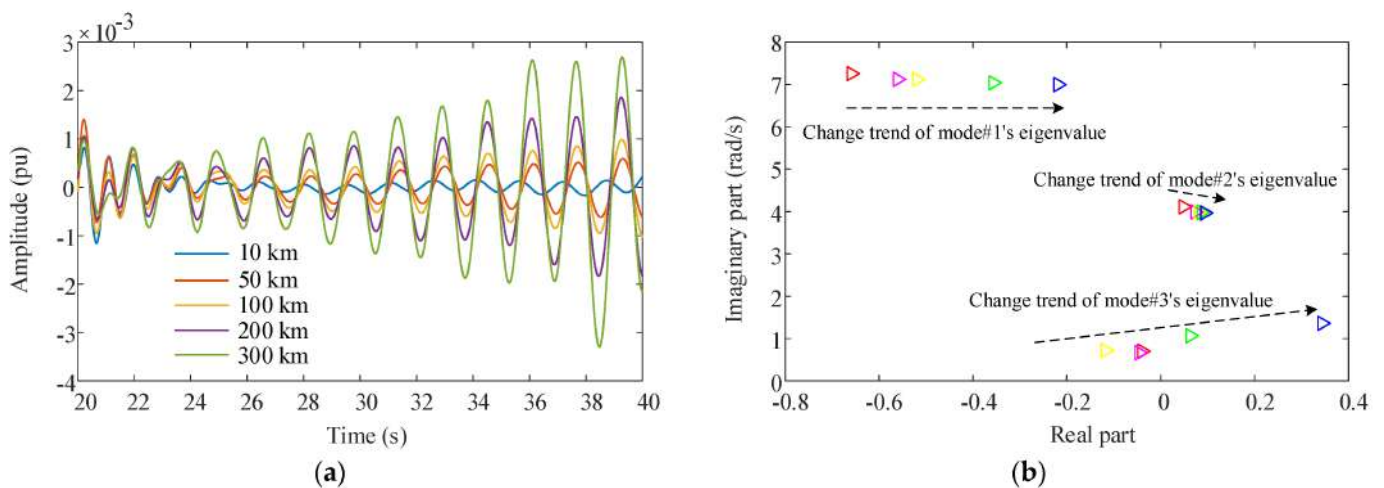
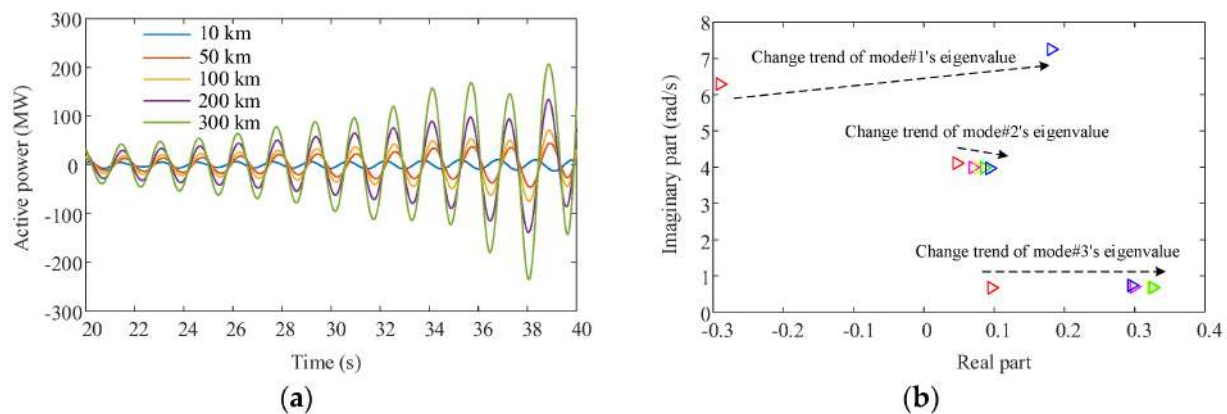


Figure 12. Rotor angular velocity oscillation of G4: (a) Oscillation output; (b) eigenvalues distribution.





**Figure 13.** Active power oscillation of the tie line: (a) Oscillation output; (b) eigenvalues distribution.

According to Figures 9a, 10a, 11a, 12a and 13a, as the connection distance of the wind power increases from 10 km to 300 km; the vibration amplitudes of both intra-area and inter-area oscillations present an increasing trend. In the period of 20 s after the small disturbance occurs, the overall damping ratio of the system decreases. Therefore, the LFO problem worsens, and the system stability weakens.

Figure 9b, Figure 10b, Figure 11b, and Figure 12b describe the eigenvalue distributions of the oscillation modes of the rotor angular velocity of G1–G4 related to the different connection distances of the wind power. Figure 13b describes the eigenvalue distributions of the active power oscillation modes of the tie line with the connection distance changes. It is illustrated that the eigenvalues of each mode generally move to the right in the complex plane with the connection distance increased, which makes the overall system stability worse. Although mode#1's eigenvalue of G3 moves to the left in the complex plane, the weak and negative damping characteristics of the other two dominant modes determine the increasing amplitude of the intra-area LFOs. On the other hand, it is shown that the inter-area LFOs increase significantly with the connection distance increased in Figure 13.

In addition, it can be seen from Figure 14 that the damping ratio of the dominant mode of the intra-area oscillation is little changed with the increase in distance. With the change of distance from 10 km to 300 km, the damping ratios of the active power of the tie line are  $-0.0114$ ,  $-0.0174$ ,  $-0.0194$ ,  $-0.0215$ , and  $-0.0236$ , successively, showing an obvious decrease. The damping characteristic of the inter-area oscillation obviously deteriorates, and the system stability becomes worse.

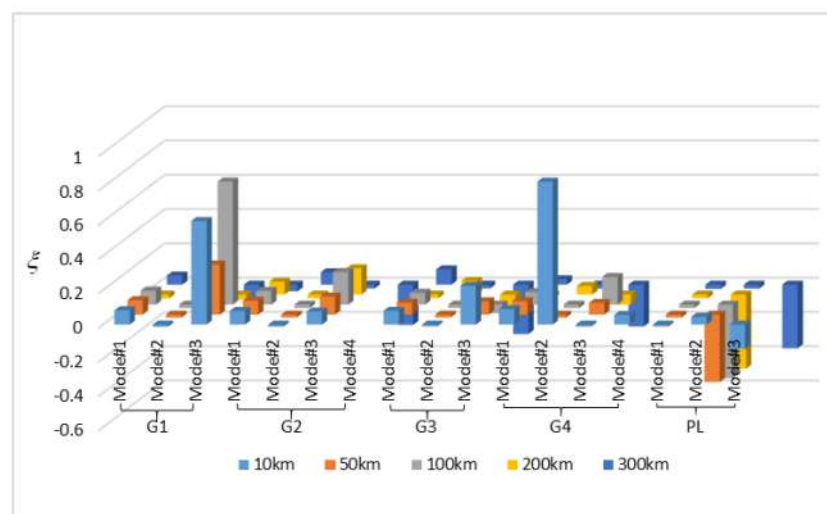


**Figure 14.** Changes of damping ratio for a different connection distance.



### 3.3. The Impact of the Capacity of the Wind Power on the System LFOs

The wind farm with adjusted capacity is integrated into the IEEE two-area four-machine power systems, as shown in Figure 15. The wind farm is equivalent to a DFIG whose capacity can be set at a different value. The equivalent DFIG is connected to bus node 7 in area A1 of the power systems. The connection distance  $l_w$  is fixed at 15 km, which benefits the wind power transmission. In order to study the impact of the capacity of the integrated wind power on the LFOs of the power systems, the capacity of the wind power is set at different values. The wind power output  $P_w$  is adjusted by the number of DFIGs of 2 MW, and the other parameters of the system were the same as those in Figure 6 in Section 3.2.

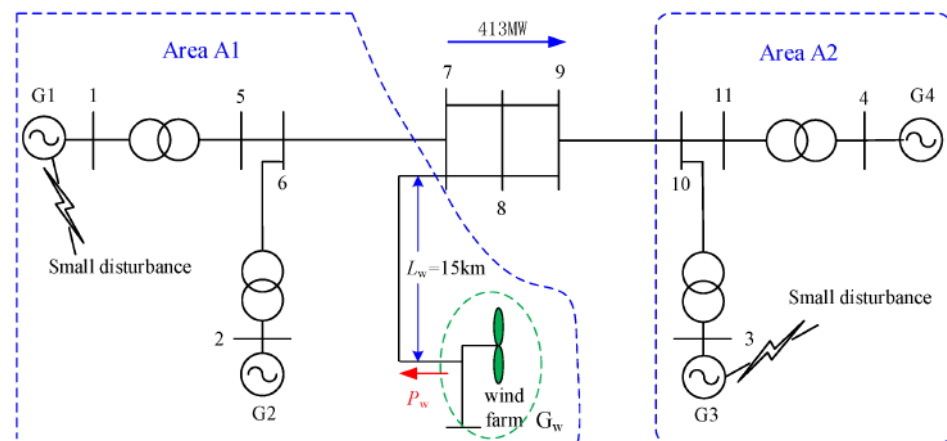


**Figure 15.** Schematic diagram of the adjustable capacity of integrated wind power.

The capacity of the integrated wind power is set as 10 MW, 50 MW, 100 MW, 300 MW, and 500 MW, respectively. The impact of different capacities on the oscillation modes of the intra-area and inter-area LFOs is tested. The oscillation modes of the rotor angular velocity of G1–G4 and the active power of the tie line are tested and shown in Tables 9–13. Figures 16a, 17a, 18a, 19a and 20a show that the amplitude of both the intra-area oscillations and the inter-area oscillations presents a decreasing trend with the capacity of the wind power increased from 10 MW to 500 MW. Figures 16b, 17b, 18b, 19b and 20b describe the eigenvalues of the oscillation modes of the rotor angular velocity of G1–G4 and the active power of the tie line with the changes of the capacity of the integrated wind power.

**Table 9.**  $P_w = 10$  MW.

Object	Mode	$\sigma$	$\omega$ (rad/s)	$\xi$
G1	Mode #1	−0.5686	±7.0010	0.0810
	Mode #2	0.0968	±4.1159	−0.0235
	Mode #3	0.0681	±0.6361	−0.1065
G2	Mode #1	−0.5362	±6.9257	0.0772
	Mode #2	0.0978	±4.1147	−0.0238
	Mode #3	−0.0478	±0.5757	0.0827
G3	Mode #1	−0.5566	±7.2391	0.0767
	Mode #2	0.0991	±4.1140	−0.0241
	Mode #3	−0.0799	±0.5212	0.1515
G4	Mode #1	−0.5426	±7.1518	0.0757
	Mode #2	0.1018	±4.1155	−0.0247
	Mode #3	−0.0372	±0.4784	0.0775
$P_L$	Mode #1	0.0988	±4.1140	−0.0240
	Mode #2	0.1435	±0.6649	−0.2110

**Table 10.**  $P_w = 50$  MW.

Object	Mode	$\sigma$	$\omega$ (rad/s)	$\xi$
G1	Mode #1	−0.5867	±7.0125	0.0834
	Mode #2	0.0464	±4.0702	−0.0114
	Mode #3	−0.0257	±0.7032	0.0365
G2	Mode #1	−0.5559	±6.9174	0.0801
	Mode #2	0.0438	±4.0686	−0.0108
	Mode #3	−0.0484	±0.6640	0.0727
G3	Mode #1	−0.5834	±7.2156	0.0806
	Mode #2	0.0430	±4.0650	−0.0106
	Mode #3	−0.1244	±0.7685	0.1598
G4	Mode #1	−0.6607	±7.2553	0.0907
	Mode #2	0.0451	±4.0676	−0.0111
	Mode #3	−0.0244	±0.7069	0.0345
$P_L$	Mode #1	0.0436	±4.0635	−0.0107
	Mode #2	0.0303	±1.1071	−0.0274

**Table 11.**  $P_w = 100$  MW.

Object	Mode	$\sigma$	$\omega$ (rad/s)	$\xi$
G1	Mode #1	−0.6124	±6.9808	0.0874
	Mode #2	0.0349	±3.9510	−0.0088
	Mode #3	−0.0466	±0.7909	0.0588
G2	Mode #1	−0.5914	±6.8905	0.0855
	Mode #2	0.0320	±3.9483	−0.0081
	Mode #3	−0.0318	±0.6593	0.0482
G3	Mode #1	−0.6149	±7.1886	0.0852
	Mode #2	0.0341	±3.9480	−0.0086
	Mode #3	−0.0616	±0.6992	0.0878
G4	Mode #1	−0.5889	±7.0858	0.0828
	Mode #2	0.0399	±3.9481	−0.0101
	Mode #3	−0.0265	±0.6084	0.0435
$P_L$	Mode #1	0.0339	±3.9422	−0.0086
	Mode #2	0.0674	±1.2951	−0.0520

**Table 12.**  $P_w = 300$  MW.

Object	Mode	$\sigma$	$\omega$ (rad/s)	$\xi$
G1	Mode #1	−0.7655	±6.8725	0.1107
	Mode #2	−0.0346	±3.6981	0.0094
	Mode #3	−0.0061	±0.6995	0.0087
G2	Mode #1	−0.7323	±6.7197	0.1083
	Mode #2	−0.0253	±3.6977	0.0068
	Mode #3	−0.0282	±0.6665	0.0423
G3	Mode #1	−0.7612	±7.0388	0.1075
	Mode #2	−0.0295	±3.7020	0.0080
	Mode #3	−0.1315	±0.7283	0.1777
G4	Mode #1	−0.7511	±6.8930	0.1083
	Mode #2	−0.0321	±3.7044	0.0087
	Mode #3	−0.0316	±0.7136	0.0442
$P_L$	Mode #1	−0.0250	±3.6985	0.0068
	Mode #2	−0.0864	±1.5045	0.0573

The following are the discussions on Figures 16–20:

According to Figures 16a, 17a, 18a, 19a and 20a, in the period of 20 s after the small disturbance occurs, the overall damping ratio of the system increases. Therefore, the LFOs have been alleviated, and the power system stability is enhanced. In addition, from the point of view of the eigenvalue change shown in Figures 16b, 17b, 18b, 19b and 20b, the

eigenvalue of each mode generally moves to the left in the complex plane. It means that the system's stability is enhanced. The imaginary part of the modal eigenvalues shows a downward trend as a whole. Therefore, the dominant mode frequency of the local oscillation and the interval oscillation decreases with the increase in the wind power output. It is worthy of attention that the damping of the dominant modes of the active power of the tie line increases significantly with the increase in the wind power output capacity. The larger capacity of the integrated wind power suppresses the LFOs better; the damping characteristics of the system are improved, and the system stability is obviously enhanced.

**Table 13.**  $P_w = 500$  MW.

Object	Mode	$\sigma$	$\omega$ (rad/s)	$\zeta$
G1	Mode #1	−0.9017	$\pm 6.6822$	0.1337
	Mode #2	−0.0750	$\pm 3.3351$	0.0225
	Mode #3	−0.0097	$\pm 0.6907$	0.0140
G2	Mode #1	−0.8103	$\pm 6.4869$	0.1240
	Mode #2	−0.0950	$\pm 3.3221$	0.0286
	Mode #3	−0.0361	$\pm 0.6752$	0.0534
G3	Mode #1	−0.7154	$\pm 6.9459$	0.1025
	Mode #2	−0.0820	$\pm 3.3208$	0.0247
	Mode #3	−0.0320	$\pm 0.7344$	0.0435
G4	Mode #1	−0.8395	$\pm 6.6771$	0.1247
	Mode #2	−0.0685	$\pm 3.3253$	0.0206
	Mode #3	−0.0496	$\pm 0.6883$	0.0719
$P_L$	Mode #1	−0.0776	$\pm 3.3239$	0.0233
	Mode #2	−0.1143	$\pm 0.7413$	0.1524

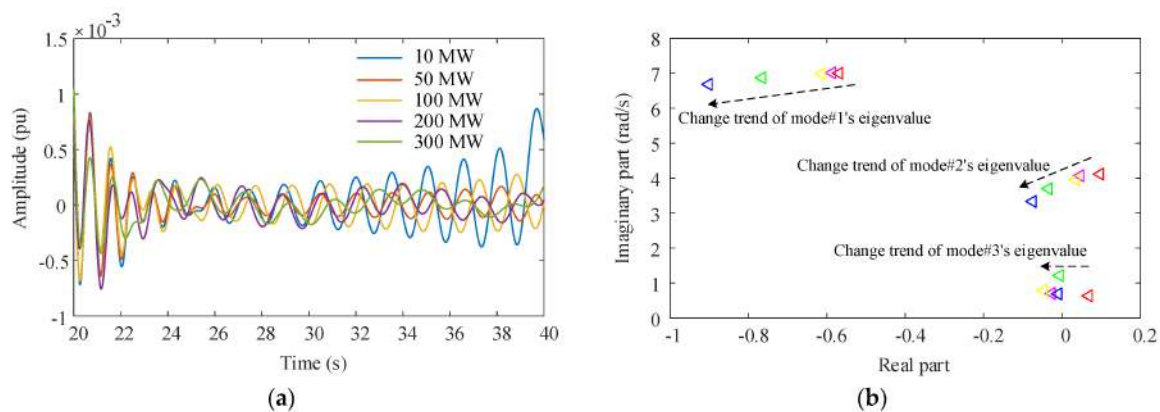


**Figure 16.** Rotor angular velocity oscillation of G1: (a) Oscillation output; (b) eigenvalues distribution.

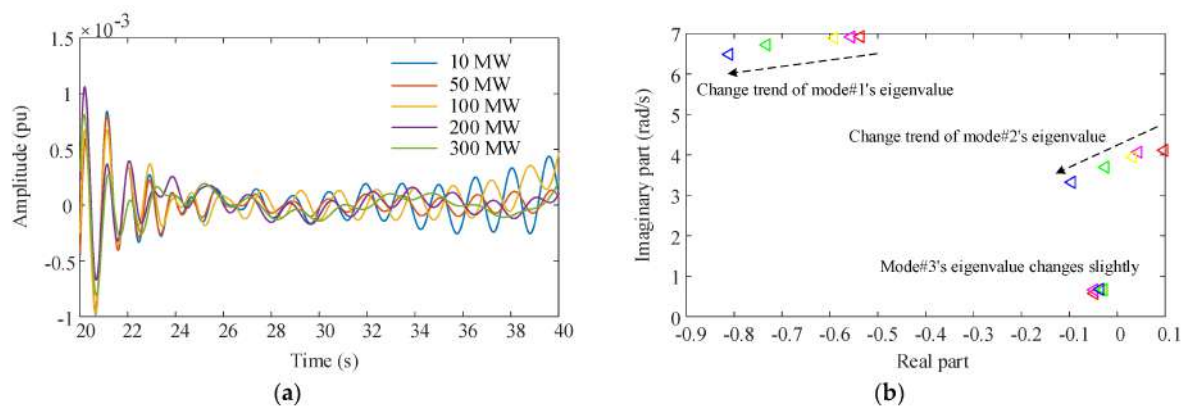


**Figure 17.** Rotor angular velocity oscillation of G2: (a) Oscillation output; (b) eigenvalues distribution.

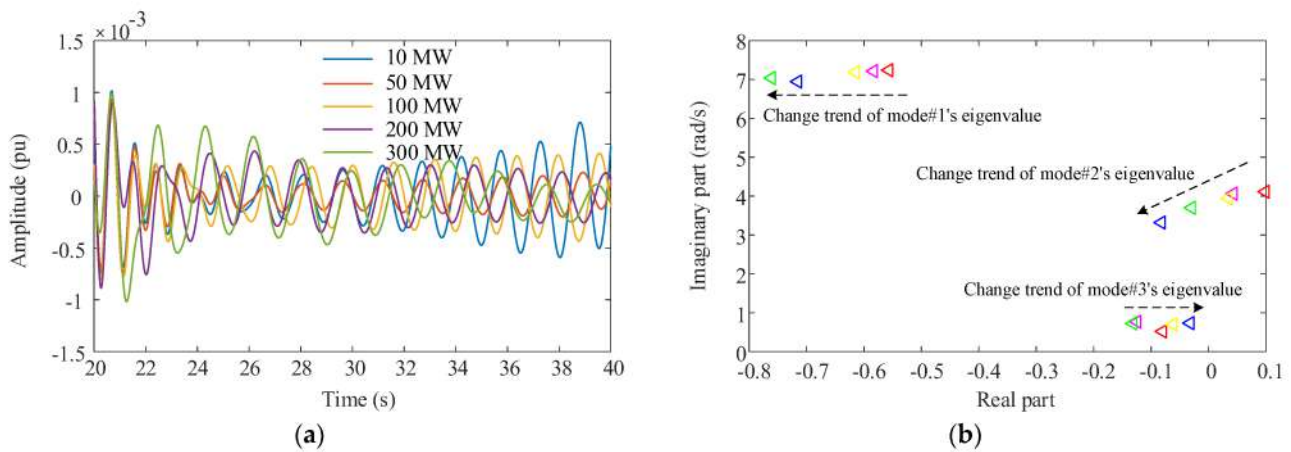


**Figure 18.** Rotor angular velocity oscillation of G3: (a) Oscillation output; (b) eigenvalues distribution.

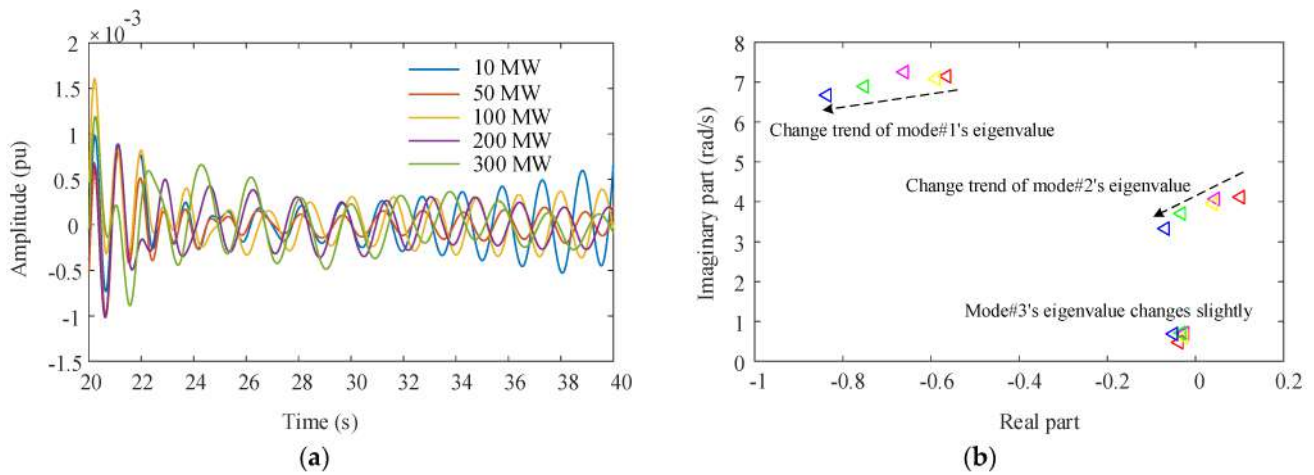


**Figure 19.** Rotor angular velocity oscillation of G4: (a) Oscillation output; (b) eigenvalues distribution.

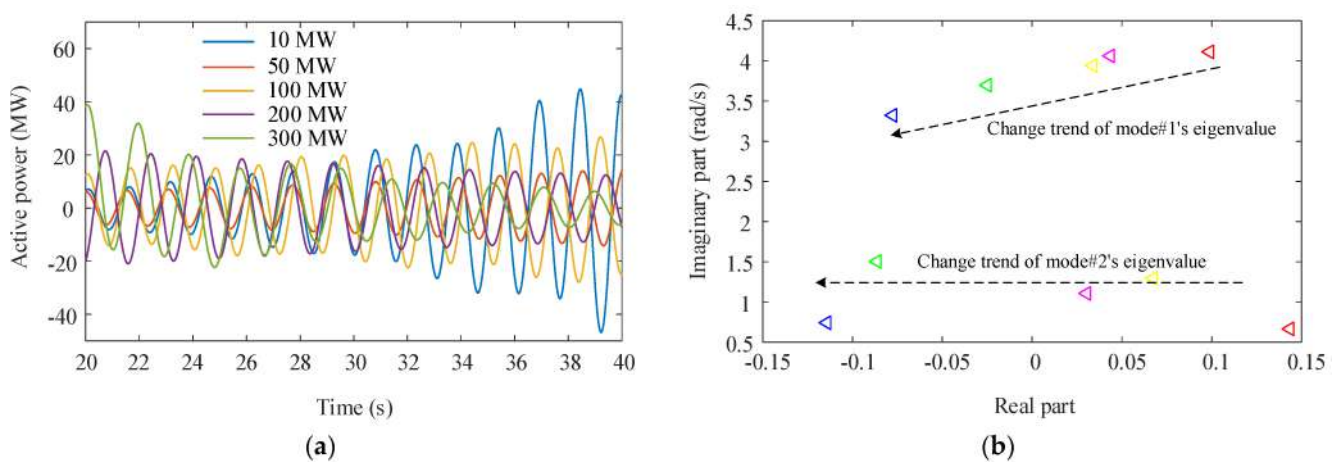


**Figure 20.** Active power oscillation of the tie line: (a) Oscillation output; (b) eigenvalues distribution.

As shown in Figure 21, the damping ratio of the dominant mode of the intra-area oscillation (Mode#1) shows an increasing trend, and the damping ratio of the dominant mode of the regional oscillation also shows an increasing trend. The maximum damping ratio will reach 0.1337 and 0.0233, respectively, and the stability of the system will be improved.

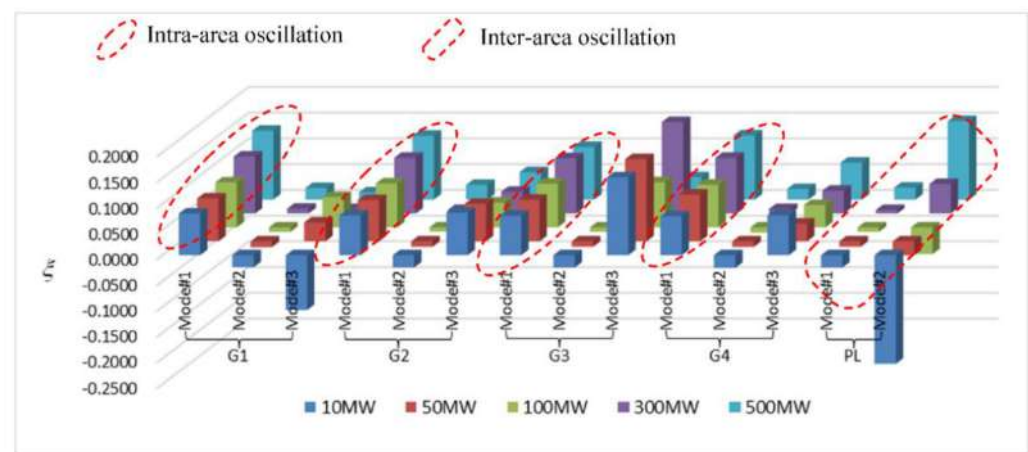


**Figure 21.** Changes of damping ratio for different output capacities.

#### 4. Conclusions

This paper conducts a detailed theoretical derivation and analysis of the damping characteristics of the two-area interconnected power system. The mathematical relations are used to analyze the changes in the damping characteristics caused by wind power integration into the two-area interconnected system. The LFO model of the IEEE two-area four-machine power system is selected as an example to analyze the impact of wind power integration on the damping characteristics of the power system. The results are summarized as follows:

- (1) The wind power consisted of DFIGs which are integrated into the PFA to suppress the system's LFOs. In contrast, the integration to the PRA increases the LFOs slightly.
- (2) With the increase in the connection distance of the wind power, the amplitudes of both the intra-area and the inter-area oscillations tend to increase. The system's LFOs increase, and its stability weakens.
- (3) As the capacity of the integrated wind power increases, the amplitudes of the intra-area and inter-area oscillations tend to decrease, and the damping ratio of the system increases as a whole. The stability of the system is enhanced, and the LFO problem is alleviated to some extent.

As is known from the analysis of the above results, wind power integration not only changes the structure of the power systems, but also alters the damping characteristics of the large-scale interconnected systems. Not only should the design and construction of the wind farms be optimized, but the appropriate grid parameters should also be constructed to improve the stability of the power system.

**Author Contributions:** Conceptualization, J.C., T.J., M.A.M., A.A. and U.D.; methodology, J.C., T.J. and M.A.M.; software, J.C., T.J. and M.A.M.; validation, J.C., T.J., M.A.M., A.A. and U.D.; formal analysis, J.C., T.J. and M.A.M.; investigation, J.C., T.J., M.A.M., A.A. and U.D.; methodology, J.C., T.J. and M.A.M.; resources, J.C., T.J. and M.A.M.; data curation, J.C., T.J., M.A.M., A.A. and U.D.; writing—original draft preparation, J.C., T.J. and M.A.M.; writing—review and editing, J.C., T.J., M.A.M., A.A. and U.D.; visualization, J.C., T.J. and M.A.M.; supervision, T.J. and M.A.M.; project administration, A.A. and U.D.; funding acquisition, A.A. and U.D.; All authors have read and agreed to the published version of the manuscript.

**Funding:** This research received no external funding.

**Institutional Review Board Statement:** Not applicable.

**Informed Consent Statement:** Not applicable.

**Data Availability Statement:** The data supporting the reported results are available in the manuscript.

**Acknowledgments:** The authors would like to thank the Estonian Centre of Excellence in Zero Energy and Resource Efficient Smart Buildings and Districts, ZEBE, grant TK146, funded by the European Regional Development Fund to support this research. Furthermore, this work was supported by the scientific research project of Fuzhou Polytechnic under Grant FZYKJRCQD202101.

**Conflicts of Interest:** The authors declare no conflict of interest.

## Nomenclature

### Subscripts, Superscripts, and Sets

$G_{eq1}, G_{eq2}$	Equivalent synchrony generator.
$j, k$	Serial number of the equivalent synchrony generator.
$\gamma$	Mark of $\frac{D_1}{T_{j1}}$ .
$G1, G2, G3, G4$	Synchrony generators of the IEEE two-area four-machine power systems.
Mode#1, Mode#2, Mode#3, Mode#4	Oscillation modes of the rotor angular velocity of the synchrony generators G1–G4 and the active power oscillation modes of the tie line from node 7 to node 9 in the IEEE two-area four-machine power systems.

### Variables and Constants

$\Delta\delta_j$	Power angle increment of the $j$ th synchrony generator.
$\Delta\omega_j$	Rotor angular velocity increment of the $j$ th synchrony generator.
$T_{jj}$	Inertia time constant of the synchrony generator $j$ .
$\Delta P_{je}$	Electromagnetic power increment of the synchrony generator $j$ .
$D_j$	Damping torque coefficient of the synchrony generator $j$ .
$K_{jk}$	Synchronous torque coefficient between the synchrony generator $j$ and $k$ , $K_{jk} = \partial P_{je} / \partial \delta_k$ .
$A_{eq}$	State matrix of the interconnected systems with two equivalent synchrony generators.
$E_1, E_2$	No-load electromotive force of the synchrony generator $G_{eq1}$ and $G_{eq2}$ .
$U_w$	Stable voltage on the integrated node of the wind power, which is assumed to be constant.
$Z_{11}, Z_{22}$	System impedance of $G_{eq1}$ and $G_{eq2}$ acting as source, respectively.
$Z_{12}, Z_{21}$	Transfer impedance between $G_{eq1}$ and $G_{eq2}$ .
$\varphi_{11}, \varphi_{12}, \varphi_{21}, \varphi_{22}$	Impedance angle of $Z_{11}, Z_{12}, Z_{21}, Z_{22}$ , respectively.
$\alpha_{11}, \alpha_{12}, \alpha_{21}, \alpha_{22}$	Impedance complementary angle of $Z_{11}, Z_{12}, Z_{21}, Z_{22}$ , respectively.
$\delta_{10}, \delta_{20}$	Rotor angle of $G_{eq1}$ and $G_{eq2}$ , respectively.
$\delta_{12}, \delta_{21}$	Rotor angle difference between $G_{eq1}$ and $G_{eq2}$ , $\delta_{12} = -\delta_{21}$ .
$\delta_{120}, \delta_{210}$	Rotor angle difference between $G_{eq1}$ and $G_{eq2}$ at some operating point, $\delta_{120} = -\delta_{210}$ .
$\delta_{w0}$	Power angle of the wind farm as an equivalent DFIG.
$\Delta\delta_w$	Power angle increment of the wind farm as an equivalent DFIG.
$X_{13}, X_{23}$	Reactance between $G_{eq1}$ and the integrated node of wind farm. Reactance between $G_{eq2}$ and the integrated node of wind farm.
$\lambda$	The eigenvalue of the equation $ A_{eq} - \lambda I  = 0$ .
$I$	Identity matrix.
$\Delta P_w$	Increment of active power provided by the wind farm.
$\Delta f_B$	Frequency increment of the integrated node of the wind farm.
$g_1$	System characteristic coefficient of the active power increment of the wind farm with respect to $\Delta f_B$ , that is, $\Delta P_w = g_1 \cdot \Delta f_B$ .
$g_2$	Proportional coefficient between $\Delta f_B$ and $\Delta\omega_1$ .
$g_3$	Proportional coefficient between $\Delta f_B$ and $\Delta\omega_2$ .
$k_1, k_2$	$k_1 = \frac{E_1 U_w}{X_{13}} \cos(\delta_{10} - \delta_{w0})$ , $k_2 = \frac{E_2 U_w}{X_{23}} \cos(\delta_{20} - \delta_{w0})$ .
$k_3, k_4$	$k_3 = g_1 \cdot g_2$ , $k_4 = g_1 \cdot g_3$ .
$\sigma$	Real part of a mode eigenvalue or damping factor.
$\omega$	Imaginary part of a mode eigenvalue or oscillation angle frequency.
$\xi$	Damping ratio, $\xi = \frac{-\sigma}{\sqrt{\sigma^2 + \omega^2}}$ .

## References

1. Tan, H.; Yan, W.; Ren, Z.; Wang, Q.; Mohamed, M.A. A robust dispatch model for integrated electricity and heat networks considering price-based integrated demand response. *Energy* **2022**, *239*, 121875.
2. Chen, J.; Alnowibet, K.; Annuk, A.; Mohamed, M.A. An effective distributed approach based machine learning for energy negotiation in networked microgrids. *Energy Strategy Rev.* **2021**, *38*, 100760.
3. Alnowibet, K.; Annuk, A.; Dampage, U.; Mohamed, M.A. Effective Energy Management via False Data Detection Scheme for the Interconnected Smart Energy Hub–Microgrid System under Stochastic Framework. *Sustainability* **2021**, *13*, 11836.
4. Mohamed, M.A.; Mirjalili, S.; Dampage, U.; Salmen, S.H.; Obaid, S.A.; Annuk, A. A cost-efficient-based cooperative allocation of mining devices and renewable resources enhancing blockchain architecture. *Sustainability* **2021**, *13*, 10382.
5. Du, W.; Bi, J.; Wang, H.; Yi, J. Inter-area low-frequency power system oscillations caused by open-loop modal resonance. *IET Gener. Transm. Distrib.* **2018**, *12*, 4249–4259.
6. Shen, C.; An, Z.; Dai, X.; Wei, W.; Ding, L. Measurement-based solution for low frequency oscillation analysis. *J. Mod. Power Syst. Clean Energy* **2016**, *4*, 406–413.
7. Kosterev, D.N.; Taylor, C.W.; Mittelstadt, W.A. Model validation for the August 10, 1996 WSCC system outage. *IEEE Trans. Power Syst.* **1999**, *14*, 967–979.
8. Fairley, P. The unruly power grid. *IEEE Spectr.* **2004**, *41*, 22–27.
9. Report of the Enquiry Committee on Grid Disturbance in Northern Region on 30th July 2012 India Northern, Eastern & North-Eastern Region on 31 July 2012. New Dehli, India, 2012. Available online: [http://nrpc.gov.in/wp-content/uploads/2017/11/grid\\_disturbance\\_report.pdf](http://nrpc.gov.in/wp-content/uploads/2017/11/grid_disturbance_report.pdf) (accessed on 13 February 2022).
10. Chen, J.; Mohamed, M.A.; Dampage, U.; Rezaei, M.; Salmen, S.H.; Obaid, S.A.; Annuk, A. A multi-layer security scheme for mitigating smart grid vulnerability against faults and cyber-attacks. *Appl. Sci.* **2021**, *11*, 9972.
11. Rezaei, M.; Alharbi, S.A.; Razmjoo, A.; Mohamed, M.A. Accurate location planning for a wind-powered hydrogen refueling station: Fuzzy VIKOR method. *Int. J. Hydrogen Energy* **2021**, *46*, 33360–33374.
12. Siootweg, J.G.; Kling, W.L. The impact of large scale wind power generation on power system oscillations. *Electr. Power Syst. Res.* **2003**, *67*, 9–20.
13. Sanchez-Gasca, J.J.; Miller, N.W.; Price, W.W. A modal analysis of a two-area system with significant wind power penetration. In Proceedings of the IEEE PES Power Systems Conference and Exposition, New York, NY, USA, 10–13 October 2004; Volume 2, pp. 1148–1152.
14. Hagstrøm, E.; Norheim, I.; Uhlen, K. Large-scale wind power integration in Norway and impact on damping in the Nordic grid. *Wind Energy* **2005**, *8*, 375–384.
15. Wu, F.; Zhang, X.P.; Godfrey, K.; Ju, P. Small signal stability analysis and optimal control of a wind turbine with doubly fed induction generator. *IET Gener. Transm. Distrib.* **2007**, *1*, 751–760.
16. Tsourakis, G.; Nomikos, B.M.; Vournas, C.D. Effect of wind parks with doubly fed asynchronous generators on small-signal stability. *Electr. Power Syst. Res.* **2009**, *79*, 190–200.
17. Yang, L.; Xu, Z.; Østergaard, J.; Dong, Z.Y.; Wong, K.P.; Ma, X. Oscillatory Stability and Eigenvalue Sensitivity Analysis of A DFIG Wind Turbine System. *IEEE Trans. Energy Convers.* **2011**, *26*, 328–339.
18. Li, H.; Liu, S.; Ji, H.; Yang, D.; Yang, C.; Chen, H.; Zhao, B.; Hu, Y.; Chen, Z. Damping control strategies of inter-area low-frequency oscillation for DFIG-based wind farms integrated into a power system. *Int. J. Electr. Power Energy Syst.* **2014**, *61*, 279–287.
19. Singh, M.; Allen, A.J.; Muljadi, E.; Gevorgian, V.; Zhang, Y.; Santoso, S. Interarea Oscillation Damping Controls for Wind Power Plants. *IEEE Trans. Sustain. Energy* **2015**, *6*, 967–975.
20. Effatnejad, R.; Zare, A.; Choopani, K.; Effatnejad, M. DFIG-based damping controller design to damp low frequency oscillations in power plant industry. In Proceedings of the 2016 International Conference on Industrial Informatics and Computer Systems (CIICS), Sharjah, United Arab Emirates, 13–15 March 2016.
21. Du, W.; Bi, J.; Cao, J.; Wang, H.F. A Method to Examine the Impact of Grid Connection of the DFIGs on Power System Electromechanical Oscillation Modes. *IEEE Trans. Power Syst.* **2016**, *31*, 3775–3784.
22. Li, C.; Zhang, W.; Liu, R. Forced low frequency oscillation of wind-integrated power systems. In Proceedings of the 2016 IEEE Power & Energy Society Innovative Smart Grid Technologies Conference (ISGT), Minneapolis, MN, USA, 6–9 September 2016.
23. Zhang, X.; Fu, Y.; Wang, S.; Wang, Y. Effects of two-area variable inertia on transient stabilisation in interconnected power system with DFIG-based wind turbines. *IET Renew. Power Gener.* **2017**, *11*, 696–706.
24. Liu, C.; Cai, G.; Ge, W.; Yang, D.; Liu, C.; Sun, Z. Oscillation Analysis and Wide-Area Damping Control of DFIGs for Renewable Energy Power Systems Using Line Modal Potential Energy. *IEEE Trans. Power Syst.* **2018**, *33*, 3460–3471.
25. Simon, L.; Swarup, K.S.; Ravishankar, J. Wide area oscillation damping controller for DFIG using WAMS with delay compensation. *IET Renew. Power Gener.* **2019**, *13*, 128–137.
26. Eshkaftaki, A.A.; Rabiee, A.; Kargar, A.; Boroujeni, S.T. An Applicable Method to Improve Transient and Dynamic Performance of Power System Equipped With DFIG-Based Wind Turbines. *IEEE Trans. Power Syst.* **2020**, *35*, 2351–2361.
27. Kundur, P. *Power System Stability and Control*; McGraw-Hill: New York, NY, USA, 1994.
28. Zhao, S.; Chang, X.; He, R.; Ma, Y. Borrow damping phenomena and negative damping effect of PSS control. *Proc. CSEE* **2004**, *24*, 7–11.



29. Chen, J.; Tao, J.; Mohamed, M.A.; Wang, M. An adaptive TLS-ESPRIT algorithm based on an S-G filter for analysis of low frequency oscillation in wide area measurement systems. *IEEE Access* **2019**, *7*, 47644–47654.
30. Tan, H.; Ren, Z.; Yan, W.; Wang, Q.; Mohamed, M.A. A wind power accommodation capability assessment method for multi-energy microgrids. *IEEE Trans. Sustain. Energy* **2021**, *12*, 2482–2492.



Article

# Management and Policy Modeling of the Market Using Artificial Intelligence

Qunpeng Fan

School of Management, Jilin Normal University, Siping 136000, China; qunpengfan@sina.com

**Abstract:** This paper investigates the market management and modeling based on advanced artificial intelligence. The proposed model deploys the combination of the support vector machine and fuzzy set theory to provide a practical and powerful prediction model for the market price over the next day. A realistic and effective model is then introduced to model the market players, such as the renewable energy sources of solar and wind turbines, as well as the fossil-fueled sources of micro turbines and fuel cells. In order to provide an optimal management program, it introduces a stochastic framework based on the point estimate method and adaptive grey wolf optimization algorithm (GWO). The proposed optimization methods use an adaptive strategy to choose the most fitting modification for enhancing the GWO performance. A realistic scenario is simulated to demonstrate the model's effectiveness and impression on the real market management. The results clearly show the effectiveness of the prediction and management model. The prediction results show the superiority of the proposed model by RMSE of 2.9643 compared to the 3.217 for SVR, 3.2364 for ANN and 3.0621 for the grey model. Moreover, the optimal MAPE is 2.7453 by the proposed method, which is much better than the 3.052 by SVR, 3.1552 by ANN and 2.9285 by the grey model. From point of view of optimization, the most fitting power dispatch has been attained with the total cost of 300.8632 over 24 h.

**Keywords:** market price prediction; modeling and management; optimization; renewable energy sources

**Citation:** Fan, Q. Management and Policy Modeling of the Market Using Artificial Intelligence. *Sustainability* **2022**, *14*, 8503. <https://doi.org/10.3390/su14148503>

Academic Editor: Mohamed A. Mohamed

Received: 7 May 2022

Accepted: 23 June 2022

Published: 11 July 2022



**Copyright:** © 2022 by the author. Licensee MDPI, Basel, Switzerland. This article is an open access article distributed under the terms and conditions of the Creative Commons Attribution (CC BY) license (<https://creativecommons.org/licenses/by/4.0/>).

## 1. Introduction

The introduction of the electricity and energy, also called power, market is a system which makes power purchasing and sales possible through bids to offer [1,2]. In this way, the demand and supply regulations are deployed for clearing the market and setting the price. The market price idea would provide a competitive environment in which electricity consumers can play a more active role in deciding what to buy and how much to pay [3–5]. Therefore, it is clear that the price of energy would be a motivating term that would increase demand if preserved low enough [6,7]. It is proved that the power market can support the social welfare of the system by decreasing the power price and letting the cheap generation players produce more power than the expensive units [8–10]. Therefore, the analysis and modeling of the market is a very critical and significant task, which requires special work and focus to enhance it [11]. Figure 1 shows the way that the market is cleared and its point of common, called MCP, is determined as a tradeoff between demand and supply. One of the most significant issues for the consumer is the estimation or prediction of the next day's market price for making clear policies and strategies. In recent years, much research has been implemented, a list of which is described in the rest of the introduction.

In [12], the market price is forecasted using a hybrid generative adversarial network model and the results are compared with the some of the most well-known algorithms in the field. It is shown in [13] that the market price and market demand both have high nonlinearity and non-stationary characteristics which, if combined with seasonality, would create a big problem for accurate prediction. In [14], a heuristic flower pollination approach is introduced in conjunction with machine learning to boost the prediction of the market

price accuracy. The proposed model considers the feature selection based on a hybrid regression model. In [15], authors assess the impact of renewable units on the market price and forecasting accuracy. A novel bootstrap gradient-based architecture is deployed for the short-term market price forecasting. In [16], a two-step market price forecasting tool is developed which uses deep learning with a loss function. The loss function would penalize any loss of spike in the price and thus some oversampling might be seen. Through the spike calibration approach, the prediction accuracy is improved in the market. The Brazil market price during the years 1998 to 2004 is assessed in [17]. It proposes a theoretical formulation based on Markov, switching to predict the market price and showing how a generator entry might be affected. In [18], the generator output power is forecasted to be an indirect way for estimating the market price. It uses machine learning models and probability sampling for analyzing the Italian electricity market. It is claimed that the proposed method does need to access all market transactions. In [19], the market price over the years January 2017–March 2020 are analyzed to forecast the price. It is shown in their research that the dominant retailers can play a critical role in controlling the market price and its growth over the year. In [20], a hybrid Bayesian extreme learning and minimum redundancy are combined to forecast the market price based on the sequence segmentation. Two market price datasets from Ontario, Canada and New York are used to check the accuracy of the proposed model hourly. The authors in [21] try to address the weather effects on market behavior, including on demand and supply, using the fractional Brownian motion. A temperature based stochastic prediction model is developed which can help much to control the market fluctuations.

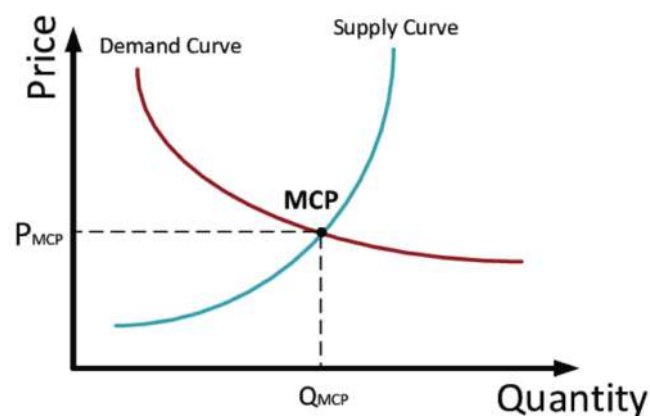


**Figure 1.** The market clearing price and the way it is determined.

According to the above explanations, it is well perceived that market modeling and analysis, especially prediction of the market price, are significant tasks which can benefit both the customers and the suppliers. This paper tries to provide market management and prediction based on artificial intelligence (AI) [22]. The proposed AI model uses support vector regression (SVR) [23] to avoid the possible overfitting concerns. It also suggests the fuzzy set theory to find a way for adjusting the kernel function parameters. In addition, the market price is then used as an input to a smart market, including several renewable or fossil fuel-based generators. An objective function is introduced to manage the power suppliers and minimize the cost of generation. Considering the very complex and nonlinear fluctuations in the market price, we need to make use of a novel smart optimization algorithm based on grey wolf optimization (GWO). It is a heuristic optimization method which has shown great abilities over the other algorithms in the literature [24,25]. Therefore, the main contributions of the paper can be shown as below:

- Proposing a fuzzy SVR-based prediction model for the market price
- Introducing a novel optimization algorithm called modified GWO for the optimal scheduling of units in an economic way

- Providing a comprehensive comparison with the most well-known algorithms in the area such ANN, Grey model, SVR, GA, PSO and original GWO

The analysis is implemented in a physical scenario to determine the effectiveness and influence of the proposed model. The simulation results obviously advocate the capabilities of the proposed prediction and management models.

The paper follows a structure organized as follows: Section 2 describes the fuzzy SVR for prediction of the market price. Section 3 describes the market model based on renewable sources and players. In Section 3, the GWO algorithm is explained in detail. Simulation results are then discussed in Section 4. At the end, the main conclusions are summarized.

## 2. Fuzzy Support Vector Regression

This section proposes a fuzzy support vector machine approach to forecast the electricity market price over the next day. The original idea of support vector machine is rooted in the nonlinear intrinsic structure of the dataset, which forces us to provide a tool for handling this nonlinearity. In this way, a support vector is able to assign a linear function on the nonlinear problem in a higher dimension. To describes this method, the sample points are shown by  $\{(x_i, y_i)\}^M$ , wherein  $M$  represents the size of the sample. In order to make a nonlinear mapping in the higher dimension,  $\Lambda(\cdot)$  is considered to form the input limited dimension to the output space with high dimension as  $\Lambda(\cdot) : \mathbb{R}^n \rightarrow \mathbb{R}^{n_h}$ . This is the core idea of the SVR, which has made it a popular and successful method in machine learning. Figure 2 shows this idea from 2D to 3D conversion. As shown in Figure 2, a nonlinear relationship which is not detectable in 2D can be easily separated by a linear function in a 3D space. The linear function, also called the SVR function, may be formulated as below:

$$f(x) = W^T \Lambda(x) + b \quad (1)$$

In the above equation, the symbols  $W$  ( $W \in \mathbb{R}^{n_h}$ ) and  $b$  ( $b \in \mathbb{R}$ ) are the model coefficients, which, if adjusted well, make the final model trustable. The training process is through optimizing the error between the real data  $W^T \Lambda(x) + b$  and the simulated data  $y$  as below:

$$R_{SVR} = \frac{1}{M} \sum_{i=1}^M E_{\epsilon}(y_i, W^T \Lambda(x_i) + b) \quad (2)$$

In this equation,  $E_{\epsilon}(y_i, f(x_i))$  plays the role of the  $\epsilon$ -insensitive loss function that is interpreted as below:

$$E_{\epsilon}(y, f(x)) = \begin{cases} |f(x) - y| - \epsilon; & |f(x) - y| \geq \epsilon \\ 0; & \text{Else} \end{cases} \quad (3)$$

Other than the training error, the SVR minimizes the structural complexity, which is shown by multiplication of weighting factors, as below:

$$\text{Min}_{W, b, \zeta^*, \zeta} R_{\epsilon}(W, \zeta^*, \zeta) = \frac{1}{2} W^T W + C \sum_{i=1}^M (\zeta_i^* + \zeta_i) \quad (4)$$

The first item in this formulation represents the model structure's complexity, which, if it becomes too high, the overfitting problem appears. In addition, the parameter  $C$  is the constant value employed in the model structure for balancing between the error and complexity. The variables  $\zeta_i^* / \zeta_i$  are errors below or above the allowed values of  $-\epsilon$  and

+  $\varepsilon$ , respectively. The dual format of the objective function in the new structure may be represented by (5), which is solvable linearly:

$$\begin{aligned} y_i - W^T \Lambda(x_i) - b &\leq \varepsilon + \xi_i^*; & i = 1, \dots, M \\ -y_i + W^T \Lambda(x_i) + b &\leq \varepsilon + \xi_i; & i = 1, \dots, M \\ \xi_i^* &\geq 0; & i = 1, \dots, M \\ \xi_i &\geq 0; & i = 1, \dots, M \end{aligned} \quad (5)$$

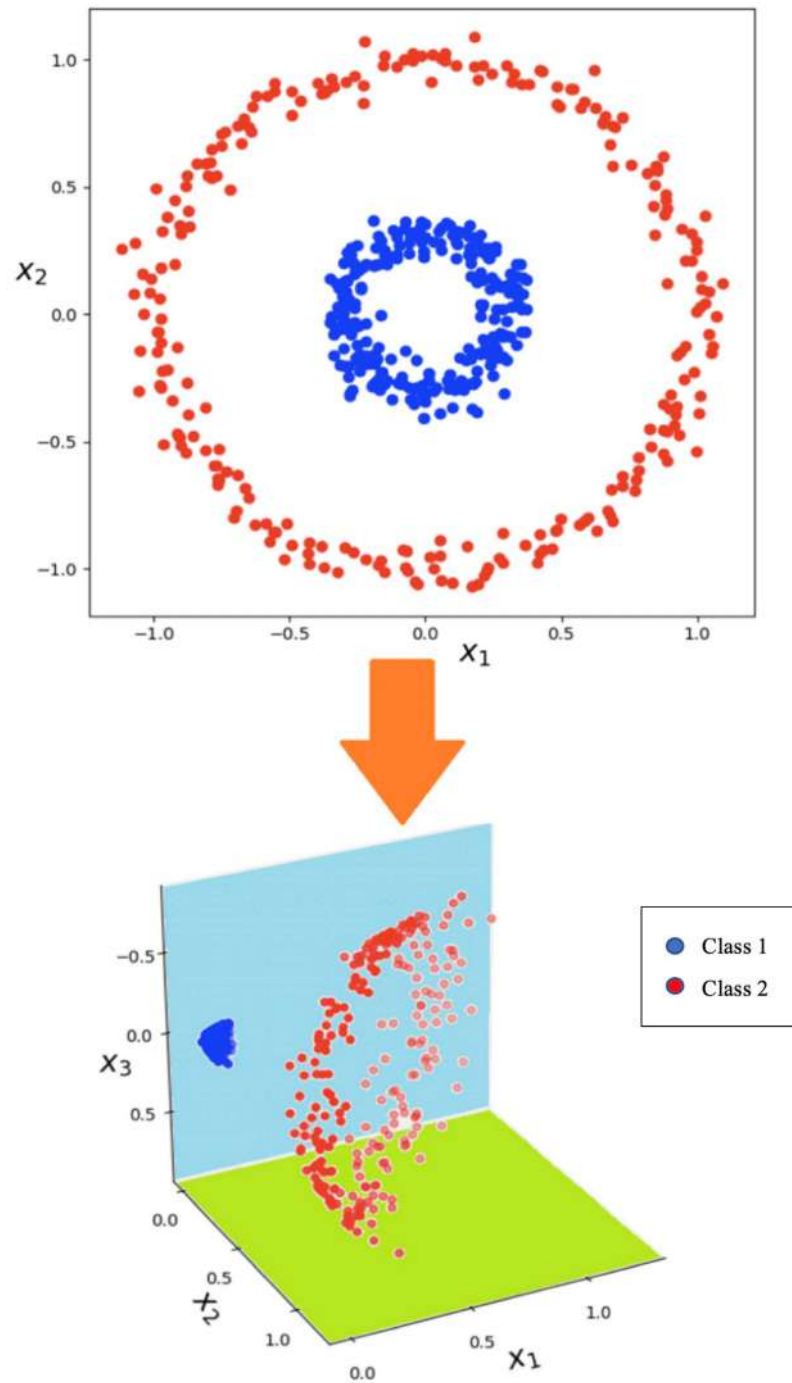


**Figure 2.** The higher dimension concept in the SVR.

A linear solution of the above equation would easily determine the optimal value of the weight factor, as below:

$$W = \sum_{i=1}^M (\beta_i^* - \beta_i) \Lambda(x_i) \quad (6)$$

In this model, the new parameters  $\beta_i^*$  and  $\beta_i$  are called the Lagrangian multipliers. Deploying  $\beta_i^*$  and  $\beta_i$  provides the dual format of the model, as below:

$$f(x) = \sum_{i=1}^M (\beta_i^* - \beta_i) K(x_i, x) + b \quad (7)$$

$$K(x_i, x) = \Lambda(x_i)^\circ \Lambda(x_j) \quad (8)$$

In (8), the term  $K(x_i, x)$  is named a kernel function. Theoretically, the kernel function meets Mercer's condition [26].

A significant point is that the kernel function can much help the mapping process, due to its role in the connection of the input and output in the dataset. Fundamentally, the kernel function is computed by the inner multiplication of  $\varphi(x_i)$  and  $\varphi(x_j)$ . There are different types of kernels, such as the Gaussian or RBF, which can be used. This article proposes a fuzzy model for the kernel function, which can enhance the model performance by suitably adjusting the fuzzy membership function. Figure 3 shows the trapezoidal fuzzy function considered as the kernel function in our model. The input feature of the function is the same as the kernel function in (7). The way that the output is determined instead can help us much in finding a better nonlinear mapping.

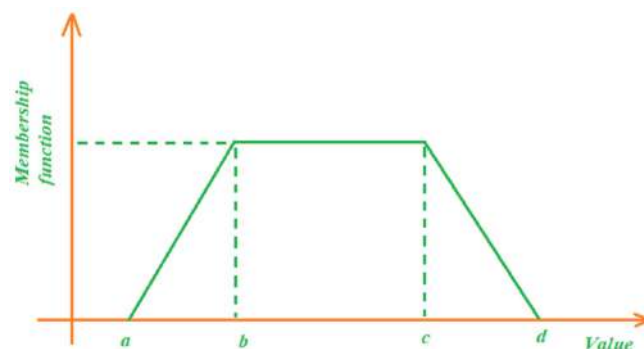


Figure 3. Fuzzy membership function used as the kernel function.

### 3. Market Economic Problem Formulation

In this section, an economic model is developed for the market players, including the consumers (loads) and generators (renewable and non-renewable sources), to make sure that the analysis can mitigate the total cost which is beneficial to both players. In order to model the market players, we first try to give a cost function which focuses on the cost of generation by the private generators, utility and battery storage. Therefore, we have considered the two renewable sources of wind turbines and solar units, and two other dispatchable units, i.e., micro turbines and fuel cells. The main goal is that the total power generation would cost the customers less based on the market hourly price. Therefore, the cost function is formulated as in (9), where the first term is the generators' power cost, the second term is the cost of On/OFF, the third term is the storage cost and the last term is the utility cost:

$$\begin{aligned} \text{Min } f(X) = \sum_{t=1}^T \text{Cost}^t = \sum_{t=1}^T \{ & \sum_{i=1}^{N_g} [u_i(t) p_{Gi}(t) B_{Gi}(t) + D_{Gi} \times \\ & \max(0, u_i(t-1) - u_i(t)) + \sum_{j=1}^{N_s} [u_j(t) p_{sj}(t) B_{sj}(t)] \\ & + p_{Grid}(t) B_{Grid}(t)] \} \end{aligned} \quad (9)$$

where  $T$  shows the time interval length (here 24 h),  $N_g$  shows the number of generators,  $u_i(t)$  is the status of a generator,  $p_{Gi}(t)$  is the generator power output,  $B_{Gi}(t)$  is the bidding of the generator,  $D_{Gi}$  is the On/Off switching cost,  $N_s$  is the number of storages,  $u_j(t)$  is storage status,  $p_{sj}(t)$  is the storage power value,  $B_{sj}(t)$  is the storage power price,  $p_{Grid}(t)$  is the main utility power value, and  $B_{Grid}(t)$  is the grid price.

The control vector which is used for optimizing (9) contains some terms, as below:

$$\begin{aligned} X &= [P_g, U_g]_{1 \times 2nT}; \\ P_g &= [P_G, P_s]; n = N_g + N_s + 1 \\ P_G &= [P_{G,1}, P_{G,2}, \dots, P_{G,N_g}]; \\ P_s &= [P_{s,1}, P_{s,2}, \dots, P_{s,N_s}] \\ P_{G,i} &= [P_{G,i}(1), P_{G,i}(2), \dots, P_{G,i}(T)]; i = 1, 2, \dots, N_g + 1 \\ P_{s,j} &= [P_{s,j}(1), P_{s,j}(2), \dots, P_{s,j}(T)]; j = 1, 2, \dots, N_s \\ U_g &= [u_1, u_2, \dots, u_n], \\ u_k &\in \{0, 1\} \\ u_k &= [u_k(1), u_k(2), \dots, u_k(T)]; k = 1, 2, \dots, n \end{aligned} \quad (10)$$

where  $P_G$  is the generator output power and  $P_s$  is the storage output power.

The above cost function is optimized by meeting some operation limits which are explained in detail. Each of the limits is explained here:

- (1) the total demand should be provided by the generators and storage, and the utility as active suppliers, to clear the market, as below:

$$\sum_{i=1}^{N_g} P_{G,i}(t) + \sum_{j=1}^{N_s} P_{s,j}(t) + P_{Grid}(t) = \sum_{l=1}^{N_L} P_{L,l}(t) \quad (11)$$

In the above,  $P_{L,l}(t)$  is the load demand at time  $t$  and  $N_L$  is the number of load levels in the system.

- (2) each dispatchable generator or unit is allowed to produce in its limited range, as below:

$$\begin{aligned} P_{Gi,\min}(t) &\leq P_{Gi}(t) \leq P_{Gi,\max}(t) \\ P_{grid,\min}(t) &\leq P_{Grid}(t) \leq P_{grid,\max}(t) \\ P_{sj,\min}(t) &\leq P_{sj}(t) \leq P_{sj,\max}(t) \end{aligned} \quad (12)$$

In (12), the min/max indices technically show the least and highest possible values.

- (3) The battery storage can only charge/discharge according to its limited charging and discharging rate, as well as the energy storage limit:

$$\Delta_{ess}(t) = \Delta_{ess}(t-1) + \eta_{charge} P_{charge} - \frac{1}{\eta_{discharge}} P_{discharge} \quad (13)$$

$$\begin{cases} \Delta_{ess,\min} \leq \Delta_{ess}(t) \leq \Delta_{ess,\max} \\ P_{charge}(t) \leq P_{charge,\max} \\ P_{discharge}(t) \leq P_{discharge,\max} \end{cases} \quad (14)$$

where  $\Delta_{ess}(t)$  is the energy stored at time  $t$ ,  $\eta_{charge}$  is the charging efficiency,  $\eta_{discharge}$  is the discharging efficiency,  $P_{charge}$  is the charging power and  $P_{discharge}$  is the discharging value.

#### 4. Adaptive Grey Wolf Optimization Method

In order to solve the problem formulation described in the last section, we need to make use of a suitable and reliable optimization algorithm. This paper proposes an adaptive grey wolf optimization (AGWO) to make sure that the optimization success is guaranteed. The original GWO is a heuristic method which uses the evolutionary habit of wolves in hunting prey. The GWO is a newly introduced algorithm which has some key features which make it a very powerful optimizer for nonlinear problems. Some of the main features

of GWO include: being a simple concept, ease of implementation, powerful local search operators, providing an appropriate balance between local and global searches, and its sub-division ability. These animals live in a group and try to make use of the experience of leaders to make the hunt a successful process. Meanwhile, the leaders can consult with each other to obtain the most promising solution. Other than that, the leaders in some circumstances listen to the wolves to make sure that the maximum efficiency is attained. This shows a low level of democracy, which can boost the optimization process. The main leader of the group is called alpha  $\alpha$ . This is the wolf with the smartest decisions in hunting. The next dominant wolf is called beta  $\beta$ , which can play the role of a leader for the group in the absence of  $\alpha$ . Moreover, in the presence of  $\alpha$ , beta can help him through consultation. In each group, the wolf with the least quality is called omega  $\omega$ , which are assumed to be workers and need to obey the leader. The remaining wolf members in the group are called delta  $\delta$ . Figure 4 provides a simple diagram showing the position of these members in the GWO.

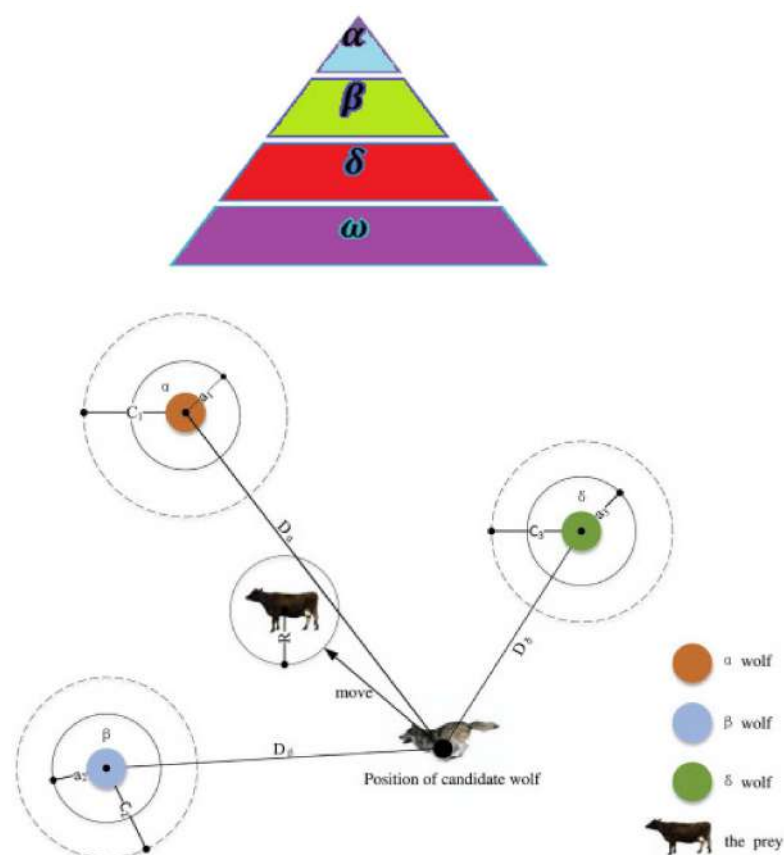


**Figure 4.** GWO algorithm structure and concept.

In order to mathematically formulate the idea of grey wolf hunting, we first produce the group of wolves, control vector, in a matrix. After calculating the cost objective for them, the population is sorted in a downward order and the alpha, beta, delta and omega members are determined. In the improvisation stage, the wolves hunt a prey which is simulated in a circle with dimension:

$$D = |\vartheta_1 \times X_p(k) - X(k)| \quad (15)$$

where  $\vartheta_1$  is a random coefficient,  $k$  shows the epoch number and  $X_p$  is the prey position. The position of each wolf is updated according to (15) as below:

$$X(k+1) = \frac{1}{3} \sum_{p=\alpha, \beta, \delta} (X_p(k) - \vartheta_2 \times D_p) \quad (16)$$

where  $\vartheta_1$  is a random coefficient. The GWO suggests to update the coefficients  $\vartheta_1$  and  $\vartheta_2$  in a recursive way. Therefore, it suggests a recursive formulation to update it, as below:

$$\vartheta_1 = 2a\lambda_1 - a \quad (17)$$

$$\vartheta_2 = 2a\lambda_2 \quad (18)$$

$$a = 2 - 2(k/k_{\max}) \quad (19)$$

$$\lambda_1 \& \lambda_2 = rand \quad (20)$$

In the above equations, the parameter  $a$  is a decreasing value in the domain  $(0,2)$ . More explanations on the original GWO can be found in [19,20].

This paper proposes an adaptive formulation to enhance the search process in the GWO. The adaptive mechanism can choose the best modification in an iteration according to its success. First, the modifications are explained:

- Modification 1: This modification uses an exchange mechanism to combine two optimal solutions in the genes (like GA) in each vector randomly. Each grey wolf would attend this operator and exchange data with the leader alpha  $X_\alpha$ :

$$x_{i,j}^{new} = \begin{cases} x_{\alpha,j}; & \vartheta_3 < \vartheta_4 \\ x_{i,j}^{rand}; & \vartheta_3 > \vartheta_4 \end{cases} \quad (21)$$

$$X_\alpha = [x_{\alpha,1}, \dots, x_{\alpha,d}]$$

$$X_i^{rand} = [x_{i,1}^{rand}, \dots, x_{i,d}^{rand}]$$

where  $\vartheta_3/\vartheta_4$  are random variables in the range  $(0,1)$ .

- Modification 2: This modification would try to enhance the mean of the grey wolf population using a motivating operator as below:

$$X_i^{new} = X_i^{old} + L_F(X_\alpha - X_\beta) \quad (22)$$

where  $L_F$  is an integer value of either 1 or 2.

Each grey wolf is allowed to pick one of these two modifications which best fits its situation. The probability of success for each modification is determined by an  $n$  index called  $Prb_\theta = 0.5$  &  $\theta = 1,2$ . Moreover, a storage is considered whose value is zero at the beginning, but as time passes, it is updated as below:

$$Acum_\theta = Acum_\theta + \frac{\kappa_l}{n_{Mod_\theta}} l = 1, \dots, n_{Mod_\theta} \quad (23)$$

$$\kappa_j = \frac{\log(N-j+1)}{\sum_{i=1}^n \log(i)}; j = 1, \dots, N \quad (24)$$

In the above,  $\kappa_j$  is the weight each solution  $X_j$  and  $N$  is the size of the population. The probability of any modification method is updated as below:

$$Prb_\theta = (1 - \varepsilon) \times Prb_\theta + \varepsilon \times \frac{Acum_\theta}{k}, (\theta = 1,2) \quad (25)$$



where  $\varepsilon$  is a constant value for balancing the two modifications. In the last step, the  $Prb_\theta$  is normalized as follows:

$$Prb_\theta = \frac{Prb_\theta}{\left( \sum_{\theta=1}^2 Prb_\theta \right)} \quad (26)$$

## 5. Simulation Results

In this section, a test system is used for examining the proposed model. The test system structure is shown in Figure 5. As is seen here, there is a wind turbine, a fuel cell, a micro turbine and a solar panel installed in the system as the generators. In addition, battery is considered to play the role of an active player as ancillary services. The utility, also as a big supplier, can attend the market and sell its power. The total power generation of the wind and solar units are plotted in Figures 6 and 7, respectively. Furthermore, the market demand is considered as shown in Figure 8. It is worth noting that this demand can also be predicted, but since the paper's focus is on the market price, it is ignored in this research, though the solution procedure is the same.

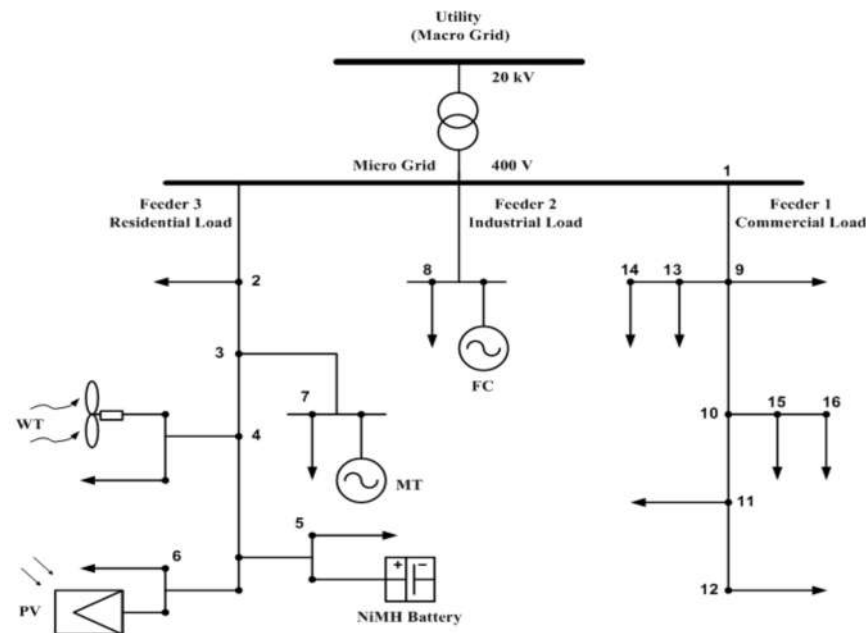


Figure 5. Single line diagram of the MG test system [27].

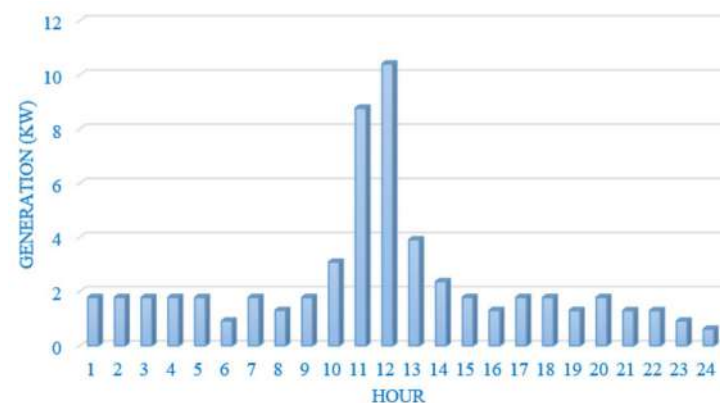
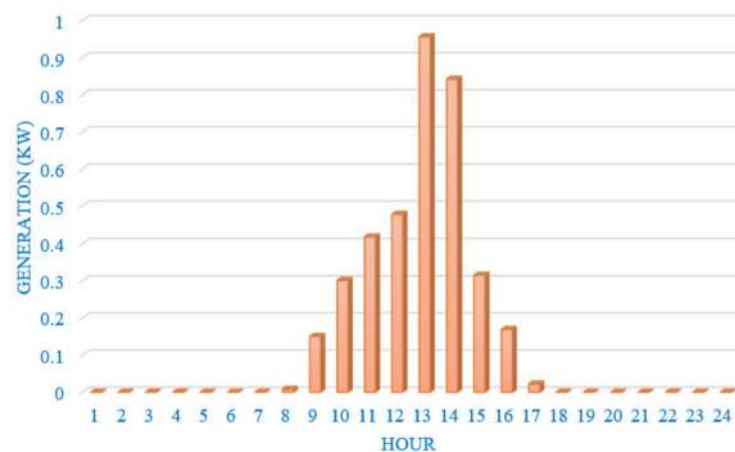
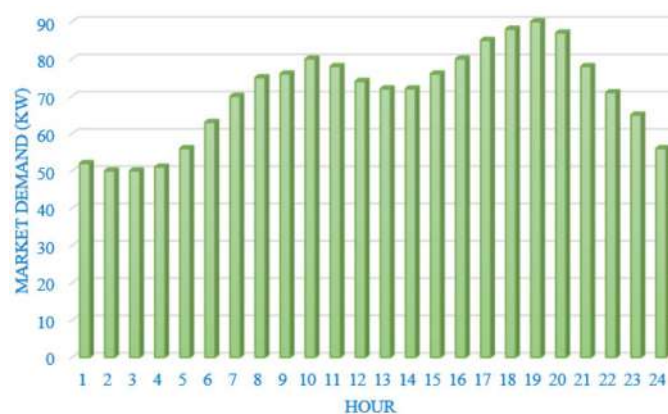


Figure 6. Wind turbine output power.



**Figure 7.** Solar panel output power.



**Figure 8.** Market demand production.

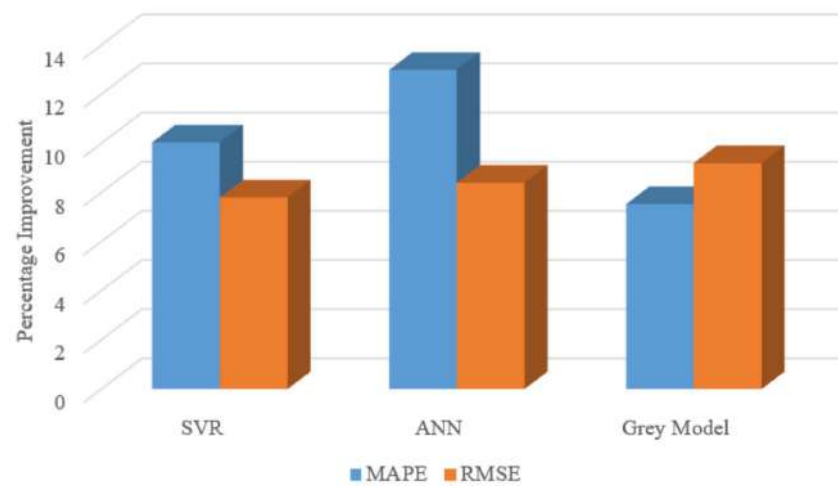
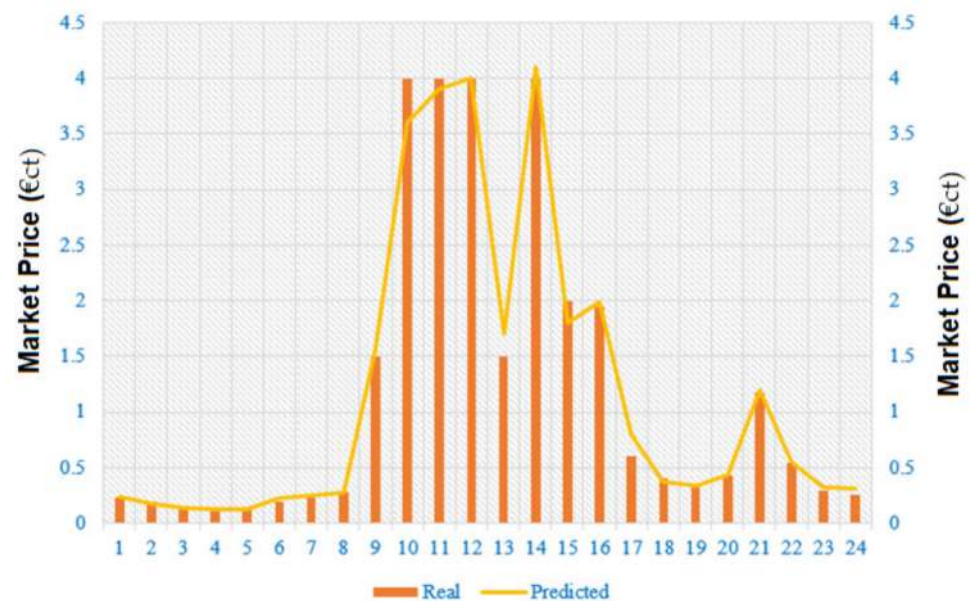
Table 1 summarizes the test system data, including the capacity and prices of each generator. In order to show first the accuracy of the proposed prediction model for market price forecasting, the historical data over a year of Tehran Electricity market are considered as the benchmark [28]. The recorded data include the hourly market price over 480 h in 2018, from which 90% is used as the training set, 5% as the validation set and 5% as the test set. Therefore, we consider the next 24 h as the prediction time horizon. The comparisons are made according to MAPE and RMSE, as described in [29]. For the sake of simplicity, the formulations are not provided here but can be found in [29]. Table 2 shows the prediction results using the proposed fuzzy SVR (FSVR), the original support vector machine, artificial neural network (ANN) and the grey model. As can be seen in this table, the proposed FSVR shows a higher training result, as reflected in the MAPE and RMSE. The proposed model could enhance the RMSE rather than the SVR, ANN and grey model by 7.8%, 8.4% and 9.2%, respectively. A complete comparison is provided in Figure 9. Almost similar improvements can be seen for the MAPE. The same conclusion might be made for the RMSE, of which the low value shows the very high robustness. Figure 10 shows the forecast curve plotted in the same figure with the real data. The appropriate accuracy can be deduced from the following nature of the forecast signal that can be seen here.

**Table 1.** Data of the test system.

Type	Min Power (kW)	Max Power (kW)	Offer (EUR/kWh)	Start-Up/Shut-Down Cost (EURct)
Micro turbine	6	30	0.457	0.96
Fuel cell	3	30	0.294	1.65
Solar unit	0	25	2.584	0
Wind unit	0	15	1.073	0
Battery	−30	30	0.38	0
Utility	−30	30	-	-

**Table 2.** The results of prediction by the fuzzy SVR for the market price.

Type	Grey Model	ANN	SVR	FSVR
MAPE	2.9285	3.1552	3.052	2.7453
RMSE	3.0621	3.2364	3.217	2.9643

**Figure 9.** The percentage improvement made by the proposed prediction model compared to SVR, ANN and Grey model.**Figure 10.** Forecast market price value versus real data.

Considering the market price, as shown in Figure 10, the cost minimization problem is solved using the AGWO algorithm. It is assumed that the battery has an initial charge of zero. The optimal scheduling is for 24 h (a full day). However, in order to see the search ability of the algorithm, the optimization process is repeated 25 times. Through this repetition, the best solution, the average of the optimal solutions and standard deviation values, would be achieved. This is a well-defined approach for assessing the stability of the algorithm. The simulation results are repeated 25 times and the final results are provided in Table 3. Accordingly, it is seen here that the proposed algorithm has discovered a more optimal solution than the other algorithms. The performance of the proposed algorithm is compared with the PSO, GA, FSAPSO and original GWO, and the results clearly show the superiority of the algorithm. Not only the best solution, but also the worst solution and standard deviation values, are still optimal compared with the other algorithms. These results show the robustness of the algorithm. The very time saving nature of the AGWO may be deduced from the last column, showing the CPU time. This is especially important if the operation time interval is reduced in the management (such as to 10 min or less). The results evidently reveal the high quality and search features of the algorithm for solving the problem. The optimal power generation and charging values of each unit is plotted as a bar diagram in Figure 11. According to this bar diagram, the battery is trying charge during the first hours and discharge during the mid-hour times. Moreover, the fuel cell, as a cheap unit, is attending with the maximum capacity. The utility is changing to a buyer of the power at the middle of the day to let the market increase its profit. The renewable wind and solar energy sources are also producing as forecasted in their initial power curves.

**Table 3.** Simulation results of optimizing cost function over 25 times.

Method	Best Solution (EURct)	Worst Solution (EURct)	Standard Deviation (EURct)	CPU Time (s)
GA [27]	335.0707	345.4849	20.9302	17.451
PSO [27]	329.4922	341.9583	15.2483	16.263
FSAPSO [27]	328.6594	336.5502	12.8409	15.685
GWO	320.3640	334.3312	8.84420	16.862
AGWO	300.8632	305.8774	0.75270	9.1673

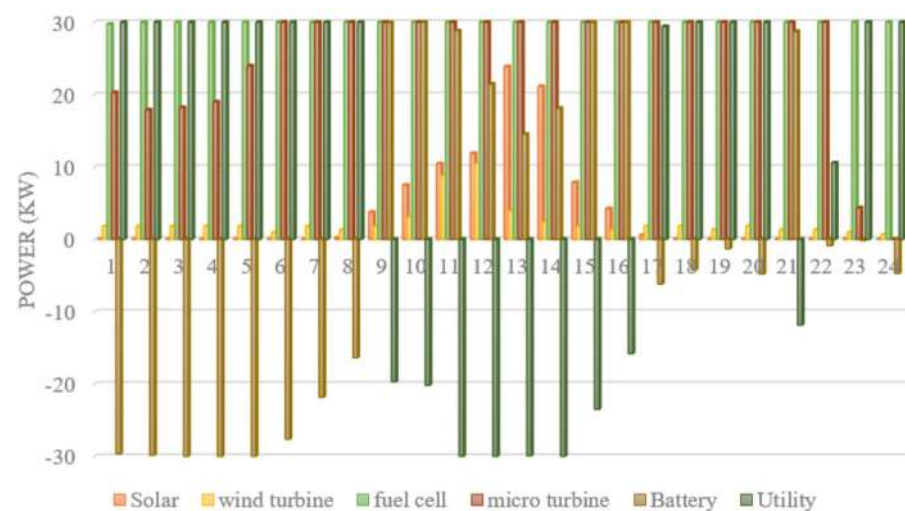


**Figure 11.** Output Power of RESs evaluated by the proposed method.

## 6. Conclusions

The focus of this work is to study market management and modeling based on AI. The proposed model uses the fuzzy-based SVR for the prediction of the market price with high accuracy. A management model based on cost minimization and unit dispatch is

developed in the study, which can help scheduling the units. A novel adaptive-modified GWO is also devised which can help to minimize the operation cost over the next 24 h. The adaptive formulation is such that it allows the algorithm to choose the best modification according to its success rate and probability. The simulation results show that the proposed model has an appropriate performance for market price prediction with low MAPE and RMSE. Furthermore, it is seen that the test system model can suitably optimize the total cost of operations, including the solar and wind renewable energy sources, as well as the fossil fuel-based models, such as fuel cell, micro turbine and battery. The AGWO's superiority over the set of algorithms is well proved.

**Funding:** This research received no external funding.

**Institutional Review Board Statement:** Not applicable.

**Informed Consent Statement:** Not applicable.

**Data Availability Statement:** This study did not report any data.

**Conflicts of Interest:** The authors declare no conflict of interest.

## References

1. Mohamed, M.A.; Mirjalili, S.; Dampage, U.; Salmen, S.H.; Al Obaid, S.; Annuk, A. A Cost-Efficient-Based Cooperative Allocation of Mining Devices and Renewable Resources Enhancing Blockchain Architecture. *Sustainability* **2021**, *13*, 10382. [CrossRef]
2. Zeng, L.; Xia, T.; Elsayed, S.; Ahmed, M.; Rezaei, M.; Jermisittiparsert, K.; Dampage, U.; Mohamed, M. A Novel Machine Learning-Based Framework for Optimal and Secure Operation of Static VAR Compensators in EAFs. *Sustainability* **2021**, *13*, 5777. [CrossRef]
3. Abera, T.; Dereje, F.; Larago, B. Mobile Backhaul in Release 8 and Beyond: Benefits, Challenges, Market Status and Impact Analysis. *Int. J. Wirel. Microw. Technol.* **2020**, *10*, 9–15. [CrossRef]
4. Beni, S.A.; Sheikh-El-Eslami, M.K. Market power assessment in electricity markets based on social network analysis. *Comput. Electr. Eng.* **2021**, *94*, 107302. [CrossRef]
5. Yildirim, C.; Kasman, A.; Hamid, F.S. Impact of foreign ownership on market power: Do regional banks behave differently in ASEAN countries? *Econ. Model.* **2021**, *105*, 105654. [CrossRef]
6. Kamala, H. Development of an Effective Method of Data Collection for Advertising and Marketing on the Internet. *Int. J. Math. Sci. Comput.* **2021**, *7*, 1–11. [CrossRef]
7. Hossain, M.A.; Pota, H.R.; Squartini, S.; Abdou, A.F. Modified PSO algorithm for real-time energy management in grid-connected microgrids. *Renew. Energy* **2019**, *136*, 746–757. [CrossRef]
8. Rizwan, M.; Waseem, M.; Liaqat, R.; Sajjad, I.A.; Dampage, U.; Salmen, S.H.; Obaid, S.A.; Mohamed, M.A.; Annuk, A. SPSO Based Optimal Integration of DGs in Local Distribution Systems under Extreme Load Growth for Smart Cities. *Electronics* **2021**, *10*, 2542. [CrossRef]
9. Bui, V.-H.; Hussain, A.; Kim, H.-M. A Multiagent-Based Hierarchical Energy Management Strategy for Multi-Microgrids Considering Adjustable Power and Demand Response. *IEEE Trans. Smart Grid* **2018**, *9*, 1323–1333. [CrossRef]
10. Fan, W.; Huang, L.; Cong, B.; Tan, Z.; Xing, T. Research on an optimization model for wind power and thermal power participating in two-level power market transactions. *Int. J. Electr. Power Energy Syst.* **2021**, *134*, 107423. [CrossRef]
11. Liu, Y.-W.; Li, L.-L.; Tseng, M.-L.; Lim, M.K.; Helmi Ali, M. Optimal scheduling of combined cooling, heating, and power microgrid based on a hybrid gray wolf optimizer. *J. Ind. Prod. Eng.* **2022**, *39*, 277–292. [CrossRef]
12. Mahedy, A.; Abdelsalam, A.; Mohamed, R.; El-Nahry, I. Utilizing Neural Networks for Stocks Prices Prediction in Stocks Markets. *Int. J. Inf. Technol. Comput. Sci.* **2020**, *12*, 1–7. [CrossRef]
13. Amjady, N.; Daraeepour, A. Mixed price and load forecasting of electricity markets by a new iterative prediction method. *Electr. Power Syst. Res.* **2009**, *79*, 1329–1336. [CrossRef]
14. Sahoo, S.; Swain, S.; Subburaj, V. Novel Gaussian flower pollination algorithm with IoT for unit price prediction in peer-to-peer energy trading market. *Energy Rep.* **2021**, *7*, 8265–8276. [CrossRef]
15. Bhatia, K.; Mittal, R.; Tripathi, M.M. An ensemble approach for electricity price forecasting in markets with renewable energy resources. *Util. Policy* **2021**, *70*, 101185. [CrossRef]
16. Shi, W.; Wang, Y.; Ma, J. An effective Two-Stage Electricity Price forecasting scheme. *Electr. Power Syst. Res.* **2021**, *199*, 107416. [CrossRef]
17. Daglish, T.; de Bragança, G.G.F.; Romano, T. Pricing effects of the electricity market reform in Brazil. *Energy Econ.* **2021**, *97*, 105197. [CrossRef]
18. Flammini, M.G.; Pretico, G.; Chicco, G. Reducing fossil fuel-based generation: Impact on wholesale electricity market prices in the North-Italy bidding zone. *Electr. Power Syst. Res.* **2021**, *194*, 107095. [CrossRef]

19. Correa-Giraldo, M.; Garcia-Rendon, J.J.; Perez, A. Strategic behaviors and transfer of wholesale costs to retail prices in the electricity market: Evidence from Colombia. *Energy Econ.* **2021**, *99*, 105276. [CrossRef]
20. Shao, Z.; Zheng, Q.; Liu, C. Modeling and forecasting the electricity clearing price: A novel BELM based pattern classification framework and a comparative analytic study on multi-layer BELM and LSTM. *Energy Econ.* **2020**, *86*, 104648. [CrossRef]
21. Prabakaran, S.; Garcia, I.C.; Mora, J.U. A temperature stochastic model for option pricing and its impacts on the electricity market. *Econ. Anal. Policy* **2020**, *68*, 58–77. [CrossRef]
22. Prasenjit, C.; Banerjee, I.; Rahaman, H. Load management scheme for energy holes reduction in wireless sensor networks. *Comput. Electr. Eng.* **2015**, *48*, 343–357.
23. Xiang, Z.; Cao, J.; Guo, Q.; Wen, T. A novel network security algorithm based on improved support vector machine from smart city perspective. *Comput. Electr. Eng.* **2018**, *65*, 67–78.
24. Liu, M.; Luo, K.; Chen, S. A stock selection algorithm hybridizing grey wolf optimizer and support vector regression. *Expert Syst. Appl.* **2021**, *179*, 115078. [CrossRef]
25. Khalid, A.; Annuk, A.; Dampage, U.; Mohamed, M.A. Effective Energy Management via False Data Detection Scheme for the Interconnected Smart Energy Hub–Microgrid System under Stochastic Framework. *Sustainability* **2021**, *13*, 11836.
26. Figuera, C.; Barquero-Pérez, Ó.; Caamaño, A.J. Spectrally adapted Mercer kernels for support vector nonuniform interpolation. *Signal Process.* **2014**, *94*, 421–433. [CrossRef]
27. Baziar, A.; Kavousi-Fard, A. Considering uncertainty in the optimal energy management of renewable micro-grids including storage devices. *Renew. Energy* **2013**, *59*, 158–166. [CrossRef]
28. IREMA Website. Available online: <https://www.irema.ir/market-data/statistical-report/daily-data/price/average> (accessed on 30 March 2021).
29. Kavousifard, A.; Samet, H. A novel method based on modified shuffled frog leaping algorithm and artificial neural network for power system load prediction. *Emerg. Intell. Technol. Ind.* **2012**, *369*, 35–46.

## Article

# Parameters Identification of Photovoltaic Cell and Module Models Using Modified Social Group Optimization Algorithm

Habib Kraiem <sup>1,2,\*</sup>, Ezzeddine Touti <sup>1,3,\*</sup>, Abdulaziz Alanazi <sup>1</sup>, Ahmed M. Agwa <sup>1,4</sup>, Tarek I. Alanazi <sup>5</sup>, Mohamed Jamli <sup>3</sup> and Lassaad Sbita <sup>2</sup>

<sup>1</sup> Department of Electrical Engineering, College of Engineering, Northern Border University, Arar 73222, Saudi Arabia

<sup>2</sup> Processes, Energy, Environment and Electrical Systems, National Engineering School of Gabes, University of Gabes, Gabes 6029, Tunisia

<sup>3</sup> Laboratory of Industrial Systems and Renewable Energies, National Higher Engineering School of Tunis, Tunis 1008, Tunisia

<sup>4</sup> Department of Electrical Engineering, Faculty of Engineering, Al-Azhar University, Cairo 11651, Egypt

<sup>5</sup> Department of Physics, College of Science, Northern Border University, Arar 73222, Saudi Arabia

\* Correspondence: alhabeeb.kareem@nbu.edu.sa (H.K.); esseddine.touti@nbu.edu.sa (E.T.)

**Abstract:** Photovoltaic systems have become more attractive alternatives to be integrated into electrical power systems. Therefore, PV cells have gained immense interest in studies related to their operation. A photovoltaic module's performance can be optimized by identifying the parameters of a photovoltaic cell to understand its behavior and simulate its characteristics from a given mathematical model. This work aims to extract and identify the parameters of photovoltaic cells using a novel metaheuristic algorithm named Modified Social Group Optimization (MSGO). First, a comparative study was carried out based on various technologies and models of photovoltaic modules. Then, the proposed MSGO algorithm was tested on a monocrystalline type of panel with its single-diode and double-diode models. Then, it was tested on an amorphous type of photovoltaic cell (hydrogenated amorphous silicon (a-Si: H)). Finally, an experimental validation was carried out to test the proposed MSGO algorithm and identify the parameters of the polycrystalline type of panel. All obtained results were compared to previous research findings. The present study showed that the MSGO is highly competitive and demonstrates better efficiency in parameter identification compared to other optimization algorithms. The Individual Absolute Error (IAE) obtained by the MSGO is better than the other errors for most measurement values in the case of single- and double-diode models. Relatedly, the average fitness function obtained by the MSGO algorithm has the fastest convergence rate.

**Keywords:** photovoltaic cells; modeling; parameters estimation; MSGO algorithm; optimization

**Citation:** Kraiem, H.; Touti, E.; Alanazi, A.; Agwa, A.M.; Alanazi, T.I.; Jamli, M.; Sbita, L. Parameters Identification of Photovoltaic Cell and Module Models Using Modified Social Group Optimization Algorithm. *Sustainability* **2023**, *15*, 10510. <https://doi.org/10.3390/su151310510>

Academic Editor: Mohamed A. Mohamed

Received: 9 May 2023

Revised: 17 June 2023

Accepted: 21 June 2023

Published: 4 July 2023



**Copyright:** © 2023 by the authors. Licensee MDPI, Basel, Switzerland. This article is an open access article distributed under the terms and conditions of the Creative Commons Attribution (CC BY) license (<https://creativecommons.org/licenses/by/4.0/>).

## 1. Introduction

In recent decades, due to their inexhaustibility, non-polluting nature, and highly adaptable properties to decentralized generation, renewable energies have been the ecological alternative to fossil fuels and nuclear energy [1,2]. For these reasons, advanced technologies are currently being developed to benefit from these types of energy sources. Photovoltaic (PV) panels, which generate electricity using the sun's energy as a renewable energy source, are one of the most prevalent forms of renewable energy [3]. Solar energy is growing exponentially. Its main characteristic is to be a form of decentralized production, making it possible to meet strong demand from citizens and local authorities and to produce energy where it is consumed. Consequently, significant losses can be avoided during energy transportation. The PV industry has been overgrowing in recent years [4] because it is not only inexhaustible but also silent and non-disturbing for residents, unlike wind turbines which cause visual and acoustic disturbances. In addition, the market to produce electricity from



solar energy is proliferating [5,6]. In this context, the importance of photovoltaic generators connected to the electricity distribution network is growing rapidly [7]. Hence, assessing and studying the performance of the photovoltaic module, which is the fundamental component of these generators, appears to be highly significant [8]. The manufacturers typically tend to provide only limited operational data for PV panels. These data are only available under standard conditions of  $1000 \text{ W/m}^2$  irradiation,  $25^\circ\text{C}$  cell temperature, and air mass of 1.5 [9]. Therefore, it is essential to understand each cell element's physical properties and electrical characteristics before developing an equivalent circuit for a photovoltaic cell. Performance evaluation of PV modules and the design of energy systems are derived from the electrical characteristic current–voltage (I–V) of the modules under different radiation levels and different temperatures of the PV cell [10,11]. There are three forms of solar cell technologies available on the market: amorphous, monocrystalline, and polycrystalline [12]. Monocrystalline and polycrystalline cells are found in rigid panels. The difference between the two types is mainly based on their efficiency. To achieve maximum performance, crystalline panels should be installed perpendicular to the sun's rays. Generally abbreviated a-Si, amorphous silicon is the non-crystallized allotropic variety of silicon; crystalline structures of the a-Si are formed from disordered atoms that are not arranged regularly. Thin layers of amorphous silicon can be deposited at low temperatures on a wide variety of substrates. Hence, a wide range of microelectronic applications can be envisaged. The advantage of amorphous silicon cells is that they are environmentally friendly because they do not use toxic heavy metals, such as cadmium or lead. Compared to amorphous cells, crystalline panels do not perform as well in partial shadowing, and they lose a tiny percentage of their output as the temperature rises over  $25^\circ\text{C}$ . Various equations can be used to model PV cells and modules approximated to differing degrees of accuracy from the actual device. This modeling offers essential advantages, such as ease of use, thanks to the equivalent electrical circuit and the popularization of the system properties. Therefore, the understanding of complex phenomena will be facilitated. Therefore, solar cells are considered power generators and will be modeled by equivalent circuits and electric models. The most commonly used are the single-diode model [13], the model with two diodes [14], and the one with three diodes [15]. Each of these models has some unknown parameters that characterize and describe the behavior of a PV generator. In addition, the behavior of PV generators is influenced by various parameters related to electrical modeling [16]. The power output of a photovoltaic (PV) cell is influenced by several factors such as the orientation of the panels, quality factor, kind of material, absorbent layer, and optical window. The optimal orientation of panels should be perpendicular to the sun's direction to maximize the power output. The quality factor of the cell is a measure of its efficiency to convert sunlight into electricity, and it involves a trade-off between efficiency and cost. The choices of material and the thickness and composition of the absorbent layer also play a significant role in determining the power output. Additionally, optimizing the optical window requires a balance between light transmission and absorption by the window. The PV cell's performance is interdependent on various parameters, such as efficiency, open-circuit voltage, fill factor, short-circuit current, and maximum power point. These parameters are interdependent, and there are constraints between them that must be considered to optimize the cell's performance. Hence, understanding the constraints between the PV cell parameters is vital for designing efficient PV systems.

In order to optimize the various characteristics and simulate the behavior of a PV generator, it is crucial to identify the physical mechanisms at play within it. The complexity of the model is determined by the number of parameters that need to be identified. The ideal model includes a current source for solar power input and a diode for the PN junction, but additional components can be added to better represent the PV cell's behavior in specific operational situations. Various methods of parameter identification have been studied in the literature, including numerical, analytical, deterministic, and metaheuristic methods. Numerical methods utilize mathematical algorithms to iteratively optimize parameter values using measured or simulated data. These methods employ numerical



optimization techniques, including iterative algorithms and metaheuristic approaches, to minimize the discrepancy between model predictions and observed data. Numerical methods offer flexibility in handling complex and nonlinear problems [17,18]. Analytical methods involve analyzing mathematical formulas to identify the parameters of PV models. These methods are characterized by their short execution time and simplicity. However, their solutions are not precise [19,20]. The deterministic methods have major drawbacks, such as the high sensitivity to the initial hypotheses and the tendency of these algorithms to converge to the local optimum [21]. Moreover, they depend on the convexity of the model [22]. However, the models of photovoltaic cells are multimodal and characterized by nonlinearities. Recently, metaheuristic methods seem to be good potential alternatives for extracting parameters from PV models [23]. Indeed, they overcome the shortcomings of the analytical and deterministic methods already cited. In the following, we mention some of the most popular metaheuristic methods: Genetic Algorithm (GA) [24], artificial bee colony algorithm (ABC) [25], differential evolution algorithm (DE) [26], bird mating optimization (BMO) [27], Ant Lion Optimizer (ALO) [28], bacterial foraging optimization (BFO) [29], gray wolf optimization (GWO) [30], whale optimization algorithm (WOA) [31], Slime Mould Algorithm (SMA) [32], Sal Swarm Algorithm (SSA) [33], and Coyote Optimization Algorithm (COA) [15].

The primary objective of this study is to investigate and analyze the efficiency of a novel algorithm called Modified Social Group Optimization (MSGO) [34] for the extraction and identification of the parameters of photovoltaic cells. To provide a comprehensive assessment, a comparative study was conducted, incorporating various technologies and models of photovoltaic panel cells.

In the initial phase of this investigation, the proposed algorithm was applied to the monocrystalline photovoltaic panel of RTC France Company, considering both single- and double-diode cell models. The outcomes obtained through the MSGO algorithm were compared with results from previous studies utilizing alternative metaheuristic algorithms, such as the Nelder–Mead method and modified particle swarm optimization (NM-MPSO) [35], Levenberg–Marquardt algorithm combined with Simulated Annealing (LMSA) [36], ABC [21], biogeography-based optimization algorithm with mutation strategies (BBO-M) [37], improved adaptive differential evolution (Rcr-IJADE) [38], artificial bee swarm optimization algorithm (ABSO) [39], and chaotic asexual reproduction optimization (CARO) [40]. All these algorithms were tested on the same photovoltaic panel, under identical lighting and temperature conditions (temperature of 33 °C and irradiation of 1000 W/m<sup>2</sup>).

Subsequently, the proposed algorithm was also evaluated on a flexible photovoltaic panel composed of hydrogenated amorphous silicon (a-Si: H). The obtained results were compared with the findings presented by authors from [41], who based their research on the optimization algorithms Quasi-Newton Method (QNM) and the Self-Organizing Migrating Algorithm (SOMA).

To validate the results obtained by the proposed MSGO algorithm, an experimental study was performed on the TITAN-12-50 panel, utilizing polycrystalline cells [42]. Finally, the paper concludes with a comparative analysis between different optimization algorithms employed for photovoltaic parameter extraction. The results obtained through the proposed MSGO algorithm are compared with those derived from other algorithms such as the WOA, SSA, Sine Cosine Algorithm (SCA), Virus Colony Search Algorithm (VCS), Gravitational Search Algorithm (GSA), and Ant Lion Optimizer (ALO). Throughout the remainder of this paper, three sections are described: Section 2 introduces PV models and problem formulation. Section 3 details the proposed MSGO algorithm. Section 4 treats the study of the MSGO algorithm efficiency by testing various pieces of technology and PV cell models. In the last section, the obtained results are compared with those given in previous studies.

## 2. Mathematical PV Model Analysis

The evaluation of the PV module performance and the power system design is based on the current–voltage electrical characteristic of the modules under different radiation levels and various temperatures of the PV cells. It is possible to model PV cells and modules by means of equations that approximate the physical cell to varying degrees. Several electrical models are proposed in the literature for simulating PV cells under different conditions. The model's complexity varies depending on the number of parameters ( $R_s$ ,  $R_{sh}$ , etc.) to be considered. Every model is basically refinements of the ideal model, which consists of a diode that represents the PN junction and a current source that represents incident solar power.

It is possible to add several additional elements to provide a better representation of the behavior of PV cells in some operating areas [43]. Single-diode models (SDMs), double-diode models (DDMs), and three-diode models (TDMs) are the most used models. Figure 1a represents the single-diode model, which is regarded as the most popular model. It is widely used because of its simplicity. It also provides high precision and simplicity in the power generation quadrant.

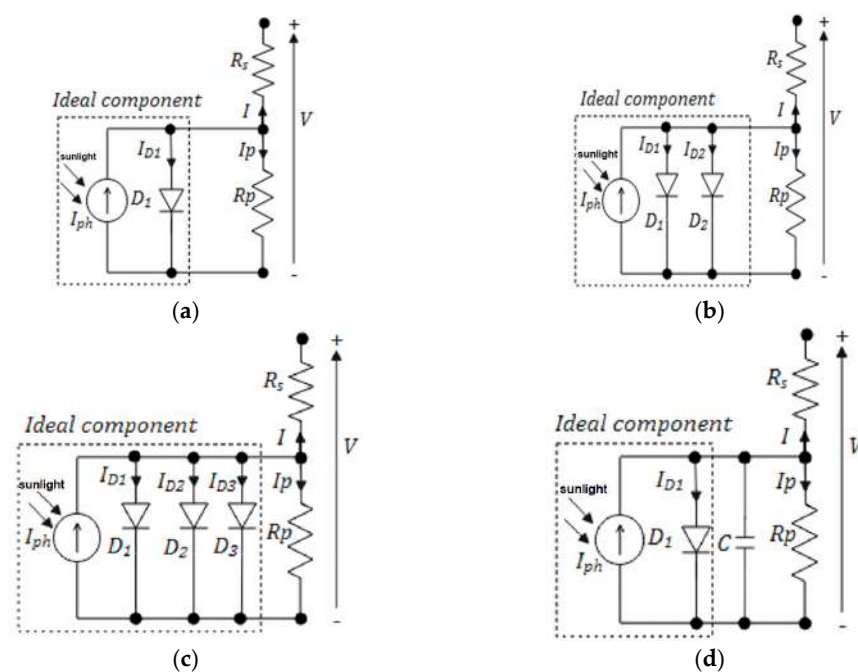


Figure 1. Solar cell models: (a) SDM, (b) DDM, (c) TDM, and (d) Dynamic Model.

The single-diode model has undergone various advancements that have led to the development of more accurate models, such as the Bishop model, which explains the behavior of the PV cell under reverse polarization. The double-diode model, shown in Figure 1b, considers losses due to various resistances and devices in the different electric components that constitute the circuit [44]. An enhanced model considers the effects of grain boundaries and leakage currents. This model involves three diodes as it is shown in Figure 1c. Although this model meets most of the physical requirements of solar cells, it involves computing nine parameters that require exceptionally high numerical execution. In addition, dynamic models are proposed by introducing the capacity to model the dynamic behavior of the PV cell. This model type is shown in Figure 1d. All these models differ in the number of parameters required for computing the I–V characteristic [45].

$I_{ph}$  is the photo-generated current source;  $I_{D1}$ ,  $I_{D2}$ ,  $I_{D3}$  are the currents of diodes  $D_1$ ,  $D_2$ , and  $D_3$ ;  $R_p$  is the shunt resistance;  $R_s$  is the series resistance;  $I$  is the output current; and  $V$  is the output voltage.

## 2.1. Mathematical Development

### 2.1.1. Crystalline Cells

From the equivalent circuit (Figure 1a), it is evident that the current produced by the solar cell is equal to that produced by the current source ( $I_{ph}$ ), minus that which flows through the diode ( $I_d$ ), minus that which flows through the shunt resistor ( $I_p$ ).

$$I = I_{ph} - K_i I_d - I_p \quad (1)$$

$$\text{where } K_i = \begin{cases} K_1 = \begin{bmatrix} 1 & 0 & 0 \end{bmatrix}, i = 1 \text{ in case of SDM} \\ K_2 = \begin{bmatrix} 1 & 1 & 0 \end{bmatrix}, i = 2 \text{ in case of DDM} \\ K_3 = \begin{bmatrix} 1 & 1 & 1 \end{bmatrix}, i = 3 \text{ in case of TDM} \end{cases}, \text{ where } I_d = \begin{bmatrix} I_{d1} \\ I_{d2} \\ I_{d3} \end{bmatrix}, \text{ and } I_p = \frac{V + R_s I}{R_p}.$$

The current in the  $j^{\text{th}}$  diode is given by

$$I_{dj} = I_{sdj} \left( e^{\left( \frac{q(V + R_s I)}{n_j K T} \right)} - 1 \right), (j = 1, 2, 3) \quad (2)$$

Then, the current given in Equation (1) is given by Equation (3), where  $I_{SDM}$ ,  $I_{DDM}$ , and  $I_{TDM}$  are the total output current when considering the SDM, DDM, and TDM, respectively.

$$\begin{cases} I_{SDM} = I_{ph} - I_{sd} \left( e^{\left( \frac{q(V + R_s I)}{n_1 K T} \right)} - 1 \right) - \frac{V + R_s I}{R_p} \\ I_{DDM} = I_{ph} - I_{sd1} \left[ e^{\left( \frac{q(V + R_s I)}{n_1 K T} \right)} - 1 \right] - I_{sd2} \left[ e^{\left( \frac{q(V + R_s I)}{n_2 K T} \right)} - 1 \right] - \frac{V + R_s I}{R_p} \\ I_{TDM} = I_{ph} - I_{sd1} \left[ e^{\left( \frac{q(V + R_s I)}{n_1 K T} \right)} - 1 \right] - I_{sd2} \left[ e^{\left( \frac{q(V + R_s I)}{n_2 K T} \right)} - 1 \right] - I_{sd3} \left[ e^{\left( \frac{q(V + R_s I)}{n_3 K T} \right)} - 1 \right] - \frac{V + R_s I}{R_p} \end{cases} \quad (3)$$

where  $n_1$ ,  $n_2$ , and  $n_3$  are the ideality factors of the diodes  $D_1$ ,  $D_2$ , and  $D_3$ ;  $K$  is the Boltzmann constant ( $1.380649 \times 10^{-23}$  Joule/Kelvin);  $T$  is the temperature of the PV panel (Kelvin); and  $q$  is the charge of the electron ( $1.602176634 \times 10^{-19}$  Coulomb).

The TDM does not seem suitable for fast computations and has complex nonlinear analytic expressions; therefore, this model will be excluded from the parametric identification tests.

### 2.1.2. Amorphous Silicon Cell

Equation (4) defines the current–voltage characteristic for an amorphous silicon cell:

$$I = I_{ph} \left( 1 - \frac{d_i^2}{\mu_{eff} [V_b - (V + IR_s)]} \right) - I_s \left[ \exp \left( \frac{V + IR_s}{a V_T} - 1 \right) \right] - \frac{V + IR_s}{R_{sh}} \quad (4)$$

$d_i$  denotes the width of the  $i^{\text{th}}$  layer in the (a-Si) p\_i\_n diode,  $\mu_{eff}$  represents the mobility-lifetime product of the electron and hole, and  $V_{bi}$  is the built-in field voltage.

The diode reverse saturation current and the photo-generated current of an (a-Si) cell under constant light and temperature are given, respectively, by

$$I_{ph} = q A g(x) (L_p + L_n + W) \quad (5)$$

$$I_0 = J_s \times A = \left( \frac{q D_p p_{n0}}{L_p} + \frac{q D_n n_{p0}}{L_n} \right) \times A \quad (6)$$

where  $A$  is the  $p_n$  junction area,  $L_p$  is the carrier diffusion length of the  $p$ -type area,  $L_n$  is the carrier diffusion length of the  $n$ -type area,  $W$  is the depletion layer,  $D_p$  and  $D_n$  are the holes and electrons diffusion coefficient,  $p_{n0}$  and  $n_{p0}$  are the minority carrier concentration in the  $P$  region and  $N$  region, and  $g(x)$  is the electron hole formation ratio.

## 2.2. The Objective Functions

The term objective function is used in mathematical optimization and operations research to refer to a function that acts as a criterion for identifying the best solution to an optimization problem.

The objective function of the SDM may be written as

$$f_{SDM}(V, I, X) = I - X(1) + X(2) \left[ e^{\left( \frac{q(V+X(3)I)}{X(4)KT} \right)} - 1 \right] + \frac{V + X(3)I}{X(5)} \quad (7)$$

$$X = [I_{ph} \quad I_{sd} \quad R_s \quad n_1 \quad R_p]$$

For the DDM, the error function is expressed by

$$f_{DDM}(V, I, X) = I - X(1) + X(2) \left[ e^{\left( \frac{q(V+X(3)I)}{X(4)KT} \right)} - 1 \right] + X(5) \left[ e^{\left( \frac{q(V+X(3)I)}{X(6)KT} \right)} - 1 \right] + \frac{V + X(3)I}{X(7)} \quad (8)$$

where  $X = [I_{ph} \quad I_{sd1} \quad R_s \quad n_1 \quad I_{sd2} \quad n_2 \quad R_p]$ .

Whereas, the error function for the TDM is defined by

$$f_{TDM}(V, I, X) = I - X(1) + X(2) \left[ e^{\left( \frac{q(V+X(3)I)}{X(4)KT} \right)} - 1 \right] + X(5) \left[ e^{\left( \frac{q(V+X(3)I)}{X(6)KT} \right)} - 1 \right] + X(7) \left[ e^{\left( \frac{q(V+X(3)I)}{X(8)KT} \right)} - 1 \right] + \frac{V + X(3)I}{X(9)} \quad (9)$$

where  $X = [I_{ph} \quad I_{sd1} \quad R_s \quad n_1 \quad I_{sd2} \quad n_2 \quad I_{sd3} \quad n_3 \quad R_p]$ .

It is necessary to use  $Ne$  samples (data points number) to widen the scope of the search and reach the global optimum. Equation (10) gives us a description of the cost function:

$$RMSE(x) = \sqrt{\frac{1}{Ne} \sum_{C=1}^{Ne} (f_M^C(V^C, I^C, x))^2} \quad (10)$$

## 3. Procedure of Social Group Optimization for PV Parameters Estimation

The past twenty years have seen a remarkable rise in interest in metaheuristic optimization algorithms. The research work developed has enabled the appearance of new algorithms which are generally based on the following:

- A new idea inspired by a natural, physical, chemical phenomena;
- A modification of an existing algorithm to improve its performances;
- The hybridization of two methods allows the strengths to merge and the weaknesses to be eliminated of the two algorithms.

However, no algorithm can be adapted to all types of problems. In 2016, a new metaheuristic optimization algorithm appeared, known as Social Group Optimization (SGO) [46]. To solve complex problems, the new algorithm was inspired by the social behavior of individuals in groups. Each individual's knowledge is mapped by its fitness. The algorithm contains two phases. The first phase is called the improving phase in which each individual interacts with the best person (best solution) to improve his knowledge by interacting. The second phase is named the acquiring phase, during which the individuals acquire knowledge when they interact with the best person and randomly selected individuals simultaneously. A comparative study is carried out to show the performance of the new method. Detailed information on the SGO algorithm can be found in the following articles [47,48]. The SGO algorithm is described with the following:

$P_i$ , ( $i = 1, 2, 3, \dots, N$ ):  $P_i$  is the social group persons, and  $N$  is the total number of people in the social group.

$P_{ij}$ , ( $j = 1, 2, \dots, D$ ):  $D$  is the traits number related to a person which allows us to determine the dimensions of a person.

$f_i$ , ( $i = 1, 2, \dots, N$ ) is their corresponding fitness value.

### Improving phase

In each social group, the role of the best person ( $P_{best}$ ) is to propagate knowledge between all persons. As a result, others in the group enhance their knowledge.

$$[minvalue, index] = \min\{f(P_i), i = 1, 2, 3, \dots, N\}$$

$$gbest = P(index, :)$$

The following algorithm (Algorithm 1) can be used to calculate how often each person's knowledge is updated:

---

#### Algorithm 1 Improving phase

---

```

for i = 1: N
  for j = 1: D
     $P_{new_{ij}} = c * P_{ij} + r * (P_{best}(j) - P_{ij})$ 
  end for
end for

```

---

$r$ : random number, and  $r \in [0, 1]$ . If  $P_{new}$  provides higher fitness than  $P_{old}$ , it is accepted [34].  $c$  is the parameter of self-introspection  $c \in [0, 1]$ .

### Acquiring Phase

In the acquiring phase (Algorithm 2), a person acquires new knowledge by interacting with other persons of the group. The interaction can be with the best person ( $P_{best}$ ) or randomly with other persons who have more knowledge. To acquire knowledge, a person always interacts with the  $P_{best}$  and with any other person of the group who has more knowledge than him. The ability to obtain a quantity of knowledge from another person is defined by the self-awareness probability (SAP). The modified acquiring phase is computed as

$$[value, index\_num] = \min\{f(P_i), i = 1, 2, 3, 4, \dots, N\}$$

$$P_{best} = P(index\_num, :)$$

where  $P_i$  is the updated value at the completion of the improving phase.

---

#### Algorithm 2 Acquiring phase

---

```

for i = 1: N
  Randomly select one person  $P_r$  where  $i \neq r$ 
  If  $f(P_i) < f(P_r)$ 
    If  $rand > SAP$ 
      for j = 1: D
         $P_{new_{i,j}} = P_{i,j} + rand_1 * (P_{i,j} - P_{r,j}) + rand_2 * (best_p(j) - P_{i,j})$ 
      end for
    else
      for j = 1: D
         $P_{new_{i,j}} = lb + rand_2 * (ub - lb)$ 
      end for
    end if
  else
    for j = 1: D
       $P_{new_{i,j}} = P_{i,j} + rand_1 * (P_{r,j} - P_{i,j}) + rand_2 * (best_p(j) - P_{i,j})$ 
    end for
  end if
end for

```

---

$P_{new}$  is accepted if it provides a higher level of fitness than  $P$ .

The general steps to use the MSGO algorithm to extract parameters of a PV cell include:

Step 1: Define the objective function which describes the behavior of the PV cell under different conditions. This function takes input parameters, such as the cell's temperature, irradiance, and voltage, and outputs a value that represents the cell's performance. The goal is to find the values of these input parameters that maximize the output value of the objective function.

Step 2: Define the parameter space. The parameter space defines the objective function constraints for each parameter, such as the temperature may range from  $-10\text{ }^{\circ}\text{C}$  to  $100\text{ }^{\circ}\text{C}$ , the irradiance may range from  $0\text{ W/m}^2$  to  $1000\text{ W/m}^2$ , and the voltage may range from  $0\text{ V}$  to  $1\text{ V}$ . All other range parameters are declared in Equations (15)–(17).

Step 3: Initialize the population. The population ( $P_i$ ) is a set of solutions that are randomly generated within the parameter space. Each solution corresponds to a set of input parameters that are used to evaluate the objective function.

Step 4: Evaluate the fitness. The fitness is a measure of how well each solution performs with respect to the objective function. The fitness function takes as input the output value of the objective function and returns a scalar value that represents the quality of the solution. The higher the fitness, the better the solution.

Step 5: Update the population. The MSGO algorithm updates the population in two phases: the improving phase and the acquiring phase. In the improving phase, each individual interacts with the best person in the social group to improve its knowledge. In the acquiring phase, each individual acquires knowledge by interacting with the best person and randomly selected individuals. The updating of each person's knowledge can be calculated using the formula described in the improving phase.

Step 6: Repeat steps 4 and 5 until convergence. The optimization process continues until the fitness values converge to a satisfactory level or the maximum number of iterations is reached. The best solution found during the optimization process corresponds to the set of input parameters that maximizes the output value of the objective function. These parameters can be used to characterize the behavior of the PV cell under the given conditions.

#### 4. Results

The technical details of the software and hardware used for the extraction of the various simulation results are given in Table 1.

**Table 1.** Software and hardware details.

Hardware and Software	Setting
CPU	Intel (R) Core (TM) i7—7500U
Frequency	2.9 GHz
RAM	12 Gb
Simulation software	Matlab R2018b
Operating System	Windows 10

The adjustable parameters of the MSGO algorithm include: the population size is 40, and the maximum number of iterations is 3000. However, the parameters of other comparative algorithms are given in references cited in the first section.

All simulation work was conducted under the following solar irradiance and temperature conditions:  $1000\text{ W/m}^2$  and  $33\text{ }^{\circ}\text{C}$ . The obtained results of our parameter identification algorithm were compared to other optimization algorithms to determine the accuracy of the fitted curve between the MSGO algorithm values and experimental data. Table 2 summarizes the comparison work established in this paper.

**Table 2.** Summary of comparative study.

Types of Tested Panels	PV Cell Model	Examined Algorithms during the Comparison
RTC France Company monocrystalline	Single diode Double diode	NM-MPSO, LMSA, ABC, BBO-M, Rcr-IJADE
Hydrogenated Amorphous Silicon a-Si: H	Single diode	NM-MPSO, Rcr-IJADE, ABSO, CARO, ABC
TITAN-12-50 Polycrystalline	Single diode Double diode	SOMA, QNM SCA, ALO, GSA, VCS, WOA, SSA

#### 4.1. MSGO Implementation

To verify the accuracy of the fitted curve obtained by the MSGO algorithm using experimental data, a comparison is made against other algorithms. Tables 3 and 4 present a statistical analysis of the contrasted results for each model. The statistical errors used to demonstrate the performance of the proposed algorithm are presented below.

**Table 3.** Extracted parameters in case of an SDM.

Algorithm	$I_{ph}$ (A)	$I_0$ ( $\mu$ A)	$n$	$R_s$ ( $\Omega$ )	$R_p$ ( $\Omega$ )
<b>MSGO</b>	0.7607877	0.31058918	1.47725615	0.0365470	52.88998
<b>BBO-M</b>	0.760781	0.318743	1.479842	0.036422	53.36226
<b>Rcr-IJADE</b>	0.760775	0.323022	1.481183	0.036376	53.718525
<b>LMSA</b>	0.760781	0.318492	1.479764	0.036433	53.326441
<b>CARO</b>	0.760792	0.317243	1.481681	0.036443	53.08930
<b>ABC</b>	0.76082	0.325155	1.481731	0.036443	53.64332
<b>NM-MPSO</b>	0.760781	0.323065	1.481202	0.036384	53.72221

**Table 4.** The estimated data and the resulted IAE obtained by the proposed algorithm **MSGO** compared with other algorithms in the case of an SDM.

	$V_{exp}$ (V)	$I_{exp}$ (A)	$I_{est}$ (A)	MSGO	Rcr-IJADE	BBO-M	ABC	LMSA	NM-MPSO
1	−0.2057	0.764	0.764149248	0.00014925	0.00009559	0.000006	0.0001	0.000115762	0.000087
2	−0.1291	0.762	0.762293808	0.00029381	0.00066611	0.000604	0.0006	0.000680672	0.000662
3	−0.0588	0.7605	0.761373566	0.00087357	0.00085473	0.000817	0.0008	0.000863281	0.000854
4	0.0057	0.7605	0.7601543024	0.00034570	0.00035034	0.000364	0.0003	0.000346856	0.000346
5	0.0646	0.76	0.759038854	0.00096115	0.00094298	0.000946	0.0009	0.000953669	0.000945
6	0.1185	0.759	0.758010563	0.00098944	0.00095528	0.000943	0.0009	0.000973813	0.000957
7	0.1678	0.757	0.757045517	0.00004552	0.00009510	0.000120	0.0001	0.0000690271	0.000091
8	0.2132	0.757	0.756084674	0.00091533	0.00084950	0.000817	0.0008	0.000886778	0.000858
9	0.2545	0.7555	0.755022264	0.00047774	0.00041823	0.000361	0.0004	0.000445307	0.000413
10	0.2924	0.754	0.753597432	0.00040257	0.00032967	0.000276	0.0003	0.000370139	0.000336
11	0.3269	0.7505	0.751327686	0.00082769	0.00089542	0.000953	0.0008	0.000858429	0.000888
12	0.3585	0.7465	0.747306479	0.00080648	0.00085737	0.000914	0.0008	0.000827345	0.000848
13	0.3873	0.7385	0.740087107	0.00158711	0.00160420	0.001668	0.0016	0.00160213	0.001596
14	0.4137	0.728	0.727430948	0.00056905	0.00059912	0.000583	0.0006	0.000616337	0.000604
15	0.4373	0.7065	0.707034237	0.00053424	0.00044631	0.000485	0.0004	0.000492923	0.000452
16	0.459	0.6755	0.675413782	0.00008622	0.00019600	0.000230	0.0002	0.000182486	0.000206
17	0.4784	0.632	0.631018287	0.00098171	0.00110900	0.001271	0.0012	0.001194906	0.001117
18	0.496	0.573	0.572202755	0.00079724	0.00091027	0.001112	0.0011	0.001026552	0.00092
19	0.5119	0.499	0.499575662	0.00057566	0.00049902	0.000563	0.0005	0.000638902	0.00049
20	0.5265	0.413	0.413530488	0.00053049	0.00049030	0.000612	0.0006	0.00065758	0.000492
21	0.5398	0.3165	0.31721586	0.00071586	0.00071532	0.000985	0.001	0.000992379	0.000718
22	0.5521	0.212	0.212079153	0.00007915	0.00010468	0.000142	0.0001	0.000112783	0.000102
23	0.5633	0.1035	0.102706638	0.00079336	0.00078397	0.001254	0.0012	0.001305993	0.000779
24	0.5736	−0.01	−0.009221842	0.00077816	0.00075437	0.001268	0.0013	0.001228583	0.000751
25	0.5833	−0.123	−0.12427906	0.00127906	0.00137750	0.002537	0.0024	0.002545248	0.001381
26	0.59	−0.21	−0.209015291	0.00098471	0.00080320	0.001469	0.0015	0.001522512	0.000807

- The Individual Absolute Error (IAE) is defined by

$$\text{IAE} = |I_{\text{measured}} - I_{\text{estimated}}| \quad (11)$$

- The Median Absolute Error (MAE) is expressed as

$$\text{MAE} = \sum_{i=1}^m \frac{|I_{\text{measured}} - I_{\text{estimated}}|}{m} \quad (12)$$

- The Residual Sum of Squares (SSE) is defined by

$$\text{SSE} = \sum_{i=1}^{N_e} (I_{\text{measured}} - I_{\text{estimated}})^2 \quad (13)$$

- The Root Mean Square Error (RMSE) is given by

$$\text{RMSE} = \sqrt{\frac{1}{N_e} \sum_{i=1}^{N_e} (I_{\text{measured}} - I_{\text{estimated}})^2} \quad (14)$$

The equations below present the objective function constraints for each model, both for single and double diodes. The objective function constraints for the SDM is given by

$$\begin{cases} 0 \leq I_{ph} \leq 1 \text{ A} \\ 0 \leq I_{01} \leq 1 \times 10^{-7} \text{ A} \\ 1 \leq n_1 \leq 2 \\ 0 \leq R_s \leq 0.8 \Omega \\ 0 \leq R_p \leq 100 \Omega \end{cases} \quad (15)$$

The objective function constraints for the DDM are

$$\begin{cases} 0 \leq I_{ph} \leq 1 \text{ A} \\ 0 \leq I_{01} \leq 1 \times 10^{-7} \text{ A} \\ 0 \leq I_{02} \leq 1 \times 10^{-7} \text{ A} \\ 1 \leq n_1 \leq 2 \\ 1 \leq n_2 \leq 2 \\ 0 \leq R_s \leq 0.5 \Omega \\ 0 \leq R_p \leq 100 \Omega \end{cases} \quad (16)$$

The objective function constraints for (a-Si: H) are

$$\begin{cases} 0 \leq I_{ph} \leq 1 \mu\text{A} \\ 0 \leq d \leq 10 \times 10^{-8} \text{ m} \\ 0 \leq \mu_{eff} \leq 10 (\text{cm}^2/\text{V}) \\ 0 \leq V_{bi} \leq 1.5 \text{ V} \\ 0 \leq R_s \leq 0.5 \Omega \\ 0 \leq I_s \leq 5 \times 10^{-14} \\ 1 \leq a \leq 2.5 \\ 0 \leq R_{sh} \leq 50 \Omega \end{cases} \quad (17)$$

#### 4.1.1. A Comparative Study of Extraction Parameters for the SDM

The extracted parameters using the MSGO algorithm for the SDM are presented in Table 3. These values are compared to those obtained by other algorithms such as **BBO-M**, **R<sub>cr</sub>-IJADE**, **LMSA**, **CARO**, **ABC**, and **NM-MPSO**.

The estimated current values obtained by the proposed algorithm and the resulted IAE are given in Table 4. These results are compared to those obtained by the **R<sub>cr</sub>-IJADE**,



**BBO-M, ABC, LMSA, and NM-MPSO** algorithms. As it is shown, the IAE (IAT) obtained by the MSGO algorithm is better than the other errors for most measurement values.

The various statistical errors already defined by Equations (11)–(14) are presented in Table 5 and compared with those obtained by the other algorithms. One can remark that the MSGO error IAT (IAE) has the lowest value, which proves the robustness of the used algorithm.

**Table 5.** Statistical results for the SDM.

	MSGO	BBO-M	R <sub>cr</sub> -IJADE	LMSA	CARO	ABC	NM-MPSO
<b>IAT</b>	0.01738	0.0213	0.017704	0.0215	0.0182	0.0205	0.0177
<b>RMSE</b>	$7.21 \times 10^{-4}$	$9.86 \times 10^{-4}$	$7.75 \times 10^{-4}$	$9.86 \times 10^{-4}$	$9.87 \times 10^{-4}$	$9.49 \times 10^{-4}$	$7.75 \times 10^{-4}$
<b>SSE</b>	$1.355 \times 10^{-5}$	$2.529 \times 10^{-5}$	$1.562 \times 10^{-5}$	$2.529 \times 10^{-5}$	$2.531 \times 10^{-5}$	$2.343 \times 10^{-5}$	$1.563 \times 10^{-5}$
<b>MAE</b>	$6.68 \times 10^{-4}$	$8.19 \times 10^{-4}$	$6.81 \times 10^{-4}$	$8.27 \times 10^{-4}$	$6.98 \times 10^{-4}$	$7.88 \times 10^{-4}$	$6.81 \times 10^{-4}$

The different IAE results given in Table 4 are illustrated in Figure 2. One can notice that the IAE obtained by the MSGO algorithm (red color) is the lowest error for most values.

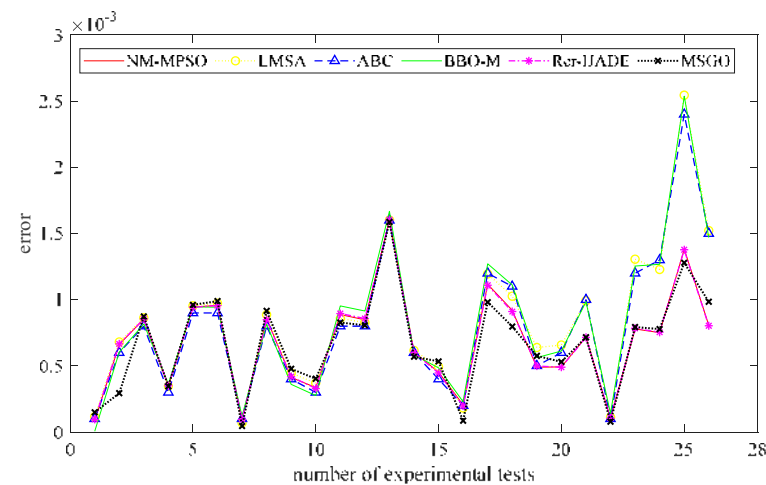


**Figure 2.** Calculated errors IAE obtained with the MSGO, R<sub>cr</sub>-IJADE, BBO-M, ABC, LMSA, and NM-MPSO algorithms: case of SDM.

In order to assess the precision of the extracted parameters, one compares the I–V and P–V characteristics obtained from the estimated parameters using the MSGO method with the experimental data. Figure 3 illustrates this comparison, specifically for a single-diode case. These figures allow us to evaluate the quality of the parameter estimation process.

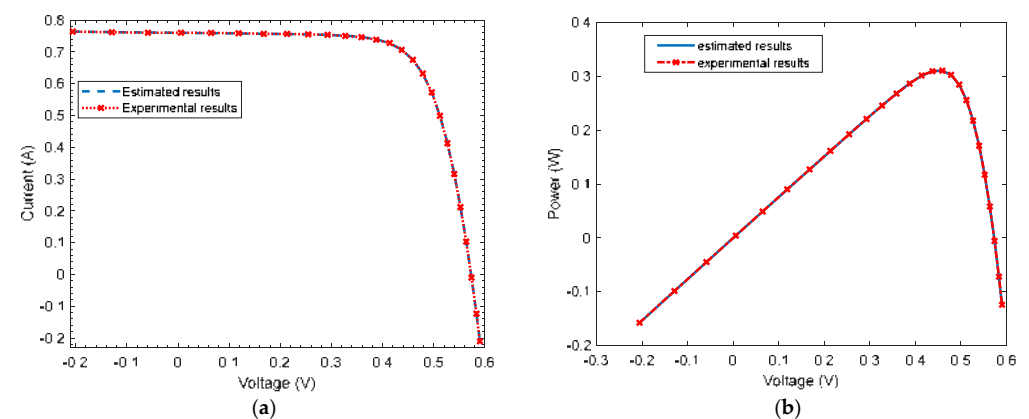


**Figure 3.** Experimental and estimated results obtained by the proposed MSGO algorithm in the case of an SDM: (a) Current\_Voltage; (b) Power\_Voltage.

The results depicted in Figure 3 indicate that the reconstructed SDM aligns well with the experimental data.

#### 4.1.2. A Comparative Study of Extraction Parameters for the DDM

The extracted parameters using the MSGO algorithm for the DDM are presented in Table 6. These values are compared to those obtained by other algorithms, such as **BBO-M**, **R<sub>cr</sub>-IJADE**, **LMSA**, **CARO**, **ABC**, and **NM-MPSO**.

**Table 6.** Extracted parameters in the case of double-diode model.

Algorithm	$I_{ph}$ (A)	$I_{01}$ ( $\mu$ A)	$I_{02}$ ( $\mu$ A)	$n_1$	$n_2$	$R_s$ ( $\Omega$ )	$R_p$ ( $\Omega$ )
MSGO	0.7607	0.1465	0.6300	1.4190	1.8075	0.0371	54.7897
R <sub>cr</sub> -IJADE	0.760821	0.225974	0.749347	1.451017	2.0000	0.036740	55.485443
CARO	0.760752	0.293151	0.090982	1.473383	1.77322	0.036414	54.39674
ABSO	0.760783	0.267135	0.381914	1.465125	1.98152	0.036572	54.62193
ABC	0.760825	0.040712	0.287433	1.449541	1.48852	0.036445	53.78046
NM-MPSO	0.760782	0.224761	0.755245	1.45054	1.99998	0.036752	55.52967

The estimated current values obtained by the proposed algorithm and the resulted IAE are given in Table 7. These results are compared to those obtained by the **R<sub>cr</sub>-IJADE**, **BBO-M**, **ABC**, **LMSA**, and **NM-MPSO** algorithms. As it is shown, the IAE (IAT) obtained by the MSGO algorithm is better than the other errors for the majority of measurement values.

**Table 7.** Estimated data and the resulted IAE obtained by the proposed algorithm **MSGO** compared with other algorithms.

	$V_{exp}$ (V)	$I_{exp}$ (A)	$I_{est}$ (A)	MSGO	ABC	CARO	ABSO	R <sub>cr</sub> -IJADE	NM-MPSO
1	−0.2057	0.764	0.76402813	0.0000281297	0.000092908	0.00031	0.000031	0.00009268	0.000023
2	−0.1291	0.762	0.762630936	0.000630936	0.0006	0.000629	0.000629	0.00065394	0.000598
3	−0.0588	0.7605	0.761348408	0.000848408	0.0008	0.000843	0.000843	0.00085755	0.000832
4	0.0057	0.7605	0.760170729	0.000329271	0.0003	0.000338	0.000338	0.00033747	0.00033
5	0.0646	0.76	0.759091932	0.000908068	0.0009	0.00092	0.00092	0.00094	0.000895
6	0.1185	0.759	0.758093995	0.000906005	0.0009	0.000919	0.000919	0.00094935	0.00088
7	0.1678	0.757	0.757150045	0.000150045	0.0001	0.000139	0.000139	0.00009635	0.000187
8	0.2132	0.757	0.756196358	0.000803642	0.0008	0.000807	0.000807	0.00085535	0.000757
9	0.2545	0.7555	0.755121281	0.000378719	0.0004	0.000368	0.000368	0.00041885	0.000323
10	0.2924	0.754	0.753659367	0.000340633	0.0003	0.000306	0.000306	0.00033126	0.000277
11	0.3269	0.7505	0.751329108	0.000829108	0.0008	0.000892	0.000892	0.00089511	0.000896
12	0.3585	0.7465	0.74723368	0.00073368	0.0008	0.000822	0.000822	0.00084939	0.000798
13	0.3873	0.7385	0.739947501	0.001447501	0.0016	0.001544	0.001544	0.00160214	0.0001495
14	0.4137	0.728	0.727258182	0.000741818	0.0006	0.000669	0.000669	0.00061216	0.000729
15	0.4373	0.7065	0.706880574	0.000380574	0.0004	0.000396	0.000396	0.00045162	0.000344
16	0.459	0.6755	0.675327647	0.000172353	0.0002	0.000235	0.000235	0.00019888	0.000259
17	0.4784	0.632	0.631016281	0.000983719	0.0012	0.001111	0.001111	0.00111234	0.0001099
18	0.496	0.573	0.572261627	0.000738373	0.0011	0.000886	0.000886	0.00092523	0.000845
19	0.5119	0.499	0.499644454	0.000644454	0.0005	0.000533	0.000533	0.00049417	0.000586
20	0.5265	0.413	0.413556808	0.000556808	0.0006	0.000525	0.000525	0.00049125	0.000571
21	0.5398	0.3165	0.317169103	0.000669103	0.001	0.00073	0.00073	0.00071918	0.000753
22	0.5521	0.212	0.211959679	0.0000403211	0.0001	0.00009	0.00009	0.00010831	0.00088
23	0.5633	0.1035	0.102545511	0.000954489	0.0012	0.000806	0.000806	0.00077968	0.000827
24	0.5736	−0.01	−0.009374369	0.000625631	0.0012	0.00073	0.00073	0.00075539	0.000711
25	0.5833	−0.123	−0.124360342	0.001360342	0.0025	0.00139	0.00139	0.00137667	0.0001388
26	0.59	−0.21	−0.209001839	0.000998161	0.0014	0.00083	0.00083	0.00080501	0.000865

The various statistical errors already defined by Equations (11)–(14) are presented in Table 3 and compared with those obtained by the other algorithms. One can remark that the MSGO error IAT (IEA) has the lowest value, which proves the robustness of the used algorithm.

The various IAE results given in Table 7 are illustrated in Figure 4. One can notice that the IAE obtained by the MSGO algorithm (red color) is the lowest error for most values.

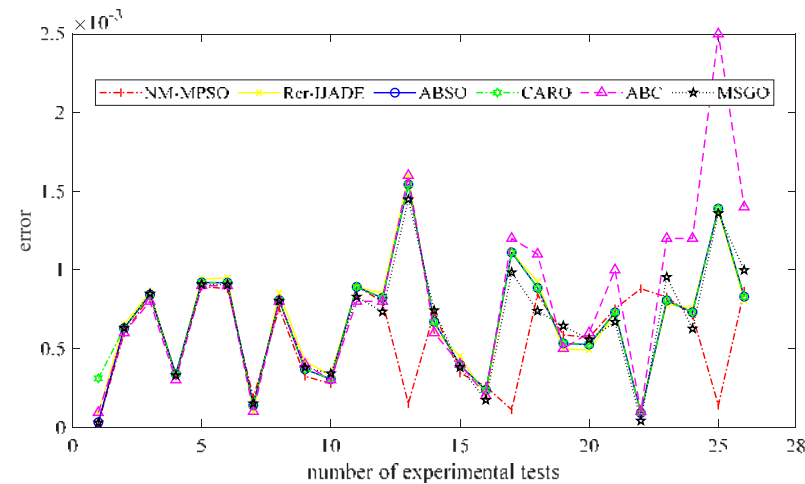


**Figure 4.** Calculated errors IAE obtained using the MSGO, ABC, CARO, ABSO, Rcr-IJADE, and NM-MPSO algorithms: case of DDM.

The I–V and P–V characteristics resulting from the parameters identified using the MSGO algorithm are compared to both experimental and estimated data to evaluate their quality. Figure 5 provides a comparison for a scenario involving two diodes, allowing us to determine the accuracy of the parameter estimation achieved through the MSGO algorithm. The results of the parameter identification using the MSGO algorithm and experimental data are compared with the estimated data to investigate the quality of the extracted parameters.

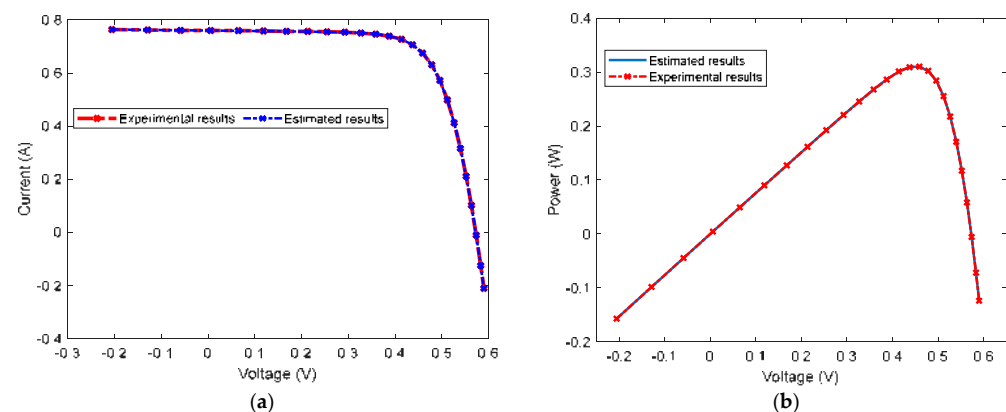


**Figure 5.** Experimental and estimated results obtained by the proposed MSGO algorithm in the case of a DDM: (a) Current\_Voltage; (b) Power\_Voltage.

Figure 6a,b illustrate the estimated I–V characteristic of the SDM and DDM compared with the experimental one. It is noted that there is a slight advantage of the DDM compared to the SDM, which is not clear enough in the figure. Upon closer inspection of the corresponding statistical results given in Tables 5 and 8, it becomes evident that the DDM outperforms the SDM by a small margin.

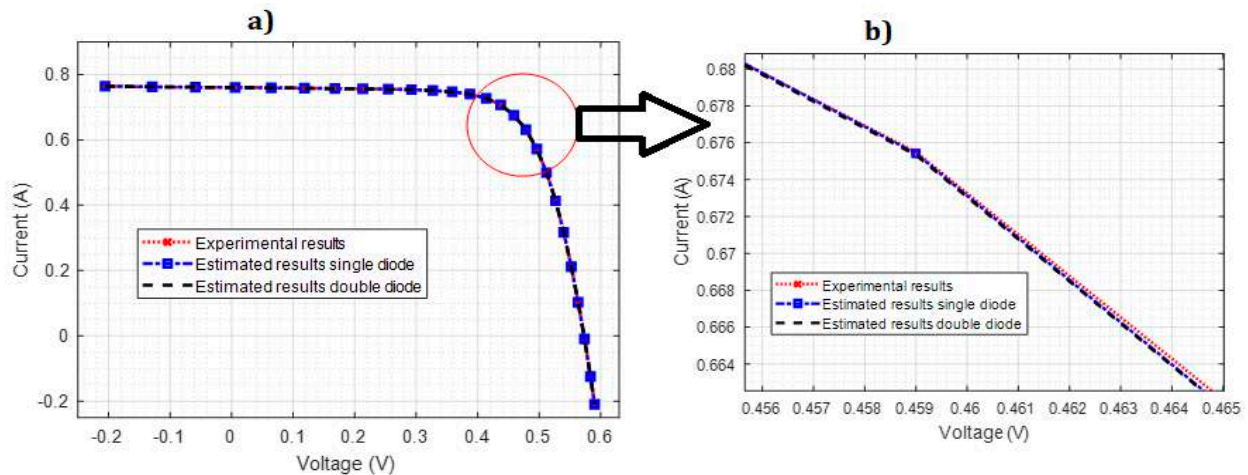


**Figure 6.** Experimental and estimated results: (a) I–V characteristic for SDM and DDM, and (b) Zoom of I–V characteristic in Figure 5a.

**Table 8.** Statistical results for the DDM (RTC France Company).

	MSGO	R <sub>cr</sub> -IJADE	CARO	ABSO	ABC	NM-MPSO
Total IAE	0.0172	0.0177	0.0693	0.0178	0.0204	0.0174
RMSE	$7.514 \times 10^{-4}$	$7.754 \times 10^{-4}$	$8.1 \times 10^{-4}$	$7.682 \times 10^{-4}$	$9.922 \times 10^{-4}$	$7.581 \times 10^{-4}$
SSE	$1.468 \times 10^{-5}$	$1.56 \times 10^{-5}$	$1.7 \times 10^{-5}$	$1.53 \times 10^{-5}$	$2.56 \times 10^{-5}$	$1.49 \times 10^{-5}$
MAE	$6.62 \times 10^{-4}$	$6.81 \times 10^{-4}$	$2.67 \times 10^{-4}$	$6.83 \times 10^{-4}$	$7.84 \times 10^{-4}$	$6.68 \times 10^{-4}$

#### 4.1.3. A Comparative Study of Extraction Parameters for the Amorphous PV Cell

The extracted parameters using the **MSGO** algorithm for the amorphous model are presented in Table 9. These values are compared to those obtained by other algorithms such as **QNM** and **SOMA**.

**Table 9.** Extracted parameters in case of amorphous cell.

Algorithm	$I_{ph}$ (A)	$d$ ( $10^{-8}$ m)	$\mu_{eff}$ ( $cm^2/V$ )	$V_{bi}$ (V)	$R_s$ ( $\Omega$ )	$I_s$ (A)	$a$	$R_{sh}$ ( $\Omega$ )
MSGO	0.3123	4.72	3.03	0.97	0.295	1.5	1.918	11.07
QNM	0.3043	5.8065	4.8812	0.9759	0.4242	3.0691	1.999	11.9138
SOMA	0.3181	4.9743	3.3277	0.9963	0.4706	3.0783	1.9931	13.9288

The various IAE results given by Table 10 are illustrated in Figure 7. One can notice that the IAE obtained by the MSGO algorithm (red color) is the lowest error for most values, as is confirmed in Table 11.

**Table 10.** Estimated data and resulted IAE obtained by the proposed algorithm **MSGO**.

	$V_{exp}$ (V)	$I_{exp}$ (A)	$I_{est}$ (A)	IAE		
				MSGO	QNM	SOMA
1	1.525	0	−0.00328	0.00328	0.0041	0.00086
2	1.515	0.0158	0.0137831	0.002017	0.0058	0.0027
3	1.5	0.0302	0.0378181	0.007618	0.0003	0.0032
4	1.4775	0.0619	0.0701493	0.008249	0.0028	0.0004
5	1.47	0.0868	0.0798933	0.006907	0.0188	0.0153
6	1.445	0.1142	0.1085644	0.005636	0.0187	0.0138
7	1.37	0.1604	0.1623759	0.001976	0.0055	0.0075
8	0	0.3044	0.3042089	0.000191	0.0209	0.0026

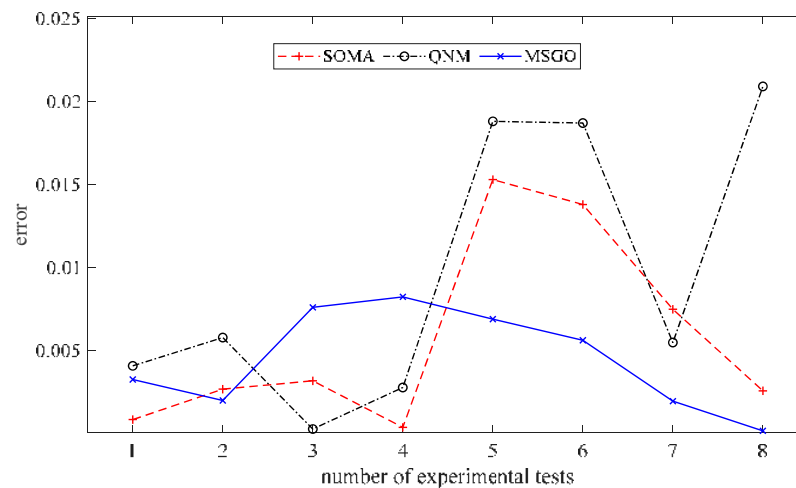


**Figure 7.** Estimated errors IAE.

**Table 11.** Statistical results for amorphous model.

	MSGO	SOMA	QNM
<b>Total IAE</b>	0.03587	0.04636	0.07690
<b>RMSE</b>	$5.295 \times 10^{-3}$	$7.952 \times 10^{-3}$	$1.239 \times 10^{-2}$
<b>SSE</b>	$2.243 \times 10^{-4}$	$5.059 \times 10^{-4}$	$1.228 \times 10^{-3}$
<b>MAE</b>	$4.484 \times 10^{-3}$	$5.796 \times 10^{-3}$	$9.612 \times 10^{-3}$

#### 4.2. Experimental Validation

The I–V and P–V characteristics of the TITAN-12-50 photovoltaic panel are implemented using the experimental test bench shown in Figure 8. The Parameter Specification of the TITAN-12-50 PV module is given in Table 12. To determine the various parameters of the photovoltaic generator, voltage and current measurements are required. These measurements are carried out using the LV25-P voltage sensor (Octapart, New York, NY, USA) and LA25-NP current sensor (Infineon, Munich, Germany). The solar sensor based on TLO82 is used to measure solar irradiation; meanwhile, the temperature is measured with an LM335 temperature sensor (ES Systems, Neo Psychico, Greece). The voltage and current are varied utilizing a variable resistor. The electronic oscilloscope scopiX, II (OX 7104) (TiePie, Sneek, The Netherlands) is used to display and record this variation.

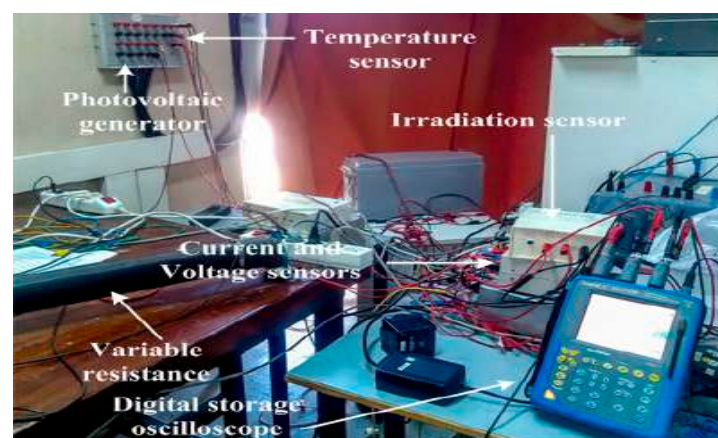


**Figure 8.** Experimental test bench.

**Table 12.** Parameter Specification of the TITAN-12-50 PV module.

Characteristics	Value
$I_{sc}$ (A)	3.2
$V_{oc}$ (V)	21
$P_{mpp}$ (W)	50
$I_{mpp}$ (A)	2.9
$V_{mpp}$ (V)	17.2
Cells number	32

Several experiments are conducted in this study to evaluate the I–V and P–V characteristics of the developed models under various lighting and temperature conditions. Various environmental factors affect the performance of a PV generator under real-life conditions. Consequently, four different tests are performed, and their data are recorded and presented in Figures 9 and 10.

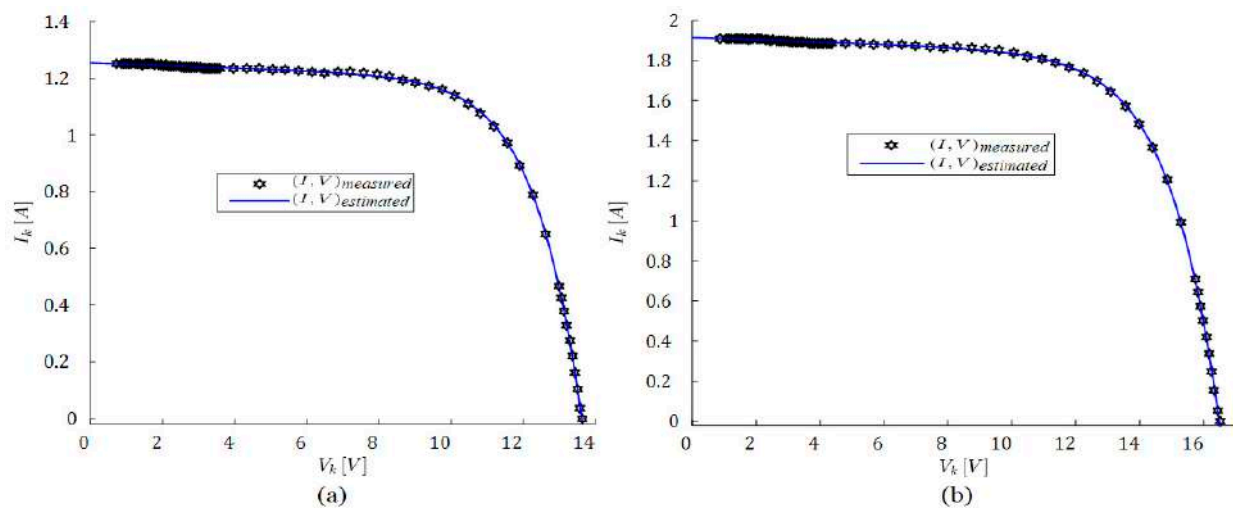


**Figure 9.** Comparison of I–V curves for TITAN-12-50 PV module using MSGO algorithm: (a)  $G = 360 \text{ W/m}^2$  and  $T = 18 \text{ }^\circ\text{C}$ ; and (b)  $G = 556 \text{ W/m}^2$  and  $T = 20.5 \text{ }^\circ\text{C}$ .

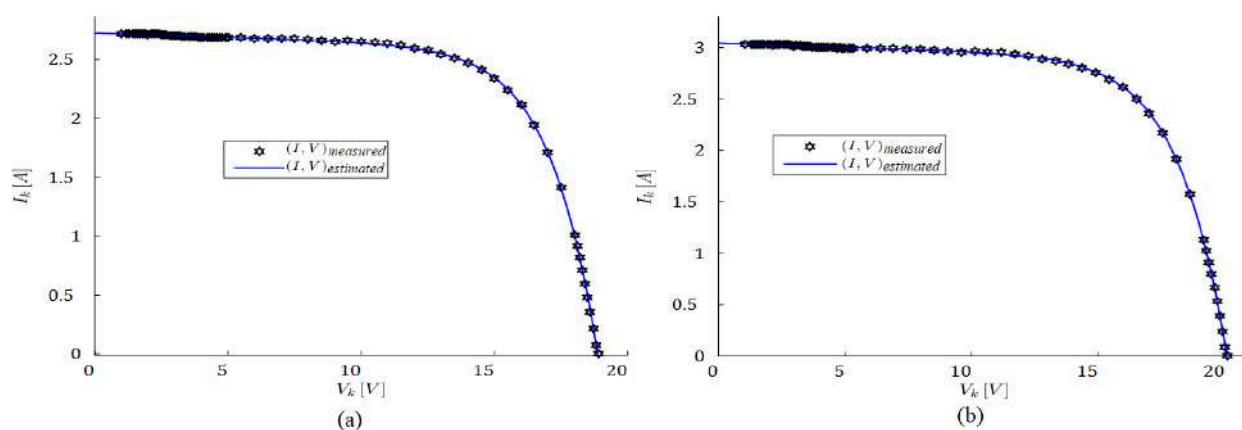


**Figure 10.** Comparison of I–V curves for TITAN-12-50 PV module using MSGO algorithm: (a)  $G = 810 \text{ W/m}^2$  and  $T = 22.60 \text{ }^\circ\text{C}$ ; and (b)  $G = 900 \text{ W/m}^2$  and  $T = 23.80 \text{ }^\circ\text{C}$ .

According to the presented results in Figures 9 and 10, it can be noticed that the estimated current coincides with the measured current for the different cases of environmental factors.

This shows the effectiveness of the MSGO algorithm against changes in temperature and irradiation.

The convergence curves of various algorithms are illustrated in Figure 11. The average fitness functions ALO, WOA, VCS, GSA, SSA, and SCA are given in Ref. [40]. The MSGO results are presented in Figure 11 in black. In general, all algorithms exhibit an acceptable variation in the fitness function. The fastest convergence rate is seen in the MSGO results.

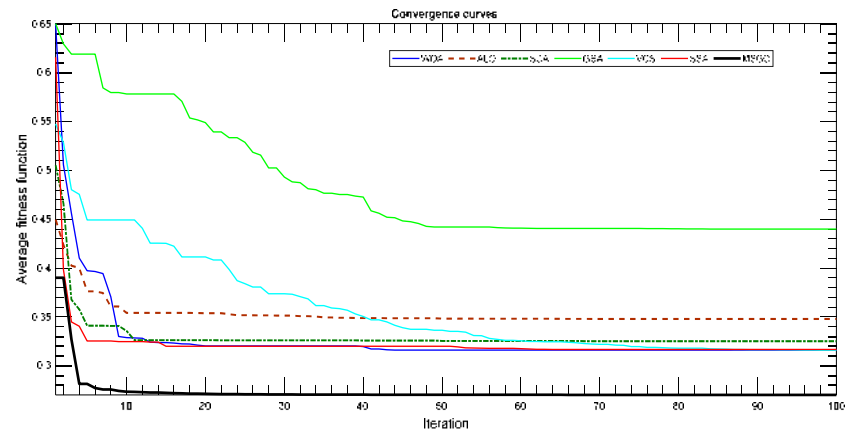


Figure 11. Average fitness functions.

All different parameters of the TITAN-12-50 solar panel extracted under  $G = 810 \text{ W/m}^2$  and  $T = 22.70 \text{ }^\circ\text{C}$  are illustrated in Table 13.

Table 13. Obtained RMSE values and estimated parameters of PV cells.

Parameters	$I_{ph}$ (A)	$R_s$ ( $\Omega$ )	$R_p$ ( $\Omega$ )	$\alpha_1$	$\alpha_2$	$I_{01}$ ( $\mu\text{A}$ )	$I_{02}$ ( $\mu\text{A}$ )	RMS
MSGO	3.2810	0.3562	105.6204	1.4046	1.4046	4.48	4.48	$1.3637 \times 10^{-6}$
SCA	2.74	0.169	72.000	1.456	1.200	9	9	$1.3937 \times 10^{-5}$
ALO	2.733	0.489	50	1	1	0.6869	0.6786	$1.5665 \times 10^{-4}$
GSA	2.716	0.818	140.659	1.013	1.058	0.6999	0.6405	$4.8032 \times 10^{-5}$
VCS	2.734	0.333	70.189	1.003	1.002	0.6990	0.6993	$1.6188 \times 10^{-6}$
WOA	2.75	0.351	90	1.60	1.48	7	7	$3.6935 \times 10^{-4}$
SSA	2.722	0.174	98	1.2	1.3	7.8	7.8	$1.5777 \times 10^{-6}$

Table 13 shows the extracted parameters of the TITAN-12-50 PV module at  $G = 810 \text{ W/m}^2$  and  $T = 22.70 \text{ }^\circ\text{C}$ . The MSGO parameter results are compared with previous results, given by Ref. [40], taking into account the same temperature and irradiation conditions. The proposed MSGO algorithm achieved the lowest RMSE value compared to all other algorithms by  $1.3637 \times 10^{-6}$ . After analyzing the data presented in Table 13, Figure 10, and Figure 11, it can be inferred that the MSGO algorithm exhibits several advantages, such as rapid convergence and minimal errors.

## 5. Discussion

The MSGO algorithm was developed to enhance the precision of solar cell parameter extraction. It was tested on monocrystalline, polycrystalline, and amorphous PV cells with the SDM and DDM to evaluate its performance. The MSGO algorithm was then compared to other techniques in the literature to determine its effectiveness. Results from statistical analysis and figures indicate that the MSGO algorithm is highly accurate and robust. Additionally, the results obtained from the MSGO algorithm are more promising than those of other previously proposed methods.

To further confirm the accuracy of the simulation model, experimental tests were conducted. The results of these tests indicate that the proposed MSGO algorithm is remarkably accurate, fast, and convergent, outperforming other similar algorithms proposed in the literature.



**Author Contributions:** All authors contributed to formulating the research idea, algorithm design, result analysis, writing, and reviewing the research. Conceptualization, H.K. and E.T.; data curation, E.T.; funding acquisition, E.T. and A.M.A.; investigation, M.J.; methodology, A.A. and A.M.A.; project administration, H.K.; resources, L.S.; software, T.I.A.; validation, A.A.; writing—original draft, H.K. and A.M.A.; writing—review and editing, T.I.A. All authors have read and agreed to the published version of the manuscript.

**Funding:** This work is funded by the Deanship of Scientific Research at Northern Border University under research group grant number (RG-NBU-2022-1215).

**Institutional Review Board Statement:** Not applicable.

**Informed Consent Statement:** Not applicable.

**Data Availability Statement:** Not applicable.

**Acknowledgments:** The authors extend their appreciation to the Deanship of Scientific Research at Northern Border University for funding this work through research group No. (RG-NBU-2022-1215). The authors gratefully thank the Prince Faisal bin Khalid bin Sultan Research Chair in Renewable Energy Studies and Applications (PFCRE) at Northern Border University for their support and assistance.

**Conflicts of Interest:** The authors declare no conflict of interest.

## References

1. Ezzeddine, T. Reactive power analysis and frequency control of autonomous wind induction generator using particle swarm optimization and fuzzy logic. *Energy Explor. Exploit.* **2019**, *38*, 755–782. [CrossRef]
2. Touti, E.; Zayed, H.; Pusca, R.; Romary, R. Dynamic Stability Enhancement of a Hybrid Renewable Energy System in Stand-Alone Applications. *Computation* **2021**, *9*, 14. [CrossRef]
3. Kariem, H.; Touti, E.; Fetouh, T. The efficiency of PSO-based MPPT technique of an electric vehicle within the city. *Meas. Control.* **2020**, *53*, 461–473. [CrossRef]
4. Gul, M.; Kotak, Y.; Muneer, T. Review on recent trend of solar photovoltaic technology. *Energy Explor. Exploit.* **2016**, *34*, 485–526. [CrossRef]
5. Kihlström, V.; Elbe, J. Constructing Markets for Solar Energy—A Review of Literature about Market Barriers and Government Responses. *Sustainability* **2021**, *13*, 3273. [CrossRef]
6. Aminian, E.; Saffari, H. Experimental analysis of dropwise condensation heat transfer on a finned tube: Impact of pitch size. *Proc. Inst. Mech. Eng. Part A J. Power Energy* **2021**, *236*, 752–759. [CrossRef]
7. Belloni, M.; Conti, T.D.N. The Connection of Solar Generators to the Electricity Distribution Network as a Means of Mitigating Environmental Impacts by Dispensing the Banks of Accumulators. *Energy Power Eng.* **2019**, *11*, 392–397. [CrossRef]
8. Kumar, R.; Deshmukh, V.; Bhari, R.S. Performance enhancement of photovoltaic modules by nanofluid cooling: A comprehensive review. *Int. J. Energy Res.* **2020**, *44*, 6149–6169. [CrossRef]
9. Silva, P.R.; da Silva Jota, P.R.; Batista, A.P. PV Characterization System Outdoors—Case Study in Brazil. *J. Power Energy Eng.* **2017**, *05*, 119–132. [CrossRef]
10. Mokarram, M.; Mokarram, M.J.; Khosravi, M.R.; Saber, A.; Rahideh, A. Determination of the optimal location for constructing solar photovoltaic farms based on multi-criteria decision system and Dempster–Shafer theory. *Sci. Rep.* **2020**, *10*, 8200. [CrossRef]
11. Kraiem, H.; Aymen, F.; Yahya, L.; Triviño, A.; Alharthi, M.; Ghoneim, S.S.M. A Comparison between Particle Swarm and Grey Wolf Optimization Algorithms for Improving the Battery Autonomy in a Photovoltaic System. *Appl. Sci.* **2021**, *11*, 7732. [CrossRef]
12. Stutenbaeumer, U.; Mesfin, B. Equivalent model of monocrystalline, polycrystalline and amorphous silicon solar cells. *Renew. Energy* **1999**, *18*, 501–512. [CrossRef]
13. Anani, N.; Ibrahim, H.K. Adjusting the Single-Diode Model Parameters of a Photovoltaic Module with Irradiance and Temperature. *Energies* **2020**, *13*, 3226. [CrossRef]
14. Taherbaneh, M.; Rezaie, A.H.; Ghafoorifard, H.; Rahimi, K.; Menhaj, M.B.; Milimonfared, J.M. Evaluation of two-diode-model of a solar panel in a wide range of environmental conditions. *Int. J. Electron.* **2011**, *98*, 357–377. [CrossRef]
15. Qais, M.H.; Hasanien, H.M.; Alghuwainem, S.; Nouh, A.S. Coyote optimization algorithm for parameters extraction of three-diode photovoltaic models of photovoltaic modules. *Energy* **2019**, *187*, 116001. [CrossRef]
16. Premkumar, M.; Subramaniam, U.; Babu, T.S.; Elavarasan, R.M.; Mihet-Popa, L. Evaluation of Mathematical Model to Characterize the Performance of Conventional and Hybrid PV Array Topologies under Static and Dynamic Shading Patterns. *Energies* **2020**, *13*, 3216. [CrossRef]
17. Muhammadsharif, F.F.; Hashim, S.; Hameed, S.S.; Ghoshal, S.; Abdullah, I.K.; Macdonald, J.; Yahya, M.Y. Brent’s algorithm based new computational approach for accurate determination of single-diode model parameters to simulate solar cells and modules. *Sol. Energy* **2019**, *193*, 782–798. [CrossRef]



18. Muhammadsharif, F.F.; Hashim, S. A Simple and Efficient Determination of the Ideality Factor of Solar Cells and Modules from the Knee Point of the Shunt Resistance Curve. *Arab. J. Sci. Eng.* **2023**, *48*, 8217–8225. [CrossRef]
19. DChan, D.S.H.; Phang, J.C.H. Analytical methods for the extraction of solar-cell single- and double-diode model parameters from I-V characteristics. *IEEE Trans. Electron Devices* **1987**, *34*, 286–293. [CrossRef]
20. Ibrahim, H.; Anani, N. Evaluation of Analytical Methods for Parameter Extraction of PV modules. *Energy Procedia* **2017**, *134*, 69–78. [CrossRef]
21. Oliva, D.; Cuevas, E.; Pajares, G.J.E. Parameter identification of solar cells using artificial bee colony optimization. *Energy* **2014**, *72*, 93–102. [CrossRef]
22. Narasimman, K.; Iniyar, S.; Goic, R. Experimental investigation of ridge concentrator PV-based solar water pumping system for small-scale applications. *Energy Sources Part A Recover. Util. Environ. Eff.* **2019**, *42*, 1844–1860. [CrossRef]
23. Fadlallah, S.O.; Serradj, D.E.B. Determination of the optimal solar photovoltaic (PV) system for Sudan. *Sol. Energy* **2020**, *208*, 800–813. [CrossRef]
24. Bastidas-Rodriguez, J.; Petrone, G.; Ramos-Paja, C.; Spagnuolo, G. A genetic algorithm for identifying the single diode model parameters of a photovoltaic panel. *Math. Comput. Simul.* **2017**, *131*, 38–54. [CrossRef]
25. Chen, X.; Xu, B.; Mei, C.; Ding, Y.; Li, K. Teaching–learning–based artificial bee colony for solar photovoltaic parameter estimation. *Appl. Energy* **2018**, *212*, 1578–1588. [CrossRef]
26. Yang, X.; Gong, W.; Wang, L. Comparative study on parameter extraction of photovoltaic models via differential evolution. *Energy Convers. Manag.* **2019**, *201*, 112113. [CrossRef]
27. Askarzadeh, A.; dos Santos Coelho, L. Determination of photovoltaic modules parameters at different operating conditions using a novel bird mating optimizer approach. *Energy Convers. Manag.* **2015**, *89*, 608–614. [CrossRef]
28. Kanimozhi, G.; Kumar, H. Modeling of solar cell under different conditions by Ant Lion Optimizer with LambertW function. *Appl. Soft Comput.* **2018**, *71*, 141–151. [CrossRef]
29. Subudhi, B.; Pradhan, R. Bacterial Foraging Optimization Approach to Parameter Extraction of a Photovoltaic Module. *IEEE Trans. Sustain. Energy* **2017**, *9*, 381–389. [CrossRef]
30. Saxena, A.; Sharma, A.; Shekhawat, S. Parameter extraction of solar cell using intelligent grey wolf optimizer. *Evol. Intell.* **2020**, *15*, 167–183. [CrossRef]
31. Elazab, O.S.; Hasanien, H.M.; Elgendy, M.A.; Abdeen, A.M. Parameters estimation of single- and multiple-diode photovoltaic model using whale optimisation algorithm. *IET Renew. Power Gener.* **2018**, *12*, 1755–1761. [CrossRef]
32. Kumar, C.; Raj, T.D.; Premkumar, M. A new stochastic slime mould optimization algorithm for the estimation of solar photovoltaic cell parameters. *Optik* **2020**, *223*, 165277. [CrossRef]
33. Ben Messaoud, R. Extraction of uncertain parameters of single and double diode model of a photovoltaic panel using Salp Swarm algorithm. *Measurement* **2019**, *154*, 107446. [CrossRef]
34. Naik, A.; Satapathy, S.C.; Abraham, A. Modified Social Group Optimization—A meta-heuristic algorithm to solve short-term hydrothermal scheduling. *Appl. Soft Comput.* **2020**, *95*, 106524. [CrossRef]
35. Hamid, N.F.A.; Rahim, N.A.; Selvaraj, J. Solar cell parameters identification using hybrid Nelder-Mead and modified particle swarm optimization. *J. Renew. Sustain. Energy* **2016**, *8*, 015502. [CrossRef]
36. Dkhichi, F.; Oukarfi, B.; Fakkar, A.; Belbounaguia, N. Parameter identification of solar cell model using Levenberg–Marquardt algorithm combined with simulated annealing. *Sol. Energy* **2014**, *110*, 781–788. [CrossRef]
37. Niu, Q.; Zhang, L.; Li, K. A biogeography-based optimization algorithm with mutation strategies for model parameter estimation of solar and fuel cells. *Energy Convers. Manag.* **2014**, *86*, 1173–1185. [CrossRef]
38. Gong, W.; Cai, Z. Parameter extraction of solar cell models using repaired adaptive differential evolution. *Sol. Energy* **2013**, *94*, 209–220. [CrossRef]
39. Askarzadeh, A.; Rezazadeh, A. Artificial bee swarm optimization algorithm for parameters identification of solar cell models. *Appl. Energy* **2013**, *102*, 943–949. [CrossRef]
40. Yuan, X.; He, Y.; Liu, L. Parameter extraction of solar cell models using chaotic asexual reproduction optimization. *Neural Comput. Appl.* **2014**, *26*, 1227–1239. [CrossRef]
41. Wang, Y.; Xi, J.; Han, N.; Xie, J. Modeling method research of flexible amorphous silicon solar cell. *Appl. Sol. Energy* **2015**, *51*, 41–46. [CrossRef]
42. Abbassi, R.; Abbassi, A.; Heidari, A.A.; Mirjalili, S. An efficient salp swarm-inspired algorithm for parameters identification of photovoltaic cell models. *Energy Convers. Manag.* **2018**, *179*, 362–372. [CrossRef]
43. Rodrigo, P.; Fernández, E.; Almonacid, F.; Pérez-Higueras, P. Models for the electrical characterization of high concentration photovoltaic cells and modules: A review. *Renew. Sustain. Energy Rev.* **2013**, *26*, 752–760. [CrossRef]
44. Bishop, J. Computer simulation of the effects of electrical mismatches in photovoltaic cell interconnection circuits. *Sol. Cells* **1988**, *25*, 73–89. [CrossRef]
45. Sulyok, G.; Summhammer, J. Extraction of a photovoltaic cell’s double-diode model parameters from data sheet values. *Energy Sci. Eng.* **2018**, *6*, 424–436. [CrossRef]
46. Elazab, O.S.; Hasanien, H.M.; Alsaidan, I.; Abdelaziz, A.Y.; Muyeen, S.M. Parameter Estimation of Three Diode Photovoltaic Model Using Grasshopper Optimization Algorithm. *Energies* **2020**, *13*, 497. [CrossRef]

47. Satapathy, S.; Naik, A. Social group optimization (SGO): A new population evolutionary optimization technique. *Complex Intell. Syst.* **2016**, *2*, 173–203. [CrossRef]
48. Naik, A.; Satapathy, S.C.; Ashour, A.S.; Dey, N. Social group optimization for global optimization of multimodal functions and data clustering problems. *Neural Comput. Appl.* **2016**, *30*, 271–287. [CrossRef]

**Disclaimer/Publisher’s Note:** The statements, opinions and data contained in all publications are solely those of the individual author(s) and contributor(s) and not of MDPI and/or the editor(s). MDPI and/or the editor(s) disclaim responsibility for any injury to people or property resulting from any ideas, methods, instructions or products referred to in the content.

## Article

# A New Five-Port Energy Router Structure and Common Bus Voltage Stabilization Control Strategy

Xianyang Cui <sup>1,2</sup>, Yulong Liu <sup>1,2</sup>, Ding Yuan <sup>1,2</sup>, Tao Jin <sup>1,2,\*</sup> and Mohamed A. Mohamed <sup>3,\*</sup>

<sup>1</sup> College of Electrical Engineering and Automation, Fuzhou University, Fuzhou 350108, China

<sup>2</sup> Fujian Province University Engineering Research Center of Smart Distribution Grid Equipment, Fuzhou 350108, China

<sup>3</sup> Electrical Engineering Department, Faculty of Engineering, Minia University, Minia 61519, Egypt

\* Correspondence: jintly@fzu.edu.cn (T.J.); dr.mohamed.abdelaziz@mu.edu.eg (M.A.M.)

**Abstract:** Multi-port energy routers are a core device that integrates distributed energy sources and enables energy-to-energy interconnections. For the energy routing system, the construction of its topology, the establishment of internal model switching and the control of common bus voltage stability are the key elements of the research. In this paper, a five-port energy router structure is proposed, including a PV port, an energy storage port, a grid-connected port, a DC load port, and an AC load port. Among them, the energy storage port and the grid-connected port involve bidirectional energy flow, which are the core ports of control. For the system state, a model switching strategy is proposed based on the topology and the port energy flow direction. When the external conditions change, the system can be stabilized by means of a quick response from the energy storage port. When the energy storage is saturated, the state is switched, and the grid-connected port works to achieve system stability. The rapid stabilization of the bus voltage and the free flow of energy are achieved by combining the fast response of the model predictive control with the properties of multiple model switching. Finally, the feasibility of this energy router topology and control strategy is verified by building simulations in MATLAB.

**Keywords:** energy internet; energy router; common bus voltage; cooperative control; model transformation

**Citation:** Cui, X.; Liu, Y.; Yuan, D.; Jin, T.; Mohamed, M.A. A New Five-Port Energy Router Structure and Common Bus Voltage Stabilization Control Strategy. *Sustainability* **2023**, *15*, 2958. <https://doi.org/10.3390/su15042958>

Academic Editor: Pablo García Triviño

Received: 21 December 2022

Revised: 1 February 2023

Accepted: 2 February 2023

Published: 6 February 2023



**Copyright:** © 2023 by the authors. Licensee MDPI, Basel, Switzerland. This article is an open access article distributed under the terms and conditions of the Creative Commons Attribution (CC BY) license (<https://creativecommons.org/licenses/by/4.0/>).

## 1. Introduction

With the shortage of energy and the increasing problem of environmental pollution, distributed energy has gradually come into people's view, and the energy internet (EI), with electricity at its core, has come to be paid more attention [1,2]. The energy router (ER) is the core equipment for energy internet architecture, effectively integrating distributed energy sources, realizing AC–DC free conversion and multi-directional flow of energy, and effectively reducing the impact brought about by distributed energy sources and AC–DC load access to the power system [3–5], and the popular use of energy routers is an essential trend for the future development of the energy internet. For interconnected systems of distributed energy sources, a reasonable energy router architecture, suitable energy scheduling and coordination control strategy are the key factors for determining the stable operation of the system [6,7]. ER can not only solve the problem of distributed energy grid connection, but also provide a plug-and-play interface for different devices. ER can achieve the goal of power system control integration. Therefore, research on ER is very urgent.

Depending on the demand and the location, energy routers with different classifications are also used, and can mainly be divided into terminal energy routers, regional energy routers, and backbone energy routers [8–10]. Normally, energy routers applied to the backbone and area are relatively mature, while those applied to the terminal have been less thoroughly researched. Energy routers for terminal applications are widely used,

and can effectively utilize distributed energy and meet the development goal of “double carbon”, having high research significance.

Therefore, energy routers have accordingly been studied in terms of overall architecture [11], control strategy [12,13], internal communication design [14], and key parameters [15], but so far, no expert scholars have proposed a general energy router architecture and a control strategy that can satisfy various operating conditions. Ref. [16] proposed a coordinated control strategy for AC–DC hybrid ER based on energy storage and voltage stabilization that used multiple sets of converters to provide a wealth of AC–DC ports, and also classified the external ports for consideration, but its module control strategy was relatively simple, and the dynamic performance required improvement. Ref. [17] proposed a multi-LAN port energy router that could easily connect distributed power sources and AC–DC loads to the backbone grid, but did not consider the access of energy storage systems, and the energy router architecture was not complete. Ref. [18] provided the design idea of a community energy router, giving different operating states of the energy router under distribution network failure. However, no specific feasible topology was given. In [19], a power allocation strategy for seamless switching conditions was proposed, but it lacked precise consideration of the battery. In [20], a two-level modular ER structure that could be applied to DC microgrid clusters was proposed to realize the function of flexible interconnection of microgrids. In [21], the impact on the energy router under grid fault conditions and the balancing strategy of the capacitor voltage under various conditions were analyzed, but only situations under single-phase grid faults were considered, without considering two-phase or multiple three-phase faults.

The study of ER is at this stage no longer limited to the ER itself, as the grid-connected port is connected to the distribution grid. Therefore, research on the power quality of the distribution grid port and the energy allocation and optimization of the distribution grid side is also meaningful. In ref. [22], the authors proposed a hierarchical grid model to enhance the resilience of DC-MGs. In refs. [23,24], the researchers studied energy hubs. These include wind power, solar power, and energy storage. The management of distributed energy sources and the improvement of distribution network reliability, respectively, were studied. However, these papers are all macroscopic studies, but do not explain the details of ER.

Due to the nature of the energy router, the presence of a grid-connected port is necessary. When the energy router is connected to the grid, if it is not established with a battery or the battery is not properly controlled and directly connected to the grid, it will result in high network loss. The battery is able to play the role of a bridge for energy circulation, carry out energy buffering, and can also help the energy router to stabilize the bus voltage. For the regulation of the energy router, the use of the battery, the state of charge of the battery, and the comprehensive deployment of the battery discharge power also need to be considered [25–28]. Refs. [29,30] mention a variety of optimization algorithms that serve as a theoretical basis for the future expansion of ER and its integration with power systems, and the future expansion of power systems will be studied in depth on the basis of the algorithms. Refs. [31,32] propose optimization algorithms in combination with biology, and these algorithms are better able to optimize the energy allocation strategy of energy routers and improve their efficiency.

On the basis of the existing research, the study of ER has primarily focused on structure as well as on control. Therefore, in this paper, we design a five-port energy router topology in consideration of these two points and propose a corresponding control strategy for this structure.

The first point is the design of the topology. In accordance with the requirements, an ER including PV, energy storage, grid-connected, AC, and DC ports was proposed. All ports are connected by a DC bus, and are unified and controlled by a central processor. The topologies of different ports are designed to realize the energy flow.

The second point is the implementation of the control strategy. The control strategy is divided into two layers, which are the independent control of the ports and the overall

coordinated control. For the port functions, each port designs an independent control strategy to maintain stability. At the same time, the top-level control is designed to divide the working modes, and the different ports operate in a coordinated fashion under different working modes to finally work stably.

## 2. Energy Router Topology Creation and Analysis

In the original model, the ER system integrates the PV, the AC load, and the DC load. In response to the need to provide various ports involved in energy routers, this paper proposes a five-port energy router for a wide range of applications. The router architecture is shown in Figure 1, and the five groups of ports are the PV port, the energy storage port, the grid-connected port, the DC load port, and the AC load port. All ports of the energy router converge into a DC common bus (CB), and  $U_{CB}$  is the common bus voltage.  $i_1 \sim i_5$  are the output current values of the five ports, which can represent the interaction with the common bus energy handover.

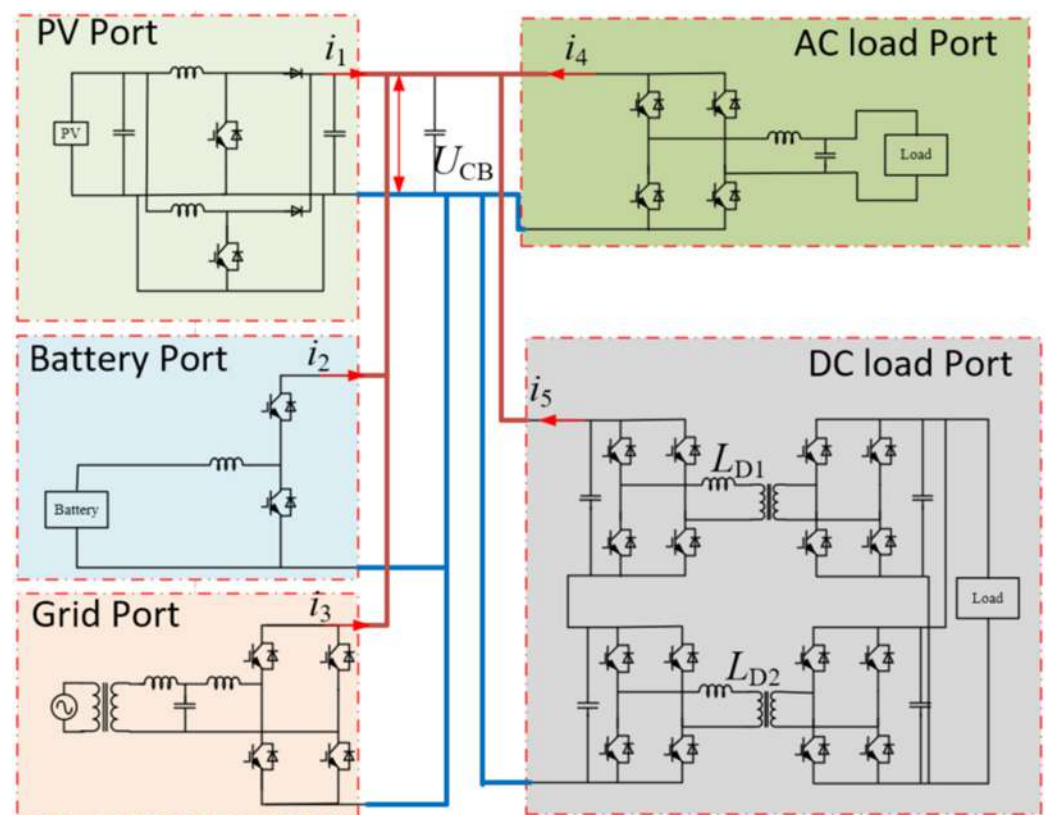


**Figure 1.** The architecture of five-port ER.

Port 1 is the PV port structure, considering the low voltage level of solar power (PV) and the high voltage level of the common bus, the boost topology is used, and considering the switching tube current stress and ripple, this port adopts the interleaved parallel boost structure.  $i_1$  is the PV port and common bus interaction current, the PV port and common bus interaction power  $P_1 = i_1 U_{CB}$ , for the energy storage port, the adopted structure is a two-level converter;  $i_2$  is the storage port, and the common bus current storage port interaction power  $P_2 = i_2 U_{CB}$ , where the port plays the role of stabilizing the DC bus voltage. For the grid-connected port, the structure of a two-level converter combined with an LCL filter is used, which is connected to the grid to realize the interaction of energy with the grid, and the interaction power is  $P_3 = i_3 U_{CB}$ , for the AC load port, the structure of a two-level converter and an LC filter is used, and the interaction power with the common bus is  $P_4 = i_4 U_{CB}$ ; for the DC load port, a parallel input structure is used. For the DC load

port, the structure used is an input parallel-type double active bridge converter (ISOP DAB), and the interaction power of the port with the common bus is  $P_5 = i_5 U_{CB}$ .

The system has a total of five groups of ports, ignoring port losses, and the real-time power balance of the system using the common bus is shown below.

$$P_1 \Delta t + P_2 \Delta t + P_3 \Delta t + P_4 \Delta t + P_5 \Delta t + P_{non} \Delta t = 0 \quad (1)$$

$$P_{non} \Delta t = \frac{1}{2} C_{CB} U_{CB}^2 \quad (2)$$

$$\sum_{k=1}^5 i_k U_{CB} + \frac{1}{2} C_{CB} U_{CB}^2 = 0 \quad (3)$$

where  $U_{CB}$  is the current common bus voltage value,  $C_{CB}$  is the DC bus capacitance value,  $i_k$  is the interaction power generated by each port with the DC bus, and  $P_{non}$  is the unbalanced power of the system at the current moment. Due to the changes in PV, load, etc., fluctuations in  $P_{non}$  will be caused, and will be accompanied by fluctuations in  $U_{CB}$ . Therefore, the overall coordination control starts from the stable control of  $U_{CB}$ , and stable operation of the system is finally realized by controlling the energy interaction status of the energy storage port and the grid-connected port with the main line.

For the energy router, the five groups of ports involved are divided into two parts, consisting of the functional port, for the unidirectional flow of energy, and the voltage stabilization port, for the bidirectional flow of energy. Among them, the PV, AC and DC load ports are the functional ports, and the grid-connected energy storage ports are the voltage stabilization ports.

The structural design of the PV port adopts the structure presented in Figure 2.

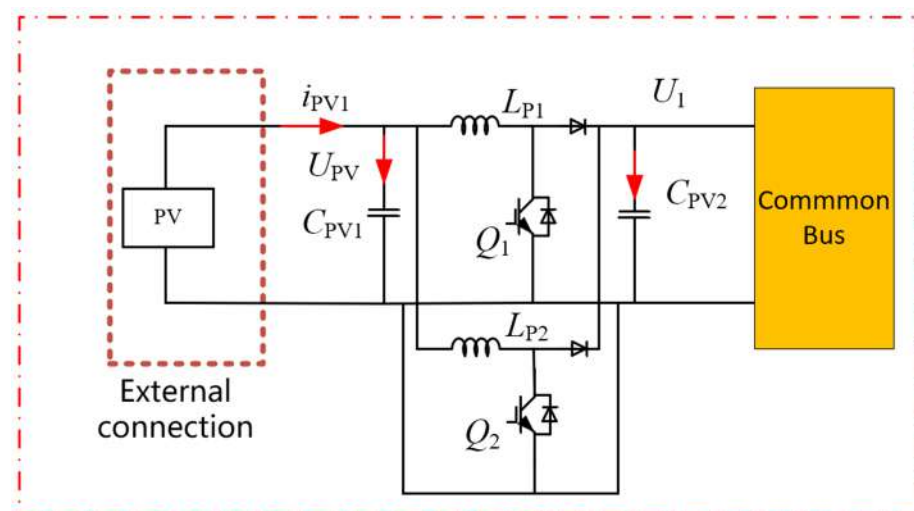


**Figure 2.** The architecture of the PV port.

The function of the PV port is to incorporate solar energy into the energy router system, and the criterion of its work is the full utilization of light energy without considering factors such as energy flow system stability, so the design and control of the PV port start from the efficient acquisition of energy without involving other factors. Considering the characteristics of low PV voltage level, multiple parallel PV cells, and high DC bus voltage level, a boost converter is used as the port, and considering the expandability and the current stress of the switching devices, the boost converter structure adopts an interleaved parallel boost circuit. When the power is the same, the current stress of the staggered parallel booster structure switch tube is lower than that of the ordinary booster circuit; the current ripple is also smaller, which is advantageous for the stability of the common bus voltage and current control.

For the design of the AC load port, considering the controllability of the system and the overall control difficulty, the AC port is not involved in internal voltage stabilization, and is only used as a functional port to supply the load, so the control method and basic structure are the same as those of the conventional inverter. It is sufficient to ensure the output stability and realize the basic external functions. Figure 3 shows the topology of the AC load port, with the output connected to the outside through an LC filter.

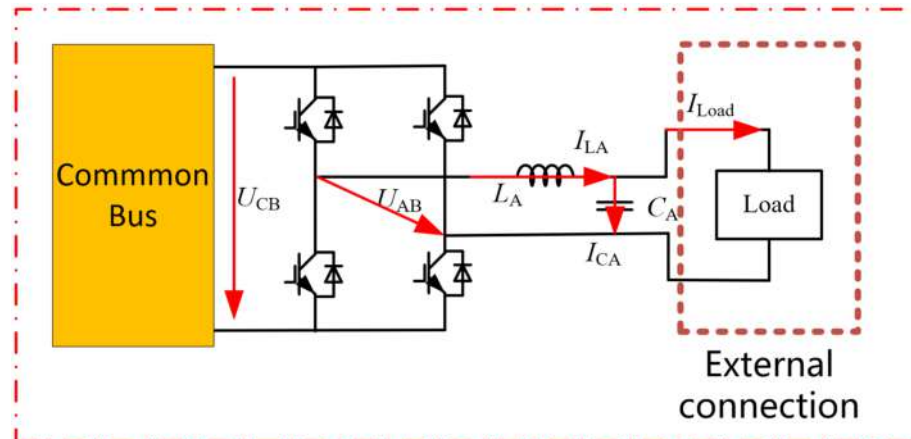


Figure 3. Topology of AC load port.

For the DC port shown in Figure 4, the overall situation is similar to that of the AC port, which is also only used as a functional port to provide DC output without participating in system regulation, and only needs to ensure output stability and achieve basic functions. Considering the widespread use of electric vehicles, the DC port usually needs to provide a greater amount of power, and in terms of electrical isolation, the output of the two modules is connected in series with the output of the parallel-type double active bridge converter (ISOP DAB) to realize the external connection. This structure can effectively increase the output power and reduce the device's current stress.

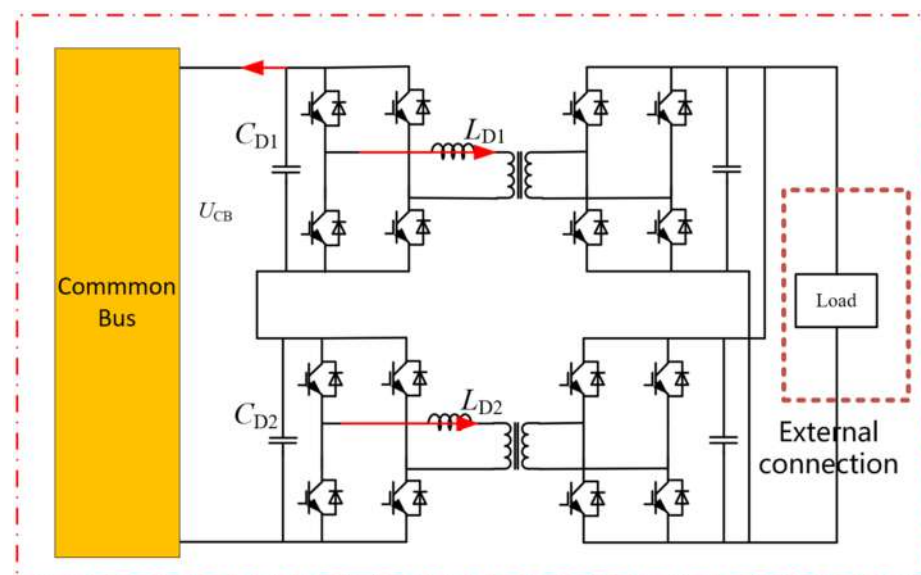


Figure 4. Topology of the DC load port.

For a two-module ISOP-type DAB structure, as described in Figure 5, the modules at the input are voltage-divided, and the voltage at the output is automatically equalized. Due to the manufacturing process, the parameters between the modules are not exactly the



same, and the power balance between the modules needs to be considered. When the input voltage equalization loop is in stable operation, the system achieves power equalization among modules and current equalization at the output with  $I_{21} = I_{22}$ . When the input voltage of the system is disturbed, the input voltage equalization loop can be controlled so that the input voltage of each module receives equalized control. When the output current of the module is disturbed and increases, the output voltage of the module decreases, because the input voltage equalization loop has already achieved system power balance.

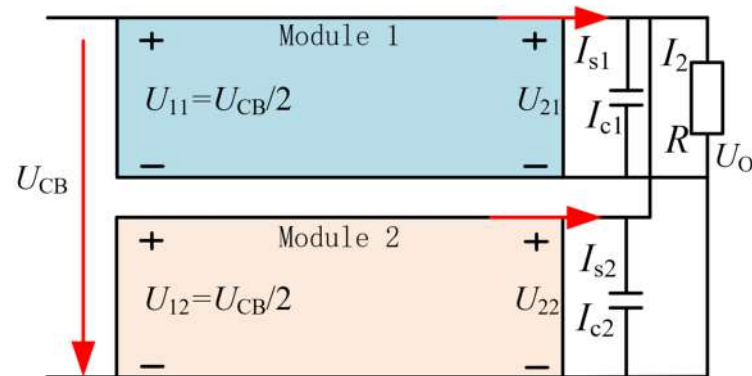


Figure 5. Equivalent diagram of ISOP DAB converter.

The output voltage drop leads to the current flowing to the load becoming smaller and the current flowing to the inductor becoming larger, at which time the inductor is charged and the voltage increases, forming negative feedback regulation, and the system output voltage restores a stable value again. As can be observed, the input voltage equalization loop can simultaneously control the system input voltage waveform and the system output current fluctuation, and ensure the power balance between the system modules from the input side and the output side at the same time.

The grid-connected port is different from the two load ports and the PV port in that it assumes the function of bidirectional energy flow, and is thus an important structure for realizing the energy routing function by obtaining energy from the grid to provide loads when the system energy is insufficient and feeding the excess energy back to the grid when the system energy is excessive. For the grid-connected ports, the structure used is the single-phase rectifier structure shown in Figure 6.

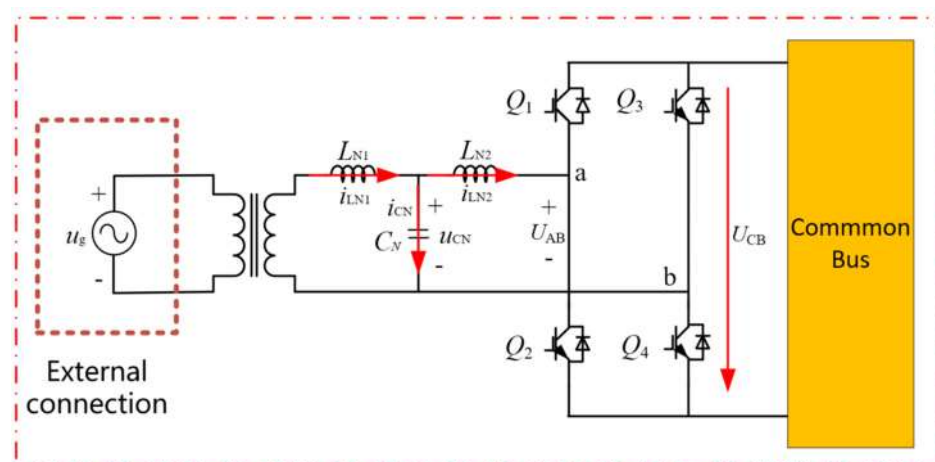


Figure 6. Topology of the grid-connected port.

The grid-connected port is connected to the grid through a set of LCL filters. As a third-order system, LCL filters are small in size and have good high-frequency filtering



performance, but the structure has resonant peaks, which can reduce the stability of the system. In the control, the resonant peaks are suppressed by adding virtual resistors.

The energy storage port plays the role of stabilizing the DC bus voltage, connecting the battery, and buffering the energy, and is the most critical port in terms of the control of the energy router. This port needs to realize the bidirectional flow of energy, and also requires rapid control that is able to quickly sense the fluctuation of the common bus voltage and make adjustments in the control. Therefore, a bidirectional buck–boost structure, as shown in Figure 7, was chosen, and its control adopts the faster model predictive control.

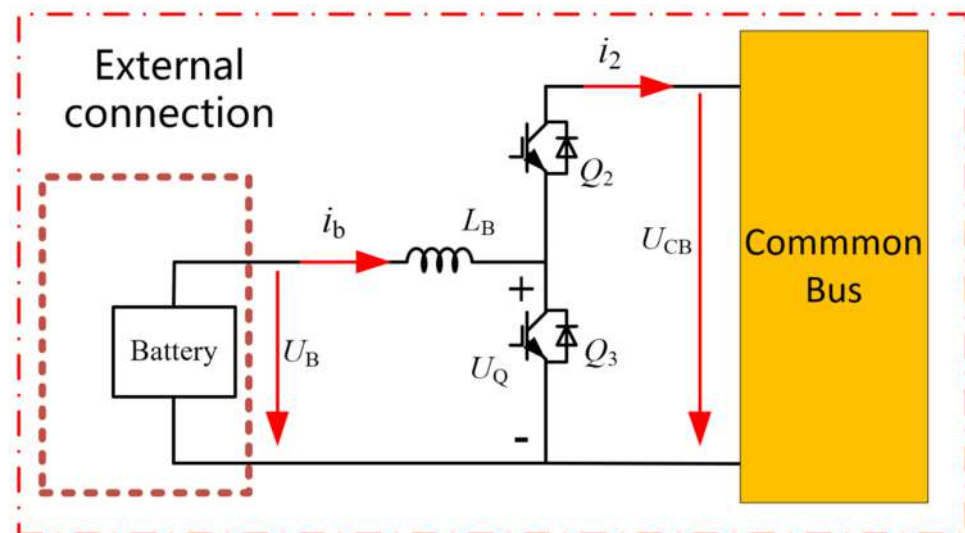


**Figure 7.** Structure of the energy storage part.

The port realizes the bidirectional flow of energy by controlling the opening and closing of switch tubes  $Q_2$  and  $Q_3$ . When  $Q_3$  is cut off, the opening and closing of  $Q_2$  are controlled, meaning that the circuit works in the boost mode, whereby energy is transferred from the battery to the DC bus. When  $Q_2$  is cut off, the opening and closing of  $Q_3$  are controlled, and the circuit works in the buck mode, whereby energy is transferred from the DC bus to the battery, thus realizing the bidirectional flow of energy.

An overview of the energy flow directions and functions of the five ports is provided in Table 1. Obviously, the energy of the first two ports flows in both directions, and the functions are more complex and have more important positions. The last three ports only function to perform energy transfer, and do not play a dominant role in the control.

**Table 1.** ER ports and functional description.

Port	Direction of Energy Flow	Function
Battery Port	Bidirectional	1. Coordinated energy flow 2. Stabilize UCB 3. Coordinated energy storage batteries
Grid port	Bidirectional	1. Coordinated energy flow 2. Stabilize UCB 3. Integrating ER with the grid
PV Port	Unidirectional external to ER	Transferring solar energy to the ER.
AC load port	Unidirectional ER to external	Provide power for AC load
DC load port	Unidirectional ER to external	Provide power for the DC load

### 3. Energy Router Control Strategy Research

#### 3.1. Overall Control Architecture and Control Strategy

For the control of the energy router, the most effective current is achieved using the hierarchical control strategy; in this control strategy, the port controller performs control using local information, and on this basis maintains two-way contact with the central controller. The control architecture is shown in Figure 8, where the overall control architecture is divided into four layers, comprising (from top to bottom) the top-level control platform, the information collection platform, decision control and the bottom-level control platform. Information enters the controller at the bottom and flows upwards, and control signals enter the port at the top and flow downwards.

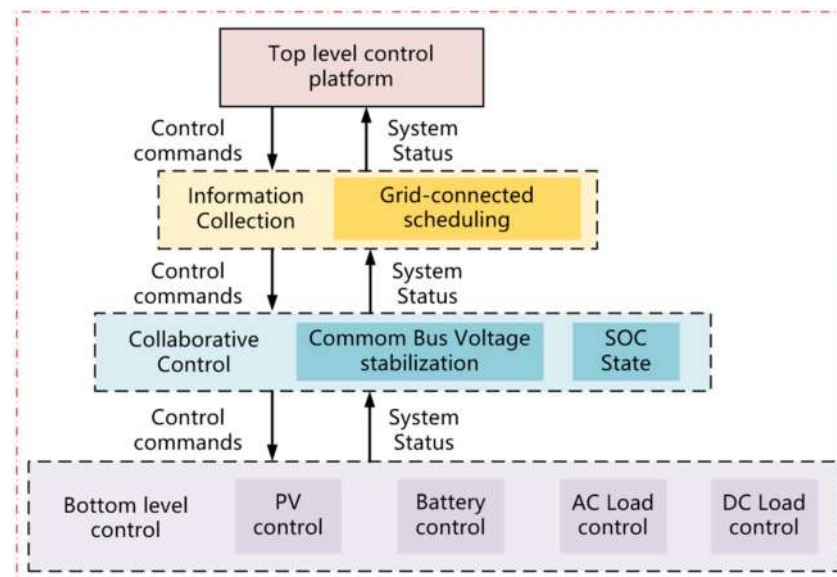


**Figure 8.** Hierarchical control architecture of five-port ER.

For the proposed five-port energy router topology and the hierarchical control architecture used in this paper, the bottom-level control layer and the cooperative control layer are the core of the study. The bottom-level control layer corresponds to the independent control of the five ports, and the cooperative control performs overall control of the ports' operating states by means of bus voltage and battery charge state. The cooperative control layer includes two points, bus voltage stabilization and battery charge state adjustment, both of which are closely related to the energy storage ports. Therefore, this study focuses on the energy storage port in the design and control of the bottom-level port, and establishes an overall control strategy for the port that is able to realize reasonable control of the bus voltage and stability, as well as the battery charge state, so as to finally realize the free flow among multiple energy sources and the stable operation of the energy router. The energy router works stably.

#### 3.2. Five-Port Control Strategy Design

The first is the control of the PV port, which is a unidirectional functional port, and its control goal is to inject as much light energy as possible into the common bus. For this system, in order to ensure that the load attains maximum power, proper load matching is required. When the load resistance is equal to the internal resistance of the power supply system, the load receives the maximum power, with such a load matching process being referred to as maximum power point tracking (MPPT) [33,34]. Figure 9 shows the process of MPPT for the PV port. By collecting the power at the current moment and comparing it with the power at the previous moment, the switching tubes are controlled by judging the change in power, while using a staggered parallel boost structure, where the control

signals of the two groups of switching tubes are the same, but the delta carrier signals are staggered by half a cycle to achieve harmonic offset.

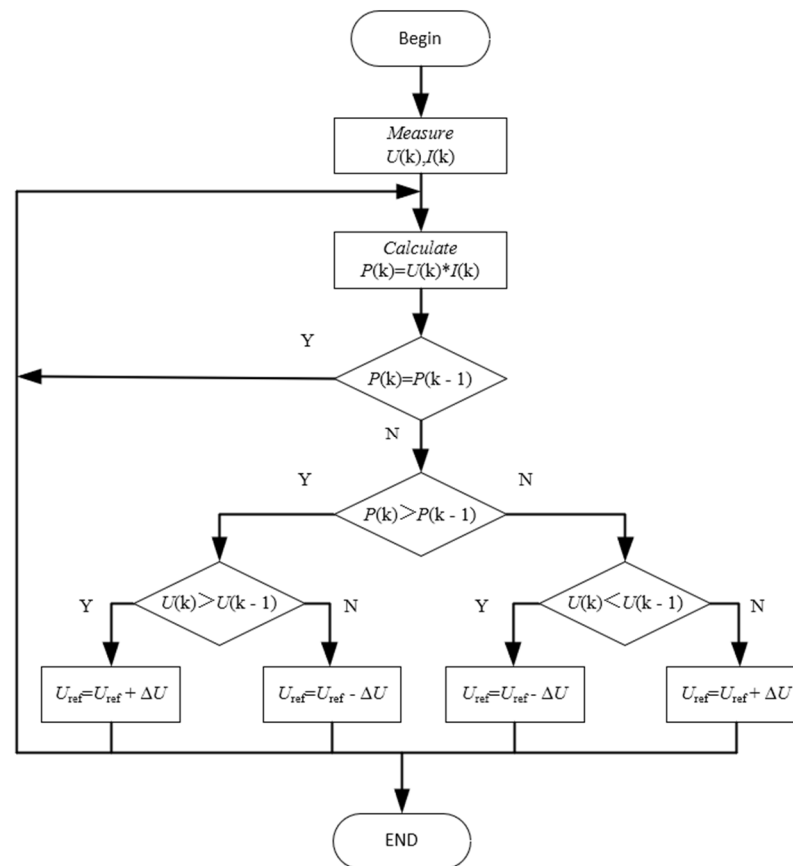


**Figure 9.** PV module structure and control block diagram.

For the AC load port, as can be seen from the structure topology diagram in Figure 3, the output is connected to the load using an LC filter. It is not a bad idea to set the load as a resistive load with resistance  $R$ . Then, in the complex frequency domain, we have:

$$\begin{cases} I_{LA}(s) = \frac{U_{AB}(s) - U_C(s)}{L_A s} \\ (I_{L1}(s) - I_{Load}(s)) \frac{1}{Cs} = U_C(s) \\ I_{Load}(s) = \frac{U_C(s)}{R} \end{cases} \quad (4)$$

Using bipolar SPWM modulation, in one switching cycle:

$$\overline{U_{AB}} = (2D - 1)U_{CB} \quad (5)$$

$$D = \frac{1}{2} \left( 1 + \frac{V_m}{V_{tri}} \right) \quad (6)$$

where  $D$  is the duty cycle,  $V_m$  is the reference sine wave, which is the input to the modulator, and  $V_{tri}$  is the peak delta carrier wave.

$$\overline{U_{ab}} = (2D - 1)U_{CB} \quad (7)$$

$$\overline{U_{ab}} = \left[ 2 \times \frac{1}{2} \left( 1 + \frac{V_m}{V_{tri}} \right) - 1 \right] U_{CB} = \frac{V_m}{V_{tri}} U_{CB} \quad (8)$$

Then, the transfer function of the AC port can be obtained as follows:

$$G_0(s) = \frac{U_0(s)}{V_m(s)} = \frac{1}{L_A C s^2 + \frac{L_A}{R} s + 1} \frac{U_{CB}}{V_{tri}} \quad (9)$$

For the AC load port, a dual closed-loop voltage and current control are used, and the control strategy is shown in Figure 10.

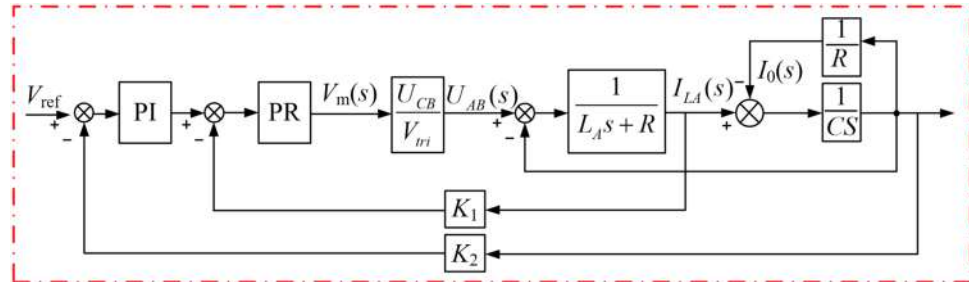


**Figure 10.** AC load port control structure diagram.

The voltage outer loop is the error signal obtained by comparing the reference value with the sampled value of the output voltage, and then the current reference value of the inner loop is generated by the PI controller; the current reference value of the inner loop and the inductor current obtained from the actual sampling are used to generate the current error, and the modulated wave is obtained from the proportional resonance of the inner loop. The feedforward of the reference value is also added to improve the time response characteristics.

For the DC port, an ISOP DAB topology is used, as shown in Figure 4. For this structure, a centralized dual-loop voltage equalization control strategy is used, which is based on the principle whereby a voltage loop is used to control the output voltage, and an independent input voltage loop is used to equalize the input voltage. When the input voltage of a module in the system is disturbed and increases, it can be seen from Figure 11 that the offset control amount of the module also increases, so the output phase shift duty cycle increases, the output power increases, the system input side capacitor is in a discharged state, and the voltage drops, thus stabilizing the output voltage [35].

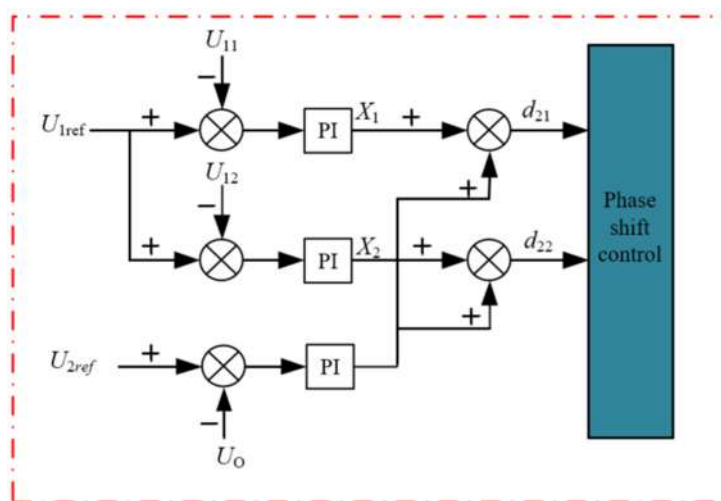


**Figure 11.** Block diagram of the double-loop voltage equalization control system for DAB.

For the grid-connected port, a single-phase rectifier structure is used, as shown in Figure 6: the grid side and the LCL filter and rectifier are isolated using a transformer, and the LCL filter circuit is connected to the DC bus side using the single-phase rectifier.

For the single-phase rectifier, the mathematical model in the complex frequency domain is as follows:

$$\begin{cases} L_{N1}s \cdot i_{LN1}(s) = -u_{CN}(s) + u_g(s) \\ C_N s \cdot u_{CN}(s) = u_g(s) - i_{LN2}(s) \\ L_{N2}s \cdot i_{LN2}(s) = u_{CN}(s) - U_{AB}(s) \end{cases} \quad (10)$$

For SVPWM, the following can be obtained:

$$\frac{U_{AB}(s)}{U_m(s)} = \frac{U_{CB}}{U_{tri}} \quad (11)$$

where  $U_{AB}(s)$  is the actual output voltage,  $U_m(s)$  is the modulating waveform,  $U_{CB}$  is the DC bus voltage, and  $U_{tri}$  is the carrier peak. The actual grid current is obtained, as well as the reference value for the purpose of comparison, and the modulating signal is obtained using a proportional resonant controller, which obtains the capacitor current reference value  $i_{CN\_ref}$  and then compares it with the actual capacitor current  $i_{CN}$ .

With respect to the resonance of the LCL filter, the passive damping method is used to suppress the system resonance, and the control strategy with full feedback of the grid voltage is adopted in consideration of the influence that the voltage fluctuation of the grid has on the system. Figure 12 shows the grid voltage full-feedback control block diagram of the grid-connected port.

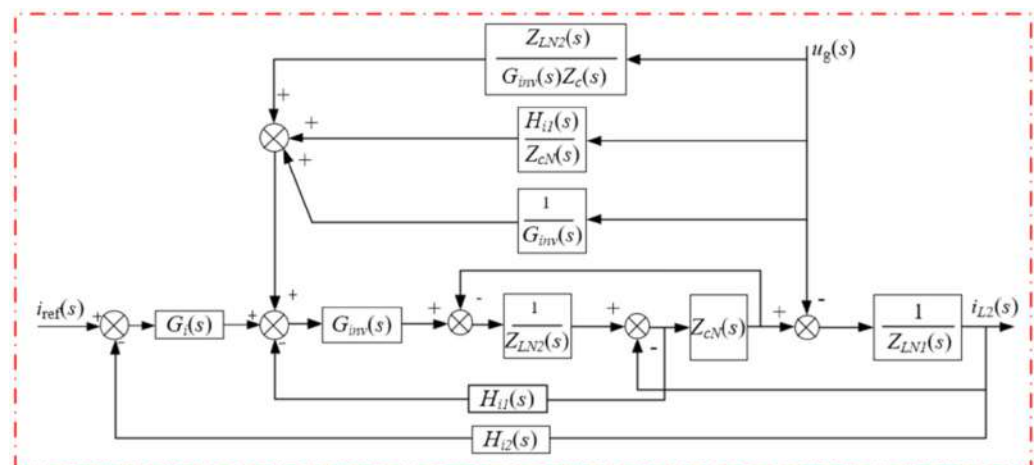


**Figure 12.** Grid voltage full-feedback control block diagram of the grid-connected port.

$H_{i1}(s)$  and  $H_{i2}(s)$  in Figure 12 are the current sensor gain and  $G_i(s)$  is the transfer function of the outer loop, respectively. Figure 13 shows the block diagram of the grid-connected port control, which is used to build the grid-connected port and realize grid-connected port control of the ER.

The energy storage port of the ER can play the role of energy buffer and dissipate the unbalanced energy in a timely fashion, thus playing a role in stabilizing the voltage of the common bus. As a core port, the sensitive control of the energy storage port is of great significance. Model predictive control, as a mature control strategy, has excellent dynamic performance, while the control structure is simple and can be combined with different control strategies such as PI to achieve even better control performance by combining their advantages.

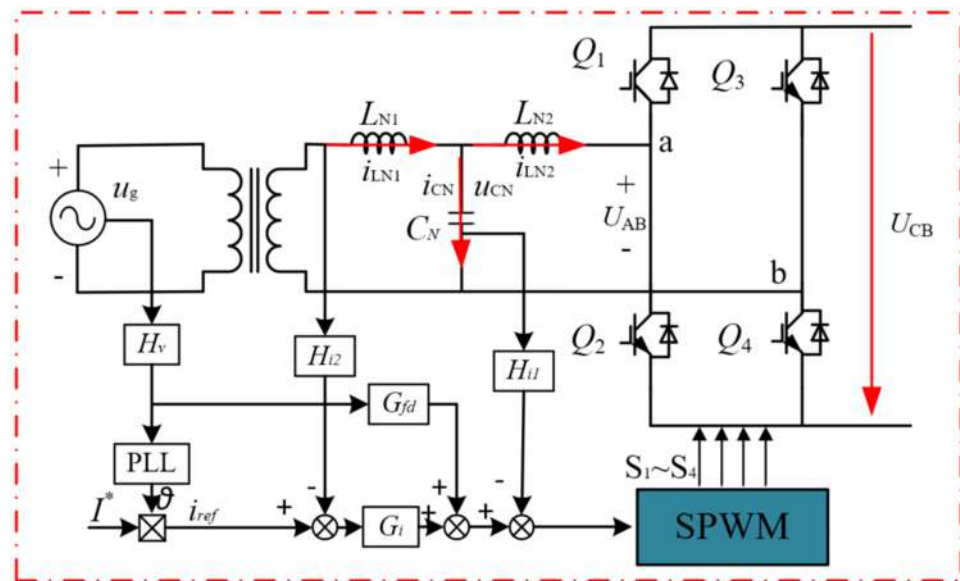


Figure 13. Control block diagram of the structure of the grid-connected port.

As can be observed from the energy storage port structure diagram depicted in Figure 7,

$$U_Q = L_B \frac{di_b}{dt} + U_b \quad (12)$$

Using a discretized form, the transformation of Equation (7) yields

$$i_L(k+1) = (U_Q - U_b) \frac{T_s}{L_B} + i_L(k) \quad (13)$$

Using the sensor, we can get  $i_l$  at moment  $K$ . On the basis of prediction, we can get  $i_{lK+1}$ . Let's assume that the converter is working in the buck mode at this time; then, we have

$$i_L(k+1) = (DU_{CB} - U_B) \frac{T_s}{L_B} + i_L(k) \quad (14)$$

Usually, for digital control systems, there is a certain delay time, which is expressed as follows:

$$i_L(k+1) = (D_{old}U_{CB} - U_B) \frac{T_s}{L} + i_L(k) \quad (15)$$

where  $D_{old}$  is the duty cycle of the previous moment. Generally, a constant voltage is considered for a given sampling period; therefore, we have

$$D = \frac{(i_{Lref} - i_L(k+1))L}{T_s U_{CB}} + \frac{U_B}{U_{CB}} \quad (16)$$

The block diagram of the energy storage converter control is shown in Figure 14. First, the  $U_{CB}$  and the given reference voltage  $U_{CBref}$  are sent to the proportional-integral PI for comparison, at which time a reference current is output for comparison with the actual inductor current and sent to the model predictive controller in order to generate the duty cycle, and the output is compared with the carrier waveform to generate the control signal. When the bus voltage fluctuates, it can be adjusted by this model predictive control strategy.

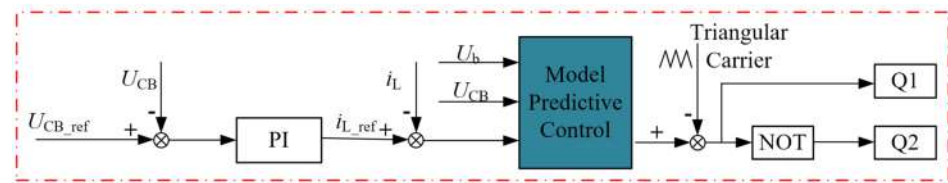


**Figure 14.** Control block diagram of energy storage converter.

### 3.3. Five-Port Energy Router Cooperative Control Strategy

In the energy router, the grid-connected port and the energy storage port are bidirectional ports, which, in addition to their basic functions, also assume the role of stabilizing the common bus voltage,  $U_{CB}$ , which are now defined as voltage stabilization ports. The PV port and the DC and AC load ports are unidirectional ports, which realize the basic function of the energy router is to transmit energy in one direction, which will be defined as the functional port.

The cooperative control of the five ports of the energy router starts with the current common bus voltage  $U_{CB}$ , compares it with the theoretical  $U_{CB\_ref}$ , and also analyzes the state of charge (SOC) of the battery, combining the current PV output with the actual consumption, and divides the work of the energy router into 12 working models, which can be classified into five groups of working models, and the cooperative control of the functional ports and the voltage stabilization ports. The synergistic control of the functional ports and voltage stabilization ports makes it possible to realize the stable operation of the energy router. Figure 15 presents a flowchart of the model discrimination used in the volume router, and Table 2 presents the detailed model classification criteria.

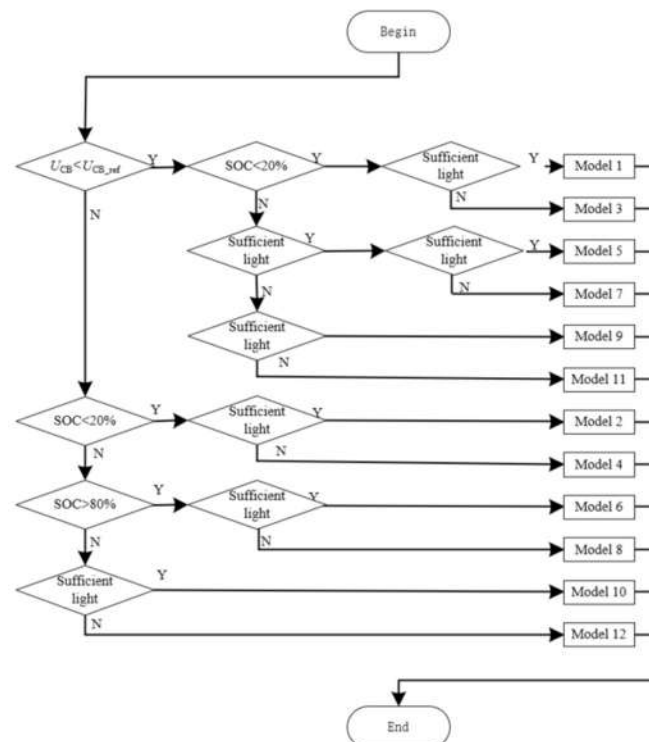


**Figure 15.** Flowchart of model switching of energy router.

According to Table 2, the common bus, energy storage and PV states are delineated as models A, B, C, D and Z.

Model A is an “off-grid charging model”; in this state, the energy supply of storage is insufficient and PV is sufficient. While the energy supply comes from the PV port, the



storage port receives energy from the bus, and the grid-connected port does not participate in the work.

**Table 2.** The working model of ER.

Model	$U_{CB}$	SOC	Illumination	Model
Model A	$U_{CB} < U_{CB\_ref}$	$SOC < 20\%$	Sufficient	Model 1
Model A	$U_{CB} > U_{CB\_ref}$	$SOC < 20\%$	Sufficient	Model 2
Model B	$U_{CB} < U_{CB\_ref}$	$SOC < 20\%$	Insufficient	Model 3
Model B	$U_{CB} > U_{CB\_ref}$	$SOC < 20\%$	Insufficient	Model 4
Model C	$U_{CB} < U_{CB\_ref}$	$SOC > 80\%$	Sufficient	Model 5
Model C	$U_{CB} > U_{CB\_ref}$	$SOC > 80\%$	Sufficient	Model 6
Model D	$U_{CB} < U_{CB\_ref}$	$SOC > 80\%$	Insufficient	Model 7
Model D	$U_{CB} > U_{CB\_ref}$	$SOC > 80\%$	Insufficient	Model 8
Model Z	$U_{CB} < U_{CB\_ref}$	$20\% < SOC < 80\%$	Sufficient	Model 9
Model Z	$U_{CB} > U_{CB\_ref}$	$20\% < SOC < 80\%$	Sufficient	Model 10
Model Z	$U_{CB} < U_{CB\_ref}$	$20\% < SOC < 80\%$	Insufficient	Model 11
Model Z	$U_{CB} > U_{CB\_ref}$	$20\% < SOC < 80\%$	Insufficient	Model 12

Model B is the “grid-connected charging model”, where the energy router storage port is “non-stocked” and the PV is insufficient, and it is necessary to get energy from the grid to meet the requirements of load consumption.

Model C is a “grid-connected power generation model”, where the energy router is full of energy storage and the PV is sufficient to feed the acquired energy back to the grid.

Model D is an “off-grid discharge model”, where the energy router has sufficient energy storage and the PV is insufficient, and the energy router supplies the AC/DC port consumption from its own energy storage.

Model Z is the “intermediate model”, which is the middle model among Models A–D, indicating that the energy router is self-sufficient and works normally, and this intermediate state is off grid, which is the ideal working state, and the energy router is regarded as a “micro grid” without an external connection. The energy is generated and consumed by the system itself, without any interaction with the outside world.

The five-port energy router transitions between the above five working models, and the different working models represent the different working states of the energy storage and grid-connected ports, thus realizing the stable overall control.

#### 4. Simulation Verification and Analysis

In order to verify that the energy router topology proposed in this paper and the corresponding control strategy are feasible, an energy router model based on model predictive control was built using the MATLAB/Simulink platform, and its main parameter settings are shown in Table 3.

Considering the battery storage state and the limitation of simulation time, the initial storage value of the battery, SOC, in the energy router “Model Z” was set to 60%, and its range was set to  $59.993 < SOC < 60.009$ . The initial light intensity of the simulation was set to  $1000 \text{ w/m}^2$ , and the output power of the PV port was about 10 kW at this time. The initial light intensity of the simulation was set to  $1000 \text{ w/m}^2$ , and the output power of the PV port was about 10 kW at this time. The light dropped at 1.1 s and then dropped again to 0 at 1.3 s, after which the PV port stops working.

The system functional port states are as follows: the initial state is set to have only the AC port working, the load power is about 1 kW, and the initial working model of the system is the Z-intermediate model. The system puts the DC port into operation at 0.6 s, the light starts to drop at 1.1 s, and decreases to 0 at 1.3 s, the DC load port < at 1.6 s, the AC port increases the load at 1.9 s, and the load further increases at the AC port at 2.2 s.

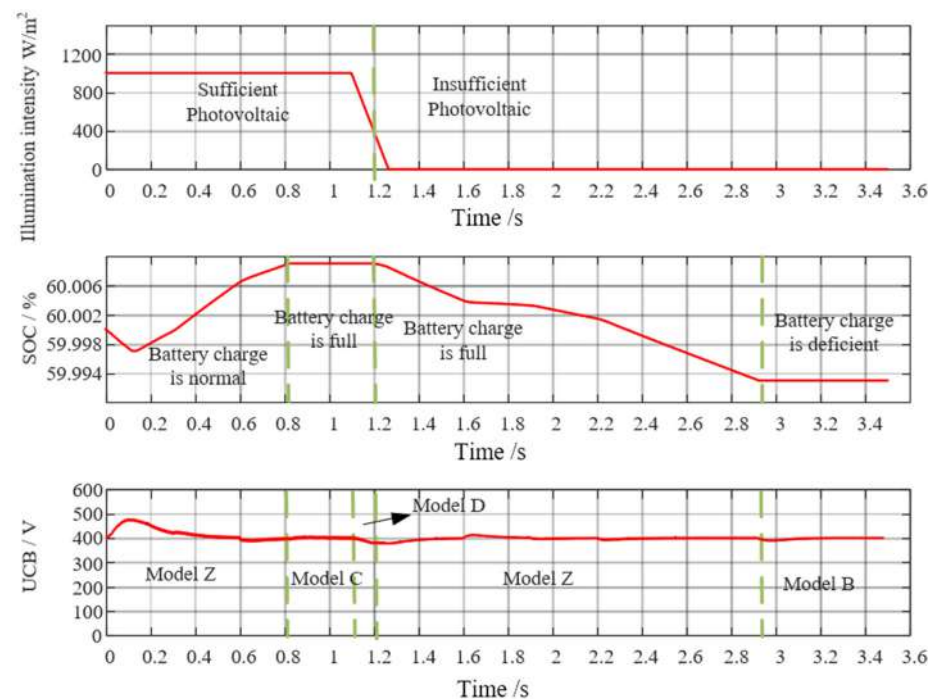


**Table 3.** Parameters of ER.

Parameters	Value
Common Bus voltage $U_{CB\_ref}$	400 V
PV port inductors $L_{P1}, L_{P2}$	5 mH
PV module open circuit voltage	309 V
PV port capacitor $C_{P1}$	3300 $\mu$ F
Energy storage inductor $L_B$	5 mH
Grid port inductor $L_{N1}$	0.6 mH
Grid port inductor $L_{N2}$	0.2 mH
Grid port capacitor $C_N$	10 $\mu$ F
AC load port inductor $L_A$	5 mH
AC load port capacitor $C_A$	6 $\mu$ F
DC load inductor $L_{D1}$	50 mH
DC load inductor $L_{D2}$	47 mH
DC load capacitor $C_{D1}$	470 $\mu$ F
DC load capacitor $C_{D2}$	500 $\mu$ F
Initial light intensity $I_0$	1 kW/m <sup>2</sup>
Initial SOC	60%

The system voltage regulator ports work as follows: 0–0.8 s, only the energy storage port works, and the battery is charged; 0.8–1.2 s, the grid-connected port works and outputs energy to the grid; 1.2–2.9 s, the energy storage port works, and the battery is discharged. Then, 2.9 s later, the grid-connected port works, and obtaining energy from the grid.

The light intensity, battery SOC, and common bus voltage  $U_{CB}$  waveforms are plotted in Figure 16. The plot characterizes the expected battery storage state with the change in external model change and the throwing of AC and DC loads, with the common bus changing with the load.

**Figure 16.** Lighting intensity, energy storage, common bus voltage.

As can be seen in Figure 16, the simulation is started, and the system is in model Z at 0–0.8 s. At 0.8 s, the animal battery is fully charged, and the system enters model C. At 1.1 s, the PV drops to 0, and the system enters model D. The system stabilizes and re-enters model Z. The battery SOC drops further until the system enters model C at 2.9 s.

Different model switching methods correspond to different converter operating states, and the steady-state operation of the energy router can be observed on the basis of the DC bus voltage, which fluctuates with load switching and model change, but can be stabilized quickly.

Figure 17 shows the PV port power curve, which reaches the light inflection point at 1.1 s, after which the PV power gradually decreases to 0, which is consistent with the light situation in Figure 16, and the PV port works normally.

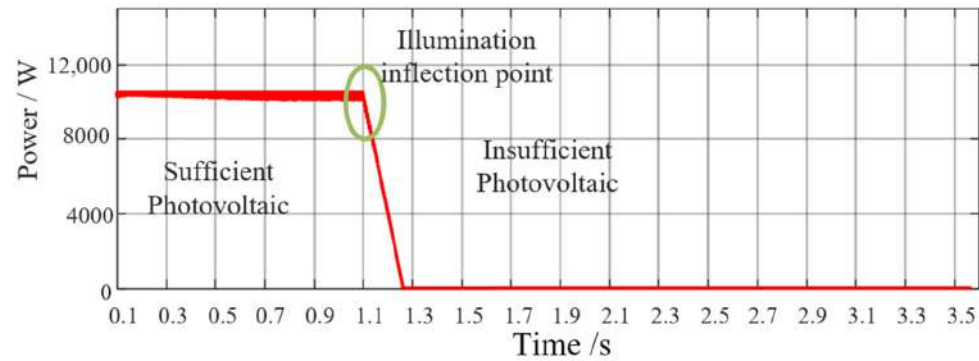


Figure 17. PV port power curve.

Figure 18 shows the power fluctuation of the AC and DC load ports and the bus voltage fluctuation. The four graphs represent the AC port load power, DC port load power, total load power, and the fluctuation of bus voltage when the load is switched. The AC load increases from 1 kW to 3 kW to 5 kW, and its output power is rapidly stabilized, while the DC load increases from 0 to 5 kW and then decreases. From the power fluctuation graph and the DC bus voltage fluctuation graph, it can be seen that the AC and DC load ports are able to realize basic functions, and the bus voltage can quickly return to stability when the AC and DC loads are added and removed.

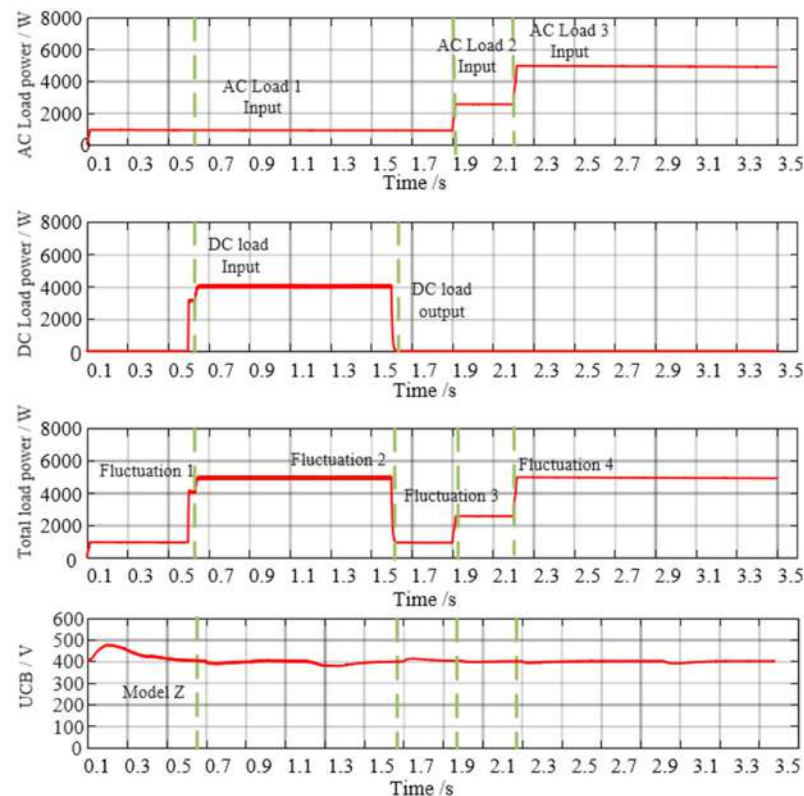
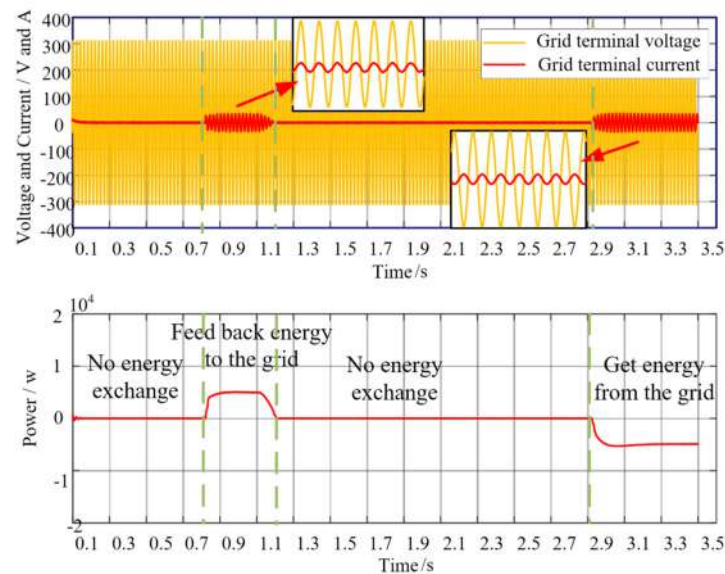


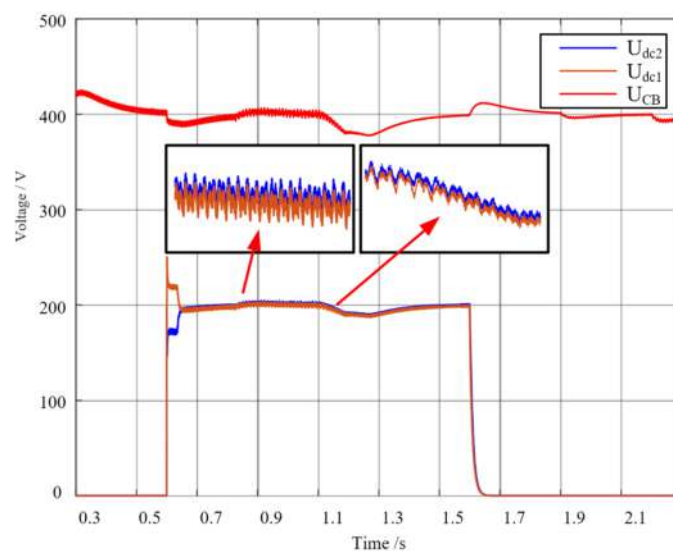
Figure 18. Power fluctuation and common bus voltage diagram.

Figure 19 shows the voltage and current power of the grid-connected port of the energy router; there is no energy exchange at the power port before 0.8 s, and at 0.8 s, the power port delivers energy to the grid, corresponding to model C in Figure 14; the corresponding battery is full of electricity, and the PV port continues to generate energy, at which time the excess energy is fed back to the grid. At 1.1 s, the PV exits, and the AC/DC port is supplied with energy from the battery, at which point the grid-connected port stops working. At 2.9 s, the storage port stops working, and the load continues to consume energy, at which point it enters model B. The grid-connected port receives energy from the grid in order to provide the required load for consumption.



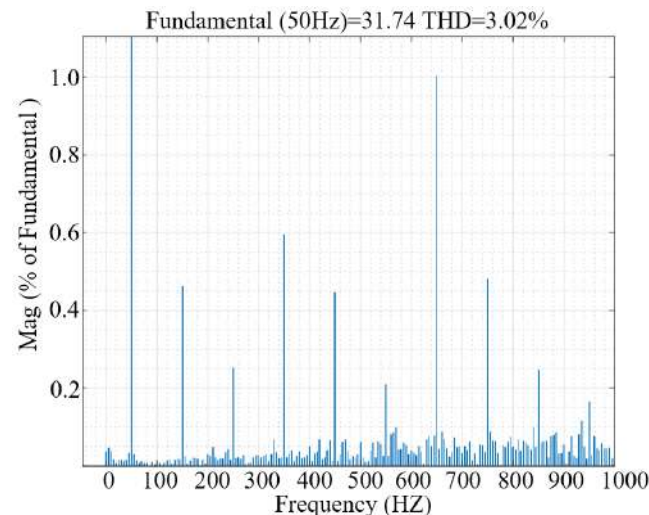
**Figure 19.** Voltage, current and power diagram of grid-connected port.

Figure 20 shows the voltage at the input of the ISOP DAB and the division of the CD1, CD2, and DC load voltage is implemented at 0.6 s. Due to the different input parameters of the ISOP DAB, the voltage division at the input is different. Under the double closed-loop voltage division control designed as shown in Figure 11, the two sets of input voltages are rapidly equalized, while at the same time, due to the change in the model, it is possible to satisfactorily follow the voltage at the input.



**Figure 20.** Capacitive voltage at the DAB input.

Figure 21 presents a spectral analysis of the grid-connected port, where the harmonic distortion rate is only 3.02%. Using the energy router topology and the corresponding control method proposed in this paper, the output current waveform is good, and the impact on the grid is small.



**Figure 21.** Spectral analysis of the grid-connected port.

The study of ERs is divided into analysis at the module level and at the system level. The study in this article also starts from these two levels.

As shown in Table 1, at the module level, the system is divided into five ports. The first port is the energy storage port. As shown in Table 1, the functions of the energy storage port are divided into three parts. These three functions are verified in Figure 16. Figure 16 shows the change in the SOC of the energy storage port and the corresponding change in the ER operating mode. The second is the grid-connected port, as shown in Table 1, the functions of which can be divided into three parts. These functions are demonstrated in Figure 19, as well as in Figure 21. Figure 19 shows the direction of energy flow in the grid-connected port and the role played by the energy storage port in stabilizing the bus voltage. From Figure 21, it can be observed that the grid-connected port not only fulfills the function of energy coordination, but also has less impact on the distribution network. The third is the photovoltaic port; Figures 16 and 17 show the functionality of the photovoltaic port with different current light intensities and different levels of output power. Finally, there are two load ports, and Figure 18 shows the stability of the system when the two load ports are working in alternation.

System-level studies are effectively equivalent to all ports working in coordination, with energy flowing freely and on demand. All ports are able to work properly throughout this process, thus reflecting the stable operation of the system.

Figure 22 shows the working status of different ports at different points in time, as well as the coordinated work of all ports, which makes it possible to finally realize the free flow of energy.

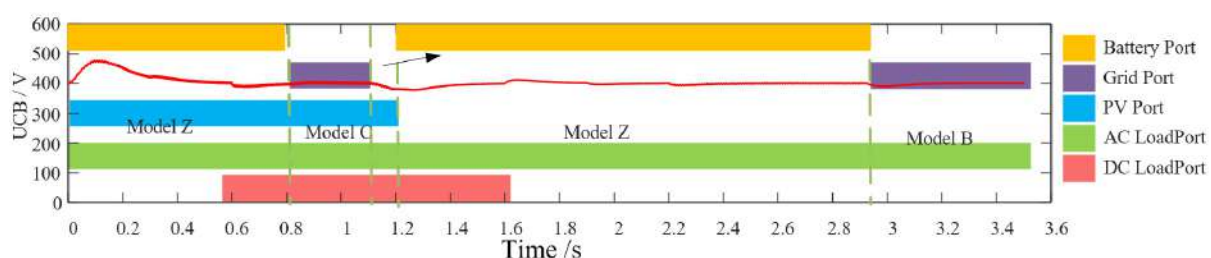


**Figure 22.** Model switching and port coordination diagram.

## 5. Conclusions

In this paper, a five-port energy router topology was designed on the basis of the basic function of the energy router, where the five external groups of ports correspond to the five groups of topologies, and a corresponding control strategy is designed for each port. At the same time, an energy router model switching strategy was designed according to the flow of energy and the storage of that state. Through the switching of different models, the external state changes can be satisfied, while stability is achieved for the voltage of the bottom bus. The feasibility of this energy router was subsequently verified. Compared with previous studies, the innovations presented in this study are as follows:

- (1) At the module control level, model predictive control was applied to the module control of ER, resulting in the common bus voltage having a faster stabilization speed. At the module topology level, for high-power modules, such as photovoltaic modules, a staggered parallel structure was used in order to reduce the current stress and improve feasibility. Finally, a reasonable and feasible five-port topology and control structure was designed.
- (2) A corresponding modal division strategy was proposed for the internal energy storage state and energy flow direction of the energy router, and through the division of this strategy, reasonable control of the energy storage port and the grid-connected port is realized, and the effective switching of the working modalities reflects the characteristics of the interactive flow of energy, which has a certain practical value in engineering applications.

**Author Contributions:** Conceptualization, X.C., Y.L., D.Y., T.J. and M.A.M.; Methodology, X.C., Y.L., D.Y., T.J. and M.A.M.; Software, X.C. and Y.L.; Validation, X.C., D.Y., T.J. and M.A.M.; Formal analysis, M.A.M.; Investigation, D.Y. and T.J.; Writing—original draft, X.C., Y.L., T.J. and M.A.M.; Writing—review and editing, X.C., Y.L., D.Y., T.J. and M.A.M.; Supervision, T.J. and M.A.M. All authors have read and agreed to the published version of the manuscript.

**Funding:** This work was supported by the Chinese National Natural Science Foundation (grant number 51977039) and the central government guiding local science and technology development project under grant number 2021L3005.

**Data Availability Statement:** Not applicable.

**Conflicts of Interest:** The authors declare no conflict of interest.

## References

1. Huang, A.Q.; Crow, M.L.; Heydt, G.T.; Zheng, J.P.; Dale, S.J. The Future Renewable Electric Energy Delivery and Management (FREEDM) System: The Energy Internet. *Proc. IEEE* **2010**, *99*, 133–148. [CrossRef]
2. Wen, J.; Zhou, B.; Wei, L. Preliminary study on an energy storage grid for future power system in China. *Power Syst. Prot. Control* **2022**, *50*, 1–10.
3. Guo, H.; Wang, F.; Zhang, L.; Luo, J. Technologies of energy router-based smart distributed energy network. *Proc. CSEE* **2016**, *36*, 3314–3324.
4. Liu, Y.; Yuan, D.; Gong, Z.; Jin, T.; Mohamed, M.A. Adaptive spectral trend based optimized EWT for monitoring the parameters of multiple power quality disturbances. *Int. J. Electr. Power Energy Syst.* **2023**, *146*, 108797. [CrossRef]
5. Zhao, D.; Hu, N.; Fu, J.; Ben, J.S.; Zi, N.Z. Research on the practice and road map of enhancing the flexibility of a new generation power system in China. *Power Syst. Prot. Control* **2020**, *53*, 1–9.
6. Loh, P.C.; Li, D.; Chai, Y.K.; Blaabjerg, F. Autonomous operation of hybrid microgrid with AC and DC subgrids. *IEEE Trans. Power Electron.* **2012**, *28*, 2214–2223. [CrossRef]
7. Zheng, L.; Chunming, T.; Fan, X.; Jun, G.; Songhui, X. The power control of power electronic transformer in hybrid AC-DC microgrid. *Trans. China Electrotech. Soc.* **2015**, *30*, 50–57.
8. Wang, S.; Su, S.; Wang, H.; Ouyang, Z.; Wang, H.; Zhou, W. An energy routing control method for a terminal energy router based on switching system theory. *Power Syst. Prot. Control* **2022**, *50*, 81–90.
9. Chen, R.; Yang, Y.; Jin, T. A hierarchical coordinated control strategy based on multi-port energy router of urban rail transit. *Prot. Control Mod. Power Syst.* **2022**, *7*, 15. [CrossRef]
10. Cui, X.; Jin, T.; Dai, Q. Research on Key Technologies of Energy Router for Urban Rail Transit. In Proceedings of the 2022 IEEE 5th International Conference on Electronics Technology (ICET), Chengdu, China, 16 May 2022; pp. 1250–1254.

11. Bu, Z.; Sun, X.; Teng, J.; Zhao, W.; Li, X.; Wang, B. A Compact Energy Router Scheme Based on MMC. *Proc. CSEE* **2022**, *42*, 4536–4546.
12. Li, P.; Sheng, W.; Duan, Q.; Li, Z.; Zhu, C.; Zhang, X. A Lyapunov Optimization-Based Energy Management Strategy for Energy Hub with Energy Router. *IEEE Trans. Smart Grid* **2020**, *11*, 4860–4870. [CrossRef]
13. Tu, C.; Lan, Z.; Luan, S.; Xiao, F. A Coordinated Power Control Strategy of Three-port DC Energy Router Based on Droop Phase-shift. *Power Syst. Technol.* **2019**, *43*, 4105–4114.
14. Hussain, S.M.S.; Aftab, M.A.; Nadeem, F.; Ali, I.; Ustun, T.S. Optimal Energy Routing in Microgrids with IEC 61850 Based Energy Routers. *IEEE Trans. Ind. Electron.* **2019**, *67*, 5161–5169. [CrossRef]
15. Cao, Y.; Yuan, L.; Zhu, S.; Huang, R.; Feng, G.; Zhao, Z. Parameter Design of Energy Router Orienting Energy Internet. *Power Syst. Technol.* **2015**, 3094–3101. [CrossRef]
16. Li, Z.; Sheng, W.; Duan, Q. Coordinated control strategy of AC/DC hybrid power router based on energy storage and voltage stabilization. *Autom. Electr. Power Syst.* **2019**, 121–129. [CrossRef]
17. Shi, L.; Liu, G. Research on switching control strategy for the multi-LAN-port energy router. *J. Electr. Power Sci. Technol.* **2015**, 3094–3101. [CrossRef]
18. Xu, M.; Tai, N.; Huang, W. Energy router design based on community energy network. *Power Syst. Prot. Control* **2016**, *44*, 177–183.
19. Li, S.; Wu, C.; Jiang, X.; Pan, P.; Ke, Z. Coordinated Control of Multiple Operation Conditions for Multi-port Energy Router in Energy Internet Framework. *Autom. Electr. Power Syst.* **2020**, *44*, 32–45.
20. Tu, C.; Xiao, F.; Lan, Z.; Guo, Q.; Shuai, Z. Analysis and Control of a Novel Modular-Based Energy Router for DC Microgrid Cluster. *IEEE J. Emerg. Sel. Top. Power Electron.* **2018**, *7*, 331–342. [CrossRef]
21. Xiao, Q.; He, J.; Wang, H.; Jia, H. Voltage balance control strategy for DC capacitor of electrical energy router under power grid failure. *Autom. Electr. Power Syst.* **2018**, *42*, 20–25.
22. Mansouri, S.A.; Nematbakhsh, E.; Ahmarinejad, A.; Jordehi, A.R.; Javadi, M.S.; Marzband, M. A hierarchical scheduling framework for resilience enhancement of decentralized renewable-based microgrids considering proactive actions and mobile units. *Renew. Sustain. Energy Rev.* **2022**, *168*, 112854. [CrossRef]
23. Nasir, M.; Jordehi, A.R.; Tostado-Véliz, M.; Tabar, V.S.; Mansouri, S.A.; Jurado, F. Operation of energy hubs with storage systems, solar, wind and biomass units connected to demand response aggregators. *Sustain. Cities Soc.* **2022**, *83*, 103974. [CrossRef]
24. Matin, S.A.A.; Mansouri, S.A.; Bayat, M.; Jordehi, A.R.; Radmehr, P. A multi-objective bi-level optimization framework for dynamic maintenance planning of active distribution networks in the presence of energy storage systems. *J. Energy Storage* **2022**, *52*, 104762. [CrossRef]
25. Zhang, Y.; Du, G.; Lei, Y.; Zheng, H. Current status and prospects of control strategy for a DC micro grid hybrid energy storage system. *Power Syst. Prot. Control.* **2021**, *49*, 177–187.
26. Ramos, F.; Pinheiro, A.; Nascimento, R.; de Araujo Silva, W., Jr.; Mohamed, M.A.; Annuk, A.; Marinho, M.H.N. Development of Operation Strategy for Battery Energy Storage System into Hybrid AC Microgrids. *Sustainability* **2022**, *14*, 13765. [CrossRef]
27. Nascimento, R.; Ramos, F.; Pinheiro, A.; Junior, W.d.A.S.; Arcanjo, A.M.C.; Filho, R.F.D.; Mohamed, M.A.; Marinho, M.H.N. Case Study of Backup Application with Energy Storage in Microgrids. *Energies* **2022**, *15*, 9514. [CrossRef]
28. Chen, W.; Liu, B.; Nazir, M.S.; Abdalla, A.N.; Mohamed, M.A.; Ding, Z.; Bhutta, M.S.; Gul, M. An Energy Storage Assessment: Using Frequency Modulation Approach to Capture Optimal Coordination. *Sustainability* **2022**, *14*, 8510. [CrossRef]
29. Dehghani, M.; Shiraz University of Technology; Montazeri, Z.; Givi, H.; Guerrero, J.; Dhiman, G.; University of Shahreza; Aalborg University; Government Bikram College of Commerce. Darts Game Optimizer: A New Optimization Technique Based on Darts Game. *Int. J. Intell. Eng. Syst.* **2020**, *13*, 286–294. [CrossRef]
30. Dehghani, M.; Montazeri, Z.; Dhiman, G.; Malik, O.; Morales-Menendez, R.; Ramirez-Mendoza, R.; Dehghani, A.; Guerrero, J.; Parra-Arroyo, L. A Spring Search Algorithm Applied to Engineering Optimization Problems. *Appl. Sci.* **2020**, *10*, 6173. [CrossRef]
31. Dhiman, G.; Oliva, D.; Kaur, A.; Singh, K.K.; Vimal, S.; Sharma, A.; Cengiz, K. BEPO: A novel binary emperor penguin optimizer for automatic feature selection. *Knowl. Based Syst.* **2020**, *211*, 106560. [CrossRef]
32. Dhiman, G. ESA: A hybrid bio-inspired metaheuristic optimization approach for engineering problems. *Eng. Comput.* **2019**, *37*, 323–353. [CrossRef]
33. Ali, A.I.M.; Alaas, Z.M.; Sayed, M.A.; Almalaq, A.; Farah, A.; Mohamed, M.A. An Efficient MPPT Technique-Based Single-Stage Incremental Conductance for Integrated PV Systems Considering Flyback Central-Type PV Inverter. *Sustainability* **2022**, *14*, 12105. [CrossRef]
34. Rao, C.; Hajjiah, A.; El-Meligy, M.A.; Sharaf, M.; Soliman, A.T.; Mohamed, M.A. A Novel High-Gain Soft-Switching DC-DC Converter with Improved P&O MPPT for Photovoltaic Applications. *IEEE Access* **2021**, *9*, 58790–58806. [CrossRef]
35. Mohamed, M.A.; Awwad, E.M.; El-Sherbeeney, A.M.; Nasr, E.A.; Ali, Z.M. Optimal scheduling of reconfigurable grids considering dynamic line rating constraint. *IET Gener. Transm. Distrib.* **2020**, *14*, 1862–1871. [CrossRef]

**Disclaimer/Publisher’s Note:** The statements, opinions and data contained in all publications are solely those of the individual author(s) and contributor(s) and not of MDPI and/or the editor(s). MDPI and/or the editor(s) disclaim responsibility for any injury to people or property resulting from any ideas, methods, instructions or products referred to in the content.



## Article

# Cost Estimation Process of Green Energy Production and Consumption Using Probability Learning Approach

Jian Xiao <sup>1,\*</sup> and Wei Hou <sup>2,3</sup>

<sup>1</sup> Dong Fureng Economic & Social Development School, Wuhan University, Wuhan 430072, China

<sup>2</sup> Chakrabongse Bhuvanarth International Institute for Interdisciplinary Studies, Rajamangala University of Technology Tawan-Ok, Bangkok 10400, Thailand; houwei9999@gmail.com

<sup>3</sup> State Grid Beijing Electric Power Corporation, Beijing 100031, China

\* Correspondence: hbbj1108@163.com

**Abstract:** With electric vehicle (EV) charging, green energy production costs could be reduced, and smart grid (SG) reliability improved. Nevertheless, the vast number of EVs could adversely affect the stability of the voltage and cost of operation. The present study designs a new security-based system based on a new EV participation charging method for a decentralized blockchain-enabled SG system. It is aimed at minimizing the level of power alternation in the electrical network and the total charging costs of EVs as mobile systems. In the first step, the power alternation level issue of the SG is formulated based on the capacity of EV batteries, the rate of charging, and EV users' charging behavior. Next, a new adaptive blockchain-based EV participation (AdBEV) method is proposed, using the Iceberg order execution algorithm for improving EV discharging and charging schedules. Simulated outcomes demonstrate that the suggested method is superior to the genetic algorithm method when it comes to reducing power fluctuation levels and total charging cost.

**Keywords:** smart grid; modern transportation system; hybrid blockchain technology; EV mobility; machine learning

## 1. Introduction

The introduction of electric vehicles (EVs) brings the idea of vehicle-to-grid (V2G) and grid-to-vehicle (G2V) into the energy market, which will convert the overloaded network into a valuable source. EVs are supplied with proper control methods to fatten the load, shave the peak, and regulate the frequency. EV charging and discharging via a bidirectional power flow in a smart grid (SG) is expected to decrease the cost of subsidiary (reserved) energy production and improve the system's robustness [1]. In more detail, as an example, when many EVs begin charging simultaneously throughout peak energy consumption periods, the large power generators must begin the subsidiary generators (with a shorter response time) to supplement the energy demand, and this results in a delay for the subsidiary generators to begin producing energy. Ten to fifteen min is needed for energy to be provided. Ref [2] proposes game theory structures such as the energy grid, EVs, and smart communities, providing insight into possible optimization techniques for achieving efficient and intelligent energy management. In spite of this, large penetrations of EVs into the electrical system raise issues regarding the impact on electrical system stability and operational costs [3].

Refs [4,5] examined a centralized information center operator as the aggregator for gathering energy consumption demand and further commanding the transfer of energy in the traditional EV discharging/charging method. Utilizing the aggregator, control methods are used for controlling power flow during peak and off-peak hours, respectively. Since the behavior of EV users is uncontrollable, EVs are considered a widely distributed power load on the power grids. This makes it possible to schedule the exchange of energy, even if a predetermined scheduling process does not consider every factor affecting the electrical

**Citation:** Xiao, J.; Hou, W. Cost Estimation Process of Green Energy Production and Consumption Using Probability Learning Approach. *Sustainability* **2022**, *14*, 7091. <https://doi.org/10.3390/su14127091>

Academic Editor: Mohamed A. Mohamed

Received: 23 April 2022

Accepted: 27 May 2022

Published: 9 June 2022



**Copyright:** © 2022 by the authors. Licensee MDPI, Basel, Switzerland. This article is an open access article distributed under the terms and conditions of the Creative Commons Attribution (CC BY) license (<https://creativecommons.org/licenses/by/4.0/>).

grid [6]. Although SG aggregators are designed for decentralizing traditional energy grids and supporting micro-distributed renewable generators, they compromise the purpose of the SGs [7]. As a result of the centralized-based system, decision-making is delayed and grid participants' autonomy is undermined, in that users cannot control the discharging or charging of their processes. The current average cost of electricity that users are paying at the time of consumption is generally not indicative of the actual wholesale costs. When operating costs vary, it is difficult to adjust to fluctuating power demand [8,9].

Several control methods for EV discharging and charging techniques have been presented before to control the duration and amount of energy transferred in order to enhance grid performance. Smart charging planning for low-voltage residential grids based on the state-of-charge (SOC) amounts like battery residual and battery capacity, thus impacting the entire grid offloading, is presented in ref [5]. In ref [4], automatic generation control signals are applied for regulating EV discharging and charging schedules for enhancing the frequency regulation service's efficiency is examined by considering the dynamic departure time and arrival time of EVs. Ref [10] examined an aggregated based on the optimization model of the EV charging process by considering the stochastic characteristics of the charging process and applied the Genetic Algorithm (GA) for determining the parameters of the system model. The proposed EV discharging/charging schedule algorithms in [5] assumed static parameters for the EV's accessible charging time. It is important to note that in [4,10] the suggested charging layout was on the basis of parameter estimations and theoretical calculations which did not completely account for the flexibility of EVs. Thus, it would be difficult for the blockchain (BC) platform to be adapted to the kinds of battery and consumer behavior associated with EVs.

Due to a large number of EV charging and dispatching demands, a BC idea has been developed for providing peer-to-peer transferred structures, which utilize decentralized storage for whole transferred information data. Therefore, BC technology will enable a non-trusting network to eliminate the operational costs of the intermediaries, which would result in a cheaper, faster, and more reliable way of reflecting fluctuating wholesale costs to consumers. BC technology can also shift high-load equipment to off-peak hours for reducing energy prices and assist in reducing the overloaded peaks [11,12]. Therefore, ref [13] examined a new scheme to trade energy on the basis of BC technology for adopting the decentralized and competitive environment of local energy production, however, the BC was only utilized as a data storage warehouse for transaction recording. A detailed analysis of the economic assessment of the market mechanism for local energy trading can be found in ref [14]. According to ref [15], BCs and decentralized consensus methods were applied for coordinating the planning of distributed power sources in a microgrid and guaranteeing fair payments with no need for a centralized aggregator.

In order to charge EVs on a large scale, simple control methods are required for reducing operating delay and investment costs. As a result, an adaptive EV discharging/charging planning algorithm is presented in this study according to the BC platform, called Adaptive BC-based EV Participation (AdBEV) for executing the data sharing and decision-making method.

As a method of solving the problem, the Iceberg order management algorithm [16] is widely applied in the digital financial trading market and is assumed a powerful machine learning approach that can be used for managing EV discharging and charging demands. In summary, the study makes the following contributions:

- (1) A new EV participation method, which can introduce the idea of decentralized EV discharging and charging on a BC-enabled SG system is presented in this study.
- (2) A discharging and charging plan issue related to EVs on the BC-enabled SG network is formulated for the EV charging schedule.
- (3) The AdBEV layout on the basis of the iceberg order algorithm, which executes the optimal order process for matching the SG electricity discharging and charging demand is proposed in order to reduce the power fluctuation level.



- (4) AdBEV has been shown to have a better power fluctuation level in comparison with the benchmark method that utilizes GA. Besides, it has been shown that the suggested algorithm achieves low computation prices in comparison with the benchmark layout in the Ethereum platform.

Following are the remaining parts of this study. The system model according to the matching imbalances of the EV consumer profile related to discharging/charging is built in Section 2. The problem formulation and the algorithm definition are presented in Section 3. The simulation outcomes and the AdBEV vs. GA comparison are demonstrated in Section 4. Section 5 presents the conclusions.

## 2. System Model

As an extension to the system model developed in [17], a residential district that has a substation transformer whose maximum power capacity is  $P_{max}$ , is considered here. On the supplier side, there are traditional extend power plants, distributed micro renewable generators, and storage. In addition, the user power loads, such as residential areas and hospitals, are linked to the public BC energy exchange platform that allows for the transmission, encryption, and storage of information about electricity supply and demand. Figure 1 illustrates the architecture of the power network including the public BC platform to trade power.

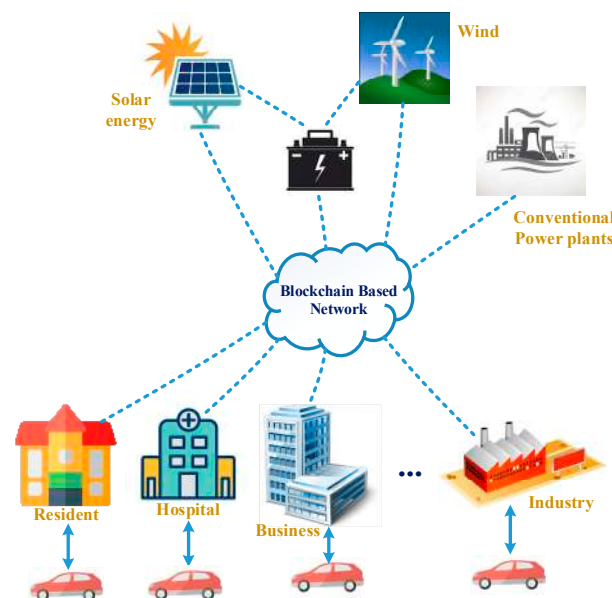


**Figure 1.** The SG diagram contains the public BC trading platform.

This model assumes that EVs can publish and transmit the discharging or charging orders to the SG public BC trading platform. EVs are able to be charged and discharged using a programmable charging installation. Using this design, the grid operator will be able to switch the power transmission for the EV instantly on/off (presuming the switches are complicated). Figure 2 illustrates the process for processing the transaction in the BC platform. Driver owners initiate the power orders including buying and selling, and once the identity of the initiator has been verified, orders can be entered on the BC-based trading platform. After that, the AdBEV layout is used to process the orders, which are then published in the open order book. Peers in the grid transact and verify the matched orders. Both parties must confirm orders before they can be stored in a distributed manner.

$$X_{i,t} = \begin{cases} 1, & \text{if } EV_i \text{ is connected at } t \\ 0, & \text{otherwise} \end{cases} \quad (1)$$

where  $X$  represents the EV status matrix as Equation (2). It should be noted that in our research, we considered 100 households, where every household is assumed to own an EV. Hence, the dimension of this matrix of our research is  $100 \times 1$ .

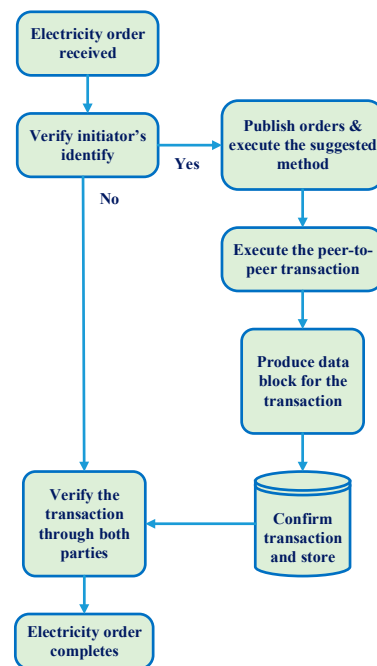


**Figure 2.** The process for transferred execution in the BC-enabled SG network.

Battery residual for every EV is  $(SOC_{ini})$  and the predicted SOC when charging determines the power demand for EV is  $(SOC_{exp})$ . The formula looks like this:

$$P_{EV}(t) = \sum_{i=1}^I (X_{i,t} (SOC_{exp}(i) \pm SOC_{ini}(i))) \quad (2)$$

When scheduling EV discharging/charging, it is essential to take into consideration how many EVs remain linked to the system in order to determine the maximum waiting time for the order. According to this study, the duration of the charging, and the amount of energy transferred, are combined to predict the hourly charging demand pattern throughout the day for achieving minimal energy fluctuations and consumer satisfaction.

Profiles of vehicle activity related to the normal residential EV charging demands are modeled using [18]. The pattern of the charging demand on a daily basis can be inferred by combining the duration of the charging and the amount of energy transferred. Equation (3) can be used to model the amount of energy transferred during EV charging based on the balance between complexity and precision, and this is expressed using a time segment vector  $\eta(t)$  comprised of the percentage of stay-on-line EV in Equation (4).

$$k_j(t) = \sum_{j=1}^J \sum_{t=T_f}^{T_s} (a_j \sin(b_j t + c_j)) + \varepsilon \quad (3)$$

$$\vec{\eta}(t) = [k_1(t), k_2(t), \dots, k_j(t)]\% \quad (4)$$

The  $T_f$  refers to the first time step and while  $T_s$  refers to the second time step elapsed that can enable the formation of a certain fitting in  $j^{th}$  order of sine series. The  $j$  shows the order for the total of sine series derived from the Matlab curve fitting toolbox, in which  $J$  indicates the model complexity of the sum of the sines. The parameters in the sum of the sine series are shown by the  $a_j$ ,  $b_j$ , and  $c_j$ . In view of the charging load profile (LP) indication

that a specific number of EVs should remain online during the procedure, Equation (4) is rewritten accordingly:

$$N_{car}(t) = \Omega \cdot [k_1(t), k_2(t), \dots, k_j(t)] \quad (5)$$

Here, the whole number of EVs in an area is shown by  $\Omega$ . The power demand for one-time segment changes during every iteration of order execution. Accordingly, Equation (2) is reformulated with the amount of power exchange  $Q_i$  according to the order category:

$$P_{EV}(t) = \sum_{i=1}^I (X_{i,t} Q_i) \quad (6)$$

Therefore, the whole residential load is described as the total demand for EV discharging/charging and LP excluding EV for formulating EV charging problems.

$$P_{total}(t) = P_{home}(t) + P_{EV}(t), \quad t \in T \quad (7)$$

$$P_{total}(t) + \varsigma(t) \leq P_{sub}, \quad \forall t, \quad (8)$$

$$V_{min} \leq V(t) \leq V_{max}, \quad \forall t, \quad (9)$$

Here, the power load excluding EV is shown by  $P_{home}$ . Aggregating the above random process (7) with the suggested algorithm can solve the EV discharging/charging scheduling problem. In order to enhance the operation of the electric grid, it is advisable not to exceed the peak transformer substation load following the implementation of EV discharging and charging to the residential electricity demand. In limitation (8), the error item  $\varsigma(t)$  shows power losses or branch overloaded plus the total power load should not exceed the substation power capacity  $P_{sub}$ . Hence, there is a maximum number of EV  $\max(N_{car}(t))$ , which is employed in the system to prevent exceeding the substation capacity. The levels of the voltage in buses have been limited, and cannot exceed the minimum and maximum limits in limitation (9).

### 3. Formulation of the Problem and Explanation of the Algorithm

EV discharging and charging demand is scheduled to minimize the effect of consuming or injecting excessive amounts of energy on the network. The paper examines an adaptive discharging/charging method for different kinds of EVs for flattening the LP of transformer substations in distribution networks.

#### A. Formulation of the problem

As input data, the daily 30 min power interchange order book profile of a residential grid has been used, with EV charging/discharging demands on a daily basis as the decision parameter. A schedule that is adaptive for filling in the gaps in the residential LP is essential for equalizing the level of alternation of the entire system. Accordingly, the total function of utility for measuring the level of alternations in 2-time parts of a network is:

$$P_{PFL} = \sum_{t=1}^T \|P_{total}(t) - P_{total}(t-1)\| \quad (10)$$

Here, the total power alternation level during 24 h with 30 min temporal resolution is shown by  $P_{PFL}$ ,  $P_{total}(t)$ , and the overall power in the transformer at hour  $t$  and  $t-1$  is represented by  $P_{total}(t-1)$ . This system is aimed at minimizing the power alternation level criteria  $P_{PFL}$  of the total energy network using a set of variables to be optimized for related  $i$  and its related  $SOC_{exp}$ , as shown below:

$$\min_{\forall SOC_{exp}(i) \in I} P_{PFL} \quad (11)$$

$$S \cdot T \cdot \sum_{t=1}^T \sum_{i=1}^I (SOC_{exp}(i) \pm (SOC_{ini}(i))) = \sum_{t=1}^T P_{EV}(t) \quad (12)$$

$$SOC_{ini}(i) \in (0, 1), \forall i, \quad (13)$$

$$SOC_{exp}(i) \leq P_{max}, \forall i, \quad (14)$$

$$X_{i,t} = \{0, 1\}, \quad \forall i, \quad \forall t, \quad (15)$$

Using Equation (12), the charging and discharging power from EVs is limited to the order demand based on the existing EV number  $i$  and the obtained  $SOC_{exp}(i)$ . In Equation (13), the initial SOC is set between (0,1). Despite the fact that this limitation might lead to a less flattened power LP, users' requirements are met as a consequence of this limitation. The limitation (14) ensures that the maximum SOC following charging is not greater than the EV battery capacity  $P_{max}$  for every EV  $i$ . As explained in (13), an EV could have just 2 states, one being connected to the network and one being disconnected.

As Equation (15) has a binary constraint for EV connection state  $X_{i,t}$ , the formulation of the issue is a mixed combinatorial nonconvex issue. The optimal solution to this problem is not a systematic method with an effective computational method. The optimization problem can be to determine how many EVs should be used for transferring energy (discharging/charging) to reduce the total power fluctuations. It should be noted that the required infrastructures to deploy the proposed technique are including, but are not limited to, open cloud, reliable and scalable hardware, updated software, a stable internet connection, databases, battery, several energy resources, different levels of load demand, EV, point of sales terminals, crypto automated teller machines (ATMs), etc.

#### B. ADBEV layout

This part proposes an ADBEV layout for solving this issue by utilizing the power exchange book as a trading system. A scheduling result in the previous time slot can affect the power demand in the next one as well. The grid system needs to be kept at a minimum power fluctuation so as to provide the total power charging demand of EVs.

##### a. Normal electricity exchange order

In the case of a small quantity power exchange order, the demand has been formatted as an input that can be sent to the power exchange stand book  $Std_{in}$  via a vector as shown below:

$$\vec{Q}_i = (\gamma, Id_i, \sigma_i, Q_i) \quad (16)$$

Here, the specific identifier for the discharging/charging initiators is shown by the  $Id_i$  in which they are EVs or other equipment, the confirmed agent price for the power order is represented by the  $\sigma_i$ , the power demand amount of the order is shown by the  $Q_i$ , and  $\gamma$  presents a matrix showing if it is a power discharging or charging order:

$$\gamma = \begin{cases} 1, & \text{charging order} \\ 0, & \text{discharging order} \end{cases} \quad (17)$$

To produce every matched trade, the solution must be used in the existing book  $Std_{in}$  for each inserted order message, and whole non-error output must be directed to the  $Std_{out}$ . The trade information format can be described in the following way:

$$\vec{T}_i = (Id_{sell}, Id_{buy}, \sigma_m, Q_m) \quad (18)$$

Here, the  $Id_{buy}$  and  $Id_{sell}$  indicate the matched power buy and sell order identifier respectively, this matched price in pence is shown by the  $\sigma_m$  and the matched amount for the order is represented by the  $Q_m$ . The solutions must display the existing full order book in the previous format upon receiving an order message and upon receiving every matching entry in the book.

### b. ICEBERG power interchange structure

An extend user can hold an overall exchange demand ( $\phi_0$ ) and intend to liquidate it before time  $T_{max}$ , in which case the peak size  $\phi_P$  and a limit  $\bar{S}$  to the demand of the iceberg are assigned. The latter exceeds the initial optimal bid price  $S_0$  on the charging side, as shown below:

$$S_0 < \bar{S} \quad (19)$$

The first portion of the order cannot be quickly executed, and the reverse is also true.

For ensuring the smooth running of the iceberg power exchange and the advantage achieved by participants, choosing the right price is critical. Based on ref [16], a jump-diffusion process is used to model the optimal charging price  $S_t$ . This paper aimed at building an electricity exchange market for EV consumers, to find a guide price related to every period of time, when  $S_t < \bar{S}$ , the extensively applied geometric Brownian motion for the stock price is adopted for modeling the real-time power price on a daily basis:

$$dS_t = \mu S_t dt + \sigma S_t dW_t, \quad \text{with } S_t < \bar{S} \quad dS_t = \mu S_t dt + \sigma S_t dW_t, \quad \text{with } S_t < \bar{S}, \quad (20)$$

Here, it is possible to set the percentage drift  $\mu$  and percentage volatility  $\sigma$  as constants, and a Wiener process is shown by  $W_t$ . So, the next equations allow obtaining the optimal iceberg price  $S_t$  for a certain top price value  $S_0$ :

$$S_t = S_0 \exp\left(\left(\mu - \frac{\sigma^2}{2}\right)t + \sigma W_t\right) \quad (21)$$

$$E(S_t) = S_0 e^{\mu t} \quad (22)$$

In Equation (22), the iceberg format is given by the vector integrating the order optimal price  $\sigma_{S_i}$  and the overall demand  $\phi_i$ . In theory,  $Q_{pi}$  shows the peak for a single trading period that will never exceed  $\phi_i$ :

$$\vec{Q}_i = (\gamma, Id_i, \sigma_{S_i}, \phi_i, Q_{pi}) \quad (23)$$

Based on the priority function, both normal and iceberg power exchanges must be depicted in the order book:

$$f(P_{1p}(n); P_{2t}(n)) = \alpha Rank(Pr) + \beta Rank(T) \quad (24)$$

Here, the ranking for the price is shown by  $Rank(Pr)$ , and the ranking for generation time is indicated by  $Rank(T)$ , and  $\alpha = 10\beta$  for building a price-competitive market. In Figure 3, the algorithm first determines the normal and iceberg orders after initializing the demand for power discharging and charging. Following that, entire orders are sorted based on the ranking function  $f(P_{1p}(n); P_{2t}(n))$  for matching them for exchange. Following the execution of entire orders in every trade frame period, provides a respective response for the orders.

Figure 4 illustrates the optimal order method for matching the power discharging and charging demand for three different scenarios. The algorithm can execute whole matching orders in the order of price ranking provided that the power demand is satisfied in a manner that minimizes power fluctuations. Those orders whose priority amounts are the highest are executed initially, even when the overall amount of power sell orders is lower compared to the overall amount of power buy orders. Afterward, the iceberg execution strategy has been applied to the unmatched electricity demand orders for matching the orders in the one-time frame ( $t \in T$ ). Iceberg orders that equal 1 ( $N_{Q_i} = 1$ ) are held until the next cycle with a similar priority value, or, they are allocated new priorities. When there are a larger number of sell orders, the iceberg execution is applied to passively wait for the next cycle execution. Order books are built and updated for every time frame ( $t \in T$ ).

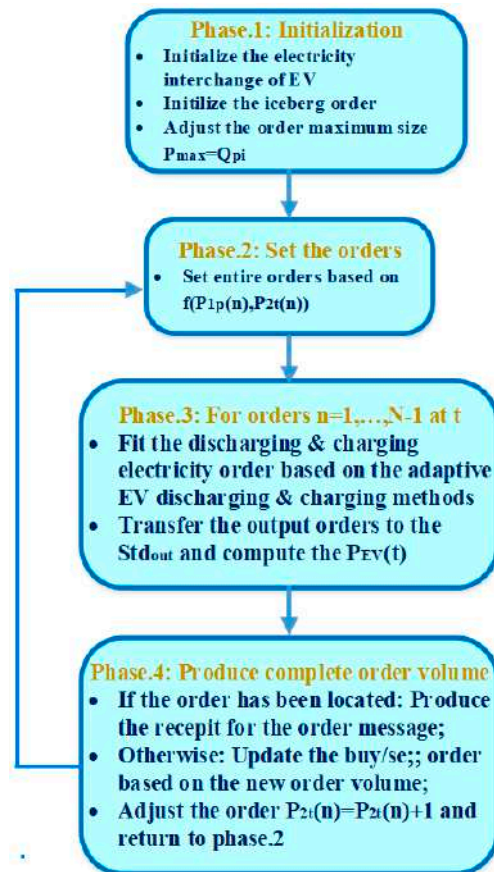


Figure 3. Electricity trading network with order book initialization.

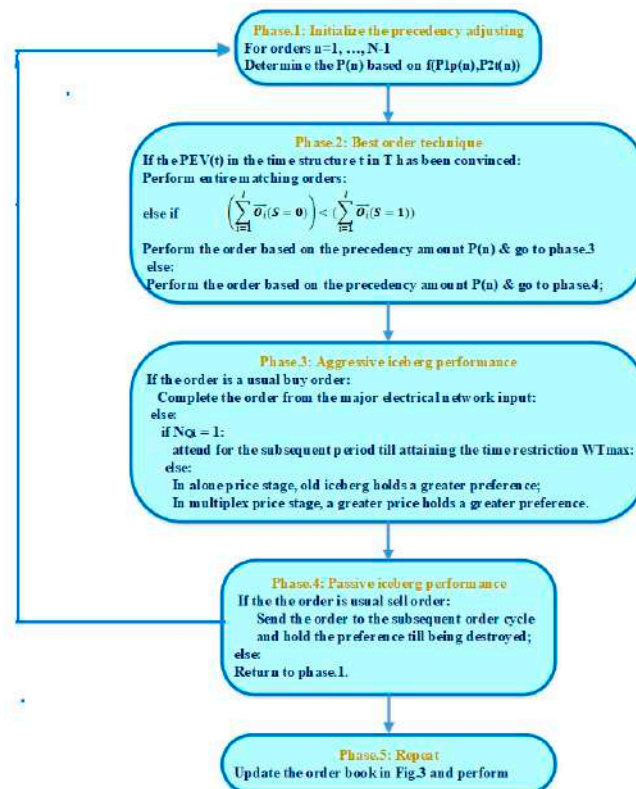


Figure 4. Adaptive BC-based EV participation plan.

Because AdBEV can optimize charging patterns in day-ahead markets, when one day all the time slots have been allocated, the suggested scheduling layout can execute just once a day according to the prior EV arrival pattern and residential LPs.

#### 4. Simulation Outcomes

##### A. Experiment setup

AdBEV is evaluated using the residential region substation transformer with a  $P_{max} = 250$  kVA serving 100 households. Every household is assumed to own an EV. Taking into account the different kinds of EVs in the market, 2 kinds of the most common battery sizes of 8.8 kWh (Toyota Prius), and 60 kWh (Tesla model S) are selected. In terms of charging rates, various manufacturers have various connector kinds, with slow charging and fast charging compatible with 3 kW (16 A), and 43 kW (63 A) chargers, respectively. Based on the charging port availability, the number of EVs for fast and slow charging has been assigned at a ratio of 1:4 in the simulation procedure. There are 2 parts to the EV charge connection state, the first one is between 06:00 and 18:00, and the other one is between 18:30 and 05:30 (+1). EV batteries have an initial residual voltage ( $SOC_{ini}$ ) created at random, while the battery level ( $SOC_{exp}$ ) following charging has been assigned to 80% for battery protection, whereas the SOC following discharging has been assigned to 50% to make it easier to use.

The Ethereum platform is used for implementing the developed algorithm by taking into account the distributed trading platform for the power interchange market. Platforms such as Ethereum allow consumers running distributed applications on public BCs [19]. The Solidity language with version 0.4.0 has been applied for deploying the suggested smart contract for executing the AdBEV layout. As a result, gas consumption from the Ethereum platform can provide a direct indication of the algorithm's operational difficulty. Consumers of the public BC platform must pay *gas* costs for executing smart contract commands in the Ethereum platform [20]. The cost of executing a complicated algorithm vastly increases the trade cost for the power, as the number of peers in the grid increases.

The simulation consists of 2 kinds of orders: iceberg and normal orders based on Equations (5) and (16). Applying iceberg orders can decrease the power load fluctuations caused by large trading volume orders. For the simulation, the iceberg and normal orders have a ratio of about 1:1. Furthermore, the peak size of the trading quantity (Q) for every order has been set at 4 kW. Table 1 shows the simulation of a partial order book. The system model determines data architecture (described in Section 2). Orders on the buy-side have been ranked in ascending order based on the cost, while they are ranked in descending order on the sell-side that is comparable to a stock exchange market with price competition. Those iceberg orders are highlighted with bold figures in the quantity (Q) column. This exchange process with the order input is simulated for calculating the total cost fluctuation based on the real-time price.

**Table 1.** Electricity interchange order book.

S(Buy/Sell)	Buy	Buy	Buy	...	Sell	Sell	Sell
Q (kW)	2.14	<b>4.0</b>	1.07	...	4.0	0.44	1.80
Price (pence)	13	12	11		17	15	14
Id	0	70	12		0	18	48

Prices of power exchange markets vary based on the iceberg order execution algorithm, in which the drift of the optimal bid cost is taken as constant. It is assumed that a simple scenario is used for keeping the setup tractable for exposition: the optimal bid cost shows a zero-drift  $\mu = 0$  before iceberg orders are submitted. As a result, the original cost fluctuation interval has been assigned at  $\sigma_i(10; 30)$  based on the local area and as a consequence, the order price  $\sigma_t$  has been adjusted throughout particular times of the day for simulating the

retail power costs as shown in Figure 5. Every hour's price has been determined from the average price of whole deal orders for every time interval from the order book.

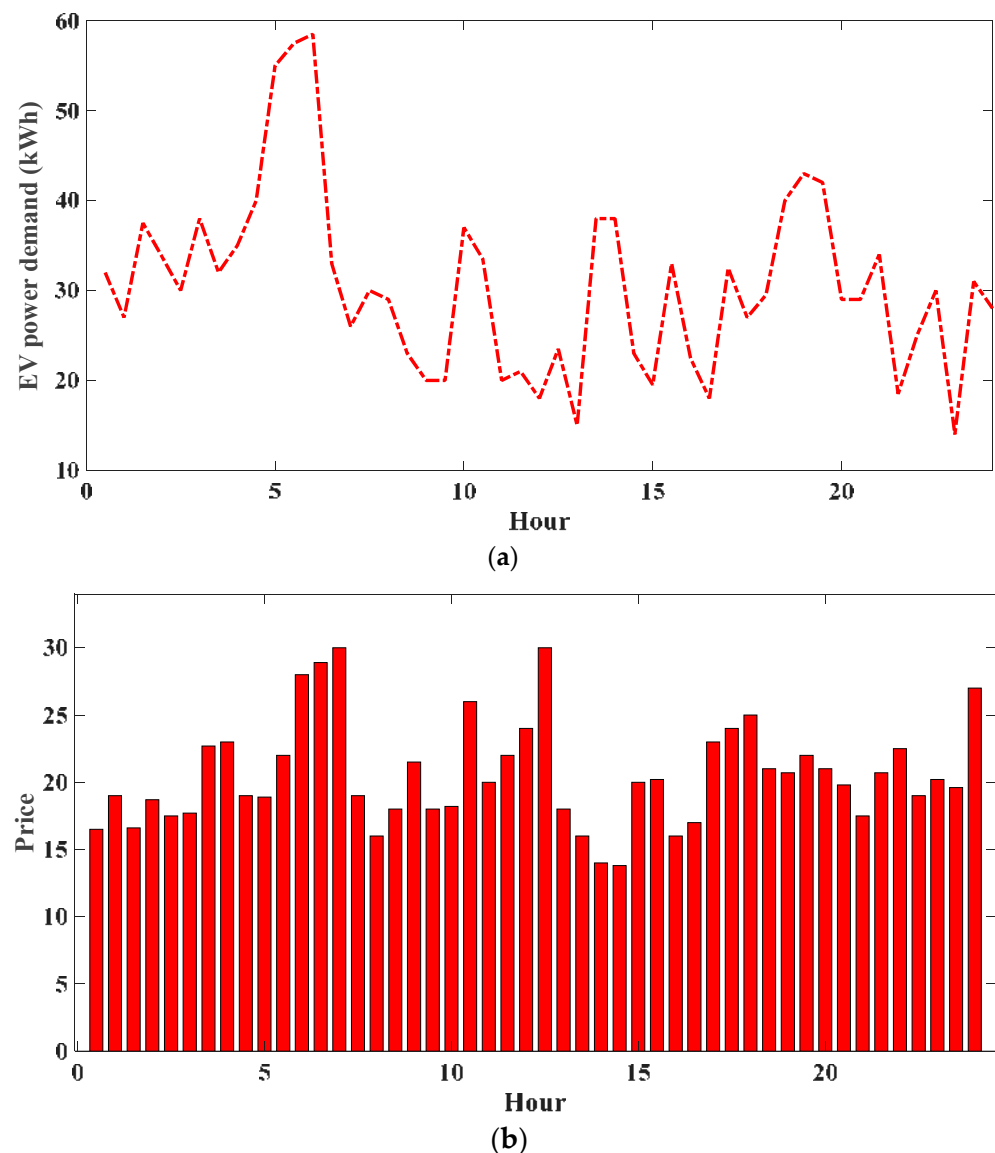


**Figure 5.** Mean generated trading cost within a day: (a) EV power demand; (b) price.

#### B. Power alteration amount minimization

Figure 6 illustrates the impact of the algorithm on the power load alternation. Here is a comparison of the daily half-hourly resolution of LP in a residential area excluding each EV charging scheduling optimization (top panel) and with scheduling method utilizing GA (bottom panel). The daily profile of the domestic residential from the Elexon report is used in the simulation [21]. Charging demand of EV and residential load is represented by the red dashed line  $v$  in every timeframe. Because of the high number of charging requirements during this period, the overall electricity consumption at 20:30 exceeds the power capacity, with  $P_{PFL} = 1.15$  by Equations (7)–(9). As described in [17], following the application of a planning algorithm, the load of charging has been moved to the off-peak time and the discharging characteristics have been taken into account.



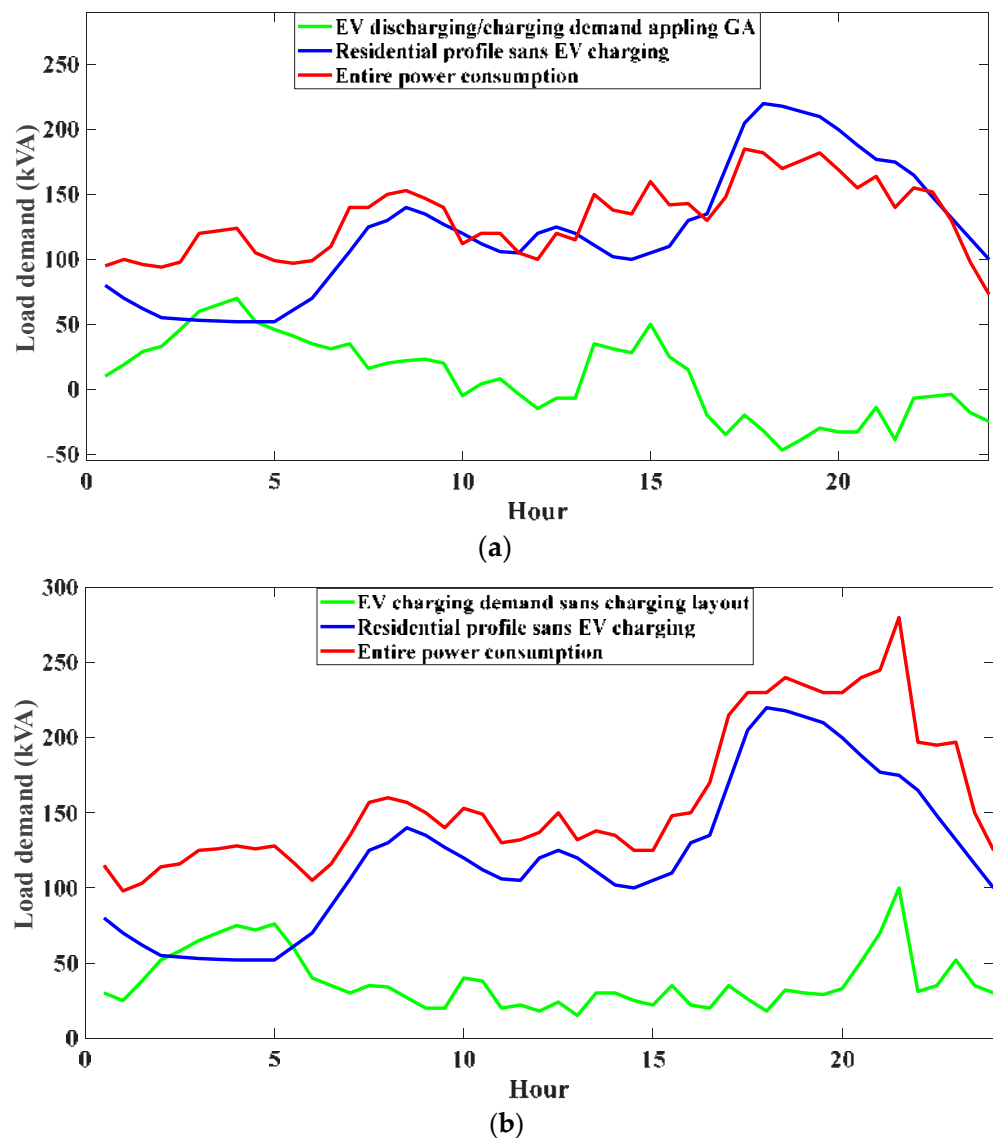


**Figure 6.** A comparison of the domestic 30 min LP. (a) LP applying charging/discharging scheme; (b) LP sans charging method.

The suggested AdBEV scheduling layout allows EVs for generating discharging and charging orders for the market based on their states of connection, battery capacities, and discharging/charging limitations. By using the proposed algorithm, the total power demand fluctuation level can be reduced, with the optimized outcome  $P_{PFL}^*$  with the algorithm being 0.63, determined through Equations (7) to (9), which results in a reduction of 25.9 by comparison with the  $P_{PFL}$  applying the GA scheduling algorithm. Figure 7 illustrates how the index P is better suited to flatten consumption loads by applying the optimized EV charging layout in ref [17]. In addition, by increasing the number of EVs in the system, the  $P_{PFL}^*$  would rise linearly since the SOC is assumed to be normally distributed [10]. The total utility function Equation (8) shows that the power fluctuation level  $P_{PFL}$  has been aggregated with the absolute difference of power consumption over two consecutive hours, in which the ability to minimize power fluctuation increases linearly as  $P_{EV}(t)$  increases.

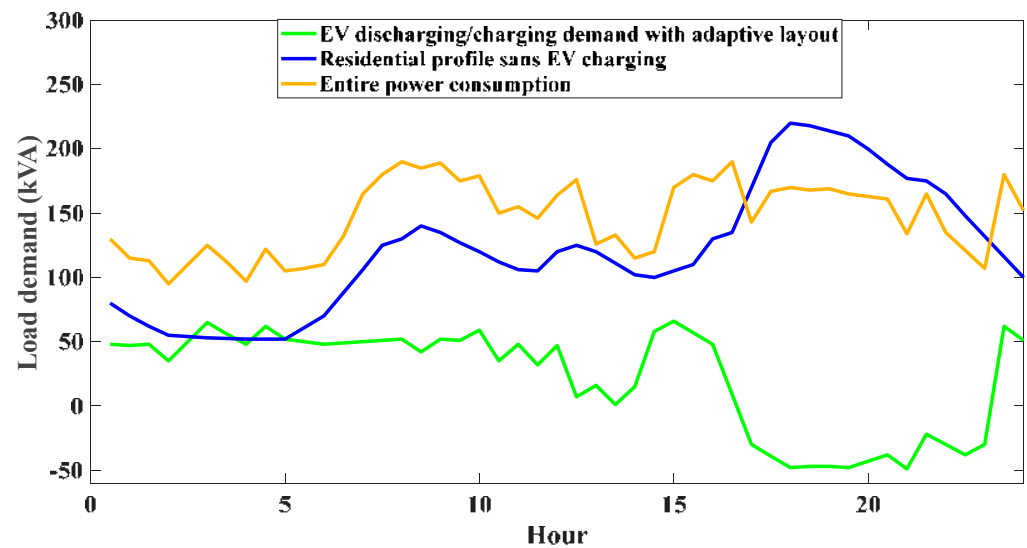


**Figure 7.** Domestic half-hourly LP applying the offered adaptive EV discharging/charging demand matching scheme.

### C. Discussion and analyzing computation cost

The computational complexity should be noted because calculation complexity directly affects exchange performance and cost. A *gas* computation can correspond to a low-level operation in the Ethereum Virtual Machine, in which every opcode can have its own *gas*. The operators *add* applies 3 *gas*, whereas multiplication 2 integers apply 5 *gas*. The total *gas* cost is 21,000 *gas* as a base despite not having interacted with the contract, and every *gas* resulting from running a contract plus 21,000 *gas* is included in the overall *gas*. As shown in Figure 8, the theoretical computation cost for Ethereum based on the number of peers for every system is modeled [22–24]. As it is inferred from Figure 5, the power cost goes up from 6:00 to 8:00, 11:00 to 13:00, and 17:00 to 19:00 corresponding to the higher energy demand  $P_{EV}$  for EV charging periods. In Figure 6, it is seen that when the GA scheduling algorithm is used, the peak time power consumption is reduced with less energy fluctuation index at  $P_{PFL} = 0.85$ . In comparison to the  $PPFL$  index with no scheduling algorithm, there is a 26.1% reduction in the index, and the transformer load has been reduced. It is deduced from the results that as the number of EVs in the system increases, the  $P_{PFL}^*$  will linearly since the SOC is assumed to be normally distributed. Moreover, it is observed that the total utility function, as calculated and represented in Equation (8), shows that the power fluctuation level  $P_{PFL}$  has been aggregated with the absolute difference in power consumption over two consecutive hours. The simulation results show that the proposed technique not only helps the policymakers to reduce the price but also provides a dynamic and transparent environment that can mitigate possible fraud within the system. The appropriate performance and high quality of the proposed model are well proved in the results.

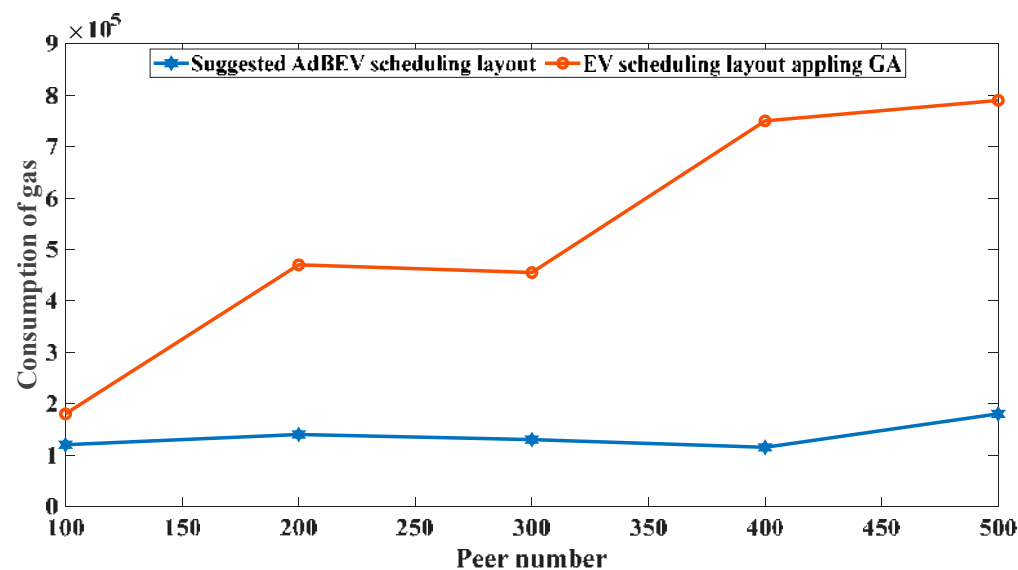


Figure 8. Comparison of calculation cost among the EV scheduling layout applying GA and the AdBEV.

## 5. Conclusions

An AdBEV scheduling layout for minimizing power fluctuations in order to provide a reliable and safe trading platform is examined in the present study. The EV stay-on-line model has been modeled for controlling the accessibility of discharging/charging amounts in the market. Most scheduling demands are processed using the iceberg order execution algorithm. The outcomes of the simulation are satisfactory and suggest that the proposed hybrid blockchain and machine learning algorithm can significantly lower power fluctuation levels, while also maximizing EV driver usefulness. The discharging and charging procedure can be controlled dynamically by adapting the very popular EV battery kinds and charging rates. AdBEV can provide insights into the construction of buildings in the transactional power market in the context of BC technology for improving decentralizing of the SGs. By reducing gas consumption, the suggested algorithm increases the performance of order trading. The future requires finding a balance between the on- and off-chain complexity, whilst taking advantage of BC's decentralized nature. It is worth noting that the main shortcoming of the proposed technique is the required space for the BL technique. Indeed, after a long time, storing all these transactions on a database requires a huge amount of space. Moreover, in the case of an attack, the retrieval of data would be challenging.

**Author Contributions:** Data curation, W.H.; Investigation, J.X. and W.H.; Project administration, W.H.; Resources, J.X.; Supervision, J.X.; Visualization, J.X. All authors have read and agreed to the published version of the manuscript.

**Funding:** This research received no external funding.

**Institutional Review Board Statement:** Not applicable.

**Informed Consent Statement:** Not applicable.

**Data Availability Statement:** This study did not report any data.

**Conflicts of Interest:** The authors have no conflict of interest to declare.

## References

1. Alnowibet, K.; Annuk, A.; Dampage, U.; Mohamed, M.A. Effective Energy Management via False Data Detection Scheme for the Interconnected Smart Energy Hub–Microgrid System under Stochastic Framework. *Sustainability* **2021**, *13*, 11836. [CrossRef]
2. Mohamed, M.A.; Mirjalili, S.; Dampage, U.; Salmen, S.H.; Al Obaid, S.; Annuk, A. A cost-efficient-based cooperative allocation of mining devices and renewable resources enhancing blockchain architecture. *Sustainability* **2021**, *13*, 10382. [CrossRef]

3. Wang, B.; Dabbaghjamanesh, M.; Kavousi-Fard, A.; Mehraeen, S. Cybersecurity enhancement of power trading within the networked microgrids based on blockchain and directed acyclic graph approach. *IEEE Trans. Ind. Appl.* **2019**, *55*, 7300–7309. [CrossRef]
4. Taherzadeh, E.; Javadi, S.; Dabbaghjamanesh, M. New optimal power management strategy for series plug-in hybrid electric vehicles. *Int. J. Automot. Technol.* **2018**, *19*, 1061–1069. [CrossRef]
5. Dabbaghjamanesh, M.; Kavousi-Fard, A.; Dong, Z.Y. A novel distributed cloud-fog based framework for energy management of networked microgrids. *IEEE Trans. Power Syst.* **2020**, *35*, 2847–2862. [CrossRef]
6. Angelim, J.H.; Affonso, C.D.M. Probabilistic assessment of voltage quality on solar-powered electric vehicle charging station. *Electr. Power Syst. Res.* **2020**, *189*, 106655. [CrossRef]
7. Dehghani, M.; Kavousi-Fard, A.; Dabbaghjamanesh, M.; Avatefipour, O. Deep learning based method for false data injection attack detection in AC smart islands. *IET Gener. Transm. Distrib.* **2020**, *14*, 5756–5765. [CrossRef]
8. Rajić, M.N.; Maksimović, R.M.; Milosavljević, P.; Pavlović, D. Energy management system application for sustainable development in wood industry enterprises. *Sustainability* **2019**, *12*, 76. [CrossRef]
9. Shojaei, F.; Rastegar, M.; Dabbaghjamanesh, M. Simultaneous placement of tie-lines and distributed generations to optimize distribution system post-outage operations and minimize energy losses. *CSEE J. Power Energy Syst.* **2020**, *7*, 318–328.
10. Aghajan-Eshkevari, S.; Azad, S.; Nazari-Heris, M.; Ameli, M.T.; Asadi, S. Charging and Discharging of Electric Vehicles in Power Systems: An Updated and Detailed Review of Methods, Control Structures, Objectives, and Optimization Methodologies. *Sustainability* **2022**, *14*, 2137. [CrossRef]
11. Dabbaghjamanesh, M.; Wang, B.; Kavousi-Fard, A.; Hatziargyriou, N.D.; Zhang, J. Blockchain-based stochastic energy management of interconnected microgrids considering incentive price. *IEEE Trans. Control. Netw. Syst.* **2021**, *8*, 1201–1211. [CrossRef]
12. Dabbaghjamanesh, M.; Wang, B.; Kavousi-Fard, A.; Mehraeen, S.; Hatziargyriou, N.D.; Trakas, D.N.; Ferdowsi, F. A novel two-stage multi-layer constrained spectral clustering strategy for intentional islanding of power grids. *IEEE Trans. Power Deliv.* **2019**, *35*, 560–570. [CrossRef]
13. Aslam, S.; Javaid, N.; Khan, F.A.; Alamri, A.; Almogren, A.; Abdul, W. Towards efficient energy management and power trading in a residential area via integrating a grid-connected microgrid. *Sustainability* **2018**, *10*, 1245. [CrossRef]
14. Antal, C.; Cioara, T.; Antal, M.; Mihailescu, V.; Mitrea, D.; Anghel, I.; Salomie, I.; Raveduto, G.; Bertoncini, M.; Croce, V.; et al. Blockchain based decentralized local energy flexibility market. *Energy Rep.* **2021**, *7*, 5269–5288. [CrossRef]
15. Vilathgamuwa, M.; Mishra, Y.; Yigitcanlar, T.; Bhaskar, A.; Wilson, C. Mobile-Energy-as-a-Service (MEaaS): Sustainable Electromobility via Integrated Energy–Transport–Urban Infrastructure. *Sustainability* **2022**, *14*, 2796. [CrossRef]
16. Zeng, L.; Xia, T.; Elsayed, S.; Ahmed, M.; Rezaei, M.; Jermisittiparsert, K.; Dampage, U.; Mohamed, M. A novel machine learning-based framework for optimal and secure operation of static VAR compensators in EAFs. *Sustainability* **2021**, *13*, 5777. [CrossRef]
17. Ghaffari, S.; Ashkaboosi, M. Applying Hidden Markov Model Baby Cry Signal Recognition Based on Cybernetic Theory. *IJEIR* **2016**, *5*, 243–247.
18. Lehtinen, O.; Pitkäniemi, S.; Weckman, A.; Aikio, M.; Mabano, M.; Lehtonen, M. Electric Vehicle Charging Loads in Residential Areas of Apartment Houses. In Proceedings of the 2020 21st International Scientific Conference on Electric Power Engineering (EPE), Prague, Czech Republic, 19–21 October 2020; IEEE: Piscataway, NJ, USA, 2020; pp. 1–6.
19. Ashkaboosi, M.; Ashkaboosi, F.; Nourani, S.M. *The Interaction of Cybernetics and Contemporary Economic Graphic Art as “Interactive Graphics”*; University Library of Munich: Munich, Germany, 2016.
20. Badruddoja, S.; Dantu, R.; He, Y.; Upadhayay, K.; Thompson, M. Making smart contracts smarter. In Proceedings of the 2021 IEEE International Conference on Blockchain and Cryptocurrency (ICBC), Sydney, Australia, 3–6 May 2021; IEEE: Piscataway, NJ, USA; pp. 1–3.
21. Rizwan, M.; Waseem, M.; Liaqat, R.; Sajjad, I.A.; Dampage, U.; Salmen, S.H.; Al Obaid, S.; Mohamed, M.A.; Annuk, A. SPSO Based Optimal Integration of DGs in Local Distribution Systems under Extreme Load Growth for Smart Cities. *Electronics* **2021**, *10*, 2542. [CrossRef]
22. Shahab, S.; Lades, L.K. Sludge and transaction costs. *Behav. Public Policy* **2021**, 1–22. [CrossRef]
23. Cavusoglu, S.S.; Macário, R. Minimum delay or maximum efficiency? Rising productivity of available capacity at airports: Review of current practice and future needs. *J. Air Transp. Manag.* **2021**, *90*, 101947.
24. Foryś, I.; Głuszak, M.; Konowalczyk, J. Compensation due to land use restrictions: The case of limited use area in the vicinity of Polish airports. *Oeconomia Copernic.* **2019**, *10*, 649–667. [CrossRef]

## Article

# Coordinated Design of Type-2 Fuzzy Lead–Lag-Structured SSSCs and PSSs for Power System Stability Improvement

Prabodh Khampariya <sup>1</sup>, Sidhartha Panda <sup>2</sup>, Hisham Alharbi <sup>3</sup>, Almoataz Y. Abdelaziz <sup>4,\*</sup>  
and Sherif S. M. Ghoneim <sup>3,\*</sup>

- <sup>1</sup> Department of EEE, Sri Satya Sai University of Technology & Medical Sciences, Sehore 466001, India; khampariya5@gmail.com  
<sup>2</sup> Department of Electrical Engineering, Veer Surendra Sai University of Technology, Odisha 768018, India; prof.dr.spanda@gmail.com  
<sup>3</sup> Electrical Engineering Department, College of Engineering, Taif University, P.O. Box 11099, Taif 21944, Saudi Arabia; h.alharbi@tu.edu.sa  
<sup>4</sup> Faculty of Engineering and Technology, Future University in Egypt, Cairo 11835, Egypt  
\* Correspondence: almoatazabdelaziz@hotmail.com (A.Y.A.); s.ghoneim@tu.edu.sa (S.S.M.G.)

**Abstract:** This work suggests a type-2 fuzzy lead–lag (T2FLL) controller structure for flexible AC transmission system (FACTS)-based damping controllers and power system stabilizers (PSSs) for power system stability improvement. The values of the suggested controller are optimized by a hybrid adaptive differential evolution and pattern search algorithm (hADE-PS) method. Initially, a single-machine infinite-bus (SMIB) system with lead–lag (LL)-structured FACTS and PSS controllers is considered, and the dominance of the hADE-PS method is established over the original differential evolution (DE), genetic algorithm (GA), and particle swarm optimization (PSO). The supremacy of T2FLL over the lead–lag (LL) controller is established under different large and small disturbance conditions, as well as varied loading conditions and fault positions. Lastly, the effectiveness of T2FLL is evaluated in a multimachine power system (MMPS). It is demonstrated that the suggested T2FLL offers better performance than the LL controller under various large and small disturbance conditions by providing significantly more damping to all modes of oscillations.

**Citation:** Khampariya, P.; Panda, S.; Alharbi, H.; Abdelaziz, A.Y.; Ghoneim, S.S.M. Coordinated Design of Type-2 Fuzzy Lead–Lag-Structured SSSCs and PSSs for Power System Stability Improvement. *Sustainability* **2022**, *14*, 6656. <https://doi.org/10.3390/su14116656>

Academic Editors: J. C. Hernandez and Mohamed A. Mohamed

Received: 18 April 2022  
Accepted: 26 May 2022  
Published: 29 May 2022



**Copyright:** © 2022 by the authors. Licensee MDPI, Basel, Switzerland. This article is an open access article distributed under the terms and conditions of the Creative Commons Attribution (CC BY) license (<https://creativecommons.org/licenses/by/4.0/>).

**Keywords:** power system stability; power system stabilizer; static synchronous series compensator; type-2 fuzzy lead–lag controller; differential evolution; pattern search

## 1. Introduction

Low-frequency oscillations are detected after disturbances in power systems that are joined by weak transmission lines. Under such circumstances, a lack of adequate system damping may result in sustained oscillations and, in turn, lead to the separation of the system [1,2]. To handle this issue, power system stabilizers (PSSs) are extensively favored by utilities. However, PSSs may not provide sufficient damping, and additional controllers are required. In this regard, recently developed flexible AC transmission system (FACTS) devices can be employed to provide the required damping. The static synchronous series compensator (SSSC) is an effective series FACTS device for power flow control and, hence, can be designed to provide additional damping [3].

Various soft-computing-based schemes have been suggested for damping controller design. Methodologies such as particle swarm optimization (PSO) [4,5], genetic algorithm (GA) [6,7], oppositional cuckoo algorithm [8], simulated annealing (SA) [9], tabu search (TS) [10], and bacteria foraging algorithm (BFA) [11] have been proposed in the literature. When SSSCs and PSSs are present in a power system, both should be coordinately designed. In the literature, PSSs are coordinately designed with other controllers such as PSS and SSSC by GA [12], PSS and SVC by GA [13], PSS and SSSC by hybrid PSO and gravitational search algorithm (GSA) [14], and PSS and thyristor-controlled series compensator (TCSC) [15–17].

It is observed in the literature that lead–lag (LL) controllers are commonly employed by researchers as structures of damping controllers. Recently, fuzzy logic controllers (FLCs) have been proposed by researchers, as FLCs can operate with imprecise inputs and handle nonlinearity. In [18], an improved control strategy has been proposed using a fuzzy PID regulator for a hybrid system. An FLC-based hybrid scheme is projected in [19] for power oscillation damping with FACTS and PSS controllers. In [20], a mixture of fuzzy-neural schemes is employed to capture maximum power. A hybrid firefly swarm-based type-2-based fractional-order (FO) fuzzy PID-structured PSS has been suggested in [21] for stability improvement of power systems.

Different optimization techniques such as the cuckoo search (CS) algorithm [22] and BAT search algorithm [23] have been employed in the literature for the optimal design of PSS parameters, and the superiority of the approach for system damping was demonstrated for various loading conditions. Numerous optimization-technique-based FACTS devices such as CS-based static synchronous compensator (STATCOM) [24], flower-pollination-based FACTS damping controller for a multimachine power system (MMPS) [25], and gravitational search algorithm (GSA)-based SSSCs [26] have been proposed for power system stability improvement. It is also demonstrated in the literature that when PSS and FACTS devices are present, they should be designed in a coordinated manner for achieving improved system performance [27].

From the above survey, it is evident that many optimization methods have been used for various power system problems, but no technique is exactly suited for all types of problems, and there are opportunities for performance enhancement by proposing new and modified techniques. Differential evolution (DE) is an easy but capable optimization method [28]. DE effectiveness relies on the choice of DE parameters such as crossover constant ( $Cr$ ) and scaling factor ( $F$ ) [28]. Throughout the search procedure, appropriate  $F$  and  $Cr$  parameters must be engaged in place of employing constant parameters during the evolution. An adaptive method is suggested here, where an adaptive mechanism is used for the selection of suitable  $F$  and  $Cr$  parameters during the optimization procedure. As DE is a global search method, it is intended for exploring the search area. To improve search capabilities, hybrid schemes have been recently projected for engineering design problems. A hybrid DE–PS procedure was suggested in [29] to tune the modified integral-derivative (MID) structure for frequency regulation. Fuzzy PID values are tuned by many hybrid optimization liaisons and GSAs for different systems in [30]. A hybrid-shuffled frog-leaping and PS-tuned PID has been proposed for frequency control in [31]. Recently, a hybrid-modified DE and PS (hMDE-PS)-based SSSC controller was proposed under communication constraints for stability improvement [32]. The superiority of hMDE-PS over other variants of DE such as JADE [33], CoDE [34], and SHADE [35] has been demonstrated for benchmark test functions. A hybrid adaptive DE and PS (hADE-PS)-based fractional-order fuzzy PID (FOFPID) structure for frequency regulation of power systems was reported in [36], where the performance of the FOFPID controller was equated with a double-derivative PI and PID controller for assessing frequency regulation performance using transfer function models of power systems.

Based on the above facts, this work proposes a novel scheme by employing a hybrid ADE and PS (hADE-PS) method for the coordinated design of a type-2 fuzzy lead–lag (T2FLL)-structured FACTS controller and PSS for power oscillation damping. The effectiveness of hADE-PS is compared with other popular algorithms such as GA, PSO, and the original DE. The novelties of the current work are:

- i. A new controller structure, known as type-2 fuzzy lead–lag (T2FLL), is proposed in this paper for PSS- and SSSC-based controllers for power system stability improvement.
- ii. The design task is taken as an optimization problem, and controller parameters are optimized by a recently proposed hADE-PS method.

- iii. Technique-wise, the hDE-PS method is compared with GA, PSO, and DE methods, and controller-wise, T2FLL is compared with type-1 fuzzy lead-lag (T1FLL) and widely used lead-lag (LL) controllers.
- iv. Various disturbance scenarios and changed loading/fault locations are simulated for both single-machine infinite-bus (SMIB) and MMPS, and it is seen that improved damping is attained with T2FLL related to T1FLL and LL controllers for all scenarios.

This paper is structured as follows: Section 2 introduces the systems under investigation. The projected control approach is described in Section 3. An overview of the hybrid adaptive DE and PS technique is provided in Section 4. Results are discussed in Section 5. Conclusions and future work are provided in Section 6.

## 2. Systems under Investigation

### 2.1. The SMIB System

Initially, SMIB system exposed in Figure 1 is taken. In Figure 1, the transformer is represented by  $T$ ; the infinite bus and generator terminal voltages are denoted by  $V_S$  and  $V_T$ , respectively; while  $V_1$  and  $V_2$  are the bus voltages, the SSSC converter output voltage and the DC voltage source are represented by  $V_{cnv}$  and  $V_{DC}$ , respectively; the line current is  $I$ ; the real powers in the transmission lines and one line are each represented by  $P_L$  and  $P_{L1}$ , respectively. The generator is provided with a turbine and governor, an excitation system, and a PSS. The excitation system contains a voltage regulator and exciter [37]. The system parameters are specified in Appendix A.

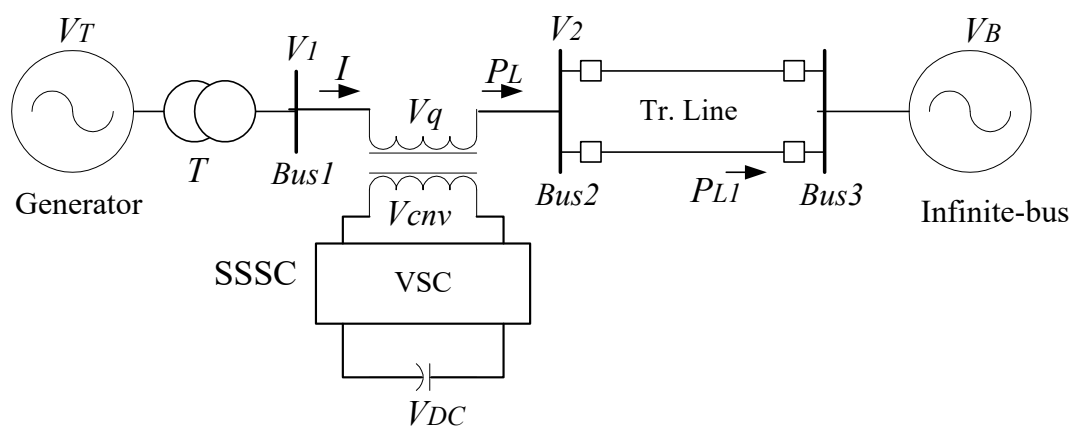


Figure 1. SMIB system.

### 2.2. Kundur's Test System (Four-Machine Two-Area)

The multi-machine power system (MMPS) contains 11 buses and 2 areas, joined by a weak transmission line as revealed in Figure 2. Loads and shunt capacitors are assumed at buses 7 and 9. The 2 areas are joined by 2 lines of 220 km. It was precisely planned to investigate low-frequency oscillations [38]. The test system follows the characteristics of usual systems in real operation. The load is characterized as constant impedances. The power transfer from area 1 to area 2 is 413 MW. The system is stressed and oscillates in the occurrence of any disturbance. The system details are taken from [38] and given in Appendix A.

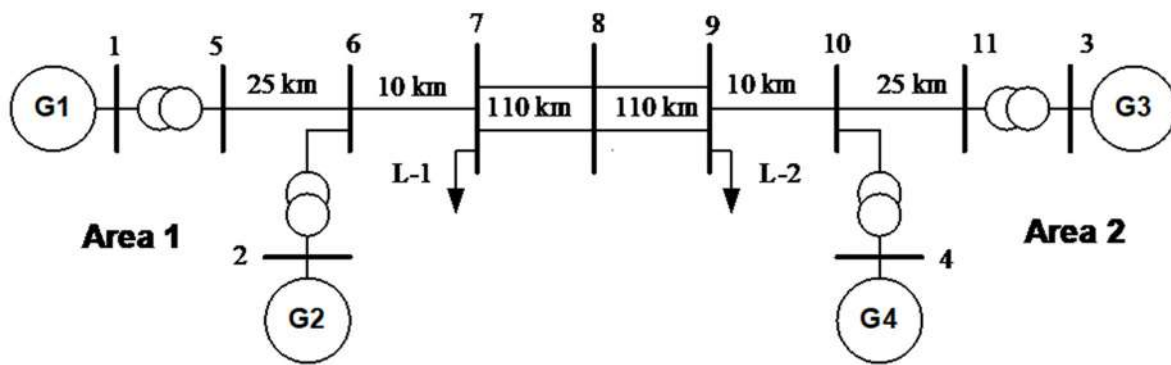


Figure 2. Kundur's 4-machine 2-area system.

### 3. The Proposed Approach

#### 3.1. Type-2 Fuzzy Logic Overview

When uncertainties are present, the conventional fuzzy logic control (FLC) may not be effective to improve the performance of the system. However, the twin membership function (MF) grounded type-2 FLC (T2F) provides improved system performance. The present study proposes a type-2 fuzzy lead-lag (T2FLL) controller as a damping controller. The MFs of the T2FLL engage upper and lower MFs (UMF and LMF). The type-2 fuzzy act includes fuzzification, knowledge base, type reducer (TR), and defuzzification.

Fuzzification is the initial phase of FLC. It processes inputs and creates the necessary prearranged fuzzy sets by the MFs. The linguistic parameters engaged for MFs are Extreme Positive (EXP), Least Positive (LP), Zero (ZER), Least Negative (LN), and Extreme Negative (EXN).

The T2F fuzzy set (FS) is formulated as:

$$FS = ((Var, a), \mu_U(Var, a)), \forall Var \in P, \forall a \in J_{Var}[0, 1] \quad (1)$$

where  $\mu_U(Var, a)$  is the UMF,  $Var$  is the main variable,  $a$  is the extra parameter in area  $J_{Var}$

The universe of discourse is formulated as:

$$FS = \int_{Var \in P} \int_{a \in J_{Var}[0, 1]} \frac{\mu_E(Var, a)}{(Var, a)} \quad (2)$$

where,  $\int \int$  = Union on ACE and  $a$

Now the membership expression is:

$$\mu_U(Var, a) = \overline{FOU(U)} \forall Var \in P, \forall a \in J_{Var}[0, 1] \quad (3)$$

where  $J_{Var}$  is expressed as:

$$J_{Var} = [\mu_U(Var, a), \mu_L(Var, a)] \forall Var \in P, \forall a \in J_{Var}[0, 1] \quad (4)$$

The MF associated with type-I FLC inspires to develop MFs of T2F.

The rule base and interface engine form the knowledge base. The rule base is demonstrated in Table 1. Individually,  $Var$  and  $dAVar$  are the inputs to T2F and  $y$  is the output.



**Table 1.** Rule base of fuzzy controller.

$\dot{e}$ \ $e$	EXN	LN	ZER	LP	EXP
EXN	EXN	EXN	LN	LN	ZER
LN	EXN	LN	EXN	ZER	LP
ZER	LN	LN	ZER	LP	LP
LP	LN	ZER	LP	LP	EXP
EXP	ZER	LP	LP	EXP	EXP

The characteristic of the type-2 FLC is

$$LMF : for Var = \underline{LN}; dVar = \underline{Z}; Y = \underline{LN} \quad (5)$$

$$UMF : for Var = \overline{LN}; dVar = \overline{Z}; Y = \overline{LN} \quad (6)$$

where  $\underline{LN}$ ,  $\underline{Z}$  and  $\overline{LN}$ ,  $\overline{Z}$  are related to  $LMF$  and  $UMF$ , respectively.

The related FS firing forte is

$$\underline{f^s} = \min(\mu_{\underline{US}}(Var, a), \mu_{\underline{US}}(dVar, a)) \quad (7)$$

$$\overline{f^s} = \max(\mu_{\overline{US}}(Var, a), \mu_{\overline{US}}(dVar, a)) \quad (8)$$

$$F^s = [\underline{f^s}, \overline{f^s}] \quad (9)$$

where  $\underline{f^s}$  and  $\overline{f^s}$  are related to  $LMF$  and  $UMF$ , respectively.

Type reduction (TR) is used to modify type-2 to type-1 FS for defuzzification. The schemes for defuzzification are centroid, the center of sets (SOC), and the center of sums. Here, SOC is used as it is reported as the best scheme. The outputs are:

$$Y_{cos} = \sum_{s=1}^{25} \frac{F^s Y^s}{F^s} = [Y_{m1}, Y_{m2}] \quad (10)$$

$$Y_{m1} = \frac{\sum_{s=1}^{25} \underline{f^s} y^s}{\sum_{s=1}^{25} \underline{f^s}} \quad (11)$$

$$Y_{m2} = \frac{\sum_{s=1}^{25} \overline{f^s} y^s}{\sum_{s=1}^{25} \overline{f^s}} \quad (12)$$

where  $Y_{m1}$  and  $Y_{m2}$  are associated with MFs of type-1 FLC. The output of type-2 FLC  $Y_{cos}$  is found by averaging. The recommended T2FLL is set bearing in mind all characteristics of lead-lag controller and T2F.

### 3.2. Structure of T2FLL Controller

The configuration of the proposed type-2 fuzzy lead-lag (T2FLL) SSSC-based controller is revealed in Figure 3. It contains a sensor block, transport delay block, scaling factor blocks for fuzzy input, gain, a washout, and lead-lag (LL) blocks. The washout tie constant is generally taken as 10 s [38]. The LL blocks deliver the suitable phase lead to balance for the lag among output and input. The output of the controller is the  $V_q$ .

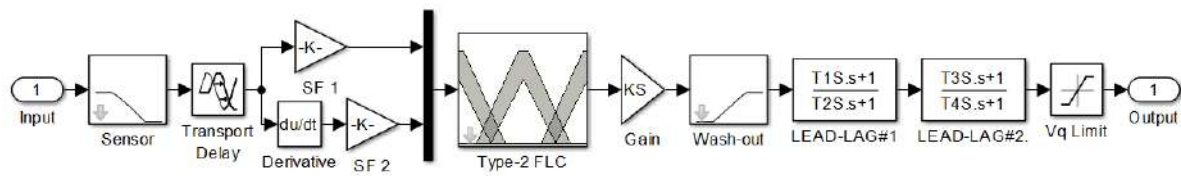


Figure 3. SSSC-based T2FLL controller.

Figure 4 shows the structure of the T2FLL-based PSS. It consists of a gain, washout, and LL block. The speed variation is fed as input to the PSS. The PSS output ( $V_s$ ) is used to change the excitation voltage.

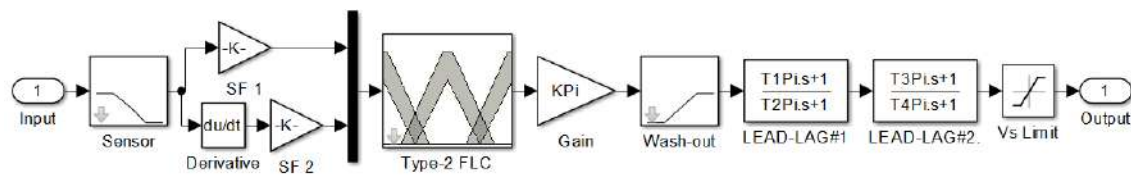


Figure 4. PSS-based T2FLL controller.

Speed deviations are selected as T2FLL controller input signals. A sensor time constant of 15 ms is assumed. A transport delay of 50 ms is assumed for the SSSC controller.

### 3.3. Optimization Problem

An integral time multiplied absolute error (ITAE) criterion is employed for the SMIB system. For MMPS, an ITAE criterion using local and inter-area modes of oscillations is selected. They are represented by:

For SMIB:

$$J = \int_{t=0}^{t=t_{sim}} |\Delta\omega| \cdot t \cdot dt \quad (13)$$

For MMPS:

$$J = \int_{t=0}^{t=t_{sim}} (\sum |\Delta\omega_L| + \sum |\Delta\omega_I|) \cdot t \cdot dt \quad (14)$$

where  $\Delta\omega$  is the speed deviance in the SMIB system,  $\Delta\omega_L$  and  $\Delta\omega_I$  are the speed deviations of MMPS related to local and inter-area modes, respectively, and  $t_{sim}$  is the simulation time.

Therefore, the design task is formulated as an optimization task as:

$$\text{Minimize } J \quad (15)$$

Subject to

$$\begin{aligned} KSF_{i_{min}} &\leq KSF_i \leq KSF_{i_{max}} (KSF_i = \text{Scaling factors}) \\ K_{i_{min}} &\leq K_i \leq K_{i_{max}} (K_i = \text{Gains}) \\ T_{i_{min}} &\leq T_i \leq T_{i_{max}} (T_i = \text{Time constants}) \end{aligned} \quad (16)$$

The limits of the parameters are [0.01–100] for  $K_i$ , [0.01–10] for  $T_i$ , and [0.01–100] for  $KFS_i$ . In the present work, the hADE-PS algorithm determines T2FLL values.

## 4. Overview of Hybrid Adaptive DE and PS Technique

The differential evolution (DE) method is a simple, competent but efficient method [28]. Encouraged by the evolution approach, the DE method is found to be a capable method for complex engineering problems. The stages of DE are:

#### 4.1. Mutation

The mutant vector  $w^j|_i$  is to be performed for each parent vector  $y^j|_i$  on each generation 'i' is:

$$w^j|_i = y^{q_1}|_i + F(y^{q_2}|_i - y^{q_3}|_i) \quad (17)$$

where  $q_1 \neq q_2 \neq q_3 \neq j$ .  $F$  indicates the scaling factor.

#### 4.2. Crossover

It is a vital method for the expansion of population diversity. In Binary crossover, the trial vector  $v^j|_i = [v_1^j|_i, v_2^j|_i, \dots, v_n^j|_i]$  can be generated through the target vector  $y^j|_i$  and its mutant vector  $w^j|_i$ . As:

$$v_l^j|_i = \begin{cases} w_l^j|_i & \text{if } \text{rand}(0,1) \leq Cr \\ y_l^j|_i & \text{otherwise} \end{cases} \quad (18)$$

where  $l \in 1, 2, \dots, n$ . For every vector  $y^j|_i$  and  $w^j|_i$ , the trial vector  $v^j|_i$  can be generated as:

$$v^j|_i = y^j|_i + F_j(w^j|_i - y^j|_i) \quad (19)$$

#### 4.3. Selection

The selection operation is engaged to maintain a fixed population size in all generations. The vector having the best fitness value replaces the fewer fit vectors.

The equation representing this process is:

$$y^j|_{i+1} = \begin{cases} v^j|_i & \text{if } f(v^j|_i) \leq f(y^j|_i) \\ y^j|_i & \text{otherwise} \end{cases} \quad (20)$$

DE is a competent method but relies on its algorithm parameters such as  $F$  and  $Cr$ . Appropriate choice of  $F$  and  $Cr$  is vital for the performance of DE. Numerous researchers have recommended different schemes to choose  $F$  and  $Cr$  values [39].

Liu and Lampinen [40] indicated the control parameters value to evaluate the robustness as well as the effectiveness of the DE algorithm. Gamperle et al. [41] have suggested the values such as 0.6 and [0.3, 0.9] for  $F$  and  $Cr$  to control the parameters. On the other hand, Ali and Torn [42] have tested their results on the values such as 0.5 and [0.4, 1] for  $F$  and  $Cr$ . Moreover, different self-adaptive approaches are proposed to select 'Cr & F' during the experimentation for effective results [43].

Selecting correct  $F$  and  $Cr$  parameters is a problem-dependent task. The projected scheme uses an adaptive approach to select  $F$  and  $Cr$  values during the optimization process. For generation  $i$ , the triangular factors such as  $\Delta F$ , and  $\Delta Cr$  have been used for evaluating  $f_F(y)|_i$  and  $f_{Cr}(y)|_i$  for each child in the population. For Triangular Distribution factor of  $F$  ( $\Delta F$ ) and  $Cr$  ( $\Delta Cr$ ), where  $\Delta F = [0.1, 1, 2]$  and  $\Delta Cr = [0.1, 0.4, 1]$  are engaged in the present study.

To select  $F^i$  and  $Cr^i$ , mx (maximum), mn (minimum), and md (median) are engaged in a generation as indicated in Equations. (21) and (22).

$$F^i = \begin{cases} F_{mn} + \sqrt{\text{rand } V * (F_{mx} - F_{mn}) / (F_{md} - F_{mn})} \\ \text{if } \text{rand } V < (F_{mx} - F_{mn}) / (F_{md} - F_{mn}) \\ F_{mx} - \sqrt{(1 - \text{rand } V) * (F_{mx} - F_{mn}) / (F_{mx} - F_{md})} \\ \text{otherwise} \end{cases} \quad (21)$$

$$Cr^i = \begin{cases} Cr_{mn} + \sqrt{\text{rand } V * (Cr_{mx} - Cr_{mn}) / (Cr_{md} - Cr_{mn})} \\ \text{if } \text{rand } V < (Cr_{mx} - Cr_{mn}) / (Cr_{md} - Cr_{mn}) \\ Cr_{mx} - \sqrt{(1 - \text{rand } V) * (Cr_{mx} - Cr_{mn}) / (Cr_{mx} - Cr_{md})} \\ \text{otherwise} \end{cases} \quad (22)$$

Here,  $rand V$  has been selected in an arbitrary distribution with a limit  $[0, 1]$ .

Before performing the mutation scheme, the  $F^i$  and  $Cr^i$  values are set which affects the mutation, cross-over, and selection process for the newly generator vector  $y^i|_{i+1}$ . Due to the easy generation of adaptive values for  $F$  and  $Cr$ , it can maintain the time complexity as compared to conventional DE.

The pattern search (PS) method is shown to be useful in numerous hybrid approaches [23,25]. The information regarding the PS algorithm is available in the literature [23,25]. At first, the ADE technique is executed and PS is then executed considering the final results of ADE as the starting points. So, the benefit of hybridizing the ADE and PS algorithms is that the hybrid algorithm will have enhanced exploring and exploiting capability.

## 5. Outcomes

### 5.1. SMIB System

The SMIB system is developed in MATLAB / SIMULINK as displayed in Figure 5. In the present study, the ode23tb (stiff/TR-BDF2) solver which is a variable-step with 1 cycle of the fundamental frequency as the maximum time step is used as in the literature [4,5]. The system is developed using the Sim Power Systems (SPS) library of SIMULINK. The dynamics of all windings are specified in the rotor reference frame (q-d frame). The Hydraulic Turbine and Governor (HTG) and Excitation system are present in the subsystem represented by the “Generator Control System” (Reg\_M).

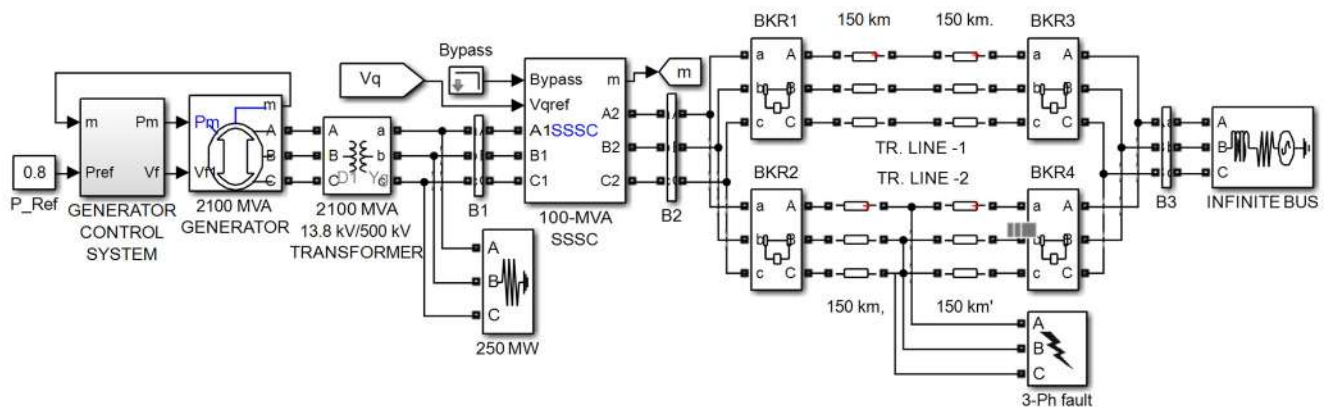


Figure 5. MATLAB/SIMULINK model of SMIB system.

The system model is constructed in the SIMULINK environment and optimization routines are specified in a separate m file. For ITAE evaluation, the model is simulated considering a severe disturbance. The  $J$  value is transferred to the optimization routine by transferring it to the workspace and used by the optimization program to minimize  $J$  value.

To validate the advantage of the hADE-PS approach, the LL controller is initially considered. For ITAE calculation, a 3-phase fault of 5 cycles is assumed at the midpoint of one transmission line. The lines are opened for 5 cycles to clear the fault. To authenticate the better performance of the hADE-PS method, the LL values are optimized by the hADE-PS, DE, PSO, and GA methods. It is worth mentioning here that, the parameters of the compared algorithm are taken from the related reference papers [44,45].

One important challenge of a hybrid global search (GS) and local search (LS) is the tradeoff between GS and LS because the cost of LS can be rather high. If LS is applied at the first stage, several solutions in the final generation may lie very close to each other at the end of LS, which makes it harder for the second stage GS method to maintain diversity in its population. This may lead the hybrid algorithm to converge to a local optimum. Therefore, the LS is performed at the second stage using the best solution provided by the GS method. This action tends to make the hybrid algorithm more computationally efficient and helps to prevent converging to a local optimum [29,31,32,36]. As the LS method is

used to improve the solution quality (fine-tuning) but not to explore the search space to find independently the global optimum, more iterations (about 90%) are assigned to the GS method and fewer iterations (about 10%) are assigned to the LS method [29–32].

For the application of DE, PSO, and GA, 50 populations and 100 generations are employed and for the hADE-PS technique, 90 generations are assigned to the ADE technique and 10 generations are assigned to the PS technique. The parameters employed for each technique are as follows: GA: Tournament selection, Crossover and mutation rates 0.9 and 0.1; PSO: Inertia weight reduces from 0.9 to 0.2, social and cognitive components 2.0; DE: DE/best/2/bin strategy, step size and crossover probability 0.2 and 0.6. The PS is executed with a mesh size of 1, mesh expansion factor of 2 and mesh contraction factor of 0.5. The maximum number of objective function evaluations is set to 10. All the techniques are executed 10 times, and optimal values (as per the least ITAE value) obtained are taken as controller parameters. The outcomes are delivered in Table 2. It is obvious from Table 2 that, with lead–lag structure, the least ITAE values ( $33.7926 \times 10^{-3}$ ) are obtained with the hADE-PS technique compared to GA ( $44.3216 \times 10^{-3}$ ), PSO ( $40.9781 \times 10^{-3}$ ) and DE ( $37.7718 \times 10^{-3}$ ) techniques. So with the identical system and controller structure, the percentage reduction in ITAE value with hADE-PS compared to GA, PSO, and DE techniques are 23.56%, 17.53%, and 10.53%, respectively. This demonstrates the dominance of hADE-PS over GA, PSO, and DE techniques. The speed deviation response is revealed in Figure 6, from which it is evident that the best system response is attained with hADE-PS related to GA, PSO, and DE.

**Table 2.** Optimized lead–lag-structured PSS and SSSC parameters for SMIB.

Technique	Controller	$K_i$	$T_{1i}$	$T_{2i}$	$T_{3i}$	$T_{4i}$	$J \text{ Value} \times 10^{-3}$
GA	SSSC	74.0740	0.4286	0.0511	0.4523	1.1098	44.3216
	PSS	19.8294	0.1415	0.0011	0.0630	1.2736	
PSO	SSSC	38.5588	1.0653	0.3218	0.6751	0.7496	40.9781
	PSS	24.2563	1.5546	1.4223	0.0134	0.4930	
DE	SSSC	50.1218	0.8175	1.1379	1.4961	0.4326	37.7718
hADE-PS	PSS	16.0860	0.1553	0.7317	1.7974	1.7974	33.7926
	SSSC	71.5265	1.2006	1.3051	0.0011	0.0012	
	PSS	18.2475	0.0011	0.5204	0.0011	0.4981	

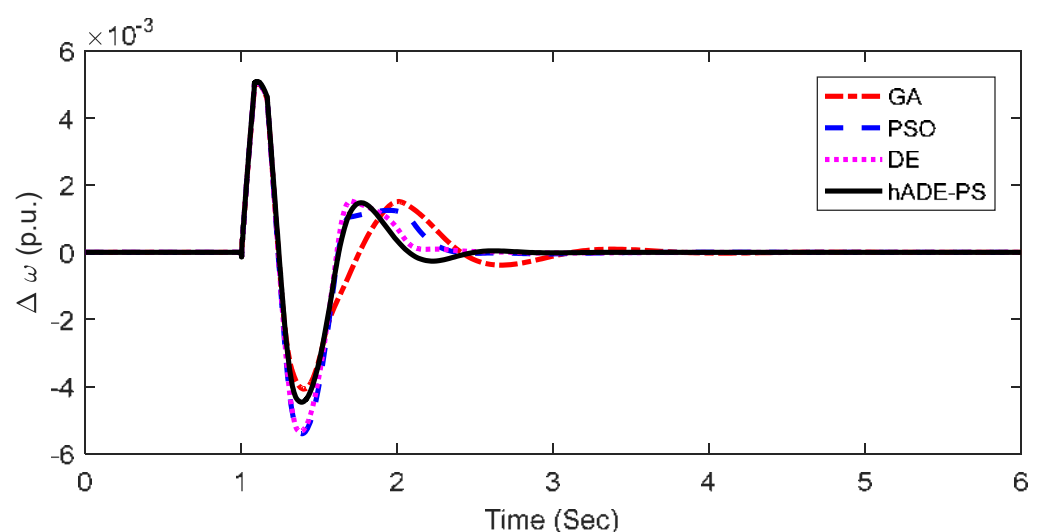


**Figure 6.**  $\Delta\omega$  response with GA-, PSO-, DE-, and hADE-PS-tuned lead–lag controller.

In the next step, the proposed Type-2 fuzzy lead–lag controller is implemented and hADE-PS-tuned parameters are specified in Table 3. For comparison, the results of the

type-1 fuzzy lead–lag (T1FLL) controller are also provided in Table 3. The type-1 fuzzy part, i.e., membership functions, range, etc. is adopted from reference [36]. It can be noticed that with the same hADE-PS technique, the ITAE value is further reduced to  $31.9342 \times 10^{-3}$  with T1FLL, and the least ITAE of  $28.6961 \times 10^{-3}$  is attained with the T2FLL controller. So there is a reduction of 10.13% and 15.08% in  $J$  value with T2FLL related to the T1FLL and LL controller, respectively.

**Table 3.** hADE-PS optimized T2FLL- and T1FLL-structured PSS and SSSC parameters for SMIB.

Controller	$KSF_1$	$KSF_2$	$K_i$	$T_{1i}$	$T_{2i}$	$T_{3i}$	$T_{4i}$	$J \text{ Value} \times 10^{-3}$
T2FLL controller								
SSSC	0.0105	0.1824	79.5279	1.9974	1.5774	1.0292	0.4604	28.6961
PSS	0.0104	0.7241	49.9350	0.0622	1.6995	0.0012	1.9974	
T1FLL controller								
SSSC	1.9093	1.4684	14.2391	0.0154	0.4538	1.9974	0.9935	31.9342
PSS	0.3209	1.2285	30.5106	0.2421	1.7827	0.4172	1.9974	

To explore the viability of T2FLL, several contingencies are taken. These scenarios are widely used in literature to evaluate the performance of and are given as follows [46–48].

#### 5.1.1. Scenario 1: Large Disturbance Condition

Initially, the performance is investigated at nominal loading ( $P_e = 0.8$  p.u.  $\delta_0 = 48.5^\circ$ ). A 3-phase fault of 5 cycles is applied at the midpoint of one transmission line. The fault is removed by opening the line for 5 cycles. The responses with the hADE-PS-tuned LL, T1FLL, and T2FLL controllers are revealed in Figure 7a–e. For comparison, the responses without any control are also shown in Figure 7a–e. Figure 7a–e displays the speed deviation response ( $\Delta\omega$ ) in p.u., power angle response ( $\delta$ ) in degrees, tie-line power in the line ( $P_L$ ) in MW SSSC output voltage ( $V_q$ ) in p.u., and PSS output ( $V_s$ ) in p.u. under above severe disturbance.

Figure 7a–e demonstrate that the proposed controller tuned by hADE-PS has a superior damping performance compared to both the T1FLL and LL controller. Figure 7a–c also indicate that T2FLL offers improved response with less overshoot/undershoot compared to both the T1FLL and LL controller.

#### 5.1.2. Scenario 2: Small Disturbance Condition

The efficiency of the T2FLL is also studied at small disturbance conditions by removing load at bus 1 for 100 ms at  $t = 1$  s. Figure 8 displays the  $\Delta\omega$  response, from which it is seen that T2FLL designed at large disturbance conditions, suppresses power system oscillations efficiently at the small disturbance, and T2FLL also delivers a better transient response compared to the T1FLL and LL in this case.

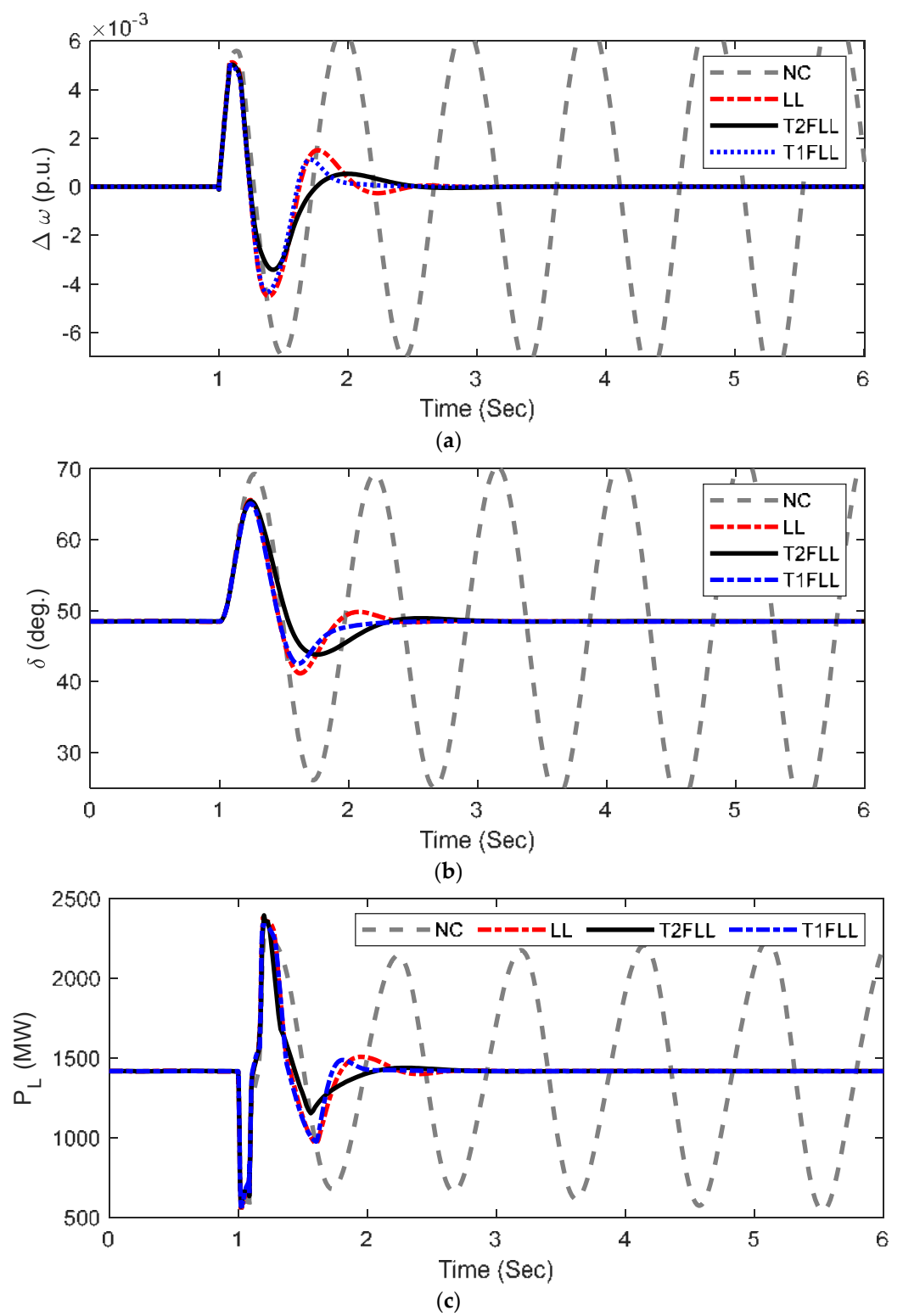


Figure 7. Cont.

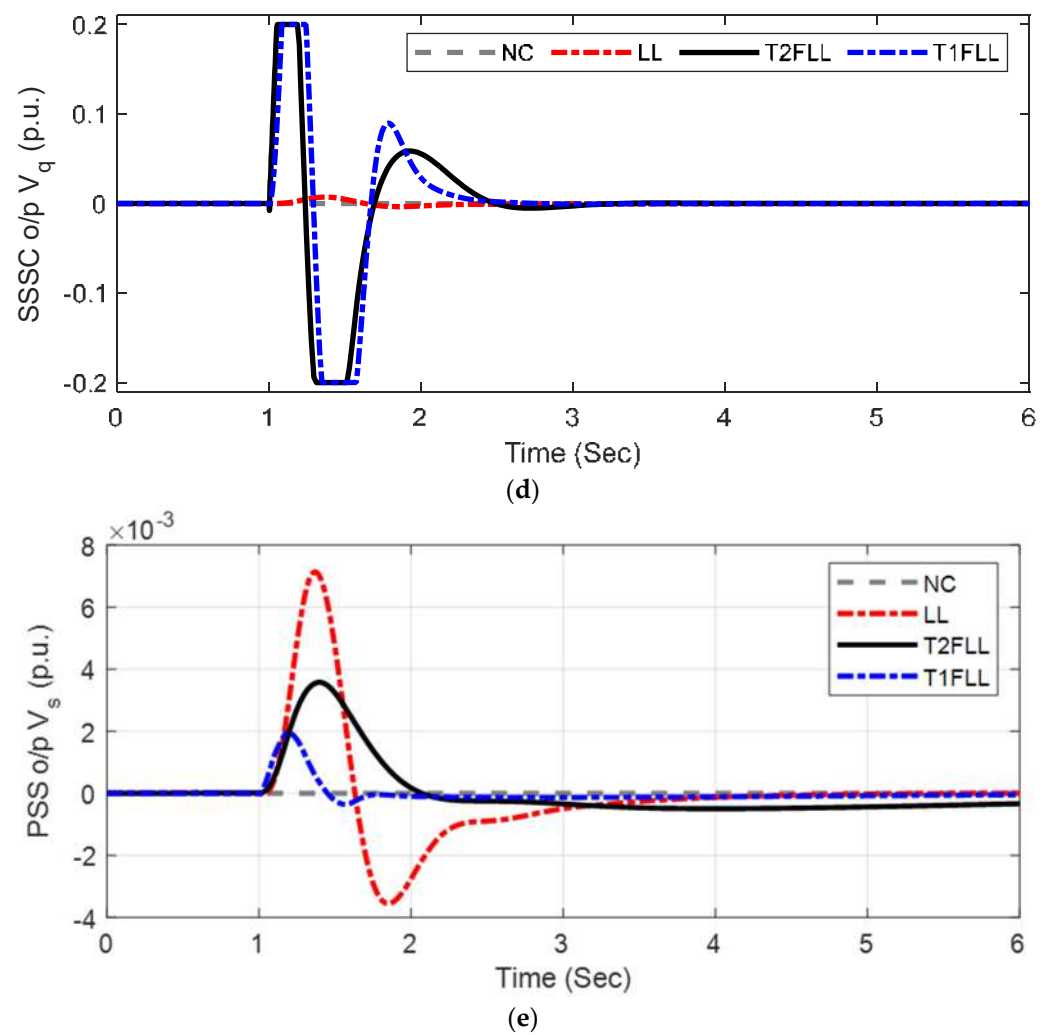


Figure 7. System response of SMIB for Scenario 1: (a)  $\Delta\omega$ , (b)  $\Delta\delta$ , (c)  $P_L$ , (d) SSSC output, (e) PSS output.

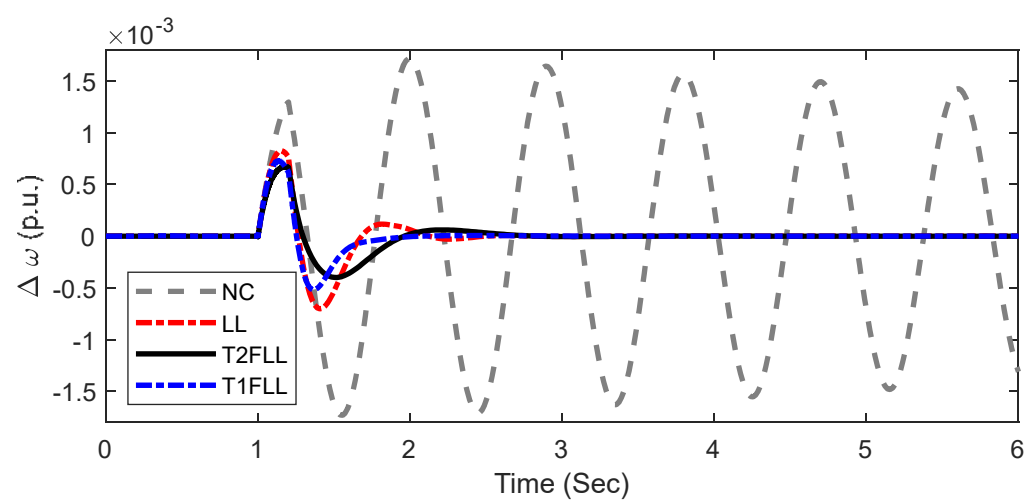


Figure 8.  $\Delta\omega$  response of SMIB for Scenario 2.

### 5.1.3. Scenario 3: Changed Loading Condition and Fault Location

Controller efficiency is also verified in changed fault location and loading conditions. A self-clearing, 5-cycle, 3-phase fault is assumed at bus 1 in light loading ( $P_e = 0.5$  p.u.,  $\delta_0 = 38.2^\circ$ ) condition. Under this contingency,  $\Delta\omega$  variation is revealed in Figure 9. It is



noticed that oscillations are damped quickly with T2FLL in comparison with the T1FLL and LL controllers and without the controllers.

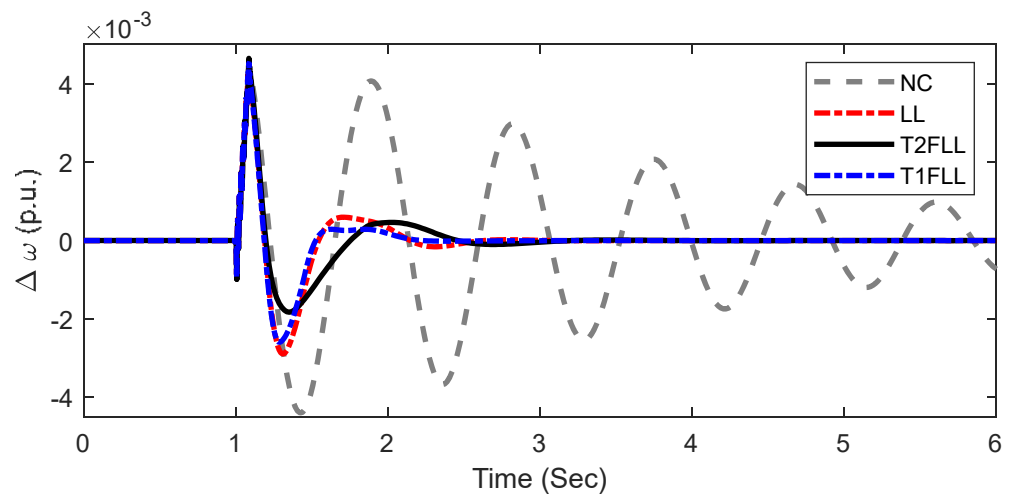


Figure 9.  $\Delta\omega$  response of SMIB for Scenario 3.

The performance for the above three scenarios is gathered in Table 4 for improved clarification of enhancement by the proposed method. It can be observed that for different scenarios, the least performance indexes are found with T2FLL related to the T1FLL and LL controller.

Table 4. Performance comparison under various scenarios for SMIB.

Scenario/Controller		ISE ( $\times 10^{-6}$ )	ITAE ( $\times 10^{-2}$ )	ITSE ( $\times 10^{-3}$ )	IAE ( $\times 10^{-6}$ )	Overshoots in $\Delta\omega$ ( $\times 10^{-3}$ )	Undershoots in $\Delta\omega$ ( $\times 10^{-3}$ )
Scenario 1	NC	256.6942	244.0563	43.0972	1493.7607	7.786	−8.6124
	LL	7.7379	3.3792	2.3878	10.1409	5.0881	−4.4641
	T1FLL	6.8863	3.1934	2.0871	8.8434	4.998	−4.3516
	T2FLL	5.8701	2.86961	2.0413	7.4721	5.0363	−3.3831
Scenario 2	NC	9.3642	42.5216	8.1817	45.9841	1.7148	1.7312
	LL	0.1951	0.4901	0.3586	0.2514	0.8321	−0.7049
	T1FLL	0.1668	0.4862	0.3398	0.2163	0.7148	−0.5189
	T2FLL	0.1162	0.4618	0.3142	0.1528	0.6732	−0.3972
Scenario 3	NC	19.6749	30.5829	9.0338	48.6916	4.6224	−4.3954
	LL	2.6978	1.825	1.3121	3.3519	4.5324	−2.8929
	T1FLL	2.4873	1.8011	1.2967	3.0572	4.5324	−2.2581
	T2FLL	2.2042	1.8169	1.2816	2.73604	4.5324	−1.8272

## 5.2. Extension to Multi-Machine System (MMPS)

The MMPS presented in Figure 2 is taken in the next stage and constructed in the MATLAB/SIMULINK setting as revealed in Figure 10. The MATLAB/SIMULINK model of Area 1 is revealed in Figure 11. In the same way, Area 2 is also modeled. The location of series FACTS devices constitutes a major step in the employment of FACTS devices in power systems. Depending on the required objective, sensitivity analysis can be performed to decide the best location of SSSC in a large power system. Keeping in view of our objective of power system stability enhancement, the SSSC is incorporated between bus 1 and bus 2, as presented in Figure 10. To design the proposed T2FLL controller, a similar approach as used in the SMIB case is followed. The objective function is defined in Equation (14) for a multi-machine system. The tuned parameters for LL, T1FLL, and T2FLL are provided in Tables 5 and 6, respectively.

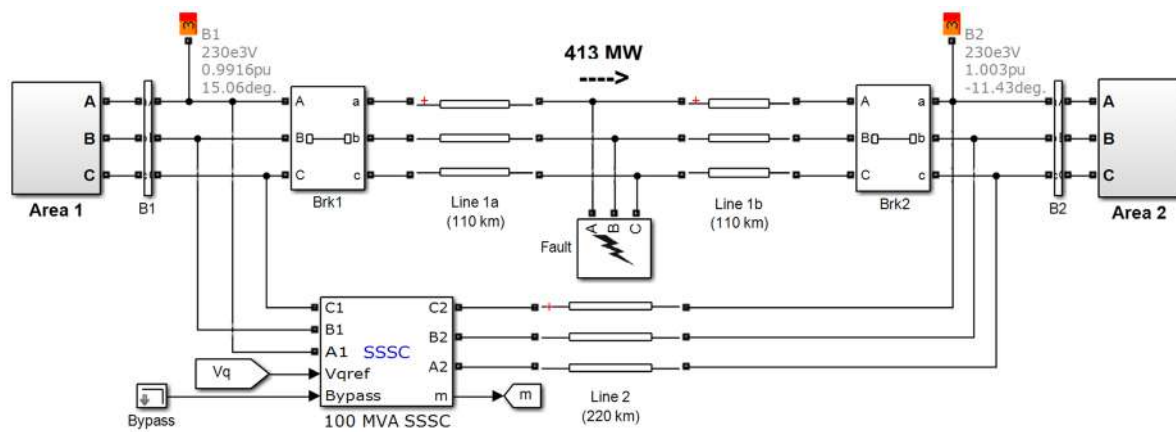


Figure 10. MATLAB/SIMULINK model of Kundur's 4-machine 2-area system.

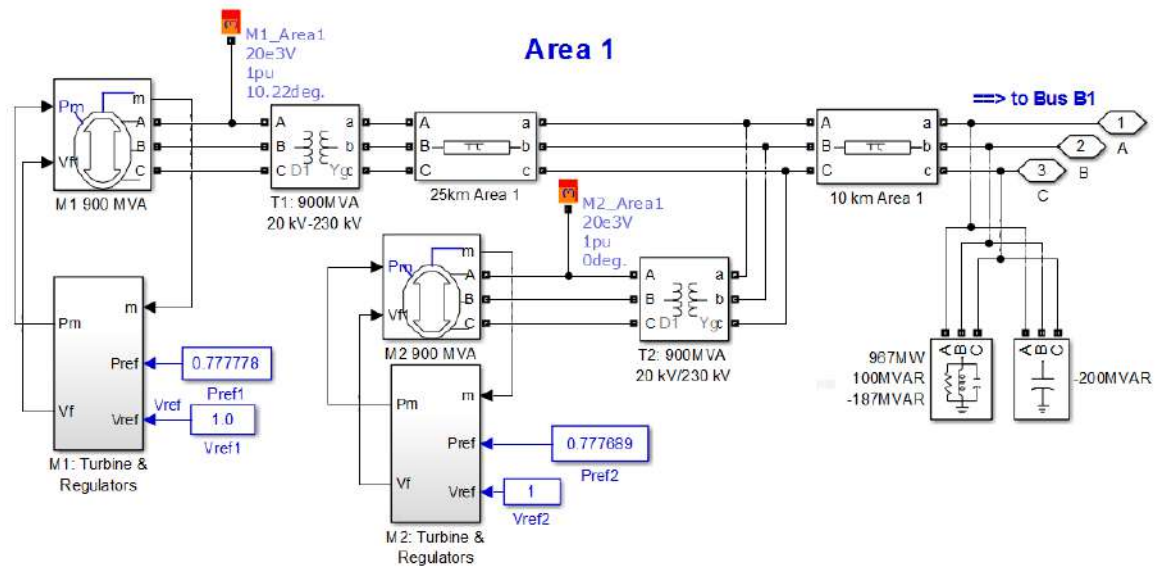


Figure 11. MATLAB/SIMULINK model of Area 1 of Kundur's 4-machine 4-area system.

Table 5. Optimized lead-lag-structured PSS and SSSC parameters for multi-machine system.

Controller	$K_i$	$T_{1i}$	$T_{2i}$	$T_{3i}$	$T_{4i}$
SSSC	92.8460	0.0885	0.0308	4.5494	7.4982
PSS1	46.8908	0.0430	0.0182	2.7794	8.8044
PSS2	48.0950	0.0114	0.0155	3.9735	3.5212
PSS3	45.8967	0.0712	0.0128	3.7749	3.2167
PSS4	27.6544	0.0974	0.0319	3.8884	3.2087

**Table 6.** Optimized T2FLL-structured PSS and SSSC parameters for multi-machine system.

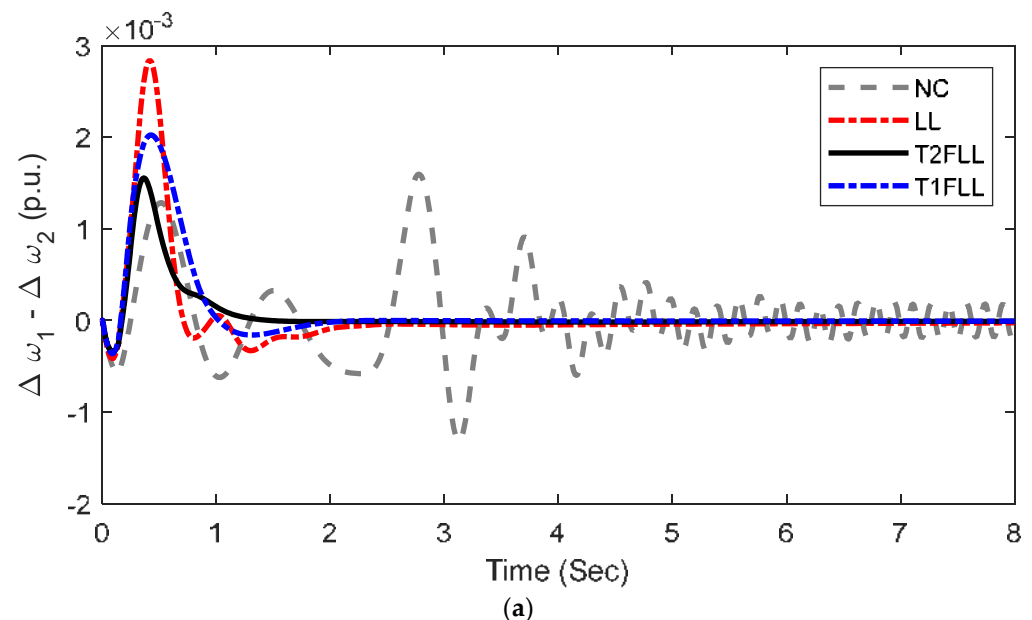
Controller	$KSF_1$	$KSF_2$	$K_i$	$T_{1i}$	$T_{2i}$	$T_{3i}$	$T_{4i}$
<b>T2FLL controller</b>							
SSSC	0.0102	0.0148	41.0552	0.0990	0.0064	1.5070	2.9408
PSS1	0.7591	0.0126	24.6432	0.0193	0.0066	2.4321	2.3374
PSS2	1.9797	0.0468	16.5071	0.0394	0.0104	1.9728	1.5423
PSS3	0.0765	0.0284	37.0997	0.0992	0.0059	2.4474	3.0812
PSS4	1.2245	0.2568	11.0542	0.0155	0.0051	1.7857	0.9991
<b>T1FLL controller</b>							
SSSC	0.2323	0.5164	2.7141	0.0103	0.0101	4.9493	2.0462
PSS1	1.0206	0.0871	11.7451	0.0194	0.0066	3.2127	3.8817
PSS2	1.5428	0.4353	40.6019	0.0415	0.0383	2.3425	3.8154
PSS3	0.9495	0.0100	49.4935	0.0121	0.0060	4.2398	4.4935
PSS4	1.4140	0.0492	35.8082	0.0115	0.0239	2.4098	3.6268

To investigate the viability of T2FLL, several contingencies are taken. These scenarios are widely used in the literature to evaluate the performance and are given as follows [46–48].

#### 5.2.1. Scenario 1: Three Phase Fault Disturbance Condition

Initially, the performance of the controller is investigated under a large disturbance scenario. A 3-phase fault (self-clearing) of 5 cycles is assumed at the middle of one transmission line at  $t = 0$  s. The local and inter-area modes of oscillations with the hADE-PS-tuned LL, T1FLL, and T2FLL controllers are shown in Figure 12a,b. For comparison, the responses without any control are also presented in Figure 12a,b.

It is obvious from Figure 12a,b that the system loses stability without control, and stability is maintained with all the controllers. It is also evident from Figure 12a,b that improved system damping performance with fewer overshoots/undershoots is attained with the proposed T2FLL controller compared to the T1FLL and LL controllers.

**Figure 12.** Cont.

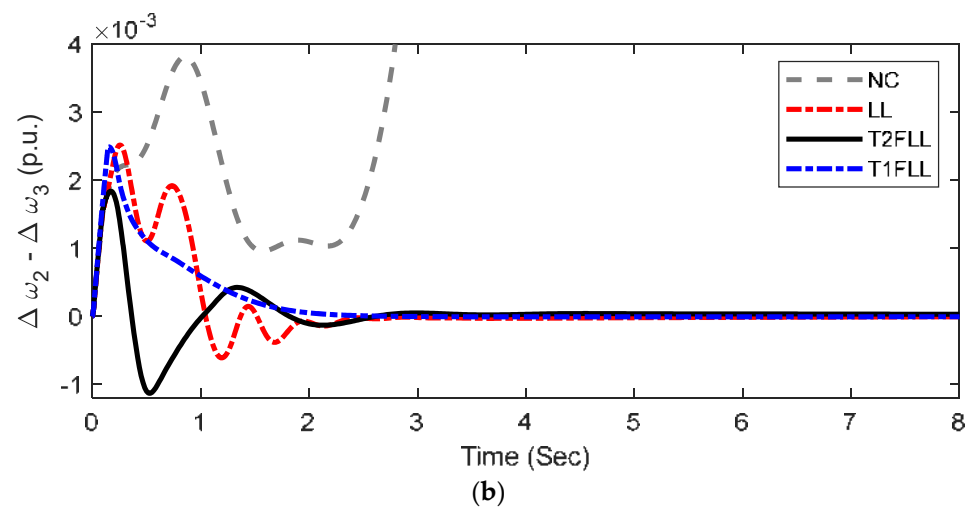


**Figure 12.** System response of MMPS system for Scenario 1: (a) local mode; (b) inter-area mode. (a) local mode of oscillation of MMPS for Scenario 1. (b) Inter-area mode of oscillation of MMPS for Scenario 1.

#### 5.2.2. Scenario 2: Line Outage Disturbance Condition

In this scenario, one of the two tie-lines is removed at  $t = 0$  sec and reclosed after 5 cycles. The responses are exposed in Figure 15a,b. It is evident from Figure 15a,b that in this scenario also, the system loses stability without control, and improved responses are attained with the T2FLL controller related to the T1FLL and LL controllers.

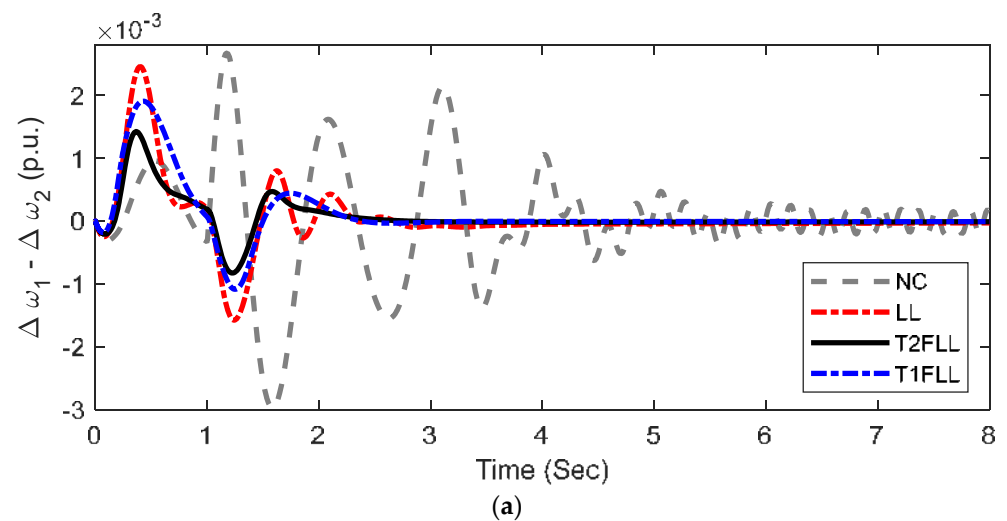


**Figure 13.** Cont.

Figure 14. Cont.

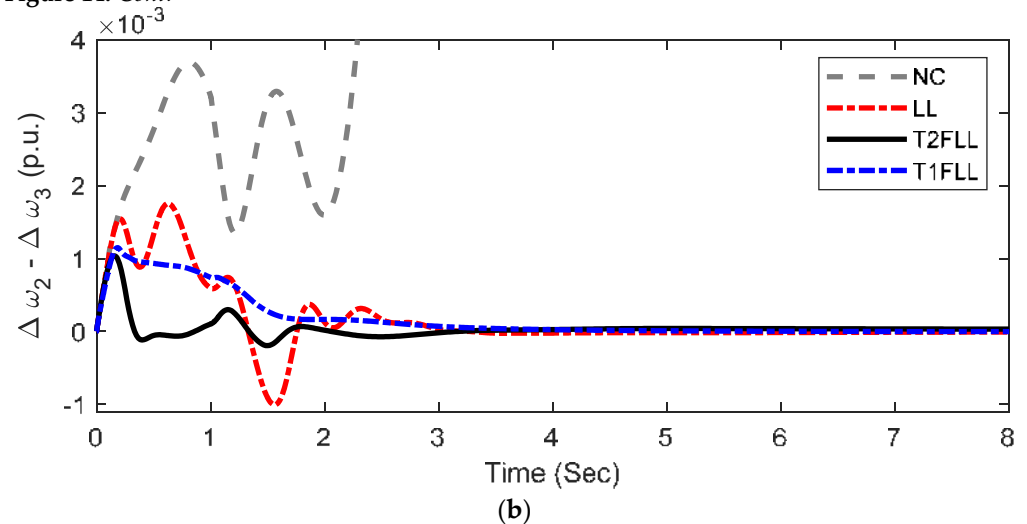


**Figure 15.** System response of MMPS system for Scenario 2: (a) local mode; (b) inter-area mode. (a) local mode of oscillation of MMPS system for Scenario 2. (b) Inter-area mode of oscillation of MMPS system for Scenario 2.

### 5.2.3. Scenario 3: Small Disturbance Condition

To simulate the small disturbance condition, the voltage reference of M1 is increased by 5% for 12 cycles, and the responses are revealed in Figure 16a,b. It is obvious from Figure 16 that both the LL and T2FLL controllers maintain stability and T2FLL is superior to the T1FLL and LL controller, providing significantly more damping to all modes. For better illustration, objective function values for MMPS for the above scenarios are presented in Table 7. It can be noticed from Table 7 that fewer  $J$  values are attained with T2FLL for all the scenarios compared to T1FLL and LL controllers.

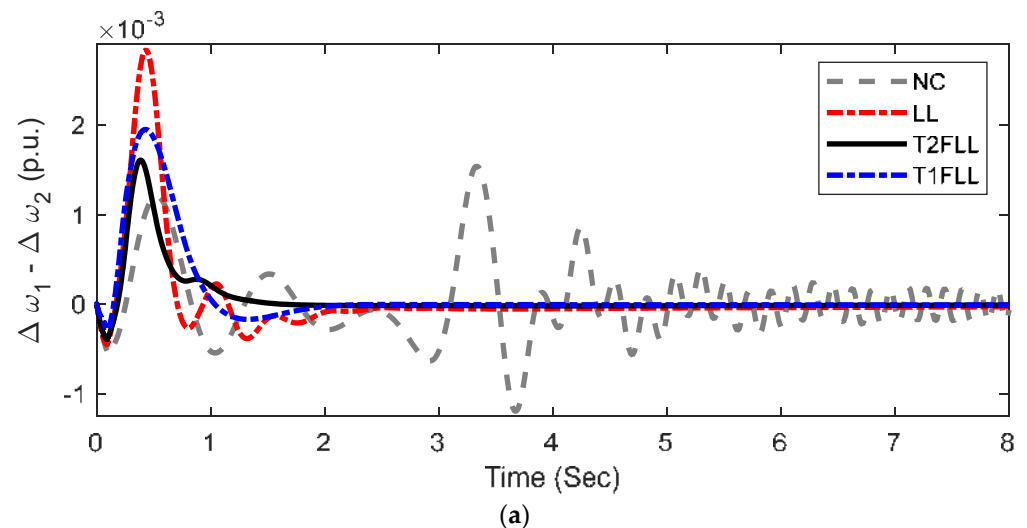
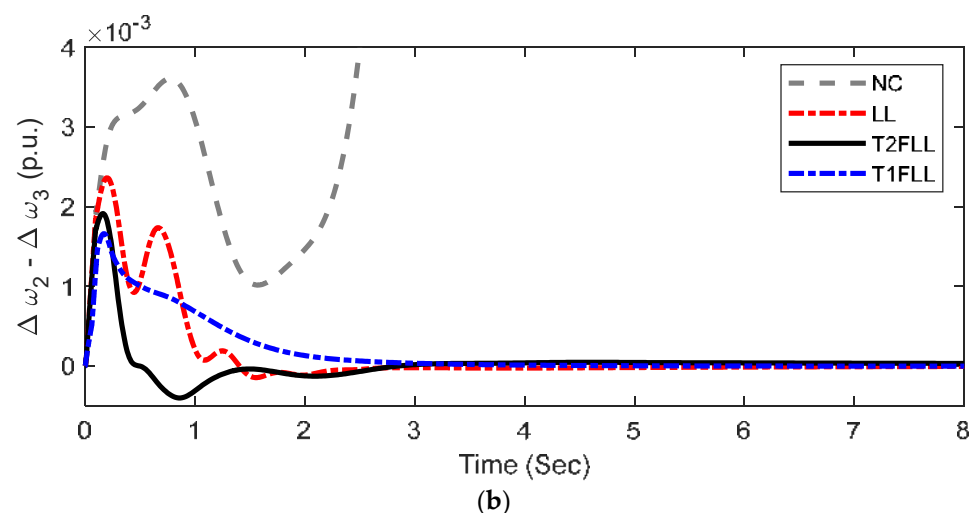


Figure 16. Cont.



**Figure 16.** System response of MMPS system for Scenario 3: (a) local mode; (b) inter-area mode. (a) Local mode of oscillation of MMPS system for Scenario 3. (b) Inter-area mode of oscillation of MMPS system for Scenario 3.

**Table 7.** Objective function value comparison under various scenario for MMPS.

Scenario/Controller	Scenario 1 ( $\times 10^{-3}$ )	Scenario 2 ( $\times 10^{-3}$ )	Scenario 3 ( $\times 10^{-3}$ )
NC	20,806.0798	21,201.1951	21,040.6094
LL	14.5224	12.8586	17.4648
T1FLL	12.6361	11.8245	13.8912
T2FLL	9.9952	10.6961	10.5976

## 6. Conclusions

In this present work, type-2 fuzzy lead-lag (T2FLL)-structured SSSC and PSS damping controller are suggested for stability improvement of power systems. The controllers are coordinated and designed using a hybrid adaptive DE-PS (hADE-PS) technique.

Initially, a SMIB system with a lead-lag controller is considered, and the dominance of hADE-PS as related to DE, PSO, and GA is demonstrated. It is noticed that for the SMIB system with LL controller, the percentage reduction in ITAE value with hADE-PS related to GA, PSO, and DE methods are 23.56%, 17.53%, and 10.53%, respectively.

Next, the T2FLL controller is designed and it is found that there is a reduction of 10.13% and 15.08% in  $J$  value with T2FLL related to the T1FLL and LL controller, respectively. Various disturbance scenarios such as large disturbance, small disturbance, and changed loading/fault location are simulated and it is seen that improved damping is attained with T2FLL related to the T1FLL and LL controllers for all the scenarios.

The study is also applied to an MMPS and it is noticed that though all controllers maintain synchronism under various scenarios, an improved system response is attained with T2FLL compared to others. For all the scenarios, the proposed T2FLL is superior to the T1FLL and LL controller, providing significantly more damping to all modes.

Extension of the presented control scheme to a large scale power system is the future scope of this work. Additionally, new hybrid optimization techniques could be implemented for improving the system performance further.

**Author Contributions:** Conceptualization, P.K. and S.P.; data curation, P.K.; formal analysis, P.K., S.P. and A.Y.A.; funding acquisition, H.A., A.Y.A. and S.S.M.G.; investigation, P.K., S.P., A.Y.A. and S.S.M.G.; methodology, P.K.; project administration, H.A., A.Y.A. and S.S.M.G.; resources, S.P. and S.S.M.G.; software, S.P.; supervision, S.P. and A.Y.A.; validation, P.K., S.P., H.A. and A.Y.A.; visualization, P.K., S.P. and S.S.M.G.; writing—original draft, P.K.; writing—review and editing,

S.P., H.A., A.Y.A. and S.S.M.G. All authors have read and agreed to the published version of the manuscript.

**Funding:** This work was supported by Taif University Researchers Supporting Project number (TURSP-2020/34), Taif University, Taif, Saudi Arabia.

**Institutional Review Board Statement:** Not applicable.

**Informed Consent Statement:** Not applicable.

**Data Availability Statement:** Not applicable.

**Acknowledgments:** The authors appreciate Taif University Researchers Supporting Project number (TURSP-2020/34), Taif University, Taif, Saudi Arabia for supporting this work.

**Conflicts of Interest:** The authors declare no conflict of interest.

## Appendix A

### SMIB Parameters

**Generator:** Nominal power ( $S_B$ ), voltage ( $V_B$ ) and frequency ( $f$ ): 2100 MVA, 13.8 kV, 60 Hz  
Parameters: Stator resistance ( $R_S$ ):  $2.8544 \times 10^{-3}$ , Reactances:  $X_d = 1.305$ ,  $X_q = 0.474$ ,  $X'_d = 0.296$ ,  $X'_q = 0.243$ ,  $X''_d = 0.252$ ,  $X''_q = 0.18$ ,  $T_d = 1.01$ s,  $T'_d = 0.053$ s,  $T''_{q0} = 0.1$ s.

Inertia constant ( $H$ ) and pole pairs ( $p$ ): 3.7 s and 32

#### Excitation System:

Gains ( $K_A$ ) and time constant ( $T_A$ ) of regulator: 200 and 0.001 s

Gains ( $K_e$ ) and time constant ( $T_e$ ) of exciter: 1 and 0 s

Gains ( $K_f$ ) and time constant ( $T_f$ ) of damping filter: 0.001 and 0.1 s

Low-pass filter time constant ( $T_{LP}$ ): = 0.02 s,

Transient gain reduction ( $T_b, T_c$ ): 0

Regulator output limits ( $E_{fmax}/E_{fmin}$ ) and gain ( $K_p$ ): 7/0 and 0

#### Hydraulic Turbine and Governor:

Gains ( $K_a$ ) and time constant ( $T_a$ ) of Servo-motor: 3.33 and 0.07 s

Limits of Gate opening ( $G_{max}/G_{min}$  and  $V_{gmax}/V_{gmin}$ ): 0.97518/0.01 and 0.01/−0.1 pu/s

Permanent droop ( $R_p$ ): = 0.05, Hydraulic turbine:  $\beta = 0$ ,  $T_w = 2.67$  sPID regulator ( $K_p, K_i, K_d, T_d$ ): 1.163, 0.105, 0, 0.01 s

#### Transformer:

Nominal power ( $S_B$ ) = 2100 MVA, Winding connection:  $D_1/Y_g$ , Primary and secondary voltage ( $V_1/V_2$ ): 13.8/500 kV, Resistance ( $R$ ): 0.002 p.u., Inductances ( $L_1/L_2$ ): 0/0.12, Magnetization resistance ( $R_m$ ) and reactance ( $L_m$ ): 500  $\Omega$

#### Transmission line:

Line length and no. of phases: 300 km, 3-Ph, Resistance per unit length ( $R_1/R_0$ ): 0.02546/0.3864  $\Omega$ / km, Inductance per unit length ( $L_1/L_0$ ):  $0.9337 \times 10^{-3}$  /  $4.1264 \times 10^{-3}$  H/km, Capacitance per unit length ( $C_1/C_0$ ):  $12.74 \times 10^{-9}$  /  $7.751 \times 10^{-9}$  F/ km

#### Load at Bus2:

250 MW (500 kV, 60 Hz, Y-grounded)

### Kundur's 4-machine 2-area system

textbfGenerator: Nominal powers: 900 MVA each, Nominal voltages: 20 kV each, frequency ( $f$ ): 60 Hz

Parameters: Stator resistance ( $R_S$ ):  $2.8544 \times 10^{-3}$ , Reactances:  $X_d = 1.8$ ,  $X_q = 1.7$ ,  $X'_d = 0.3$ ,  $X'_q = 0.55$ ,  $X''_d = 0.25$ ,  $X''_q = 0.25$ ,  $T'_{do} = 8$  s,  $T''_{do} = 0.03$  s,  $T'_{q0} = 0.4$  s,  $T''_{q0} = 0.05$  s, Stator resistance ( $R_S$ ): 0.0025  $\Omega$

**Excitation Systems:** Each same as SMIB system

#### Steam Turbine and Governor:

Regulator Gain ( $K_p$ ) = 1, Permanent droop ( $R_p$ ): 0.05, Dead zone ( $D_z$ ): 0, Speed relay and servo-motor time constants ( $T_{sr}/T_{sm}$ ): 0.001/0.15 s, Limits of gate opening ( $G_{max}/G_{min}$  and  $V_{gmax}/V_{gmin}$ ): 4.496/0 and 0.01/−0.1 pu/s, time constants of steam turbine ( $T_1, T_2, T_3, T_4$ ): 0, 10, 3.3, 0.5 s, Turbine torque fractions ( $F_1, F_2, F_3, F_4$ ): 0, 0.36, 0.36, 0.28

#### Transformers:

Nominal powers = 900 MVA each, Winding connection:  $D_1/Y_g$ , Primary and secondary voltage ( $V_1/V_2$ ): 20/230 kV, Resistance ( $R$ ):  $1 \times 10^{-6}$ , Inductances ( $L_1/L_2$ ): 0/0.15, Magnetization resistance ( $R_m$ ) and reactance ( $L_m$ ): 500  $\Omega$

#### Transmission lines:

*Distributed parameter line* (110 km line sections) and *PI section line* (10 km and 25 km line sections)

Line length and n0. of phases: 300 km, 3-Ph, Resistance per unit length ( $R_1/R_0$ ): 0.0529/1.61  $\Omega$ /km, Inductance per unit length ( $L_1/L_0$ ): 0.0014/0.0061 H/km, Capacitance per unit length ( $C_1/C_0$ ):  $8.7749 \times 10^{-9}$ /5.2489  $\times 10^{-9}$  F/km

#### Loads:

**Area-1:** Active power: 967 MW, Inductive reactive power: 100 MVAR, Capacitive reactive power: 387 MVAR

**Area-2:** Active power: 1767 MW, Inductive reactive power: 100 MVAR, Capacitive reactive power: 537 MVAR

#### SSSC Data

Converter rating = 100 MVA, Nominal voltage: 500 kV, Frequency ( $f$ ): 60 Hz, Maximum rate of change in reference voltage = 3 pu/s, Converter impedances ( $R/L$ ): 0.00533/0.16, DC link voltage: 40 kV, DC link equivalent capacitance:  $375 \times 10^{-6}$  F, Injected Voltage regulator gains ( $K_P/K_I$ ): 0.00375/0.1875, DC Voltage regulator gains ( $K_P/K_I$ ):  $0.1 \times 10^{-3}/20 \times 10^{-3}$ , Limits of injected voltage:  $\pm 0.2$

## References

1. Yu, Y.N. *Electric Power System Dynamics*; Academic Press: New York, NY, USA, 1983.
2. Sauer, P.W.; Pai, M.A. *Power System Dynamics and Stability*; Prentice-Hall: Englewood Cliffs, NJ, USA, 1998.
3. Gyugyi, L.; Schauder, C.D.; Sen, K.K. Static synchronous series compensator: A solid-state approach to the series compensation of transmission lines. *IEEE Trans. Power Deliv.* **1997**, *12*, 406–417. [CrossRef]
4. Panda, S.; Ardil, C. Robust coordinated design of multiple power system stabilizers using particle swarm optimization technique. *Int. J. Electr. Syst. Sci. Eng.* **2008**, *1*, 41–48.
5. Panda, S.; Padhy, N.P. Robust power system stabilizer design using particle swarm optimization technique. *Int. J. Electr. Syst. Sci. Eng.* **2008**, *1*, 2260–2267.
6. Abdel-Magid, Y.L.; Abido, M.A.; Al-Baiyat, S.; Mantawy, A.H. Simultaneous stabilization of multi-machine stabilizers via genetic algorithm. *IEEE Trans. Power Syst.* **1999**, *14*, 1428–1439. [CrossRef]
7. Sebba, K.; Boudour, M. Optimal locations and tuning of robust power system stabilizer using genetic algorithms. *Int. J. Electr. Power Syst. Res.* **2009**, *79*, 406–416. [CrossRef]
8. Paul, S.; Roy, P.K. Oppositional cuckoo optimization algorithm for optimal tuning of power system stabilizers. In Proceedings of the Michael Faraday IET International Summit, Kolkata, India, 12–13 September 2015; pp. 176–181.
9. Abido, M.A. Robust design of multi-machine power system stabilizers using simulated annealing. *IEEE Trans Energy Convers.* **2000**, *15*, 297–304. [CrossRef]
10. Abdel-Magid, Y.L.; Abido, M.A.; Mantawy, A.H. Robust tuning of power system stabilizers in multi-machine power systems. *IEEE Trans Power Syst.* **2000**, *15*, 735–740. [CrossRef]
11. Mishra, S.; Tripathy, M.; Nanda, J. Multi-machine power system stabilizer design by rule based bacteria foraging. *Int. J. Electr. Power Syst. Res.* **2007**, *77*, 1595–1607. [CrossRef]
12. Jolfaei, M.G.; Sharaf, A.M.; Shariatmadar, S.M.; Poudeh, M.B. A hybrid PSS-SSSC GA-stabilization scheme for damping power system small signal oscillations. *Electr. Power Energy Syst.* **2016**, *75*, 337–344. [CrossRef]
13. Falehi, A.D.; Rostami, M.; Doroudi, A.; Ashrafi, A. Optimization and coordination of SVC-based supplementary controllers and PSSs to improve power system stability using a genetic algorithm. *Turk. J. Elec. Eng. Comp. Sci.* **2012**, *20*, 639–654.
14. Khadanga, R.K.; Satapathy, J.K. Time delay approach for PSS and SSSC based coordinated controller design using hybrid PSO-GSA algorithm. *Int. J. Electr. Power Energy Syst.* **2015**, *71*, 262–273. [CrossRef]
15. Tripathy, M.; Mishra, S. Coordinated tuning of PSS and TCSC to improve hopf bifurcation margin in multi-machine power system by a modified bacteria foraging algorithm. *Int. J. Electr. Power Energy Syst.* **2015**, *66*, 97–109. [CrossRef]
16. Ali, E.S.; Abd-Elazim, S.M. Coordinated design of PSSs and TCSC via bacterial swarm optimization algorithm in a multi-machine power system. *Int. J. Electr. Power Energy Syst.* **2012**, *36*, 84–92. [CrossRef]
17. Shayeghi, H.; Safari, A.; Shayanfar, H.A. PSS and TCSC damping controller coordinated design using PSO in multi-machine power system. *Energy Convers Manag.* **2010**, *51*, 2930–2937. [CrossRef]
18. Dadfar, S.; Wakil, K.; Khaksar, M.; Rezvani, A.; Miveh, M.R.; Gandomkar, M. Enhanced control strategies for a hybrid battery/photovoltaic system using FGS-PID in grid-connected mode. *Int. J. Hydrog. Energy* **2019**, *44*, 14642–14660. [CrossRef]
19. Khaksar, M.; Rezvani, A.; Moradi, M.H. Simulation of novel hybrid method to improve dynamic responses with PSS and UPFC by fuzzy logic controller. *Neural Comput. Appl.* **2018**, *29*, 837–853. [CrossRef]



20. Rezvani, A.; Esmaeily, A.; Etaati, H.; Mohammadinodoushan, M. Intelligent hybrid power generation system using new hybrid fuzzy-neural for photovoltaic system and RBFNSM for wind turbine in the grid connected mode. *Front. Energy* **2019**, *13*, 131–148. [CrossRef]
21. Ray, P.K.; Paital, S.R.; Mohanty, A.; Eddy, F.Y.S.; Krishnan, A.; Gooi, H.B.; Amaratunga, G.A.J. A hybrid firefly-swarm optimized fractional order interval type-2 fuzzy PID-PSS for transient stability improvement. *IEEE Trans. Ind. Appl.* **2019**, *55*, 6486–6498. [CrossRef]
22. Elazim, S.M.A.; Ali, E.S. Optimal power system stabilizers design via cuckoo search algorithm. *Int. J. Electr. Power Energy Syst.* **2016**, *75*, 99–107. [CrossRef]
23. Ali, E.S. Optimization of power system stabilizers using BAT search algorithm. *Int. J. Electr. Power Energy Syst.* **2014**, *61*, 683–690. [CrossRef]
24. Elazim, S.M.A.; Ali, E.S. Optimal location of STATCOM in multimachine power system for increasing loadability by cuckoo search algorithm. *Int. J. Electr. Power Energy Syst.* **2016**, *80*, 240–251. [CrossRef]
25. Abdelaziz, A.Y.; Ali, E.S. Static VAR compensator damping controller design based on flower pollination algorithm for a multi-machine power system. *Electr. Power Compon. Syst.* **2015**, *43*, 1268–1277. [CrossRef]
26. Abd Elazim, S.M.; Ali, E.S. Optimal SSSC design for damping power systems oscillations via gravitational search algorithm. *Int. J. Electr. Power Energy Syst.* **2016**, *82*, 161–168. [CrossRef]
27. Elazim, S.M.A.; Ali, E.S. Coordinated design of PSSs and SVC via bacteria foraging optimization algorithm in a multi-machine power system. *Int. J. Electr. Power Energy Syst.* **2012**, *41*, 44–53. [CrossRef]
28. Storn, R.; Price, K. Differential evolution—A simple and efficient adaptive scheme for global optimization over continuous spaces. *J. Glob. Optim.* **1997**, *11*, 341–359. [CrossRef]
29. Sahu, R.K.; Gorripotu, T.S.; Panda, S. A hybrid DE-PS algorithm for load frequency control under deregulated power system with UPFC and RFB. *Ain Shams Eng. J.* **2015**, *6*, 893–911. [CrossRef]
30. Mohanty, P.; Sahu, R.K.; Panda, S. A novel hybrid many optimizing liaisons gravitational search algorithm approach for AGC of power systems. *Autom. J. Control. Meas. Electron. Comput. Commun.* **2020**, *61*, 158–178. [CrossRef]
31. Khadanga, R.K.; Kumar, A.; Panda, S. A hybrid shuffled frog-leaping and pattern search algorithm for load frequency controller design of a two-area system composing of PV grid and thermal generator. *Int. J. Numer. Modeling* **2020**, *33*, e2694. [CrossRef]
32. Rout, B.D.; Pati, B.B.; Panda, S. A hybrid modified differential evolution-pattern search approach for SSSC based damping controller design under communication constraints. *Int. J. Syst. Assur. Eng. Manag.* **2018**, *9*, 962–971. [CrossRef]
33. Zhang, J.; Sanderson, A.C. JADE: Adaptive differential evolution with optional external archive. *IEEE Trans. Evol. Comput.* **2009**, *13*, 945–958. [CrossRef]
34. Wang, Y.; Cai, Z.; Zhang, Q. Differential evolution with composite trial vector generation strategies and control parameters. *IEEE Trans. Evol. Comput.* **2011**, *15*, 55–66. [CrossRef]
35. Tanabe, R.; Fukunaga, A. Success-history based parameter adaptation for differential evolution. In Proceedings of the IEEE CEC, Cancun, Mexico, 20–23 June 2013; pp. 71–78.
36. Mohanty, P.; Sahu, R.K.; Sahoo, D.K.; Panda, S. Adaptive differential evolution and pattern search tuned fractional order fuzzy PID for frequency control of power systems. *Int. J. Model. Simul.* **2022**, *42*, 240–254. [CrossRef]
37. SimPowerSystems 4.3 User's Guide. Available online: <http://www.mathworks.com/products/simpower/> (accessed on 3 March 2022).
38. Kundur, P. *Power System Stability and Control*; McGraw-Hill: Irvine, CA, USA, 1994; p. 813, Example 12.6.
39. Chintu, J.M.; Sahu, R.K.; Panda, S. Adaptive differential evolution tuned hybrid fuzzy PD-PI controller for automatic generation control of power systems. *Int. J. Ambient. Energy* **2019**, *17*, 1–6. [CrossRef]
40. Liu, J.; Lampinen, J. A fuzzy adaptive differential evolution algorithm. *Soft Comput.* **2005**, *9*, 448–462. [CrossRef]
41. Gamperle, R.; Muller, S.D.; Koumoutsakos, P. A parameter study for differential evolution. *Adv. Intell. Syst. Fuzzy Syst. Evol. Comput.* **2002**, *10*, 293–298.
42. Ali, M.M.; Torn, A. Population set-based global optimization algorithms: Some modifications and numerical studies. *Comput. Oper. Res.* **2004**, *31*, 1703–1725. [CrossRef]
43. Biswas, P.P.; Suganthan, P.N.; Wu, G.; Amaratunga, G.A. Parameter estimation of solar cells using datasheet information with the application of an adaptive differential evolution algorithm. *Renew. Energy* **2019**, *132*, 425–438. [CrossRef]
44. Panda, S.; Padhy, N.P. Comparison of Particle Swarm Optimization and Genetic Algorithm for FACTS-based Controller Design. *Appl. Soft Comput.* **2008**, *8*, 1418–1427. [CrossRef]
45. Mohanty, B.; Panda, S.; Hota, P.K. Controller parameters tuning of differential evolution algorithm and its application to load frequency control of multi-source power system. *Int. J. Electr. Power Energy Syst.* **2014**, *54*, 77–85. [CrossRef]
46. Swain, S.C.; Panda, S.; Mahapatra, S. A multi-criteria optimization technique for SSSC based power oscillation damping controller design. *Ain Shams Eng. J.* **2016**, *7*, 553–565. [CrossRef]
47. Panda, S.; Yegireddy, N. Multi-input single output SSSC based damping controller design by a hybrid improved differential evolution-pattern search approach. *ISA Trans.* **2015**, *58*, 173–185. [CrossRef] [PubMed]
48. Panda, S.; Kiran, S.H.; Dash, S.S.; Subramani, C. A PD-type multi input single output SSSC damping controller design employing hybrid improved differential evolution-pattern search approach. *Appl. Soft Comput.* **2015**, *32*, 532–543. [CrossRef]

## Article

# Development of Operation Strategy for Battery Energy Storage System into Hybrid AC Microgrids

Felipe Ramos <sup>1</sup>, Aline Pinheiro <sup>2</sup>, Rafaela Nascimento <sup>1</sup>, Washington de Araujo Silva Junior <sup>1</sup>, Mohamed A. Mohamed <sup>3,\*</sup>, Andres Annuk <sup>4</sup> and Manoel H. N. Marinho <sup>1,\*</sup>

<sup>1</sup> Polytechnic School of Pernambuco, University of Pernambuco (UPE), Recife 50720-001, PE, Brazil

<sup>2</sup> Energy Storage Division, Edson Mororó Moura Institute of Technology (ITEMM), Recife 51020-280, PE, Brazil

<sup>3</sup> Department of Electrical Engineering, Faculty of Engineering, Minia University, Minia 61519, Egypt

<sup>4</sup> Institute of Forestry and Engineering, Estonian University of Life Sciences, 51006 Tartu, Estonia

\* Correspondence: dr.mohamed.abdelaziz@mu.edu.eg (M.A.M.); marinho75@poli.br (M.H.N.M.)

**Abstract:** With continuous technological advances, increasing competitiveness of renewable sources, and concerns about the environmental impacts of the energy matrix, the use of hybrid microgrids has been promoted. These generation microsystems, historically composed basically of fossil fuels as the main source, have experienced an energy revolution with the introduction of renewable and intermittent sources. However, with the introduction of these uncontrollable sources, the technical challenges to system stability, low diesel consumption, and security of supply increase. The main objective of this work is to develop an operation and control strategy for energy storage systems intended for application in hybrid microgrids with AC coupling. Throughout the work, a bibliographic review of the existing applications is carried out, as well as a proposal for modification and combination to create a new control strategy. This strategy, based on optimized indirect control of diesel generators, seeks to increase generation efficiency, reduce working time, and increase the introduction of renewable sources in the system. As a result, there is a significant reduction in diesel consumption, a decrease in the power output variance of the diesel generation system, and an increase in the average operating power, which ensures effective control of hybrid plants.

**Keywords:** renewable Resources; microgrids; generation efficiency; energy management; battery energy storage system

**Citation:** Ramos, F.; Pinheiro, A.; Nascimento, R.; de Araujo Silva Junior, W.; Mohamed, M.A.; Annuk, A.; Marinho, M.H.N. Development of Operation Strategy for Battery Energy Storage System into Hybrid AC Microgrids. *Sustainability* **2022**, *14*, 13765. <https://doi.org/10.3390/su142113765>

Academic Editor: Alberto-Jesus Perea-Moreno

Received: 11 September 2022

Accepted: 11 October 2022

Published: 24 October 2022



**Copyright:** © 2022 by the authors. Licensee MDPI, Basel, Switzerland. This article is an open access article distributed under the terms and conditions of the Creative Commons Attribution (CC BY) license (<https://creativecommons.org/licenses/by/4.0/>).

## 1. Introduction

The hybridization of microgrids integrated with photovoltaic generation systems plays an important role as an alternative to reduce diesel consumption and consequent reduction in operating costs [1]. In this context, energy storage systems act as enablers and enhancers of this integration, since several instability factors can be found when only the photovoltaic system is introduced, mainly due to the lack of control of the solar source [2].

This work has as its main proposal the development of a parameterizable operating strategy for energy storage systems applied to hybrid microgrids.

The textual body of the work is organized into five sections, and in Section 2—Theoretical Reference, the definition of microgrids, their main components, and classifications are presented. Furthermore, a detailed description of the Battery Energy Storage System (BESS) applications associated with the scope of this work or the use in isolated systems is provided. In Section 3—Methodology, the applications that make up the proposed control strategy, the changes made to the traditional methodology, and the way in which they are combined are described. At the end, the proposed system for validation is detailed, as well as the analysis methods. In Section 4—Results, the effectiveness of the operation is demonstrated through the analysis of the main energy parameters of the microgrid. In addition, a sensitivity analysis regarding the integration of the PV array (Photovoltaic) and

BESS is performed. Finally, in Section 5—Conclusions, the results are consolidated and future work is proposed.

## 2. Theoretical Reference

### 2.1. Literature Review

In this section, a bibliographic review is carried out covering topics related to the operation of microgrids in their various configurations.

In [3], an operation strategy proposal was made that uses a day-ahead forecast model to optimize the response to demand, seeking the lowest overall cost of the operation. The proposal, which relies on the connection of the electricity grid, resulted in a sensitivity analysis indicating a microgrid composed of BESS, PV generation, and wind power, reaching lower cost levels when compared to the traditional model of single supply through the distributor.

In [4], a study was carried out based on the application of BESS and renewable energy sources for the short-term energy market, basing the operation on generation and cost forecast models. As a result, there is a cost reduction in the global operation of the system, proving the effectiveness of the proposed algorithm.

A review of the applications of hybrid energy storage systems, based on the combination of batteries and supercapacitors, was presented in [5], focusing on renewable power smoothing strategies, voltage and frequency control, lifetime and optimization, among others. Furthermore, a comparison between storage technologies based on batteries and capacitors is developed.

A comparison of operating strategies for microgrids was presented in [6]. As a base case, the traditional model of load following the electrical network is used, where load fluctuations are absorbed by the main source. Two additional strategies for controlling the supply of the network are proposed: the first is the stabilization of a constant daily supply power and the second is the stabilization of a constant annual supply power. The proposed cases presented a lower total cost of supply than the base case, although they also presented a greater waste of energy.

A comparative study of three operating strategies for microgrids was carried out in [7]: i. Load following, ii. Cycle charging, and iii. Combined dispatch. The strategy iii. operates as a combination of the two previous strategies, aiming at the best option depending on the conditions. The evaluated microgrid is composed of PV generation, Diesel generation, and BESS, based on the Homer (Hybrid Optimization of Multiple Energy Resources) software. In response, for the proposed scenario, the combined dispatch strategy is proven to be more effective, with lower CO<sub>2</sub> emissions and lower global cost of supply.

In [8], a study similar to the one discussed in [7] is presented, evaluating the operating strategies available in the Homer software, these being i. Load following, ii. Cycle charging, and iii. Combined dispatch. Additionally, studies are carried out regarding the storage technology used, with analyses for Lead-Acid, Lithium-Ion, Vanadium Flux, Supercapacitors, and Reversible Hydroelectric Batteries.

In [9], a control algorithm for supercapacitors in dynamic frequency regulation applications was developed. Based on this use, an option is presented to reduce the traditional load-sharing strategies, with sudden variations being absorbed by the storage system. The article also shows that although the supercapacitor was used as a base, other technologies can be used to perform the function.

In [10], a study of PV insertion in electrical networks was developed, applying two strategies that make it possible to increase the share of PV generation. The first strategy is based on changing the consumption profile, using variable pricing for energy depending on resource availability. The second strategy uses storage systems as sources of generation stabilization and peak absorption, allowing insertions above 50% of the total energy balance.

A case study of a microgrid composed of diesel, PV, wind, and BESS generation was presented by [11]. The strategy, based on BESS's SoC (State-of-Charge) steps, ensures that the operation of the diesel generator is minimized and at rated power, being used to

recharge the BESS at times of low renewable generation. Optimization and dimensioning studies based on the global cost of the operation are also presented.

More recently, [12] carried out a case study to complement a ship's energy generation system with fuel cells and BESS. In the proposed strategy, which uses Homer as a simulation platform, the scenario with the lowest possible CO<sub>2</sub> emission is sought, so that the ship's original energy generator is maintained. The study also shows that the result of the reduction and optimal scenario for the insertion of additional elements varies according to the load profile considered.

The literature review contributed to the consolidation of the knowledge base and an investigation of the current technological stage of the topic. Of great importance for the construction of the work methodology, this review also made it possible to identify the gaps in the current proposals for microgrid control. As described in this section, a proposal was not identified in the evaluated works that combined the applications of power smoothing applied to Load and PV, optimal dispatch of BESS to increase the efficiency of diesel generation, sharing of the rotating reserve, and use of the surplus energy generated by PV, which is the focus of this work.

## 2.2. Microgrids

Microgrids can be defined as independent generation structures composed minimally of one or more generation sources and interconnected loads. These microgrids can have in their generation matrix elements such as renewable energy sources, mainly solar and wind, storage systems, and generation based on fossil fuels. In addition to the generation and consumption components, the importance of the control and protection elements of the system is also highlighted, which guarantees the integrity and correct functioning of the integrated systems [13].

According to [13], microgrids can be classified in different ways, and the main ones can be cited: i. Generation capacity, ii. Type of installation and load, iii. Network connection and supply nature. Other classifications may consider the number of phases, voltage level, and other technical aspects.

Microgrids that work in AC (Alternate Current), DC (Direct Current), and hybrid models of work, both continuous and alternating, can also be classified according to the type of load to be supplied.

For direct current microgrids, the main highlight is the greater efficiency due to reduced energy conversion processes, in addition to facilitating the process of integrating renewable sources. On the other hand, it is important to consider that most loads used today were designed and operated only with AC supply, bringing the need for at least one DC to AC conversion system.

For DC microgrids, the main advantage is the high level of maturity of the global electricity sector on the subject since traditional electrical networks are developed in AC and there are no major complications for connection to the grid or grid conventional electrical, if necessary. However, for the system to function as desired, a robust control and operation structure is required, combined with a good management system.

In addition to the aforementioned options, there is also the possibility of integrating hybrid systems from the point of view of load supply and connection, using part of the system in direct current and part of the system in AC.

Another relevant point in the classification and design of microgrids refers directly to the control modes applied to this structure. For master-slave controls, a structure is used where only one of the generation sources represents the voltage and frequency parameters, whereas the others act as current sources, following the standards established by the main source.

With the use of Peer-to-Peer topology, the figure of the main source is not necessary, since all installed sources work in automatic load sharing mode. In this scenario, all sources are configured with an operating droop curve, where active and reactive power is automatically generated through voltage and frequency parameters at the connection point.

For this classification scenario there are also hybrid models, where part of the sources work in Slave mode and part of the sources in Peer-to-Peer mode. For the system analyzed in this work, the term hybrid refers to the fact that different sources of generation and control are considered, unlike traditional microgrids that are based on only one generation source.

### 2.3. BESS Applications

According to [14], it is possible to differentiate applications of energy storage systems between five main categories as shown in Figure 1, so that applications related to use in microgrids are directly or indirectly related to one of these proposed items.

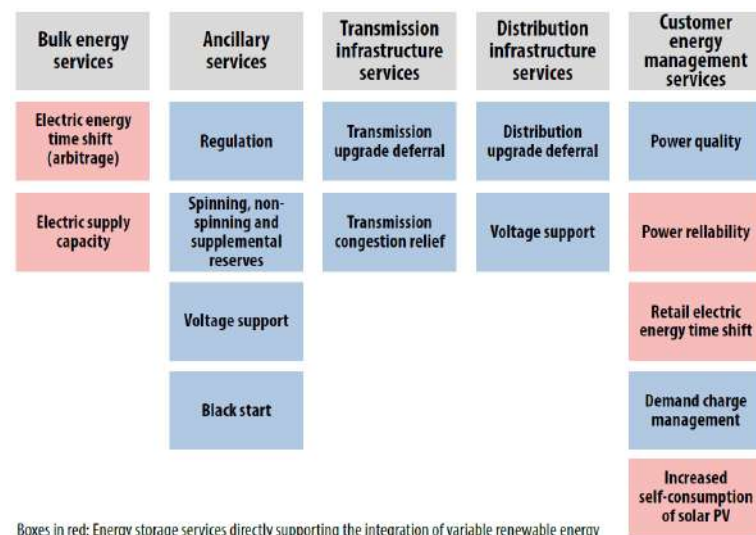


**Figure 1.** BESS Applications.

#### 2.3.1. Energy Arbitrage

This application, used both in isolated and grid-connected systems, consists of storing energy in periods of high generation and use in periods of low resource availability and/or high consumption. With this strategy it is possible to store energy in periods when energy is cheaper and use it in periods when production is more expensive [15]. In addition, especially in microgrids with high insertion of renewable sources, energy waste is common due to the imbalance between generation and consumption, thus, storage plays a fundamental role in the technical and economic feasibility of these systems [16].

Illustrating this behavior, Figure 2 shows a typical operation of a storage system connected to the electricity grid, charging between 01:00 and 10:00 and discharging between 17:00 and 20:00.

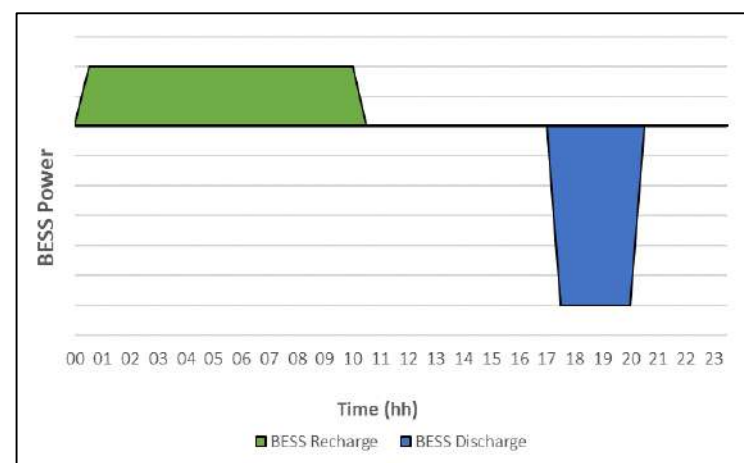


**Figure 2.** A typical operation of a storage system connected to the electricity grid.

In this work, a method of performing the energy displacement function is proposed, based on intelligent discharge control. This method is detailed in Section 4.

### 2.3.2. Increase Electric Supply Capacity

In order to meet consumption peaks, this functionality is characterized by the complementation of the storage system to power not available in the generation system, using the stored energy to supply the excess part of consumption [17]. This application makes it possible to install generation systems smaller than the peak consumption required for service, especially in cases where these do not occur continuously and frequently [18].

### 2.3.3. Upgrade Deferral

This application is used in both transmission and distribution, and characterized by the inhibition or postponement of the need for investments in electrical infrastructure reinforcements.

Usually, the repowering of electrical systems occurs due to sporadic peaks in demand, lasting for a few hours. In this scenario, the investment in storage systems can be reduced when compared to the traditional method of meeting these peaks [19].

Figure 3 shows the typical operation of a storage system performing the investment postponement function.

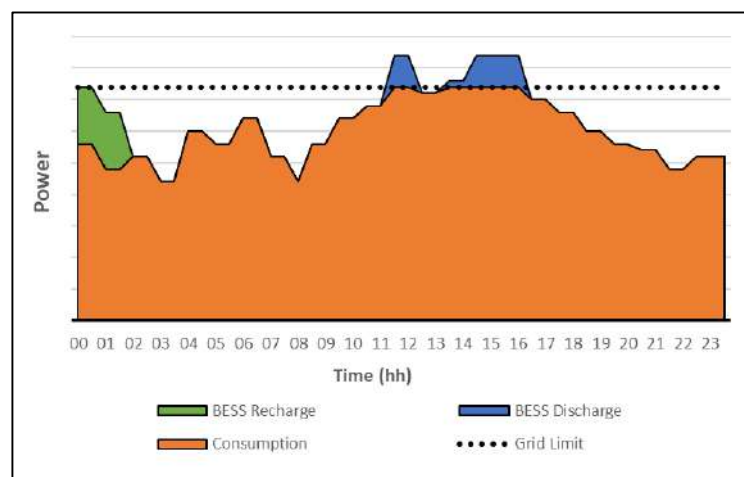


**Figure 3.** Upgrade Deferral Application.

### 2.3.4. Black Start

This function is characterized by the capacity of the storage system to restore the electrical grid after a complete system collapse, serving as a voltage and frequency source until synchronization and connection of other generation sources [20].

### 2.3.5. Load Leveling

This application, typically used in transmission and distribution systems, aims to ensure that energy consumption at a given point is always within pre-established maximum and minimum limits, increasing the predictability of energy supply [21]. If consumption is lower than the established limit, the storage system recharges; if consumption is greater than the established limit, discharge is carried out [22].

Figure 4 shows the typical operation of a storage system performing the leveling function of a hypothetical load.

In this work, a method of performing the load-leveling function is proposed, based on the combination of power smoothing algorithms. This method will be detailed in Section 4.

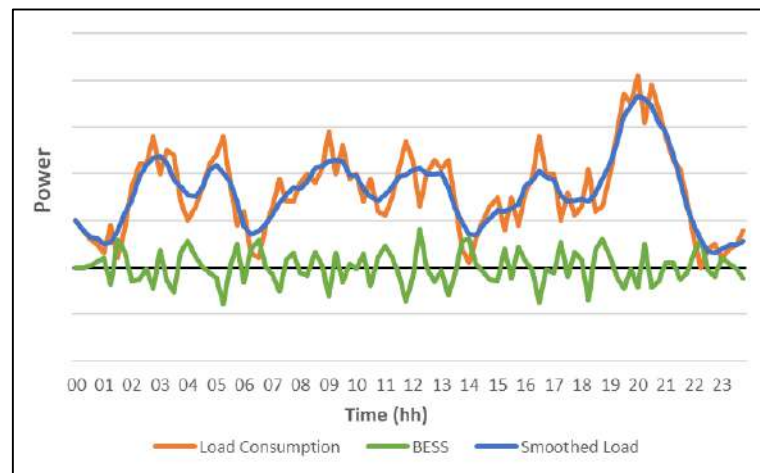


**Figure 4.** Load Leveling.

### 2.3.6. Power Smoothing

Renewable energy sources are becoming increasingly present in the world's electricity generation. For example, according to [23], photovoltaic solar energy has increased its capacity by almost nine times in 9 years, from 381.6 GW in 2010 to 3.4 TW in 2019. On the other hand, energy fluctuations caused by weather conditions bring several technical challenges related to power quality, protection, dispatch control, and reliability, reducing the possibility of massive insertion of this source [24].

An alternative to maintain the stability of the network is to smooth the output of the intermittent source with the use of energy storage systems, so that, providing or absorbing power, it stabilizes the variation in the connection point to an acceptable range [25].

Figure 5 shows the typical operation of a storage system connected to a photovoltaic system, performing power smoothing.

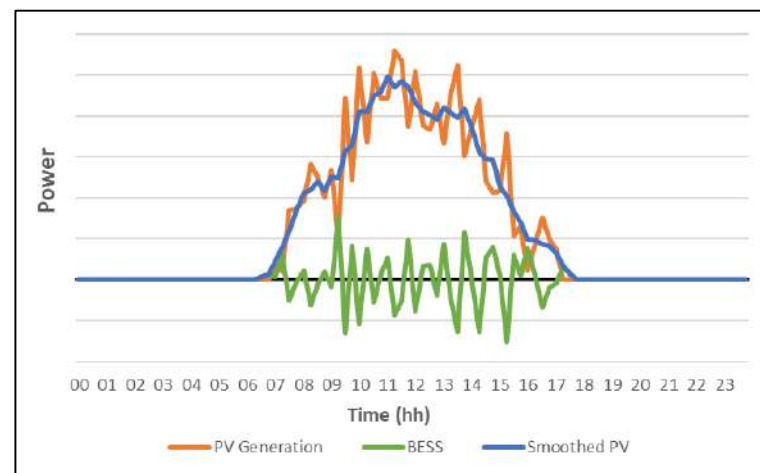


**Figure 5.** Typical operation of a storage system connected to a photovoltaic system.

The main ways of performing this control are described below:

**Moving Average:** This technique is widely used in stock analysis, smoothing out volatility and making it easier to see the price trend of a security. It can also be applied to smooth power outputs, being known for its computational simplicity. The basic operation of this algorithm is to sum the recent output power values and then divide by the number of periods in the calculation average.

The only input parameter used for this technique is the analyzed time interval, so that, regardless of the weather conditions, longer intervals will generate smoother curves. However, the greater the gap and smoothing, the greater the energy storage system and its utilization [26].



**Double Moving Average:** In order to enhance the power smoothing of the single moving average method, the double moving average applies the above technique twice, the first being on the original data and the second on the response data. Similar to the previous scenario, although this strategy produces greater smoothing, the energy and utilization of the storage system is also intensified [27].

**Exponential Moving Average:** Similar to the simple moving average algorithm, this strategy uses historical data to generate its smoothed output. However, a multiplication constant is also used, which has greater weight for more recent data.

**Moving Median:** This smoothing algorithm applies a similar concept to the simple moving average, however, using the median instead of the arithmetic average. From a statistical point of view, the moving median can reach the power trend more quickly; however, in certain scenarios, this behavior can be negative, since the algorithm can present sudden transitions.

**Ramp Rate:** Unlike previous algorithms, the ramp rate method calculates the power variation and uses the storage system only if the variation exceeds the established threshold, for example, 10% per minute. This proves attractive for most scenarios as it minimizes battery usage and sizing. The percentage change is calculated by the difference between the current output and the previous output, divided by the rated power of the plant. This variation can remain within the established limits or exceed positively or negatively [28].

In this work, a method of performing the power smoothing function based on the modification of the ramp rate control algorithm is proposed. This method will be detailed in Section 4.

### 2.3.7. Clipping Recapture

With the traditional oversizing of DC power against the AC power of photovoltaic systems, it is common for an effect known as “clipping” to occur, where the power available on the DC bus exceeds the rated power of the inverters to which the bus is connected. In this way, the output power of the system is limited, even if the photovoltaic modules have more power available for generation.

This oversizing is generally used for several technical and economic reasons, which are beyond the scope of this work; however, it is possible to direct the additional energy to the storage system and later use, aiming to maximize the gains of the generation system as a whole.

This application has a relatively simple operating logic, since whenever the DC power exceeds the PV inverter’s transformation capacity, the excess power is directed to the batteries, which are connected to the photovoltaic module’s busbars through a DC/ AC [29].

Figure 6 shows the typical operation of a storage system performing the clipping utilization function.

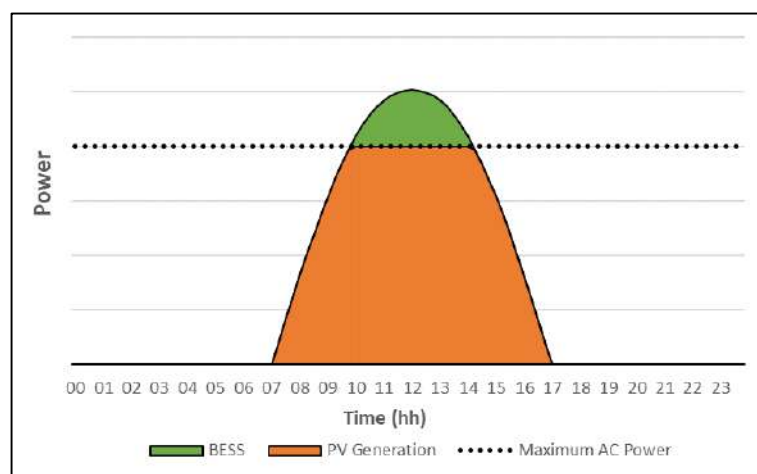


**Figure 6.** Typical operation of a storage system performing the clipping utilization function.



### 2.3.8. Capacity Reserve

The capacity reserve can be defined as energy available for use in sudden load variations or partial failures in the generation system. These reserves can be divided into a few categories, which are mainly related to the time of operation [30].

**Spinning Reserve:** Generation capacity connected to the grid with a response between seconds to a few minutes, sufficient to compensate for load increases or partial drops of generation systems. This service can be provided in a simple way by storage systems, since the response to commands sent takes place on a millisecond scale, depending on the priority of the application [31].

**Supplementary Reserve:** Generation capacity used after the entry of the rotating reserve, which may be disconnected from the network, with a response in tens of minutes [32].

In this work, a method of performing the capacity reservation function based on the load state of the storage system is proposed. This method will be detailed in Section 4.

### 2.3.9. Frequency and Voltage Regulation

Aimed at guaranteeing the stability of the network, these functions have as their main objective the guarantee of the dynamic balance of power between generation and consumption. To carry out this application, the storage system performs fast and high-power operations, discharging in situations where the frequency has values lower than those established and recharging at times when the frequency has high values. In a similar way to frequency regulation, with in voltage regulation it is possible to control the bus where the system is connected, but with the use of reactive power [33].

Figure 7 shows the typical operation of a storage system performing the frequency control function.

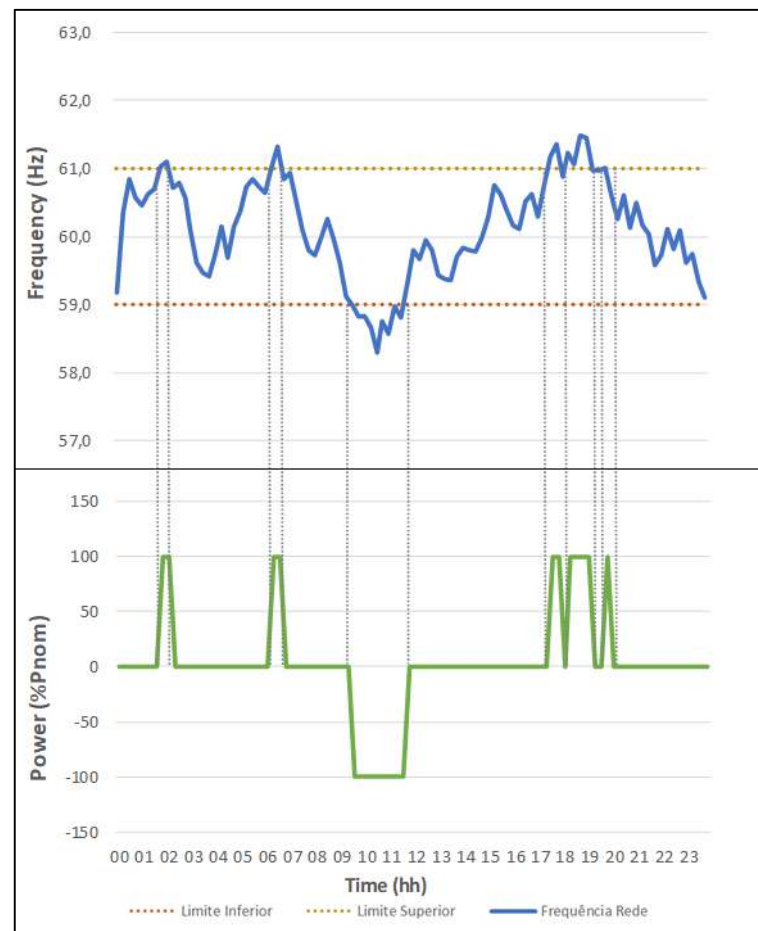


**Figure 7.** Typical operation of a storage system performing the frequency control function.

### 2.3.10. Virtual Inertia

With the massive penetration of non-rotating energy sources in electrical power systems, it is expected that part of the traditional generation systems will lose space, reducing their participation. However, traditional generation systems operate predominantly with synchronous machines, which in their working principle present mechanical inertia, hence being able to respond to frequency variations instantaneously.

This effect of substitution of generation sources causes the weakening of electrical networks, since most power generation systems based on power electronics cannot perform these functions.

An alternative to solve this problem is the use of energy storage systems operating as a voltage source, performing the virtual inertia function in parallel to the electrical grid, associated with control techniques for “damping” the system response.

The main difference between this functionality and traditional frequency regulation is in the connection/operation mode of the storage system, which directly affects the response time. For frequency regulation, the system is connected as a current source, in this way, in an event of frequency variation, it is necessary for the system to perform the measurement, process the information, and then act to correct it. For the virtual inertia function, as the system remains in voltage source mode, the response is instantaneous to frequency variations, whether positive or negative [34].

Figure 8 shows the frequency control levels for traditional electrical systems, as follows:

Mech Inertia: Mechanical inertia, provided by synchronous generators;

Inertia Emu.: Virtual inertia, provided by BESS, topic 2.3.10;

Primary Control: Frequency Regulation, topic 2.3.9;

Secondary Control: Rotating Reserve, topic 2.3.8;

Tertiary Control: Supplementary Reserve, topic 2.3.8;

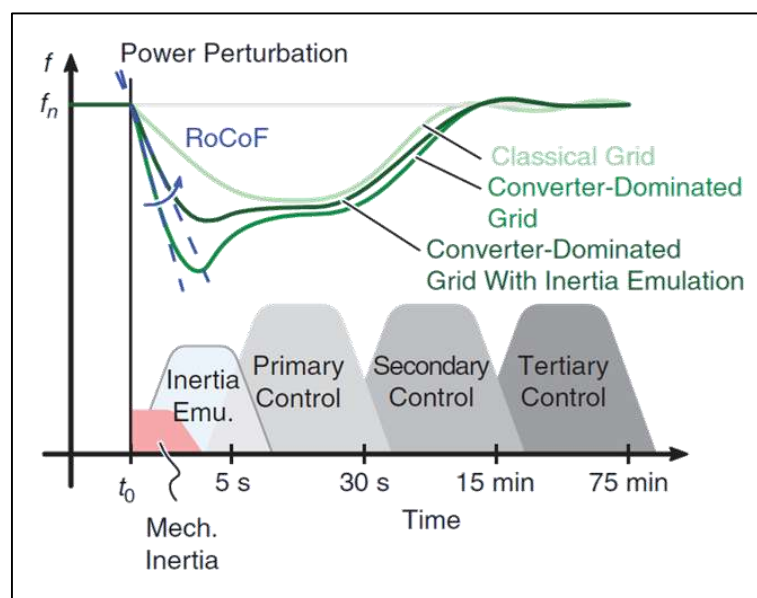


Figure 8. Energy Reserve.

### 3. Methodology

The methodology used in this work consists of the combination of several applications of storage systems aimed at microgrids, with the main objectives of enhancing the diesel economy generated by the photovoltaic system and minimizing the power variations imposed on the Diesel Genset. For the proposed study, it was considered that the Gensets always operate in load sharing mode, where all generated power is divided equally between the connected machines, respecting the minimum operating limit of the machines. The following topics describe the operating modes of each of the storage system applications.

### 3.1. Applications

#### 3.1.1. Excess Energy Recapture

In traditional isolated systems, the balance between generation and consumption is carried out through the control of the Genset's, so that load variations are compensated by an increase or decrease in the generation. However, with the application of photovoltaic systems, due to the lack of control of the main source, it is possible the occurrence of scenarios where the generation exceeds the load consumption, causing a waste of energy. This scenario intensifies as the power of the PV system increases.

Figure 9 shows the PV generation and consumption curves for a hypothetical day, highlighting the effect of surplus energy, which can be used to recharge the storage system and later use.

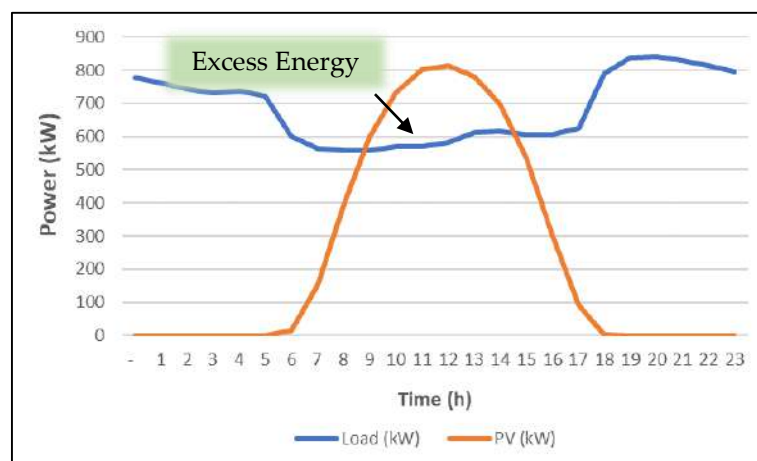


Figure 9. Microgrid with PV Generation.

Storage systems are an alternative for the use of surplus energy and subsequent use, enhancing the economy of diesel since more energy comes from a renewable source. As the PV system grows, more surplus energy is generated, bringing greater viability to the application of storage systems. Since this is the application with the highest economic return for BESS in the microgrid, priority is given to its execution over other functionalities.

In line with the strategy of prioritizing the recharge of the storage system with surplus energy, a controlled discharge is proposed in two scenarios. The first scenario occurs when more than one Genset is in operation; in this way, the calculation of the required discharge power of the storage system for the sequential shutdown of the machines is performed. In this way, based on the power and energy available in BESS, as many machines as possible are turned off, ensuring that the machines that remain on continue their operation at the optimum point of efficiency.

This strategy aligns the decrease in diesel consumption by reducing the energy demanded by the Genset's with the increase in the generation efficiency of the remaining Genset's, seeking the optimal point of operation.

For example, if three Gensets are operating at 80% of their power ( $3 \times 80\% = 240\%$ ), the power required to turn off a machine will be equal to 40% of its rated power. If the storage system has enough power and energy to shut down a machine, it will discharge the equivalent of 40% of the Genset power, causing its shutdown, keeping the two remaining machines at their optimal operating point. If the storage system has available power and energy equivalent to 140% of the Genset power, it will shut down two machines, keeping the remaining machine at its optimal operating point.

The second algorithm control scenario occurs when only one Genset is in operation. In the proposed configuration, at least one Genset must remain connected and generating, in order to guarantee the voltage and frequency of the network. Based on this, it is not possible to discharge the storage system to the point of causing the total shutdown of the Diesel generation system.

However, it is proposed to configure a target power of operation of the Genset until the storage system can perform the discharge. Ideally, this target power should not present low Genset efficiency values.

For example, if the configured target power is 75% of the rated power and the generator is operating at 100% of the rated power, the storage will discharge with a power equivalent to 25%. In another hypothetical scenario, using the same target power setting of 75%, but operating the Genset at 50% of rated power, the storage system does not perform unloading or recharging operations.

It is worth mentioning that this configured parameter is different from the minimum operating power of the Genset. The minimum operating power is an immutable value, so continuous operation below the minimum power can cause irreversible damage to the machine.

### 3.1.2. Power Smoothing of Photovoltaic Generation

As pointed out in topic 2.3.6, the power smoothing of photovoltaic generation is an important service provided by storage systems. In this work, two modifications are proposed to the commonly used methods.

In traditional microgrids, power generation is based on Gensets; in this way, since this is the main source, all load variations are absorbed by this set. Based on this, it is proposed to apply power smoothing in the sum of the load consumption data with the PV generation, creating a real smoothing scenario for the Genset's, unifying the power smoothing and load leveling applications in a single algorithm.

This modification aims to focus the application of the storage system on reducing the variations imposed on the Genset and not on the output of the PV system. As an example, if the PV system has a positive variation in generation and the load also presents an increase in consumption, this variation against the Genset can be cancelled without interference from storage, depending on the amplitude of the events. The opposite is also valid, since a drop in generation can be potentiated with an increase in consumption, generating a high-power ramp in the Genset's.

Figures 10–16 are possible to observe, for a hypothetical day: i. PV generation; ii. load consumption; iii. load consumption + PV generation; iv. smoothed load consumption + PV generation; v. load consumption + smoothed PV generation; saw. smoothed load consumption and PV generation; vii. Comparison of smoothing.

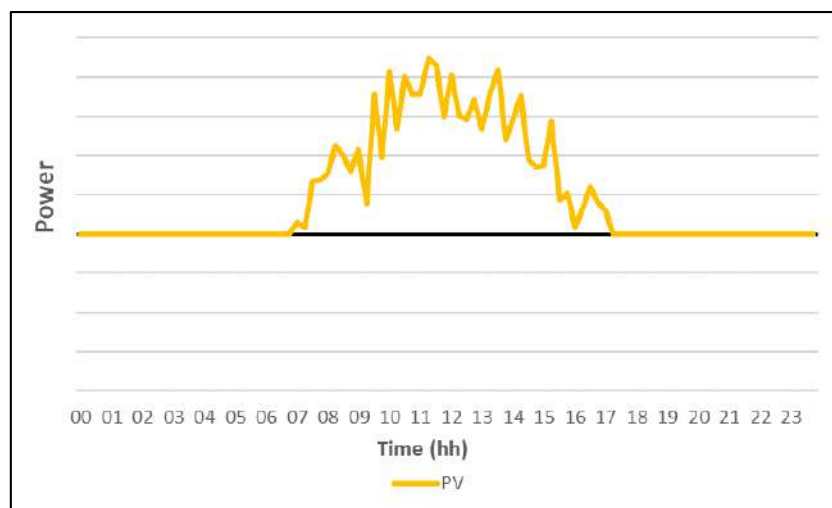


Figure 10. PV Generation.

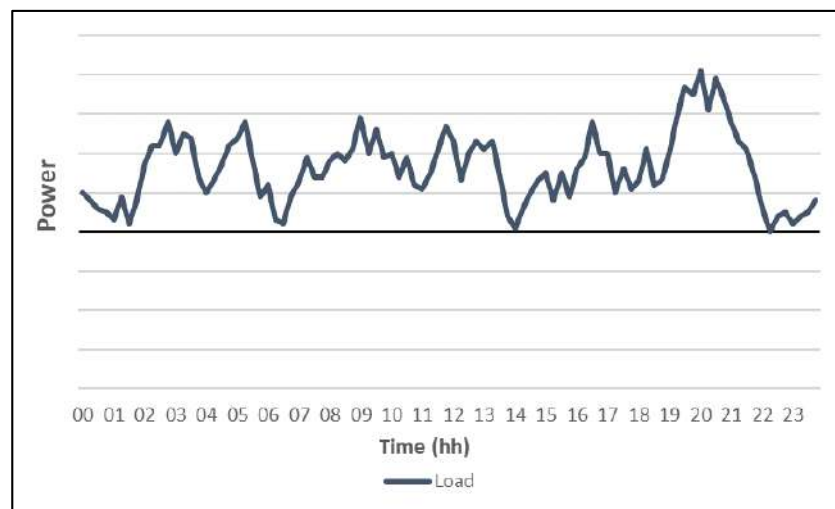


Figure 11. Load Power.

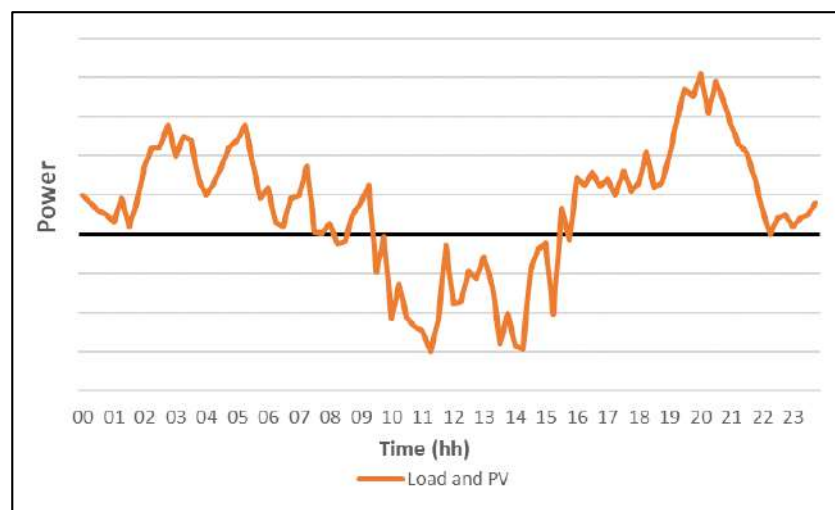


Figure 12. Load and PV Power.



Figure 13. Smoothed Load and Natural PV.

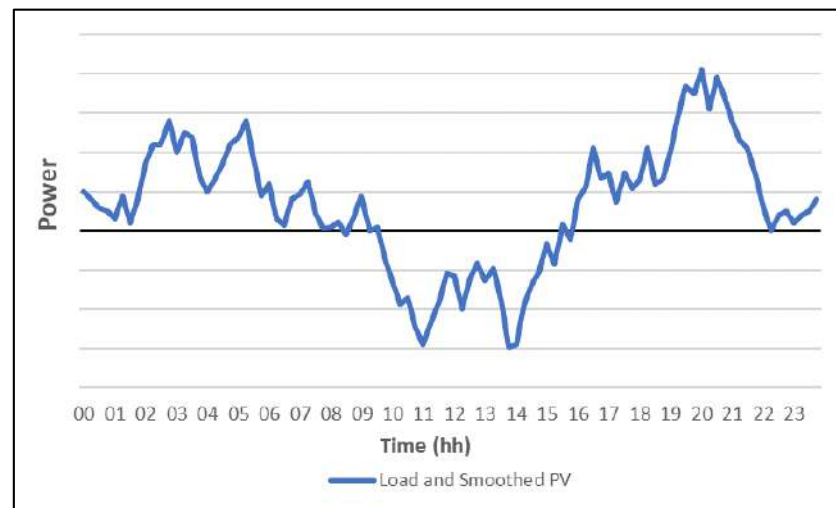


Figure 14. Natural Load and Smoothed PV.

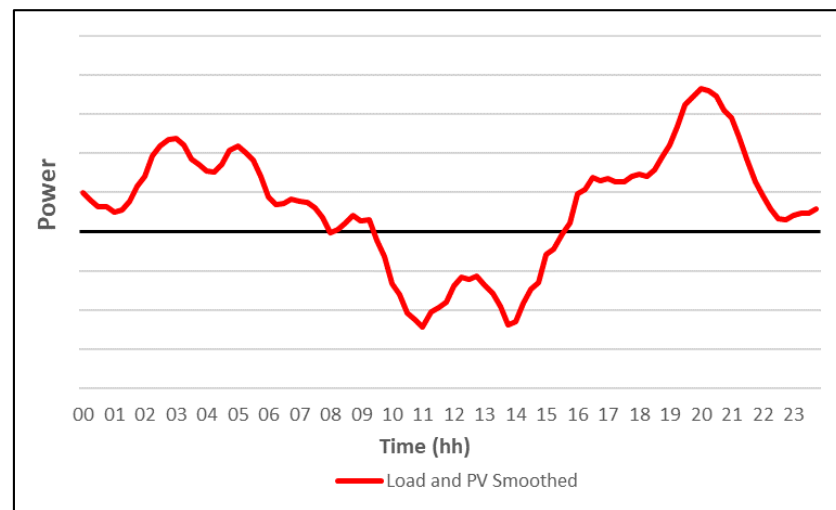


Figure 15. Load and Smoothed PV.

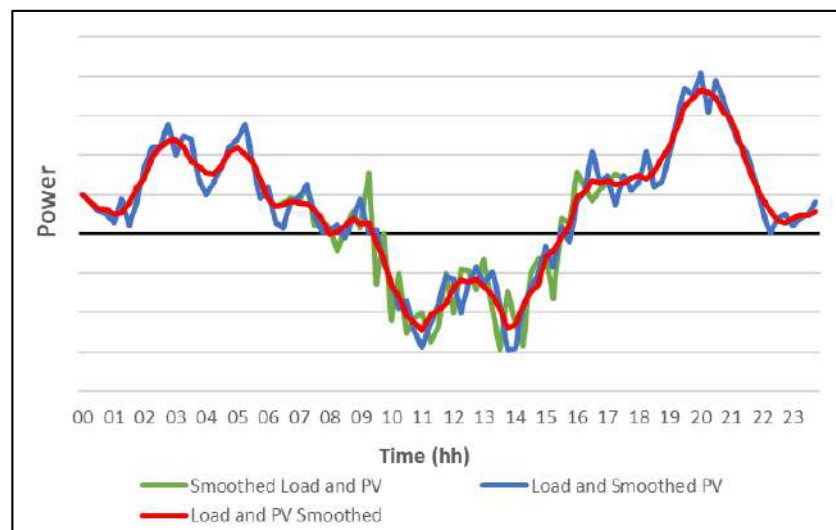


Figure 16. Smoothing Comparison.

Another point of great importance for the correct application of smoothing methods, as studied by Pinheiro, A. in [35], refers to the SoC level of the storage system. Depending on load and PV generation variations, scenarios may occur where the consumption increase always happens abruptly and the drops in soft variations, causing an imbalance in the SoC at the beginning and end of the day, since BESS would only carry out operations to smooth out the abrupt rise in consumption, without carrying out recharging operations, as the drop in consumption did not exceed the threshold rate.

Based on this, the proposed smoothing method is a modification of the ramp rate strategy, recharging or discharging the system to reach the desired SoC with energy from the Gensets, without extrapolating the designated threshold rate.

In other words, if the Load + PV set decreases consumption in relation to the previous smoothed power, enough to exceed the threshold rate, the battery bank must consume part of this power, recharging to keep the variation seen by the Genset within the admissible limit, and vice versa. However, if the variation is within the limits (that is, no limit exceeded), the BESS can perform the function of returning to the ideal SoC, recharging or discharging, without extrapolating the limit rate of change.

### 3.1.3. Capacity Reserve

As presented in 2.3.8, isolated generation systems must work with an available reserve power so that any sudden load increases or partial failures in the generation system can be met without violating the established voltage and frequency values. However, due to this reserve percentage, it is likely that the generators will start to operate outside the optimal consumption ranges, since this value is found close to the rated power of the machine.

As storage systems are capable of providing power and energy quickly, this power reserve can be shifted from the Genset's to the storage system, so that the optimal range of consumption of the Genset can be reached more easily, since there is greater use of available power.

In this work, it is proposed to perform the capacity reserve function of the generation system in the storage system. For the execution of this functionality, the power available by the storage system is verified, conflicting with the state of load and power limits of the equipment. If full power is not available, the diesel generation system returns to the execution of the functionality, which can also be shared, with part of the reserve coming from storage and part from the Genset's.

### 3.2. Proposed System

In the proposed microgrid, the PV system, five Gensets of equal power, and the storage and load system are connected to the AC bus, as illustrated in Figure 17.



**Figure 17.** AC Microgrid Topology.

**PV system:** With peak power being an input variable, the simulated PV system has an average monthly generation of 120 kWh/kWp/month and a monthly generation profile as shown in Figure 18. To perform the simulations, the generation profile was determined as equivalent to 1 kWp, so multipliers on top of the base profile were applied to reach the peak power target. Figure 18 presents the monthly generation for a simulated 100 kWp system.



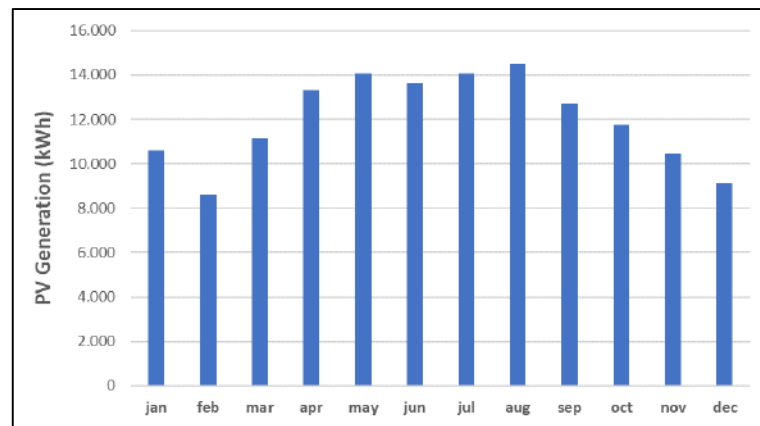


**Figure 18.** PV Monthly Generation Profile.

**Genset:** The simulated Gensets have a nominal power of 500 kW and a minimum operating power of 125 kW, with the five machines having the same configuration. The consumption curve, shown in Figure 19, is based on the data presented in [36].

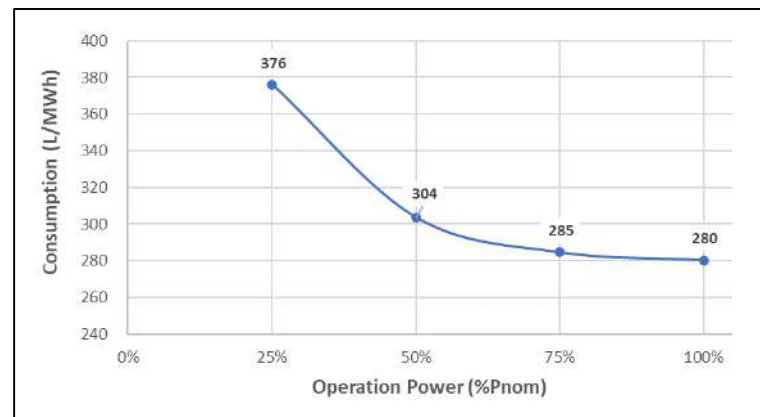


**Figure 19.** Consumption Curve of Diesel Genset.

**Storage System:** With useful energy being an input variable, the simulated storage system has a round-trip efficiency of 85% and a power/useful energy ratio of 1.

**Load:** The base load for the simulations has a peak consumption of 1.25 MW and an average consumption of 500 MWh/month. The typical consumption curve is shown in Figure 20 and the monthly consumption is shown in Figure 21.

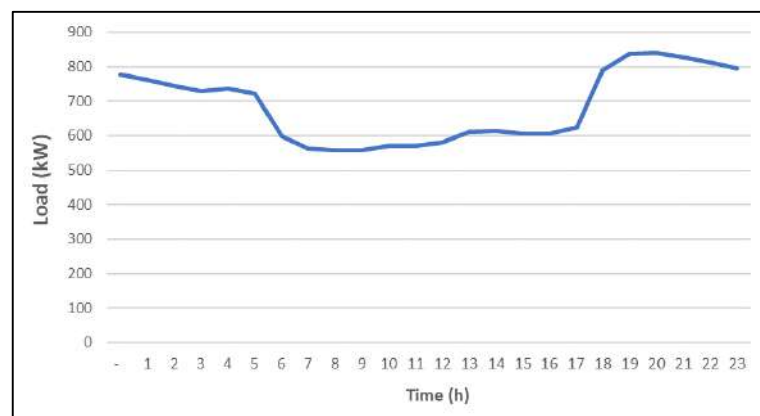


**Figure 20.** Daily Consumption Profile.



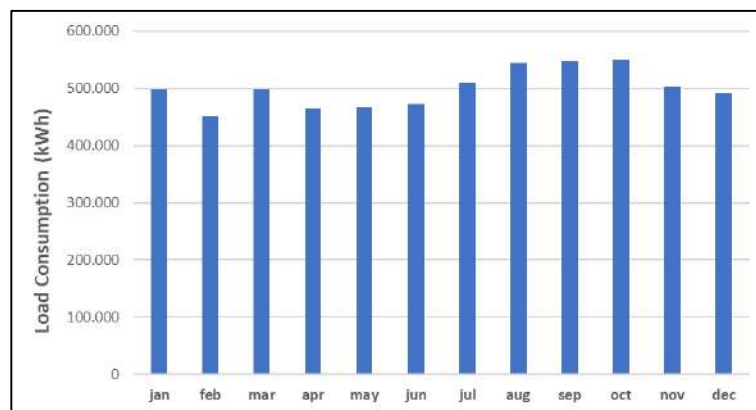


**Figure 21.** Monthly Consumption Profile.

### 3.3. Simulations and Results Analysis

The simulations were carried out for a period of one year of consumption and generation, with a time interval of 5 min between samples, thus, dynamic stability studies are not contemplated in this work.

For the amplitude of the subsystems, analyses were carried out with photovoltaic systems from 0 to 4 MWp, in steps of 500 kWp, and storage system from 0 to 6 MWh, in steps of 500 kWh.

For the analysis of results, the microgrids operation indicators were standardized, as follows:

1. Diesel consumption (L);
2. Surplus Energy (kWh);
3. Energy Recharged by BESS (kWh);
4. PV generation (kWh);
5. PV share in the energy matrix (%);
6. Hours of Operation of Gensets (h);
7. Average operating power of Gensets (kW);
8. Percentage of Gensets power variation within the established limits (%);
9. Variation in the average power of the Gensets;
10. Distribution of power variation bands for Gensets.

## 4. Results

### 4.1. Energy Balance

In this section, the energy balance of the microgrid will be analyzed, presenting the effectiveness of the implementation of the hybrid system to reduce diesel consumption, increase the PV share, energy recharged by BESS, and the sensitivity analysis with the variation of these components.

Seeking to simplify the understanding of the behavior of the microgrid and the results achieved by the operation algorithm, Figures 22–24 show the standard operation data for scenarios of low, medium, and high penetration of renewables.

In the scenario of low penetration of renewables (Figure 22), it is possible to observe a decrease in the operating power of the Genset in relation to the consumption of the load during the period of higher PV generation, followed also by a slight reduction, where the discharge of the BESS is found. This reduction in operating power is due to PV participation in the generation matrix and storage as an element for absorbing excess energy.

In this scenario, it is possible to point out that even if the PV generation does not exceed the consumption of the load, there is surplus energy in the microgrid, since the minimum generation to be exported by the Gensets is 125 kW.

In the scenario of medium penetration of renewables (Figure 23), it is possible to observe that the PV system has greater participation in the microgrid, with more surplus energy being

generated. In the same way, BESS recharges and discharges more expressively, extending the time in which the generator operates with less power than the load consumption.

For this result, it is possible to observe that close to 11:00 am, BESS decreases the recharge power, even if there is excess energy in the microgrid. This happens because the state of charge has reached the maximum value and there is no more storage capacity, causing this excess energy to be wasted.

In the scenario of high penetration of renewables (Figure 24), the surplus energy due to high generation during the day is even more evident. The PV overtakes the load during almost the entire generation period and is followed by a controlled discharge of the storage system, causing the generator to operate at close to its minimum power throughout the entire period.

Similar to the previous analysis, around 11:00 a.m. the charging power of BESS decreases, since charging is complete and there is no space for storage.

As the main parameter to be evaluated in economic analyses, since it corresponds to the component with the highest operating cost in a microgrid, diesel consumption is presented in Figure 25. The operation analysis is performed for systems PV from 0 to 4 MWp, in steps of 500 kWp and BESS from 0 to 6 MWh, in steps of 500 kWh.

At points of lower PV insertion (0 and 500 kWp), it is noted that the change in the size of the storage system does not present significant differences in diesel consumption. This is mainly due to the low surplus energy generated in these scenarios, the main source of BESS recharge. As the PV system grows, the more effective the storage system is, as there is more surplus energy available for recharging.

As an analysis of the operating trends, it is highlighted that the increase in the PV system presents greater effectiveness for the relative reduction in diesel consumption in the first steps (0 to 1 MWp). This is because most of the energy generated in these scenarios is used by the microgrid. With the increase in the PV system, it is possible to observe a stabilization trend in the reduction in diesel consumption, so that this stabilization behavior is observed earlier in scenarios with lower insertion of BESS.

As a complement to the PV trend analysis, it is noteworthy that the first step of inserting storage (0 to 500 kWh) presents a greater percentage reduction in diesel consumption, since the power smoothing and capacity reservation services pass to be performed.

In addition, with the increase in BESS, it is possible to notice that in the final stages (5.5 MWh to 6 MWh) the reduction in diesel losses percentage effectiveness, also reaching a stabilization trend. This behavior is mainly due to the high energy stored and the need to keep at least one generator in operation to guarantee the voltage and frequency reference, even at minimum power.

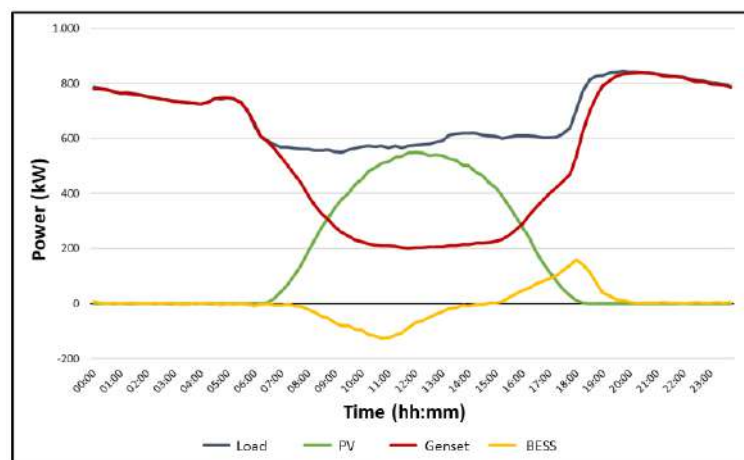


**Figure 22.** Average Operation–Low Renewables Penetration Rate (1 MWp–0.5 MWh).

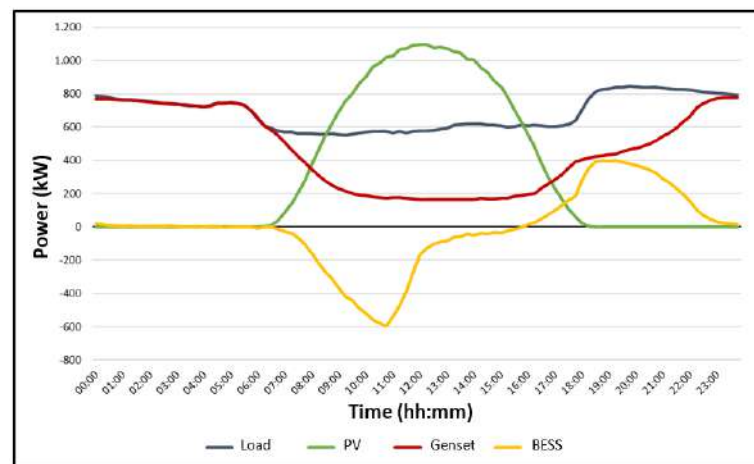


Figure 23. Average Operation–Medium Renewables Penetration Rate (2 MWp–2 MWh).

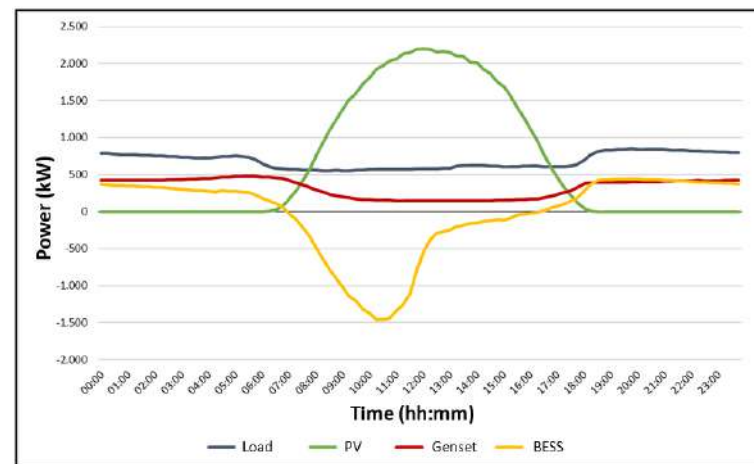


Figure 24. Average Operation–High Renewables Penetration Rate (4 MWp–6 MWh).

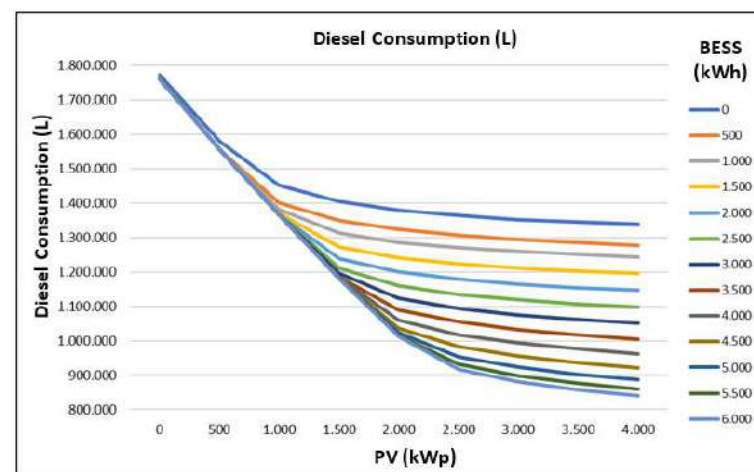
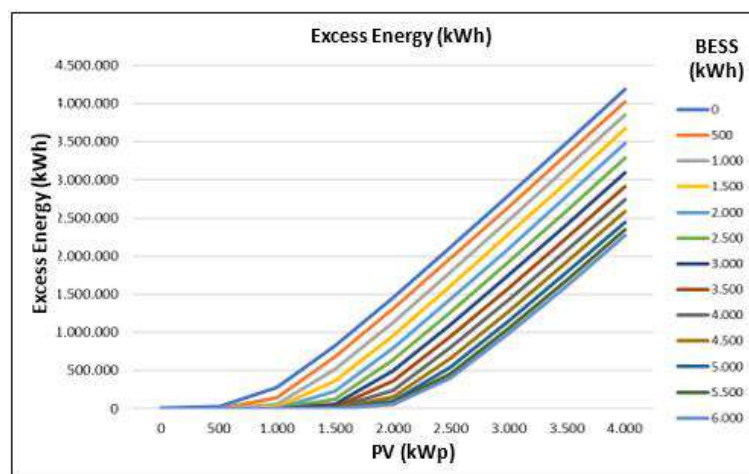


Figure 25. Diesel Consumption vs. PV and BESS insertion.

Complementary to the analyses carried out for diesel consumption, Figure 26 shows the surplus energy of the microgrid with the increase in PVS (Photovoltaic System) and BESS. For the lower PV insertion scenarios (0 to 500 kWp) there is no surplus energy, since the load consumption remains above the PV generation + Genset minimum generation. However, it is noted that the increase in PVS is accompanied by an increase in excess energy, even if minimized with the insertion of BESS.

The trend of constant increase in excess energy, even with the insertion of larger BESS is noticeable, explained by the need to keep at least one Genset in operation, even at minimum power.



**Figure 26.** Excess Energy vs. PV and BESS insertion.

For the recharged energy of the BESS (Figure 27), it is noted that the stabilization of the parameter is reached earlier for smaller storage capacities. Similar to previous analyses, this occurs due to the limitation of BESS recharge to absorb excess energy from the plant. This analysis becomes important, mainly for economic aspects, as it details the real need for storage capacity through BESS recharge.

Taking the 1 MWp PVS as an example, it is possible to infer that from the point of view of energy use, there is no considerable difference between using a 2 MWh or 6 MWh BESS, since the energy recharged by both systems is close. In this scenario, using a higher capacity system would bring an extra cost to the system, which could lead to the economic unfeasibility of the investment.

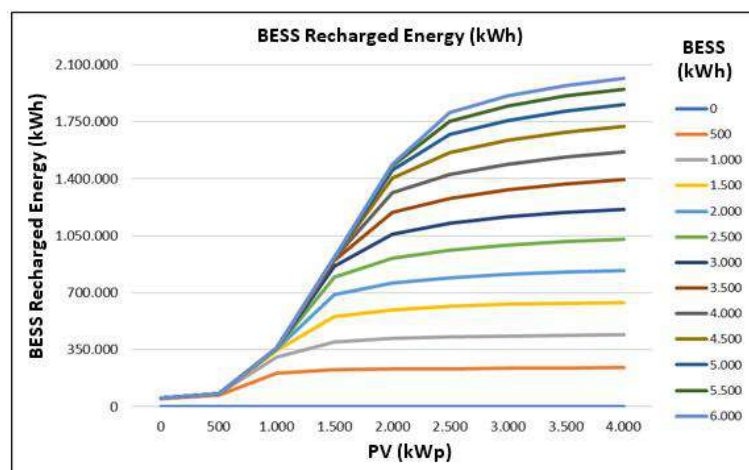


**Figure 27.** BESS Recharged Energy vs. PV and BESS Integration.

Adding to the analysis of the energy balance of the microgrid, Figure 28 shows the PV participation in meeting the load in view of the increase in the generation and storage system. Additionally, the percentage of PV generation was inserted in relation to the total consumption of the load, in order to illustrate the low use of generated energy for larger systems.

With the low penetration of PVS, it is clear that the PV share follows the percentage generation compared to consumption, as there is low surplus energy in these scenarios. As the PV insertion increases, the greater the dispersion between generation and use, even with the increase in BESS, and a trend towards stabilization of participation is noted.

As already pointed out in previous analyses, this stabilization takes place far from the point of 100% renewable penetration due to the need to guarantee the operation of at least one Genset. It is important to emphasize that different load profiles will bring different results regarding the penetration of renewables in the system, being the analysis of varied loads outside the scope of this work.

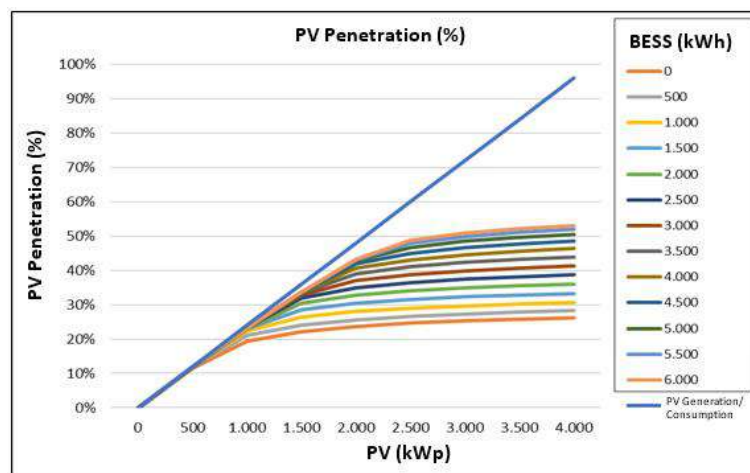


**Figure 28.** Renewable Penetration vs. PV and BESS Integration.

#### 4.2. Capacity Reserve

One of the functions developed for the operation algorithm refers to the capacity reservation of the microgrid. In this proposal, the reserve power is transferred to BESS, if available. This feature aims to reduce operating time and increase the average working power of the Genset's.

To exemplify the proposed strategy, considering a scenario with exclusive generation by Genset's and 30% of the capacity reserve, for a load of 500 kW, a minimum available power of 650 kW will be required. As the generator simulated for this microgrid has a maximum power of 500 kW, two generators would be needed working in parallel. If this functionality is performed by another system, this load could be serviced with only one generator connected.

In the scenario where the reserve function is not performed by the Genset, the operation is based on one generator, with a working power of 500 kW, compared to two generators with a working power of 250 kW. Note, for this example, that performing the capacity reserve function reduces the operating time by half and the operating power remains at the optimal point, bringing better efficiency in the generated L/kWh ratio and lower maintenance costs, since the machine spends less time in operation.

Figure 29 shows the graph with the two extremes of the BESS analyzes (0.5 MWh and 6 MWh). For the system with a capacity of 0.5 MWh, it is possible to achieve a reduction of approximately 900 h of operation for smaller PVSs (0.5 to 1 MWp) and 1500 h for the PVS of 4 MWp.

For the system with a capacity of 6 MWh, the same reduction is achieved for scenarios with lower penetration of renewables and a reduction of approximately 1000 h considering PVS of 6 MWp.

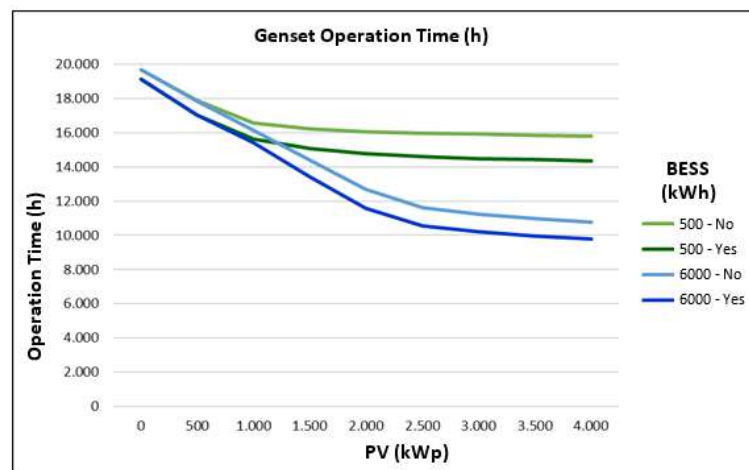


Figure 29. Diesel Genset Operating Hours vs. Capacity Reserve (500 kWh e 6000 kWh).

As a consequence of the reduction in the reserve percentage of the Genset's, an increase in the average operating power of the machines is observed. Figure 30 shows the average power data for the 500 kWh BESS. Of note is an average power increase of 15 kW for scenarios with lower PV penetration and 28 kW for the scenario with higher penetration.

Figure 31 shows the average power data for the 6 MWh BESS. The same reduction of 15 kW for smaller PVSs and 41 kW for the scenario of higher penetration stands out.

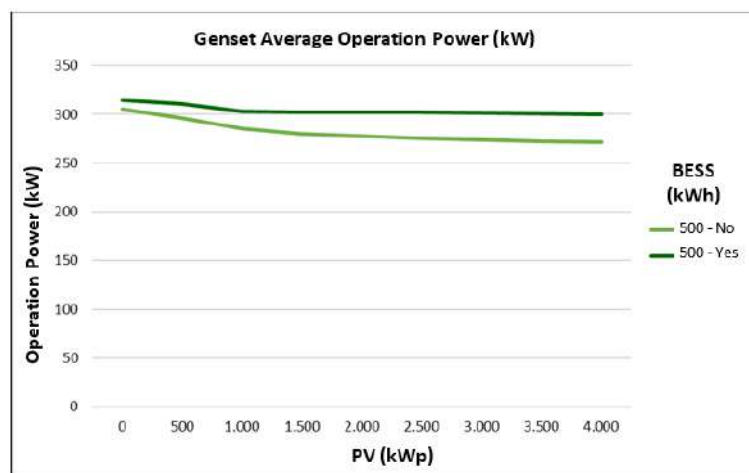


Figure 30. Average Diesel Genset Operating Power vs. Capacity Reserve (500 kWh).

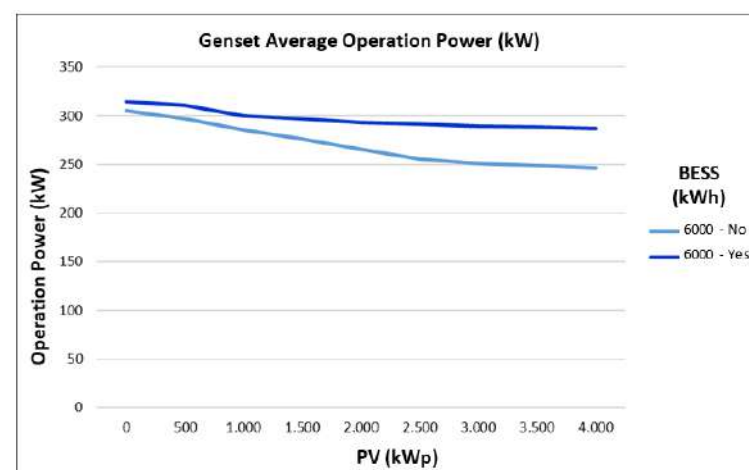


Figure 31. Average Diesel Genset Operating Power vs. Capacity Reserve (6000 kWh).



#### 4.3. Power Smoothing

The power smoothing functionality has a main objective to limit the variation imposed on the Genset, which is caused by the load or PVS. This variation minimization seeks to increase the voltage and frequency stability of the network (parameters not analyzed in this work) and minimize the chance of damage to the Genset's due to the inertia found in the motors, which contrast with abrupt load variations.

In short, when executing the functionality, BESS analyzes the working power of the Genset in the previous instant and controls the maximum variation in  $\pm 1\%$ /minute. It should be noted that this parameter can be configured according to the needs of the Gensets used.

Figure 32 shows the power variation data within the limits of  $\pm 1\%$ /min for a BESS of 500 kWh. It is possible to notice that, without the execution of the functionality, the limits present a high rate of violation, remaining below 80% for low penetration of renewables (0.5 to 1.5 MWp) and close to 83% for higher penetrations.

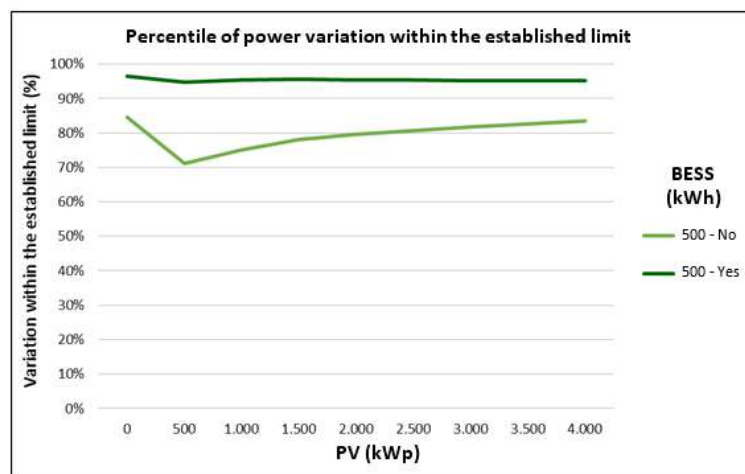


**Figure 32.** Power Variation of the Diesel Genset within the Established Limit (500 kWh).

The increase in data with a variation rate within the limits for larger PVSs is basically due to the generation limitation at times when the generation exceeds the load consumption. As illustrated in Figures 23 and 24, in high-generation scenarios, the Genset output is kept fixed at the minimum power, making the observed variation null. With the functionality running, all scenarios are kept above 95%, proving the effectiveness of the proposed solution even for low storage capacity.

Figure 33 shows the power variation data within the limits of  $\pm 1\%$ /min for a BESS of 6 MWh. In a similar way to the behavior of the lower capacity system, the effectiveness of the functionality stands out, guaranteeing 95% of the variation within the limit established for low PV penetration (0.5 MWp) and above 98% for medium and large systems (2 to 4 MWp).

Without functionality running, data within limits remains below 80% for low penetration of renewables (0.5 to 1.0 MWp) and increases up to 94% as PVS increases. As explained in the previous analysis, the increase in the percentage of data within the established variation rate is due to the limitation of PV generation to guarantee the minimum operating power of the Genset.

As a consequence of BESS operation, keeping the power variation within the established limit of  $\pm 1\%$ /min, it is also possible to observe a considerable reduction in the average power variation, in kW/min. Figure 34 shows the power variation data, in kW/min, for the 500 kWh BESS, with and without the power smoothing function. For systems with low penetration of renewables it is possible to observe a reduction of approximately 20% of the average variation (10.4 kW to 8.4 kW). For the highest PV insertion point (4 MWp) a reduction of approximately 29% of the average variation is achieved (10.1 kW to 7.2 kW).

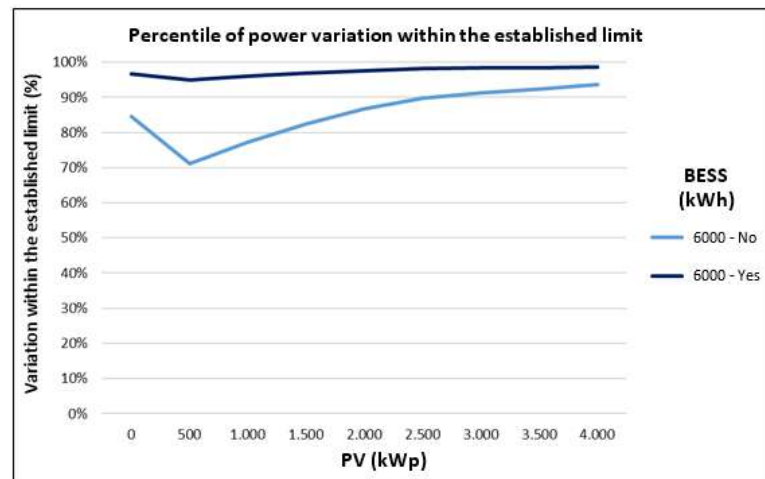


Figure 33. Power Variation of the Diesel Genset within the Established Limit (6000 kWh).

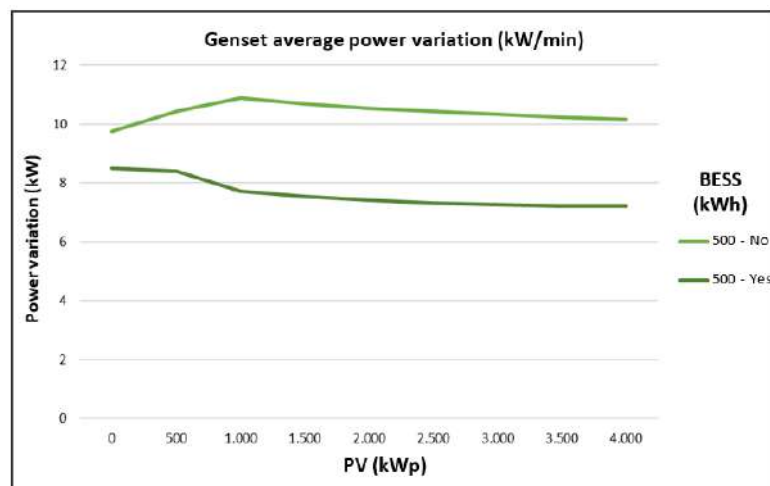


Figure 34. Average Power Variation of Diesel Genset vs. PV Power Smoothing (500 kWh).

For the analysis of the system with a BESS of 6 MWh, shown in Figure 35, it is possible to observe a reduction of the same 20% in low PV insertion (10.4 kW to 8.4 kW) and of 22% for higher insertions (4.3 kW to 3.3 kW). Additionally, noteworthy is the natural reduction in the average power variation for scenarios with greater PV insertion, since, due to the phenomenon presented in the previous analyses, the larger the PV + BESS set, the longer the generator remains at minimum operating power, or with the output power controlled by the action of BESS, according to the strategy of using surplus energy and optimized discharge, presented in Figure 34.

Figure 36 shows the power variation distribution for the simulation performed, 2 MWp–500 kWh. This representation illustrates the scenario with and without the application of the power smoothing strategy, where BESS performs the variation limitation if it has a modulus greater than 1%. As seen from this scenario, it is possible to detect that without the application of the smoothing strategy, there are variations that violate these limits.

It is also noted from Figure 36 that all data with a population outside the allowed variation zone of  $-1\%$  to  $1\%$  had a reduction in their occurrence, due to the application of the smoothing strategy.



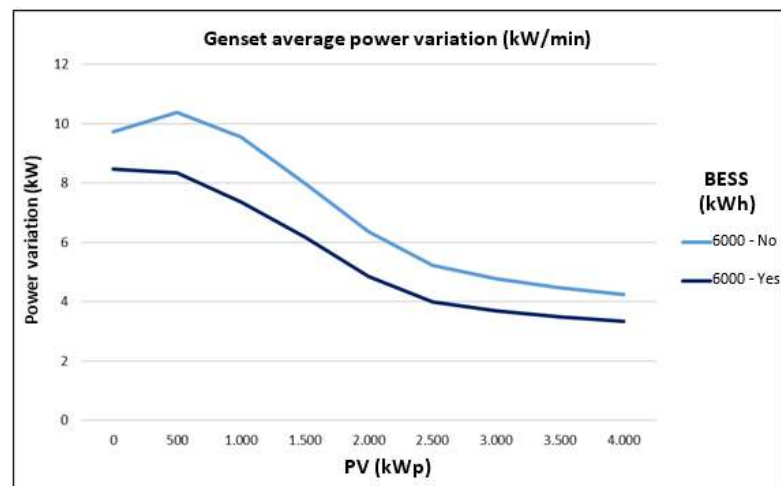


Figure 35. Average Power Variation of Diesel Genset vs. PV Power Smoothing (6000 kWh).

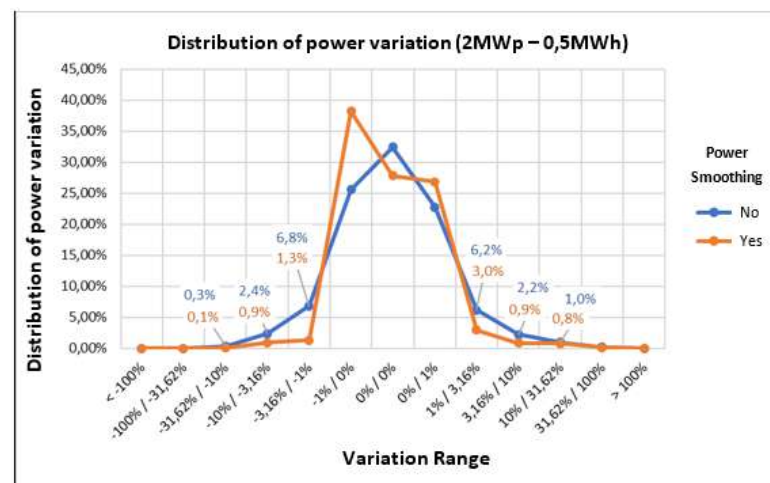


Figure 36. Distribution of Power Variation of Diesel Genset (2 MWp–500 kWh).

## 5. Conclusions

Throughout this work, in which the control strategy for microgrids was developed and applied, it was possible to verify the effectiveness of the proposal with reductions in diesel consumption with values greater than 50%, reduction in Genset operating time by up to 50%, increase in the average operating power, and guarantee of power variation within the limits with the confidence of up to 99%, all results being variable according to the level of PV + BESS penetration. The proposed strategy contributes with a new perspective of BESS applications in microgrids, enabling the realization of simultaneous and combined functionalities, such as intelligent discharge control, Genset power smoothing, and sharing of the rotating reserve. The proposed study was limited to the construction and demonstration of the effectiveness of the strategy for applications in microgrids with AC coupling, with the guarantee of at least one generator working as a voltage and frequency reference source. For future work, a detailed economic analysis of each of the components and of the complete microgrid is suggested, in order to evaluate the combination of PVS, BESS, and Genset that best relates to the technical and economic benefits, being able to use sensitivity matrices for different estimates of the cost of components, diesel, and maintenance.

**Author Contributions:** Conceptualization, F.R., A.P., R.N., W.d.A.S.J., M.A.M. and M.H.N.M.; data curation, F.R., W.d.A.S.J., M.A.M. and M.H.N.M.; formal analysis, R.N. and M.H.N.M.; investigation, F.R., A.P., W.d.A.S.J., M.A.M., A.A. and M.H.N.M.; methodology, R.N., M.A.M. and M.H.N.M.; resources, A.P., R.N. and W.d.A.S.J.; software, F.R. and M.H.N.M.; supervision, M.A.M. and M.H.N.M.; validation, A.A.; visualization, A.P. and A.A.; writing—original draft, F.R., A.P., R.N., W.d.A.S.J., M.A.M. and M.H.N.M.; writing—review and editing, F.R., A.P., R.N., W.d.A.S.J., M.A.M., A.A. and M.H.N.M. All authors have read and agreed to the published version of the manuscript.

**Funding:** This research received no external funding.

**Institutional Review Board Statement:** Not applicable.

**Informed Consent Statement:** Not applicable.

**Data Availability Statement:** Not applicable.

**Conflicts of Interest:** The authors declare no conflict of interest.

## References

- Dayalan, S.; Gul, S.S.; Rathinam, R.; Fernandez Savari, G.; Aleem, S.H.A.; Mohamed, M.A.; Ali, Z.M. Multi-Stage Incentive-Based Demand Response Using a Novel Stackelberg–Particle Swarm Optimization. *Sustainability* **2022**, *14*, 10985. [CrossRef]
- Chen, W.; Liu, B.; Nazir, M.S.; Abdalla, A.N.; Mohamed, M.A.; Ding, Z.; Bhutta, M.S.; Gul, M. An Energy Storage Assessment: Using Frequency Modulation Approach to Capture Optimal Coordination. *Sustainability* **2022**, *14*, 8510. [CrossRef]
- Peng, F.; Su, H.; Li, P.; Song, G.; Zhao, J. *An Interactive Operation Strategy for Microgrid Cooperated with Distribution System Based on Demand Response*; IEEE: New York, NY, USA, 2015; ISBN 9781467371063.
- Zhang, Y.; Liu, B.; Zhang, T.; Guo, B. An Intelligent Control Strategy of Battery Energy Storage System for Microgrid Energy Management under Forecast Uncertainties. *Int. J. Electrochem. Sci.* **2014**, *9*, 4190–4204.
- Khalid, M. A Review on the Selected Applications of Battery-Supercapacitor Hybrid Energy Storage Systems for Microgrids. *Energies* **2019**, *12*, 4559. [CrossRef]
- Huang, Y.; Masrur, H.; Shigenobu, R.; Hemeida, A.M.; Mikhaylov, A.; Senjyu, T. A Comparative Design of a Campus Microgrid Considering a Multi-Scenario and Multi-Objective Approach. *Energies* **2021**, *14*, 2853. [CrossRef]
- Aziz, A.S.; Tajuddin, M.F.N.; Adzman, M.R.; Ramli, M.A.M.; Mekhilef, S. Energy Management and Optimization of a PV/Diesel/Battery Hybrid Energy System Using a Combined Dispatch Strategy. *Sustainability* **2019**, *11*, 683. [CrossRef]
- Arévalo-Cordero, P.; Benavides, D.J.; Espinoza, J.L.; Hernández-Callejo, L.; Jurado, F. Optimal Energy Management Strategies to Reduce Diesel Consumption for a Hybrid Off-Grid System. *Rev. Fac. Ing.* **2020**, *98*, 47–58. [CrossRef]
- Delille, G.; François, B.; Malarange, G. Dynamic Frequency Control Support: A Virtual Inertia Provided by Distributed Energy Storage to Isolated Power Systems. In Proceedings of the 2010 IEEE PES Innovative Smart Grid Technologies Conference Europe (ISGT Europe), Gothenburg, Sweden, 11–13 October 2010; pp. 1–8.
- Denholm, P.; Margolis, R.M. Evaluating the Limits of Solar Photovoltaics (PV) in Electric Power Systems Utilizing Energy Storage and Other Enabling Technologies. *Energy Policy* **2007**, *35*, 4424–4433. [CrossRef]
- Zhao, B.; Zhang, X.; Li, P.; Wang, K.; Xue, M.; Wang, C. Optimal Sizing, Operating Strategy and Operational Experience of a Stand-Alone Microgrid on Dongfushan Island. *Appl. Energy* **2014**, *113*, 1656–1666. [CrossRef]
- Vieira, G.T.T.; Pereira, D.F.; Taheri, S.I.; Khan, K.S.; Salles, M.B.C.; Guerrero, J.M.; Carmo, B.S. Optimized Configuration of Diesel Engine-Fuel Cell-Battery Hybrid Power Systems in a Platform Supply Vessel to Reduce CO<sub>2</sub> Emissions. *Energies* **2022**, *15*, 2184. [CrossRef]
- Mohamed, M.A. A relaxed consensus plus innovation based effective negotiation approach for energy cooperation between smart grid and microgrid. *Energy* **2022**, *252*, 123996. [CrossRef]
- Ralon, P.; Taylor, M.; Ila, A.; Diaz-Bone, H.; Kairies, K. *Electricity Storage and Renewables: Costs and Markets to 2030*; International Renewable Energy Agency: Abu Dhabi, United Arab Emirates, 2017; ISBN 9789292600389.
- Mohamad, F.; Teh, J.; Lai, C.M. Optimum allocation of battery energy storage systems for power grid enhanced with solar energy. *Energy* **2021**, *223*, 120105. [CrossRef]
- Ramos, F.O.; Neto, M.M.B.; Pinheiro, A.L.; Junior, W.A.S.; Lima, R.N. A Real Case Analysis of a Battery Energy Storage System for Energy Time Shift, Demand Management, and Reactive Control. In Proceedings of the 2021 IEEE PES Innovative Smart Grid Technologies Conference-Latin America (ISGT Latin America), Quito, Ecuador, 15 September 2021.
- Metwally, M.K.; Teh, J. Optimum network ageing and battery sizing for improved wind penetration and reliability. *IEEE Access* **2020**, *8*, 118603–118611. [CrossRef]
- Ribeiro, P.F.; Johnson, B.K.; Crow, M.L.; Arsoy, A.; Liu, Y. Energy Storage Systems for Advanced Power Applications. *Proc. IEEE* **2001**, *89*, 1744–1756. [CrossRef]
- Fidalgo, J.N.; Couto, M.; Fournié, L. The worth of network upgrade deferral in distribution systems—Truism or myth? *Electr. Power Syst. Res.* **2016**, *137*, 96–103. [CrossRef]

20. Liu, L.; Wang, Y.; Zhao, Y. The Energy Storage System Control Research Based on Black-Start. In Proceedings of the 2014 China International Conference on Electricity Distribution (CICED), Shenzhen, China, 23 September 2014; pp. 1472–1476.
21. Mielczarski, W. Impact of Energy Storage on Load Balancing. In Proceedings of the 2018 15th International Conference on the European Energy Market (EEM), Lodz, Poland, 27–29 June 2018; Institute of Electrical and Electronics Engineers (IEEE): New York, NY, USA, 2018; pp. 1–5.
22. Izidio, D.M.F.; de Mattos Neto, P.S.G.; Barbosa, L.; de Oliveira, J.F.L.; da Marinho, M.H.N.; Rissi, G.F. Evolutionary Hybrid System for Energy Consumption Forecasting for Smart Meters. *Energies* **2021**, *14*, 1794. [CrossRef]
23. IRENA. *Renewable Capacity Statistics 2020*; International Renewable Energy Agency: Abu Dhabi, United Arab Emirates, 2020; ISBN 9789292602390.
24. de Mattos Neto, P.S.G.; de Oliveira, J.F.L.; Domingos, D.S.; Siqueira, H.V.; Marinho, M.H.N.; Madeiro, F. An Adaptive Hybrid System Using Deep Learning for Wind Speed Forecasting. *Inf. Sci.* **2021**, *581*, 495–514. [CrossRef]
25. Mohamed, M.A.; Almalaq, A.; Abdullah, H.M.; Alnowibet, K.A.; Alrasheedi, A.F.; Zaindin, M.S.A. A distributed stochastic energy management framework based-fuzzy-PDMM for smart grids considering wind park and energy storage systems. *IEEE Access* **2021**, *9*, 46674–46685. [CrossRef]
26. Haque, M.E.; Sakib Khan, M.N.; Islam Sheikh, M.R. *Smoothing Control of Wind Farm Output Fluctuations by Proposed Low Pass Filter, and Moving Averages*; International Conference on Electrical & Electronics Engineering: New York, NY, USA, 2015; ISBN 9781467378192.
27. Alevizakos, V.; Chatterjee, K.; Koukouvinos, C.; Lappa, A. A Double Moving Average Control Chart. *Commun. Stat. Simul. Comput.* **2020**, *37*, 1696–1708. [CrossRef]
28. Martins, J.; Spataru, S.; Sera, D.; Stroe, D.I.; Lashab, A. Comparative Study of Ramp-Rate Control Algorithms for PV with Energy Storage Systems. *Energies* **2019**, *12*, 1342. [CrossRef]
29. Mohamed, M.A.; Abdullah, H.M.; Al-Sumaiti, A.S.; El-Meligy, M.A.; Sharaf, M.; Soliman, A.T. Towards energy management negotiation between distributed AC/DC networks. *IEEE Access* **2020**, *8*, 215438–215456. [CrossRef]
30. Al-Shamma'a, A.A.; Hussein Farh, H.M.; Noman, A.M.; Al-Shaalan, A.M.; Alkuhayli, A. Optimal Sizing of a Hybrid Renewable Photovoltaic-Wind System-Based Microgrid Using Harris Hawk Optimizer. *Int. J. Photoenergy* **2022**, *2022*, 4825411. [CrossRef]
31. Teh, J.; Lai, C.M. Reliability impacts of the dynamic thermal rating and battery energy storage systems on wind-integrated power networks. *Sustain. Energy Grids Netw.* **2019**, *20*, 100268. [CrossRef]
32. Al-Shamma'a, A.A.; Alturki, F.A.; Farh, H.M. Techno-economic assessment for energy transition from diesel-based to hybrid energy system-based off-grids in Saudi Arabia. *Energy Transit.* **2020**, *4*, 31–43. [CrossRef]
33. Zeng, L.; Xia, T.; Elsayed, S.K.; Ahmed, M.; Rezaei, M.; Jermstipparsert, K.; Dampage, U.; Mohamed, M.A. A novel machine learning-based framework for optimal and secure operation of static VAR compensators in EAFs. *Sustainability* **2021**, *13*, 5777. [CrossRef]
34. Unamuno, E.; Paniagua, J.; Barrena, J.A. Unified Virtual Inertia for Ac and Dc Microgrids. *IEEE Electr. Mag.* **2019**, *7*, 56–68. [CrossRef]
35. Pinheiro, A.L.; Ramos, F.O.; Neto, M.M.B.; Lima, R.N.; Bezerra, L.G.S.; Junior, W.A.S. A Review and Comparison of Smoothing Methods for Solar Photovoltaic Power Fluctuation Using Battery Energy Storage Systems. In Proceedings of the 2021 IEEE PES Innovative Smart Grid Technologies Conference-Latin America (ISGT Latin America), Quito, Ecuador, 15 September 2021.
36. Caterpillar Inc. *C18 500kW Diesel Generator Sets*; Caterpillar Inc.: Peoria, IL, USA, 2019.

Article

# A Vector Inspection Technique for Active Distribution Networks Based on Improved Back-to-Back Converters

Weiming Zhang <sup>1</sup>, Hui Fan <sup>1</sup>, Jiangbo Ren <sup>2</sup>, Xianzhi Wang <sup>1</sup>, Tiecheng Li <sup>1</sup> and Yibo Wang <sup>3,\*</sup>

<sup>1</sup> State Grid Hebei Electric Power Research Institute, Shijiazhuang 050021, China

<sup>2</sup> State Grid Hebei Electric Power Co., Ltd., Shijiazhuang 050021, China

<sup>3</sup> Wuhan Kemov Electric Co., Ltd., Wuhan 430223, China

\* Correspondence: yibowangwuh@gmail.com

**Abstract:** In this paper, an improved back-to-back converter is proposed, and the converter is used as a test power source for vector inspection of relay protection in an active distribution network, which effectively solves the problem that the output voltage and current of the test power source cannot be continuously and stably adjusted. Firstly, a three-phase back-to-back cascade converter is established to analyze the impedance characteristics of its DC terminal. Then a feedforward voltage is added to the inverter to improve the input impedance characteristics of the inverter. Secondly, the system stability and parameter stability of the improved back-to-back converter are analyzed. Finally, the improved converter is used as the test power source for vector inspection of relay protection in the active distribution network. The simulation results show that the stability of the improved back-to-back converter system is greatly improved. The experiment shows that the vector check technology based on an improved back-to-back converter can effectively check the vector of relay protection in an active distribution network and find various installation problems.

**Keywords:** active distribution network; relay protection; vector inspection; back-to-back converter; stability

**Citation:** Zhang, W.; Fan, H.; Ren, J.; Wang, X.; Li, T.; Wang, Y. A Vector Inspection Technique for Active Distribution Networks Based on Improved Back-to-Back Converters. *Sustainability* **2023**, *15*, 750. <https://doi.org/10.3390/su15010750>

Academic Editor: Mohamed A. Mohamed

Received: 25 November 2022

Revised: 23 December 2022

Accepted: 27 December 2022

Published: 31 December 2022



**Copyright:** © 2022 by the authors. Licensee MDPI, Basel, Switzerland. This article is an open access article distributed under the terms and conditions of the Creative Commons Attribution (CC BY) license (<https://creativecommons.org/licenses/by/4.0/>).

## 1. Introduction

Vector inspection of relay protection is important to enact before the power grid is put into operation. Vector error will lead to false-action or non-action of relay protection in a normal operation state and fault state. Therefore, relevant power grid regulations stipulate that the correctness of the relay protection vector must be strictly checked comprehensively before newly installed equipment or devices with great changes in the circuit are put into operation [1]. At the same time, the relay protection vector inspection technology, applied before commissioning, reduces the safety risk caused by a system switching operation during the commissioning process and reduces the operation workload [2].

In recent years, vector inspection technology that has first been applied in newly built high-voltage substations and transmission networks is put into operation before relay protection [3,4], but there are some difficulties in its application to distribution networks. Compared with the high-voltage substation and transmission network, the line distance of the distribution network is shorter and the transformer capacity is smaller. As a result, the output voltage and output current of the test power source cannot be adjusted continuously and stably, which cannot satisfy the requirements of relay protection vector inspection of the distribution network [5,6].

Back-to-back converters have the advantages of four-quadrant operation, low current harmonic content, and controllable DC voltage, which attracts more and more scholars' attention and research. In this paper, the control strategy and stability of back-to-back converters are analyzed and studied. Ref. [7] adopts a no-difference beat current control and active power feedback compensation mechanism to improve the harmonic current of the back-to-back converter system and grid-connection reliability. Ref. [8] proposed

a coordinated control strategy of two-end converters, which can enhance the stable and reliable operation of the back-to-back MMC-HVDC transmission system. Ref. [9] uses the harmonic state space method to study the stability of back-to-back converters in wind turbines. Impedance matching theory points out that the stability of a cascade system not only depends on the stability of a single converter itself, but also the impedance matching between converters will affect the stability of the system to a large extent [10]. The impedance matching analysis method can be applied to improve and evaluate the stability of AC grid-connected inverters [11–13]. In refs. [14,15], the output impedance of the grid-connected inverter is constructed by virtual impedance correction to improve grid-connected stability. Refs. [16,17] proposed an active full bridge converter (DAB)—inverter cascade topology. The control link is designed according to the DC impedance of the cascade system to improve the impedance characteristics of the system and enhance its stability of the system. Ref. [18] studies the dynamic interaction between photovoltaic grid-connected inverters and power grids based on impedance analysis. None of the above references have been able to analyze the stability of the back-to-back converter from an impedance perspective and propose an improvement plan.

To solve these problems, an improved AC/DC-DC/AC cascade converter is proposed, and the converter is used as the test power source for relay protection vector inspection of the active distribution network in this paper. The main innovations of this paper are as follows:

- (1) Adding a feedforward voltage to the inverter end of the converter can effectively improve the input impedance characteristics of the inverter, and thus the system stability of the converter;
- (2) The vector inspection technology based on the improved back-to-back converter is applied to the vector inspection of the active distribution network for the first time, which can accurately find various installation problems of relay protection.

This paper is organized as follows: in Section 2, the three-phase back-to-back cascaded converter is established to analyze the impedance characteristics of its DC terminal; in Section 3, the system stability and parameter stability of the improved back-to-back converter are analyzed; in Section 4, the principle and flow of distribution network vector inspection are introduced; in Section 5, the improved converter is used as the test power source for vector inspection of relay protection, and vector inspection of relay protection of the active distribution network is carried out; in Section 6, conclusions are drawn.

## 2. Impedance Characteristics of the Converter

This section analyzes the system impedance of the three-phase back-to-back converter, the output impedance of the rectifier at the DC terminal, and the input impedance of the inverter. When analyzing the input impedance of the inverter, feedforward voltage is added to the inverter end, which can effectively improve the input impedance characteristics of the inverter.

### 2.1. Converter System Impedance

Firstly, we set up the back-to-back cascading converter topology as shown in Figure 1. The converter on both terminals is composed of three pairs of switch tubes in a three-phase bridge circuit.  $e_1$  is the grid voltage at the rectifier end,  $L_1$  and  $r_1$  are the filter inductance and parasitic resistance of the rectifier converter, respectively,  $C$  is DC filter capacitor,  $u_{dc}$  and  $i_{dc}$  are DC voltage and current, respectively,  $L_2$  and  $r_2$  are the filter inductance and parasitic resistance of the inverter converter, respectively, and  $e_2$  is the grid-connected voltage of the inverter.

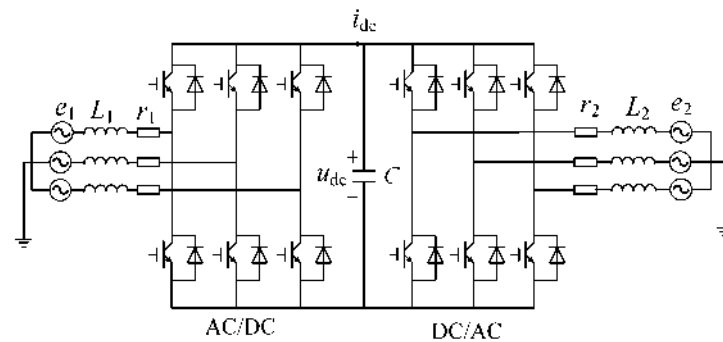


Figure 1. Topology of back-to-back converters.

The block diagram of the impedance principle of a back-to-back converter cascade system is shown in Figure 2.  $G_A$ ,  $G_B$  are transfer functions of rectifier  $A$  and inverter  $B$ , respectively [19].

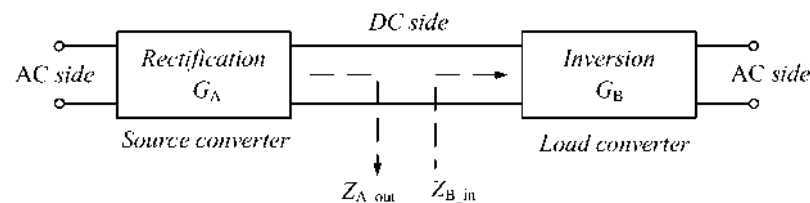


Figure 2. Schematic block diagram of cascade system impedance.

The transfer function  $G$  of the converter cascade system is:

$$G = G_A G_B \frac{1}{1 + T_m} \quad (1)$$

As can be seen from the transfer function of the cascade system, the system stability is not only dependent on the stability of a single system but also related to the impedance matching between subsystems. According to the principle of automatic control, if the open loop transfer function of a system is stable, the system is stable. Therefore,  $T_m$  can be regarded as the open loop transfer function of the cascade system, which is called the minimum loop ratio. Thus, on the premise that all subsystems are stable, the stability of the whole cascade system can be judged by the stability of the  $T_m$ .  $T_m$  is related to the control mode of the subsystem. If  $A$  is the voltage source converter and  $B$  is the current source converter, then  $T_m$  is the output impedance of rectifier  $A$  compared with the input impedance of inverter  $B$  [20], as shown in Equation (2):

$$T_m = \frac{Z_{A\_out}}{Z_{B\_in}} \quad (2)$$

where  $Z_{A\_out}$  represents the output impedance of source converter  $A$ , and  $Z_{A\_in}$  represents the input impedance of load converter  $B$ .

If  $A$  and  $B$  have opposite characteristics—that is,  $A$  is the power converter and  $B$  is the voltage source converter—then  $T_m$  is the input impedance ratio of inverter  $B$  to the output impedance of rectifier  $A$  [21], as shown in Equation (3):

$$T_m = \frac{Z_{B\_in}}{Z_{A\_out}} \quad (3)$$

Input impedance  $Z_{in}$  and output impedance  $Z_{out}$  can be obtained by constructing a small signal model of the system at the static operating point, and the calculation method is shown in Equations (4) and (5):

$$Z_{in} = \frac{\hat{u}_{in}}{\hat{i}_{in}} \quad (4)$$

$$Z_{out} = -\frac{\hat{u}_{out}}{\hat{i}_{out}} \quad (5)$$

where  $\hat{u}_{in}$  and  $\hat{i}_{in}$  are the input voltage and current small signal disturbance, respectively. Similarly,  $\hat{u}_{out}$  and  $\hat{i}_{out}$  are the input voltage and current small signal disturbance, respectively.

## 2.2. Rectifier Impedance

The control block diagram of the voltage and current double closed-loop control rectifier is established in the  $dq$  coordinate system, as shown in Figure 3. In the figure,  $i_{id}$  and  $i_{iq}$ , respectively, represent axis  $d$ - and  $q$ -axis components of grid-connected current at the rectifier terminal.  $d_{id}$  and  $d_{iq}$ , respectively, represent the  $d$  and  $q$  axis components of the rectifier switch duty cycle.  $e_{id}$  and  $e_{iq}$ , respectively, represent the components of axis  $d$  and axis  $q$  of rectifier grid-connected voltage. The symbol “\*” represents the given value of the corresponding variable, and the symbol “^” below represents the small signal disturbance of the corresponding variable [22].

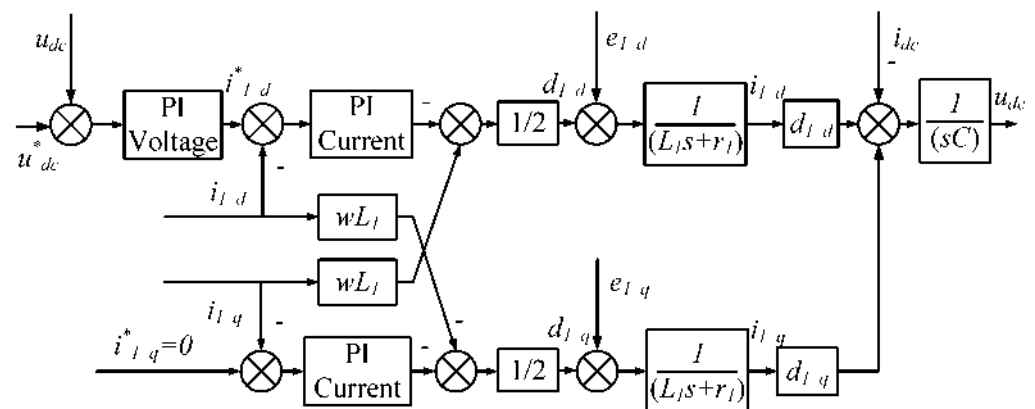


**Figure 3.** Control block diagram of the rectifier in  $dq$  coordinate system.

The small signal model of the rectifier is established by the small signal analysis method, as shown in Equation (6):

$$L_1 \frac{d}{dx} \begin{bmatrix} \hat{i}_{1d} \\ \hat{i}_{1q} \end{bmatrix} = \begin{bmatrix} -r_1 & 0 \\ 0 & -r_1 \end{bmatrix} \begin{bmatrix} \hat{i}_{1d} \\ \hat{i}_{1q} \end{bmatrix} + \begin{bmatrix} \hat{e}_{1d} \\ \hat{e}_{1q} \end{bmatrix} - \left( \begin{bmatrix} \hat{d}_{1d} \\ \hat{d}_{1q} \end{bmatrix} U_{dc} + \begin{bmatrix} D_{1d} \\ D_{1q} \end{bmatrix} \hat{u}_{dc} \right) \quad (6)$$

where  $D_{1d}$  and  $D_{1q}$  are, respectively, the  $d$ - and  $q$ -axis components of the DC duty ratio of the rectifier system, and  $U$  is the steady-state DC voltage.

According to the power balance principle, when the loss in the power transmission process is ignored, the power at the input and output sides of the rectifier should be equal.

$$P = 1.5(e_{1d}i_{1d} + e_{1q}i_{1q}) = u_{dc}i_{dc} \quad (7)$$

Assuming that the three-phase input voltage is symmetrical and balanced without disturbance, while  $\hat{e}_{1d} = 0$ ,  $\hat{e}_{1q} = 0$ , small signal analysis is performed on Equation (7), and the results are shown in Equation (8):

$$1.5E_{1d}\hat{i}_{1d} = \hat{u}_{dc}I_{dc} + U_{dc}\hat{i}_{dc} \quad (8)$$

where  $E_{1d}$  is the voltage of the d-axis of the rectifier system grid in steady state and  $I_{dc}$  is the steady-state current.

Let the current transfer function from voltage to axis  $D$  be  $G_{u_{dc}i_{1d}} = \hat{i}_{1d}/\hat{u}_{dc}$ , then the small signal equation of power balance is shown in Equation (9), and Equation (10) is the output impedance of the DC terminal of the rectifier:

$$1.5E_{1d}G_{u_{dc}i_{1d}}\hat{u}_{dc} = \hat{u}_{dc}I_{dc} + U_{dc}\hat{i}_{dc} \quad (9)$$

$$Z_{rec\_out} = -\frac{\hat{u}_{dc}}{\hat{i}_{dc}} = \frac{-U_{dc}}{1.5E_{1d}G_{u_{dc}i_{1d}} - I_{dc}} \quad (10)$$

Since the rectifier in this paper adopts voltage and current double closed-loop control, the axis components of duty cycle disturbance  $d$  and  $q$  are, respectively:

$$\begin{bmatrix} \hat{i}_{1d} \\ \hat{i}_{1q} \end{bmatrix} = \frac{1}{2} \begin{bmatrix} H_{1i}(-H_u\hat{u}_{dc} - \hat{i}_{1d}) \\ -H_{1i}\hat{i}_{1q} \end{bmatrix} = \begin{bmatrix} -\frac{H_{1i}}{2} & 0 \\ 0 & -\frac{H_{1i}}{2} \end{bmatrix} \begin{bmatrix} \hat{i}_{1d} \\ \hat{i}_{1q} \end{bmatrix} + \begin{bmatrix} -\frac{H_{1i}H_u}{2} \\ 0 \end{bmatrix} \hat{u}_{dc} \quad (11)$$

where  $H_{1i}(s)$  is the transfer function of the current loop PI regulator in rectifier control and  $H_u(s)$  is the transfer function of the voltage loop PI regulator.

Substitute Equation (11) into Equation (10), then the rectifier model is as follows.

$$M_1 \begin{bmatrix} \hat{i}_{1d} \\ \hat{i}_{1q} \end{bmatrix} = \begin{bmatrix} \hat{e}_{1d} \\ \hat{e}_{1q} \end{bmatrix} + \begin{bmatrix} -D_{1d} + H_{1i}H_u/2 \\ -D_{1q} \end{bmatrix} \hat{u}_{dc} \quad (12)$$

where  $M_1 = \begin{bmatrix} L_1s + r_1 - H_{1i}/2 & 0 \\ 0 & L_1s + r_1 - H_{1i}/2 \end{bmatrix}$ . Then, the transfer function of DC voltage to d-axis current is shown in Equation (13):

$$G_{u_{dc}i_{1d}} = \frac{\hat{i}_{1d}}{\hat{u}_{dc}} = \frac{-D_{1d} + H_{1i}H_u/2}{L_1s + r_1 - H_{1i}/2} \quad (13)$$

By substituting Equation (13) into Equation (10), the expression of output impedance  $Z_{rec\_out}$  at the DC terminal of the rectifier can be obtained.

### 2.3. Inverter Impedance

We establish the control block diagram of the inverter in the converter in the  $dq$  coordinate system, as shown in Figure 4.

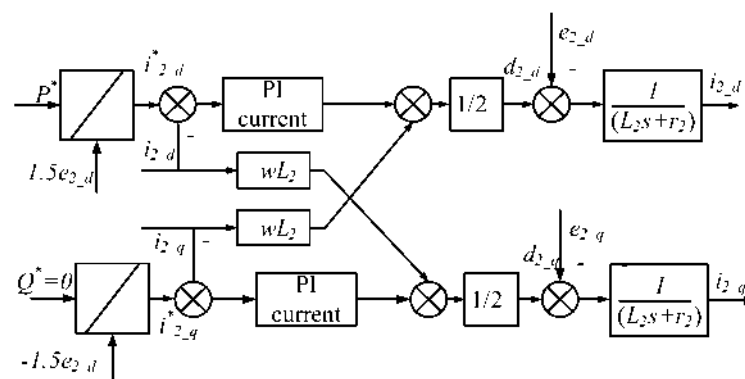


Figure 4. Control block diagram of an inverter in  $dq$  coordinate system.

In this figure,  $P$  and  $Q$  represent active and reactive power respectively,  $e_{2d}$  and  $e_{2q}$ , respectively, represent axis  $d$  and axis  $q$  components of the grid-connected voltage of the inverter system,  $i_{2d}$  and  $i_{2q}$ , respectively, represent  $d$ - and  $q$ -axis components of



inductance current, and  $d_{2\_d}$  and  $d_{2\_q}$ , respectively, represent the  $d$ - and  $q$ -axis components of the inverter switch duty cycle [23].

Similar to the derivation of the rectifier model, the small signal model of the inverter is shown in Equation (14):

$$L_2 \frac{d}{dx} \begin{bmatrix} \hat{i}_{2\_d} \\ \hat{i}_{2\_q} \end{bmatrix} = \begin{bmatrix} -r_2 & 0 \\ 0 & -r_2 \end{bmatrix} \begin{bmatrix} \hat{i}_{2\_d} \\ \hat{i}_{2\_q} \end{bmatrix} + \begin{bmatrix} \hat{e}_{2\_d} \\ \hat{e}_{2\_q} \end{bmatrix} - \left( \begin{bmatrix} \hat{d}_{2\_d} \\ \hat{d}_{2\_q} \end{bmatrix} U_{dc} + \begin{bmatrix} D_{2\_d} \\ D_{2\_q} \end{bmatrix} \hat{u}_{dc} \right) \quad (14)$$

where  $D_{2\_d}$ ,  $D_{2\_q}$  are the DC duty cycle  $d$ - and  $q$ -axis components of the inverter system. Similar to rectifier analysis, the loss in the process of power transmission is ignored, and the impedance of the DC terminal is obtained according to the power balance equation, as shown in Equation (15):

$$Z_{inv\_in} = \frac{\hat{u}_{dc}}{\hat{i}_{dc}} = \frac{U_{dc}}{1.5E_{2\_d}G_{u_{dc}i_{1\_d}} - I_{dc}} \quad (15)$$

where  $E_{2\_d}$  is the grid  $d$ -axis voltage of the inverter system at a steady state.

The inverter adopts constant power control, so the duty cycle disturbance is shown in Equation (16):

$$\begin{bmatrix} \hat{d}_{2\_d} \\ \hat{d}_{2\_q} \end{bmatrix} = \begin{bmatrix} -H_{2\_i}\hat{i}_{2\_d} \\ -H_{2\_i}\hat{i}_{2\_q} \end{bmatrix} = - \begin{bmatrix} -H_{2\_i}/2 & 0 \\ 0 & -H_{2\_i}/2 \end{bmatrix} \begin{bmatrix} \hat{i}_{2\_d} \\ \hat{i}_{2\_q} \end{bmatrix} \quad (16)$$

where  $H_{2\_i}(s)$  is the transfer function of the  $PI$  regulator of the current loop in the control loop of the inverter system. Substitute Equation (16) into Equation (14), then the small signal model of the inverter is shown in Equation (17):

$$M_2 \begin{bmatrix} \hat{i}_{2\_d} \\ \hat{i}_{2\_q} \end{bmatrix} = - \begin{bmatrix} \hat{e}_{2\_d} \\ \hat{e}_{2\_q} \end{bmatrix} + \begin{bmatrix} D_{2\_d} \\ D_{2\_q} \end{bmatrix} \hat{u}_{dc} \quad (17)$$

where  $M_2 = \begin{bmatrix} L_2s + r_2 - H_{2\_i}/2 & 0 \\ 0 & L_2s + r_2 - H_{2\_i}/2 \end{bmatrix}$ . Then, the current transfer function  $G_{u_{dc}i_{2\_d}}$  of the inverter DC terminal voltage to axis  $D$  is shown in Equation (18):

$$G_{u_{dc}i_{2\_d}} = \frac{\hat{i}_{2\_d}}{\hat{u}_{dc}} = \frac{D_{2\_d}}{L_2s + r_2 + H_{2\_i}/2} \quad (18)$$

After substituting Equation (18) into Equation (15), the input impedance  $Z_{inv\_in}$  expression of the DC inverter can be obtained.

#### 2.4. Improved Inverter Impedance

The DC terminal voltage error is used as a given compensation for the inverter  $d$ -axis power loop, and the improved inverter transfer function  $G_{u_{dc}i_d}$  block diagram is shown in Figure 5. The transfer function of inverter DC terminal voltage to  $d$ -axis current can be directly derived from Figure 5, as shown in Equation (19):

$$G'_{u_{dc}i_d} = \frac{\hat{u}_{dc}}{\hat{i}_{dc}} = \frac{D_d + kH_i/2}{L_2s + r_2 + H_{2\_i}/2} \quad (19)$$

where  $k$  is the voltage feedforward coefficient and  $H_i(s)$  is the transfer function of the current loop  $PI$  regulator. Substitute Equation (19) into Equation (18) to obtain the improved input impedance of the DC inverter  $Z'_{inv\_in}$ :

$$Z'_{inv\_in} = \frac{\hat{u}_{dc}}{\hat{i}_{dc}} = \frac{U_{dc}}{1.5E_d G'_{u_{dc}i_d} - I_{dc}} \quad (20)$$

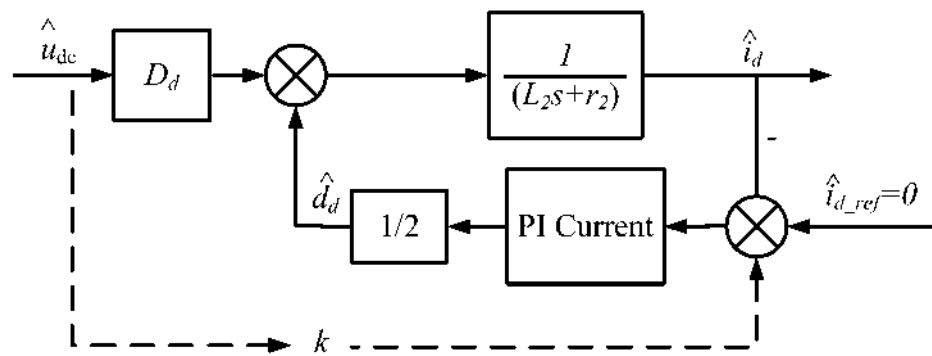


Figure 5. Improved inverter transfer function block diagram.

### 3. Stability Analysis

The stability of the improved back-to-back converter directly determines the feasibility of its application in relay protection vector inspection of the distribution network. Therefore, this section analyzes the stability of the improved back-to-back converter from two aspects of subsystem and parameter influence.

#### 3.1. Subsystem Stability Analysis

From the above analysis, the mathematical models of the output impedance  $Z_{rec\_out}$  of the rectifier and the input impedance  $Z_{inv\_in}$  of the inverter before and after optimization have been obtained. Because the rectifier acts as a voltage source converter, the minimum loop ratio of the cascade system is the ratio of the rectifier's output impedance to the inverter's input impedance. Under the condition of a given power of 5 kW, the output impedance of the rectifier at the DC terminal, the input impedance of the inverter, and the porter diagram of the optimized input impedance of the inverter are shown in Figure 6.

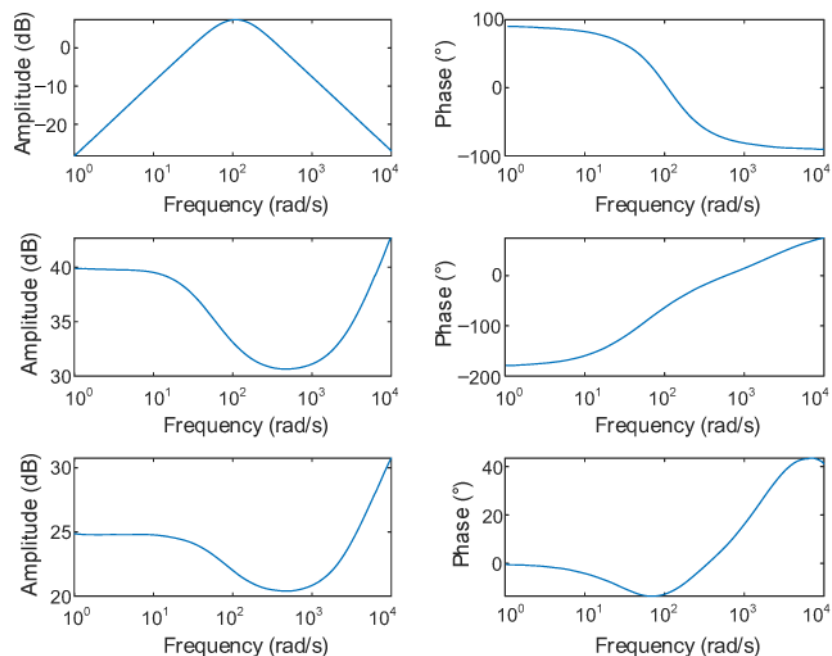


Figure 6. Bode diagram of input/output impedance of converter.

Figure 6 shows that the output impedance amplitude of the DC rectifier is smaller, and the phase ranges from  $90^\circ$  in the low-frequency band to  $-90^\circ$  in the high-frequency band. Compared with the output impedance, the input impedance amplitude of the DC inverter is larger. Its low-frequency phase is  $-180^\circ$  showing negative impedance, which is also an

important reason for the instability of the cascade system. After the voltage feedforward is introduced into the inverter, the impedance amplitude is reduced and the low-frequency phase is  $0^\circ$ , which shows resistance. Theoretically, it is beneficial to system stability.

### 3.2. Influence of Parameters on System Stability

First, three parameters  $K_1$ ,  $K_2$ , and  $K_3$  are introduced, which represent the common gain coefficients of the rectifier current loop PI controller, the voltage loop PI controller, and the inverter power loop PI controller, respectively. Equation (21) is the transfer function of the PI controller after introducing the common gain coefficient of the PI parameter:

$$H(s) = K_i(k_p + \frac{k_i}{s}) \quad (21)$$

where  $k_p, k_i$  are the ratio and integral coefficient.

When the common gain coefficient  $K_1$  of the rectifier current loop parameter changes, the bode diagram of the output impedance of the DC terminal is shown in Figure 7a. It can be seen from the figure that when the coefficient  $K_1$  changes from 0.1 to 1.5, the amplitude and phase of the output impedance do not change. That is to say, the current loop parameters of the rectifier under the voltage and current double closed-loop control have little effect on the output impedance characteristics, and they are not the dominant factor affecting the instability of the system.

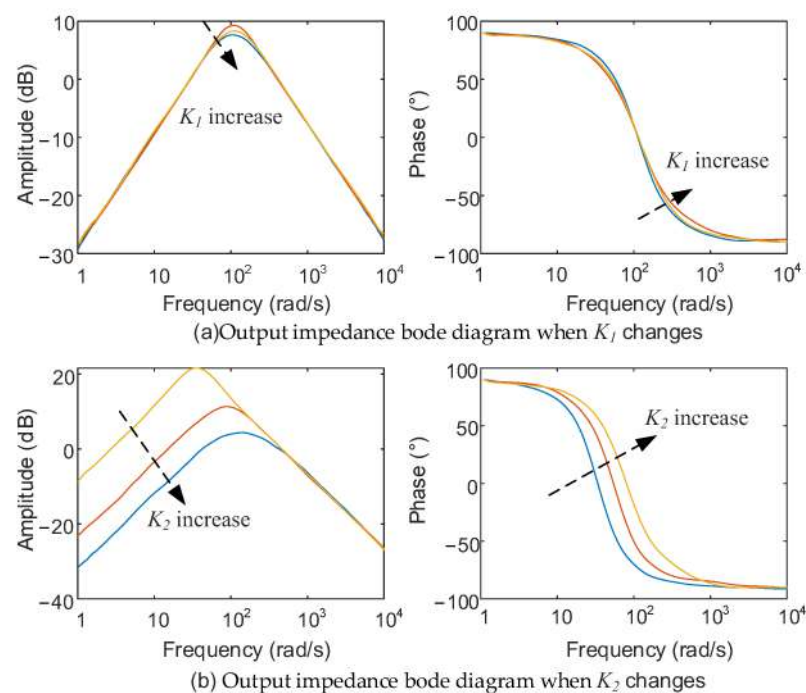


**Figure 7.** Output impedance bode diagram when coefficients  $K_1$  and  $K_2$  change. (a) Output impedance bode with  $K_1$  changes. (b) Output impedance bode with  $K_2$  changes.

When the common gain coefficient  $K_2$  of the voltage loop PI parameter of the rectifier changes, the bode diagram of the output impedance of the DC terminal is shown in Figure 7b. In general, the increase in the voltage loop PI parameter will lead to the increase in high-frequency resonant amplitude in the system, which is not conducive to system stability. In this paper, the influence of impedance on system stability is studied under the premise of system stability. It can be seen from Figure 7 that when the coefficient  $K_2$  increases from 0.1 to 1.5, the impedance amplitude of low-frequency rectifier decreases, and the capacitive impedance characteristic of high-frequency rectifier weakens. The increase in coefficient leads to the reduction of impedance amplitude, which is beneficial to the

cascade system impedance matching. Therefore, the stability of back-to-back converters will be positively affected.

When the feedforward voltage is introduced into the power loop of the inverter, only the input impedance of the inverter is affected, and it has nothing to do with the rectifier side. Therefore, the change in the input impedance of the optimized inverter is analyzed. Figure 8 shows the input impedance bode diagram before and after optimization when the coefficient  $K_3$  changes.

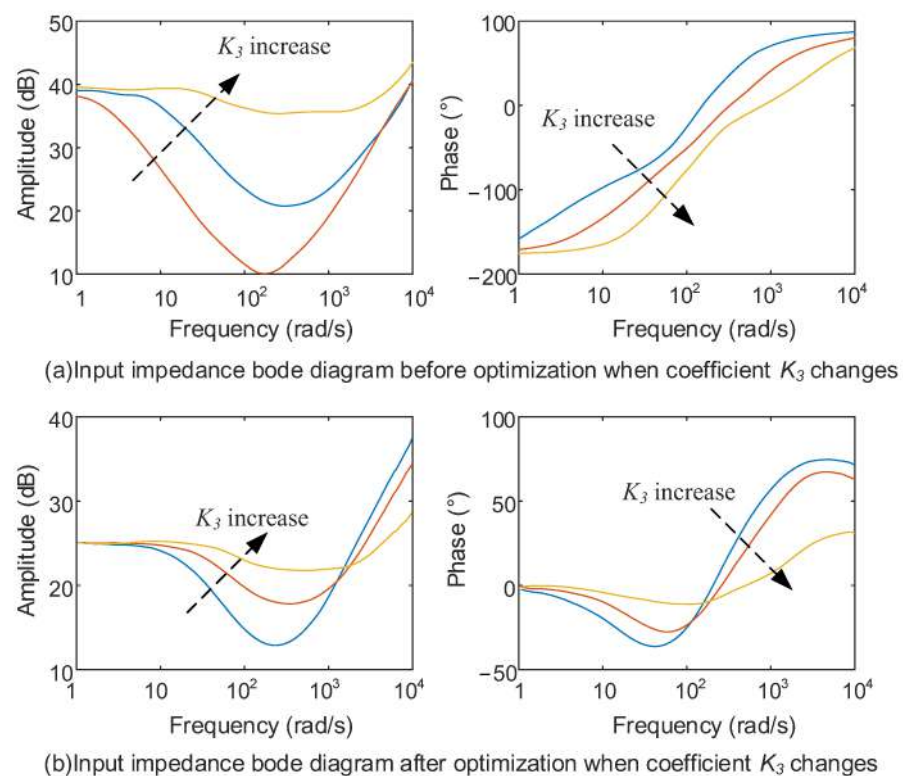


**Figure 8.** Input impedance bode diagram before and after optimization when coefficient  $K_3$  changes. (a) Input impedance bode diagram before optimization with  $K_3$  changes. (b) Input impedance bode diagram after optimization with  $K_3$  changes.

When the common gain coefficient  $K_3$  of the inverter power loop  $PI$  parameter changes, the bode diagram of the input impedance of the DC terminal is shown in Figure 8a. When the coefficient  $K_3$  changes from 0.1 to 1.5, the high-frequency input impedance amplitude increases, and the negative impedance characteristic of low-frequency inverter increases. Figure 8b is the bode diagram of the optimized input impedance at the DC terminal when the coefficient  $K_3$  changes. By comparing Figure 8a,b, it is obvious that the amplitude of the input impedance after optimization decreases. In addition, the low frequency band changes from the negative impedance characteristic which endangers the stability of the system to the pure resistive characteristic which is beneficial to the stability of the system. It can be seen that the input impedance of inverter with feedforward voltage is beneficial to the stability of cascade system.

Figure 9 shows the bode diagram of the input impedance of the DC inverter before optimization when the power changes. When the power changes from 1 kW to 6 kW, the amplitude of the input impedance of the low-frequency inverter decreases, and the negative impedance characteristic increases. The decrease in the input impedance amplitude can easily cause instability in the cascade system, so the stability of the system can be improved by increasing the amplitude of the input impedance.

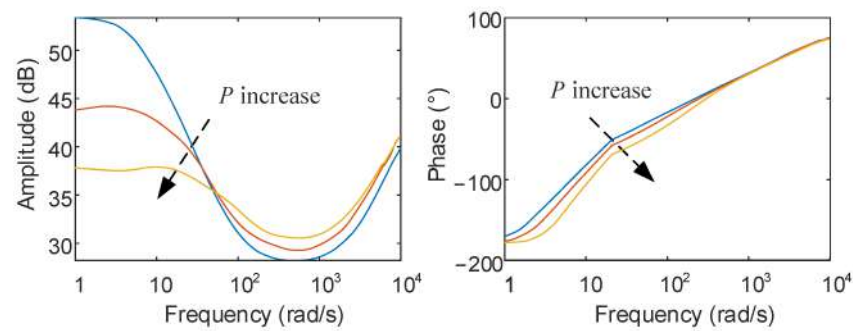


Figure 9. Input impedance bode diagram before optimization when power changes.

#### 4. Principle of Vector Inspection

Vector inspection of relay protection includes secondary voltage value, secondary current value, the angle between secondary voltage, the angle between secondary current, and the correspondence between angle value and amplitude, etc. Vector inspection mainly checks the current transformer ratio range, polarity selection, voltage, and current secondary circuit wiring correctness. The test device for relay protection vector inspection of the distribution network is shown in Figure 10, which includes the current converter, test device, simulated load, and protection device.

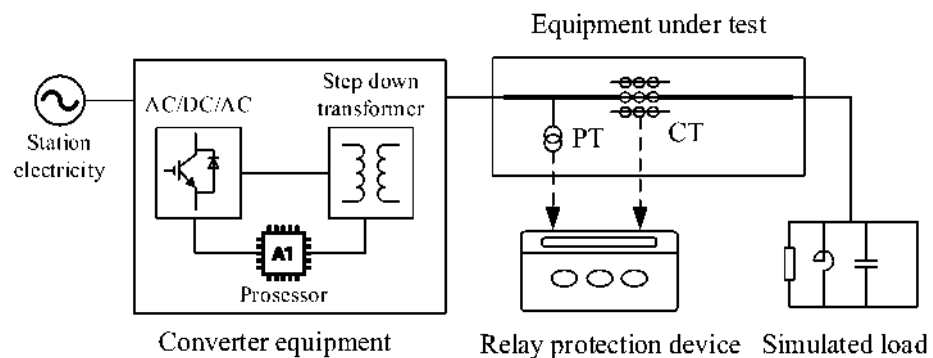


Figure 10. Vector inspection test device structure.

The input end of the current transformer is connected to 380 V mains power, and the output end is connected to the reception test equipment. The output end of the equipment to be tested is connected to the analog load, and the protection device is connected to the equipment to be tested through the voltage transformer and current transformer.

The current converter includes AC/DC-DC/AC cascade converter module, step-down transformer module, and processor module. The converter module can output continuous, stable, and adjustable current and voltage. Step-down transformers are used for voltage regulation. The processor controls and adjusts the converter module according to the output voltage and current of the converter. The whole converter equipment is required to be able to output the required load current stably and quickly respond to the required pulse current. Its nominal design is 50 kVA, 100 A/150 V phase voltage.

The analog load includes parallel test inductance, inductive analog load, capacitive analog load, and analog grounding line, which can form a variety of loops with the equipment to be tested. The test inductance adopts a fixed value of 0.5  $\Omega$ . The inductive analog load is for star connection access, which has an adjustable range of 0–1.0  $\Omega$ . The capacitive analog load is for angular connection access, which has an adjustable range of 50  $\mu\text{F}$ –200  $\mu\text{F}$ . The dynamic stability of the analog ground cable must be at least 150 A/min.

The impedance of the test system load is the sum of the impedance of the device under test and the impedance of the simulated load. During the test, we adjust the simulated

load to compensate for the test equipment and adjust the system load to the inductive or capacitive load of  $1\ \Omega$ .

The relay protection vector inspection process of the whole distribution network is as follows:

- According to the type of relay protection, select different locations to connect to the converter equipment and simulated loads;
- Adjust the output voltage and current of the converter equipment and calculate the impedance of the test system load;
- Subtract the simulated load impedance from the system load impedance to obtain an estimated impedance value of the device under test;
- According to the estimated impedance value of the device under test and the test type, adjust the converter device and the simulated load to compensate the system load impedance to the preset value;
- Connect the protection device to the test system and start the test. Check the correctness of the vector according to the secondary voltage and secondary current collected by the protection device.

## 5. Simulation and Experimental Verification

In this section, the stability of the improved converter is verified by simulation. Then, the improved converter is used as the test power source to verify the relay protection vector inspection technology in the distribution network.

### 5.1. Converter Stability Verification

For the above theoretical analysis, this paper built a three-phase back-to-back converter cascade system on the MATLAB/SIMULINK simulation platform. Table 1 shows the main circuit parameters in the simulation, and Table 2 shows the PI parameters of each control link. In accordance with the theoretical analysis, the rectifier adopts the DC voltage and filter inductor current double closed-loop control strategy, while the inverter adopts the constant power control mode. Figures 11–13, respectively, show the changes in DC terminal voltage, rectifier, and inverter power of the cascade system before and after optimization when the coefficients  $K_1$ – $K_3$  change. Figure 14 shows the changes in DC terminal voltage, rectifier, and inverter power when output power changes.

**Table 1.** Main circuit parameters of the back-to-back converter cascade system.

Parameter	Value
The effective value of grid voltage(e)/V	220
Rectifier side inductance (L1)/mH	2
Rectifier side inductance parasitic resistance (r1)/ $\Omega$	0.16
Capacitance (C)/mF	2.35
Switching frequency (fs)/k Hz	10
Inverter inductance (L2)/mH	3
Inverter inductance parasitic resistance (r2)/ $\Omega$	0.16
Specifies the DC terminal voltage (UDC)/V	700

**Table 2.** Controller parameters.

PI Control Loop	Scale Parameter	Integral Parameter
Rectifier current loop	50.87	103.49
Rectifier voltage loop	0.58	42.2
Inverter current loop	15	1520

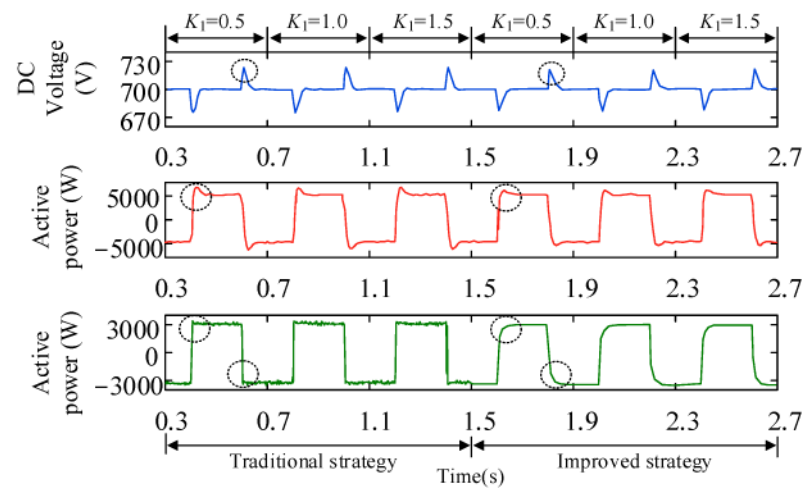


**Figure 11.** Waveform of DC terminal voltage, rectifier and inverter power output when coefficient  $K_1$  changes.

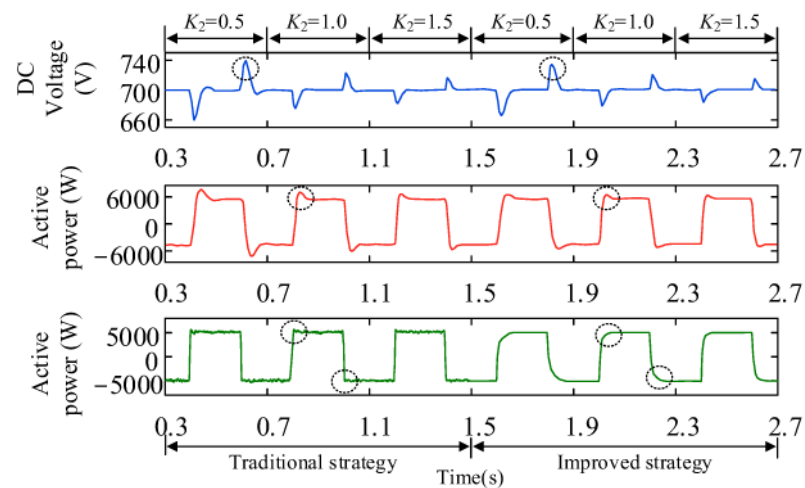


**Figure 12.** Waveform of DC terminal voltage, rectifier, and inverter power output when coefficient  $K_2$  changes.

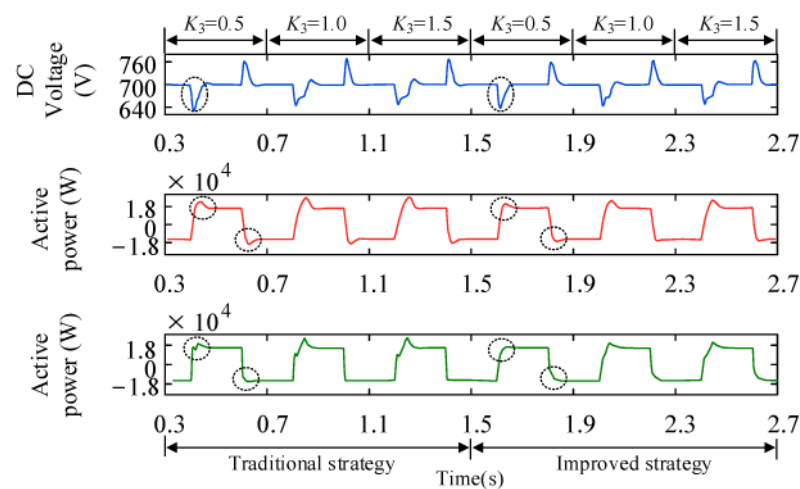


**Figure 13.** Waveform of DC terminal voltage, rectifier and inverter power output when coefficient  $K_3$  changes.



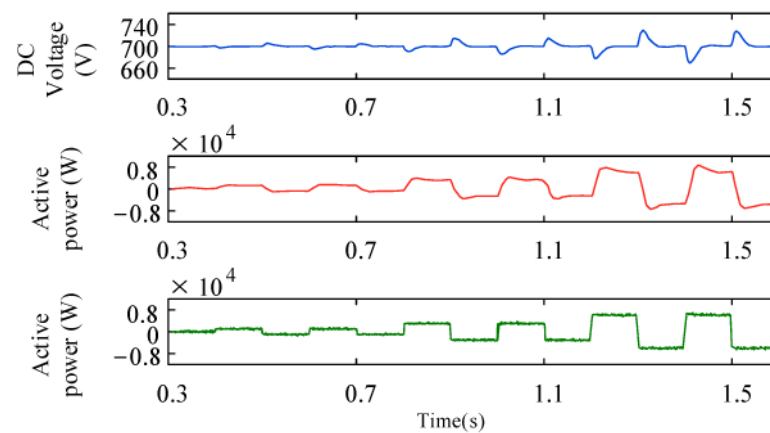


**Figure 14.** Waveform of DC terminal voltage, rectifier, and inverter power output when power changes.

Figure 11 shows the waveforms of the DC terminal voltage, rectifier, and inverter power output optimized when coefficient  $K_1$  is 0.5, 1.0, and 1.5, respectively. In each case, when the coefficient  $K_1$  changes, the system voltage and power are not greatly disturbed. Comparing the two cases, it is obvious that the peak value of the output voltage of the optimized system is smaller. The power transition process is relatively gentle, which has a favorable effect on the system.

Figure 12 shows the waveforms of DC terminal voltage, rectifier, and inverter power output when coefficient  $K_2$  is 0.5, 1.0, and 1.5, respectively. As  $K_2$  increases, the peak value of DC terminal voltage gradually weakens, and the short-term impact on the system gradually decreases. At the same time, the inverter power output waveform gradually flattens with the increase in the coefficient. According to the above analysis, the increase in the  $K_2$  coefficient reduces the output impedance of the rectifier, which is conducive to system stability. The input impedance amplitude of the DC inverter decreases after the feedforward voltage is introduced. Regulating voltage is no longer only the responsibility of the rectifier. At this time, the inverter is also sharing part of the work of regulating voltage, and the system's adjustability has also been improved.

Figure 13 shows the waveforms of DC terminal voltage, rectifier, and inverter power output when coefficient  $K_3$  is 0.1, 0.5, and 0.9, respectively. With the increase in the coefficient, DC terminal voltage distortion and voltage peak value gradually increase. At the same time, the harmonic wave of the rectifier and inverter output power becomes larger under forward power. The increase in inverter power loop parameters enhances the negative impedance characteristics of the inverter, which is not conducive to the stability of the cascade system. Compared with the waveform before and after optimization, the introduction of feedforward voltage effectively reduces the voltage harmonics of the DC terminal, and the output power distortion rate of the rectifier and inverter decreases.

Figure 14 shows the DC terminal voltage, rectifier, and inverter power output of the improved converter when output power  $P$  is 1 kW, 3 kW, and 7 kW, respectively. As the power increases, the voltage spike generated by the DC terminal voltage at the power mutation increases. The power variation of the rectifier and inverter gradually becomes uneven, and the stability of the converter system becomes worse.

## 5.2. Distribution Network Vector Inspection Application

First, the analog load is adjusted so that the end of the device to be tested is connected to the three-phase test inductance, the impedance of which is  $X_S$ . Adjust the output voltage and current of the converter. The test device automatically reads current, voltage, and active power values, then the impedance of the test system load is calculated as  $X_L$ . The system load impedance minus the analog load impedance, the estimated value of the impedance to



be tested equipment  $X_d = X_L - X_s$ . Under different test devices, the estimated impedance values of the devices to be tested are shown in Table 3.

**Table 3.** Main circuit parameters of the back-to-back converter cascade system.

Type	System Load Impedance $X_L$	Analog Load Impedance $X_s$	Estimated Impedance $X_d$
Bus	0.5037 $\Omega$	0.5 $\Omega$	0.0037 $\Omega$
Line	0.7524 $\Omega$	0.5 $\Omega$	0.2524 $\Omega$
Distribution converter	18.5495 $\Omega$	0.5 $\Omega$	18.0495 $\Omega$

Secondly, according to the estimated impedance value of the equipment to be tested, the simulation load is adjusted to compensate for the system load impedance to 1  $\Omega$ . When adjusting the current converter device for vector inspection, the current output by the converter device should meet certain requirements. Its size is related to the primary current of the device to be tested, as shown in Table 4.

**Table 4.** Output current requirements of converter equipment.

Primary Current of the Device	Current Converter Output Current
Rated current $\geq 500$ A	$\geq 10$ A
Rated current $\geq 1000$ A	$\geq 20$ A
Rated current $\geq 2000$ A	$\geq 40$ A
Fault current	$\leq 100$ A

### 5.2.1. Bus and Feeder Vector Inspection

The wiring diagram of the vector inspection of the 10 kV bus and feeder is shown in Figure 15. The power source of the test system comes from the station power, and the currency converter is connected to the equipment under test from the incoming line of the bus I. The simulated load is connected to the device under test from feeder F12. The protection device is connected to the device to be tested through the voltage transformer and current transformer. We adjust the system load to inductive 1  $\Omega$ , and then adjust the output current and output voltage of the converter equipment. The relay protections that can be tested are bus low voltage overcurrent protection, feeder F12 overcurrent protection, and quick break protection. The inspection results are shown in Table 5.

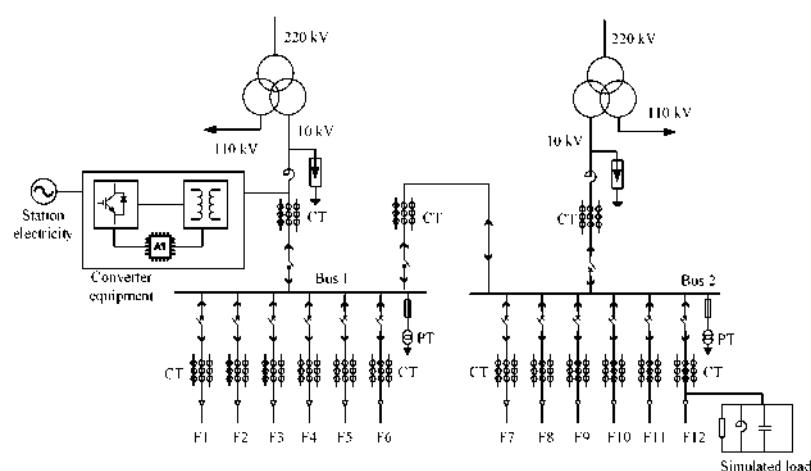


**Figure 15.** Relay protection vector inspection wiring diagram of feeder and bus.

**Table 5.** Busbar protection test data.

Transformer	U Phase	V Phase	W Phase
PT of bus I	1.274V $\angle$ 0°	1.271V $\angle$ 239°	1.281V $\angle$ 118°
Incoming CT of bus I	0.082A $\angle$ 270°	0.082A $\angle$ 150°	0.082A $\angle$ 31°
Bus coupler CT	0.082A $\angle$ 270°	0.082A $\angle$ 150°	0.082A $\angle$ 31°

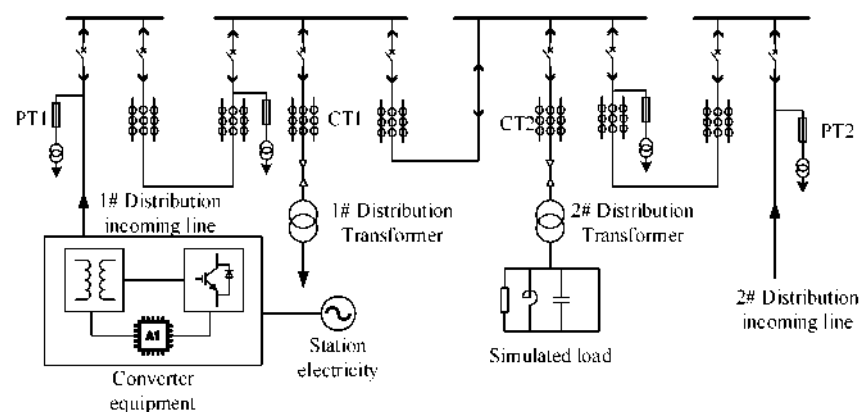
It can be seen from Tables 5 and 6 that the secondary voltage and secondary current of bus protection and feeder F12 protection are both greater than 0.02 A and 0.2 V, and the secondary current lags almost 90° behind the secondary voltage. Therefore, it can be judged that the vectors of bus protection and feeder F12 protection are correct. Similarly, by changing the position of the converter device and the simulated load, vector inspections can be carried out on other protections of the bus and feeder.

**Table 6.** Feeder protection test data.

Transformer	U Phase	V Phase	W Phase
PT for bus II	0.358A $\angle$ 5°	0.354A $\angle$ 242°	0.359A $\angle$ 124°
CT of feeder 12	0.082A $\angle$ 270°	0.082A $\angle$ 150°	0.082A $\angle$ 31°

### 5.2.2. Distribution Vector Inspection

The wiring diagram for vector inspection of the distribution transformer is shown in Figure 16. The power source of the test system is from the station electricity, and the currency converter is connected to the equipment to be tested from the 1# incoming line of the distribution transformer box, and the analog load is connected to the equipment to be tested from the 1# outgoing line of the distribution transformer. Vector inspection can be carried out for overcurrent protection and quick break protection of the 1# distribution transformer. The current converter is connected to the equipment to be tested from the 2# incoming line of the distribution transformer box, and the analog load is connected to the equipment to be tested from the 2# outgoing line of the distribution transformer. Vector inspection can be carried out for overcurrent protection and quick break protection of the 2# distribution transformer. The inspection results are shown in Table 7.

**Figure 16.** Vector inspection wiring diagram of relay protection of distribution transformer.**Table 7.** Test data of transformer protection.

Transformer	U Phase	V Phase	W Phase
1# Incoming cabinet PT1	1.238V $\angle$ 2°	1.236V $\angle$ 237°	1.242V $\angle$ 121°
1# Distribution converter CT1	0.075A $\angle$ 272°	0.071A $\angle$ 153°	0.078A $\angle$ 29°
2# Incoming cabinet PT2	1.242V $\angle$ 3°	1.248V $\angle$ 247°	1.261V $\angle$ 119°
2# Distribution converter CT2	0.062A $\angle$ 264°	0.064A $\angle$ 159°	0.068A $\angle$ 27°

As can be seen from Table 7, the secondary voltage and secondary current of distribution transformer overcurrent protection and quick break protection are both greater than 0.02 and 0.2 V. Moreover, the secondary current lags behind the secondary voltage by almost  $90^\circ$ , so the vector of distribution protection is judged to be correct. Similarly, vector inspection can be carried out on other measurement and control devices of the distribution transformer box by changing the position of the current converter and the simulated load. It is not discussed here.

### 5.2.3. Installation Problems Were Found in Application

The test device constructed in this paper was used to carry out vector inspection on relay protection of a 10 kV distribution network in a certain area, and several installation problems were found, as shown in Table 8. This shows that the vector inspection technology based on improved back-to-back converters can accurately carry out vector inspection of relay protection in the active distribution network and find various installation problems.

**Table 8.** Installation problems were found in the application.

Installation Problem	Annotation
The cable connection of the digital input optical fiber of the voltage combination unit is incorrect	In the process of a line protection vector inspection test, an error in voltage phase sequence was found, which was considered a phase sequence error of line interval combination unit voltage input optical fiber. It belonged to misconnection.
The remote module of the voltage transformer is incorrectly connected	During the protection vector inspection test of a certain line, the protection device shows no voltage of a certain phase, and the quality problem of the remote module is determined by the inspection
The polarity of the busbar current is incorrectly configured	In the process of vector inspection of bus protection, the polarity of the current is wrong. After checking, the polarity of the bus current is wrong, which belongs to the fixed value configuration error

## 6. Conclusions

This paper presents an improved back-to-back converter which is used as a test power source for relay protection vector inspection. The simulation results show that adding feed-forward voltage to the inverter can effectively improve the input impedance characteristics of the inverter, thus improving the system stability of the converter. At the same time, the vector inspection technology based on the improved back-to-back converter can meet the requirements of the distribution network and find various installation problems of the relay protection. Due to the limited laboratory conditions, this paper only uses simulation to verify the stability of the improved converter. In future work, experiments will be used to further verify the stability of the improved converter.

**Author Contributions:** Conceptualization, W.Z., J.R., X.W., T.L., Y.W. and H.F.; software, H.F., T.L.; validation, W.Z. and Y.W.; formal analysis, W.Z., J.R., X.W. and Y.W.; investigation, H.F.; data curation, X.W., T.L. and Y.W.; writing—original draft preparation, H.F., X.W., T.L. and Y.W.; writing—review and editing, H.F., J.R., T.L. and Y.W.; visualization, J.R.; supervision, Y.W.; All authors have read and agreed to the published version of the manuscript.

**Funding:** This research was funded by Science and Technology Project of State Grid Hebei Electric Power Co., Ltd. (kj2022-001).

**Institutional Review Board Statement:** Not applicable.

**Informed Consent Statement:** Not applicable.

**Data Availability Statement:** Not applicable.

**Conflicts of Interest:** The authors declare no conflict of interest.

## References

- Li, T. Research on vector inspection technology of relay protection before operation. *Hebei Electr. Power Technol.* **2013**, *32*, 2.
- Zhang, B.; Hao, X.; Cao, S.; Li, T.; Zhao, C. Research on vector inspection technology of relay protection before operation using capacitor compensation. *Hebei Electr. Power Technol.* **2013**, *32*, 1–3.
- Wang, Q.; Jin, T.; Mohamed, M.A. A Fast and Robust Fault Section Location Method for Power Distribution Systems Considering Multisource Information. *IEEE Syst. J.* **2021**, *16*, 1954–1964. [CrossRef]
- Rao, C.; Hajjiah, A.; El-Meligy, M.A.; Sharaf, M.; Soliman, A.T.; Mohamed, M.A. A novel high-gain soft-switching DC-DC converter with improved P&O MPPT for photovoltaic applications. *IEEE Access* **2021**, *9*, 58790–58806.
- Ma, H.; Liu, Z.; Li, M.; Wang, B.; Si, Y.; Yang, Y.; Mohamed, M.A. A two-stage optimal scheduling method for active distribution networks considering uncertainty risk. *Energy Rep.* **2021**, *7*, 4633–4641. [CrossRef]
- Wang, Q.; Jin, T.; Mohamed, M.A. An innovative minimum hitting set algorithm for model-based fault diagnosis in power distribution network. *IEEE Access* **2019**, *7*, 30683–30692. [CrossRef]
- Zhou, S. *Research on Harmonic Elimination and Reliability of Three-Level back to back Converter*; Anhui university: Hefei, China, 2017.
- Yang, Y.; Yang, J.; He, Z.; Li, Q.; Xu, W. Control strategy of MMC based back-to-back HVDC transmission system. *Autom. Electr. Power Syst.* **2017**, *41*, 120–124.
- Kwon, J.; Wang, X.; Bak, C.L.; Blaabjerg, F. Analysis of harmonic coupling and stability in back-to-back converter systems for wind turbines using Harmonic State Space (HSS). In Proceedings of the Energy Conversion Congress and Exposition, Montreal, QC, Canada, 20–24 September 2015; IEEE: Manhattan, NY, USA, 2015; pp. 730–737.
- Gao, J.; Zhao, J.; Qu, K.; Li, F. Reconstruction of impedance-based stability criteria in weak grid. *Power Syst. Technol.* **2017**, *41*, 2762–2768.
- Cespedes, M.; Sun, J. Impedance modeling and analysis of grid-connected voltage-source converters. *IEEE Trans. Power Electron.* **2013**, *29*, 1254–1261. [CrossRef]
- Xu, J.; Zhang, B.; Qian, Q.; Meng, X.; Xie, S. Robust control and design based on impedance-based stability criterion for improving stability and harmonics rejection of inverters in weak grid. In Proceedings of the Applied Power Electronics Conference and Exposition, Tampa, FL, USA, 26–30 March 2017; IEEE: Manhattan, NY, USA, 2017; pp. 3619–3624.
- Lissandron, S.; Dalla Santa, L.; Mattavelli, P.; Wen, B. Experimental validation for impedance-based small-signal stability analysis of single-phase interconnected power systems with grid-feeding inverters. *IEEE J. Emerg. Sel. Top. Power Electron.* **2016**, *4*, 103–115. [CrossRef]
- Yang, D.; Ruan, X.; Wu, H. Virtual impedance method to improve LCL grid-inverter's adaptability in weak power grid. *Proc. CSEE* **2014**, *34*, 2327–2335.
- Wei, S.; Tian, Y.; Wang, Y. Virtual Inductance Control for Enhancing Stability of LCL Inverter in Weak Grid. *High Volt. Eng.* **2019**, *45*, 1827–1834.
- Tian, Y.; Loh, P.C.; Deng, F.; Chen, Z.; Sun, X.; Hu, Y. Impedance coordinative control for cascaded converter in bidirectional application. *IEEE Trans. Ind. Appl.* **2015**, *52*, 4084–4095. [CrossRef]
- Tian, Y.; Loh, P.C.; Deng, F.; Chen, Z.; Hu, Y. DC-Link voltage coordinated proportional control for cascaded converter with zero steady-state error and reduced system type. *IEEE Trans. Power Electron.* **2015**, *31*, 3177–3188. [CrossRef]
- Chen, X.; Zhang, Y.; Wang, Y. Research on the dynamic interaction of photovoltaic grid-connected inverter and power grid based on impedance analysis. *Proc. CSEE* **2014**, *34*, 459–4567.
- Raza, M.; Prieto-araujo, E.; Gomis-bellmunt, O. Small signal stability analysis of offshore AC network having multiple VSC-HVDC system. *IEEE Trans. Power Deliv.* **2018**, *33*, 830–839. [CrossRef]
- Zhang, X.; Ruan, X.; Zhong, Q.C. Improving the stability of cascaded DC/DC converter systems via shaping the input impedance of the load converter with a parallel or series virtual impedance. *IEEE Trans. Ind. Electron.* **2015**, *62*, 7499–7512. [CrossRef]
- Aapro, A.; Messo, T.; Roinila, T.; Suntio, T. Effect of active damping on output impedance of three-phase grid-connected converter. *IEEE Trans. Ind. Electron.* **2017**, *64*, 7532–7541. [CrossRef]
- Alenius, H.; Roinila, T. Impedance-based stability analysis of paralleled grid-connected rectifiers: Experimental case study in a data center. *Energies* **2020**, *13*, 2109. [CrossRef]
- Yadav, A.; Chandra, S.; Bajaj, M.; Sharma, N.K.; Ahmed, E.M.; Kamel, S. A Topological Advancement Review of Magnetically Coupled Impedance Source Network Configurations. *Sustainability* **2022**, *14*, 3123. [CrossRef]

**Disclaimer/Publisher's Note:** The statements, opinions and data contained in all publications are solely those of the individual author(s) and contributor(s) and not of MDPI and/or the editor(s). MDPI and/or the editor(s) disclaim responsibility for any injury to people or property resulting from any ideas, methods, instructions or products referred to in the content.

## Article

# Experimental Investigation of an Adaptive Fuzzy-Neural Fast Terminal Synergetic Controller for Buck DC/DC Converters

Badreddine Babes <sup>1</sup>, Nouredine Hamouda <sup>1</sup>, Fahad Albalawi <sup>2</sup>, Oualid Aissa <sup>3</sup>, Sherif S. M. Ghoneim <sup>2,\*</sup> and Saad A. Mohamed Abdelwahab <sup>4,5</sup>

<sup>1</sup> Research Center in Industrial Technologies (CRTI), P.O. Box 64, Cheraga 16014, Algeria; elect\_babes@yahoo.fr (B.B.); n.hamouda@crti.dz (N.H.)

<sup>2</sup> Department of Electrical Engineering, College of Engineering, Taif University, P.O. Box 11099, Taif 21944, Saudi Arabia; f.albiloi@tu.edu.sa

<sup>3</sup> LPMRN Laboratory, Faculty of Sciences and Technology, University of Bordj Bou Arreridj, El Anseur 34000, Algeria; oualid.aissa@univ-bba.dz

<sup>4</sup> Electrical Department, Faculty of Technology and Education, Suez University, Suez 43533, Egypt; saad.abdelwahab@suezuniv.edu.eg

<sup>5</sup> Department of Computers & Systems Engineering, High Institute of Electronic Engineering, Ministry of Higher Education, Bilbis-Sharqiya 44621, Egypt

\* Correspondence: s.ghoneim@tu.edu.sa

**Abstract:** This study proposes a way of designing a reliable voltage controller for buck DC/DC converter in which the terminal attractor approach is combined with an enhanced reaching law-based Fast Terminal Synergetic Controller (FTSC). The proposed scheme will overcome the chattering phenomena constraint of existing Sliding Mode Controllers (SMCs) and the issue related to the indefinite time convergence of traditional Synergetic Controllers (SCs). In this approach, the FTSC algorithm will ensure the proper tracking of the voltage while the enhanced reaching law will guarantee finite-time convergence. A Fuzzy Neural Network (FNN) structure is exploited here to approximate the unknown converter nonlinear dynamics due to changes in the input voltage and loads. The Fuzzy Neural Network (FNN) weights are adjusted according to the adaptive law in real-time to respond to changes in system uncertainties, enhancing the increasing the system's robustness. The applicability of the proposed controller, i.e., the Adaptive Fuzzy-Neural Fast Terminal Synergetic Controller (AFN-FTSC), is evaluated through comprehensive analyses in real-time platforms, along with rigorous comparative studies with an existing FTSC. A dSPACE ds1103 platform is used for the implementation of the proposed scheme. All results confirm fast reference tracking capability with low overshoots and robustness against disturbances while comparing with the FTSC.

**Keywords:** synergetic control (SC) law; fuzzy neural network (FNN) approximator; fast terminal synergetic controller (FTSC); finite-time convergence; DC/DC buck converter

**Citation:** Babes, B.; Hamouda, N.; Albalawi, F.; Aissa, O.; Ghoneim, S.S.M.; Abdelwahab, S.A.M. Experimental Investigation of an Adaptive Fuzzy-Neural Fast Terminal Synergetic Controller for Buck DC/DC Converters. *Sustainability* **2022**, *14*, 7967.

<https://doi.org/10.3390/su14137967>

Academic Editors: Luigi Aldieri and Mohamed A. Mohamed

Received: 2 June 2022

Accepted: 26 June 2022

Published: 29 June 2022



**Copyright:** © 2022 by the authors. Licensee MDPI, Basel, Switzerland. This article is an open access article distributed under the terms and conditions of the Creative Commons Attribution (CC BY) license (<https://creativecommons.org/licenses/by/4.0/>).

## 1. Introduction

### 1.1. Motivation

The buck DC/DC converter is a common choice in many applications in electric power supply systems, including DC motor drives, DC microgrids, automobiles, sailboats, airplanes, solar systems, and many more. Its mathematical model is a nonlinear and time-varying system based on state-space equations. These equations must be treated around the steady-operating point with a small-signal linearization approach before being studied with PID controllers. When a severe disturbance causes a substantial divergence from the typical operating point, it is difficult for a standard buck DC/DC converter to achieve perfect stability [1]. In light of this, adjusting the output voltage of the buck DC/DC converter is a challenging task. Realizing a robust control strategy for buck DC/DC converter is a critical challenge for better understanding the design aspect of the regulator and stability

problem [2]. Furthermore, it can aid to enhance transient and steady-state conditions under a variety of disturbances. To overcome some of the previously mentioned challenges, this work suggests an AFN-FTSC algorithm for the output voltage control without complete converter model knowledge. FNN model, and universal approximator, are utilized in an adaptive scheme to approximate the converter nonlinear dynamics, while the FTSC algorithm is utilized to guarantee robustness through an easy-to-implement chatter-free continuous control law [1].

### 1.2. Related Work

To provide better performance for buck DC/DC converters, numerous intelligent and nonlinear control techniques have been introduced over the last decade. In paper [3], the performance of the buck DC/DC converter is evaluated by variable structure controllers in which the output voltage is tracked and regulated in a good way; however, the robustness of these controlling techniques is not acceptable against noise, chattering, parametric variations, and disturbances, which makes them practically unsuitable [4]. Otherwise, because of the switching properties of buck DC/DC converter, digital discrete control methods like repetitive [5], dead beat [6], and internal model [7] controllers have been recommended for buck DC/DC converter. The main advantage of a repetitive controller is low output distortion; however, it has some limitations such as poor tracking, large memory capacity, poor performance, and slow dynamics. Nevertheless, the internal model and dead beat controller can provide output voltage tracking without ringing and overshoot; however, the complex controlling structure of the internal model and dead beat controllers have influenced their efficiency.

In paper [8], a feedback linearization scheme is utilized for the buck DC/DC converter to control the output voltage, and model predictive controllers are presented in [9], and [10] to achieve the same goal. Both feedback linearizing and model predictive controllers provide similar advantages such as reliable reference tracking, constant switching frequency, and fast dynamic response; these controllers do not perform well under the variation in parameters due to their requirements of using precise parametric information during the implementation, and it is quite impossible to precisely know the parameters of the system as many of these vary with operating scenarios. An adaptive model predictive controller is introduced in [11] by capturing linear parameter variations so that parameter sensitivity can be alleviated. However, the inclusion of such parameter variations complicates the process of solving the optimization problem for the model predictive scheme. The Synergetic Controller (SC) is another useful alternative way of controlling the buck DC/DC converters, which can also ensure the robustness against parameter variations and disturbances by using a generalized state-space averaged representation of the system. The SC inherently alleviates the effects of external disturbances, nonlinearities, and uncertainties [12]. For all these features, SCs are extensively used for power electronic applications, including the buck DC/DC converter [13]. The standard SC scheme uses the linear manifold as a macro-variable as presented in [14] to guarantee the asymptotic convergence of the error. However, such a macro-variable makes the system static during the fluctuations in the load voltage, and therefore, it results in poor voltage tracking during transients in the system [14]. Although the gain parameters for such traditional SCs can be adjusted to ensure better transients, there are no guarantees that the system variable reaches their equilibriums in a finite time. These problems can be overcome by using SC schemes such as the Non-Singular Terminal Synergetic Control and FTSC that ensure finite-time convergence, as presented in [15,16]. However, these methods slow down the dynamic response by reducing the likelihood of overshoots during load changes and other transients during the starting. The dynamic response for regulating the output voltage during transients is accelerated in [13] using an adaptive FTSC based on dual Radial Basis Function Neural Networks (RBFNN-FTSC) control. Moreover, all adaptive SC approaches in the existing literature on the buck DC/DC converters use classical adaptive law, for which there is a possibility to induce the chattering causing ripples at the output voltage during their practical or real-time

implementations. In recent years, FNN models are a hybrid approach that combines the learning ability of a neural network with the noise-handling capabilities of fuzzy logic (FL). They are commonly used in adaptive control to cope with uncertainties and attain improved performance standards. [17,18]. Although the FNNs have extensively been utilized in different adaptive controls, the applications of FNNs for uncertain nonlinear systems are relatively new and only a few applications can be seen throughout the literature. Based on the author's knowledge, the applications of AFN-FTSC for DC/DC buck converters have not been investigated until now. Motivated by the existing literature, the considered controller design process in the current research investigates a new digital controller based on AFN-FTSC for buck DC/DC converters without the previously mentioned problems.

### 1.3. Novelty and Principal Contributions

The main innovative features of the proposed scheme are:

- (i) It is the first time a FNN model has been developed based on FTSC for DC/DC buck converters;
- (ii) Unlike closely related work, the proposed AFN-FTSC is created by incorporating the macro-variable to tackle the chattering effects, decrease the time of convergence, simplify the expression of the controller, and ensure a fast transient reaction, low steady-state error, and high output voltage tracking accuracy;
- (iii) A Lyapunov stability theorem is rigorously used to demonstrate the overall stability of the system and to obtain the updated rules for the FNN weights.
- (iv) The removal of demand for an accurate model by using a FNN approximator to estimate an unknown buck DC/DC converter functions;
- (v) Experiments are carried out to demonstrate efficiency while assisting to achieve desired goals under a variety of operating situations.
- (vi) It simultaneously ensures the higher output voltage tracking accuracy, swift transient responses, and less impact by disturbances and uncertainties due to the use of adaptive time-varying reaching law.

### 1.4. Organization of the Paper

The remaining part of the study is structured as follows. The basic requirements for SC and FNNs are briefly discussed in Section 2. The representation of the DC/DC buck converter is introduced in Section 3. The steps for designing the AFN-FTSC algorithm are presented in Section 4, including the stability and reachability analysis. Afterward, results from experimental tests are presented in Section 5 to illustrate the efficacy and practicality of the designed AFN-FTSC algorithm. Finally, the conclusions and some recommendations for further investigation are given in Section 6.

## 2. Preliminaries

### 2.1. Principle of Synergetic Control (sc)

SC algorithm is effectively a nonlinear control strategy based on the principle of directional self-organization theory and the usage of the standard nonlinear characters of dynamic systems. The fundamental idea of the SC algorithm is as follows:

1. Invariant manifold is created in the state-space of a controllable system. On this attractor, we guarantee the organization of the preferred static and dynamic behavior of the controllable system. The design of the attractor is the indication of a directed self-organization principle.
2. The most important premise in the theory of SC is the principle of compression–decompression of the phase flow of the controllable objects.
3. The designer's necessities are given in the form of an affine system that describes the preferred operating modes of the controlled systems.

Consider the nonlinear affine dynamical system of degree  $n$  given by:

$$\dot{x} = \frac{dx}{dt} = f(x, u, t) \quad (1)$$

where  $x \in R^n$ ,  $u \in R^m$ , indicating the state-variable and control-variables, respectively. The  $f(\cdot)$  indicates a continuous nonlinear function. The SC design structure starts with defining a macro-variable  $\varphi$  as a function of the state variables [19]:

$$\varphi = \varphi(x, t) \quad (2)$$

The primary goal of the SC is to force the system to function on a pre-determined manifold  $\varphi = 0$ . Develop a SC that forces system variables to approach the desired manifold exponentially, with an evolution constraint that may be expressed as:

$$\kappa \dot{\varphi} + \varphi = 0, \kappa > 0 \quad (3)$$

where  $\varphi$  is the derivative of the aggregated macro-variables, and  $\kappa$  is a positive integer that enables the designer to choose the rate of convergence to the selected attractor. The solution of (3) gives the following function for  $\varphi(t)$ :

$$\varphi(t) = \varphi_0 e^{-t/\kappa} \quad (4)$$

It affirms that  $\varphi(t) \rightarrow 0$  at  $t \rightarrow \infty$ , which implies that  $\varphi(t)$  is attracted to  $\varphi = 0$  from any starting location  $\varphi_0$  (Figure 1). Since the time constant  $\kappa > 0$ , the macro-variable  $\varphi$  will decay exponentially with a speed determined by  $\kappa$ . As long as the system is stable, the smaller value of  $\kappa$  is faster than the macro-variable decays. When  $\varphi$  approaches zero, the system converges to the manifold and then functions on the manifold without interruption.

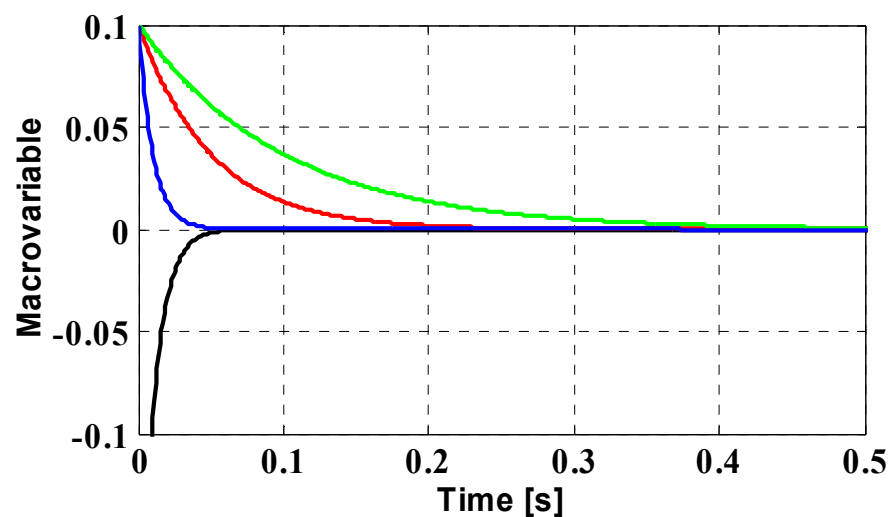


Figure 1. Convergence of macro-variable for various starting locations to the attractor.

Considering the differentiation chain provided by:

$$\dot{\varphi} = \frac{d\varphi(x, t)}{dt} = \frac{\partial \varphi(x, t)}{\partial x} \cdot \frac{dx(t)}{dt} \quad (5)$$

When (1) and (3) are substituted into (5), we get (6):

$$\kappa \frac{d\varphi(x, t)}{\partial x} f(x, u, t) + \varphi(x, t) = 0 \quad (6)$$



Resolving (6) for the control vector  $u$  gives the SC law as:

$$u = g(x, \varphi(x, t), \kappa, t) \quad (7)$$

The SC law (7) permits state trajectories to follow certain paths (3). Proper selection of the macro-variable (2) and judicious manifolds ensure the necessary performance and stability [20]. It is worth noting that SC law (7) can be rewritten as a solution to a Kolesnikov's problem (8). Choose the performance index as follows [21]:

$$J_{\Sigma} = \int_0^{\infty} \Gamma(\dot{\varphi}, \varphi) dt = \int_0^{\infty} \left( \sum_{k=1}^m \kappa_k^2 \dot{\varphi}_k^2 + \varphi_k^2 \right) dt \quad (8)$$

A Lyapunov function candidate as in (9) can be used to determine the system's asymptotic stability:

$$V(t) = 0.5 * \varphi(x, t)^2 \quad (9)$$

The following inequality is fulfilled when the condition of  $\kappa > 0$  is met:

$$\dot{V}(t) = \varphi(x, t) \dot{\varphi}(x, t) = -\frac{1}{\kappa} \varphi(x, t)^2 < 0 \quad (10)$$

Figure 2 illustrates the system's phase profile as well as the SC law's stability features, and also shows the convergence to the manifold. The steady-state operating point is the origin if the error is equal to 0. A straight line through the origin with a slope  $(-1/\kappa)$  is represented by Equation (3). The operational point of the system converges to the straight line (the control manifold) and then moves along it to the origin.

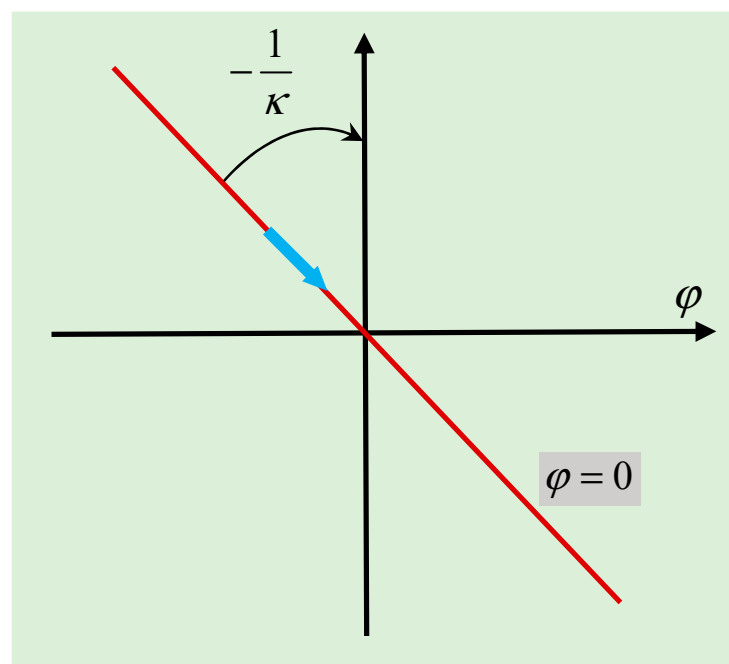


**Figure 2.** Geometric description of SC in the phase plane.

The schematic representation, illustrating the suggested controller's computations, is shown in Figure 3.

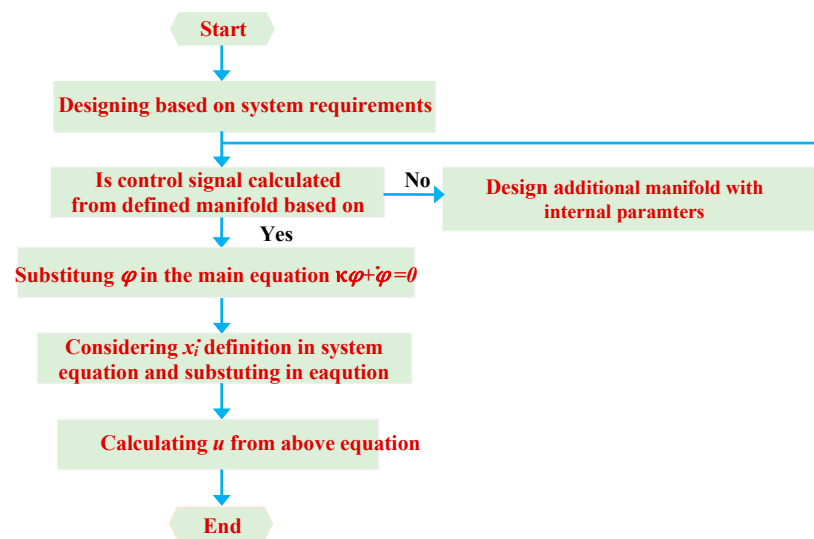


Figure 3. Schematic diagram of the proposed SC algorithm.

## 2.2. Principle of Fnn Approximator

It is known that FNNs are universal estimators and have exceptional functions in controller design and identification. The properties of the FNN, such as accelerating the learning process and finer granularity to make decisions [22], make it appropriate for real-time control systems and are capable of enhancing the control precision, stability, and flexibility of the system. The FNN is an implementation of fuzzy logic (FL) with trainable parameters similar to an ANN, which comprises four layers of neurons. They are the input layer-1; the membership layer-2; the rule layer-3; and the output layer-4, respectively, all of which are depicted in Figure 4. The key characteristic of the FNN is its ability to describe the human-like reasoning and successfully cope with experience by using conditional fuzzy IF-THEN rules to build a mapping from an input vector  $x$  to an output vector  $y$ , which may be expressed as:

$$R^l : \text{If } x_1 \text{ is } A_1^l(x_1), x_2 \text{ is } A_2^l(x_2), \dots, x_n \text{ is } A_n^l(x_n) \text{ Then } y_1 \text{ is } B_1^l, y_2 \text{ is } B_2^l, \dots, y_m \text{ is } B_m^l \quad (11)$$

where  $L = 1, 2, \dots$ , with  $L$  representing the overall number of IF-THEN rules,  $x = [x_1, x_2, \dots, x_n]^T$  and  $y = [y_1, y_2, \dots, y_m]^T$  characterize the input and output parameter vectors of FNN.  $A_1^l$  and  $B_1^l$  are the linguistic variables of the fuzzy sets, expressed by their membership function vectors  $\mu_{A_1^l}(x_i)$  and  $\mu_{B_1^l}(y)$ , respectively.

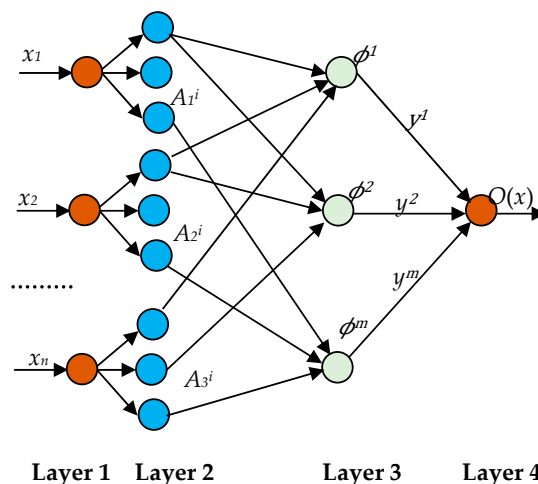


Figure 4. Structure of a FNN approximator with four layers.

Based on the singleton fuzzifier, product inference model, and center-average defuzzifier, the final output  $O(x)$  can be obtained by the FNN estimator as in [22]:

$$o(x) = \frac{\sum_{l=1}^L \left( \prod_{i=1}^n \mu_{A_i^l}(x_i) \right) \bar{y}_j^l}{\sum_{l=1}^L \left( \prod_{i=1}^n \mu_{A_i^l}(x_i) \right)} \quad (12)$$

where  $\bar{y}_j^l$  is the point in at which  $\mu_{B_j^l}(y_j)$  attains its optimal value ( $\mu_{B_j^l}(y_j) = 1$  considering).

If  $\bar{y}_j^l$  are selected as the free parameter vector, the FNN approximator (12) becomes an adaptive FNN. Then, it can be expressed in compact form as:

$$y_j(x) = \sum_{l=1}^L \bar{y}_j^l = w^T \phi(x) \quad (13)$$

where  $w = [\bar{y}_j^1, \bar{y}_j^2, \dots, \bar{y}_j^L]^T \in R^L$  is called the regulating parameter vector, and  $\phi(x) = [\phi_1(x), \phi_2(x), \dots, \phi_L(x)]^T \in R^L$  is the vector of fuzzy primary function, or the fuzzy basis function (FBFs) is obtained by (14):

$$\phi_j(x) = \frac{\prod_{i=1}^n \mu_{A_i^l}(x_i)}{\sum_{j=1}^L \left( \prod_{i=1}^n \mu_{A_i^l}(x_i) \right)} \quad (14)$$

**Remark 1.** It ought to be indicated that the complexity of the designed AFN-FTSC algorithm is dependent on the complexity of FNN approximator. Suppose that the number of FNN inputs is  $n$ , and the number of fuzzy variables is  $m$ .

The complexity of the AFN-FTSC is composed of the fuzzy layer (layer 2) and fuzzy inference layer (layer 3). The complexity of the fuzzy layer is  $O(n \times m)$ , and the complexity for the fuzzy inference production layer is  $O(m^2)$ . The total complexity of the AFN-FTSC algorithm is  $O(n \times m) + O(m^2)$ .

### 3. Mathematical Model of Buck DC/DC Converter

Figure 5 shows a buck DC/DC converter that connects an input DC voltage  $V_{in}$  with a DC load  $R_o$  having its output voltage as  $V_o$ . The buck DC/DC converter encompasses an adjustable switch  $Q$ , diode  $D$ , an inductor  $L$  with  $i_L$  as the current flowing through it, a capacitor  $C$  with  $i_C$  as the current flowing through it, and a load resistor  $R_o$  where  $i_R$  is the load current.

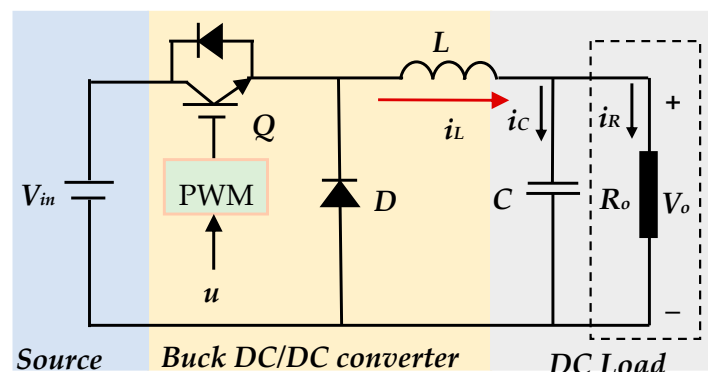


**Figure 5.** The circuit model of buck DC/DC converter.

Due to the nonlinear behavior of the diode and MOSFET/IGBT switch, the buck DC/DC converter has a nonlinear structure. Moreover, there are two charging elements

an inductor and capacitor for which the mathematical model for the system will be a second-order one.

The dynamic of the system in Figure 5 will be represented by the change in the voltage  $V_o$  across  $R_o$ , which is also the voltage across  $C$ . Similarly,  $i_L$  will change as it flows through  $L$ . Since the switch will be in two modes, ON and OFF, there will be two stages.

When the switch is turned ON in the first stage, equations representing the state-space model can be stated in the following way [23]:

$$\begin{cases} \frac{di_L}{dt} = -\frac{1}{L}V_o + \frac{V_{in}}{L}u \\ \frac{dV_o}{dt} = \frac{1}{C}i_L - \frac{1}{RC}V_o \end{cases} \quad (15)$$

In the second stage, the switch is turned OFF. In this case, the diode  $D$  is in forwarding bias and the circuit is then equivalent to a parallel RLC circuit.

For this circuit, the equation representing the state-space model can be written as follows:

$$\begin{cases} \frac{di_L}{dt} = -\frac{1}{L}V_o + \frac{V_{in}}{L}u \\ \frac{dV_o}{dt} = \frac{1}{C}i_L - \frac{1}{RC}V_o \end{cases} \quad (16)$$

At this stage, the complete dynamical average model can be obtained by combining (15) and (16) as:

$$\begin{cases} \frac{di_L}{dt} = -\frac{1}{L}V_o + \frac{V_{in}}{L}u \\ \frac{dV_o}{dt} = \frac{1}{C}i_L - \frac{1}{RC}V_o \end{cases} \quad (17)$$

Where  $u$  is the control input, which is recognized as 0 when the switch  $Q$  is turned OFF and 1 when it is turned ON, considering the capacitor voltage and its derivative as system state variables  $x_1$  and  $x_2$ , respectively. Equation (18) represents the final model of the buck DC/DC converter, which is utilized to design the proposed composite controller as discussed in the section below:

$$\begin{cases} \dot{x}_1 = x_2 \\ \dot{x}_2 = -\frac{x_1}{LC} - \frac{x_2}{RC} + \frac{V_{in}}{LC}u \end{cases} \quad (18)$$

#### 4. Proposed Robust AFN-FTSC Design

This section focuses on determining the switching control input  $u$  using the proposed AFN-FTSC law for system (18) as a function of state coordinates ( $e_1, e_2$ ), which gives the desired value of converter output voltage  $V_{o-ref}$  without the prior modeling information and is subject to the requirement that the voltage error converges to origin asymptotically in finite-time  $t_r$ , i.e., Further analyses are presented to comprehensively analyze the stability and reachability of the proposed method. The determination of the switching control law is presented below.

##### 4.1. Determination of the Control Law

Since the regulation of  $V_o$  is the main task, the design process needs to start by defining the error for this output voltage.

(1) Step 1:

Based on the design criterion, the tracking error ( $e_1$ ) for  $V_o$  can be expressed as:

$$e_1 = x_1 - V_{o-ref} \quad (19)$$

$$\dot{e}_1 = e_2 = x_2 - \dot{V}_{o-ref} \quad (20)$$

where  $V_{o-ref}$  is the reference output voltage and its dynamic will be as:

$$\dot{e}_1 = e_2 = \frac{i_L}{C} - \frac{V_o}{RC} - \dot{V}_{o-ref} \quad (21)$$

## (2) Step 2:

As seen in [24], a special variable referred to as the nonlinear macro-variable function must be added as follows:

$$\varphi = \dot{e}_1 + ae_1 + be_1^{p/q} \quad (22)$$

where  $a$  and  $b$  are the macro-variable parameters,  $p$  and  $q$  are positive odd constants, which satisfy the following criterion:  $1 < p/q < 2$ .

## (3) Step 3:

A constraint imposing preferred dynamics to the macro-variable is chosen as:

$$\kappa \dot{\varphi} + \varphi = 0 \quad (23)$$

where  $\kappa$  is a positive parameter that obliges the designer select speed convergence to the desired attractor.

## (4) Step 4:

To determine the control input while satisfying the synergetic mode reaching condition,  $\varphi = 0$ , the dynamics of the system (22) may be described as:

$$\dot{e}_1 + ae_1 + be_1^{p/q} = 0 \quad (24)$$

At this point, the reaching time  $t_r$  for  $e_1$  can be obtained by integrating Equation (20), which may be calculated as:

$$\dot{\varphi} = \dot{e}_2 + a\dot{e}_1 + b\frac{p}{q}e_1^{(p/q)-1}\dot{e}_1 \quad (25)$$

where  $e_1(0)$  is the initial value of  $e_1(t)$ . The time derivative of  $\varphi$  can be determined as:

$$\dot{\varphi} = \dot{e}_2 + a\dot{e}_1 + b\frac{p}{q}e_1^{(p/q)-1}\dot{e}_1 \quad (26)$$

By combining (23) and (26), we get (27):

$$\dot{e}_2 + a\dot{e}_1 + b\frac{p}{q}e_1^{(p/q)-1}\dot{e}_1 = -\frac{1}{\kappa}\varphi \quad (27)$$

Rewriting Equation (27), can be expressed as:

$$\dot{e}_2 = -\frac{x_1}{LC} - \frac{x_2}{RC} + \frac{V_{in}}{LC}u - \ddot{V}_{o-ref} \quad (28)$$

We specified the following abstractions for the controller design:

$$g(x) = \frac{V_{in}}{LC} \text{ and } f(x) = -\frac{x_1}{LC} - \frac{x_2}{RC}$$

Solving for the FTSC law,  $U_{FTSC}$ , guides to an enhanced reaching law (29):

$$u_{FTSC} = \frac{1}{g(x)} \left[ \ddot{V}_{o-ref} - f(x) + \frac{1}{\kappa}\varphi - a\dot{e}_1 - b\frac{p}{q}e_1^{(p/q)-1}\dot{e}_1 \right] \quad (29)$$

The next subsection follows the overall stability analysis with this SC law.

#### 4.2. Stability Analysis

The Lyapounov theorem can be used to assess the stability of the system as in (30):

$$V_1 = 0.5 * \varphi^2 \quad (30)$$

The time derivative of Equation (30), using Equations (23) and (27), can be written as:

$$\dot{V}_1 = \varphi \dot{\varphi} = \varphi \left( \dot{e}_2 + a\dot{e}_1 + b \frac{p}{q} e_1^{(p/q)-1} \dot{e}_1 \right) = \varphi \left( -\frac{1}{\kappa} \varphi \right) = -\frac{1}{\kappa} \varphi^2 \leq 0 \quad (31)$$

As a result, the regulator (29) may satisfy the system's overall stability criteria.

#### 4.3. Approximation of $f(x)$ and $g(x)$ Based on FNN

Sadly, in the practical application, the nonlinear system terms  $f(x)$  and  $g(x)$  are unknown and difficult to determine precisely. As a consequence, there is no way to apply the conventional FTSC law (29), of which the terms  $f(x)$  and  $g(x)$  are known to be scalar. To tackle this difficulty and guarantee global stability, a FNN model using the universal approximation approach is developed in the following theorem to approximate the nonlinear and unknown terms  $f(x)$  and  $g(x)$  in (29) through adaptive laws.

**Theorem 1.** Considering system (18) with unknown terms  $f(x)$  and  $g(x)$ , and design the macro-variable in the form of (22). If the updated AFN-FTSC controller  $u_{AFN-FTSC}$  is constructed as (32):

$$u_{AFN-FTSC} = \frac{1}{\hat{g}(x|w_g)} \left[ \ddot{V}_{o-ref} - \hat{f}(x|w_f) + \frac{1}{\kappa} \varphi - a\dot{e}_1 b \frac{p}{q} e_1^{(p/q)-1} \dot{e}_1 \right] \quad (32)$$

Next, the tracking error and its first derivative converge to zero in finite-time, where  $\hat{f}(x|w_f)$  and  $\hat{g}(x|w_g)$  represent the FNN estimates of the terms  $f(x)$  and  $g(x)$ . These functions can be estimated through Equations (33) and (34):

$$\hat{f}(x|w_f) = w_f^T \phi_f(x) \quad (33)$$

$$\hat{g}(x|w_g) = w_g^T \phi_g(x) \quad (34)$$

where  $\phi_f(x)$  and  $\phi_g(x)$  are the transfer functions from the input layer to the rule layer,  $w_f$  and  $w_g$  are the connection weights of FNN. By updating the network weights, the system uncertainties can be estimated adaptively.

**Theorem 2.** Considering the nonlinear model (18) with the input signal (32), and if the FNN-based adaptive laws are designed as:

$$\dot{\hat{w}}_f = -\mu_1 \varphi \phi_f(x) \quad (35)$$

$$\dot{\hat{w}}_g = -\mu_2 \varphi \phi_g(x) \quad (36)$$

where  $\eta_1$  and  $\eta_2$  are arbitrary positive parameters.

**Assumption 1.** Suppose  $x$  be a member of a compact set  $R^n = \{x \in R^n : |x| \leq K_x < +\infty\}$ , with  $K_x$  is a constant. The ideal FNN weights  $w_f^*$  and  $w_g^*$  are located in the convex area shown below:

$$\Delta_f = \{w_f \in R^n : |w_f| \leq H_f\} \quad (37)$$

$$\Delta_g = \{w_g \in R^n : |w_g| \leq H_g\} \quad (38)$$

where  $H_f$  and  $H_g$  are designed parameters, and the radius  $\Delta_f$  and  $\Delta_g$  are limitations for  $w_f$  and  $w_g$ . The universal approximation theory states that there is an ideal FNN weights  $w_f^*$  and  $w_g^*$  satisfies:

$$w_f^* = \underset{w_f \in \Delta_f}{\operatorname{argmin}} \left\{ \sup_{x \in R^n} |\hat{f}(x|w_f) - f(x)| \right\} \quad (39)$$

$$w_g^* = \underset{w_g \in \Delta_g}{\operatorname{argmin}} \left\{ \sup_{x \in R^n} |\hat{g}(x|w_g) - g(x)| \right\} \quad (40)$$

Consequently,  $f(x)$  and  $g(x)$  are approximated to arbitrary accuracy by the FNN approximators (35) and (36) as the below assumption.

**Assumption 2 (See [25]).** For each given real smooth variable  $f(x)$  and  $g(x)$  defined on a compact set  $x \in R^n$  and for any arbitrary  $\varepsilon_f > 0$  and  $\varepsilon_g > 0$ , there exists a FNN approximator and in the formula of (41) and (42) so that:

$$\sup_{x \in R^n} |\hat{f}(x|w_f) - f(x)| < \varepsilon_f \quad (41)$$

$$\sup_{x \in R^n} |\hat{g}(x|w_g) - g(x)| < \varepsilon_g \quad (42)$$

**Remark 2.** By using the FNN approximator designed above, the FNN gains  $\phi_f(x)$  and  $\phi_g(x)$  can be scheduled adaptively according to the variety of  $x_1$  and  $x_2$ . Then, the minimum approximation error can be obtained as:

$$\varepsilon = [\hat{f}(x|w_f^*) - f(x)] + [\hat{g}(x|w_g^*) - g(x)]u \quad (43)$$

where  $\varepsilon$  is bounded by a positive constant  $\varepsilon \leq \varepsilon_{\max}$ . The dynamic of the macro-variable is calculated by replacing (43) into (23):

$$\dot{\varphi} = [\hat{f}(x|w_f^*) - f(x)] + [\hat{g}(x|w_g^*) - g(x)]u - \frac{1}{\kappa}\varphi + \varepsilon \quad (44)$$

Leading, after some straightforward manipulations, to:

$$\dot{\varphi} = (w_f^{*T} - w_f^T)\phi(x) + (w_g^{*T} - w_g^T)\phi(x)u - \frac{1}{\kappa}\varphi + \varepsilon \quad (45)$$

From the above expression, one may write:

$$\dot{\varphi} = \hat{w}_f^T \phi(x) + \hat{w}_g^T \phi(x)u - \frac{1}{\kappa}\varphi + \varepsilon \quad (46)$$

where  $\hat{w}_f = w_f^* - w_f$  and  $\hat{w}_g = w_g^* - w_g$  are the error between  $w$  and the ideal weight  $w^*$ .

Stability demonstration: Let us choose the Lyapunov function candidate as:

$$V = 0.5 * \varphi \left( \varphi^2 + \frac{1}{\mu_1} \hat{w}_f^T \hat{w}_f + \frac{1}{\mu_2} \hat{w}_g^T \hat{w}_g \right) \quad (47)$$

The time derivative of Equation (47) gives:

$$\dot{V} = \varphi \dot{\varphi} + \frac{1}{\mu_1} \hat{w}_f^T \dot{\hat{w}}_f + \frac{1}{\mu_2} \hat{w}_g^T \dot{\hat{w}}_g \quad (48)$$

Substituting (46) into (48), we can get (49):

$$\dot{V} = \varphi \left( \hat{w}_f^T f(x) + \hat{w}_g^T f(x)u - \frac{1}{\kappa}\varphi + \varepsilon \right) + \frac{1}{\mu_1} \hat{w}_f^T \dot{\hat{w}}_f + \frac{1}{\mu_2} \hat{w}_g^T \dot{\hat{w}}_g \quad (49)$$

We utilize the following Equations (50) and (51):

$$\dot{\hat{w}}_f = \dot{w}_f \quad (50)$$

$$\dot{\hat{w}}_g = \dot{w}_g \quad (51)$$

Substituting (50) and (51) into (49) leads to:

$$\dot{V} = -\frac{1}{\kappa}\varphi^2 + \varphi\varepsilon + \frac{1}{\mu_1}\hat{w}_f^T(\mu_1\varphi f(x) + \dot{w}_f) + \dots + \frac{1}{\mu_2}\hat{w}_g^T(\mu_2\varphi f(x)u + \dot{w}_g) \quad (52)$$

The parameter vector  $\dot{w}_f$  and  $\dot{w}_g$  is adapted according to the (35) and (36) laws. Then, Equations (23) and (52) bring about the following result:

$$\dot{V} \leq -\frac{1}{\kappa}\varphi^2 + \varphi\varepsilon \quad (53)$$

**Remark 3.** The FNN approximation error  $\varepsilon$  should preferably be equal to zero, in this situation  $\dot{V} \leq -\frac{1}{\kappa}\varphi^2 \leq 0$  emphasizes the definiteness of the negative, thus the regulated system is stable. In reality, the estimation error is always present, hence the stability of the system cannot be assured. To finish the analysis and check the asymptotic convergence of the tracking error, we must demonstrate that  $\varphi \rightarrow 0$  as  $t \rightarrow \infty$ . Besides, suppose that  $\|\varphi\| \leq \tau$ , then Equations (53) can be reformulated as:

$$\dot{V} \leq -\frac{1}{\kappa}\tau|\varphi| + \tau|\varepsilon| \quad (54)$$

Integration on both sides of Equation (54) provides:

$$\int_0^t |\varphi| dt \leq \frac{\kappa}{\tau} (|V(0)| - |V(t)|) + \kappa \int_0^t |\varepsilon| dt \quad (55)$$

Equation (42) means that all the signals are homogeneously bounded in the closed-loop system. Then, we do have  $\varphi \in L_1$ , from (41), we recognize that the macro-variable is limited and every term in (42) is limited, hence  $(\varphi, \dot{\varphi}) \in L_\infty$ , making use of the Barbalat lemma [26]. We can conclude that the tracking error converges to zero asymptotically, which confirms the stability condition of a closed-loop system. Consequently, the stable control performance of the buck DC/DC converter can be ensured without the necessity of system information. Figure 6 shows the overall schematic diagram of the developed AFN-FTSC algorithm.

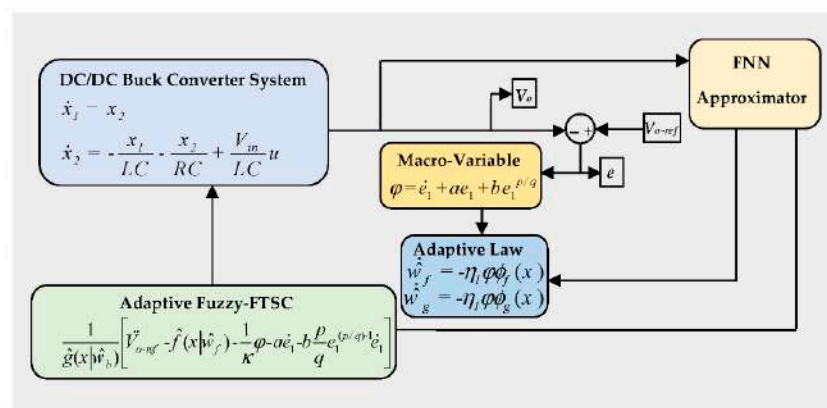


Figure 6. Block diagram for proposed AFN-FTSC controller.

## 5. Controller Performance Evaluation

Since the satisfactory control performance will require properly selecting user-defined parameters (please note that the proposed method is less sensitive than existing control methods), some discussions have been included in the following subsection.



### 5.1. Selection of the User-Defined Parameters

One of the key goals to design and implement new controllers is to achieve a faster response during the transient [27]. For the proposed AFN-FTSC scheme, the larger values of these user-defined parameters will ensure fast-transient performance. However, such large user-defined parameters or gains are not always used, as these degrade the performance of the controller by amplifying the overshoot and providing the undesirable disturbance rejection. Therefore, it is essential to make a trade-off among various performance factors while tuning these gains. These performance factors must include the desired criteria for tracking (e.g., fewer or no offsets, small overshoots, fast settling time, etc.), the appropriate level of the disturbance rejection, and robustness against parametric constraints. Since the major focus of this work is on the disturbance rejection and resilience against uncertainties, tall user-defined parameters are carefully chosen to ensure an appropriate tracking performance. For the proposed AFN-FTSC algorithm, it is found that the most sensitive parameter is  $(p/q)$ , which is basically associated with the voltage tracking error. The dynamic performance depicting the output voltage with the proposed AFN-FTSC is depicted in Figure 7 for various values of  $(p/q)$ . This figure shows the minimum value of the voltage overshoot when the value of  $(p/q)$  is equal to 2; however, the settling time is much higher than other values of  $(p/q)$ . At the same time, the voltage overshoot and the settling time are 0.15 V and 9.44 ms, respectively, when the value of  $(p/q)$  is 1.5, and this is more acceptable as compared to other values in terms of both voltage overshoot and settling time.

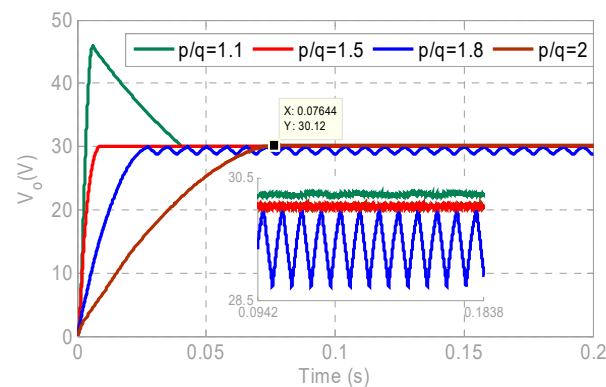


**Figure 7.** The output voltage of the converter for different values of  $(p/q)$  with the designed controller.

The voltage overshoot and settling time for different values of  $(p/q)$  with the designed AFN-FTSC are detailed in Table 1.

**Table 1.** Parameter sensitivity analysis.

$p/q$	1.1	1.5	1.8	2.0
<b>Voltage overshoot (V)</b>	15.85	0.13	0.11	0.07
<b>Settling-time (ms)</b>	42.96	9.44	27.60	75.44

To ensure a fair comparison, the acquired results are compared to that of the existing FTSC while maintaining the same value of the most sensitive gain parameter, i.e.,  $(p/q = 1.5)$  for both controllers. Similarly, the values of other user-defined parameter values can be determined, and these are presented in Table 2.

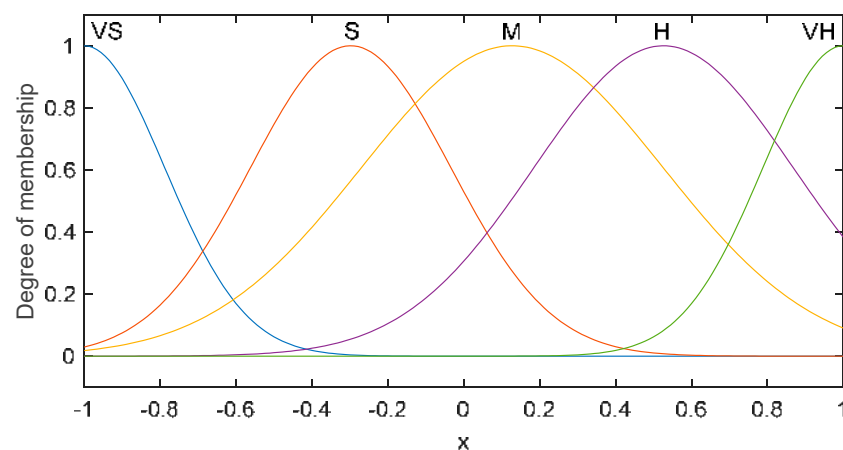
**Table 2.** Regulator Specifications.

Regulator	Parameters	Gain Value
AFN-FTSC	$\kappa$	0.005
	$a$	200
	$b$	300
	$p$	3
	$q$	2
	$\mu_1$	500
	$\mu_2$	800
FTSC	$\kappa$	0.005
	$a$	200
	$b$	300
	$p$	3
	$q$	2

In the FNN estimator, we can specify a set of five decision variables regularly distributed on a universe of discourse  $[-1,1]$ , as follows:

$$\mu_f^k = \mu_g^k = \exp[-(x + 4 - 1.6(k - 1)^2)], k = 1, \dots, 5 \quad (56)$$

$i = 5$ , which means that there are 25 rules to estimate the unknown terms. The selected 25 rules can cover the entire space and approximate any non-linear function. The member function degree is illustrated in Figure 8.

**Figure 8.** Membership function of  $x$ .

The FNN weights are selected as follows:

$$\begin{bmatrix} w_f \\ w_g \end{bmatrix} = \begin{bmatrix} w_f^1 & w_f^2 & w_f^3 & w_f^4 & w_f^5 \\ w_g^1 & w_g^2 & w_g^3 & w_g^4 & w_g^5 \end{bmatrix} \quad (57)$$

The initial values for the FNN weights are selected in a random way, and the vector of fuzzy basis functions was constructed by (12). Using these gain parameters, the designed AFN-FTSC and existing FTSC are implemented in the following under different operating points of the buck DC/DC converter.

### 5.2. Experimental Validation

In this part, the efficacy of the suggested AFN-FTSC technique for regulating the output voltage of a buck DC/DC converter is demonstrated through a real-time implementation on dSPACE 1103 platforms (Figure 9). All system parameters are carefully chosen by keeping the practical conditions in mind, which are given in Table 3.

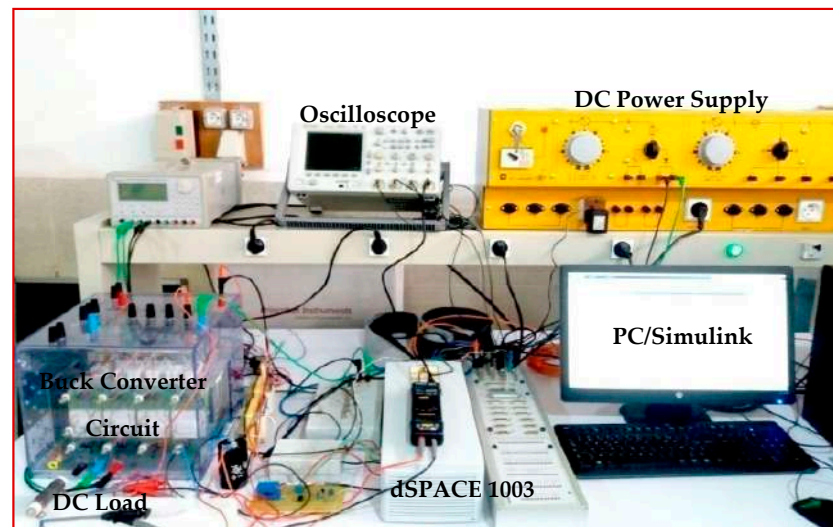


**Figure 9.** The experimental prototype of the buck DC/DC converter.

**Table 3.** System Parameters.

Parameter	Value
$V_{in}$	100 V
$R_o$	40/80/40 $\Omega$
$V_{o\_ref}$	20/30/50 V
$L$	7 mH
$C$	800 $\mu$ F
$f_s$	20 kHz

To show the efficacy of the designed AFN-FTSC algorithm, variations in the output reference voltage, input supply voltage, and load resistance are done based on the values in Table 3. However, the nominal output voltage of the converter is set at 50 V with an input voltage of 100 V during the standard conditions, i.e., while considering no disturbances. To deploy the AFN-FTSC algorithm for the buck DC/DC converter, the sampling frequency, and the switching frequency are considered as 200 kHz and 20 kHz, respectively. The superiority of the AFN-FTSC is analyzed against an existing FTSC as proposed in [14] in terms of tracking error, overshoot, and settling time. The performance of the designed AFN-FTSC algorithm is validated under a variety of operating scenarios: variations in input supply voltage, load resistance, and output reference voltage as demonstrated through the following four cases:

- Controller performance under variations in the load resistance,
- Controller performance under variations in the input supply voltage,
- Controller performance under start-up transient,
- Controller performance under variations in the output reference voltage,

**Case I:** Output voltage regulation with variations in the load resistance.

In this scenario, the test is conducted to justify the load disturbance rejection capacity of the proposed AFN-FTSC algorithm while making a comparison with the FTSC algorithm. For this purpose, the effects of only variations in the load resistance are considered, while the output reference voltage remains constant at 50 V. In this test, the load resistance of the buck DC/DC converter is decreased from 80  $\Omega$  to 40  $\Omega$ , conversely. With such changes in the load resistance, the dynamic responses of the Buck DC/DC converter are represented by two states: output voltage ( $V_o$ ) and inductor current ( $i_L$ ), as illustrated in Figure 10. The output voltage quickly settles down to its reference value without affecting the steady-state behavior while the designed one is used. However, the overshoots are a bit higher with higher settling times, especially at the instant of changes, i.e., at the decrease in load

resistance when the existing FTSC is used. Hence, Figure 10a provides an observation that the designed AFN-FTSC controller can stabilize the output voltage very quickly to its desired value without having any significant impact even with a large variation in the load resistance. Figure 10a also confirms the faster settling time with less transient with the AFN-FTSC controller during the post-disturbance operation while making its comparison with the FTSC controller.

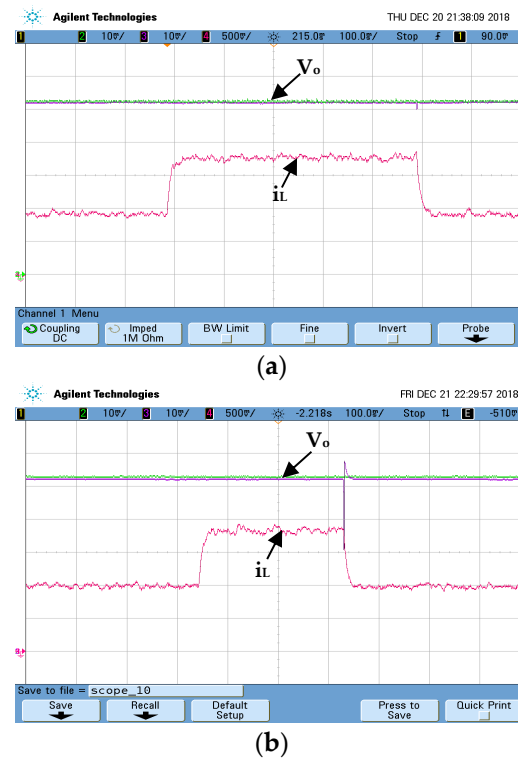


**Figure 10.** Dynamic performance of the converter under load-resistance variations ( $V_o$ : 10 V/div,  $i_L$ : 0.25 A/div and time: 100 ms/div): (a) AFN-FTSC controller, (b) FTSC controller.

Several quantitative factors such as the peak value, overshoot, undershoot, and settling time are calculated to validate the performance of the designed AFN-FTSC against the FTSC, where these values for both controllers are captured in Table 4. The designed AFN-FTSC outperforms the existing FTSC in all aspects that can also be found in Table 4. The next case study analyzes and compares the performance of the designed and existing controllers against variations in the input supply voltage.

**Table 4.** Peak value, overshoot, undershoot, and settling time with variations in the load.

Controller	Peak Value (V)	Overshoot (%)	Undershoot (%)	Settling Time (ms)
AFN-FTSC	0	0	6.66	2
FTSC	8	16	40	20

#### Case II: Output voltage regulation with variations in the input supply voltage

This test considers the variation in the input supply voltage to show the superiority of the designed AFN-FTSC over the existing FTSC algorithm. The input voltage is rated at 0 V at the start of the test, and it is suddenly raised to 100 V at  $t = 0.25$  s. However, the output reference voltage is kept constant at 30 V. The corresponding dynamic responses of different states for the converter are shown in Figure 11. As illustrated in Figure 11a, the designed AFN-FTSC can efficiently eliminate the effects of fluctuations in the input as evidenced by the proper tracking of the output reference voltage. On the other hand, the existing FTSC fails to realize the desired voltage tracking performance when responding

to changes in input supply voltage. The result in Figure 11b shows that the FTSC cannot cope with changes in the input supply voltage, however, the designed AFN-FTSC does not experience any problem to maintain the desired performance.

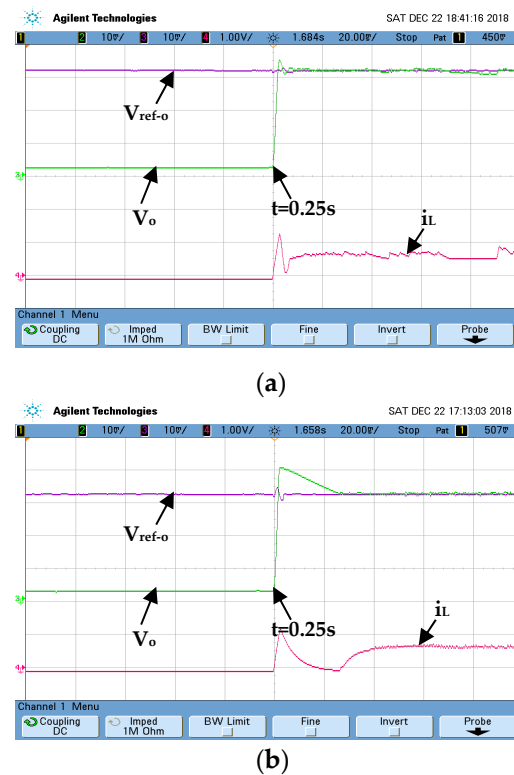


**Figure 11.** Dynamic performance of the converter under input supply voltage variations ( $V_o$ : 10 V/div,  $i_L$ : 0.5 A/div and time: 20 ms/div): (a) AFN-FTSC controller, (b) FTSC controller.

The peak value, overshoot, and settling time are calculated for this scenario and presented in Table 5, which clearly demonstrates the effectiveness of the AFN-FTSC over the FTSC. From Table 5, it can be seen that the output voltage recovery time of the AFN-FTSC is 5 ms, whereas it is 28 ms for the existing FTSC. Furthermore, from Table 5, it can be seen that the voltage fluctuation with the designed AFN-FTSC is 3 V, while it is 11 V with the existing FTSC. In comparison to the existing FTSC controller, the designed AFN-FTSC controller has a shorter settling time and lower voltage changes, as shown by the data analysis.

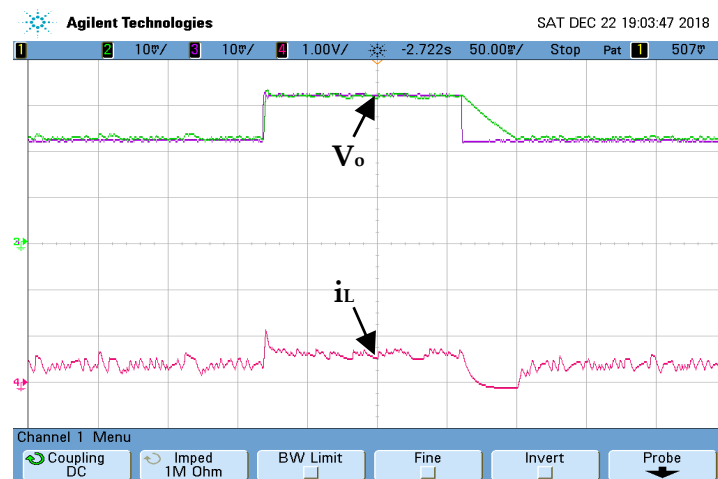
**Table 5.** Peak value, overshoot, and settling time with variations in the input voltage.

Control Strategy	Peak Value (V)	Overshoot (%)	Undershoot (%)	Settling Time (ms)
AFN-FTSC	3	10	0	5
FTSC	11	36.66	0	28

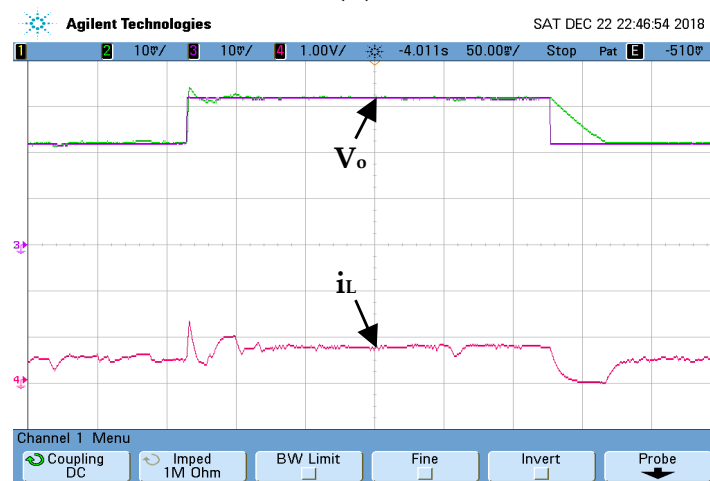
In the next case, the converter's reference output voltage variation is regarded as an external perturbation to the converter, which is discussed in the following subsection.

### Case III: Output voltage regulation with variations in the output reference voltage.

This test counts variations in the output reference voltage to demonstrate the robustness of both controllers. At the start of the test, the reference voltage is rated at 20 V and then suddenly changed to 30 V and vice-versa. Under this disturbance, the dynamic responses of both states ( $V_o$  and  $i_L$ ) are depicted in Figure 12a,b. These responses clearly demonstrate the superior capability of the AFN-FTSC controller (Figure 12a) for tracking output reference voltage, as the existing FTSC controller fails to do so (Figure 12b).



(a)



(b)

**Figure 12.** Dynamic performance of the converter under output reference voltage variations ( $V_o$ : 10 V/div,  $i_L$ : 0.5 A/div and time: 50 ms/div): (a) AFN-FTSC controller, (b) FTSC controller.

The peak value, overshoot, undershoot, and settling time are calculated for this scenario and presented in Table 6. This table clearly shows very satisfactory performance in terms of both settling time and overshoot with the designed AFN-FTSC over the FTSC.

**Table 6.** Peak value, overshoot, undershoot, and settling time with variations in the reference voltage.

Control Strategy	Peak Value (V)	Overshoot (%)	Undershoot (%)	Settling Time (ms)
AFN-FTSC	0	0	0	2
FTSC	2	6.66	0	40

The voltage tracking capability of each controller is evaluated using a sin-wave reference output voltage. As illustrated in Figure 13, the AFN-FTSC not only offers better precise results, but it also eliminates chattering.

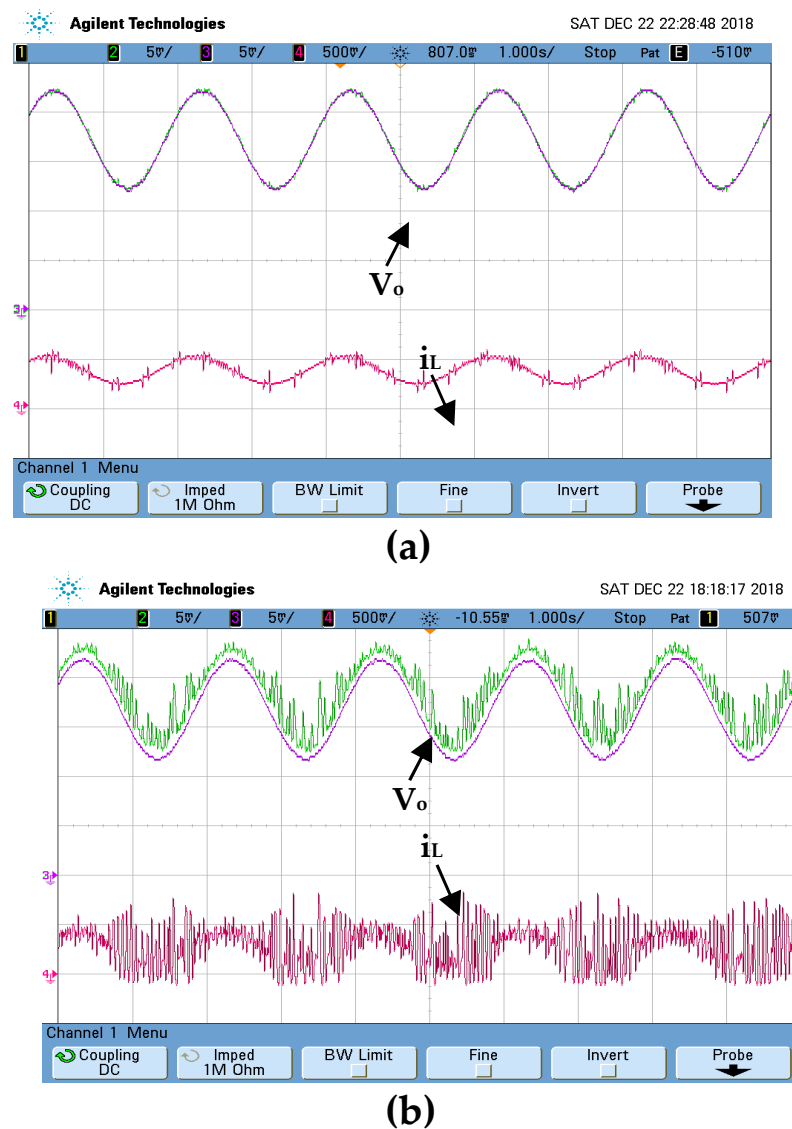


**Figure 13.** Dynamic performance of the converter under sinusoidal wave in the output voltage reference ( $V_o$ : 10 V/div,  $i_L$ : 0.5 A/div, and time: 1 s/div): (a) AFN-FTSC controller, (b) FTSC controller.

The voltage tracking capability of each controller is evaluated using a triangular-wave reference output voltage (Figure 14). The results indicate the advantage of the considered AFN-FTSC over the FTSC algorithm in terms of output voltage tracking. The studied AFN-FTSC displays a small tracking error (Figure 14a).

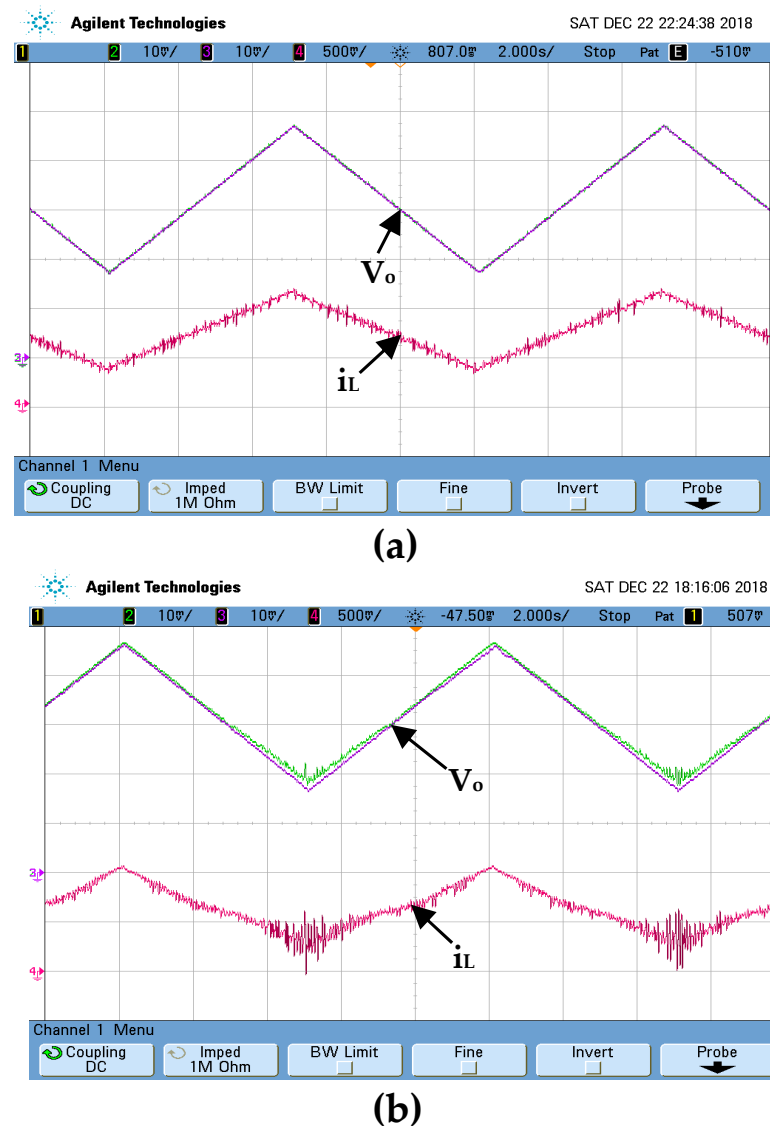


**Figure 14.** Dynamic responses of the converter with triangular-wave variations in the output voltage reference ( $V_o$ : 10 V/div,  $i_L$ : 0.25 A/div and time: 2 s/div): (a) AFN-FTSC controller, (b) FTSC controller.

**Case IV:** Output voltage regulation under nominal start-up in the reference voltage.

The purpose of this test is to evaluate the robustness of both controllers under nominal start-up in the output voltage reference. The output voltage of the converter, as presented in Figure 15, is observed for this case, which clearly shows the settling time as almost 5 ms with the AFN-FTSC. However, this settling-time is a bit larger, i.e., around 20 ms if the FTSC is used. Similarly, the FTSC exhibits an overshoot of 20%, while there are no overshoots when the AFN-FTSC is used. Therefore, it is also possible to deduce that the AFN-FTSC method provides a superior dynamic response to the existing FTSC method.

The peak value, overshoot, undershoot, and settling time are calculated for this case study and presented in Table 7. This table clearly shows very satisfactory performance in terms of both maximum overshoot and settling time with the suggested AFN-FTSC over the FTSC. Hence, the overall performance of the AFN-FTSC significantly dominates that of the FTSC for all cases.



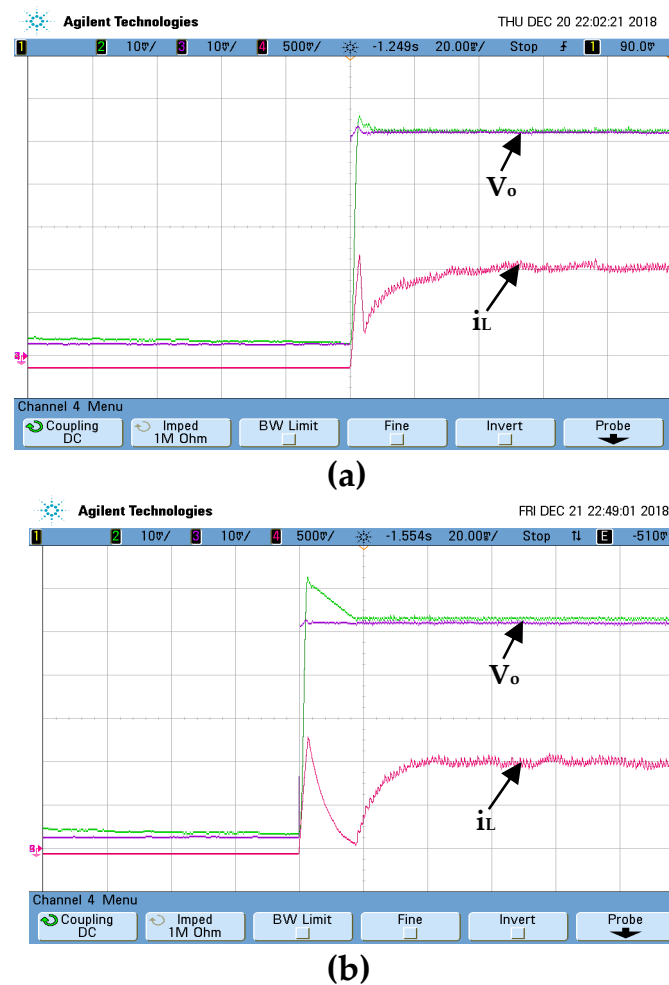


**Figure 15.** Dynamic responses of the converter under nominal start-up in the output voltage reference ( $V_o$ : 10 V/div,  $i_L$ : 0.25 A/div and time: 20 ms/div): (a) AFN-FTSC controller, (b) FTSC controller.

**Table 7.** Peak value, overshoot, undershoot, and settling time with variations in reference voltage.

Controller	Peak Value (V)	Overshoot (%)	Undershoot (%)	Settling Time (ms)
AFN-FTSC	3	2	0	5
FTSC	10	20	0	20

### 5.3. Experimental Validation

A comparative study between the proposed and existing controllers was performed, using integrals of error-based performance indices that are defined as the integral of absolute error (IAE), integral of squared error (ISE), and an integral of time-weighted squared error (ITSE). The mathematical expressions for these indices can be expressed as in [26]:

$$IAE = \int_0^T |e(t)| dt, ISE = \int_0^T e(t)^2 dt, \&ITSE = \int_0^T te(t)^2 dt \quad (58)$$

where  $T$  denotes simulation time with  $e(t)$  as the error signal. The smaller value of these indices indicates the better performance, as these indices basically represent the deviation from the ideal condition. All these three indices are calculated for both controllers and presented in Figure 16, which clearly demonstrates significantly smaller values for the AFN-FTSC algorithm when compared with the FTSC algorithm.

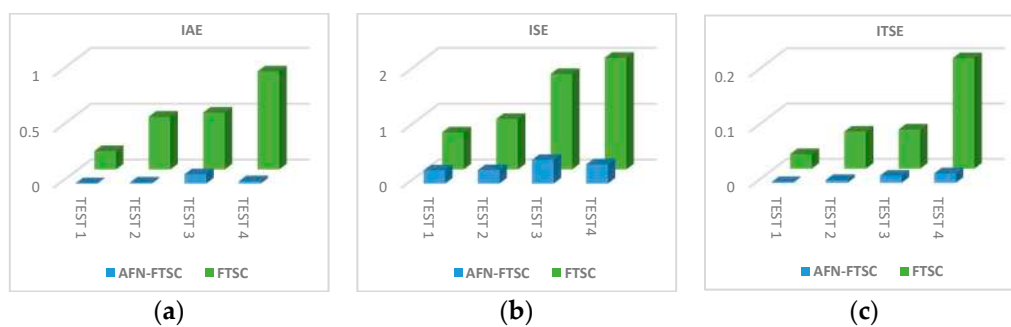


**Figure 16.** Integral-error-performance indices: (a) IAE, (b) ISE, and (c) ITSE.

## 6. Conclusions

In this study, a robust regulator is developed by combining the synergetic theory of control (STC) with a terminal attractor method to track the desired output voltage across the load connected to a buck DC/DC converter. The time-varying dynamic reaching law is employed to ensure the finite-time convergence of the tracking voltage errors and the FNN model guarantees the estimation of the unknown converter nonlinear dynamics. Experimental results are analyzed under various conditions including qualitative and quantitative ways. Comparisons were made with an existing FTSC, and the newly designed AFN-FTSC performs better in all conditions. Based on the analyses presented in this study, the key findings can be summarized as:

- The designed AFN-FTSC properly tracks the reference value of the output voltage with the minimum overshoot and faster settling time—even variations in the input voltage, load resistance, and reference voltage.
- The steady-state is significantly low under any operating scenario.

The impacts of model perturbations and external disturbances are not incorporated into the mathematical model, although these have been included during the analysis in different platforms. Future work will further improve the AFN-FTSC design process by capturing these impacts within the model.

**Author Contributions:** Conceptualization, B.B. and F.A.; Data curation, B.B., N.H. and O.A.; Formal analysis, N.H., O.A. and S.A.M.A.; Funding acquisition, F.A. and S.S.M.G.; Investigation, S.S.M.G.; Methodology, B.B., N.H., O.A. and S.A.M.A.; Project administration, B.B., F.A. and S.S.M.G.; Resources, B.B., F.A. and S.S.M.G.; Software, B.B., N.H. and O.A.; Supervision, B.B. and S.S.M.G.; Validation, N.H., O.A. and S.A.M.A.; Visualization, F.A. and S.A.M.A.; Writing—original draft, B.B., N.H. and O.A.; Writing—review & editing, F.A., S.S.M.G. and S.A.M.A. All authors have read and agreed to the published version of the manuscript.

**Funding:** This work funded by Taif University Researchers Supporting Project TURSP-2020/97, Taif University, Taif, Saudi Arabia.

**Acknowledgments:** The authors thank Taif University Researchers Supporting Project TURSP-2020/97, through Taif University, Taif, Saudi Arabia for supporting this work.

**Conflicts of Interest:** The authors declare no conflict of interest.

## References

1. Babes, B.; Boutaghane, A.; Hamouda, N.; Mezaache, M. Design of a robust voltage controller for a dc-dc buck converter using fractional-order terminal sliding mode control strategy. In Proceedings of the International Conference on Advanced Electrical Engineering (ICAEE), Algiers, Algeria, 19–21 November 2019.
2. Amir, M.; Prajapati, A.K.; Refaat, S.S. Dynamic Performance Evaluation of Grid-Connected Hybrid Renewable Energy-Based Power Generation for Stability and Power Quality Enhancement in Smart Grid. *Front. Energy Res.* **2022**, *10*, 861282. [CrossRef]
3. Yan, Y.; Liu, J. Analysis of passivity-based sliding-mode control strategy in DC/DC converter. In Proceedings of the Chinese Control Conference, Harbin, China, 7–11 August 2006; pp. 171–174.
4. Young, D.S.; Hen, T.-W.; Santi, E.; Monti, A. Synergetic control approach for induction motor speed control. In Proceedings of the Annual Conference of IEEE Industrial Electronics Society, Busan, Korea, 2–6 November 2004. IECON 2004.

5. Dehri, K.; Nouri, A.S. A discrete repetitive adaptive sliding mode control for DC-DC buck converter. *Inst. Mech. Eng. Part I J. Syst. Control. Eng.* **2021**, *235*, 1698–1708. [CrossRef]
6. Chen, J.J.; Hwang, Y.S.; Lin, J.Y.; Ku, Y. A dead-beat-controlled fast-transient-response buck converter with active pseudo-current-sensing techniques. *IEEE Trans. Very Large Scale Integr. (VLSI) Syst.* **2019**, *27*, 1751–1759. [CrossRef]
7. Kumar, V.I.; Kapat, S. Mixed-signal hysteretic internal model control of buck converters for ultra-fast envelope tracking. In Proceedings of the IEEE Applied Power Electronics Conference and Exposition (APEC), Long Beach, CA, USA, 20–24 March 2016; pp. 3224–3230.
8. Linares-Flores, J.; Hernandez Mendez, A.; Garcia-Rodriguez, C.; Sira-Ramirez, H. Robust nonlinear adaptive control of a boost converter via algebraic parameter identification. *IEEE Trans. Ind. Electron.* **2014**, *61*, 4105–4114. [CrossRef]
9. Xu, Q.; Yan, Y.; Zhang, C.; Dragicevic, T.; Blaabjerg, F. An offset-free composite model predictive control strategy for DC/DC buck converter feeding constant power loads. *IEEE Trans. Power Electron.* **2020**, *35*, 5331–5342. [CrossRef]
10. Hausberger, T.; Kugi, A.; Eder, A.; Kemmetmüller, W. High-speed nonlinear model predictive control of an interleaved switching DC/DC-converter. *Control. Eng. Pract.* **2020**, *103*, 104576. [CrossRef]
11. Albira, M.E.; Zohdy, M.A. Adaptive model predictive control for DC-DC power converters with parameters uncertainties. *IEEE Access* **2021**, *9*, 135121–135131. [CrossRef]
12. Hamouda, N.; Babes, B.; Boutaghane, A. Design and analysis of robust nonlinear synergetic controller for a PMDC motor driven wire-feeder system (WFS). In *Lecture Notes in Electrical Engineering*; Springer: Singapore, 2020; pp. 373–387.
13. Babes, B.; Boutaghane, A.; Hamouda, N. Design and real-time implementation of an adaptive fast terminal synergetic controller based on dual RBF neural networks for voltage control of DC–DC step-down converter. *Electr. Eng.* **2021**, *104*, 945–957. [CrossRef]
14. Hamouda, N.; Babes, B. A DC/DC Buck converter voltage regulation using an adaptive fuzzy fast terminal synergetic control. In *Lecture Notes in Electrical Engineering*; Springer: Singapore, 2020; pp. 711–721.
15. Hadjer, A.; Ameer, A.; Harmas, N.M. Adaptive non-singular terminal synergetic power system control using PSO. In Proceedings of the 8th International Conference on Modelling, Identification and Control (ICMIC-2016), Algiers, Algeria, 15–17 November 2016.
16. Babes, B.; Boutaghane, A.; Hamouda, N.; Mezaache, M.; Kahla, S. A robust adaptive fuzzy fast terminal synergetic voltage control scheme for DC/DC buck converter. In Proceedings of the International Conference on Advanced Electrical Engineering (ICAEE), Algiers, Algeria, 19–21 November 2019.
17. Wen, S.; Chen, M.Z.Q.; Zeng, Z.; Huang, T.; Li, C. Adaptive neural-fuzzy sliding-mode fault-tolerant control for uncertain nonlinear systems. *IEEE Trans. Syst. Man Cybern. Syst.* **2017**, *47*, 2268–2278. [CrossRef]
18. Chen, Z.; Li, Z.; Chen, C.L.P. Adaptive neural control of uncertain MIMO nonlinear systems with state and input constraints. *IEEE Trans. Neural Netw. Learn. Syst.* **2017**, *28*, 1318–1330. [CrossRef]
19. Santi, E.; Monti, A.; Proddatur, D.; Li, K.; Dougal, R.A. Synergetic control for power electronics applications: A comparison with the sliding mode approach. *J. Circuits Syst. Comput.* **2004**, *13*, 737–760. [CrossRef]
20. Shahgholian, G. Power system stabilizer application for load frequency control in hydro-electric power plant. *Int. J. Theor. Appl. Math.* **2017**, *3*, 148. [CrossRef]
21. Rubaai, A.; Young, P. Hardware/software implementation of fuzzy-neural-network self-learning control methods for brushless DC motor drives. *IEEE Trans. Ind. Appl.* **2016**, *52*, 414–424. [CrossRef]
22. Nettari, Y.; Kurt, S. Design of a new non-singular robust control using synergetic theory for DC-DC buck converter. *Electrica* **2018**, *18*, 292–329. [CrossRef]
23. Zerroug, N.; Harmas, M.N.; Benaggoune, S.; Bouchama, Z.; Zehar, K. DSP-based implementation of fast terminal synergetic control for a DC–DC Buck converter. *J. Frankl. Inst.* **2018**, *355*, 2329–2343. [CrossRef]
24. Ullah, N.; Shaoping, W. High performance direct torque control of electrical aerodynamics load simulator using adaptive fuzzy backstepping control. *Proc. Inst. Mech. Eng. Part G J. Aerosp. Eng.* **2015**, *229*, 369–383. [CrossRef]
25. Sastry, S.; Bodson, M. *Adaptive Control: Stability, Convergence, and Robustness*; Englewood Cliffs, N.J., Ed.; Prentice-Hall: Hoboken, NJ, USA, 1989.
26. Babes, B.; Mekhilef, S.; Boutaghane, A.; Rahmani, L. Fuzzy Approximation-Based Fractional-Order Nonsingular Terminal Sliding Mode Controller for DC–DC Buck Converters. *IEEE Trans. Power Electron.* **2022**, *37*, 2749–2760. [CrossRef]
27. Alanqar, A.; Durand, H.; Albalawi, F.; Cristofides, P.D. An economic model predictive control approach to integrated production management and process operation. *AIChE J.* **2017**, *63*, 1892–1906. [CrossRef]

MDPI  
St. Alban-Anlage 66  
4052 Basel  
Switzerland  
[www.mdpi.com](http://www.mdpi.com)

*Sustainability* Editorial Office  
E-mail: [sustainability@mdpi.com](mailto:sustainability@mdpi.com)  
[www.mdpi.com/journal/sustainability](http://www.mdpi.com/journal/sustainability)



Disclaimer/Publisher's Note: The statements, opinions and data contained in all publications are solely those of the individual author(s) and contributor(s) and not of MDPI and/or the editor(s). MDPI and/or the editor(s) disclaim responsibility for any injury to people or property resulting from any ideas, methods, instructions or products referred to in the content.



Academic Open  
Access Publishing

[mdpi.com](http://mdpi.com)

ISBN 978-3-7258-0088-9